Hadron-pair production on transversely polarized targets in semi-inclusive deep inelastic scattering

Der Naturwissenschaftlichen Fakultät

der Friedrich-Alexander-Universität
Erlangen-Nürnberg
zur
Erlangung des Doktorgrades Dr. rer. nat.
vorgelegt von
Christopher Braun
aus Erlangen

Als Dissertation genehmigt
von der Naturwissenschaftlichen Fakultät
der Friedrich-Alexander-Universität Erlangen-Nürnberg
Tag der mündlichen Prüfung: 29.07.2014

Vorsitzender des Promotionsorgans:	Prof. Dr. Johannes Barth
Gutachter:	Prof. Dr. Wolfgang Eyrich
	Prof. Dr. Klaus Rith

Abstract

Nucleons such as protons and neutrons are composite objects made of quarks, which are bound together by the strong force via the exchange of gluons. The probability of finding a quark of flavor q carrying the momentum fraction x of the fast moving parent nucleon is described by a parton distribution function (PDF) $f_1^q(x)$, the number density. The spin, an intrinsic angular momentum of elementary particles such as quarks but also of composite objects like nucleons, couples with magnetic fields, which allows one to align it. Taking into account this additional parameter, the spin, the scheme of PDFs in leading twist is expanded by the helicity distribution $g_1^q(x)$ and the transversity distribution $h_1^q(x)$. The first distribution covers the case where the nucleon and the quark are longitudinally polarized, while a transverse polarization is taken into account by the latter.
A tool for the investigation of the PDFs is inclusive deep inelastic scattering (DIS) of electromagnetic probes off (un)polarized nucleons at fixed-target experiments. This only gives access to $f_1^q(x)$ and $g_1^q(x)$, while the chiral-odd nature of the transversity distribution prevents a measurement without detecting the final hadronic states. However, $h_1^q(x)$ can be observed in semi-inclusive DIS (SIDIS) in combination with another chiral-odd function like the dihadron fragmentation function $H_1^{\sphericalangle q}$ in the production of a hadron-pair. The resulting experimental challenge is the reason why $f_1^q(x)$ and $g_1^q(x)$ have been investigated for almost four decades, while $h_1^q(x)$ is still subject to recent measurements and analyses.
The $160\,\mathrm{GeV}/c$ polarized muon beam of CERN's M2 beamline allows the COMPASS experiment to investigate spin effects using polarized solid-state targets. Since the year 2002 COMPASS has collected unique data sets on transversely polarized targets of lithium deuteride and ammonia, serving as deuteron and proton targets, respectively. The work of this thesis started with the analysis of asymmetries of h^+h^- hadron-pairs from the 2010 high statistic data. The subsequent implementation of particle identification using the data from the RICH detector allowed discrimination between pure pion and kaon pairs, as well as mixed pairs. The results obtained motivated for an extension of this identification analysis to the previous deuteron 2003-2004 and proton 2007 data sets using the same methods and requirements as for the 2010 data. Hence, the full set of identified hadron-pair asymmetries from the COMPASS data on the deuteron and the proton target are presented in this work. The results are compared to model predictions and results from the HERMES collaboration. Finally an extraction of the transversity distribution function $h_1(x)$ for u and d valence quarks was carried out with these new results.
In its second phase the COMPASS experiment will test a fundamental QCD relation linking SIDIS and Drell-Yan processes. An advanced type of scintillation fiber detector is crucial to the success of this measurement. The R&D efforts and the construction of this high rate capable detector requiring new approaches to the topic, are also described as part of this work.

Zusammenfassung

Nukleonen sind aus Quarks zusammengesetzte Objekte, welche durch die starke Wechselwirkung mittels Gluonenaustausch aneinander gebunden sind. Die Wahrscheinlichkeit, dass ein Quark der Art q den Impulsanteil x des Nukleons trägt, wird durch die Partonenverteilungsfunktion $f_1^q(x)$ beschrieben. Der Spin, eine intrinsische Eigenschaft von Elementarteilchen wie etwa Quarks lässt sich mittels magnetischer Felder ausrichten. Der Spin tritt jedoch auch bei zusammengesetzten Objekten wie den Nukleonen auf. Diese Eigenschaft erlaubt es, zwei weitere Partonenverteilungsfunktionen in führender Ordnung einzuführen, die Helizitätsverteilungsfunktion $g_1^q(x)$ und die transversale Verteilungsfunktion $h_1^q(x)$, auch Transversity genannt. Erstere beschreibt den Fall, dass die Spins des Nukleons und des Quarks longitudinal polarisiert sind, die zweite Funktion den Fall transversaler Polarisation beider.
Eine Methode zur Untersuchung der Partonenverteilungsfunktionen ist die inklusive tiefinelastische Streuung (DIS) von elektromagnetischen Proben an (nicht) polarisierten Nukleonen. Diese erlaubt jedoch nur einen Zugang zu $f_1^q(x)$ und $g_1^q(x)$, da die transversale Verteilungsfunktion aufgrund ihrer chiral ungeraden Eigenschaft nicht ohne den Nachweis der hadronischen Endzustände bei Streuexperimenten mit leptonischen Proben gemessen werden kann. In dieser sogenannten semi-inklusiven tiefinelastischen Streuung (SIDIS) benötigt $h_1^q(x)$ daher eine weitere chiral ungerade Funktion, wie zum Beispiel die zwei Hadronen Fragmentationsfunktion $H_1^{\sphericalangle q}$, um beobachtet werden zu können. Die daraus resultierenden experimentellen Anforderungen sind ein Grund dafür, dass $f_1^q(x)$ und $g_1^q(x)$ bereits seit vier Jahrzehnten untersucht werden, $h_1^q(x)$ jedoch weiterhin Bestandteil aktueller Messungen und Analysen ist.
Das COMPASS Experiment am CERN nutzt einen polarisierten Muonenstrahl mit einem Impuls von $160\,\mathrm{GeV}/c$ und ein polarisiertes Target, um diese Spin-Effekte zu untersuchen. Seit dem Jahr 2002 hat COMPASS mehrere Datensätze an transversal polarisierten Targets bestehend aus Lithiumdeuterid und Ammoniak, welche effektiv als Deuteronen- und Protonentarget dienen, aufgenommen. Der erste Schritt dieser Arbeit war die Analyse der mit hoher Statistik gemessenen zwei Hadronen Asymmetrien aller möglichen Kombinationen h^+h^- aus dem Datensatz des Jahres 2010. In einem nächsten Schritt wurde die Identifikation der Hadronenpaare in Pionen-, Kaonen- und gemischte Paare mittels der Daten des RICH-Detektors durchgeführt. Die daraus gewonnenen Resultate motivierten dazu, diese Analyse mit identifizierten Hadronen auch auf die vorhergehenden Datensätze am Deuteronentarget von 2003-2004 und am Protonentarget von 2007 zu erweitern. Dabei wurden einheitliche Methoden und Datenschnitte verwendet. Somit kann der gesamte Satz an zwei Hadronen Asymmetrien des COMPASS Experiments in dieser Arbeit konsistent präsentiert werden.
Diese werden mit den Resultaten von Modellrechnungen und den Ergebnissen der HERMES Kollaboration verglichen. Schließlich wurden die Transversity Funktionen der Up- und Down-Valenzquarks mit Hilfe dieser neuen Ergebnisse extrahiert.
In seiner zweiten Projektphase wird das COMPASS Experiment versuchen, eine fundamentale QCD Beziehung, welche SIDIS- und Drell-Yan Reaktion verbindet, nachzuweisen. Dabei ist ein weiterentwickeltes Faserhodoskop unverzichtbar für das Gelingen der Messung. Die F&E-Arbeiten und die Konstruktion dieses hochratenverträglichen Detektors erfordern neue Ansätze, welche auch Teil dieser Dissertation sind und kurz beschrieben werden.

Contents

1. Introduction **1**

2. Theory and experimental overview **5**
2.1. Deep inelastic scattering 5
2.1.1. Structure functions and the inclusive cross-section 7
2.2. Parton distribution functions 11
2.2.1. The naïve parton model 11
2.2.2. The parton model and its distribution functions 11
2.2.3. The first moments of the PDFs 14
2.3. Semi-inclusive deep inelastic scattering 17
2.3.1. Quarks with transverse momentum 18
2.3.2. The SIDIS cross-section in single hadron production 21
2.3.3. Single hadron asymmetries 23
2.3.4. The hadron-pair asymmetry 26
2.4. Experimental overview 34
2.4.1. The single hadron asymmetries 34
2.4.2. The hadron-pair asymmetry 40

3. The COMPASS experiment **43**
3.1. The polarized beam 44
3.2. The polarized target 45
3.3. Tracking detectors 47
3.3.1. Scintillating-fiber hodoscopes 49
3.3.2. Silicon microstrip detectors 51
3.3.3. Micromegas detectors 51
3.3.4. GEM detectors 52
3.3.5. Drift chambers 53
3.3.6. Straw tube detectors 54
3.3.7. Multi wire proportional chambers 54
3.4. Particle identification 55
3.4.1. Ring-imaging Cherenkov detector (RICH) 55
3.4.2. Calorimeters 57
3.4.3. Muon walls 58
3.5. The trigger system 60

3.6. Data acquisition (DAQ) and track reconstruction . . . 62
3.7. Event reconstruction . . . 64

4. Data analysis **65**
4.1. General information on the transverse data taking . . . 66
4.2. General data quality . . . 68
4.2.1. Detector profile analysis of 2010 data . . . 68
4.2.2. Bad spill analysis . . . 69
4.2.3. Stability of neutral kaon mass . . . 70
4.2.4. Kinematic stability . . . 71
4.3. Event selection . . . 73
4.3.1. General DIS events cuts . . . 73
4.3.2. Primary vertex and muon selection . . . 75
4.3.3. Hadron and hadron-pair selection . . . 76
4.3.4. Particle identification . . . 77
4.3.5. RICH stability check . . . 78
4.3.6. RICH efficiency and purity . . . 79
4.3.7. Cuts for pion and kaon identification . . . 81
4.4. Final statistics of deuteron and proton data . . . 82
4.5. Extraction of the asymmetries . . . 84
4.5.1. Quadrupole ratio method . . . 84
4.5.2. Unbinned maximum likelihood method . . . 86
4.5.3. From raw to final asymmetries . . . 87
4.6. Systematic studies . . . 88
4.6.1. Azimuthal stability . . . 88
4.6.2. False asymmetries . . . 95
4.6.3. Compatibility among periods . . . 96
4.6.4. Comparison of estimators . . . 99
4.6.5. Cross-check of results . . . 100
4.6.6. Systematic effects from the spectrometer acceptance . . . 101
4.6.7. Overall systematic uncertainty . . . 104
4.7. Purity correction . . . 105
4.8. Improvements to previous analyses of deuteron and 2007 proton data . . . 109
4.9. Combination of 2007 and 2010 proton data . . . 111

5. Results **115**
5.1. Results from the deuteron data . . . 115
5.1.1. All hadron-pair asymmetry from the deuteron data . . . 116
5.1.2. Identified hadron-pair asymmetry from the deuteron data . . . 116
5.2. Results from the proton target . . . 118
5.2.1. All hadron-pair asymmetry from the proton data . . . 118
5.2.2. Identified hadron-pair asymmetries from the proton data . . . 121

6. Interpretation of the results and extraction of the transversity PDF 125
6.1. General assumptions on the parton distribution and fragmentation functions . . 125
6.2. Interpretation of the asymmetries from single hadron production 127
6.2.1. Transversity and the Sivers PDF from single hadron asymmetries . . . 130
6.2.2. Advanced interpretation of the single hadron asymmetries 133
6.3. Interpretation of the asymmetry from hadron-pair production 134
6.3.1. Description of the observations 135
6.3.2. Comparison with other experimental results 136
6.3.3. Comparison with model predictions 137
6.3.4. Extraction of the Transversity PDF from hadron-pair data 143
6.3.5. Interpretation approaches 152

7. Future prospects 161
7.1. Further prospects on the hadron-pair asymmetry 161
7.2. The Drell-Yan measurement at COMPASS-II 162
7.2.1. The Drell-Yan process 162
7.2.2. Measuring Drell-Yan at COMPASS-II 165
7.2.3. A new absorber vertex detector for the Drell-Yan measurement 169

8. Summary 181

A. Appendix 183
A.1. Theory and experimental overview 184
A.2. The COMPASS experiment 190
A.3. Data analysis 193
A.4. Results 227
A.5. Interpretation of the results and extraction of the transversity PDF 240
A.6. Future prospects 246
A.6.1. A SciFi beam telescope for the Drell-Yan measurement at COMPASS . 251
A.7. Multiplicities 253
A.8. Notations and conventions 255

List of Figures 259

List of Tables 265

Bibliography 267

1. Introduction

The modern investigation of the structure of matter started with the scattering experiments of Rutherford and collaborators in 1911. The discovery of the atom's mass and charge being concentrated in a small nucleus has been a trigger for further investigations, which revealed that the nucleus is also an object composed by protons and neutrons, the nucleons. Even these are not elementary particles, having a substructure, as has been discovered in 1957 by Hofstaedter and collaborators [Hof56] at the Stanford Linear Accelerator Center (SLAC), using elastic scattering of electrons off nucleons.

The key to the nucleon's inner dynamics is the detection of the scattered lepton, which undergoes changes in its energy and direction of motion after having interacted with the nucleon's constituents via the exchange of a virtual photon. This method, deep inelastic scattering (DIS), became a common tool for the investigation of the structure of the nucleon. The very first DIS experiment, performed at SLAC, revealed the point-like nature of the constituents of the nucleon [B$^+$69], using a hydrogen target. In parallel, theoretical efforts and progresses had been made by Gell-Mann [GM64], Zweig [Zwe64] in 1964 and Feynman [Fey69] in 1969. Feynman called the constituents partons, being almost massless compared to the nucleon, while Gell-Mann and Zweig proposed three so-called *quarks* carrying one-third of the nucleon's mass each. Most important is that in both models the particles are described as fermions, which have a spin of $\frac{1}{2}\hbar$. The parton and the quark pictures were unified by Gross and Wilczek [GW73] and Politzer [Pol73] in 1973. They described the quarks as a sub-group of the partons, where the other sub-group consists of the so-called *gluons*. The latter are the exchange particles or gauge bosons for an attractive force between the quarks, the so-called strong force, and were experimentally confirmed in 1979 [BGGo79]. This basic concept of quantum chromodynamics (QCD) also describes the decay of the gluons into quark-antiquark pairs, which subsequently annihilate back into gluons. The quarks generated in such loops are referred to as *sea* quarks, while the the three constituent quarks are the so-called *valence* quarks. Protons and neutrons were found to consist of two different types of valence quarks, known as flavors, up (u) and down (d). Thus their electric charge has to be quantized in thirds of e. Four more flavors have been discovered subsequently. In order to describe the intrinsic dynamics of a nucleon, the number density $f_1^q(x)$ is defined as the probability of finding a quark of the flavor q with momentum fraction x of the momentum of the parent nucleon. Another long-known property of the nucleons, the spin, an intrinsic analog to the orbital angular momentum, then came into the focus. If the nucleons are composite objects, their total spin must arise from the sum of the orbital angular momenta and the spins of its constituents. Describing the difference in probabilities of finding a quark with spin parallel or anti-parallel w.r.t. the one of the nucleons,

which is longitudinally polarized w.r.t. its momentum, the helicity distribution function $g_1^q(x)$ was the next object to be studied.

The simple assumption that the spin of valence quarks sums up to the known nucleon spin of $\frac{1}{2}\hbar$ has been proven wrong by the results of the EMC experiment at CERN in 1988. They found a value of $0.120 \pm 0.094 \pm 0.138$ [EMC89] for the sum of the spin contributions of quarks and antiquarks to the total nucleon spin. Known as the *spin crisis*, this result served as a trigger for increased experimental and theoretical efforts in the understanding of the composition of the nucleon spin. Subsequent experiments, like SMC at CERN, E143 and E155 at Fermilab, and HERMES at HERA found this value to be $\lesssim 30\,\%$ [E15500]. In the scattering of a lepton off a longitudinally polarized target, the nucleon spin can be expressed as $\frac{1}{2}\hbar = \left(\frac{1}{2}\Delta\Sigma + \Delta G + L_q + L_g\right)\hbar$, according to Jaffe and Manohar [JM90],where $\Delta\Sigma$ is the sum of the spin contributions of quarks and antiquarks. The contribution resulting from the spin of the gluons is ΔG, while L_q and L_g are the orbital angular momenta of the quarks and gluons, respectively. Some terms occurring in this expression have been measured, like ΔG, which was found to be small and compatible with zero within the uncertainties [COMPASS09b]; others, like the angular momentum terms are still experimentally challenging.

A third function, the so-called transversity distribution $h_1^q(x)$ [RS79], completes the set of distribution functions needed for a description of the structure of the nucleon in leading twist. Here the nucleon is transversely polarized w.r.t. its momentum and the quark polarization is again parallel or anti-parallel to the one of the nucleon. A simple rotational invariance between $g_1^q(x)$ and $h_1^q(x)$ is not given, since the relativistic nature of the partons together with their nonzero masses prohibit this. From the experimental point of view the chiral-odd property of the transversity distribution makes it difficult to access because an additional chiral-odd function has to be combined with it. The fragmentation functions (FF), which describe the hadronization of the struck quark when leaving the parental nucleon, are ideal chiral-odd partners to $h_1^q(x)$. But the measurement has to be expanded to the detection of at least one hadron in the outgoing channel, that is what the term semi-inclusive DIS (SIDIS) describes. The Collins FF $H_1^{\perp q}$ [Col93] and the dihadron FF (DiFF) $H_1^{\sphericalangle q}$ contain information on the process of one or a pair of hadrons being produced in the fragmentation of a transversely polarized quark.

The polarization state of the quark does not necessarily have to be (anti)parallel to that of the nucleon, for instance unpolarized quarks in transversely polarized nucleons, described by the Sivers function [Siv90a], couple to the unpolarized FF D_1^q. The underlying effect is an intrinsic transverse momentum of the quark inside the nucleon, which started to be investigated after the observation of large asymmetries in the production of pions from proton-proton scattering [AAB$^+$91].

All three cases (Collins, Sivers and hadron-pair) lead to a modulation in the azimuthal distribution of the hadrons or hadron-pairs produced. The latter, the so-called hadron-pair asymmetry is a relatively new object in the theoretical and experimental investigations. The extraction of the transversity distribution is simplified in the hadron-pair case since it appears in the expression of the asymmetry as a product with the DiFF and not as a convolution with a FF like in the single hadron case.

Meanwhile, the effects discussed above have been measured by various collaborations such as BELLE at KEK, HERMES at DESY, and COMPASS at CERN. The latter two are fixed-target experiments, where leptonic probes ($e^{\pm}$ or muons) were/are scattered off transversely polarized proton targets, or in the case of COMPASS off an additional deuteron target. The first observation of the pion pair asymmetry from a transversely polarized proton target was made by the HERMES collaboration in 2008 [HERMES08]. COMPASS followed in 2012 [COMPASS12c] with proton and deuteron results of h^+h^- from the 2007 and 2002-2004 data, respectively. The polarized DiFF was measured by the BELLE collaboration in e^+e^- collisions [BELLE11].

This thesis is organized as follows. In Chapter 2 an introduction to the theoretical framework is given, where the main focus is on the transversity distribution which enters together with the DiFFs into the measured hadron-pair asymmetry. In the production of a single hadron the transversity distribution appears together with the Collins FF, the description of which, together with that of the Sivers function, allows for a more complete picture of the field. The COMPASS apparatus is introduced in Chapter 3 as an appropriate tool for the investigation of these processes, including a short description of its various detector types. In Chapter 4, the complete analysis chain, starting from basic detector stability studies, through the investigation of the data quality in terms of physical stabilities to the applied selection cuts on the data and the particle identification, is specified. Furthermore, the methods used to extract the asymmetry are discussed. The results on the hadron-pair asymmetry of unidentified and identified pairs obtained from the data taking periods on the transversely polarized proton, but also on the deuteron target, are presented in Chapter 5. The interpretation of the results is given in Chapter 6, not only in the case of the hadron-pair, but also briefly for the single hadron asymmetries. In particular, the measured signal of the Collins asymmetry shows similarities w.r.t. the hadron-pair signal, which is examined more closely. The comparison to corresponding results from the HERMES collaboration is supplemented by a comparison with results from model calculations. Finally, a point-by-point extraction of the transversity distribution of u and d valence quarks is performed using the complete set of pion pair asymmetries.

The hardware-related part of this thesis is covered by Chapter 7 and Section 7.2.3. An advanced type of scintillating fiber detector will play a crucial role in the investigation of perturbative QCD predicted effects at the measurement of the polarized Drell-Yan process at COMPASS-II, which are related to the Sivers function for instance.

2. Theory and experimental overview

The aim of this chapter is a moderately detailed introduction into the underlying theory of mechanisms of the physical processes analyzed in this work. The argumentation will follow the works of [AEL95, BDR02, BR04] while summarizing and giving links to the experimental field. The basic concept of studies on the structure of the nucleon, the process of deep inelastic scattering (DIS), is introduced. It already offers a broad range of possibilities like measuring density distributions. Still many distribution functions, like the transversity PDF, remain inaccessible as long as one does not measure at least some of the produced particles in the scattering process, like in semi-inclusive deep inelastic scattering (SIDIS). The transversity PDF, often just called *Transversity* is related to a nonzero transverse momentum of the quarks, which enters the full SIDIS cross-section in various terms. A brief overview of all will be given. In this context the difference between the single hadron and the hadron-pair production process, as well as the advantages which are offered by the latter are disclosed. Possible experimental accesses are introduced, were the transversity parton distribution function appears together with a fragmentation function (FF). Finally an overview of the experimental results is given, with a brief discussion on the single hadron asymmetry results and a special focus on the hadron-pair results.

2.1. Deep inelastic scattering

A common tool for the investigation of the nucleon structure is the scattering of a lepton ℓ with the four-momentum l, and a certain orientation of its spin $\boldsymbol{s}$, off a nucleon N with a certain four-momentum P and vector of its spin orientation $\boldsymbol{S}$. Please note that three-momenta are quoted in bold math-italic letters, while four-momenta are written in simple math-italic; for instance $\boldsymbol{k}$ and k, respectively. The process is called "deep inelastic" if the negative squared momentum transfer Q^2 is larger than $1\,(\mathrm{GeV}/c)^2$. The reaction can be expressed as

$$\ell(l, \boldsymbol{s}) + N(P, \boldsymbol{S}) \rightarrow \ell'(l', \boldsymbol{s}') + X, \tag{2.1}$$

where ℓ' is the scattered lepton with its four-momentum l' and its spin orientation $\boldsymbol{s}'$. The undetected final hadronic state is denoted as X. The process is induced through the exchange of a boson, here the assumption of a pure, one-photon exchange holds true since the center of mass energy achievable at the COMPASS experiment is at about $18\,\mathrm{GeV}$.

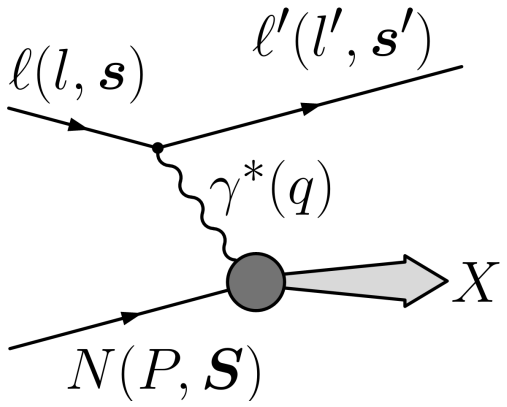

Figure 2.1.: Simplified scheme of the DIS process: The incoming lepton ℓ emits a virtual photon γ^*, denoted as ℓ' after the process. The virtual photon is scattered off a nucleon N, but the final state X remains undetected.

In general the exchange particle, therefore denoted as "virtual", can be a γ, $W^{\pm}$ or Z^0 boson. A simple scheme of a DIS process is shown in Fig. 2.1, where q is the four-momentum transfer by the virtual photon γ^*. For a detailed description and discussion of the DIS process at fixed target experiments, the definition of a set of characteristic quantities is useful. It is convenient to define them in the laboratory frame, where $\boldsymbol{P}$ is zero (see Tab. 2.1). The Bjorken scaling variable will be denoted as x in the following. For notations and conventions see Sec. A.8.

Table 2.1.: Kinematic variables for the description of the DIS process

mass of target nucleon	M
mass of incoming lepton	m
total energy of incoming and scattered lepton	E, E'
four-momentum of the target nucleon	$P \overset{\text{lab}}{=} (Mc, \boldsymbol{P} = 0)$
four-momentum of the incoming and outgoing lepton	$l = (\frac{E}{c}, \boldsymbol{l})$, $l' = (\frac{E'}{c}, \boldsymbol{l'})$
four-momentum of the virtual photon	$q = l - l'$
lepton scattering angle	ϑ
negative squared four-momentum transfer	$Q^2 = -q^2 = \frac{4}{c^2} EE' \sin^2 \frac{\vartheta}{2}$
energy transfer in the lab. system from the lepton to the nucleon	$\nu = \frac{P \cdot q}{M} \overset{\text{lab}}{=} E - E'$
fractional energy of the virtual photon	$y = \frac{P \cdot q}{P \cdot l} \overset{\text{lab}}{=} \frac{\nu}{E}$
Bjorken scaling variable	$x_{bj} = \frac{Q^2}{2P \cdot q} = \frac{Q^2}{2M\nu}$
squared invariant center of mass energy	$s = (P + l)^2 c^2$
squared invariant mass of the γ^*-nucleon system	$W^2 = (P + q)^2 c^{-2}$
	$= M^2 + \frac{2}{c^2} M\nu - \frac{1}{c^2} Q^2$

2.1.1. Structure functions and the inclusive cross-section

An ansatz by a general tensor structure is a reasonable starting point in order to determine the DIS cross-section in a theoretical way. Therefore the information on the states of the lepton before and after a scattering process is represented by the leptonic tensor $L_{\mu\nu}$, while the hadronic tensor $W^{\mu\nu}$ contains the information on the process related to the nucleon. Then the general inclusive cross-section of a DIS process can be written as [BR03b]

$$\frac{\mathrm{d}^3\sigma}{\mathrm{d}x\,\mathrm{d}y\,\mathrm{d}\phi} = \frac{\alpha^2\hbar^2 y}{2Q^2} L_{\mu\nu} W^{\mu\nu}, \tag{2.2}$$

where $\alpha = \frac{e^2}{4\pi}$ is the fine structure constant and ϕ is the azimuthal angle between the scattering plane and the target nucleon spin $\boldsymbol{S}$. The vectors of the incoming $\boldsymbol{l}$ and the scattered $\boldsymbol{l'}$ lepton span the scattering plane, as shown in Fig. 2.2.
Quantum Electro Dynamics (QED) allows for the complete calculation of the leptonic tensor, as it contains the information on the emission of the virtual photon by the incoming lepton under conservation equations. Thereby, a summation over all possible spin states $\boldsymbol{s'}$ of the outgoing lepton is performed. This spin-dependent anti-symmetric part (A) factorizes from the spin-independent symmetric part (S) under μ, ν interchange [AEL95]

$$L_{\mu\nu}(l, \boldsymbol{s}; l') = L^{(S)}_{\mu\nu}(l, l') + \imath L^{(A)}_{\mu\nu}(l, \boldsymbol{s}, l'). \tag{2.3}$$

The emitted photon then interacts with the nucleon. However, the complex structure of the nucleon arising from non-perturbative effects of the strong interaction precludes a full calculation using QCD. Nevertheless, an ansatz by symmetries and conservation equations allows for a parametrization by two spin-dependent and two spin-independent structure functions, F_1 & F_2 and g_1 & g_2, depending on x and Q^2 [Jaf96, Man92]. A further factorization in a symmetric and an antisymmetric part leads to [AEL95]

$$W^{\mu\nu} = W^{\mu\nu(S)}(P, q) + W^{\mu\nu(A)}(P, \boldsymbol{S}, q). \tag{2.4}$$

In general, the contraction of an antisymmetric and a symmetric tensor cancels out, thus the mixed terms of Eq. 2.2, which arise if Eq. 2.3 and 2.4 are inserted, cancel. Only two terms remain, one which does not depend on any spin contribution, neither the spin of the lepton nor the hadron spin, and a term containing both of them [AEL95]

$$\frac{\mathrm{d}^3\sigma}{\mathrm{d}x\,\mathrm{d}y\,\mathrm{d}\phi} = \frac{\alpha^2\hbar^2 y}{2Q^4} \Big[L^{(S)}_{\mu\nu}(l, l') W^{\mu\nu(S)}(P, q) - L^{(A)}_{\mu\nu}(l, \boldsymbol{s}, l') W^{\mu\nu(A)}(P, \boldsymbol{S}, q) \Big]. \tag{2.5}$$

Applied to the inclusive DIS process this requires a polarized beam as well as a polarized target in order to measure the complete set of spin related properties of the nucleon.
From the experimental point of view a decomposition to the level of the target spin being parallel to the incoming lepton spin $\mathrm{d}^3\sigma_{\parallel}$, being perpendicular $\mathrm{d}^3\sigma_{\perp}$ and without a certain polarization $\mathrm{d}^3\bar{\sigma}$ is useful [AEL95]

$$\frac{\mathrm{d}^3\sigma}{\mathrm{d}x\,\mathrm{d}y\,\mathrm{d}\phi} = \frac{\mathrm{d}^3\bar{\sigma}}{\mathrm{d}x\,\mathrm{d}y\,\mathrm{d}\phi} - \lambda_\ell \cos\beta \frac{\mathrm{d}^3\sigma_{\parallel}}{\mathrm{d}x\,\mathrm{d}y\,\mathrm{d}\phi} - \lambda_\ell \sin\beta\cos\phi \frac{\mathrm{d}^3\sigma_{\perp}}{\mathrm{d}x\,\mathrm{d}y\,\mathrm{d}\phi}, \tag{2.6}$$

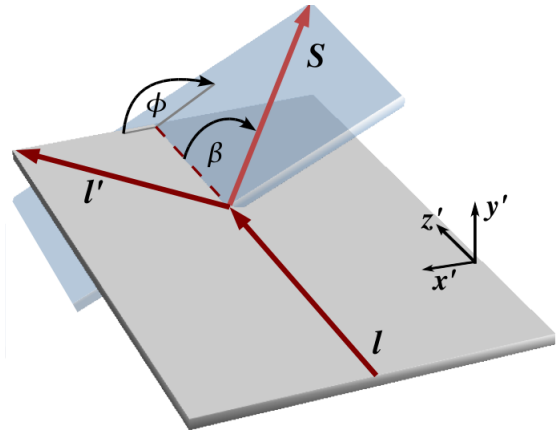

Figure 2.2.: Definition of the azimuthal angle ϕ measured around the direction of incoming lepton ℓ, and definition of the angle β between $\boldsymbol{l}$ and $\boldsymbol{S}$ [Wol10].

where β is the angle between $\boldsymbol{l}$ and $\boldsymbol{S}$, shown in Fig. 2.2. Further $\lambda_\ell = \pm 1$ is the helicity of ℓ, defined as $\lambda = \frac{\boldsymbol{s}\cdot\boldsymbol{l}}{|\boldsymbol{s}|\cdot|\boldsymbol{l}|}$; the projection of the spin onto the direction of the momentum [PRSZ06]. Thus the parallel part vanishes for a transversely polarized target due to the $\cos\beta$ dependence, and vice versa. The full expressions of the three parts read [AEL95]

$$\frac{\mathrm{d}^3\bar{\sigma}}{\mathrm{d}x\,\mathrm{d}y\,\mathrm{d}\phi} = \frac{4\alpha^2\hbar^2}{Q^2}\left[\frac{y}{2}F_1(x,Q^2) + \frac{1}{2xy}\left(1-y-\frac{y^2\gamma^2}{4}\right)F_2(x,Q^2)\right], \tag{2.7a}$$

$$\frac{\mathrm{d}^3\sigma_{\parallel}}{\mathrm{d}x\,\mathrm{d}y\,\mathrm{d}\phi} = \frac{4\alpha^2\hbar^2}{Q^2}\left[\left(1-y-\frac{y^2\gamma^2}{4}\right)g_1(x,Q^2) - \frac{y}{2}\gamma^2 g_2(x,Q^2)\right], \tag{2.7b}$$

$$\frac{\mathrm{d}^3\sigma_{\perp}}{\mathrm{d}x\,\mathrm{d}y\,\mathrm{d}\phi} = \frac{4\alpha^2\hbar^2}{Q^2}\left[\gamma\sqrt{1-y-\frac{y^2\gamma^2}{4}}\left(\frac{y}{2}g_1(x,Q^2) + g_2(x,Q^2)\right)\right], \tag{2.7c}$$

where $\gamma = \frac{2xM}{Q}$ is decreasing to zero for $Q^2 \to \infty$.
The unpolarized cross-section (Eq. 2.7a), depending on F_1 and F_2, was the first term to be studied experimentally due to the earlier availability of unpolarized targets. Furthermore the spin dependent parts in Eqs. 2.7b and 2.7c, g_1 and g_2 suffer from suppression with different powers of γ. For a longitudinal polarized target g_2 is strongly suppressed by γ^2, hence the cross-section is mostly sensitive to g_1. Further the whole term for a transversely polarized target is suppressed by a factor γ with equal strength of g_1 and g_2.
An experimental verification of the Bjorken limit [Bjo69], meaning the dependencies of $F_1(x,Q^2)$ and $F_2(x,Q^2)$ on x and on Q^2 in the limit of

$$\nu, Q^2 \to \infty \tag{2.8}$$

in $x = \frac{Q^2}{2M\nu}$ was performed with the high accuracy data for proton and deuteron targets [PDG12]. Figure 2.3 shows the results for F_2 as a function of Q^2 for different bins in x measured by different experiments covering a wide range of x and Q^2.

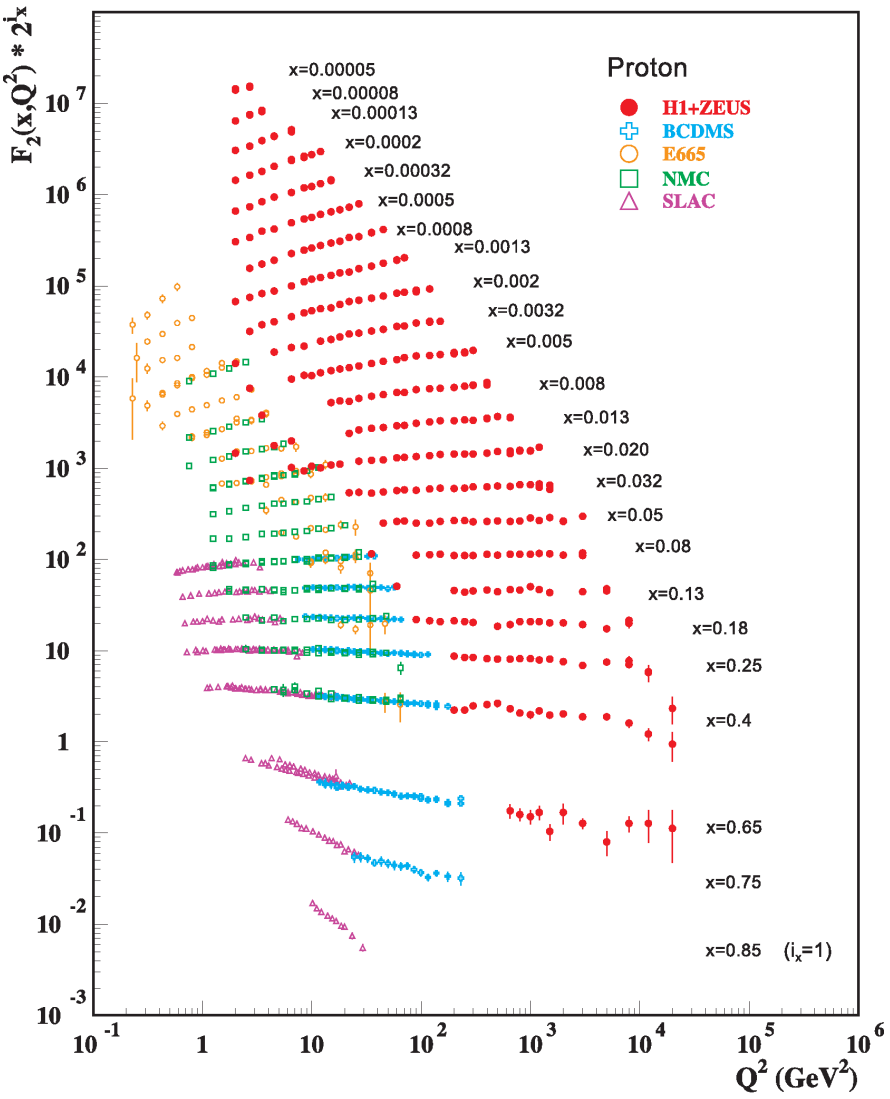

Figure 2.3.: The proton structure function F_2^p measured in electromagnetic scattering of electrons and positrons off protons (collider experiments H1 and ZEUS for $Q^2 \geq 2\,(\mathrm{GeV}/c)^2$), in the kinematic domain of the HERA data, and for electrons (SLAC) and muons (BCDMS, E665, NMC) on a fixed target. Statistical and systematic uncertainties added in quadrature are shown. The data are plotted as a function of Q^2 in bins of fixed x. Some points have been slightly offset in Q^2 for clarity. The H1 and ZEUS combined binning in x is used in this plot; all other data are rebinned to the x values of the data. For the purpose of plotting, F_2^p has been multiplied by 2^{i_x}, where i_x is the number of the x bin, ranging from $i_x = 1$ ($x = 0.85$) to $i_x = 24$ ($x = 5 \times 10^{-5}$) [PDG12].

Here the Bjorken scaling variable x is a quantity of the elasticity of the process, hence an inelastic scattering process is characterized by $0 < x < 1$, while x is equal to one in the elastic case.
An additional relation which could be proven with this data is the Callan-Gross relation [CG69]

$$2xF_1(x) = F_2(x), \tag{2.9}$$

which needs further knowledge of the nucleons structure to be interpreted, see Sec. 2.2.
The experimental access to the structure functions g_1 and g_2 is possible by the construction of spin-spin asymmetries, where the differential cross-sections from different spin orientations are combined such that [AEL95]

$$A_{\parallel} = \frac{\mathrm{d}\sigma^{\rightarrow\Rightarrow} - \mathrm{d}\sigma^{\rightarrow\Leftarrow}}{\mathrm{d}\sigma^{\rightarrow\Rightarrow} + \mathrm{d}\sigma^{\rightarrow\Leftarrow}}, \tag{2.10a}$$

$$A_{\perp} = \frac{\mathrm{d}\sigma^{\rightarrow\Uparrow} - \mathrm{d}\sigma^{\rightarrow\Downarrow}}{\mathrm{d}\sigma^{\rightarrow\Uparrow} + \mathrm{d}\sigma^{\rightarrow\Downarrow}}. \tag{2.10b}$$

The orientation of the lepton spin is indicated by a simple arrow, for instance $\rightarrow$ in the case of spin along its direction of motion, and a double arrow represents the nucleons spin, for instance $\Uparrow$ means an upwards orientation perpendicular to the beam direction. Due to the appearance of g_1 and g_2 being in linear combinations only (cf. Eqs. 2.7b, 2.7c) this does not allow for a direct measurement of only one of them. However the strong kinematical suppression by γ^2 of g_2 w.r.t. g_1 in Eq. 2.7b gives an approximate access to g_1, which then can be used to deduce g_2 from Eq. 2.7c.

2.2. Parton distribution functions

The parton distribution functions (PDFs) are quantities describing the probability of finding a parton of a certain flavor q inside the nucleon, which carries a fraction x of the total momentum of the (fast moving) nucleon. The different polarization states of the nucleon and the parton give rise to a variety of corresponding PDFs.

2.2.1. The naïve parton model

The Callan-Gross relation in Eq. 2.9 and the constancy of F_1 and F_2 over a wide Q^2 range (see Fig. 2.3), the so-called scaling behavior, gave rise to a new model of the structure of the nucleon. There the nucleon is considered to be composed of point-like particles named partons, having a spin of $\pm\frac{1}{2}\hbar$. Thus the virtual photon does not scatter off the nucleon as a whole, but off individual partons, in the case of sufficiently high momentum transfer $Q^2 \gtrsim 1\,(\mathrm{GeV}/c)^2$. A common frame to describe the reaction is the so-called "infinite momentum" frame, where the nucleon moves with high momentum while assuming the partons to be massless and neglecting their motion transverse to the nucleon's motion. In this case the Bjorken scaling variable x gets a descriptive meaning, as the momentum fraction of the nucleon carried by the struck quark. This approximation gives rise to a new way of describing the kinematics inside the nucleon by a parton distribution function, $f_1^q(x)$, giving the probability of finding a parton q carrying a momentum fraction of the parenting nucleon in an interval $[x, x + \mathrm{d}x]$. This distribution function, also called number density, describes the unpolarized state where neither the nucleon nor the parton have a defined spin orientation. If the nucleons are polarized for instance parallel to a certain direction, such as in the case of a longitudinally polarized target, the PDF $g_1^q(x) = q^+(x) - q^-(x)$ gives the difference in the probabilities of finding a parton $q(x)$ with spin parallel $+$ or anti-parallel $-$ to the spin of the parent nucleon.

2.2.2. The parton model and its distribution functions

In the naïve parton model only one type of constituent to the nucleon is assumed, the partons. Further measurements accompanied by further theoretical efforts reveal the nucleon as a complex structure containing so-called *quarks* bound together by a strong force, which is carried by so-called *gluons*. Thus a nucleon, like the proton or the neutron, consists of three valence quarks of the flavors u or d, gluons and sea quarks; quark-antiquark pairs appear from loops created by gluons. The structure functions $F_1(x)$, $F_2(x)$, and $g_1(x)$ can be written as a sum over all quark

and antiquark flavors q of $f_1^q(x)$ or $g_1^q(x)$ according to [AEL95]

$$F_1(x) = \frac{1}{2}\sum_q e_q^2 f_1^q(x), \tag{2.11a}$$

$$F_2(x) = x\sum_q e_q^2 f_1^q(x), \tag{2.11b}$$

$$g_1(x) = \frac{1}{2}\sum_q e_q^2 g_1^q(x), \tag{2.11c}$$

where e_q is the charge of a parton q in units of the elementary charge e. The structure function $g_2^q(x)$ has no interpretation in the naïve parton model, thus it is expected to be zero [AEL95]. Since the scattering takes place off a single quark inside the nucleon, the DIS scheme (see Fig. 2.1) has to be adapted. A so-called "handbag" diagram, shown in Fig.2.4, describes the process divided into two parts. At first, the incoming lepton ℓ (not shown in Fig. 2.4) scatters off a quark q by the exchange of a virtual photon γ^* with momentum q. The quark with the four-momentum k is then separated from the nucleon, which carries the total momentum P. The interaction of the quark with the photon, the called "hard" process, can be calculated explicitly via QED while the decoupling of the quark from the residual nucleon is not calculable in perturbative QCD. Instead of a direct determination, the corresponding hadronic tensor $W^{\mu\nu}$, an approach via a quark-quark-correlation matrix $\Phi_{ij}(k, P, \boldsymbol{S})$ can be performed [BDR02]. The correlator is a sum over all possible hadronic final-states X with their four-momenta $P_X = (E_X, \boldsymbol{P}_X)$ depending on the momentum of the nucleon P, of the struck quark k, and the spin of the nucleon $\boldsymbol{S}$ [BDR02]

$$\Phi_{ij}(k, P, \boldsymbol{S}) = \sum_X \int \frac{\mathrm{d}^3\boldsymbol{P}_X}{(2\pi)^3 2E_X}\,(2\pi)^4\delta^{(4)}\big(P-k-P_X\big)\,\big\langle P, \boldsymbol{S}\,\big|\,\bar{\psi}_j(0)\,\big|\,X\big\rangle\,\langle X\,|\,\psi_i(0)\,|\,P, \boldsymbol{S}\rangle\,. \tag{2.12}$$

The $\psi_{i,j}$ are the quark fields with the Dirac spinor indices i and j, see Fig. 2.4 and Sec. A.8. Momentum and energy conservation are preserved by the fourfold delta function. The completeness of all possible outgoing states $|X\rangle$ and the demanded translational invariance of the correlator itself allow one to write it as a Fourier transformation [BDR02]

$$\Phi_{ij}(k, P, \boldsymbol{S}) = \int \mathrm{d}^4\xi\,\mathrm{e}^{\imath k\cdot\xi}\,\big\langle P, \boldsymbol{S}\,\big|\,\bar{\psi}_j(0)\psi_i(\xi)\,\big|\,P, \boldsymbol{S}\big\rangle\,, \tag{2.13}$$

where the integration runs over all possible states ξ of the second quark spinor. Accordingly the hadronic tensor is given by an integral over traces of Φ_{ij} summed over all quark flavors q [BDR02]

$$W^{\mu\nu} = \sum_q e_q^2 \int \frac{\mathrm{d}^4k}{(2\pi)^4}\delta\big((k+q)^2\big)\,\mathrm{Tr}\big[\Phi(k, P, \boldsymbol{S})\gamma^\mu(\not{k}+\not{q})\gamma^\nu\big]. \tag{2.14}$$

The slash in e.g. $\not{q}$ is the so-called "Feynman slash", which generates a matrix from the four-vector according to Eq. A.13. As shown in [MR01] the quark-quark correlator also has to fulfill

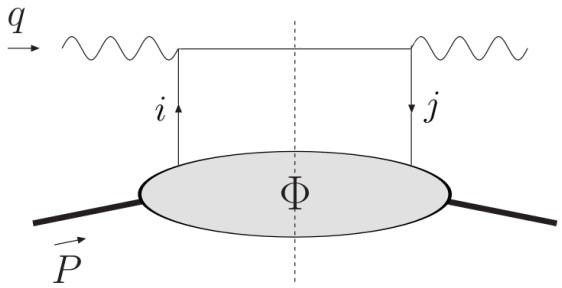

Figure 2.4.: A handbag diagram depicting an inclusive DIS process [BDG+07]. The photon-quark scattering (top part) is often referred to as the hard part of the process, and quark-remnant interactions as the soft part. The latter is described by the quark-quark correlator Φ with the Dirac spinor indices i and j.

hermiticity, parity and time reversal invariance. This allows for a decomposition in a basis of Dirac matrices, see Sec. A.8 [BDR02],

$$\Phi(x) = \frac{1}{2}\big(f_1^q(x)\not{P} + \lambda_N g_1^q(x)\gamma_5\not{P} + h_1^q(x)i\sigma\gamma_5\not{S}_T\big), \tag{2.15}$$

still in the Bjorken limit where x is equal to the Bjorken scaling variable x, see Eq. 2.8. In the infinite momentum frame it is convenient to calculate x in the light cone coordinates, where x is the fraction of the quark light cone momentum k_+ w.r.t. the nucleon light cone momentum P_+. For more details on this Sudakov decomposition of vectors into light cone coordinates see Sec. A.8. Furthermore, λ_N is the helicity and $\boldsymbol{S} \approx \lambda_N \frac{\boldsymbol{P}}{M} + \boldsymbol{S}_T$ the spin of the nucleon. A probabilistic interpretation of the PDFs $f_1^q(x)$ and $g_1^q(x)$ has already been given in the framework of the parton model, see Sec. 2.2.1. In Eq. 2.15 $h_1^q(x)$ enters as a third distribution function. It describes again the difference in the probabilities of finding a quark q with its spin parallel or anti-parallel to the spin of the parent nucleon, but this time the nucleon and the quark are transversely polarized, see diagonal elements of matrix in Tab. 2.4 for a schematic classification of the distribution functions as a function of the quark and nucleon spin polarization. While $f_1^q(x)$ and $g_1^q(x)$ are directly related to the structure functions F_1 and F_2 as in Eqs. 2.11a to 2.11c, g_1 is not related to $h_1^q(x)$ in inclusive DIS. The reason is that it is a chiral-odd object, which would require a helicity flip of the struck quark. But such a flip is forbidden in leading-twist inclusive DIS.
If the correlation matrix is known the three individual PDFs can be accessed by taking traces of products of the quark-quark correlator [BDR02]:

$$f_1(x) = \frac{1}{2}\int \frac{\mathrm{d}^4k}{(2\pi)^4}\delta\big(k^+ - xP^+\big)\,\mathrm{Tr}\big[\gamma^+\,\Phi(x)\big], \tag{2.16a}$$

$$g_1(x) = \frac{1}{2}\int \frac{\mathrm{d}^4k}{(2\pi)^4}\delta\big(k^+ - xP^+\big)\,\mathrm{Tr}\big[\gamma^+\gamma_5\,\Phi(x)\big], \tag{2.16b}$$

$$h_1(x) = \frac{1}{2}\int \frac{\mathrm{d}^4k}{(2\pi)^4}\delta\big(k^+ - xP^+\big)\,\mathrm{Tr}\big[\imath\sigma^{i+}\gamma^5\,\Phi(x)\big]. \tag{2.16c}$$

Here $\gamma^{\pm}$ are Dirac matrices in their light-cone representation, see Sec.A.8. In general the index i in $\imath\sigma^{i+}\gamma^5 = \gamma^+\gamma^i\gamma^5$ can be 1 or 2, which would lead to two expressions. But due to the convention of setting the nucleons helicity λ to 1 and $S_T = (1, 0)$, only one trace $\gamma^+\gamma^1\gamma^5$ remains. According to standard naming conventions [MT96a], the letters f, g, and h indicate the polarizations of the quark inside the nucleon as being unpolarized, longitudinally and transversely polarized. An alternative nomenclature is given by $g_{1L}^q := g_1^q := \Delta q$ and $h_1^q := \delta q := \Delta_T q$ [ABD$^+$09a].

2.2.3. The first moments of the PDFs

The first moments of the parton distribution functions are obtained by integrating them over the whole x range. These integrals are identified as the fundamental vector-, axial-, and tensor-charges denoted with g_V, g_A, and g_T which can be calculated in lattice QCD models, see [Gup97] for a general introduction on lattice QCD. This allows for a comparison of the measured transversity distributions and the results from model calculations [CBT08].
The three PDFs f_1, g_1, and h_1 behave different under charge conjugation $q \to \bar{q}$, namely like vector, axial and tensor objects, respectively [BDR02]

$$f_1^{\bar{q}}(x) = -f_1^q(-x), \tag{2.17a}$$

$$g_1^{\bar{q}}(x) = g_1^q(-x), \tag{2.17b}$$

$$h_1^{\bar{q}}(x) = -h_1^q(-x), \tag{2.17c}$$

which is important in order to describe the complete nucleon by including also the antiquarks. Their contributions are taken into account by a continuation of the quark distributions into the negative x region of the sea. These properties of f_1 and g_1 being chiral-even while h_1 is chiral-odd are the consequence of the applied Dirac structures in Eqs. 2.16a.
Taking into account Eq. 2.17a the first moments of the PDFs can be written as [BDR02]

$$\sum_q \int_{-1}^{1} \mathrm{d}x\; f_1^q(x) = \sum_q \int_0^1 \left(f_1^q(x) - f_1^{\bar{q}}(x)\right) = g_V, \tag{2.18a}$$

$$\sum_q \int_{-1}^{1} \mathrm{d}x\; g_1^q(x) = \sum_q \int_0^1 \left(g_1^q(x) + g_1^{\bar{q}}(x)\right) = g_A, \tag{2.18b}$$

$$\sum_q \int_{-1}^{1} \mathrm{d}x\; h_1^q(x) = \sum_q \int_0^1 \left(h_1^q(x) - h_1^{\bar{q}}(x)\right) = g_T, \tag{2.18c}$$

where anticommutation relations for the quark field have been used. In the vector charge and the tensor charge the distributions of the sea quarks cancel out since g_V and g_T are related to the difference of quark and anti-quark contributions, which give zero for the pairs of the sea. Therefore g_V is fully determined by the number density $f_1^q(x)$ of valence quarks [JJ91]. The tensor charge g_T is a measure for the absolute number of transversely polarized valence quarks inside of a transversity polarized nucleon.

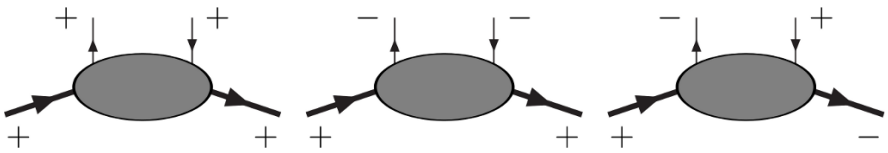

Figure 2.5.: The handbag diagrams of the three possible helicity amplitudes from left to right $\mathcal{A}_{++,++}$, $\mathcal{A}_{+-,+-}$ and $\mathcal{A}_{+-,-+}$ [BDR02].

Quark-nucleon helicity amplitudes

An alternative approach to the hadronic tensor which was introduced in Eq. 2.4 can be performed via the imaginary part of the forward virtual Compton scattering amplitude $T_{\mu\nu}$ [BDR02] through

$$W^{\mu\nu} = \frac{1}{2\pi} \operatorname{Im} T^{\mu\nu} \,. \tag{2.19}$$

The scattering amplitudes are of the general form $\mathcal{A}_{\Lambda\lambda,\Lambda'\lambda'}$, in which Λ and Λ' are the helicities of the incoming and outgoing nucleon. Correspondingly, λ and λ' are the quark helicities before and after the scattering process. The parity invariance is expressed by [BDR02]

$$\mathcal{A}_{\Lambda\lambda,\Lambda'\lambda'} = \mathcal{A}_{-\Lambda'-\lambda',-\Lambda-\lambda} \,, \tag{2.20}$$

where the helicity conservation via $\Lambda + \lambda = \Lambda' + \lambda'$ and the time-reversal invariance $\mathcal{A}_{\Lambda\lambda,\Lambda'\lambda'} = \mathcal{A}_{\Lambda'\lambda',\Lambda\lambda}$ are constraints to the possible 16 scattering amplitudes. Three amplitudes fulfill these two equations [BDR02], they are

$$\mathcal{A}_{++,++},\ \mathcal{A}_{+-,+-},\ \mathcal{A}_{+-,-+} \,. \tag{2.21}$$

In Fig. 2.5 the corresponding handbag diagrams of these three amplitudes are shown. By the application of the optical theorem it can be demonstrated that the transversity PDF is related to the amplitude $\mathcal{A}_{+-,-+}$ which represents the demanded helicity flip of both (see Sec. 2.2.2), the nucleon and the quark. The number density and the helicity PDFs are related to the sum and the difference of the $\mathcal{A}_{++,++}$ and $\mathcal{A}_{+-,+-}$ amplitudes, respectively [BDR02]

$$f_1^q(x) \propto \operatorname{Im}\big(\mathcal{A}_{++,++} + \mathcal{A}_{+-,+-}\big), \tag{2.22a}$$
$$g_1^q(x) \propto \operatorname{Im}\big(\mathcal{A}_{++,++} - \mathcal{A}_{+-,+-}\big), \tag{2.22b}$$
$$h_1^q(x) \propto \operatorname{Im}\big(\mathcal{A}_{+-,-+}\big). \tag{2.22c}$$

In the helicity basis $\mathcal{A}_{+-,-+}$ is off-diagonal and has no probabilistic interpretation. The other two PDFs are diagonal, keeping their interpretation. Transforming $\mathcal{A}_{+-,-+}$ in a transversity basis which is defined by the two vectors [BDR02]

$$|\uparrow\rangle = \frac{1}{\sqrt{2}}\big(|+\rangle + \imath\,|-\rangle\big) \quad \text{and} \quad |\downarrow\rangle = \frac{1}{\sqrt{2}}\big(|+\rangle - \imath\,|-\rangle\big), \tag{2.23}$$

provides a remedy analogous to $g_1^q(x)$. In this new basis the transversity PDF $h_1^q(x)$ is connected to a diagonal amplitude and gets a probabilistic interpretation [BDR02]

$$h_1^q(x) \propto \mathrm{Im}\big(\mathcal{A}_{\uparrow\uparrow,\uparrow\uparrow} - \mathcal{A}_{\uparrow\downarrow,\uparrow\downarrow}\big). \tag{2.24}$$

But the transversity PDF remains not measurable in inclusive DIS since it is a chiral-odd function, see Sec. 2.2.3. An access to $h_1^q(x)$ requires another chiral-odd partner which can be found in semi-inclusive DIS by a chiral-odd fragmentation function. These functions describe the fragmentation of a struck quark into one or two hadrons and will be disused in Sec. 2.3.2.

Mutual relative limits between PDFs

While the quarks and nucleons have a helicity of $\pm\frac{1}{2}$ at leading-twist, the gluon helicity can only have values of ± 1. Thus a flip of a gluons helicity would lead to a total change of ± 2 units, which cannot be compensated by the nucleon and forbids the existence of a gluon transversity $h_1^g(x)$. However, the helicity PDF $g_1(x)$ can contain contributions from the gluons. The number density $f_1^q(x)$ can also be written in the transversity basis, having the same value as in the longitudinal basis [BDR02]

$$f_1^q(x) = f_1^q(x)^+ + f_1^q(x)^- \equiv f_1^q(x)^\uparrow + f_1^q(x)^\downarrow. \tag{2.25}$$

From this constraint bounds on the other two PDFs can be derived [BDR02]

$$|g_1^q(x)| \leq f_1^q(x), \tag{2.26}$$
$$|h_1^q(x)| \leq f_1^q(x). \tag{2.27}$$

An inequality involving all three leading-twist PDFs, called the Soffer bound [Sof95] is given by

$$f_1^q(x) + g_1^q(x) \geq 2|h_1^q(x)|. \tag{2.28}$$

All three inequalities (Eq. 2.26 and 2.28) do not only hold true at leading-twist, since they are preserved by QCD evolution.

2.3. Semi-inclusive deep inelastic scattering

In semi-inclusive DIS, in contrast to inclusive DIS (see Sec. 2.1), at least one of the produced final-state hadrons is detected in addition to the scattered lepton. Thus the reaction equation 2.1 is extended to

$$\ell(l, \boldsymbol{s}) + N(P, \boldsymbol{S}) \to \ell'(l', \boldsymbol{s}') + h(P_h, \boldsymbol{S}_h) + X, \tag{2.29}$$

where P_h is the four-momentum of the outgoing hadron and $\boldsymbol{S}_h$ its spin-vector, usually being unobserved. An important measure is the fractional energy carried by the observed final state hadron, which is defined as

$$z = \frac{P \cdot P_h}{P \cdot p} \overset{\text{lab}}{=} \frac{E_h}{\nu}, \tag{2.30}$$

where ν is the momentum transfer of the virtual photon and E_h the energy of the hadron measured in the laboratory system.
Another possible source of hadrons, besides of the hadronization of the struck quark, is the fragmentation of target remnants. These can be separated by a minimum cut on z.
The fragmentation of the struck quark with a momentum $p = k + q$ into the final-state hadron with four-momentum P_h and spin $\boldsymbol{S}_h$ can be described by an extended fragmentation correlator Δ. The handbag diagram of inclusive DIS (cf. Fig. 2.4) extended with Δ is shown in Fig 2.6.
The fragmentation correlator is given by [BDR02]

$$\Delta_{ij}(p, P_h, \boldsymbol{S}_h) = \sum \int \frac{\mathrm{d}^3 \boldsymbol{P}_X}{(2\pi)^3 2E_X} \int \mathrm{d}^4\xi \, e^{ip\xi} \, \langle 0 \,|\, \psi_i(\xi) \,|\, P_h, \boldsymbol{S}_h, X \rangle \, \langle P_h, \boldsymbol{S}_h, X \,|\, \bar{\psi}_j(0) \,|\, 0 \rangle \,, \tag{2.31}$$

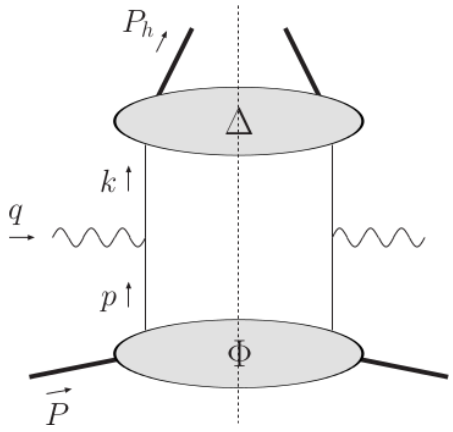

Figure 2.6.: A handbag diagram illustrating a semi-inclusive DIS reaction, where Φ is the quark-quark correlator known from inclusive DIS and Δ is the fragmentation correlator [BDG$^+$07]. At subleading twist additional gluonic loops contribute to the total cross section; the corresponding diagrams can be found in [BDG$^+$07].

summing over all final-states X and integrating over their possible momenta $\boldsymbol{P}_X$. The hadronic tensor in SIDIS is extended with the Δ correlator by [BDR02]

$$W^{\mu\nu} = \sum_q e_q^2 \int \frac{\mathrm{d}^4k}{(2\pi)^4}\frac{\mathrm{d}^4P}{(2\pi)^4}\delta^{(4)}\big(k+q-P\big)\,\mathrm{Tr}\big[\Phi(k,P,\boldsymbol{S})\gamma^\mu\Delta(p,P_h,\boldsymbol{S}_h)\gamma^\nu\big], \quad (2.32)$$

summing over all quark and anti-quark distributions and integrating over all possible quark k and hadron P momenta. Like the quark-quark correlator the fragmentation correlation can also be decomposed in a basis of Dirac matrices, see Sec. A.8. The results are the fragmentation functions, of which two survive the integration over all possible spin states $\boldsymbol{S}_h$ of the produced hadrons. These are [BDR02]

$$D_1(z) = \frac{z}{4}\int \frac{\mathrm{d}^4p}{(2\pi)^4}\delta\left(p^- - \frac{P_h^-}{z}\right)\mathrm{Tr}\Big[\gamma^-\Delta\Big], \quad (2.33a)$$

$$H_1^\perp(z) = \frac{z}{4}\int \frac{\mathrm{d}^4p}{(2\pi)^4}\delta\left(p^- - \frac{P_h^-}{z}\right)\mathrm{Tr}\Big[\imath\sigma^{1-}\gamma_5\Delta\Big]. \quad (2.33b)$$

The case of an unpolarized quark fragmenting into an unpolarized hadron is described by the unpolarized fragmentation function $D_1(z)$, while $H_1^\perp(z)$ describes the fragmentation of a transversely polarized quark into an unpolarized hadron. This function, often referred to as the Collins fragmentation [Col93], is a chiral-odd object. Thus appearing in a SIDIS process, like the one shown in Fig. 2.6 and Eq. 2.31 together with the transversity distribution function h_1 they generate a measurable chiral-even process.

2.3.1. Quarks with transverse momentum

The intrinsic transverse momentum of the struck quark inside the nucleon $\boldsymbol{k}_T$ is neglected in the infinite-momentum frame. If it is taken into account in previous equations, these still hold true if they are integrated over $\boldsymbol{k}_T$, yielding [BDR02]

$$f_1^q(x) = \int \mathrm{d}^2\boldsymbol{k}_T\, f_1^q(x,\boldsymbol{k}_T^2), \quad (2.34a)$$

$$g_1^q(x) = \int \mathrm{d}^2\boldsymbol{k}_T\, g_1^q(x,\boldsymbol{k}_T^2), \quad (2.34b)$$

$$h_1^q(x) = \int \mathrm{d}^2\boldsymbol{k}_T \left(h_{1T}^q(x,\boldsymbol{k}_T^2) - \frac{\boldsymbol{k}_T^2}{2M}h_{1T}^{q\perp}(x,\boldsymbol{k}_T^2)\right) = \int \mathrm{d}^2\boldsymbol{k}_T\, h_1^q(x,\boldsymbol{k}_T^2). \quad (2.34c)$$

With the presence of quarks transverse momenta $\boldsymbol{k}_T$ the quark-quark correlator $\phi(x,\boldsymbol{k}_T)$ has to be re-parametrized. Thus, at leading-twist five additional transverse momentum dependent parton distribution functions (TMDs) have to be taken into account,

$$f_{1T}^{q\perp},\ g_{1T}^q,\ h_{1L}^{q\perp},\ h_{1T}^{q\perp} \text{ and } h_1^{q\perp}; \quad (2.35)$$

where the indices T and L denote the transverse or longitudinal spin of the parent nucleon. They can be extracted from the correlator by tracing it with a proper Dirac matrix, like it was done in Eq. 2.16a. This leads to [BDG+07]

$$\frac{1}{2}\operatorname{Tr}\left[\phi\,\gamma^+\right] = f_1^q(x,\boldsymbol{k}_T^2) - \frac{\varepsilon_T^{ij}k_{T,i}\boldsymbol{S}_{T,j}}{M} f_{1T}^{q\perp}(x,\boldsymbol{k}_T^2), \tag{2.36a}$$

$$\frac{1}{2}\operatorname{Tr}\left[\phi\,\gamma^+\gamma^5\right] = \lambda_N g_1^q(x,\boldsymbol{k}_T^2) - \frac{\boldsymbol{k}_T\boldsymbol{S}_T}{M} g_{1T}^q(x,\boldsymbol{k}_T^2), \tag{2.36b}$$

$$\begin{aligned}\frac{1}{2}\operatorname{Tr}\left[\phi\,\imath\sigma^{i+}\gamma^5\right] &= S_T^i h_1^q(x,\boldsymbol{k}_T^2) + \lambda_N \frac{k_T^i}{M} h_{1L}^{q\perp}(x,\boldsymbol{k}_T^2) \\ &\quad - \frac{k_T^i k_T^j - \frac{1}{2}k_T^2 g_T^{ij}}{M^2} h_{1T}^{q\perp}(x,\boldsymbol{k}_T^2) - \frac{\varepsilon_T^{ij}k_{T,j}}{M} h_1^{q\perp}(x,\boldsymbol{k}_T^2).\end{aligned} \tag{2.36c}$$

While the PDFs[1] f_1, g_1 and h_1 have already been introduced, a brief description of the additional five TMDs arising from the $\boldsymbol{k}_T$-dependence is given in Tab. 2.3.
Table 2.4 shows a schematic illustrating of the properties of the eight (TMD) PDFs in terms of the polarization of the quark and of the parent nucleon.
Not only the transversity distribution is inaccessible in inclusive DIS, so is the Boer-Mulders, the Worm-gear L, and the Pretzelosity function. They require a chiral-odd function as a partner and thus are only measurable in SIDIS. The Sivers function, however shows a T-odd nature which means that it changes sign under "naïve time reversal", which is normal time reversal but without interchanging the initial- and final-state [BM98]. A final-state interaction being part of the Sivers process makes it also only measurable in SIDIS, see Sec. 6.2.2. In Table 2.2 the eight leading twist PDFs are ordered by their chirality and their properties under time reversal.
Like the quark-quark correlator, also the fragmentation correlator Δ needs to extended in terms of the transverse momentum w.r.t. the collinear case. Therefore the fragmentation functions D_1 and $H_1^\perp$ are reparametrized to a dependence on z and the transverse momentum of the quark $p_\perp = \frac{p_T^h}{z}$ after the reaction, yielding [BDG+07]

$$\Delta(z,p_T) = \frac{1}{2}\left[D_1(z,p_\perp^2)\not{n}^- + \imath H_1^\perp(z,p_\perp^2)\frac{\not{p}_\perp\cdot\not{n}^-}{2M_h}\right], \tag{2.37}$$

where $\not{n}^-$ are the Feynman slashed Sudakov vectors, see Sec. A.8.

[1] From here on the exponent q will be omitted, keeping in mind that these are PDFs and not structure functions.

Table 2.2.: Chirality and time reversal properties of leading-twist PDFs [BDR02].

T-even	chiral-even	f_1, g_1, g_{1T}
	chiral-odd	h_1, $h_{1L}^\perp$, $h_{1T}^\perp$
T-odd	chiral-even	$f_{1T}^\perp$
	chiral-odd	$h_1^\perp$

Table 2.3.: The five leading-twist transverse momentum dependent PDFs

$f_{1T}^{\perp}$	distribution of unpolarized quarks inside a transversely polarized nucleon; so-called "Sivers" function [Siv90b]
g_{1T}	distribution of longitudinally polarized quarks inside a transversely polarized nucleon; so-called "Worm-gear T" function
$h_{1L}^{\perp}$	distribution of transversely polarized quarks inside a longitudinally polarized nucleon; so-called "Worm-gear L" function
$h_{1T}^{\perp}$	distribution of quarks with a transverse polarization along their intrinsic transverse momentum in a transversely polarized nucleon; so-called "Pretzelosity" [AESY08]
$h_{1}^{\perp}$	distribution of quarks with a transverse polarization normal to the plane defined by the quark's intrinsic transverse momentum and the nucleon momentum in the unpolarized nucleon; so-called "Boer-Mulders" function

Table 2.4.: A matrix illustrating the polarization of quark (columns) and parent nucleon (rows) of the eight PDFs in terms of no defined polarization U, longitudinal polarization L, and transverse polarization T. The incident virtual photon direction is always pointing into the plane. Graphic arts in courtesy of B. Parsamyan.

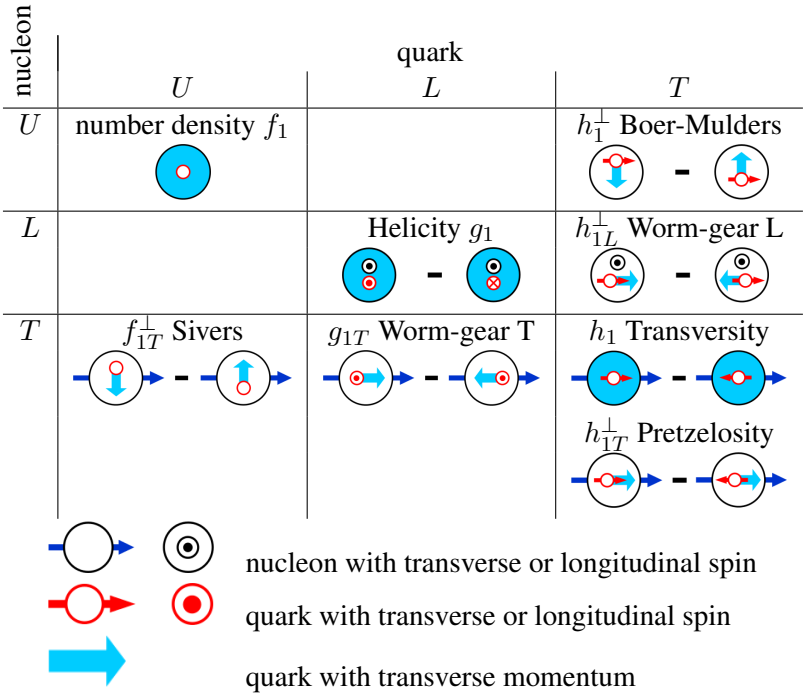

2.3.2. The SIDIS cross-section in single hadron production

The parametrization of the quark-quark correlator ϕ and the fragmentation correlator Δ, as in the previous section can be enhanced down to twist-three level [BDG$^+$07], which is sufficient at the present state of experimental possibilities. The full SIDIS cross section can be expressed as a function of eighteen structure functions

$$\begin{aligned}
\frac{\mathrm{d}^5\sigma}{\mathrm{d}x\,\mathrm{d}y\,\mathrm{d}z_h\,\mathrm{d}\phi_h\,\mathrm{d}P_{h\perp}^2} = \frac{\alpha^2\hbar^2}{xyQ^2}\,\frac{y^2}{2(1-\epsilon)}\left(1+\frac{\gamma^2}{2x}\right) \\
\Bigg[F_{UU,T} + \epsilon\, F_{UU,L} + \sqrt{2\epsilon(1+\epsilon)}\cos\phi_h\, F_{UU}^{\cos\phi_h} \\
+ \epsilon\cos 2\phi_h\, F_{UU}^{\cos 2\phi_h} + \lambda_e\sqrt{2\epsilon(1-\epsilon)}\sin\phi_h\, F_{LU}^{\sin\phi_h} \\
+ S_L\Big[\sqrt{2\epsilon(1+\epsilon^2)}\sin\phi_h\, F_{UL}^{\sin\phi_h} + \epsilon\sin 2\phi_h\, F_{UL}^{\sin 2\phi_h}\Big] \\
+ \lambda_e S_L\Big[\sqrt{1-\epsilon^2}\, F_{LL} + \sqrt{2\epsilon(1-\epsilon)}\cos\phi_h\, F_{LL}^{\cos\phi_h}\Big] \\
+ S_T\Big[\sin(\phi_h-\phi_S)\Big(\, F_{UT,T}^{\sin(\phi_h-\phi_S)} + \epsilon\, F_{UT,L}^{\sin(\phi_h-\phi_S)}\Big) \\
+ \epsilon\sin(\phi_h+\phi_S)\, F_{UT}^{\sin(\phi_h+\phi_S)} + \epsilon\sin(3\phi_h-\phi_S)\, F_{UT}^{\sin(3\phi_h-\phi_S)} \\
+ \sqrt{2\epsilon(1+\epsilon)}\sin\phi_S\, F_{UT}^{\sin\phi_S} \\
+ \sqrt{2\epsilon(1+\epsilon)}\sin(2\phi_h-\phi_S)\, F_{UT}^{\sin(2\phi_h-\phi_S)}\Big] \\
+ \lambda_e S_T\Big[\sqrt{1-\epsilon^2}\cos(\phi_h-\phi_S)\, F_{LT}^{\cos(\phi_h-\phi_S)} \\
+ \sqrt{2\epsilon(1-\epsilon)}\cos\phi_S\, F_{LT}^{\cos\phi_S} \\
+ \sqrt{2\epsilon(1-\epsilon)}\cos(2\phi_h-\phi_S)\, F_{UT}^{\cos(2\phi_h-\phi_S)}\Big]\Bigg].
\end{aligned} \tag{2.38a}$$

Here S_L and S_T denote the longitudinal and transverse orientations of the target polarization, respectively. The beam polarization is indicated by λ_e. The quantity ϵ is the ratio between the longitudinal and transverse photon flux [BDG$^+$07]

$$\epsilon = \frac{1-y-\frac{1}{4}\gamma^2y^2}{1-y+\frac{1}{2}y^2+\frac{1}{4}\gamma^2y^2}\,, \tag{2.39}$$

where $\gamma = \frac{2Mx}{Q} \overset{Q\to\infty}{\approx} 0$ and therefore will be neglected in the following. All angles are defined in the so-called gamma-nucleon system where the z-axis is assigned to the direction of the virtual photon and the xz-plane is the lepton scattering plane, as illustrated in Fig. 2.7.

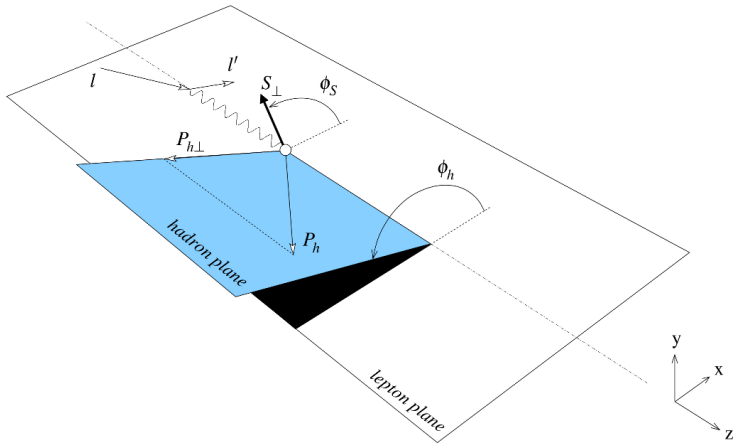

Figure 2.7.: Single hadron production in a SIDIS process: The lepton scattering plane and the hadron plane (in blue) defining the azimuthal angles of the spin of the nucleon and of the produced hadrons ϕ_S and ϕ_h, respectively [BDDM04].

The angles ϕ_S and ϕ_h arise in certain azimuthal modulations, for instance $\sin(\phi_h - \phi_S)$, which are created by a certain structure function indicated in their superscripts. Up to three subscripts are attached to the structure functions F of which the first one indicates the polarization of the beam, the second one the polarization of the target, and the optional third one the polarization of the virtual photon. All structure functions depend on the kinematic variables x, Q^2, and z (see Sec. 2.1.1), the additional dependence on p_T^h is related to the transverse momentum of the quark inside the nucleon.
Compared to the inclusive DIS case, like in Eqs. 2.11a to 2.11c, the FFs are necessary in order to describe the hadronization of the struck quark. All structure functions in Eq. 2.38a can be factorized into TMD PDFs and FFs via convolutions of the type $\mathcal{C}$. The transverse momentum of the quarks is taken into account by integrating over $\boldsymbol{k}_T^2$ and $\boldsymbol{p}_\perp$, the transverse momentum of the quark before and after the reaction, with a delta function for the conservation of momentum [BDG$^+$07]

$$\mathcal{C}[w\ \mathrm{PDF}\ \mathrm{FF}] = x \sum_q e_q^2 \int \mathrm{d}\boldsymbol{p}_\perp^2\, \mathrm{d}\boldsymbol{k}_T^2\, \delta^{(2)}\Big(\boldsymbol{p}_\perp - \boldsymbol{k}_T - \frac{\boldsymbol{P}_{h,T}}{z}\Big) w(\boldsymbol{p}_\perp, \boldsymbol{k}_T)\, \mathrm{PDF}(x, \boldsymbol{p}_\perp^2)\, \mathrm{FF}(z, \boldsymbol{k}_T^2), \quad (2.40a)$$

where $w(\boldsymbol{p}_\perp, \boldsymbol{k}_T)$ is a weight function of the transverse momenta.
The simplest case is the unpolarized structure function given by $F_{UU,T} = \mathcal{C}[f_1\, D_1]$, where f_1 is the number density PDF, D_1 the unpolarized FF, and $w = 1$ accordingly. The complete parametrization of all 18 structure functions of Eq. 2.38a can be found in [BDG$^+$07].

In this work, the parametrization up to twist-two level of PDFs and FFs is adequate, of which four of the eight TMD structure functions of Eq. 2.38a can be expressed as [BDG+07]

$$F_{UT,T}^{\sin(\phi_h-\phi_S)} = \mathcal{C}\left[-\frac{\hat{h}\cdot\boldsymbol{p}_T}{M} f_{1T}^{\perp} D_1\right], \tag{2.41a}$$

$$F_{LT}^{\cos(\phi_h-\phi_S)} = \mathcal{C}\left[\frac{\hat{h}\cdot\boldsymbol{p}_T}{M} g_{1T} D_1\right], \tag{2.41b}$$

$$F_{UT}^{\sin(\phi_h+\phi_S)} = \mathcal{C}\left[-\frac{\hat{h}\cdot\boldsymbol{k}_T}{M_h} h_1 H_1^{\perp}\right], \tag{2.41c}$$

with $\hat{h} = \frac{\boldsymbol{P}_T^h}{|\boldsymbol{P}_T^h|}$.
The structure functions $F_{UT,T}^{\sin(\phi_h-\phi_S)}$ and $F_{LT}^{\cos(\phi_h-\phi_S)}$ are convolutions of the unpolarized FF with the Sivers function $f_{1T}^{\perp}$ or the Worm-gear T function g_{1T}, respectively. The so-called "Sivers effect" (see Sec. 2.3.3) is the azimuthal asymmetry which is related to $F_{UT,T}^{\sin(\phi_h-\phi_S)}$. On the other hand the so-called "Collins" effect (see Sec. 2.3.3) arises from the $F_{UT,T}^{\sin(\phi_h+\phi_S)}$ structure function, which is a convolution of the transversity distribution function h_1 and the Collins FF$H_1^{\perp}$. The other TMD structure functions $F_{UT}^{\sin(3\phi_h-\phi_S)}$ contain terms of higher twist and have no simple interpretation in the parton model. All modulations in Eq. 2.41a are orthogonal in terms of the angles, accordingly, each term can then be extracted independently from the same data by integrating over all other terms.

2.3.3. Single hadron asymmetries

Equation 2.42a shows how a quantity can be defined to measure for instance the Collins and Sivers asymmetries. All contributions which depend on the unpolarized process vanish [BDR02] by

$$\begin{aligned} A &= \frac{\mathrm{d}^6\sigma^{\uparrow} - \mathrm{d}^6\sigma^{\downarrow}}{\mathrm{d}^6\sigma^{\uparrow} + \mathrm{d}^6\sigma^{\downarrow}} \\ &= |\boldsymbol{S}_T| D_{nn}(y) A_{raw,Collins} \sin(\phi_h + \phi_S) + |\boldsymbol{S}_T| A_{raw,Sivers} \sin(\phi_h - \phi_S). \end{aligned} \tag{2.42a}$$

The measured amplitude A_{raw} of these asymmetries, are multiplied by the inverse of the so-called depolarization factor D_{nn} which describes the fraction of the spin of the lepton which is transfered to the virtual photon. In the Collins case it is given by [BDG+07]

$$D_{NN}^{\sin(\phi_h+\phi_S)}(y) = \frac{1-y}{1-y+\frac{y^2}{2}}. \tag{2.43}$$

The depolarization factors of the other modulations can be found in Tab. A.2.

Furthermore the underlying physical asymmetry is attenuated by the fraction of polarizable material inside the target f and the target polarization itself P_T. Thus the physical asymmetry A is calculated from the measured raw asymmetry A_{raw} by

$$A = \frac{1}{f P_T D_{NN}^{\sin(\phi_h+\phi_S)}} A_{raw} \,. \tag{2.44}$$

The Collins asymmetry

The Collins asymmetry is an azimuthal modulation which arises in SIDIS by a convolution of the transversity PDF h_1 and the Collins FF $H_1^\perp$. The latter describes the fragmentation of a transversely polarized quark into an unpolarized nucleon [Col93] and the transversity TMD PDF which describes the difference in probabilities of finding quarks with spin parallel, or anti-parallel to the spin of the transversely polarized nucleon. The convolution of h_1 and $H_1^\perp$ has to be normalized to the convolution of the corresponding unpolarized functions [BDR02]

$$A_{Coll} = A_{UT}^{\sin(\phi_h+\phi_S)} \propto \frac{\sum_q e_q^2 h_1(x, \boldsymbol{k}_T^2) \otimes H_1^{\perp q}(z, \boldsymbol{p}_T^2)}{\sum_q e_q^2 f_1(x, \boldsymbol{k}_T^2) \otimes D_1^q(z, \boldsymbol{p}_T^2)}, \tag{2.45}$$

where the sum runs over all quark flavors q. The convolution integral from Eq. 2.40a of any given PDF and FF is denoted as PDF $\otimes$ FF.
A detailed interpretation and discussion on the underlying mechanisms, as well as a link to the hadron-pair asymmetry will be given in Sec. 6.3.5.

The Sivers asymmetry

The so-called "Sivers effect" has a fundamentally different origin than the Collins effect, on which a brief introduction will be given in Sec. 6.2.2. Here, the Sivers PDF $f_{1T}^\perp$ and the unpolarized fragmentation function D_1 are convoluted under the same normalization as in Eq. 2.45, as [BDR02]

$$A_{Siv} = A_{UT}^{\sin(\phi_h-\phi_S)} \propto \frac{\sum_q e_q^2 f_{1T}^\perp(x, \boldsymbol{k}_T^2) \otimes D_1^q(z, \boldsymbol{p}_T^2)}{\sum_q e_q^2 f_1(x, \boldsymbol{k}_T^2) \otimes D_1^q(z, \boldsymbol{p}_T^2)}. \tag{2.46}$$

The convolution is again performed via the convolution integral from Eq. 2.40a. In the Sivers case the depolarization factor $D_{NN}^{\sin(\phi_h-\phi_S)}(y)$ is 1, since the polarization of the virtual photon is not of impact here.

The other TMD asymmetries

Additional six asymmetry modulations in SIDIS on transversely polarized nucleons are included in the cross-section in Eq. 2.38a. Two of them are twist-two, related to the Pretzelosity TMD and the Worm-gear T TMD, $h_{1T}^{\perp}$ and g_{1T}, while the remaining four are twist-three, see also Tab. A.1.
The Pretzelosity PDF $h_{1T}^{\perp}$ describes the quark transverse polarization along the quark intrinsic transverse momentum in a transversely polarized nucleon. A common approximation of the Pretzelosity PDF is given by a linear combination of the helicity PDF and the transversity PDF $h_{1T}^{\perp}(x, \boldsymbol{k}_T^2) \approx g_1(x, \boldsymbol{k}_T^2) - h_1(x, \boldsymbol{k}_T^2)$; often referred to as one of the Wandzura-Wilczek approximations [MT96b]. It enters into the SIDIS cross-section by a convolution with the Collins FF [BDR02, BDG$^+$07]

$$A_{UT}^{\sin(3\phi_h - \phi_S)} \propto \frac{\sum_q e_q^2 h_{1T}^{\perp}(x, \boldsymbol{k}_T^2) \otimes H_1^{\perp q}(z, \boldsymbol{p}_T^2)}{\sum_q e_q^2 f_1(x, \boldsymbol{k}_T^2) \otimes D_1^q(z, \boldsymbol{p}_T^2)}. \tag{2.47}$$

From this, an azimuthal modulation with the angular dependence on $\sin(3\phi_h - \phi_S)$ is generated. Another interesting contribution is modulated by a $\cos(\phi_h - \phi_S)$ term, which is related to the Worm-gear T PDF, see Tab. 2.4. It describes the distribution of longitudinally polarized quarks in a transversely polarized nucleon. The convolution is of the type [BDR02, BDG$^+$07]

$$A_{LT}^{\cos(\phi_h - \phi_S)} \propto \frac{\sum_q e_q^2 g_{1T}(x, \boldsymbol{k}_T^2) \otimes D_1^q(z, \boldsymbol{p}_T^2)}{\sum_q e_q^2 f_1(x, \boldsymbol{k}_T^2) \otimes D_1^q(z, \boldsymbol{p}_T^2)}. \tag{2.48}$$

It gives rise to a double spin asymmetry $A_{LT}^{\cos(\phi_h - \phi_S)}$, meaning that the polarization of the target nucleon and the polarization of the incoming lepton have to be taken into account.
The depolarization factors, D_{nn}, together with all the necessary factors like the polarizations for all eight azimuthal asymmetries can be found in Tab. A.1 and Tab. A.2.
One of the twist-three structure functions, the Boer-Mulders PDF $h_1^{\perp}$ plays an important role in the future program of COMPASS. In the Drell-Yan measurement, see Sec. 7.2, its properties will be investigated; together with the Sivers function. In SIDIS processes $h_1^{\perp}$ does not appear directly, but in a linear combinations with other PDFs in the Wandzura-Wilczek approximations [MT96b, BDG$^+$07]. In the case of a SIDIS process on a transversely polarized target it enters into two asymmetries $A_{UT}^{\sin\phi_S}$ and $A_{UT}^{\sin(2\phi_h - \phi_S)}$.

2.3.4. The hadron-pair asymmetry

It has already been denoted that besides single hadron production the production of more than one hadron from one vertex, namely the production of a hadron-pair or often referred as a dihadron in literature[2], is of strong interest. The analysis of this channel is the topic of this thesis and the so far presented theoretical framework serves as the basis which now is evolved to the required full picture.
The Collins asymmetry arising from a convolution of the Collins FF and the transversity TMD PDF, see Sec. 2.3.3, allows for an experimental access to h_1, if $H_1^\perp$ is known (see Sec. 2.4.2). The hadron-pair asymmetry also depends on h_1 but the chiral-odd partner in the convolution is different. Here it is the so-called DiFF, which describes the fragmentation of a polarized quark into a pair of unpolarized hadrons, h_1 and h_2. Accordingly the process can be written as

$$\ell(l, \boldsymbol{s}) + N(P, \boldsymbol{S}) \to \ell'(l', \boldsymbol{s}') + h_1(P_{h_1}, \boldsymbol{S}_{h_1}) + h_2(P_{h_2}, \boldsymbol{S}_{h_2}) + X, \tag{2.49}$$

where P_{h_i} is the four-momentum of the outgoing hadron $i \in 1, 2$ and $\boldsymbol{S}_{h_i}$ its spin-vector[3]. In Figure 2.8 the dihadron process is depicted. The fractional energy carried by one of the observed final state hadrons is then defined as [BR03a]

$$z_i = \frac{P \cdot P_i}{P \cdot p} \overset{\text{lab}}{=} \frac{E_i}{\nu}, \tag{2.50}$$

where E_i is the energy of hadron i. Its momentum transverse w.r.t. the direction of the incoming lepton ℓ is denoted as $\boldsymbol{p}_{T,i}$. In order to ensure that the two hadrons are produced in the current fragmentation region, and not by a fragmentation of target remnants, a minimum cut on z will be applied, see Sec. 4.3.3.

The dihadron fragmentation functions (DiFF)

Analogous to the single hadron case, where the dihadron fragmentation function (DiFF) D_1^q and $H_1^{\perp q}$ describe the fragmentation of an unpolarized or a transversely polarized quark into one unpolarized hadron, the DiFFs are defined in order to describe the fragmentation into a hadron-pair. If this pair is produced via fragmentation of a unpolarized quark with flavor q the corresponding DiFF is denoted as $D_1^{\sphericalangle q}$, now depending on the kinematic variables of both hadrons. If the struck quark is transversely polarized, the so called spin-dependent DiFF $H_1^\sphericalangle$ contains the information of the fragmentation. Both DiFFs can again be extracted from a dedicated fragmentation correlator [BR06]. A handbag diagram, similar to the one describing the SIDIS process in single hadron production 2.6, is shown in Fig. 2.9.

[2] In this work both terms are used synonymously, like in most of the literature.
[3] For a better readability the subscript h_i will often be indicated as i, keeping in mind that it is the subscript denoting the hadron with index i.

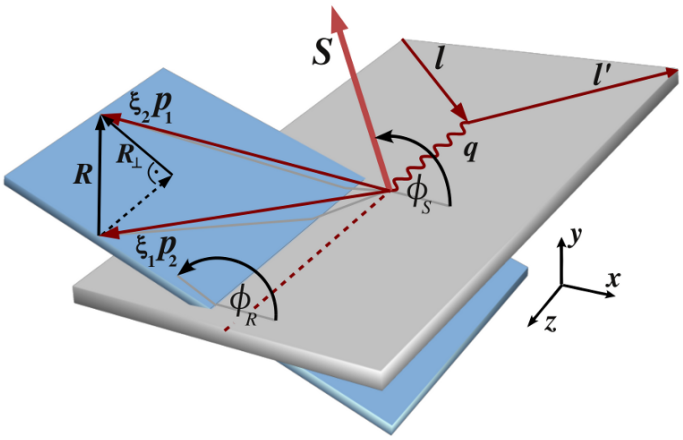

Figure 2.8.: Simplified scheme of the dihadron production process [COMPASS12c]: The incoming lepton and scattered lepton with their three-momenta $\boldsymbol{l}$ and $\boldsymbol{l}'$ define the scattering plane (in gray) and $\boldsymbol{q}$ is the three-momentum of the virtual photon. The angle ϕ_S is the azimuthal angle of the spin $\boldsymbol{S}$ of the fragmenting quark. The corresponding ξ_i values are used for the normalization of the difference vector $\boldsymbol{R}$, like $\boldsymbol{R} = (z_2\boldsymbol{p}_1 - z_1\boldsymbol{p}_2)/(z_1 + z_2) := \xi_2\boldsymbol{p}_1 - \xi_1\boldsymbol{p}_2$. Hence, ϕ_R is the azimuthal angle of $\boldsymbol{R}$ and $\boldsymbol{R}_\perp$ is its component perpendicular to $\boldsymbol{q}$. See Sec. 2.3.4 for a discussion on the difference of the definition of $\boldsymbol{R}$ as used here w.r.t. Eq. 2.52.

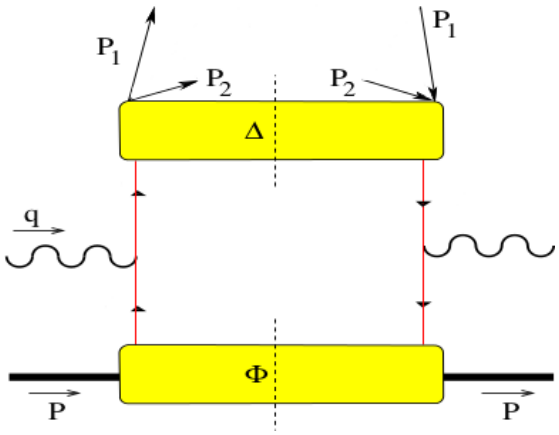

Figure 2.9.: A handbag diagram illustrating a dihadron semi-inclusive DIS reaction, where ϕ is the quark-quark correlator known from the single hadron production in SIDIS and Δ is the dihadron fragmentation correlator [BR04]. At subleading twist additional gluonic loops contribute to the total cross section; the corresponding diagrams can be found in [BR04].

The masses of the two hadrons are M_1 and M_2 (with $P_h^2 = M_h^2$) being much smaller than the hard scale Q^2 of the process. Besides the total four-momentum of the pair [BR03a]

$$P_h = P_1 + P_2 \tag{2.51}$$

also their relative momentum [BR03a]

$$R = \frac{1}{2}\big(P_1 - P_2\big) \tag{2.52}$$

will be of importance. Accordingly,the sum of their individual fractional energies is defined as [BR03a]

$$z_1 + z_2 = \frac{P \cdot P_1}{P \cdot p} + \frac{P \cdot P_2}{P \cdot p} \equiv \frac{P \cdot P_h}{P \cdot p} := z. \tag{2.53}$$

The measurable modulation is a function of two angles. One of them is again the azimuthal angle of the spin orientation of the target nucleon ϕ_S. The second angle is the azimuthal angle of the hadron-pairs relative momentum R around the direction of the incoming lepton ϕ_R, while the transverse momenta of the individual hadrons will be integrated over. The explicit form of ϕ_R and ϕ_S is [COMPASS12c]

$$\phi_R = \frac{(\boldsymbol{q} \times \boldsymbol{l}) \cdot \boldsymbol{R}}{|(\boldsymbol{q} \times \boldsymbol{l}) \cdot \boldsymbol{R}|} \arccos\left(\frac{(\boldsymbol{q} \times \boldsymbol{l}) \cdot (\boldsymbol{q} \times \boldsymbol{R})}{|\boldsymbol{q} \times \boldsymbol{l}||\boldsymbol{q} \times \boldsymbol{R}|}\right), \tag{2.54a}$$

$$\phi_S = \frac{(\boldsymbol{q} \times \boldsymbol{l}) \cdot \boldsymbol{S}}{|(\boldsymbol{q} \times \boldsymbol{l}) \cdot \boldsymbol{S}|} \arccos\left(\frac{(\boldsymbol{q} \times \boldsymbol{l}) \cdot (\boldsymbol{q} \times \boldsymbol{S})}{|\boldsymbol{q} \times \boldsymbol{l}||\boldsymbol{q} \times \boldsymbol{S}|}\right). \tag{2.54b}$$

The FF can again be extracted from the fragmentation correlator, therefore it is convenient to switch to light-cone coordinates. Here a four-vector is written as $\left[a^-, a^+, a^x, a^y\right]$ in terms of light-cone components $a^\pm = (a^0 \pm a^3)/\sqrt{2}$ (see Sec. A.8) and its transverse spatial components a_T^x and a_T^y. If this is applied, the relevant momenta can be rewritten as [BR03a, BR04, BR06, BCR13]

$$P^\mu = \left[\frac{M^2}{2P^+}, P^+, 0, 0\right], \tag{2.55a}$$

$$p^\mu = \left[\frac{p^2 + \boldsymbol{p}_T^2}{2xP^+}, xP^+, p_T^x, p_T^y\right], \tag{2.55b}$$

$$k^\mu = \left[\frac{P_h^-}{z}, \frac{z(k^2 + \boldsymbol{k}_T^2)}{2P_h^-}, k_T^x, k_T^y\right], \tag{2.55c}$$

$$P_h^\mu = \left[P_h^-, \frac{M_h^2}{2P_h^-}, 0, 0\right], \tag{2.55d}$$

$$R^\mu = \left[\frac{|\boldsymbol{R}|P_h^-}{M_h}\cos\theta, -\frac{|\boldsymbol{R}|M_h}{P_h^-}\cos\theta, R_T^x, R_T^y\right] \tag{2.55e}$$

$$= \left[\frac{|\boldsymbol{R}|P_h^-}{M_h}\cos\theta, -\frac{|\boldsymbol{R}|M_h}{P_h^-}\cos\theta, |\boldsymbol{R}|\sin\theta\cos\phi_R, |\boldsymbol{R}|\sin\theta\sin\phi_R\right], \tag{2.55f}$$

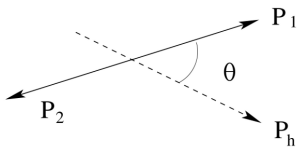

Figure 2.10.: The hadron-pair in the center of mass frame. The angle θ is the polar angle of the pair w.r.t. the direction of $P_h^\mu = [\sqrt{2}^{-1} M_{inv}, \sqrt{2}^{-1} M_{inv}, 0, 0]$ in the target rest frame.

with [BCR13]

$$|\boldsymbol{R}| = \frac{1}{2}\sqrt{M_h^2 - 2\big(M_1^2 + M_2^2\big) + \frac{\big(M_1^2 - M_2^2\big)^2}{M_h^2}}\,, \tag{2.56a}$$

$$\boldsymbol{R}_T = \boldsymbol{R}\sin\theta \tag{2.56b}$$

in the center of mass frame (cm), see Fig. 2.10.
In the basis of the hadronic and leptonic tensor, analogous to the inclusive DIS case in Eq. 2.5, the differential cross section for hadron-pair production on SIDIS can be written as a seven fold derivative [BR03a]

$$\frac{\mathrm{d}^7\sigma}{\mathrm{d}\cos\theta\,\mathrm{d}M_h^2\,\mathrm{d}\phi_R\,\mathrm{d}z\,\mathrm{d}x\,\mathrm{d}y\,\mathrm{d}\phi_S} = \sum_q \frac{\alpha^2\hbar^2 y e_q^2}{32 z Q^2} L_{\mu\nu}\; 2M\; W^{\mu\nu}, \tag{2.57}$$

where the hadronic tensor for a quark flavor q at tree level is given by [BR03a]

$$2MW_q^{\mu\nu} = 32 z\,\mathcal{I}\Big[\mathrm{Tr}\Big[\Phi_q(x,\boldsymbol{S})\gamma^\mu\Delta^q(z,\cos\theta,M_h^2,\phi_R)\gamma^\nu\Big]\Big]. \tag{2.58}$$

The shorthand notation $\mathcal{I}$ integrates over the transverse momenta of the quark and the final hadrons, to ensure the conservation of transverse momenta [BR03a]

$$\mathcal{I}\,[f] = \int \mathrm{d}\boldsymbol{p}_T\,\mathrm{d}\boldsymbol{k}_T\;\delta\left(\frac{\boldsymbol{p}_T - \boldsymbol{P}_{h\perp}}{z - \boldsymbol{k}_T}\right)[f]\;. \tag{2.59}$$

The trace of the tensor in Eq. 2.58 contains the full information of the dihadron process. The non-perturbative processes describing the distributions of quark inside the spin-$\frac{1}{2}$ target nucleon are included in the quark-quark correlator $\Phi_q(x,\boldsymbol{S})$ and the fragmentation correlator Δ_q contains information on the production of a hadron-pair in the residual jet.

The correlators are given by [BR04]

$$\Phi_q(x, \boldsymbol{S}) = \int \mathrm{d}\boldsymbol{p}_T \, \mathrm{d}p^- \Phi_q(p; P, \boldsymbol{S})\Big|_{p^+ = xP^+}, \tag{2.60a}$$

$$\Delta^q(z, \cos\theta, M_h^2, \phi_R) = \frac{z|\boldsymbol{R}|}{16 M_h} \int \mathrm{d}\boldsymbol{k}_T \, \mathrm{d}k^+ \Delta^q(k; P_h, R)\Big|_{k^- = P_h^- z^{-1}}. \tag{2.60b}$$

Furthermore the fragmentation correlator in terms of hadronic matrix elements of non-local quark operators is [BR04, BMP03]

$$\Delta^q_{ij}(k; P_h, R) = \sum_X \int \frac{\mathrm{d}^4\xi}{(2\pi)^4} \, e^{\imath k\cdot\xi} \, \langle 0 \,|\, \psi(\xi)_i \,|\, P_h, R; X\rangle \, \langle P_h, R; X \,|\, \bar\psi_j(0) \,|\, 0\rangle \,, \tag{2.61}$$

where ψ is the quark field operator. The fragmentation correlator as written above is not a color gauge invariant object, since the quark fields ψ are evaluated at two light-front separated space-time points 0 and ξ, respectively. In order to restore color gauge invariance, gauge link operators have to be included [BR04, BMP03]

$$\begin{aligned}\Delta^q_{ij}(k; P_h, R) = \sum_X \int \frac{\mathrm{d}^4\xi}{(2\pi)^4} \, e^{\imath k\cdot\xi} \left\langle 0 \,\middle|\, \mathcal{U}^{n_+}_{(-\infty,\xi)} \psi(\xi)_i \,\middle|\, P_h, R; X \right\rangle \\ \left\langle P_h, R; X \,\middle|\, \bar\psi_j(0) \mathcal{U}^{n_+}_{(0,-\infty)} \,\middle|\, 0 \right\rangle .\end{aligned} \tag{2.62a}$$

The operators $\mathcal{U}$ are gauge link operators [BR04], the so-called "Wilson lines"

$$\mathcal{U}_{(0,\xi)} = \mathcal{P}\left(-\imath g \int_0^\xi \mathrm{d}w A(w) \right), \tag{2.63}$$

where A is the gluon field with coupling constant g, and $\mathcal{P}$ indicates a path ordered exponential. It symbolically denotes all possible soft gluon lines to Δ and resumes their contributions.
After an integration over all transverse momenta $\boldsymbol{k}_T$, where the Wilson lines $\mathcal{U}$ can be reduced to unity using a light-cone gauge, only two fragmentation functions survive [BBJR00, BR03a, BR06]:

$$D_1^{\sphericalangle q}(z, \cos\theta, M_h^2) = 4\pi \, \mathrm{Tr}\big[\Delta^q(z, \cos\theta, M_h^2, \phi_R)\gamma^-\big], \tag{2.64}$$

$$\frac{\epsilon_T^{ij} R_{Tj}}{M_h} H_1^{\sphericalangle q}(z, \cos\theta, M_h^2) = 4\pi \, \mathrm{Tr}\big[\Delta^q(z, \cos\theta, M_h^2, \phi_R)\imath\sigma^{i-}\gamma_5\big]. \tag{2.65}$$

The first one is the so-called unpolarized DiFF and the latter is the polarized DiFF, since ϵ_T^{ij} serves as a projector of the polarization states[4] when applied on the correlator. From these equations two bounds can be derived [BR03a]

$$D_1^{\sphericalangle q}(z, \cos\theta, M_h^2) \geq 0, \qquad D_1^{\sphericalangle q}(z, \cos\theta, M_h^2) \geq \frac{|\boldsymbol{R}_T|}{M_h} H_1^{\sphericalangle q}(z, \cos\theta, M_h^2). \tag{2.66}$$

[4] $\epsilon_T^{ij} = \epsilon^{\rho\sigma\mu\nu} n_{+\rho} n_{-\sigma}$ with $\epsilon^{0123} = 1$

For the full derivation of the leptonic tensor and the quark-quark correlator, see [BR03a, BR04]. The full differential leading-twist cross-section from Eq. 2.57 can be rewritten in terms of the obtained FF [BR03a]

$$\begin{aligned}\frac{\mathrm{d}^7\sigma}{\mathrm{d}x\,\mathrm{d}y\,\mathrm{d}z\,\mathrm{d}\phi_R\,\mathrm{d}\phi_S\,\mathrm{d}\cos\theta\,\mathrm{d}M_h^2} =& \frac{2\alpha^2\hbar^2}{4\pi Q^2 y}\sum_q e_q^2\Big[A(y)f_1^q(x)D_1^{\sphericalangle q}(z,\cos\theta,M_h^2) \\ &+ \lambda_e S_L\frac{C(y)}{2}g_1^q(x)D_1^{\sphericalangle q}(z,\cos\theta,M_h^2) \\ &+ B(y)\frac{|\boldsymbol{S}_T||\boldsymbol{R}_T|}{M_h}\sin(\phi_R+\phi_S)h_1^q(x)H_1^{\sphericalangle q}(z,\cos\theta M_h^2)\Big],\end{aligned} \tag{2.67}$$

where $A(y) = \left(1 - y + \frac{y^2}{2}\right)$, $B(y) = (1-y)$, and $C(y) = y(2-y)$. For an experimental investigation one might consider a transversely polarized target ($|\boldsymbol{S}_T| > 0$) and an arbitrary or unpolarized beam. From the data obtained from such a measurement a single spin asymmetry (SSA) can be built [BR03a]:

$$A_{OT}^{\sin(\phi_R+\phi_S)}(y,x,z,M_h^2) = |\boldsymbol{S}_T|\frac{B(y)}{A(y)}\frac{\sum_q e_q^2 h_1^q\int\mathrm{d}\cos\theta\frac{|\boldsymbol{R}_T|}{2M_h}H_1^{\sphericalangle,q}(z,\cos\theta,M_h^2)}{\sum_q e_q^2 f_1^q\int\mathrm{d}\cos\theta D_1^{\sphericalangle q}(z,\cos\theta,M_h^2)}, \tag{2.68}$$

which gives access to the transversity TMD PDF h_1 at leading twist by measuring the standard variables x, y, z, and the angle ϕ_R and ϕ_S.
In a well-defined framework a partial wave expansion of the dihadron fragmentation functions can be performed; this procedure will be described in the course of the interpretation of the results in Sec. 6.3.3. By evolving the formalism to sub-leading twist of the TMD PDFs, as performed in [BR04], a set of additional modulations, single and double spin, appear. Two of them are currently under investigation at the CLASS Hall-B experiment [CLASS13, BR04]

$$\mathrm{d}^7\sigma_{UL} = \frac{\alpha^2\hbar^2}{2\pi Q^2 y}\boldsymbol{S}_L\sum_{aq}e_a^2 V(y)\sin\phi_R\frac{|\boldsymbol{R}_T|}{Q}\frac{M}{M_h}xh_L^q(x)H_1^{\sphericalangle q}(z,\cos\theta,M_h^2), \tag{2.69a}$$

$$\mathrm{d}^7\sigma_{LU} = \frac{\alpha^2\hbar^2}{2\pi Q^2 y}\lambda_e\sum_q e_q^2 W(y)\sin\phi_R\frac{|\boldsymbol{R}_T|}{Q}\frac{M}{M_h}xe^q(x)H_1^{\sphericalangle q}(z,\cos\theta,M_h^2). \tag{2.69b}$$

The PDFs $h_L^q(x)$ and $e^q(x)$ are of subleading nature of transversely polarized quarks inside longitudinally or unpolarized nucleons, respectively.

Lorentz invariant definition of the hadron-pair difference vector

The angle ϕ_R, as defined in Eq. 2.54a is not invariant against boosts in the direction of the virtual photon. Since P_1 and P_2 will behave differently under such a boost, this might lead to an azimuthal rotation of $\boldsymbol{R}$ like it has been defined in Eq. 2.52. Therefore an alternative definition

$$\boldsymbol{R} = \frac{z_2 \boldsymbol{P}_1 - z_1 \boldsymbol{P}_2}{z_1 + z_2} \tag{2.70}$$

was proposed by Artru [Art02]. The transverse component $\boldsymbol{R}_\perp$ is also Lorentz invariant against boosts along the virtual photon direction in leading order. Later this definition is also used in the interpretation of the hadron-pair asymmetry in the framework of the recursive string fragmentation model [Art10], see Sec. 6.3.5. In this work the Lorentz invariant form is used to evaluate the azimuthal angle ϕ_R. A study on the influence of the different definitions of $\boldsymbol{R}$ on ϕ_R was performed by Massmann [Mas08] and was found to be small.
The HERMES collaboration[5] uses an alternative definition [HERMES08]

$$\boldsymbol{R}^{\mathrm{H}} := \frac{\boldsymbol{P}_1 - \boldsymbol{P}_2}{2}\,, \tag{2.71a}$$

$$\boldsymbol{R}_T^{\mathrm{H}} := \boldsymbol{R}^{\mathrm{H}} - \left(\boldsymbol{R}^{\mathrm{H}} \cdot \hat{\boldsymbol{P}}_h\right)\hat{\boldsymbol{P}}_h\,, \tag{2.71b}$$

where $\hat{\boldsymbol{P}}_h = \frac{\boldsymbol{P}_h}{|\boldsymbol{P}_h|}$ and $\boldsymbol{P}_h = \boldsymbol{P}_{\pi^+} + \boldsymbol{P}_{\pi^-}$. Thus $\boldsymbol{R}_T^{\mathrm{H}}$ is the component of $\boldsymbol{P}_1$ perpendicular to $\boldsymbol{P}_h$ and $\phi_{R\perp}^{\mathrm{H}}$ the azimuthal angle of $\boldsymbol{R}_T^{\mathrm{H}}$ about the γ^* direction.

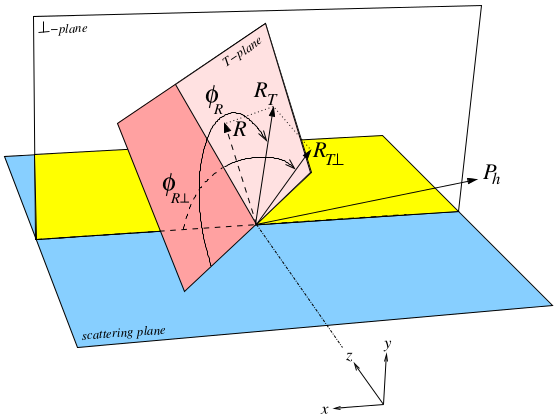

Figure 2.11.: Illustration of the difference between $\boldsymbol{R}_T$ and $\boldsymbol{R}_T^{\mathrm{H}} = \boldsymbol{R}_{T\perp}$ and thus the resulting difference of ϕ_R and $\phi_{R\perp}$ [BR04]. The $\perp$ plane is perpendicular to the scattering plane (in blue).

[5] The superscript H indicates the form of the variables used by the HERMES collaboration.

In Eq. 2.72a the expressions of ϕ_R (COMPASS) and $\phi^{\mathrm{H}}_{R\perp}$ are opposed, and an illustration of the difference between both is shown in Fig. 2.11. Correspondingly HERMES uses [HERMES08]

$$\phi_R = \frac{(\boldsymbol{q}\times\boldsymbol{l})\cdot\boldsymbol{R}}{|(\boldsymbol{q}\times\boldsymbol{l})\cdot\boldsymbol{R}|}\arccos\left(\frac{(\boldsymbol{q}\times\boldsymbol{l})\cdot(\boldsymbol{q}\times\boldsymbol{R})}{|\boldsymbol{q}\times\boldsymbol{l}||\boldsymbol{q}\times\boldsymbol{R}|}\right), \tag{2.72a}$$

$$\phi^{\mathrm{H}}_{R\perp} = \frac{(\boldsymbol{q}\times\boldsymbol{l})\cdot\boldsymbol{R}^{\mathrm{H}}_{\boldsymbol{T}}}{|(\boldsymbol{q}\times\boldsymbol{l})\cdot\boldsymbol{R}^{\mathrm{H}}_{\boldsymbol{T}}|}\arccos\left(\frac{(\boldsymbol{q}\times\boldsymbol{l})\cdot(\boldsymbol{q}\times\boldsymbol{R}^{\mathrm{H}}_{\boldsymbol{T}})}{|\boldsymbol{q}\times\boldsymbol{l}||\boldsymbol{q}\times\boldsymbol{R}^{\mathrm{H}}_{\boldsymbol{T}}|}\right). \tag{2.72b}$$

as definitions for the azimuthal angles.
The difference between ϕ_R and $\phi^{\mathrm{H}}_{R\perp}$ is in the order of Q^{-2} [Mas08, BR04] and will therefore be neglected when comparing the results of the two experiments in Secs. 2.4.2 and 6.3.2.

2.4. Experimental overview

The first measurement of transverse spin effects in SIDIS was performed by the HERMES experiment at DESY, Hamburg, in the years 2002-2004, where a $27.6\,\mathrm{GeV}/c$ electron or positron beam was scattered off a transversely polarized gaseous hydrogen target. In parallel, the COMPASS experiment at CERN, Geneva, equipped with a solid state transversely polarized deuterium target collected data with a $160\,\mathrm{GeV}/c$ muon beam. The COMPASS measurement program continued in the year 2006 using a longitudinally polarized ammonia target installed in 2005, being effectively a proton target. The years 2007 and 2010 were dedicated to the investigation of transverse spin effects. At Jefferson Laboratory, Newport News, the Hall-A experiment E06-010 has measured transverse spin effects with a $6\,\mathrm{GeV}/c$ electron beam on a polarized ^{3}He target, serving as a neutron target.

2.4.1. The single hadron asymmetries

Even though the single hadron azimuthal asymmetries are not the main topic of this work, they are part of the SIDIS cross-section and some of them contain information of the transversity TMD PDF h_1 or are part of the measuring program of the second phase of the COMPASS experiment, see Chap. 7.2, such as the Sivers function. Recently, studies suggest a possible similarity between $H_1^\perp$ and $H_1^\sphericalangle$, see Sec. 6.3.5. For completeness the results from the measurements of the other six TMD asymmetries on single hadron production (see Sec. 2.3.3) are also described briefly. Only recent results are shown in this section as such being important in the following chapters, while references to previous results will be given when they appear to be useful. The single hadron asymmetries are plotted as functions of x, z and the transverse momentum of the hadrons produce $p_{h\perp}$ (HERMES nomenclature) or p_T^h (COMPASS nomenclature) in units of GeV/c. Note that the HERMES collaboration uses natural units, where the equality $\hbar := c := 1$ is defined.

Sivers asymmetry

The Sivers asymmetry for charged pions and kaons measured by the HERMES collaboration on a gaseous proton target is shown in Fig. 2.12 [HERMES09]. The asymmetry of positively charged pions is different from zero for all three dependencies with a positive sign. It is almost constant in bins of x at around $5\,\%$, while a clear increase with higher z and $p_{h\perp}$ can be observed. In contrast the asymmetry of negatively charged pions is consistent with zero. A similar trend with almost twice the amplitude as for the π^+ is visible for the asymmetry of positively charged kaons, while the asymmetry of K^- is again compatible with zero.

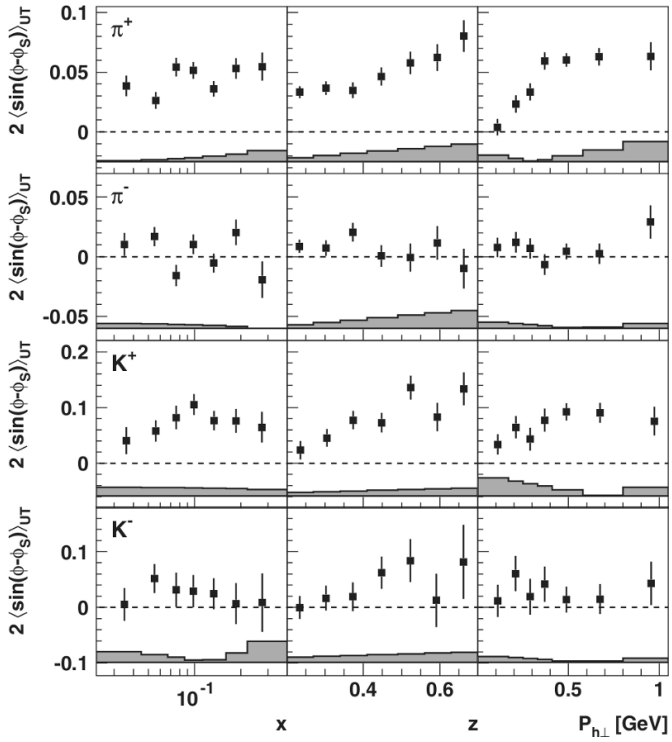

Figure 2.12.: Results of the Sivers single hadron asymmetry of charged pions $\pi^{\pm}$ (1^{st} and kaons 2^{nd} row) and $K^{\pm}$ (3^{rd} and 4^{th} row) measured by the HERMES collaboration on a transversely polarized proton target [HERMES09].

The extracted asymmetries of identified hadrons from the data on a deuteron target collected in the years 2003-2004 from the COMPASS collaboration are shown in Fig. 2.13 [COMPASS09a]. The asymmetry amplitudes are compatible with zero within the statistical uncertainties in all three dependencies for all hadrons. The results are interpreted as a close-to-complete cancellation of the u and d quark contributions from the transversity PDFs on the deuteron as an isoscalar target.
Figure. 2.14 shows the COMPASS results from a polarized proton target extracted from the data collected in 2010 [COMPASS14d]. The asymmetry of negatively charged pions is compatible with zero, while the positively charged pions is clearly different from zero but smaller than the corresponding results from HERMES. A possible Q^2 dependence of the Sivers asymmetry was investigated recently, since COMPASS covers a larger Q^2 range than HERMES, see Sec. 6.2.1. The corresponding results of unidentified charged hadrons $h^{\pm}$ from 2007 and 2010 data can be found in [COMPASS10b] and [COMPASS12b], respectively.

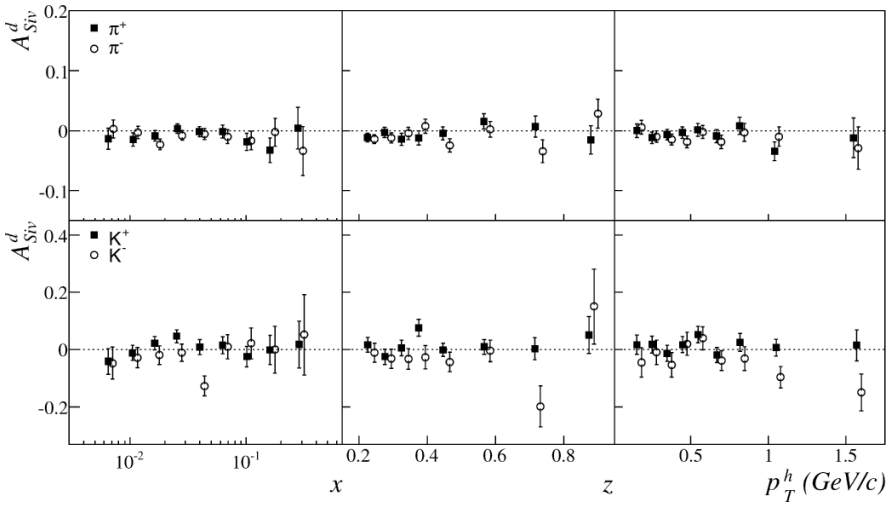

Figure 2.13.: Results of the Sivers single hadron asymmetry of charged pions $\pi^{\pm}$ (1st row) and kaons $K^{\pm}$ (2nd row) measured by the COMPASS collaboration on a transversely polarized deuteron target from the 2003-2004 data [COMPASS09a].

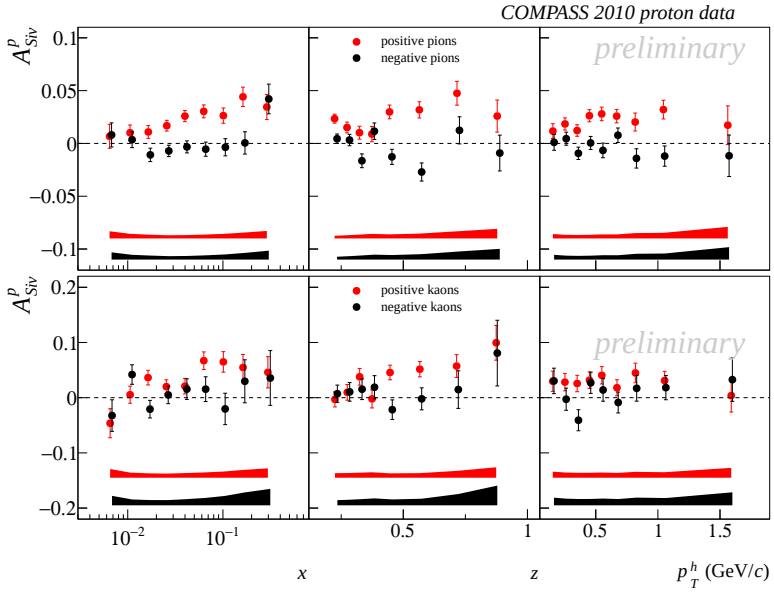

Figure 2.14.: Results of the Sivers single hadron asymmetry of charged pions $\pi^{\pm}$ (1st row) and kaons $K^{\pm}$ (2nd row) measured by the COMPASS collaboration on a transversely polarized proton target from the 2010 data [COMPASS14d].

Collins asymmetry

Figure 2.15 shows the Collins asymmetry for charged pions and kaons measured by the HERMES collaboration on a proton target [HERMES10]. The charged pions show a clear signal characterized by an increasing amplitude with higher values of x. The signs of the amplitudes are positive for π^+ and negative for π^- with a maximum at 0.03 and -0.07, respectively. The asymmetry of K^+ has a similar shape like the one of π^+ but with almost twice its amplitude. On the contrary the asymmetry of K^- is compatible with zero in all dependencies. From these results for the first time the conclusion could be made that both the transversity PDF and the Collins fragmentation function are different from zero.
The Collins angle as used by the COMPASS experiment contains an additional phase of $-\pi$ w.r.t. the definition used by HERMES, which causes a sign change of the extracted asymmetries. Figure 2.16 shows the obtained asymmetries for charged pions and kaons on a transversely polarized deuteron target; previous results can be found in [COMPASS05, COMPASS07b]. The asymmetries amplitudes of all types of identified hadrons are small and compatible with zero within the uncertainties.

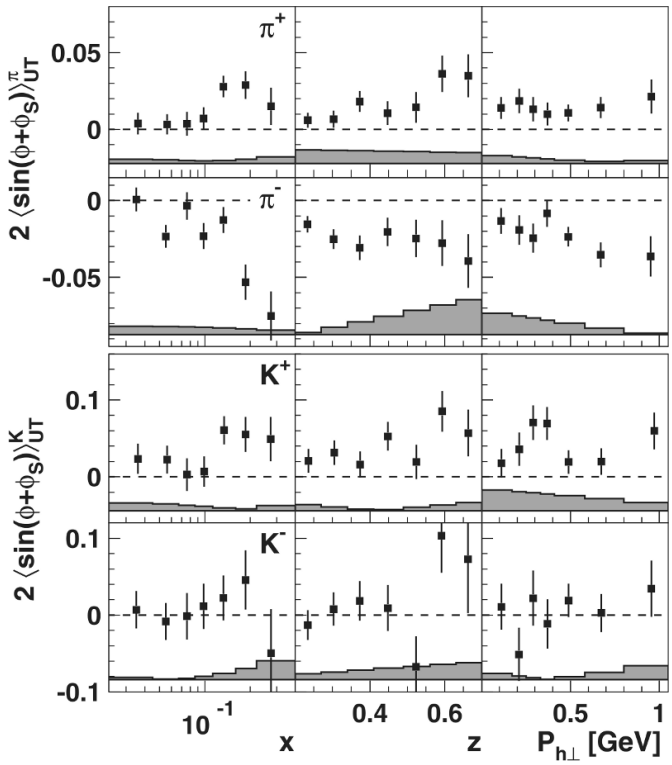

Figure 2.15.: Results of the Collins single hadron asymmetry of charged pions $\pi^{\pm}$ (1^{st} and 2^{nd} row) and kaons $K^{\pm}$ (3^{rd} and 4^{th} row) measured by the HERMES collaboration on a transversely polarized proton target [HERMES10].

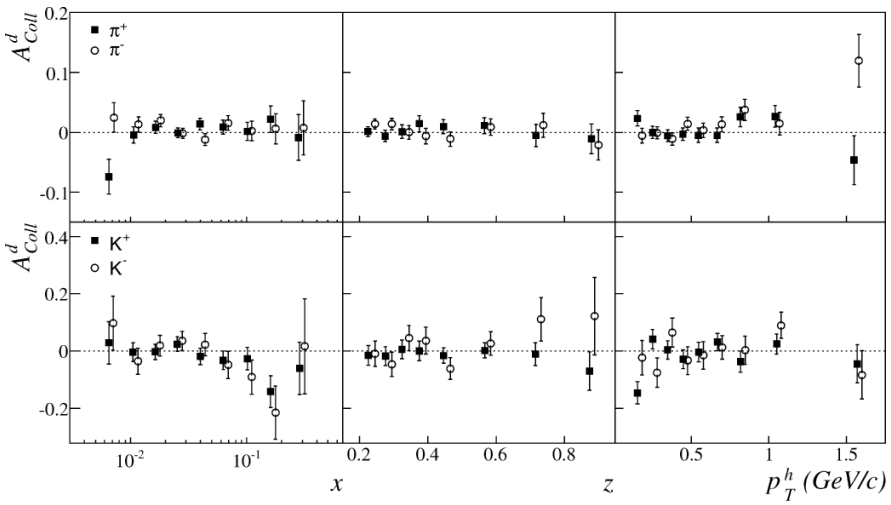

Figure 2.16.: Results of the Collins single hadron asymmetry of charged pions $\pi^{\pm}$ (1^{st} row) and kaons $K^{\pm}$ (2^{nd} row) measured by the COMPASS collaboration on a transversely polarized deuteron target from the 2003-2004 data [COMPASS09a].

The Collins asymmetries of charged pions and kaons from the data on a proton target collected in 2010 are shown in Fig. 2.17. The corresponding results of all charged hadrons $h^{\pm}$ from the data taken in the years 2007 and 2010 can be found in [COMPASS10b] and [COMPASS12a], respectively. Confirming the different sign for differently charged pions, also the amplitude of the signal is compatible with the one from HERMES. The Collins amplitude for charged kaons is small and compatible with zero within the uncertainties.
With the results shown above one can draw the conclusion that transversity distribution and the Collins fragmentation function are both nonzero, but since both experiments just measure a convolution of both, it is not possible to extract one of these two functions separately. Therefore complementary results of only e.g. the Collins FF are needed.
Collider experiments, like the BELLE experiment at KEK, Japan, can provide this information on the production of hadron-pairs from electron-positron annihilation. Figure A.1 shows the results of two different analyses of the same data set, where the Collins FF was found to be clearly nonzero with an increase of the amplitude as a function of z_1 and z_2 of the hadrons produced [BELLE08]. Results from the extracted transversity TMD PDF will be shown and discussed in Sec. 6.3.4.
The Jefferson Lab, Newport News, Hall-A experiment measured the Collins and Sivers asymmetries on a polarized ^{3}He target [A11]. The obtained amplitudes are small and compatible with zero within the uncertainties for both modulations.

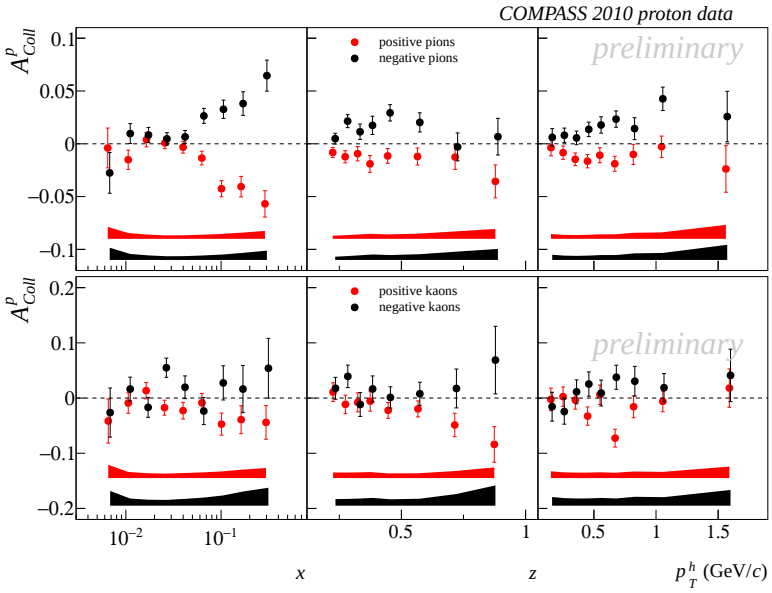

Figure 2.17.: Results of the Collins single hadron asymmetry of charged pions $\pi^{\pm}$ (1st row) and kaons $K^{\pm}$ (2nd row) measured by the COMPASS collaboration on a transversely polarized proton target from the 2010 data [COMPASS14d].

Further TMD asymmetries

Besides the Sivers and the Collins asymmetry, six additional single hadron azimuthal asymmetries arise in the SIDIS cross-section at next-to-leading order (see Sec. 2.3.3). Both experiments, HERMES and COMPASS, extracted them from their data sets on proton target and deuteron targets. The overall agreement between the results which were obtained is good. From the HERMES collaboration the asymmetries of identified hadrons are available [HERMES11], while for COMPASS the results are given for unidentified charged hadrons, which are mostly pions. Four out of the six asymmetries are small and compatible with zero within the uncertainties in the results of both experiments, these are [BDR02, BDG$^+$07]

1. $A_{LT}^{\cos\phi_S}$: related to the Worm-gear function $g_{1T}^{\perp}$,
2. $A_{LT}^{\cos(2\phi_h-\phi_S)}$: related to the Worm-gear function $g_{1T}^{\perp}$,
3. $A_{UT}^{\sin(2\phi_h-\phi_S)}$: related to the Pretzelosity $h_{1T}^{\perp}$ and Sivers $f_{1T}^{\perp}$ function,
4. $A_{UT}^{\sin(3\phi_h-\phi_S)}$: related to the Pretzelosity function $h_{1T}^{\perp}$.

The extracted asymmetries are shown in Figs. A.2 and A.3, from the COMPASS results from the 2002-2004 deuteron data and the combined 2007/2010 proton data.
However, the twist-two modulation $A_{LT}^{\cos(\phi_h-\phi_S)}$, which is related to the Worm-gear TMD PDF $g_{1T}^{\perp}$ shows a clear nonzero trend for positively charged hadrons at large x, as well as in the HERMES results [HERMES11]. A twist-three modulation was also found to be sizeable. The $A_{UT}^{\sin\phi_S}$ asymmetry, which is related to the transversity and the Sivers functions, is nonzero with an increasing trend in the x dependence for negatively charged hadrons [HERMES11, COMPASS14e].

2.4.2. The hadron-pair asymmetry

The first data on the asymmetry of dihadrons from SIDIS on a transversely polarized target was published by the HERMES collaboration in the year 2008 [HERMES08]. In Figure 2.18 these results of $\pi^+\pi^-$ pairs are shown as a function of the invariant mass of the pair M_{inv}, x and z. The mean value of the asymmetry is clearly nonzero with a positive sign. The coarse binning, which is applied due to available statistics, does not allow one to conclude any trend, but rather that the signal seems to be sizeable in the high M_{inv} range.
Also in this case, the first results of the COMPASS collaboration were extracted from the data set collected on the deuteron target. The published results of all charged hadron-pairs h^+h^- are shown in Fig. 2.19 (upper panel) [COMPASS12c]. The corresponding results of identified pairs are just available from a preliminary analysis, while a final re-analysis for publication is part of this thesis. In Figure 2.19 (lower panel) the results of the four possible pair combinations $\pi^+\pi^-$ (2^{nd} row), K^+K^- (3^{rd} row), π^+K^- (4^{th} row) and $K^+\pi^-$ (5^{th} row) are shown.

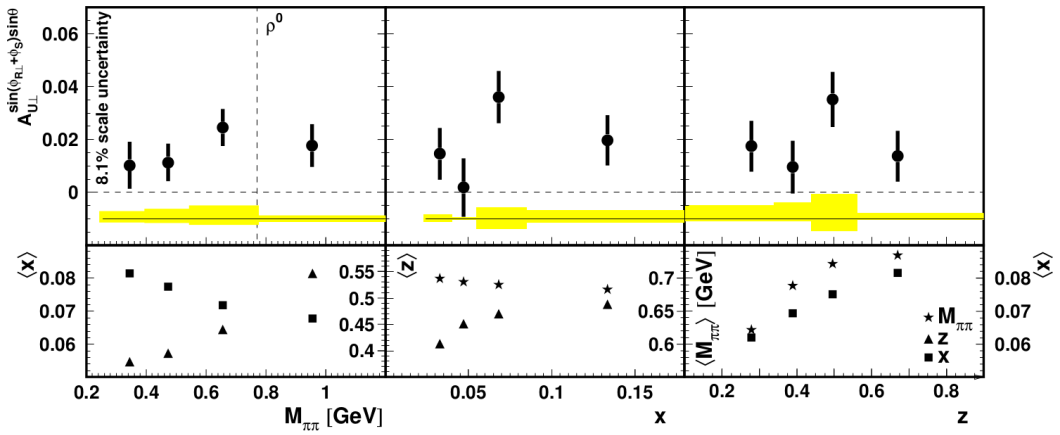

Figure 2.18.: Results of the hadron-pair azimuthal asymmetry of $\pi^+\pi^-$ pairs measured by the HERMES experiment (top panel) [HERMES08] as a function of $M_{\pi\pi}$, x, and z. The bottom panels show the average values of the variables that were integrated over.

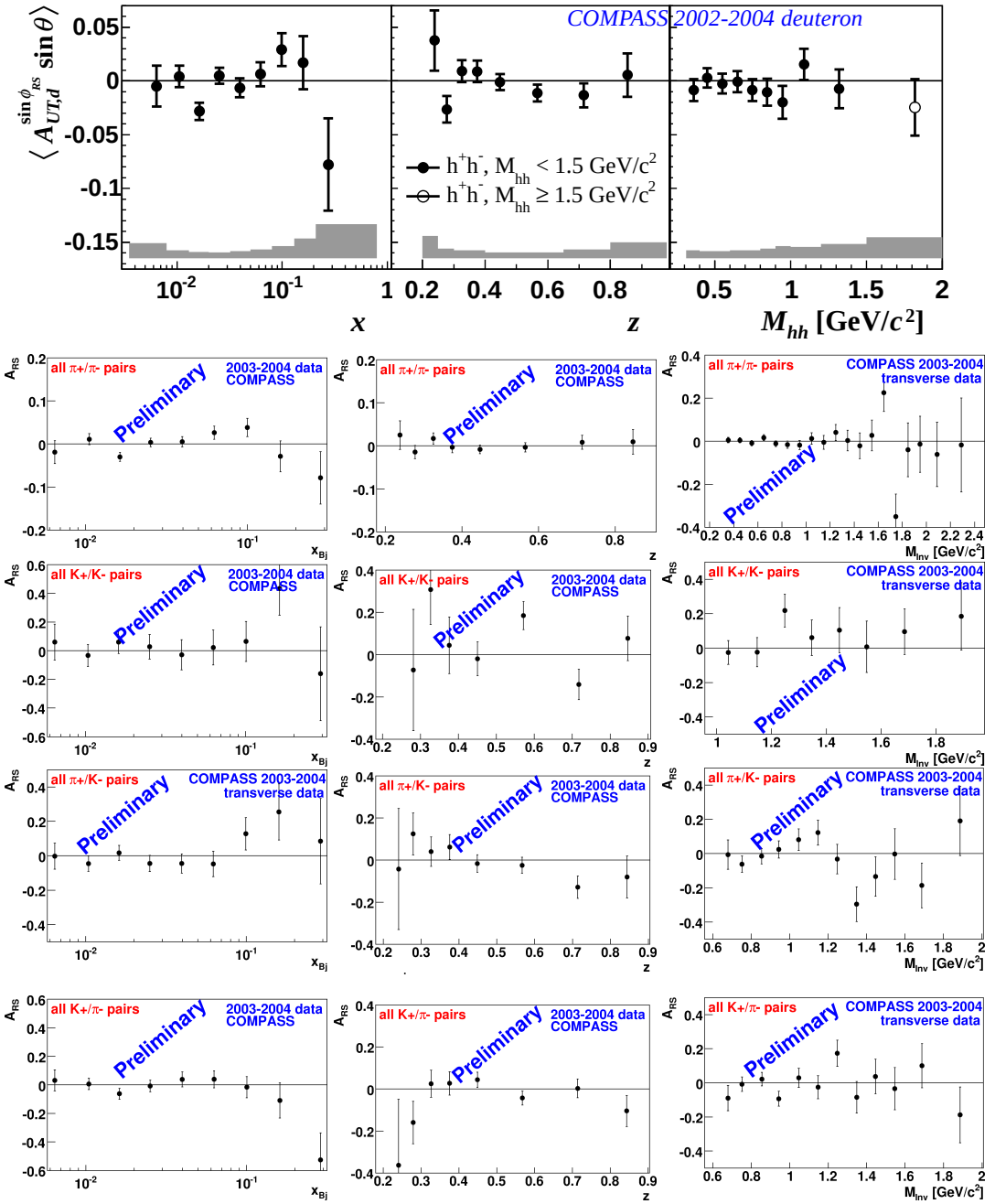

Figure 2.19.: Results of the hadron-pair azimuthal asymmetry measured by the COMPASS experiment on a deuteron target: all hadron-pairs h^+h^- (1^{st} row; 2002-2004 data) [COMPASS12c], identified hadron-pairs $\pi^+\pi^-$ (2^{nd} row), K^+K^- (3^{rd} row), π^+K^- (4^{th} row) and $K^+\pi^-$ (5^{th} row), all 2003-2004 data from [Vos08, Mas08].

All hadron-pair asymmetries on the deuteron target, unidentified and identified pairs are small and compatible with zero within the uncertainties. As in the single hadron case, this is interpreted as a an indication of equal magnitudes but different signs of the transversity PDFs of u and d quarks.
As COMPASS continued its transverse program with a proton target, the hadron-pair asymmetry could be extracted from the data collected in the year 2007, see Fig. 2.20 [COMPASS12c]. The nonzero trend measured by HERMES could be confirmed by these results. Thanks to the larger statistics in a broader kinematic range, for the first time a clear trend of increasing amplitudes with increasing x values was found. Moreover an indication of nonzero asymmetry amplitudes in the M_{inv} dependence between $500\,\mathrm{MeV}/c^2$ and $1\,\mathrm{GeV}/c^2$ is visible.
As described in Sec. 2.3.4 the hadron-pair asymmetry arises from a product of the transversity TMD PDF h_1 and the DiFF $H_1^{\sphericalangle}$. This allows an alternative approach, besides of the Collins asymmetry, to the extraction of h_1.
COMPASS already provides two key ingredients, the hadron-pair asymmetry on a deuteron and a proton target. While missing information for an extraction of the u and the d quark transversity, the DiFF has to be measured separately. As in the single hadron case the BELLE experiment did provide this data extracted from the production of two hadron-pairs in e^+e^- collisions [BELLE11]. The obtained results are shown in Fig. A.4, where the top panel shows the asymmetry arising from $H_1^{\sphericalangle}$ in bins of z of the second hadron as a function of z of the first hadron, and in the lower panel the corresponding results as functions of the masses of the hadrons produced.
A brief review of further possibilities to access the transversity and Sivers PDF is given in Sec. A.1.

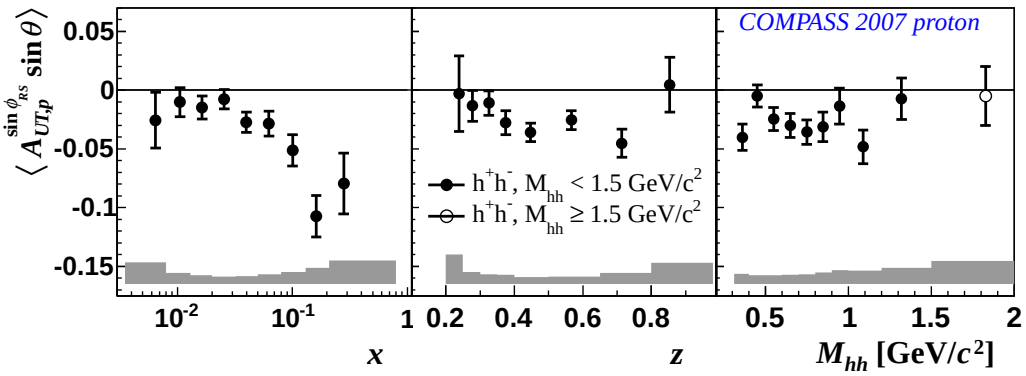

Figure 2.20.: Results of the hadron-pair azimuthal asymmetry measured by the COMPASS experiment extracted from the 2007 proton target data unidentified pairs h^+h^- [COMPASS12c].

3. The COMPASS experiment

The COMPASS (**CO**mmon **M**uon and **P**roton **A**pparatus for **S**tructure and **S**pectroscopy) experiment is a fixed target experiment at the external M2 beamline at the Super-Proton-Synchrotron (SPS) at CERN (**C**onseil **E**uropéen pour la **R**echerche **N**ucléaire) in Geneva, Switzerland. The beam line, which was also used by the former experiments EMC (**E**uropean **M**uon **C**ollaboration), NMC (**N**ew **M**uon **C**ollaboration), and SMC (**S**pin **M**uon **C**ollaboration), offers the unique possibility to switch between leptonic and hadronic probes. Therefore, the COMPASS experiment is designed for two purposes, the investigation of the nucleon spin by using a high energy muon beam and hadron spectroscopy by using hadron beams. The target region can be flexibly equipped with the corresponding target setups, namely a polarized frozen spin target or different nuclear targets, such as lead, copper and carbon. Downstream of the target a spectrometer structure, divided in two stages, follows. Each stage is equipped with a dipole magnet, SM1 and SM2, with a field strength of $1.0\,\mathrm{Tm}$ and $4.4\,\mathrm{Tm}$, respectively. The first section, called the "Large Angle Spectrometer" (LAS) covers particles with small momenta and large polar angles. The second stage with its stronger bending field, covering a phase space with high momenta and small scattering angles, is called the "Small Angle Spectrometer" (SAS). Downstream of each particular spectrometer magnet a variety of detectors for charged particle tracking is situated including muon-walls; furthermore a hadronic and an electro-magnetic calorimeter is available in each stage. In addition the LAS has a **R**ing **I**maging **Ch**erenkov Detector (RICH) at its disposal, which allows a precise particle identification [COMPASS07a]. The COMPASS experiment started its data taking in the year 2002 dedicated to the investigation of the nucleon spin with a longitudinally or transversely polarized deuterium (^{6}LiD) target off which a muon beam with a momentum of $160\,\mathrm{GeV}/c$ was scattered. A shutdown of the SPS followed in the year 2005, and the advantage was taken to upgrade the target by installing a new solenoid magnet with increased geometric acceptance and replacing the two-cell target with a three-cell target. In addition the RICH detector particle identification accurateness was improved by replacing the multi-wire proportional chambers in the central region with multi-anode photomultiplier including a new readout. Starting in the year 2006 the nucleon spin program was proceeded using a longitudinally polarized proton target and the running in the year 2007 was equally shared between this and the transversal polarization state. The long term measurements on the hadron spectroscopy took place in the years 2008 and 2009 to study the pion polarizability via Primakoff scattering and diffractive meson production. The measurement on the transversely polarized proton target was resumed in 2010 to increase the statistical precision, likewise for the longitudinal case in the year 2011. Finally the running period in 2012 had the aim to set the path towards the COMPASS-II program starting in late 2014, by performing a pilot run for the 2015

Drell-Yan measurement, see Chap. 7.2. One full year of data taking on deep virtual Compton scattering (DVCS) to investigate generalized parton distributions (GPDs) will follow, as well as another year dedicated to the study of chiral perturbation theory, via the measurement of pion and kaon polarizabilities and Primakoff Compton scattering [MM10].
This chapter briefly summarizes the content of [COMPASS07a], where the COMPASS apparatus has been introduced to the public, with an update to the 2010 data taking period. In addition more details on the scintillating-fiber hodoscopes are given, as modifications and upgrades of this detector types at the COMPASS experiment are also part of this thesis, see Sec. 7.2.

3.1. The polarized beam

The SPS beam time is partitioned in so-called super-cycles of 33 s to 39 s (for example 21.6 s in 2004) length during the 2010 running period of which the time is shared between the connected experiments and the LHC, see Figs. A.5 and A.6. The bunched beam of the SPS dedicated to the COMPASS experiment is extracted to form a flat top with almost constant rate by specialized septum magnets. This extraction time is called a spill, containing in average 2.4×10^{13} (1.2×10^{13} in 2004) protons and had a total length of 13 s with a flat top of 9.6 s in 2010 (4.8 s in 2004). This primary proton beam with a momentum of 400 GeV/c is guided onto a production target (T6) consisting of beryllium of 500 mm thickness. The majority of the secondary particles being produced there, pions with a small admixture of kaons (≈ 3.6 %) and others, are selected by an array of six acceptance quadrupoles and a set of three dipoles with a momentum band of up to ±10 % around a nominal momentum up to 225 GeV/c. During the passage of the 600 m long decay line, consisting of a series of focusing and defocussing (FODO[1]) quadrupoles, the particles of the secondary beam decay preferably into muons and muon neutrinos [PDG12]

$$\pi^+ \to \mu^+ + \nu_\mu \qquad (\text{BR } 99.98\,\%),$$
$$K^+ \to \mu^+ + \nu_\mu \qquad (\text{BR } 63.55\,\%).$$

The parity violation in this weak decay causes a natural polarization of the produced muons along their trajectory. The value of the longitudinally polarization depends strongly on the ratio between the muon and pion momenta, and is about 80 % at a muon momentum of 160 GeV/c, which is used for the measurements of the transverse spin asymmetries. Absorbers made of beryllium are used to stop the remaining hadron components, before the second 250 m long FODO transport line guides the muons to the surface level. A setup of three dipole magnets (B6), bending the beam back onto the horizontal plane at 100 m upstream of the target, is used together with six scintillator hodoscopes for the determination of the momentum of the muons, see Fig. 3.1. Three of these hodoscopes (BM01, BM05 and BM02) are grouped before the dipole magnets in front of two quadrupole magnets (Q29 and Q30) and the other three (BM03, BM06 and BM04) after Q31 and Q32. The ordering of the BMS planes is of historical reasons,

[1] The term FODO describes the setting of a beam line, where after a e.g. horizontally focusing quadrupole "F" and a drift distance "O" follows a horizontally defocussing quadrupole "D" and again a drift distance.

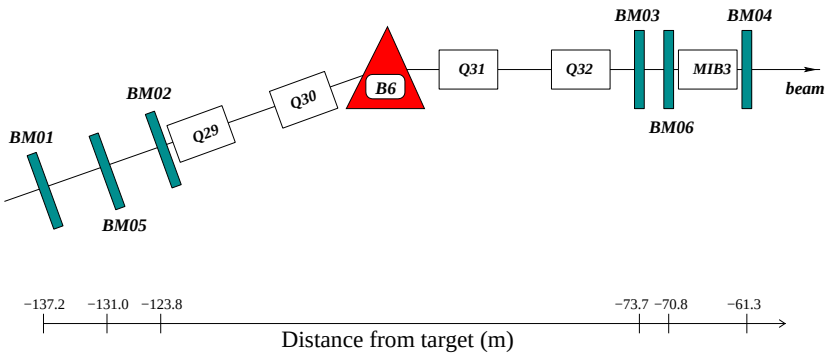

Figure 3.1.: Schematic view of the beam momentum station: BM01–BM06 indicate the BMS planes, Q29–Q32 are quadrupole magnets and B6 is an array of three bending magnets [COMPASS07a].

since BM01-BM04, which consist of horizontal scintillator strips, were already used in previous experiments [Muon81]. This existing setup was upgraded with two scintillating fiber hodoscopes, one between each pair, respectively, in oder to provide additional redundancy for the high beam intensity used by COMPASS. Both, the dimensions of the scintillator strips and of the fibers are chosen to stay below a particle flux per element (varying size) or fiber channel (2 mm diameter) of $3 \times 10^6\,\mathrm{s}^{-1}$ or $1 \times 10^7\,\mathrm{s}^{-1}$, respectively. A time resolution of ≈ 0.3 ns is achieved with a PMT readout. The momentum of each beam track can be calculated to a precision of $\leqslant 1\,\%$ with a reconstruction efficiency of $\approx 93\,\%$. Finally the beam is focused and steered on the target. The steering becomes necessary due to the dipole field of the target in transverse running. During the 2010 running period an average flux of $3.7 \times 10^7\ \mu/\mathrm{s}$, corresponding to $4 \times 10^8\ \mu/\mathrm{spill}$ was achieved.

3.2. The polarized target

Besides the polarization of the incoming muon beam, which comes naturally via parity violation in pion decay, the possibility of having the target material polarized is a key ingredient of the COMPASS experimental setup for the investigation of spin asymmetries. The full SIDIS cross-section (Sec. 2.3.2) contains terms with longitudinal and transverse polarization states of the target nucleus, thus the two frozen-spin targets used during the COMPASS measurements have the possibility to operate in both states. For the measurements on the deuteron target in the running periods of 2002 until 2004 a two-cell target, which incorporated several elements previously used by the SMC experiment [SMC99] was used, while, as already shortly mentioned, a complete new target system with three cells has been installed and operated from 2006 on. This new proton target has three main advantages, the angular acceptance increased to ± 180 mrad, while it was ± 69 mrad for the deuteron target. Furthermore the three-cell configuration allows

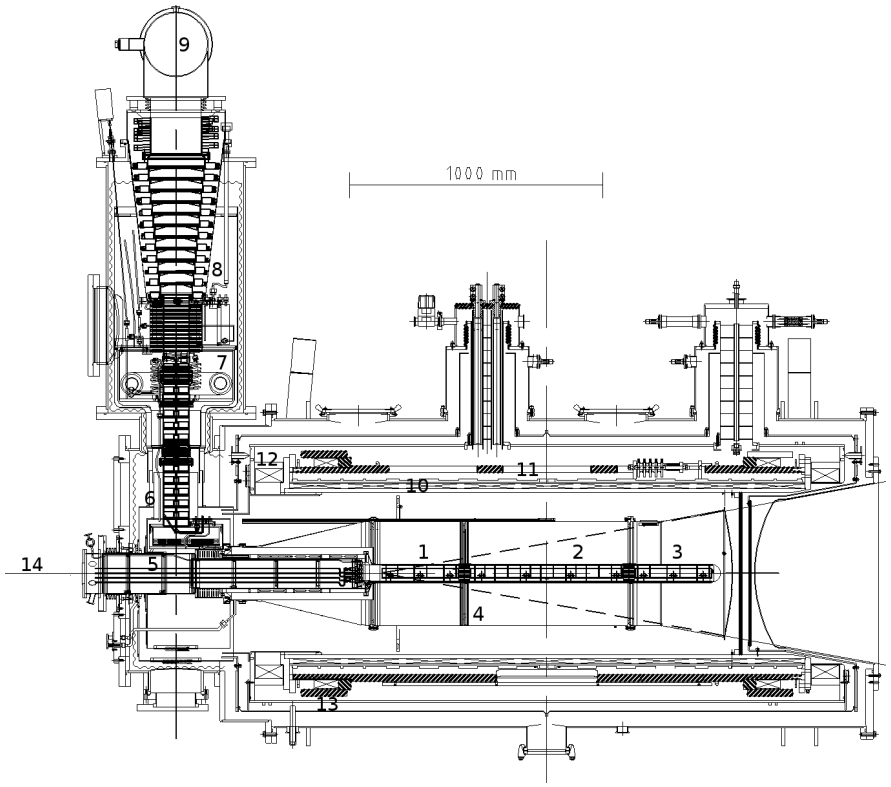

Figure 3.2.: Schematic view of the COMPASS polarized three-cell target [COMPASS07a]: 1–3: upstream, central and downstream target cell, 4: microwave cavity, 5: target holder, 6-9: ^{3}He-^{4}He refrigerator, 10: solenoid coil, 11 & 12: compensation coil, 13: dipole coil, 14: muon beam entrance (beam enters from the left).

for a more advanced cancellation of acceptance effects. The total length of the target cells was kept constant at 120 cm, but instead of two 60 cm long target cells separated by 10 cm, a middle cell with 60 cm length surrounded by two outer cells, 30 cm length each, all separated by 5 cm were installed, see Fig. 3.2. The volume of target material increased by 78 % since the diameter went up from 3 cm to 4 cm. The requirement of an isoscalar target material for the first three years of running, lead to the choice of deuterated Lithium-6 which allows for a high level of deuteron polarization of about 47 %. The fraction of polarizable material f, called dilution factor is ≈ 38 % for this target including the helium content in the target material volume. However, the proton target consisting of ammonia (NH_3), due to its azote constituent has a lower dilution factor of ≈ 15 %. On the other hand higher polarization values up to ≈ 90 % are reached.
Strong magnetic fields are necessary to build-up and to maintain the polarization of the target material by the method of Dynamic Nucleon Polarization (DNP) [Abr83]. Here the electron polarization is transfered to the nuclear spins through a microwave field, which requires paramagnetic centers created by e.g. irradiation, inside the material [Mei01]. In the longitudinal case a superconducting solenoid magnet creates a holding field of 2.5 T while microwave radiation at

material specific frequencies induces the polarization in the two cells. A dipole holding field of $0.42\,\mathrm{T}$ generated by a superconducting toroidal magnet is applied in the transverse mode. Besides of the strong magnetic fields the second key ingredient for a high value and a long decay time of the polarization is very low temperature. The ^{3}He-^{4}He dilution refrigerator cools the target material down to ≈ 60 mK via a chain of a ^{4}He liquid/gas phase separator, a ^{4}He evaporator and a ^{3}He evaporator, see Fig. 3.2.
In order to minimize the influence on the measured asymmetries of acceptance effects related to the origin coordinate of the primary vertex inside the target, the target polarization reversal is performed every five to seven days in the transversal mode by changing the microwave frequencies. The dipole field itself cannot be rotated since it bends the beam particles in contrary to the solenoid field, which is anticipated by a small offset in the incoming trajectory. Thus between every reversal the polarization has to be destroyed and rebuilt again.

3.3. Tracking detectors

The tracking system of the COMPASS beam telescope (upstream of the target) and spectrometer (downstream of the target) involves a large variety of detector types based on different principles to detect charged particles adapted to the specific requirements to the time and spatial resolution and the active area to be covered. A schematic overview on the COMPASS setup during the 2010 running is shown in Fig. 3.3.
The tracking stations, distributed over the entire length of the apparatus, are constructed to resolve possible ambiguities selecting coincidental hits of particles through several detector planes transverse to the beam direction. This principle is illustrated in Fig. A.7. To do this, at least three independent detector planes with different orientations are necessary, in most cases four or more planes are installed to have additional redundancy. The naming convention is the following: X and Y planes are segmented to measure the horizontal and vertical coordinate, additional layers called U and V are rotated clockwise and anticlockwise w.r.t. the X plane orientation. The choice of the detector type is mainly related to the expected flux of particles in the region to be covered, thus the tracking detectors can be categorized in three different radial distances to the beam axis:

Very small angle trackers (VSAT): The highest particle rates are found in the center of the muon beam to a radial distance of $\approx 3\,\mathrm{cm}$ with up to about 2×10^5 particles per second and mm^2. The track reconstruction of the incoming beam muons and the outgoing muons is important for the reconstruction of the primary vertex, in particular for the related kinematic quantities, see Sec. 4.3.2. Detectors made of scintillating fibers and silicon microstrip detectors fulfill the requirements listed above. A more detailed description of the different detector types is subsequently given.

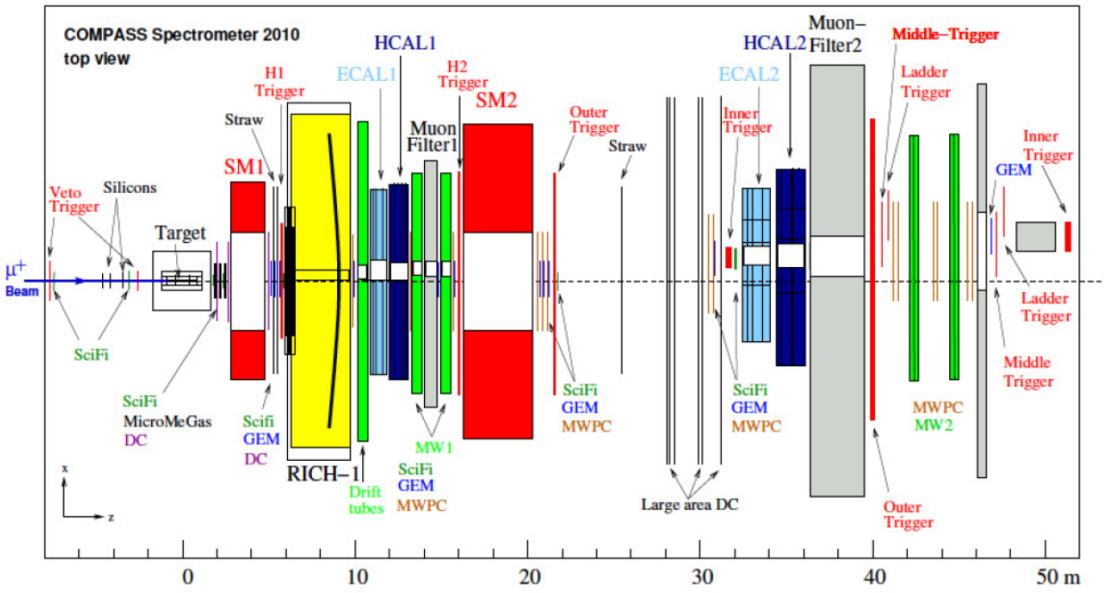

Figure 3.3.: Schematic top view on the COMPASS spectrometer in the 2010 running configuration [COMPASS07a](modified): The Z axis points in the beam direction, the X axis is the horizontal (ruling from right-hand to the left-hand side of the beam axis) and the Y axis the vertical (rising from the ground) axis in the laboratory frame.

Small angle trackers (SAT): With particle fluxes of about one order of magnitude lower then in the VSAT region, the so-called "small angle trackers" (SAT) cover a radial distance of $3-40$ cm around the beam axis. Their purpose is to detect particles with small scattering angles, thus their central region of 5 cm in diameter is deactivated or attenuated in its gain due to the high rates being caused by beam particles which have not interacted with the target material or have been scattered under very small angles. Gas filled micropattern detectors are deployed for this task, such as MicroMegas (**Micromes**h **Ga**seous **S**tructure) and GEM detectors (**G**as **E**lectron **M**ultipliers) which combine the requirements of a high rate capability and a good spatial resolution ($< 100\,\mu$m) with the advantages of being able to cover fairly large active areas while having a low material budget.

Large angle trackers (LAT): Low particle fluxes in combination with a large area to be instrumented characterize the "large angle trackers" situated more then 40 cm away from the beam center. Gaseous detectors are again the type of choice, this time with a slightly reduced resolution in time and space, but with active areas in the order of square meters. This is the domain of **D**rift **C**hambers (DC), straw tube chambers (STRAW) and **M**ulti **W**ire **P**roportional **C**hambers (MWPC). These detector types are commonly used in particle physics experiments since decades. Thus their technology is very well known, which inter alia allows for a reliable and cost efficient instrumentation of large areas w.r.t. to the types mentioned above.

3.3.1. Scintillating-fiber hodoscopes

The scintillating-fiber hodoscopes (SciFi) have the highest time resolution of all detectors of the COMPASS experiment with typical RMS values of a single plane between 400 ps in the central region and 300 ps in the low occupancy regions. Since they are constructed as stacks of overlapping fiber layers with a certain diameter, the spatial resolution is fully determined by the geometry, namely the pitch between the fibers and their diameter. A schematic view of the profile of a SciFi hodoscope is shown in Fig. 3.4, including the resulting signal distributions for different incident angles of particle crossing. In total ten SciFi stations have been operating in the 2010 running period. As a part of the beam telescope three stations were placed upstream of the target (FI01, FI15 and FI02). Together with two more stations right downstream of the target they are indispensable to provide informations in order to link the incoming muon with the track of the scattered muon. Furthermore FI01 and FI02 are also readout via scalers for the determination of the beam flux, which is important in the measurement of absolute cross-sections. In addition this time information of FI01 and FI02 is also used to link tracks reconstructed in the BMS in order to assign the correct momentum to the beam muons. To have additional redundancy for this task and to have the option to reduce the material budget in the region upstream of the target a recently developed station with reduced thickness, so-called "FI15", was installed for the 2010 running and from there on fully integrated in the data acquisition and track reconstruction, see Sec. 3.3.1. A similar arrangement of SciFi stations is situated around the second spectrometer magnet (SM2), including FI05, FI55 and FI06 upstream, and FI07 and FI08 downstream of it. Their purpose is to enable the reconstruction of scattered muon tracks in the beam region. Only FI08 has been placed outside of the beam to detect scattered muons with small scattering angles, which are leaving the spot of the remaining beam at this far downstream position. The size of the active area of the fiber layers, between $3.9 \times 3.9\,\mathrm{mm}^2$ and $12.3 \times 12.3\,\mathrm{cm}^2$, depends on the purpose and position inside the apparatus. An overview of their specifications can be found in Tab. A.3. The same applies for the used diameters of the fibers, which is 0.5, 0.74 or 1 mm, leading to a spatial resolution between 130, 170 and 210 µm increasing in beam direction. The light produced inside the scintillating material, which is of the type SCSF-78MJ fabricated by Kuraray Co. Ltd., is transmitted through clear fibers and then detected by 16-channel multi-anode PMTs (MaPMT) of the type H6568 by HAMAMATSU [BEE$^+$02, Nae02, Teu03, H$^+$04, Ado09, Sch09].

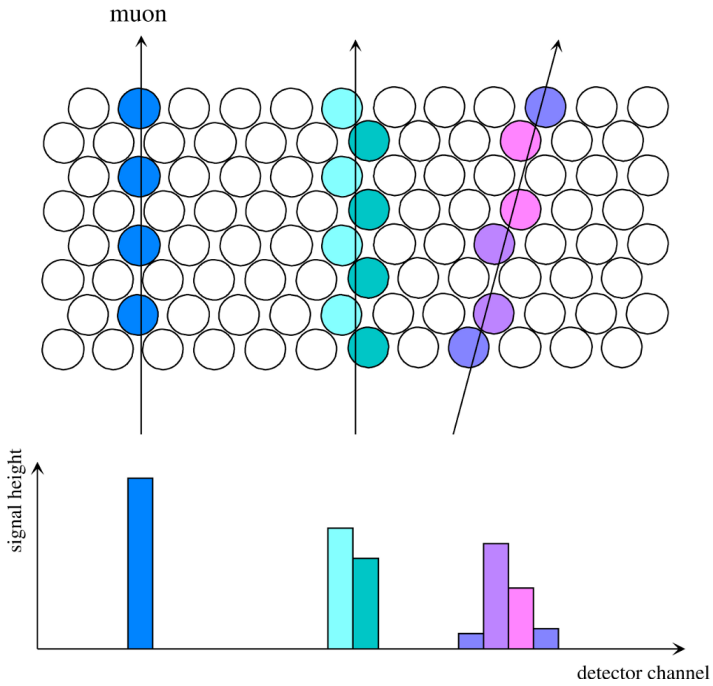

Figure 3.4.: Cross-section of a stacked hodoscope made of scintillating fibers (pointing out of the plane of projection) (top panel) and the channel-by-channel signal distributions for different incident positions and angles of an ionizing particle crossing the detector plane (bottom panel) [Teu03]

Beam Monitor/FI15

Most of the SciFi stations (except of FI55) used in the experiment since the beginning have a thickness in units of radiation lengths X_0 for electrons (for a definition of X_0 see [Leo94]) of about $2\,\%$. A new station, called FI15 with a reduced thickness has been intended as a replacement of one of the stations of the beam telescope in particular for the use during hadron beams, where the full setup of the existing stations exceeds the limit of tolerable material inside the beam. Its additional two planes contribute to a more precise determination of the incoming track parameters. This holds also true for the measurements with the muon beam, where the FI15 is situated between FI01 and FI02. The task of development and construction was performed by the groups of Bonn and Erlangen described to a large part in [Bra10], with the benefit of the experience from construction of station already in use [BEE$^+$02]. However, several modifications were applied in order to fulfill the new requirements, while maintaining basic characteristics such as the time resolution and efficiency.

Among them are the abdication of clear light guides, by attaching the scintillating fibers directly onto the entrance window of the MaPMT, in order to reduce light losses during the transmission and the passage through the welding point. Since the readout of the fibers is single sided the other one is mirrored with a MYLAR© foil resulting in a gain of $6.4\,\%$ more photons [Bra10]. Furthermore an advanced type of the MaPMT H6568 by HAMAMATSU called H6568-100 is used. They show an increased quantum efficiency of about 50 to $80\,\%$ w.r.t. the standard type H6568, achieved by an improvement of the photo cathode bi-alkali material.
The size of the new detector was chosen to be $4.5 \times 4.5\,\mathrm{cm}^2$ to cover a slightly larger area than FI01 and FI02, with two projections X and Y. Each plane consists of 64 channels, from two layers of fibers of $1\,\mathrm{mm}$ diameter. Tests have shown that this dimension is less sensitive to bending concerning its light guide properties than smaller diameters e.g. $0.75\,\mathrm{mm}$. Because the fibers have to be bent on a short distance to fit to the MaPMTs four-by-four channel pattern. The relative efficiency of FI15, determined by a track reconstruction using FI01 and FI02 gives good values of $\geqslant 97\,\%$.

3.3.2. Silicon microstrip detectors

To complement for a more precise measurement of the incoming tracks, since the SciFi detectors already have a very good time resolution but a limited spatial resolution (Sec. 3.3.1), Silicon Microstrip detectors are used. They provide a spatial resolution of $10\,\mu\mathrm{m}$ and a time resolution of about $2.5\,\mathrm{ns}$ with an active area of $5 \times 7\,\mathrm{cm}^2$. The silicon wafer itself was developed for another experiment [AMM$^+$00]. Its radiation hardness made it an excellent candidate for the high particle flux of the COMPASS environment, so they were developed further and assembled to complete detector stations [ADME$^+$03]. Each waver provides two-dimensional position information of the hits by a double sided readout via perpendicular readout strips on the front and in the back side. For the sake of redundancy and to be able to solve ambiguities (see Sec. A.7) each station consists of two sub-stations, at almost the position along the beam axis, where one is covering the X and Y projections and the second is rotated around this axis by 5° for additional U and V projections.

3.3.3. Micromegas detectors

The near-beam region of the SAT still sees a flux of scattered particles up to $450\,\mathrm{kHz/cm}^2$ in a fairly large radius around the beam. For this purpose so-called Micromegas detectors were enhanced to fulfill these requirements [T$^+$01, K$^+$03, M$^+$02]. The three MM stations consisting of four grouped planes (X, Y, U and V) cover an active area of $40 \times 40\,\mathrm{cm}^2$ with a dead zone of $5\,\mathrm{cm}$ diameter to repel the actual beam. Filled with a gas mixture of Ne/C_2H_6/CF_6 in a ratios of 80/10/10 the gaseous volume is separated by a metallic micromesh to create two sub-volumes, a conversion gap and an amplification gap.

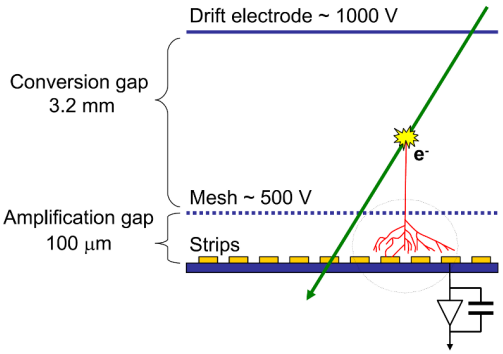

Figure 3.5.: Scheme of the principle of a Micromegas detector [COMPASS07a]

The ionization takes place in the conversion region where the produced electrons drift towards the mesh, after passing it a fifty time stronger electric field leads to the creation of avalanches resulting in a large number of electron-ion pairs, see Fig. 3.5. The positively charged ions cannot drift back to the cathode, however they are captured by the mesh. The collection of the electrons is effected by means of parallel microstrips with a pitch of 360 µm (420 µm in the outer region). This structure has two main advantages, one is the fast evacuation of ions and the second is the reduced transverse diffusion of the electrons, both together result in a high rate capability, which then reflects in a high average efficiency of $\approx 97\,\%$, a spatial resolution of 90 µm [B$^+$05] and a time resolution of 9.3 ns, whereas the thickness in radial lengths is just $0.3\,\%$ per plane.

3.3.4. GEM detectors

The second type of gaseous detectors in the SAT region are the GEM detectors, where again a gas filled volume is used to generate electron/ion pairs via ionization. In this case the multiplication of the electrons is taking place inside of micro-holes (70 µm diameter, $\approx 10^4$ holes per cm^2) in a 50 µm thin polyimide foil. A copper cladding on both sides of the foils shapes the applied electric field in a way that it is strong enough to create avalanches inside the holes volume (several 100 V across the foil) to extract them from the holes and to guide them to the next amplification stage [Sau97]. Three of these GEM foils, within a transfer gap of 2 mm between each of them, are placed inside the gaseous volume filled with a 7 to 3 ratio of Ar and CO_2 [ACD$^+$02, KWP$^+$04]. A schematic cross-section of a triple GEM detector and the configuration of the electric field inside and around the holes is shown in Fig. 3.6 (left panel). The readout is performed two-dimensionally by means of two sets of ≈ 800 strips with a pitch of 400 µm arranged in two layers perpendicular to each other, separated by a thin insulation layer (see Fig. 3.6 right panel). Thus two detectors, each $31 \times 31\,\text{cm}^2$ of this type, mounted inclined by $45°$ form one station with four projections. The material budget is in the same order as in the case of the Micromegas, at $0.4\,\%$ to $0.7\,\%$ of the radiation length. The efficiency calculated for all GEM detectors is $\approx 97.2\,\%$. The spatial resolution (70 µm with the complete GEM setup) is slightly better while the time resolution (12 ns) is slightly worse than for the Micromegas.

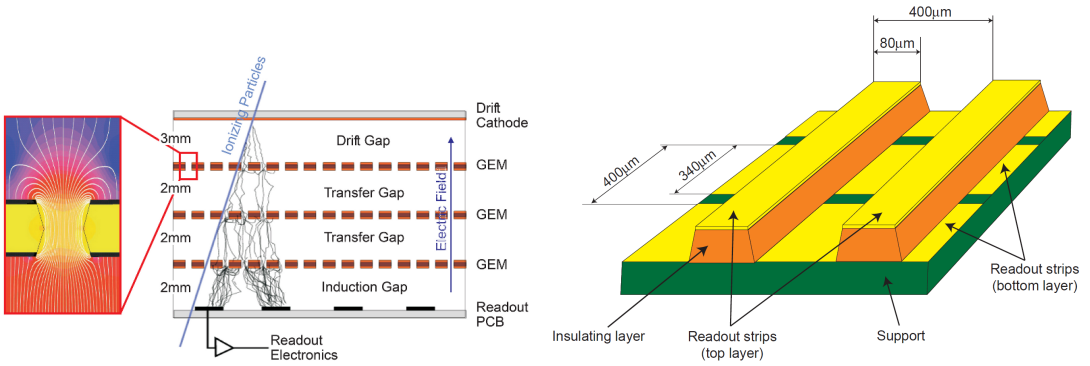

Figure 3.6.: Schematic cross-section of a triple GEM detector (left) and its two-dimensional readout structure (right) [COMPASS07a]

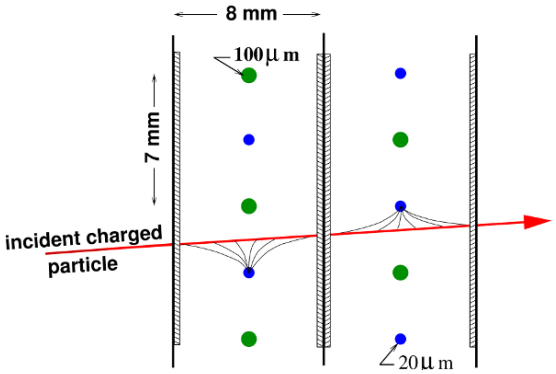

Figure 3.7.: Geometry of a DC (Drift chamber) detector with the sensitive wires (blue) and the potential wires (green), coated foils separate the gaseous volumes [COMPASS07a]

3.3.5. Drift chambers

Increasing the active detector area by an order of magnitude compared to the small area detectors, with $180 \times 127\,\mathrm{cm}^2$ the DC are particularly designed to cover the whole acceptance of SM1. A DC station consists of eight layers, with a total material budget of $0.32\,\%$ radiation length, where each inclination, X, Y, U $(20°)$, and V $(-20°)$ is covered by two layers. These layers, each has a gas gap of $8\,\mathrm{mm}$, are filled with a mixture of Ar/C_2H_6/CF_4 (45/45/10) and are separated by a $25\,\mu\mathrm{m}$ thick MYLAR© foil coated with $\approx 10\,\mu\mathrm{m}$ graphite. The electrons produced by ionization are collected by the sense-wires which alternate in an interval of $3.5\,\mathrm{mm}$ with the potential wires, see Fig. 3.7. Thus the drift cells dimensions of $8 \times 7\,\mathrm{mm}^2$ are optimized for a balance of the incident particle flux and the drift time of the electrons. With this setup an averaged spatial resolution of $\approx 270\,\mu\mathrm{m}$ after the track fitting for each wire layer is achieved, with a mean layer efficiency of $\geqslant 95\,\%$. The maximum hit rate per wire is achieved upstream of

SM1 at $800\,\text{kHz}$, caused by the low energy background which is bend away by the magnet. The actual beam spot is deactivated by a dead zone of $30\,\text{cm}$ diameter.
The drift chamber technique used for the DC detectors (see sec. 3.3.5) is applied on an even larger scale, called the large area DC [B$^+$76]. Some quantities were increased to adapt to a large active area of $500 \times 250\,\text{cm}^2$, such as the anode wire pitch to $4\,\text{cm}$ and the anode-cathode gap up to $1\,\text{cm}$. The diameters of the anode and cathode wires are the same as for the standard DC detectors, while the used gas mixture of Ar/CF_4/CO_2 with the ratio of 85/10/5 is different. The resulting increase in the spatial resolution, which was measured to be $0.5\,\text{mm}$, fulfills the requirements of the SAS. Again the employment of different inclinations is implemented.

3.3.6. Straw tube detectors

Straw tubes are a widely used detector type when large areas have to be instrumented, see also [BDD$^+$06] for a review. The tubes used at COMPASS are made of two layers of thin KAPTON© films glued onto each other, where the inner one is coated with carbon ($40\,\mu\text{m}$ thick) and the outer one with aluminum ($12\,\mu\text{m}$ thick). The anode wires consist of gold-plated tungsten and are of a diameter of $30\,\mu\text{m}$. The dead zone, in order to let the beam pass is realized by a hole of the size $20 \times 10\,\text{cm}^2$ by dividing the central straws into a lower and an upper part. A mixture of Ar/CO_2/CF_4 in the ratio 74/6/20 serves as the gas filling. Depending on the particles scattering angle, which is between 15 and 200 mrad, the straw tubes have an outer diameter of $6.14\,\text{mm}$ or $9.65\,\text{mm}$. Each straw station consists of three detector with two horizontal, two vertical and two inclined planes ($10°$) to resolve ambiguities, where the last two have an active area of $4567 \times 3160\,\text{mm}^2$ and the horizontal one $3570 \times 4117\,\text{mm}^2$. Thus the number of readout channels or single tubes per plane is 892 or 704, respectively. The probability that a charged particle is detected in one of the two planes with the same orientation is higher than $99\,\%$. The spatial resolution is of the same order as of the Drift chambers.

3.3.7. Multi wire proportional chambers

MWPCs provide another possibility to instrument large areas, such as the COMPASS SAS. The main difference w.r.t. the STRAW or DC detectors is that multiple layers of wires are embedded into a single gas volume, while the gas mixture is the same as for the STRAWs. Three different layouts of MWPC are used, common to all is the wire diameter of $20\,\mu\text{m}$, the wire pitch of 2 mm and the gap of $8\,\text{mm}$ between the anode and the cathode. What distinguish them is the the active area ($178 \times 120\,\text{cm}^2$ or $178 \times 90\,\text{cm}^2$), the number of wire layers per chamber (2, 3 or 4) and therefore the number of different inclined layers. Further details can be found in [COMPASS07a]. The residual distribution of the track, evaluated with all detectors but the MWPC and then searching for the corresponding hits in the MWPCs has a RMS of $1.6\,\text{mm}$ with an efficiency larger than $98\,\%$.

3.4. Particle identification

Even for inclusive DIS a clear identification of the scattered muon is of great importance. Whether the muons are already detected by the COMPASS tracking detectors (Sec. 3.3) or not, the muon wall system (Sec. 3.4.3) combined with hadron absorbers gives a clear proof of a charged particle being a muon or not. Both spectrometer parts of COMPASS, the LAS and the SAS possess such a medium resolution tracking detector (MW1 and MW2) each with a hadron absorber in front of it. In SIDIS reactions the produced hadrons, or at least some of them, have to be detected and their momenta have to be measured. Moreover a precise identification is aspired. Therefore the first spectrometer stage is equipped with a RICH detector, see section 3.4.1. The energy of the primarily or secondarily produced electrons, photons and hadrons is measured in electro-magnetic (ECAL1 and ECAL2) and hadronic (HCAL1 and HCAL2) calorimeters (see Sec. 3.4.2 and Sec. 3.4.2), available in each spectrometer stage.

3.4.1. Ring-imaging Cherenkov detector (RICH)

P.A. Cherenkov discovered and gave an interpretation of the observation that when certain liquids are irradiated by gamma rays a weak visible light is produced inside of them [Cer34]. This now called Cherenkov effect occurs when a particle travels through a medium with a velocity larger than the velocity of light in that medium. The observed emission of photons is not arbitrary, but occurs in a cone symmetric way. The opening angle θ_C of the cone, the Cherenkov angle, is then given by

$$\cos\theta_C = \frac{1}{\beta \cdot n}, \tag{3.2}$$

where n is the refractive index of the medium and $\beta = v/c$. From the measured Cherenkov angle θ_C, in a gaseous environment with known n, and the momentum of a particle determined inside the spectrometer, the particle type can be identified by calculating its invariant mass.
The basics of **R**ing-**i**maging **Ch**erenkov detector (RICH) are described in [YS94]. The COMPASS RICH detector, more precisely RICH-1 since it is located in the LAS, is designed to cover the whole angular acceptance [ABB$^+$05], i.e. ± 250 mrad in the horizontal and ± 180 mrad in the vertical plane. Its gas radiator vessel has a length of 3 m, determined by balancing the quest of a sufficient number of produced Cherenkov photons and minimized material budget in the spectrometer acceptance. The total volume of $80\,\mathrm{m}^3$ is filled with C_4F_{10} as a radiator gas, which has an $n-1$ of $\approx 1.53 \times 10^{-3}$ depending on the particles momentum. The refractive index is adapted to the energy range of the COMPASS experiment and allows a separation of pions, kaons and protons starting from their momentum thresholds at $2.5\,\mathrm{GeV}/c$, $9\,\mathrm{GeV}/c$ and $17\,\mathrm{GeV}/c$, respectively. The upper momentum threshold is given by $50\,\mathrm{GeV}/c$. The detection of the produced Cherenkov photons is accomplished by a two spherical mirror surfaces, which reflect and focus the photons on an array of detectors outside the LAS acceptance.

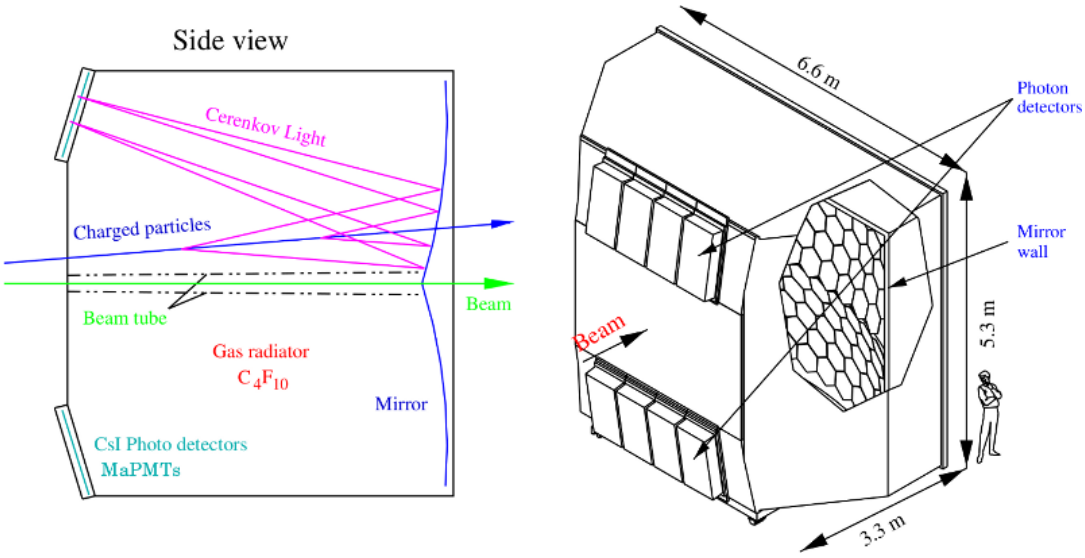

Figure 3.8.: The RICH at COMPASS: principle (left panel) and artistic view (right panel) [COMPASS07a]

The mirror substrate is a borosilicate glass of 7 mm thickness, corresponding to $\approx 5.5\,\%$ of radiation length coated with a refractive layer of aluminum (80 nm) with a reflectance in the range of $83 - 87\,\%$. Until the 2004 running the readout was entirely done by Multi Wire Proportional Chambers with CsI photo-cathodes. An upgrade was performed in 2005 in order to reduce the uncorrelated background signals, where the central region (see also Sec. 4.3.5) was replaced by 576 Multi-Anode Photomultipliers with a time resolution better than 1 ns. Details on this can be found in [AAA$^+$08a]. Figure 3.8 shows the principle (left panel) and artistic view (right panel) of the COMPASS RICH-1 detector. Figure 3.9 shows typical event pattern of hadron-generated Cherenkov rings, which is taken as the input for a likelihood fitting procedure for pattern recognition to provide certain likelihood values from which the particle type can then be determined. For further details on the pattern recognition see [AAA$^+$08b] and for the particle type determination from likelihood values for the used running periods see Sec. 4.3.7.

RICH Wall

The RICH wall is a large size tracking detector positioned between the RICH and the first electro-magnetic calorimeter, which is used for the reconstruction of the trajectory of particles which have crossed the RICH. Not only the assignment of tracks to their Cherenkov cone is improved, but it also serves as a pre-shower for the upstream ECAL1. The layout is a commonly used sandwich buildup of eight alternating layers made of stacks of steel and lead plates with **M**ini **D**rift **T**ubes (MDT, see Sec. 3.4.3) inbetween.

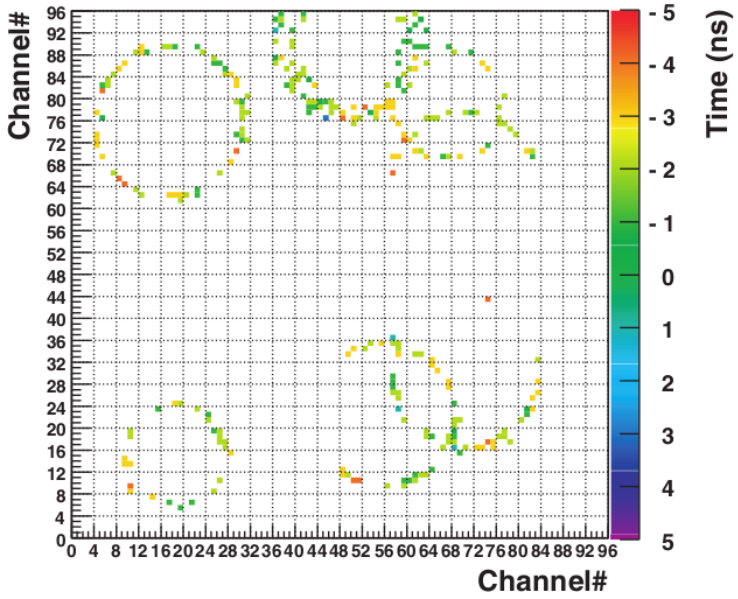

Figure 3.9.: Hadron-generated Cherenkov rings detected in 2006, seen in the on-line single event display [AAA$^+$08a]

3.4.2. Calorimeters

Although the data collected by the electro-magnetic and hadronic calorimeters are not used in this analysis a short overview of the devices will be given since consideration and first checks are currently done for the analysis of asymmetries from hadron-pairs which contain neutral pions. In each stage the corresponding HCAL is positioned directly after the corresponding ECAL, which are then followed by the muon filters with their hadron absorbers.

Electro-magnetic Calorimeters

What all detectors which were discussed up to now have in common is the ambition to minimize the material budget brought by them into the acceptance of the spectrometer. The picture changes if one wants to detect photons, i.e. from the decay of neutral pions, or to identify electrons. The aim is to have enough radiation length of material so that incoming high energy photons or electrons initiate electro-magnetic showers, which then produce Cherenkov light inside a high n medium. An array of 2973 lead glass blocks of $38 \times 28 \times 450\,\mathrm{mm}^3$ is chosen for this purpose e.g. in ECAL2, previously used in the GAMS-4000 spectrometer [LAPP81, LAPP86a, LAPP86b]. The produced light is guided inside the glass block to a PMT, see Fig. A.8. Since the amount of light is proportional to the energy deposited (linearity is better than $1\,\%$), e.g. the two γ coming

from a π^0 decay can be identified. The energy resolution $\sigma(E)/E$ and the spatial resolution $\sigma(x)$ were found to be $5.5\,\%/\sqrt{\frac{E}{\mathrm{GeV}}} \oplus 1.5\,\%$ and $6\,\mathrm{mm}/\sqrt{\frac{E}{\mathrm{GeV}}} \oplus 0.5\,\mathrm{mm}$, respectively. ECAL1 was added in the year 2005 to the COMPASS spectrometer, its layout is more advanced but the principle remains the same, details can be found in [Kur07].

Hadronic Calorimeters

With the hadronic calorimeters the amount of material is further increased to almost fully absorb hadrons and electrons in the energy range e.g. in the case of HCAL1 of 10 to 100 GeV. Again an array of calorimeter modules is used, not with a continuous material, but with a sandwich structure of alternating iron and scintillator plates. In this way the HCAL1, consisting of 480 calorimeter modules of $146 \times 142 \times 1010\,\mathrm{mm}^3$ reaches a thickness of 4.8 nuclear interaction lengths. The 220 modules of HCAL2 have dimensions of $200 \times 200 \times 1080\,\mathrm{mm}^3$ resulting in a nuclear interaction length of five for pions and seven for protons. Showers of secondary particles are created in the high Z material, here iron, when a hadron passes it, which then produce a light signal in the scintillators. A scheme of these modules showing how the light is read out by fibers from the scintillator plates is shown in Fig. A.9. The iron plates have a thickness of 20 mm for HCAL1 and 25 mm for HCAL2, while the scintillator plates are 5 mm in both cases [GKK$^+$06]. The normalized energy resolution $\sigma(E)/E$ for e.g. pions can be parameterized for HCAL1 as $(59.4 \pm 2.9)\%/\sqrt{\frac{E}{\mathrm{GeV}}} \oplus (7.6 \pm 0.4)\,\%$ and for HCAL2 as $(66/\sqrt{\frac{E}{\mathrm{GeV}}} \oplus 5)\,\%$.

3.4.3. Muon walls

A precise muon identification is important for the clear distinction of the scattered muons coming from the primary vertices from other muons or particles. This is a crucial task not only in the already realized SIDIS measurements but also for future investigations on the Drell-Yan process, see Sec. 7.2. Since COMPASS is a two-stage spectrometer, a detector system is installed in each stage, LAS and SAS, called muon wall 1 (MW1) and 2 (MW2) respectively. Both stations consist of a hadron absorber with a set of tracking station upstream and downstream of the absorbers. Both stations rely on gaseous wire detectors in different appearances, while the absorber of MW1, called Muon Filter 1 is a 60 cm thick iron wall and Muon Filter 2 is made of 2.4 m thick concrete. In the dimensioning of the active area, the corresponding acceptance was taken into account, so MW1 has an active area of $\approx 4800 \times 4100\,\mathrm{mm}^2$ and MW2 of $\approx 4500 \times 2000\,\mathrm{mm}^2$. MW1 uses modified plastic streamer tubes with fully metallic cathodes working in proportional mode [I$^+$83, Bus88]. The gas mixture used is Ar/Co_2 in a ratio of 7/3. The gold plated tungsten wires with a diameter of 50 µm are tensed in the center of cells of a comb extrusion made of aluminum.

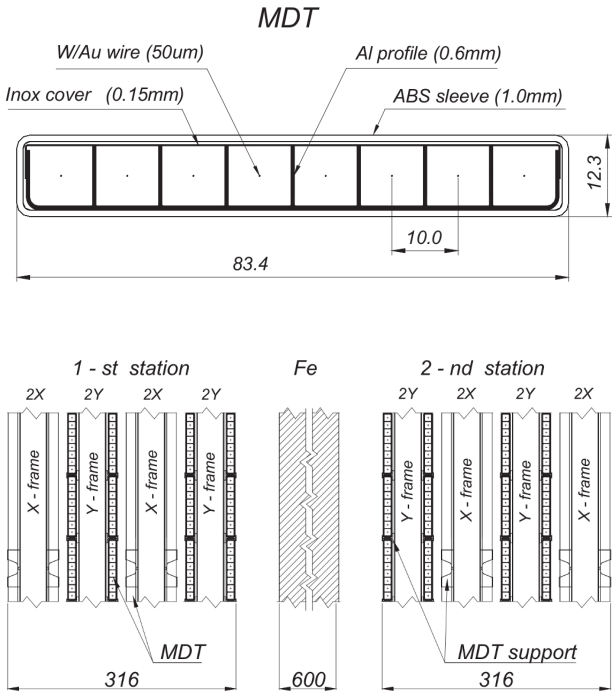

Figure 3.10.: Cross-section of a MDT module (top panel) and schematic cross-sectional view of MW1 (bottom panel), all dimensions in mm [COMPASS07a]

Each of these MDT (Mini Drift Tube) modules has eight of these cells, a cross-section is shown in Fig. 3.10 (top panel). The wire pitch is chosen to be $10\,\text{mm}$. Together with the setup of in total eight planes (four at each side of the iron wall) of MDTs in two projections (X and Y) this corresponds to a spatial resolution of $10/\sqrt{12}\,\text{mm}$. A schematic cross-section of the whole MW1 system is shown in Fig. 3.10 (bottom panel). The overall efficiency was measured to be $\approx 91\,\%$, more details are given in [A$^+$07b, A$^+$07a].
The tracking detectors of MW2 are drift tubes, which were originally designed for the D$\varnothing$ experiment [BEG$^+$89]. Upstream and downstream of the Muon Filter 2 six layers of drift tubes are mounted with a horizontal, a vertical and an inclined orientation. Two layers with the same incline make up one double layer, stacked in a similar way such as the scintillating fibers in the SciFi stations, see Fig. 3.4. The diameter of the stainless steel tubes is $30\,\text{mm}$. This implicates a wire pitch in a double layer of $16.75\,\text{mm}$, the total spatial resolution of MW2 was measured to be in the range of 0.5 to $0.9\,\text{mm}$. The gas mixture is chosen to be Ar/CH_4 in a 3 to 1 ratio. Finally the overall efficiency was measured to be $\approx 96\,\%$.

3.5. The trigger system

The trigger system of COMPASS is designed with respect to the kinematic characteristics of its physics program. The aim is to provide a readout signal to the front-end electronics of the detectors combining a very fast decision time with a low dead time. Again the high rate environment is the challenging issue here.
In order to fulfill these requirements various sets of scintillator hodoscopes are placed inside the spectrometer depending on different Q^2 ranges. Fig. 3.11 shows the location of these hodoscopes of the triggers called "inner" (IT), "middle" (MT), "ladder" (LT), and "outer" (OT) and the veto stations upstream of the target. For more details see [BBH$^+$05]. The coverage of the trigger sub-systems in a two-dimensional plane of y and Q^2 is shown in Fig. 3.12. A minimum cut on $Q^2 > 1\,(\mathrm{GeV}/c)^2$ defines the DIS region and thus is the lower limit of the data used in this analysis (see Sec. 4.3.1). The main trigger elements to cover this region are the MT, OT, and LT where the muon scattering angle in the non-bending plane is measured and compared with coincidence matrices to ensure that the muon is coming from the target region. A schematic view of this logic is shown in Fig. 3.13. The coverage of the high Q^2 range was based on a calo trigger, until in 2010 (inbetween P5 and P6) additional hodoscopes named H1 and H2 were installed to improve efficiency and time resolution. This trigger called LAST (**L**arge **A**ngle **S**pectrometer **T**rigger) extends the Q^2 range of all hadron-pairs up to a mean value of $23.0\,(\mathrm{GeV}/c)^2$ in the highest x bin in the case of the hadron-pair analysis, compared to $22.6\,(\mathrm{GeV}/c)^2$ in the 2007 data (see Tab. A.20 and Tab. A.15). H1 is placed directly upstream of the RICH and the second one downstream of Muon Filter 1. A detailed study of the performance of the LAST trigger in the running period of 2010 can be found in [BP10]. A detailed comparison on the performance of the whole COMPASS trigger system in the running periods of 2007 and 2010 can be found in [NK12], where also the high efficiencies of $\approx 97\,\%$ of the hodoscopes are evaluated. The overall time resolution is in the range of 0.5 to 1 ns depending on the size of the hodoscopes elements and the required coincidence with the calorimeter signals.
In order to avoid tracks from the halo of the beam causing wrong trigger signals a system of veto hodoscopes is placed upstream of the target. Each of them has a beam hole of 4 cm in diameter adapted to the dimensions of the target cells. A hit in already one of the vetos is enough to reject the track and thus the whole event, shown in Fig. A.10. The absolute purity of the trigger signals ranges from 15 to $35\,\%$ depending on additionally requested (anti-)coincidences with the calorimeter trigger and/or the veto system, which are both not described here, see [COMPASS07a] for more details.

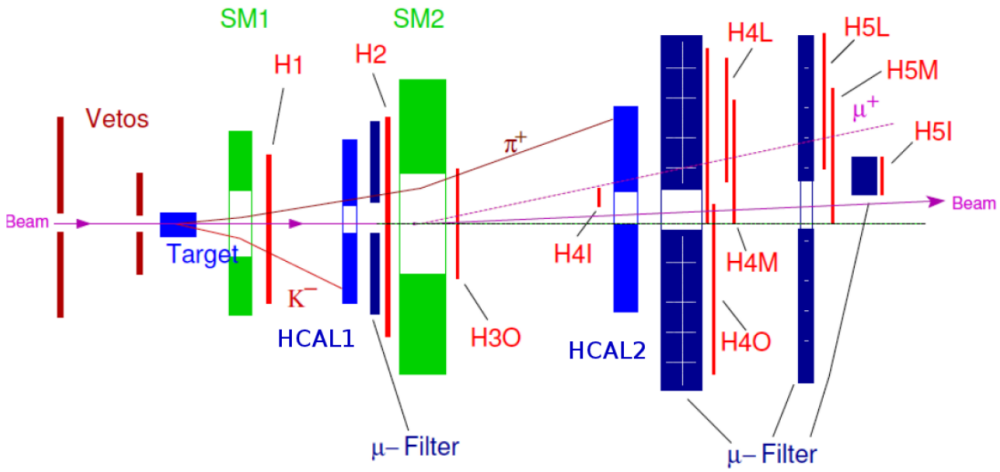

Figure 3.11.: Schematic view of the COMPASS trigger components: IT (H4I & H5I), MT(H4M & H5M), LT (H4L & H5L), OT (H3O & H4O), LAST (H1 & H2), Vetos and hadronic calorimeters [COMPASS07a].

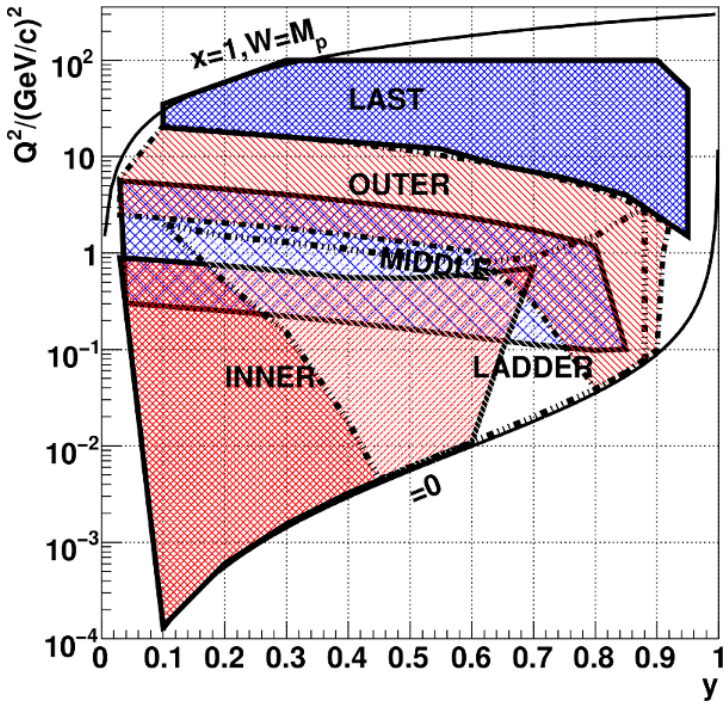

Figure 3.12.: The kinematic coverage in y and Q^2 for the trigger sub-systems. The two lines, namely $x = 1$ & $W = M_P$ and $\theta = 0$ show the kinematic limits of elastic scattering and forward scattering [COMPASS07a](modified).

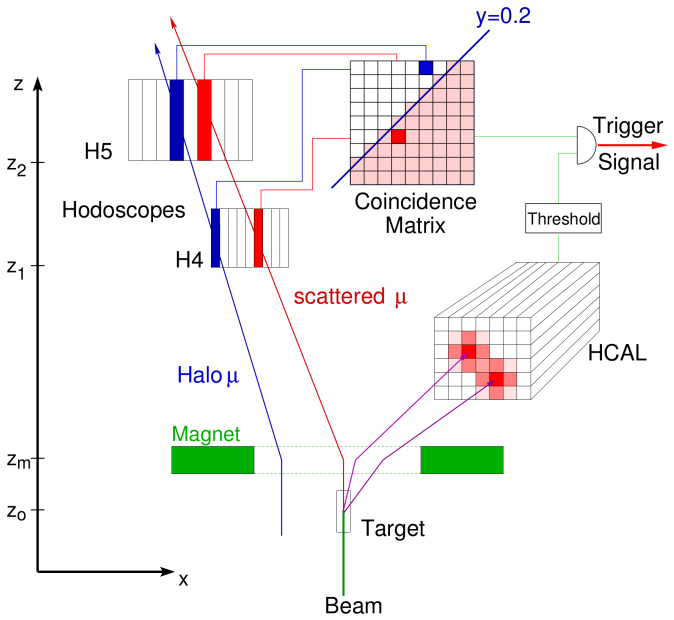

Figure 3.13.: Schematic view of the COMPASS trigger for quasi-real photoproduction with high energy loss. A coincidence of a calorimeter threshold signal and hodoscopes signal is required. Where the hodoscopes signal is derived from a coincidence matrix of two hodoscopes H4 and H5 separating events with vertex inside the target from halo muon tracks [COMPASS07a].

3.6. Data acquisition (DAQ) and track reconstruction

With the large number of more than $\approx 0.25 \times 10^6$ detector channels to be readout, the COMPASS Data Acquisition (DAQ) has to deal with a large amount of data. The triggered good events (see Sec. 3.5) come at a rate of ≈ 10 kHz during the 9.6 s flat top of the beam extraction. The aim of the developed DAQ system was to avoid losses due to additional DAQ dead times. Therefore the design scheme is a pipeline, shown in fig. 3.14, starting nearby the physical detectors with a digitalization of the analog detector outputs by Front-End (FE) boards. The digital signal is then transfered via fast links to modules called CATCH (**C**OMPASS **A**ccumulated, **T**ransfer and **C**ontrol **H**adware) and GeSiCA (**GE**M and **Si**licon **C**ontrol and **A**cquisition) which already build local sub-events for a certain time window provided by the **T**rigger **C**ontrol **S**ystem (TCS). One CATCH module can combine the data from up to 16 front-end cards. An optical link module (S-LINK [vdB97]) with a maximum bandwidth of 160 MB/s transfers the data to the Readout Buffers (ROBs) were the data arriving during the spill is stored in buffer cards still on the level of sub-events. A TCS signal is distributed from the TCS down through all stages to the FE boards for a precise time synchronization.

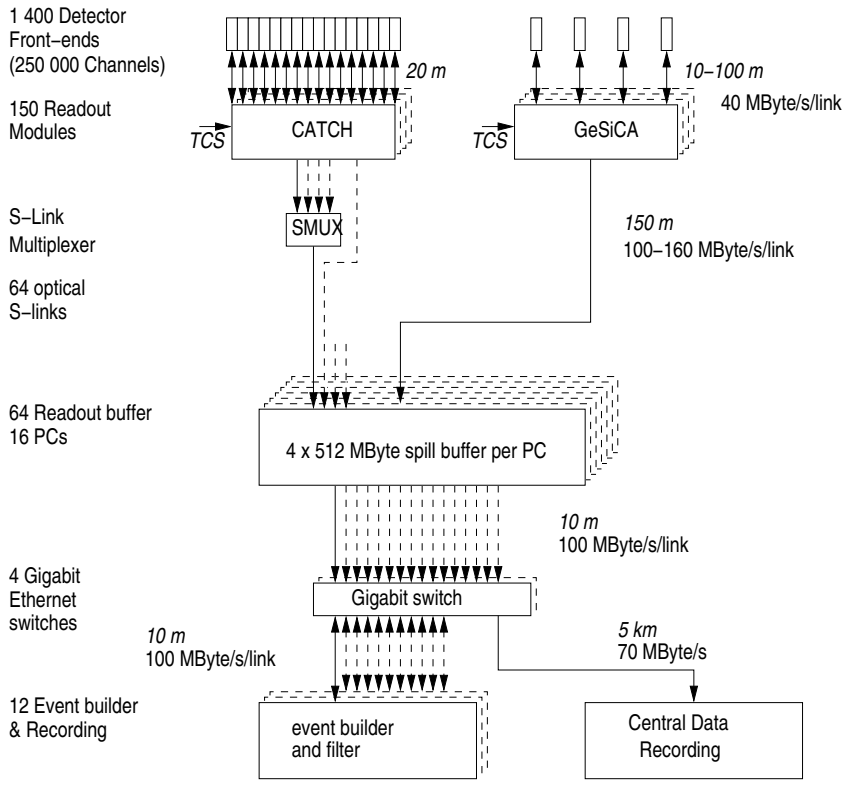

Figure 3.14.: General architecture of the COMPASS DAQ system. The data from the detectors is digitized in the front end cards. Then the readout modules named CATCH and GeSiCA combined the data. During the spill it is buffered before complete events are assembled by the Event builders. The final storage place of the files containing the collected events is the CERN computer center [COMPASS07a].

Since a complete super-cycle of the SPS machine takes approximately $40\,s$ the data collected during the spill of 9.6 s can be processed during the longer off-spill period by the Event Builders (EB). These machines combine the local sub-events to full events with the complete information of all detectors. In this way an access to whole events is already possible a few seconds after it has been recorded. As a storage unit so-called "chunks" are created with a total size of 1 GB containing the events with an average size of 45 kB. Gigabit switches provide a fast connection between the EBs, the ROBs and the CERN Computer Center, where the final chunks are transfered to, in order to be stored on the tape system CASTOR (**C**ERN **A**dvanced **STOR**age system). Currently a new Readout module with advanced feature is developed and has been tested during the 2012 running by the Freiburg group. It is specially designed for high rate applications, up to several MHz for each of its 128 channels at a time resolution of ≈ 93 ps. This will be important in particular for the measurements which are scheduled for the COMPASS-II program, see Sec. 7.2. A detail review of this project can be found in [BBF$^+$13].

3.7. Event reconstruction

The data written on tape is not ready to be used fully for the extraction of the parameters of physical processes, such as particle tracks, their charges and vertex positions. A dedicated software called CORAL (**CO**mpass **R**econstruction and **A**na**L**ysis) take the hit information from the various detector planes and tries to fit straight particle trajectories inside these patterns. This is done in different inclinations specified by the orientations of the different detector planes, at first in the sections of the spectrometer where no magnetic field from the magnets SM1 and SM2 is present. Then the recognized straight tracks are connected with curved sections by a bridging mechanism. After this, intersections of the tracks are identified in the three-dimensional space, which are then marked as vertices. The resulting fully reconstructed events are then stored in ROOT trees in a format called "mini Data Summary Tapes" (mDST), with a reduction in the amount of data at a factor of 100. This whole procedure is described in an early COMPASS note [BGKW04], however, development is continuously ongoing.
For the final analysis of physical processed a second Software called PHAST (**PH**ysics **A**nalysis **S**oftware and **T**ools) was developed which makes use of the ROOT analysis software package provided by CERN [ROOT13]. It provides several algorithms and tools to the user to have an easy access to the physical values, such as particle tracks or vertex parameters which are required for this analysis. In the next chapter the data quality tests and event selection are described which were mainly performed using PHAST. Also this program is in a continuous improvement process, for instance the difference of the two analyses of the 2007 and the 2010 data will be discussed in Sec. 4.8.

4. Data analysis

In this work the results on the measurement of spin-dependent asymmetries from five years of COMPASS data taking on transversely polarized targets are presented. In the years 2002, 2003, and 2004 a deuteron (^{6}LiD) two-cell target has been used, sharing the available beam time between longitudinal and transverse polarization of the target material. Also in the running period of the year 2007 such a sharing was performed on the upgraded three-cell NH_3 proton target. Finally the whole running period of 2010 was dedicated to the high statistics transverse measurement again on the three-cell proton target. In this chapter the applied quality checks, the event selection and the particle identification using the RICH detector are described, as well as a study dedicated to possible effects of particle misidentification. The methods used to extract the hadron-pair asymmetry are described. Furthermore a collection of tests, implemented to study the azimuthal stability of the data are introduced, which are used to determine the systematic uncertainties. Finally the results from the independent data taking periods on the proton target are combined.
The work for this thesis started in the year 2010 with the actual data taking, the studies on the data quality and the calculation of the unidentified h^+h^- asymmetries. These results have been released in August 2011 and were shown for the first time at the TRANSVERSITY 2011 conference [COMPASS12d]. As the next step, the particle identification was implemented in the analysis chain and the corresponding results for $\pi^+\pi^-$, K^+K^-, π^+K^-, and $K^+\pi^-$ pairs from the 2010 data set were released in August 2012. The first presentation to the public took place at the SPIN 2012 conference [COMPASS14b]. The aim of having a combined set of results from the 2007 and 2010 proton target data taking motivated for reanalysis on the identified pairs of the data collected in 2007[1]. In March 2012 these combined proton results have been released and shown for the first time at the DIS 2013 conference [COMPASS13]. Being the last missing element for the final step of this thesis, the extraction of the u and d valence quark transversities, the analysis of the identified pairs from the deuteron target data was finally released in November 2013[2]. The two reanalyses are crucial for this final goal, because the methods used for the previous analyses were different w.r.t. the recently used and were partly outdated. With this thesis the complete set of hadron-pair asymmetries from the transverse COMPASS data is available, extracted with homogeneous cuts and methods at the best known level, see Sec. 4.8 for a detailed description.

[1] Note that the results for unidentified pairs has been published before [COMPASS12c] and a preliminary analysis of identified pairs was performed by Wollny [Wol10].

[2] The results for unidentified pairs from the deuteron data have been published [COMPASS12c] and a preliminary analysis of identified pairs was performed by Vossen and Massmann [Mas08].

A publication on the combined 2007/2010 h^+h^- asymmetries is already available [COMPASS14a], while a paper including the complete set of identified hadron-pair asymmetries from both targets is in preparation.

4.1. General information on the transverse data taking

Starting from the first year of the data taking in 2002, the measurement of azimuthal asymmetries played a major role in the COMPASS physics program. Its aim was pursued further in the following two years. In total five periods of data on the transversely polarized deuteron target were collected: In 2002 periods P2B/C and P2H, in 2003 period P1G/H and in 2004 period W33/34 and W35/36. For the sake of simplicity these periods will sometimes be referred to as "deuteron_P1 – deuteron_P5". Please note that for the whole 2002 running period no particle identification is available, since the RICH detector was not yet fully functional. Thus the 2002 data is used for the evaluation of the unidentified hadron-pair asymmetry, but not for the identified ones. The orientations of the target nucleon spins of all running periods are shown in the Tab. 4.1, where the arrows $\Downarrow$ and $\Uparrow$ indicate the up and down states of each target cell. Only period 2010_P10 is an exception to this scheme, since in its second sub-period 2010_W39b the polarization has been reversed again, from $\Uparrow\Downarrow\Uparrow$ to $\Downarrow\Uparrow\Downarrow$ in order to have a more balanced statistic between the two configurations; the data has been allocated accordingly.

Table 4.1.: Target spin configurations for 2002 – 2004, 2007, and 2010 transversity run periods; the arrows indicate the polarization of the target cells (two cells in 2002 – 2004, three cells in 2007 and 2010).

period	1^{st} sub-period	polarization	2^{nd} sub-period	polarization
deuteron_P1	2002_P2B	⇓⇑	2002_P2C	⇑⇓
deuteron_P2	2002_P2H1	⇓⇑	2002_P2H2	⇑⇓
deuteron_P3	2003_P1G	⇓⇑	2003_P1H	⇑⇓
deuteron_P4	2004_W33	⇑⇓	2004_W34	⇓⇑
deuteron_P5	2004_W35	⇓⇑	2004_W36	⇑⇓
2007_P1	2007_W25	⇓⇑⇓	2007_W26	⇑⇓⇑
2007_P2	2007_W27	⇓⇑⇓	2007_W28	⇑⇓⇑
2007_P3	2007_W30	⇑⇓⇑	2007_W31	⇓⇑⇓
2007_P4	2007_W39	⇑⇓⇑	2007_W40	⇓⇑⇓
2007_P5	2007_W41	⇓⇑⇓	2007_W42a	⇑⇓⇑
2007_P6	2007_W42b	⇓⇑⇓	2007_W44	⇑⇓⇑
2010_P1	2010_W23a	⇓⇑⇓	2010_W23b	⇑⇓⇑
2010_P2	2010_W24a	⇑⇓⇑	2010_W24b	⇓⇑⇓
2010_P3	2010_W26a	⇓⇑⇓	2010_W26b	⇑⇓⇑
2010_P4	2010_W27a	⇑⇓⇑	2010_W27b	⇓⇑⇓
2010_P5	2010_W29a	⇑⇓⇑	2010_W29b	⇓⇑⇓
2010_P6	2010_W31a	⇓⇑⇓	2010_W31b	⇑⇓⇑
2010_P7	2010_W33a	⇑⇓⇑	2010_W33b	⇓⇑⇓
2010_P8	2010_W35a	⇓⇑⇓	2010_W35b	⇑⇓⇑
2010_P9	2010_W37a	⇑⇓⇑	2010_W37b	⇓⇑⇓
2010_P10	2010_W39a	⇓⇑⇓	2010_W39b	⇑⇓⇑ & ⇓⇑⇓
2010_P11	2010_W42a	⇓⇑⇓	2010_W42b	⇑⇓⇑
2010_P12	2010_W44a	⇑⇓⇑	2010_W44a	⇓⇑⇓

4.2. General data quality

Besides of the on-line monitoring of the data being taken by the COOOL program, various other tests are applied off-line, which means after the recorded data has been further processed, described in Sec. 3.7. For a complex apparatus such as the COMPASS spectrometer, the sources of possible instabilities are not simple to identify completely during the data taking. However, this is in particular mandatory since the measured effects are small. A main focus is on the stability of the data inside of each (sub-)period, but also on a spill-to-spill basis and on a global basis over whole running periods.
For the 2010 data taking period a detector-profile analysis tool, analyzing the hit distributions of all tracking detectors was introduced for the first time [Bra10]. After the event reconstruction done by CORAL additional studies on the data stability were performed. These are the bad spill analysis, the K^0 stability and the stability of kinematic variables.

4.2.1. Detector profile analysis of 2010 data

The first step of the off-line analysis is performed on the raw data, meaning the bare hit distributions from the tracking detectors of the whole beam telescope and spectrometer. This was applied for the first time on the 2010 data set and helped to ensure the outstanding stability of this data, see Sec. 4.6.3. Most of the common detector problems, such as noise and partly or totally dead detector layers, already show up in these histograms filled with the hit distribution normalized to the beam intensity. The normalization factor is taken from the scaler data of the FI01 detector and is in particular crucial to check for inefficiencies. If a sufficient number of hits in a run is present, ≈ 20 spills were found to be adequate, the distributions are also monitored concerning their mean values and sigma.
This detector profile analysis program searches automatically for deviations on a run-by-run basis and also in the statistical measures, mean and sigma (called RMS in the plots) values, shown in Fig. 4.1. An output list is generated, which is then discussed by detector and data production experts. Taking into account the available redundancies and the statistical balance between sub-periods a final list is generated containing the detectors which will not be used in the production process. A detailed description of the program can be found in [Bra10]. The Fig. 4.1 shows an example from period 2010_P3 where a drift chamber (DC) detector and a MWPC (PA) detector suffer from dead channels visible as white areas. Both were excluded from the data production for the whole period. The full list of rejected detectors of the 2010 running can be found in Tab. A.4.

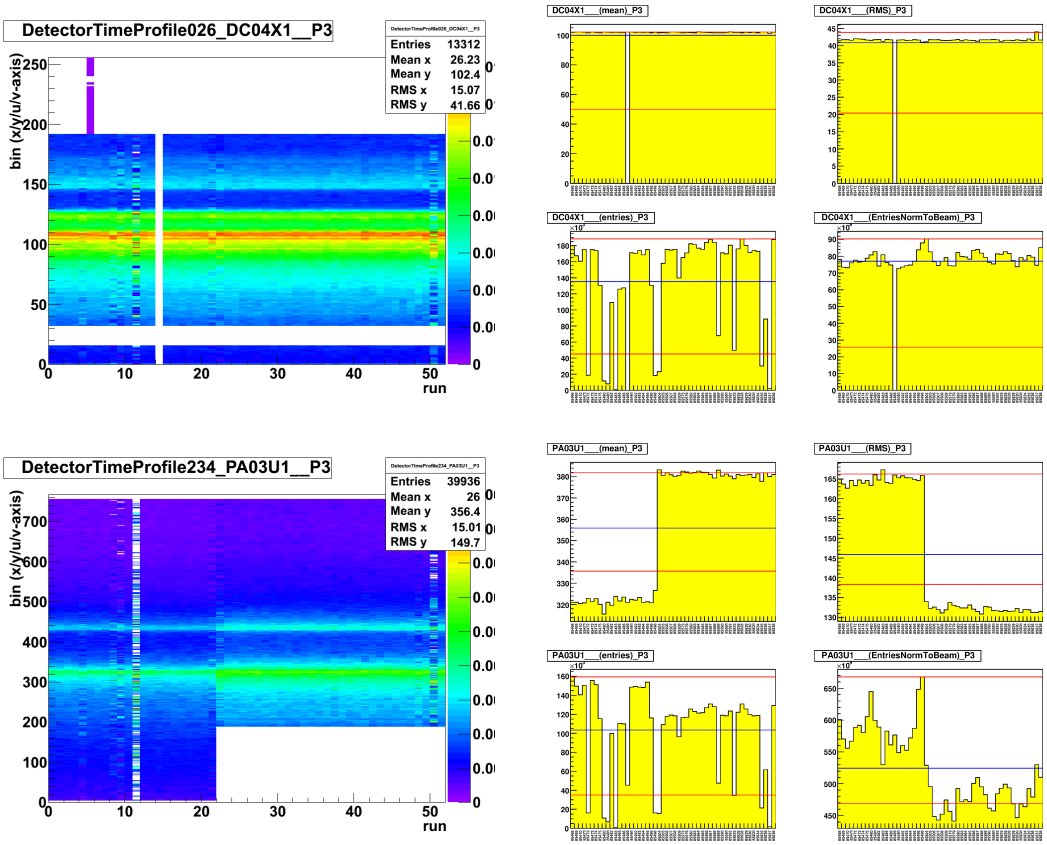

Figure 4.1.: Two examples of detectors, DC04X1 (top) PA03U1 (bottom) with partly dead channels, found with the off-line detector-profile analysis. The plots on the right side show the distributions of the mean value of the detector profiles (upper left) of the RMS value (upper right) and the number of entries, non-normalized (lower left) and normalized (lower right) as a function of runs. [Bra10]

4.2.2. Bad spill analysis

The so-called "bad spill" analysis is the first step in the line of quality studies applied on the produced data, which means event reconstructed data at the PHAST level, see Sec. 3.7. It is performed with a minimum of constraints, consisting of the basic requirement for DIS events that Q^2 is greater then $1\,(\mathrm{GeV}/c)^2$. The aim is to monitor the stability on a spill-by-spill basis of certain basic measures, which are certain vertex variables such as the number of beam particles per vertex, the number of outgoing tracks per vertex and the number of primary vertices per event. In addition the inclusive and exclusive trigger rates and the number of clusters in the hadronic calorimeters are monitored.

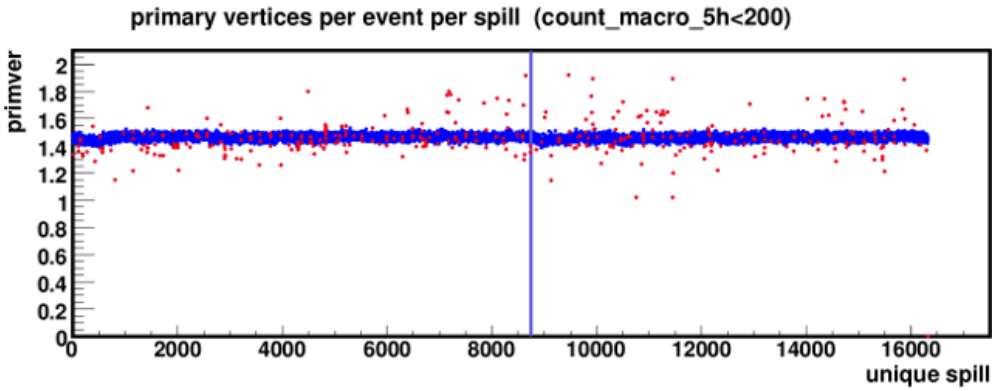

Figure 4.2.: The average number of primary vertices per event for period 2010_P8 as an example of the bad spill analysis [Ado13]. Spills which fulfill the good spill criteria are indicated in blue, spills which do not fulfill this are indicated in red. The blue vertical line indicates the changeover in the target spin orientations

The identification of bad spills is based on a statistical method by the comparison of the variables listed above of one spill to the spills in an interval of 600 spills before and after. Then a minimum number of neighboring spills, of which a measure is inside a certain limit of multiple of units of standard deviations, is required. Otherwise the spill is rejected from the analysis [Wol10, Ado13]. Spills were marked as bad if less than 200 out of the 1200 neighboring spills exceed a $5\,\sigma$ limit for the vertex variables and the inclusive trigger rates, or if less then 600 neighbors are within a $6\,\sigma$ for the others. Furthermore the beam constancy is also a criterion for exclusion, for instance if the number of muons is under a threshold of 1.5×10^8 per spill, compared to the nominal number of 2.5×10^8. Such a case indicates problems in the SPS beam extraction, which could cause large asymmetries in the beam parameters. Runs are removed from the analysis if the fraction of bad spill exceeds $80\,\%$.
For the sake of simplicity here just the results from the 2010 data are reported, the corresponding results for the other running periods can be found in [Mas08, Soz07]. The largest deviations were found in the number of clusters in the hadronic calorimeter, but since its data is not used in the analysis of azimuthal asymmetries, this was not taken into account. The rejection of spills by the remaining variables lead to a loss of $\approx 4\,\%$ of events. An example of the distribution of the average number of primary vertices per event of 2010_P8 is shown in Fig. 4.2, rejected spills are marked in red.

4.2.3. Stability of neutral kaon mass

The decay of a neutral kaon into two charged pions $K^0_S \to \pi^+\pi^-$ is not only used as a source of pions for the RICH efficiency determination (see Ref. 4.3.6), but also to test the data quality on a run-by-run basis. The selection criteria applied on the $Q^2 > 1\,(\mathrm{GeV}/c)^2$ sample is the invariant

mass of the two-pion system. Its difference to the literature value of the K^0 mass [PDG12] is calculated for each event and the resulting distribution of each run is fitted with a Gaussian. On this basis three distributions are monitored as a function of the run number for each period, they are the mean value of the Gaussian, its width (corresponding to the mass resolution) and the number of reconstructed K^0 per primary vertex. Figure 4.3 shows as an example these three distributions for P8 of the 2010 running. In the case of the 2010 data, the distributions of the Gaussian mean value and its width were found to be compatible with the literature value within the uncertainties and therefore no run was rejected due to this test. However, the distribution of reconstructed K^0 per primary vertex shows more distinct deviations from the mean value of the whole period. Hence $\pm 3\sigma$ limits were applied, and runs which exceed this were rejected from the analysis. From this test less then $1\,\%$ of the total events of the recorded 2010 data were rejected.

4.2.4. Kinematic stability

The last step of the selection for a good data quality is the study of the stability of kinematic variables. It is already related to the physics case, since runs and spills have already been rejected according to the bad spill list and the K^0 stability list and the monitored variables are essential for the evaluation of the azimuthal asymmetries. Moreover the final kinematic cuts, which will be described later in Sec. 4.3, are also applied, such that this test refers to the almost final data sample. On a run-by-run basis the distributions of the mean values of x, y, Q^2, E', E_h, $p_\perp$, ϕ, ϕ_h, the polar angles of the scattered muon, and the hadron produced are extracted. For each period the ratio of the different distributions from its two sub-periods is calculated, not only for the sum of all triggers but also for each trigger individually (see Sec. 3.5). This reveals runs with unstable trigger conditions, even if the sum over all runs might be stable. To check the stability between the sub-periods, which is crucial due to the intended cancellation of systematic effects, each run of one sub-period is compared to the whole other sub-period.
The choice to reject a run is performed on a convergence procedure, therefore the ratios of individual runs are fitted with a constant function. The χ^2 probability P of this fit is determined for each variable P_ν as well as for the sum of the variables P_{sum}. A run is kept in the sample if $P_\nu > 10^{-5}$ for a single variable and $P_{sum} > 10^{-4}$ for the sum of the variables, otherwise it is rejected. With the obtained sub-sample the procedure is repeated until the distribution are flat and no more major failures are present.
With this method an instability of the calorimeter trigger was found in P5 of the 2010 running (an exemplary distribution is shown in Fig. A.11), with the result that pure calorimeter trigger events do not enter the analysis for the whole period, the same holds true in the 2007 running data for P2, P4 and P5. Concerning the 2010 data the number of hadrons rejected by this test refers to $\approx 5\,\%$, for the other running periods the rejection rate is in the same order.
Details of the corresponding studies on the deuteron data can be found in [HK06, B$^+$06].

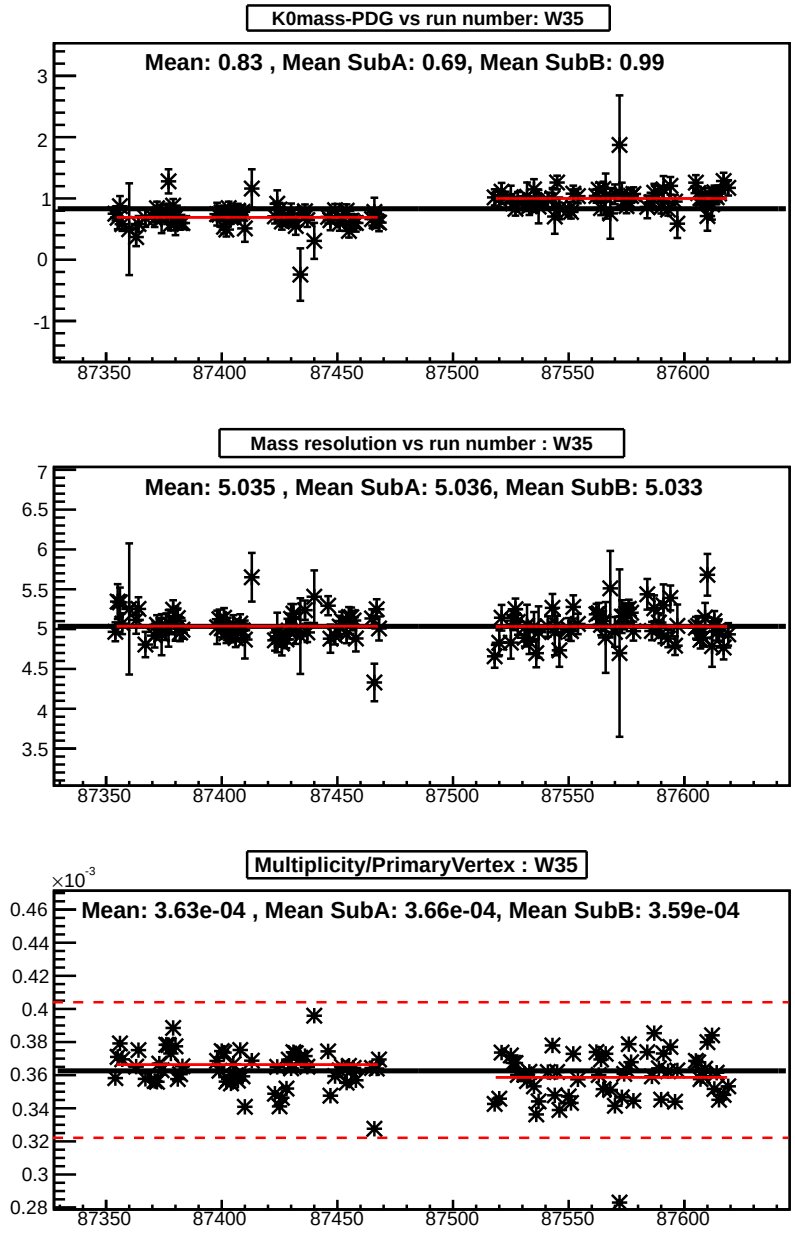

Figure 4.3.: Distribution of the K^0 stability test of period 2010_P8 as a function of the run number [Ado13]: The difference of reconstructed $\pi^+\pi^-$ mass and K^0 mass from literature [PDG12] (top panel) in MeV/c^2, mass resolution in MeV/c^2 (center panel) and the number of reconstructed K^0 per primary vertex (bottom panel). The red dashed lines indicate statistical $\pm 3\sigma$ borders. The black line is the result of a fit with a constant functional form.

4.3. Event selection

From the collectivity of the saved data, deep inelastic scattering (DIS) events are selected to extract the transverse target spin asymmetries. Basic requirement is the presence of at least a primary vertex with an incoming and an outgoing muon track. In the following section the different cuts are described to select the physics data, including the specific cuts of the particle identification using the RICH (see Sec. 4.3.4). The different types of targets and the different years of data taking cause fairly different cuts, which will be discussed in detail. Furthermore the all hadron results from the deuteron and proton data, which were already published [COMPASS12c] show some differences w.r.t. the analysis of the identified asymmetries. All events which fulfill the cuts will be referred to as the standard sample.

4.3.1. General DIS events cuts

The DIS regime is characterized by a squared four momentum transfer Q^2 of the virtual photon to be greater then $1\,(\mathrm{GeV}/c)^2$ (Sec. 2.1), the corresponding cut is chosen accordingly. The relative energy transfer y is also restricted in order to discard elastic scattering events by the requirement of y being greater than 0.1, further this ensures the rejection of events where halo or background muons are falsely identified as scattered muons. While an upper limit of $y < 0.9$ removes events which would suffer from the necessity of applying radiative corrections. The invariant mass of the final hadronic state W is strongly correlated to the relative energy transfer y, see Fig 4.4 (center right panel). With a cut at $W > 5\,\mathrm{GeV}/c^2$ not only the rejection of elastic scattering events is further improved, but also events from the resonance region are excluded. The geometric acceptance of the COMPASS target and spectrometer (see Secs. 3.2 and 3.3) together with the beam energy allow one the access to DIS events down to a limit of $x = 0.003$, while the upper limit is 0.7. The described cuts where applied on non-identified h^+h^- pairs and identified hadron-pairs from all, deuteron and proton data.
The distributions of the individual kinematic variables Q^2, y , W, and x before and after their specific cuts as well as the correlations of W with y and Q^2 with x for pion pairs from the combined 2007/2010 data sample are shown in Fig. 4.4. The distributions for the other pair combinations K^+K^-, π^+K^-, and $K^+\pi^-$ are shown in Figs. A.12 to A.18, as well as for the deuteron data. For details on the logarithmic binning see Sec. A.8.

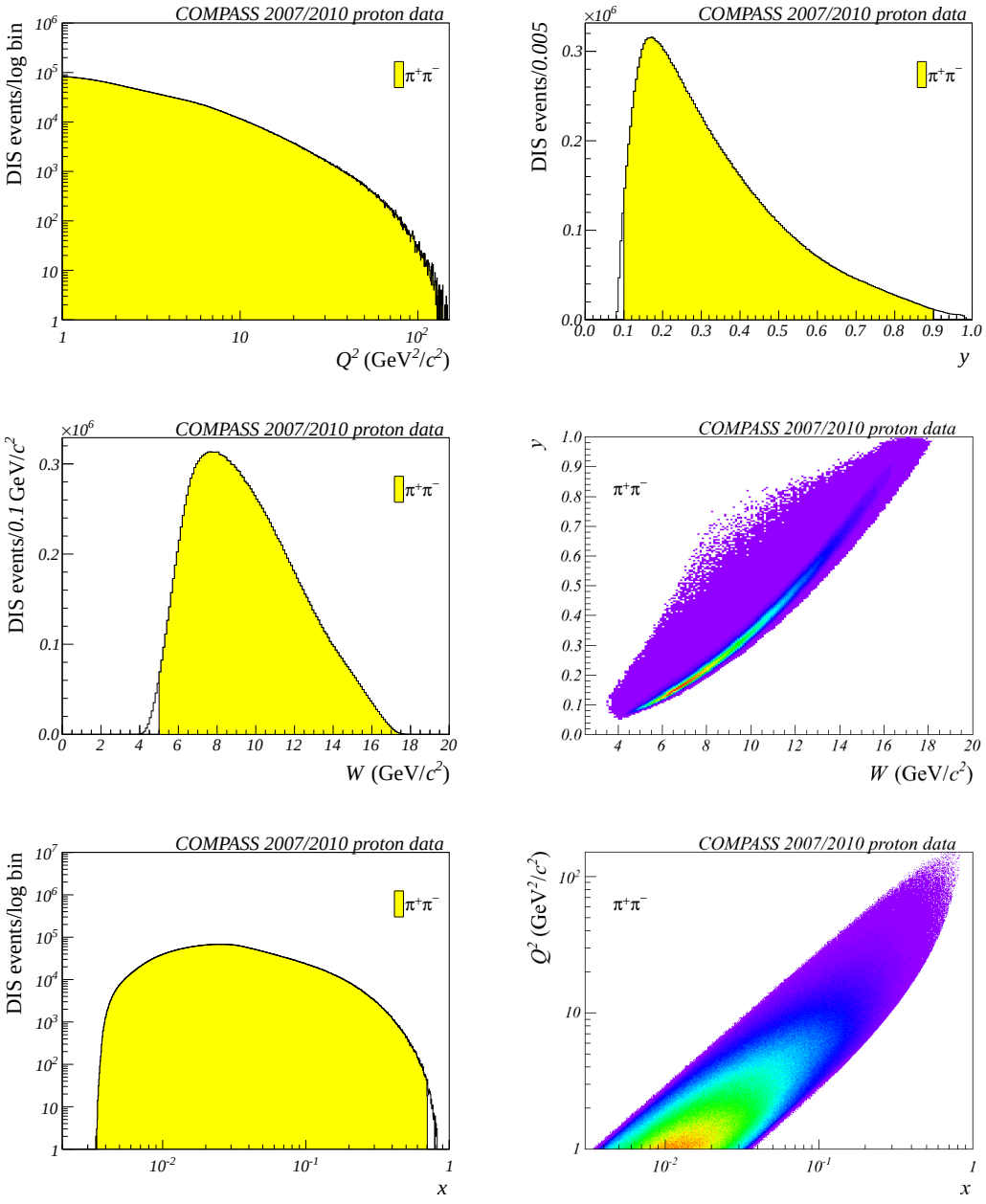

Figure 4.4.: Kinematic distribution of DIS events with $\pi^+\pi^-$ pairs in the outgoing channel before (white) and after the specific cuts (yellow) from the combined 2007/2010 proton data. From left to right in the 1$^{\text{st}}$ row: Q^2 and y distributions; 2$^{\text{nd}}$ row: W distribution and y vs. W distribution; 3$^{\text{rd}}$ row: x distribution and Q^2 vs. x distribution.

4.3.2. Primary vertex and muon selection

Primary vertex

The data collected at COMPASS is stored in the basis of events (see Sec. 3.7), where each event might contain also more than one primary vertex; such as decays of secondary particles of e.g. K^0 meson (see Sec. 4.2.3). The most promising candidate for the so-called best primary vertex (BPV), is determined by the largest number of outgoing particles, which also indicates the highest available energy most probably provided directly by a beam particle. If two vertices in an event have the same number of outgoing particles, the one with the smallest reduced χ^2 of its coordinates is chosen as the BPV. For a SIDIS measurement the detection of the outgoing muon and at least one outgoing hadron is required, further the analysis of hadron-pair asymmetries puts this number up to two. Thus just vertices with an incoming and at least three outgoing particles (scattered muon & two charged hadrons) enter this analysis.
Once a BPV is defined, its coordinates are checked to be inside the target material. The two- and three-cell target configurations of the deuteron and the proton measurements are described in Sec. 3.2. The exact positions of the two or three target cells are determined for each period by a detailed study of the distribution of vertices coming from the target material and its support structure. This is necessary because the target is not centered w.r.t. the COMPASS coordinate system, but was shifted e.g. in the year 2010 2.5 cm downstream with an offset in X of -0.2 cm and in Y of 0.02 cm. The target cells of the three-cell proton target have a diameter of 4.0 cm, a stricter cut on the radius around the target center of 1.9 cm is chosen to ensure that the vertex is inside the target material and not in the target holder material.
In addition the track projection of the incoming muon is required to cross all target cells within the radial cut to ensure equal flux in all target cells.
The distribution of the BPV coordinates of pion pairs from the deuteron, the 2007 and the 2010 proton data along the beam axis is shown in Fig. 4.5, the corresponding distribution for all other pairs are shown in Fig. A.19.

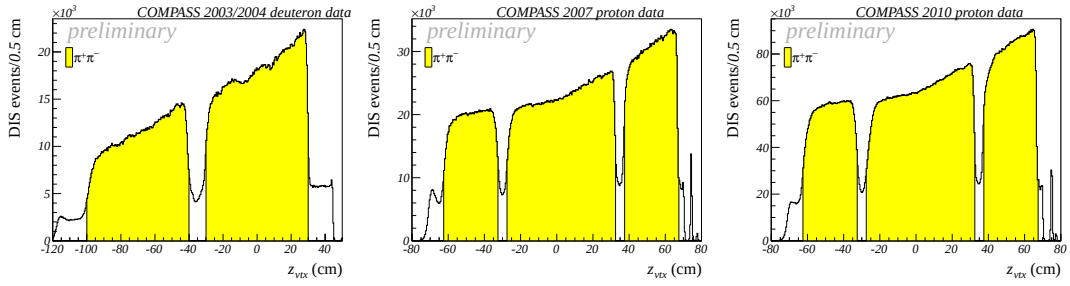

Figure 4.5.: Distribution coordinates of the primary vertices along the beam axis from deuteron data (left panel), 2007 data (center panel) and 2010 data (right panel) before (white) and after the cuts (yellow) for pion pairs.

Incoming muon

The momentum distribution of the incoming beam muon μ has a Gaussian shape, centered around 160 GeV$/c$ with a sigma of 5 GeV$/c$. To exclude the tails of this distribution the momentum range of 140 GeV$/c < p < 180$ GeV$/c$ is considered for this analysis. If the momentum of a beam muon is not reconstructed from the BMS data (sec. 3.1) the event is also rejected. The quality of the muon track is considered by the χ^2 values of the track fit inside the beam telescope, just tracks with a reduced $\chi^2 < 10$ are accepted.

Scattered muon

Like in the case of the beam muon the track of the scattered muon μ' has to fulfill the requirement of a reduced χ^2 to be smaller than 10. For a clear identification of the μ' in the spectrometer more requirements are demanded. It has to be charged positively, has to pass more then 30 units of radiation lengths nX/X_0 while is does not pass the region of the hole in the absorbers and its track has to have at least one hit before SM1 and one hit behind Muon Wall 1. If there are more than one μ' coming out of the BPV the whole event is rejected. For the deuteron and the 2007 data, the tracks passing through the yoke of SM2 have been rejected due to issues with the bridging of the tracks.

4.3.3. Hadron and hadron-pair selection

Hadron selection

All outgoing particles of the BPV (see Sec. 4.3.2), with the exception of the scattered muon, are considered as hadron candidates. Muons being misidentified as hadrons can be rejected when they pass Muon Wall 1, which means that their track have hits after $Z_{\text{MW1}} \approx 3300\,\text{cm}$. Furthermore a first hit upstream of the position of SM1 ($Z_{\text{SM1}} \approx 350\,\text{cm}$) is required. To avoid tracks that are only reconstructed in the fringe field of SM1, a hadron track has to have a hit inbetween the positions of SM1 and MW1. As in the muon case a reduced χ^2 smaller then 10 of the tracks fit is required, as well as a passed radiation lengths nX/X_0 smaller than 10. In addition two cuts on the kinematics of the hadrons are applied. The first one is on the Feynman scaling variable $x_F = 2p_L/\sqrt{s}$ and the second on the fraction of the virtual photons energy z_i carried by hadron i. Both x_F and z_i have to be in the range of $0.1 - 1.0$. Note that in contrast to the single hadron analysis no cut on the transverse momentum of the hadron p_T^h is applied.

Hadron-pair selection

After the hadrons are selected by the cuts described above, the remaining number of good hadrons is checked to be at least two hadrons of opposite charge per BPV. These two are then merged together as a hadron-pair or dihadron. If there are more then two outgoing hadrons all possible combinations of oppositely charged pairs are taken into account to the analysis, e.g. two positively and one negatively charged hadron form two pairs, which share the negatively charged one.
For these pairs the total z value is calculated by summing z_1 and z_2 (see Figs. A.22, A.23), which obviously must be smaller then 1.0. The z distribution of pion pairs from the running periods of deuteron, 2007, and 2010 is shown in Fig. 4.6, the corresponding distribution for all other pairs are shown in Fig. A.21.
In order to have a well defined angle between the two hadrons, a cut on their difference vector is applied such that $R_T > 0.07\,\mathrm{GeV}/c$, which is kind of a minimal distance of the two hadrons in momentum space to ensure that clearly two hadrons are measured. For a definition and discussion on R_T of see Sec. 2.3.4.
Finally exclusively produced ρ mesons are rejected by a cut on the missing energy of the hadron-pair. The corresponding exclusivity peak is clearly visible around zero in the E_{miss} distribution shown in Figs. 4.7, A.24, the cut was tuned to be $E_{miss} > 3\,\mathrm{GeV}$ [Wol10]. Likewise the z distributions (see Fig 4.6) show the removed exclusivity peak around a values of 1.0.

4.3.4. Particle identification

According to the kinematic domain of the COMPASS experiment the hadrons produced in SIDIS are mostly charged pions. From the final all hadron sample $\approx 67\,\%$ are identified as pions, while the charged kaons account for a fraction of $\approx 10\,\%$. The remaining particles are either protons, electrons or have not been clearly identified. Concerning the hadron-pairs $\approx 60\,\%$ of the total h^+h^- pairs are pion pairs, $\approx 2\,\%$ kaon pairs and $\approx 8\,\%$ mixed pairs. The missing fraction refers to cases where at least one of the two hadrons has not been clearly identified. This motivates the assignment of the pion mass for the extraction of the asymmetries of h^+h^- pairs, which result in a miscalculation of z in the case the hadron is a charged kaon. Thus and for the reason of a full flavor separation, an identification of the hadrons is necessary. The RICH detector described in Sec. 3.4.1 gives an unique opportunity to have a clear separation between pions and kaons for momenta above the pion threshold, see Sec. 4.3.7.

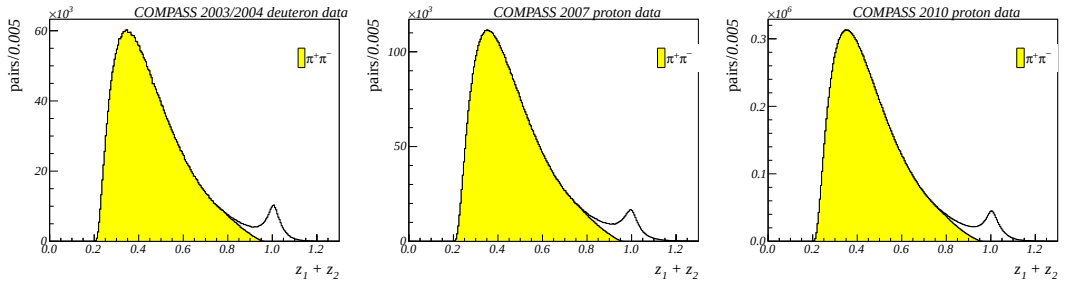

Figure 4.6.: Distribution of the variable $z = z_1 + z_2$ from deuteron data (left panel), 2007 data (center panel) and 2010 data (right panel) before (white) and after the cut on E_{miss} (yellow) for pion pairs.

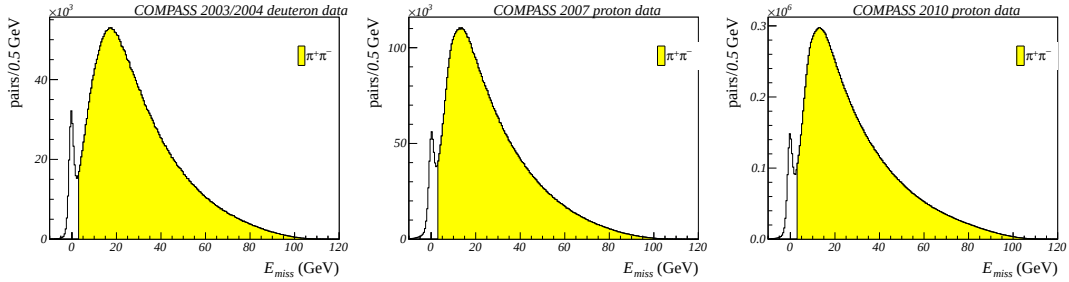

Figure 4.7.: Missing energy distribution of pion pairs from deuteron data (left panel), 2007 data (center panel) and 2010 data (right panel) before (white) and after the cut on E_{miss} (yellow) for pion pairs.

4.3.5. RICH stability check

As for all tracking detectors the RICH data is also checked to ensure a stable behavior during the running periods. The procedure of this study is shown on the example from the 2010 proton data and it was performed on the single and the hadron-pair sample. In the case of the single hadron sample the RICH has been geometrically divided into four disks of the polar angle θ_h of the hadron w.r.t. the nominal beam axis, while in the hadron-pair case the division is not useful since the single hadrons of the pairs are distributed all over the RICH active area. The values of the θ_h angle might have an influence since the RICH is equipped with different types of photo detectors (see Sec. 3.4.1), MaPMTs in the inner region and MWPC in the outer region. These four intervals extend in the ranges $0\,\text{mrad} < \theta_h < 30\,\text{mrad}$, $30\,\text{mrad} < \theta_h < 110\,\text{mrad}$, $110\,\text{mrad} < \theta_h < 200\,\text{mrad}$, and $200\,\text{mrad} < \theta_h < 400\,\text{mrad}$. The first two ranges are read out by MaPMTs, the third one is equipped partly by MaPMTs & MWPC and the latter one is instrumented with MWPC detectors only. In the study based on hadron-pairs for each run the ratio of identified $\pi\pi$, KK, and $K\pi$ pairs to the total number of hadron-pairs is evaluated and then fitted with a Gaussian distribution. In addition the ratios of pion pairs to the other identified

pairs are determined. Note that in this study no distinction between different charges has to be applied, thus $K^+\pi^-$ and π^+K^- are merged as "$K\pi$" pairs. On the resulting distributions of the mean values from the Gaussian fits as a function of the runs, shown in Fig. 4.8, a $\pm 4\sigma$ limit is applied and all runs outside of it are rejected. Among those are significant deviations for which a reason can be identified according to the logbook, such as run 86375 "methane leak", runs 87818 - 87828 "RICH photo detectors off" and runs 88165 & 88169 "RICH cooling failure". The final lists of so-called "bad RICH" runs from the single and the hadron-pair sample are largely consistent and therefore have been combined to a single list of in total 82 runs which were removed from the standard sample. This corresponds to $\approx 2\,\%$ of the total statistics.
An analog study on the 2007 proton running period data can be found in [Pes10] and for the deuteron data in [Soz07].

4.3.6. RICH efficiency and purity

To evaluate the efficiency of the RICH detector to identify a charged hadron correctly, decays with fixed types of produced hadrons are studied. Since a clear separation of pions and kaons is mandatory for this analysis, the decays of K^0 mesons into pairs of charged pions and the decays of $\Phi(1020)$ meson into pairs of charged kaons are ideal processes to study. This allows for an individual calculation of the identification efficiencies of charged pions and kaons. The identification efficiency is defined as the ratio of particles being correctly identified to the total number of particles obtained from the K^0 or $\Phi(1020)$ decays.
Two more dependencies of the efficiencies are taken into account when final efficiencies are determined. First the polar angle of the hadron track w.r.t. the beam axis, since the RICH detector is equipped with different types of photo detectors (see Sec. 4.3.5), second the hadron momentum due to the momentum dependent Cherenkov angle (see Sec. 3.4.1). The Cherenkov threshold of the kaons at $9\,\mathrm{GeV}$ implies that the impurities of the pions can only be evaluated starting from this value.
The condition of the RICH running, gas mixture and pressure were identical for the data taking periods of 2007 and 2010, therefrom studies have shown that the efficiencies as a function of the hadron angle, momentum and charge are identical [Pes10]. The results of the deuteron running periods of 2003 and 2004 are slightly lower, but compatible with the proton running periods [Soz07].
The method used to evaluate the purity corrections to the asymmetries from the identification efficiencies in the case of a single hadron analysis is described in [SSM06], while the procedure for the hadron-pair analysis is more complicated and will be discussed in detail in Sec. 4.7. The high purity values of the kaon sample ($\approx 90\,\%$) and the pion sample ($\approx 99\,\%$) also allow one for an evaluation of the hadron-pair purities, see Sec. 4.7.

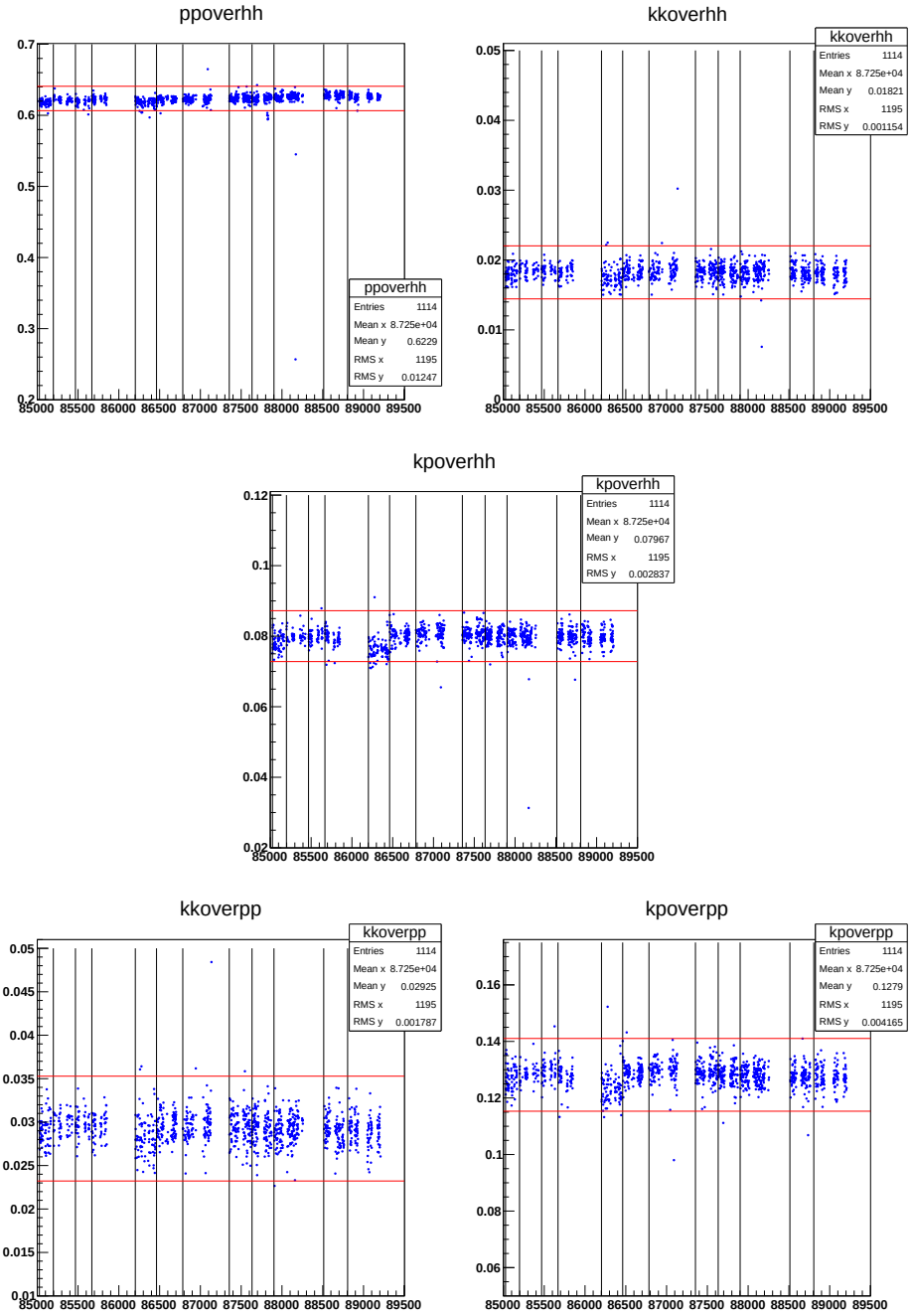

Figure 4.8.: Fraction of identified pion pairs (top left), kaon pairs (top right) and mixed pairs (middle) to all hadron-pairs as a function of runs. The ratio of mixed pairs (bottom left) and kaon pairs (bottom right) to pion pairs. Vertical lines indicate periods, horizontal red lines show the $\pm 4\,\sigma$ borders.

4.3.7. Cuts for pion and kaon identification

The assignment of the particle type to a hadron track is based on a comparison of likelihood values $\mathcal{L}$, which are calculated by the CORAL package RICHONE for different mass hypothesis corresponding to pion, kaon, electron, proton and background. The ratio of the highest to the second highest likelihood value is required to be larger than a dedicated threshold, which is tuned by balancing two competing aspects. The contamination of the sample by misidentified particles is being minimized, while RICH efficiency is kept as high as possible. The resulting demanded ratios are shown in Tab. 4.2 for the proton target and the deuteron target runnings.
The general cut on the ratio of pion or kaon likelihood values $\mathcal{L}_{max=\pi/K}$ to the second highest likelihood value $\mathcal{L}_{2ndmax}$ is in common to all data sets, see Tab. 4.2 first two lines. Then there are some specific differences between the deuteron and the proton target runnings. For the deuteron data it is explicitly requested that the ratio of the pion/kaon likelihood to the background likelihood is greater then 1.03 or 1.04. There is no such demand for the 2007 and 2010 runnings, but there the electron likelihood value is just taken into account if $\mathcal{L}_e$ is 1.8 times larger then $\mathcal{L}_\pi$. A lower threshold of the particle momentum was already discussed above, while also a general upper threshold has to be applied to guarantee a good separation between pions and kaons. For all running periods a general cut of $p_{max} < 50\,\mathrm{GeV}/c$ is applied, corresponding to a $1.5\,\sigma$ separation between K and π. Note that for the deuteron data additional cuts on the lower hadron momentum had to be applied to ensure a sufficient number of Cherenkov photons, corresponding to a mean number of four emitted photons. For the pions the physical limit of the Cherenkov threshold $\mathrm{thr}_{\mathrm{Cherenkov}} = m_{\pi/K}/\sqrt{n^2_{\mathrm{RICH}} - 1}$, where n_{RICH} is the refraction index of the RICH, is enlarged by a bias of $0.5\,\mathrm{GeV}$ and for kaons by $1.0\,\mathrm{GeV}$. The value of this lower thresholds is about $3.1\,\mathrm{GeV}/c$ for pions and $10.1\,\mathrm{GeV}/c$ for kaons. This was not necessary in the case of the 2007 and 2010 data, due to a better RICH performance after its upgrade, see Sec. 3.4.1.

Table 4.2.: Cuts on the likelihood ratio values of the RICH particle identification for proton (2007/2010) and deuteron target (2003-2004) runnings

	proton target 2007/2010	deuteron target 2003-2004
$\frac{\mathcal{L}_{max=\pi}}{\mathcal{L}_{2ndmax}}$	> 1.020	> 1.002
$\frac{\mathcal{L}_{max=K}}{\mathcal{L}_{2ndmax}}$	> 1.080	> 1.003
$\frac{\mathcal{L}_{max=\pi}}{\mathcal{L}_{background}}$	–	> 1.030
$\frac{\mathcal{L}_{max=K}}{\mathcal{L}_{background}}$	–	> 1.040
$\frac{\mathcal{L}_{max=\pi}}{\mathcal{L}_e}$	> 0.560	–

4.4. Final statistics of deuteron and proton data

After the application of all cuts and the removal of bad runs and spills, the final all hadron-pair deuteron data sample consists of 6.5×10^6 hadron-pairs. The two proton data samples from 2007 and 2010 include 10.9×10^6 and 34.6×10^6 hadron-pairs, respectively. Showing an increase in statistics by a factor of ≈ 3 using the 2010 data.
In order to get the number of identified pairs the RICH identification cuts (as described in Sec. 4.3.7) and the RICH bad run and spill list was applied.
The final statistics of all hadron and identified pairs for each period of the deuteron 2002-04 sample is shown in Tab. 4.3. The corresponding numbers from the two proton sample from 2007 and 2010 are shown in the Tabs. 4.4 and 4.5. Note the partially different set of cuts which were used for the results of h^+h^- from deuteron and 2007 data, as described in Secs. 4.3 and [COMPASS12c]. Furthermore the 2002 data was completely rejected for the particle identification due to problems of the RICH radiator transparency [Pes10]. The compatible ratios between pion pairs and the other pairs from the two proton target measurements, are an indication of the stability of the RICH detector.

Table 4.3.: Final statistics of the deuteron 2002-04 hadron-pair sample: all hadron and identified pairs.

period	week	h^+h^-	$\pi^+\pi^-$	K^+K^-	π^+K^-	$K^+\pi^-$
2002_P2B/C	deuteron_P1	514,633	–	–	–	–
2002_P2H1/H2	deuteron_P2	344,791	–	–	–	–
2003_P1G/H	deuteron_P3	1,900,946	1,295,004	31,843	84,345	101,043
2004_W33/34	deuteron_P4	1,632,825	1,156,900	28,052	75,386	87,036
2004_W35/36	deuteron_P5	2,115,180	1,517,645	36,887	100,191	115,561
total		**6,508,375**	**3,969,549**	**96,782**	**259,922**	**303,640**
ratio to $\pi^+\pi^-$				2.4 %	6.6 %	7.6 %

Table 4.4.: Final statistics of the 2007 hadron-pair sample: all hadron and identified pairs.

period	week	h^+h^-	$\pi^+\pi^-$	K^+K^-	π^+K^-	$K^+\pi^-$
W25/26	2007_P1	1,735,127	1,049,135	37,515	63,961	87,726
W27/28	2007_P2	1,719,663	997,968	28,502	50,090	69,872
W30/31	2007_P3	2,718,408	1,927,891	53,024	96,461	133,719
W39/40	2007_P4	1,946,021	1,409,017	39,854	70,507	98,610
W41/42a	2007_P5	1,849,622	1,338,269	39,015	69,057	96,799
W42b/44	2007_P6	944,239	685,087	19,443	34,302	48,379
total		**10,913,080**	**7,407,367**	**217,353**	**384,378**	**535,105**
ratio to $\pi^+\pi^-$				2.9 %	5.2 %	7.2 %

Table 4.5.: Final statistics of the 2010 hadron-pair sample: all hadron and identified pairs.

period	week	h^+h^-	$\pi^+\pi^-$	K^+K^-	π^+K^-	$K^+\pi^-$
W23	2010_P1	1,688,231	1,005,122	29,126	53,486	73,286
W24	2010_P2	1,570,083	952,157	28,398	51,151	71,454
W26	2010_P3	1,691,234	1,007,122	29,843	54,489	75,770
W27	2010_P4	1,804,717	1,076,136	31,721	57,273	80,394
W29	2010_P5	2,044,274	1,185,280	33,186	61,281	84,659
W31	2010_P6	2,982,732	1,803,243	53,534	97,346	135,494
W33	2010_P7	3,075,647	1,837,905	54,297	99,930	138,127
W35	2010_P8	3,704,061	2,224,774	65,306	120,226	166,919
W37	2010_P9	3,568,240	2,046,273	59,638	109,761	152,711
W39	2010_P10	5,312,771	3,204,887	93,629	171,668	238,508
W42	2010_P11	3,563,477	2,144,441	62,011	113,494	160,039
W44	2010_P12	3,558,312	2,112,515	61,140	112,853	156,779
total		**34,563,779**	**20,599,855**	**601,829**	**1,102,958**	**1,534,140**
ratio to $\pi^+\pi^-$				2.9 %	5.3 %	7.4 %

4.5. Extraction of the asymmetries

Different methods are available to extract the asymmetry from the collected data, among them the one-dimensional "quadrupole ratio method" (QR) and the two-dimensional "unbinned likelihood method" (UL) are the most common and trusted methods.

4.5.1. Quadrupole ratio method

The different polarizations of the two-cell deuterium target as well as the three-cell proton target open the possibility to take data on two different target spin orientations at the same time. For a further minimization of systematic effects due to acceptance effect, both used targets are split up into four parts for each period of the same polarization state, numbered from 1 to 4. In the case of the deuteron target each target cell is split into two parts, these are numbered in the way that 1 and 2 are of opposite polarization, as well as 3 and 4, see Fig. 4.9. For the proton target it is sufficient to split the middle cell into two parts to have pairs of cells with opposite spin orientations as shown in Fig. 4.9.
The position of the primary vertex of each event is assigned to one of these new defined cells, so N_i is the number of events with the BPV inside a target cell $i \in [1, 2, 3, 4]$. To indicate the results from the second sub-period with opposite target polarization the N_i are marked with a $'$. For the extraction of the asymmetry the quantity $F^{QR}(\phi)$ is defined:

$$F^{QR}(\phi) = \frac{N_1(\phi)\ N_2'(\phi)\ N_3'(\phi)\ N_4(\phi)}{N_1'(\phi)\ N_2(\phi)\ N_3(\phi)\ N_4'(\phi)}, \tag{4.1}$$

where ϕ is the angle of the specific modulation. For the hadron-pair asymmetry the N_i is given by

$$N_i(\phi) \approx N_i^0(1 \pm \epsilon \sin\phi_{RS})(1 + a_i \sin\phi_{RS}). \tag{4.2}$$

The unpolarized cross-section and the luminosity determine the constant value of N_i^0. The spin-dependent physical modulation with an amplitude ϵ depending on the target spin orientation $\pm$ is the origin of the term $(1 \pm \epsilon \sin\phi_{RS})$. Assuming the factorization of acceptance effects the term $(1 + a_i \sin\phi_{RS})$ takes them into account.
Inserting Eq. 4.2 in Eq. 4.1 gives

$$F^{QR}(\phi) \approx C \cdot \Big(1 + \big((a_1 - a_1') - (a_2 - a_2') - (a_3 - a_3') + (a_4 - a_4') + 8\epsilon\big) \sin\phi_{RS}\Big), \tag{4.3}$$

where $C = \frac{N_1^0(\phi)\ N_2'^0(\phi)\ N_3'^0(\phi)\ N_4^0(\phi)}{N_1'^0(\phi)\ N_2^0(\phi)\ N_3^0(\phi)\ N_4'^0(\phi)} \approx 1$ due to the assumption of an equal beam flux in all cells. The definition of a relative acceptance change between the sub-periods

$$e_i = a_i - a_i' \tag{4.4}$$

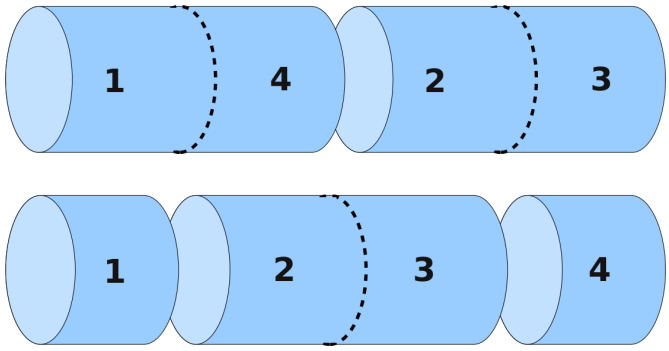

Figure 4.9.: Configuration of the target cells of the two-cell deuteron target (top panel) and the three-cell proton target (bottom panel) [Wol10].

simplifies Eq. 4.3 to

$$F^{QR}(\phi) \approx C \cdot \Big(1 + \big(e_1 - e_2 - e_3 + e_4 + 8\epsilon\big) \sin\phi_{RS}\Big). \tag{4.5}$$

To fit the $F^{QR}(\phi)$ quantity a functional form

$$f(\phi) = p_0(1 + p_1 \sin\phi_{RS}) \tag{4.6}$$

is used. Then the measured asymmetry $\epsilon_m = \frac{p_1}{8}$ is related to the real asymmetry ϵ by

$$\epsilon = \epsilon_m + \frac{(e_1 - e_2 - e_3 + e_4)}{8}. \tag{4.7}$$

From the definition leading to Eq. 4.4 a bias can only be introduced by possible changes of the cell acceptances between two sub-periods and not due to different geometrical acceptances of the cells. Furthermore the assumption is made that this change of acceptance between sub-periods is the same in each target cell, i.e. $e_1 \approx e_2 \approx e_3 \approx e_4$. This assumption, the so-called "reasonable assumption" is tested in a dedicated study (see Sec. 4.6.1) and may be used in the estimation of the systematic uncertainty.
Performing a fit in a binned distribution a possible bias due to the finite bin size has to be considered. In this case the ϕ_{RS} range is divided into 16 bins of equal width Δ. The number of events in each bin then is a constant multiplied by the mean value of the expected distribution. Accordingly the mean value in one bin is

$$\langle \sin\phi_{RS} \rangle = \frac{1}{\Delta} \int_{\phi_{RS}}^{\phi_{RS}+\Delta} f(\phi_{RS}) \mathrm{d}\phi. \tag{4.8}$$

Inserting the fit function from Eq. 4.6 one obtains

$$\frac{\epsilon_m}{\epsilon} = \frac{2}{\Delta} \sin\frac{\Delta}{2} \tag{4.9}$$

as the ratio between the measured ϵ_m and the real ϵ asymmetry. In this case with 16 bins the correction is at the level of $0.6\,\%$, which is smaller then the statistical uncertainty and is therefore neglected in the following.

4.5.2. Unbinned maximum likelihood method

Possible problems to a binned one-dimensional fit method are the statistical fluctuations in the ratio of small numbers. This is one of the reasons why the two-dimensional fit method (fit in a plane of ϕ_R and ϕ_S) suffers from larger corrections thus it is not discussed here. To overcome this, the unbinned maximum likelihood method [COMPASS10a, MPS$^+$09] has been developed. As a starting point a probability density function p_i for each target cell i is defined, which depends on the angles ϕ_R and ϕ_S. Thus $p_i(\phi_R, \phi_S)$ is proportional to the product of the acceptance of the cell i and the cross-section of the physics modulation. The cross-section used for the unbinned fit in the case of the hadron-pair asymmetry is

$$\sigma_{\pm}(\phi_R, \phi_S) \propto 1 + \varepsilon_1 \sin(\phi_R + \phi_S - \pi), \tag{4.10}$$

which is the only modulation for a unpolarized beam[3] and a transversely polarized target and remaining after the $\boldsymbol{k}_T$ integration, as described in Sec. 2.3.4. In the case of the single hadron asymmetries all eight modulations of the transverse spin dependent asymmetries are taken into account by fitting them simultaneously.
The likelihood function is built as the product of the probability densities $p_{i,k}$ corresponding to each hadron-pair k from each target cell i [MPS$^+$09]

$$\mathcal{L} = \prod_{i=0}^{4} \left[\left(e^{\mathcal{N}_i^+} \prod_{k=0}^{N_i^+} p^+(\phi_S^k, \phi_R^k) \right)^{\frac{\overline{N}}{N_i^+}} \left(e^{\mathcal{N}_i^-} \prod_{k=0}^{N_i^-} p^-(\phi_S^k, \phi_R^k) \right)^{\frac{\overline{N}}{N_i^-}} \right], \tag{4.11}$$

where $N_i^{\pm}$ is the number of hadron-pairs coming from a vertex inside of target cell i with positive or negative polarization and $\overline{N} = \frac{1}{8} \sum_{i=1}^{4} \mathcal{N}_i^+ + \mathcal{N}_i^-$. A difference in statistics is taken into account by a normalization with the exponent $\frac{\overline{N}}{N_i^{\pm}}$ to avoid a possible bias.
A simple normalization of the probability density function to 1 introduces a small bias as shown by Monte Carlo simulations in [MPS$^+$09]. Therefore a normalization to the expected number of hadrons [MPS$^+$09]

$$\mathcal{N}_i^{\pm} = \int_0^{2\pi} \int_0^{2\pi} p_i^{\pm}(\phi_R, \phi_S) \mathrm{d}\phi_R \mathrm{d}\phi_S \tag{4.12}$$

is performed. The asymmetry values are then extracted by minimization of the interest function $-\ln \mathcal{L}$ using the Broyden-Fletcher-Goldfarb-Shanno (BFGS) [Bro70, Fle69, Gol70, Sha70] algorithm from the GNU scientific library [Fou] or MINUIT contained in the ROOT analysis framework provided by CERN [ROOT13]. Both minimizers have been used in the independent analyses by the institutes of Trieste (MINUIT) and Erlangen (BFGS), the results of this comparison are shown in Sec. 4.6.5 together with the cross-checks of the results obtained with the one-dimension fit method 4.5.1 giving almost equal results.

[3] The beam polarization is not present in this modulation, see Sec. 2.3.4.

4.5.3. From raw to final asymmetries

The so-called "raw" asymmetries are the asymmetries obtained by fitting the pure ϕ_{RS} (QR) or (ϕ_R,ϕ_S) distributions (UL), without taking into account the target polarization P_T, the dilution factor f and the spin transfer coefficient D_{NN}. These are used in the cross-check procedure and might also be of interest for theoreticians to compare the data with model calculations on their level. For both estimators, the QR (Sec. 4.5.1) and the UL (Sec. 4.5.2), it is possible to obtain the final asymmetries by dividing the raw asymmetry values in each bin with the mean values $\langle P_T \rangle$, $\langle f \rangle$ and $\langle D_{NN} \rangle$ calculated in the same bin.
For both estimators also the possibility to weight the hadron-pairs with their individual dilution factor and spin transfer coefficient before the fit was implemented. Since the target polarization is assumed to be constant in defined time intervals and since it could cause a bias to the fit, it is taken into account after the fit.
Both fit methods, weighted and unweighted, give almost the same results, as shown in Fig. 4.10 for the deuteron h^+h^- pair results. In order to maintain continuity the unweighted fit has been chosen to obtain the final results. This procedure has also the advantage that one can go one step backward in the analysis, i.e. from the final to the raw asymmetry by dividing the amplitude value (and its error) in each bin by the mean values of f, D_{nn} and P_T the mean target polarization. For simplicity the final asymmetries are called asymmetries from now on.

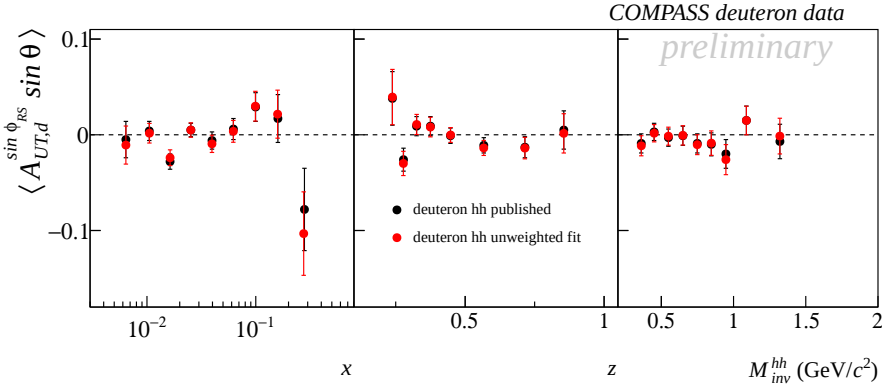

Figure 4.10.: Hadron-pair asymmetries of deuteron data h^+h^- pairs obtained with an unweighted UL fit (black dots) and with an f and D_{NN} weighted UL fit (red dots).

4.6. Systematic studies

The search for systematic uncertainties in the available data was performed by applying different tests on the final data sample. Different possible effects which can affect the measurement were taken into account.
The "R-test" gives an indication of the change in the azimuthal acceptance between the two sub-periods and its distribution is expected to be flat. The "T-test" extends this idea by testing for possible sine modulations in the acceptances of two sub-periods. In the "reasonable assumption test" (RA) also the expected physical modulation is taken into account in the search for azimuthal instabilities in the data.
One of the most powerful tests is to check for non-physical "false" asymmetries by a dedicated combination of target cells.
Furthermore the compatibility of the asymmetries between the different periods is monitored, as well as the stability of the results in terms of a virtual segmentation of the spectrometer.
Finally the determined uncertainties are combined to an overall systematic uncertainty.
Although the particle identification via the RICH-detector is precise, a study of the influence of misidentification on the asymmetries was performed.

4.6.1. Azimuthal stability

The azimuthal stability of the asymmetries is tested using three methods, namely the R-test, T-test and the RA-test.

R-test

The R-test is a measurement of the change of the azimuthal acceptance between the two sub-periods. Therefore the ratio

$$R(\phi) = \frac{N_1(\phi) + N_4(\phi)}{N'_1(\phi) + N'_4(\phi)} \cdot \frac{N_2(\phi) + N_3(\phi)}{N'_2(\phi) + N'_3(\phi)} \tag{4.13}$$

is constructed, which is expected to be flat within single data taking periods, if no change in the azimuthal acceptance occurs. As a check of the fulfillment of the flat hypothesis the χ^2 values of a fit with a constant to $R(\phi_{RS})$ are compared to a χ^2 normal distribution. The Figure 4.11 shows this comparisons of all identified pair combinations from deuteron, 2007 and 2010 proton data. The distributions of the obtained χ^2 values are well compatible with the normal distributions. In addition, Tab. A.5 contains the probabilities of these χ^2 values for each data taking period in order to check for periods with significant deviations w.r.t. the others.
For all deuteron and proton data the R-test gives reasonable χ^2 values and corresponding probabilities and is therefore not considered in the overall systematic uncertainty.

T-test

The aim for the T-test is to construct a value for which the expected modulation vanishes. If one neglects higher order terms, i.e. $\mathcal{O}(\sin^2\phi)$ and assumes that the acceptance cancels, the expression

$$T(\phi) = \frac{N_1(\phi)N_2(\phi)N_3(\phi)N_4(\phi)}{N'_1(\phi)N'_2(\phi)N'_3(\phi)N'_4(\phi)} \tag{4.14}$$

fulfills this. Inserting equation 4.2 then gives

$$T(\phi) \approx T_0 \cdot (1 + (e_1 + e_2 + e_3 + e_4)\sin\phi_{RS}), \tag{4.15}$$

where the $e_i = (a_i - a'_i)$ as in Eq. 4.4 are a measure of the change in acceptance between the sub-periods. Thus $T_0 = \frac{N^0_1(\phi)N^0_2(\phi)N^0_3(\phi)N^0_4(\phi)}{N'^0_1(\phi)N'^0_2(\phi)N'^0_3(\phi)N'^0_4(\phi)}$. To test the ideal case, where $T(\phi)$ is constant in ϕ, it is fitted with a sine modulation $f_T(\phi) = const \cdot (1 + A_T \sin\phi)$. The measured asymmetry A_m is unbiased if $e_1 = e_2 = e_3 = e_4$, see Eq. 4.7. A non-stable acceptance leads to sizeable χ^2 values for the assumption of $T(\phi)$ being compatible with zero.
The distributions of the χ^2 values in comparison to a normal χ^2 distribution for all data sets and possible pair combinations are shown in Fig. 4.12. The agreement between the data and the expected distribution is good and the number of bins with larger χ^2 of > 10 is very small. The corresponding probability values for each data taking period are shown in Tab. A.5. Please note that this test does not reveal all possible changes in acceptance; for instance two sizable e_i from different cells could cancel in the overall sum. Nevertheless, the T-test covers the most probable acceptance problems which might occur.
For a final decision on the stability the T-test results will be combined with the results from the RA-test in Sec. 4.6.1.

RA-test

The basic idea of the reasonable assumption (RA-test) was already motivated in Sec. 4.5.1, where the acceptance variation of single cells between the sub-periods was discussed. Therefore the azimuthal distribution of the two sub-periods $\frac{N_i(\phi)}{N'_i(\phi)}$ for each cell i is separately fitted with $f_{\text{RA}}(\phi) = const \cdot (1 + \varepsilon_i \sin\phi)$.
The four amplitudes ε_i obtained from the fits can be combined to the expected value of the physical modulation as

$$\varepsilon = \frac{\varepsilon_1 - \varepsilon_2 - \varepsilon_3 + \varepsilon_4}{8}, \tag{4.16}$$

and to the sum of the single amplitudes $\mathcal{E} = \varepsilon_1 + \varepsilon_2 + \varepsilon_3 + \varepsilon_4$. The expected value of the measured asymmetry of each cell $i \in [1, 2, 3, 4]$ can be written as

$$\begin{aligned}
\varepsilon_1 &\approx \quad 2 \cdot \varepsilon + \frac{\mathcal{E}}{4} =: \alpha_1, \\
\varepsilon_2 &\approx -2 \cdot \varepsilon + \frac{\mathcal{E}}{4} =: \alpha_2, \\
\varepsilon_3 &\approx -2 \cdot \varepsilon + \frac{\mathcal{E}}{4} =: \alpha_3, \\
\varepsilon_4 &\approx \quad 2 \cdot \varepsilon + \frac{\mathcal{E}}{4} =: \alpha_4.
\end{aligned} \tag{4.17}$$

As for the previous test a χ^2 value is built as a measure of the deviation from the ideal case. Here a sum running over the squared differences of the four measured amplitudes ε_i and the mean expected values α_i (Eq. 4.17) divided by the uncertainty of each amplitude is calculated

$$\chi^2_{\text{RA}} = \sum_{i=1}^{4} \Big(\frac{\varepsilon_i - \alpha_i}{\sigma_i} \Big)^2. \tag{4.18}$$

The results of this test, the χ^2 values of the RA-test of deuteron, 2007 and 2010 proton data are shown in Fig. 4.13 compared to normal χ^2 distributions. The overall agreement of the data with the expected distributions is good. The corresponding χ^2 probabilities for each period are shown in Tab. A.6, again for all data sets and all pair combinations. Most of the χ^2 probabilities are high or very high. For two periods (2010_4 and 2010_10) the values for the pion pairs are lower then $10\ \%$, but for other pairs they are in the nominal range. For a final decision the RA-test results will be combined with the results from the T-test in the next section.

Combination of T-test and RA-test

The results from the two latter tests, namely the T-test (Sec. 4.6.1) and the RA-test (Sec. 4.6.1) are combined in order to have a final result to quantify the azimuthal stability of the measurements as an unique χ^2. The final $\chi^2_{\text{T+RA}}$ is the sum of the χ^2 values from the RA-test and the T-test.
Note that in previous internal COMPASS presentations and release notes the χ^2 values of the T-test have been weighted by a factor of $\frac{1}{2}$ w.r.t. the RA χ^2 values in the combined results. The results presented in this work, based on an equal weighting, show that this more strict criterion also gives reasonable $\chi^2_{\text{T+RA}}$ distributions.
The distributions of values in comparison with the expected normal distributions are given in Fig. 4.14. Some single bins, mostly of pairs which include kaons give χ^2 values larger than ≈ 15. The corresponding χ^2 probabilities for each period and pair type from all data sets can be found in Tab. A.6.
Since no systematic effect is observed and the overall distributions show a good agreement with the χ^2 normal distributions no period is rejected and no systematic uncertainty is considered due to this combined test results.

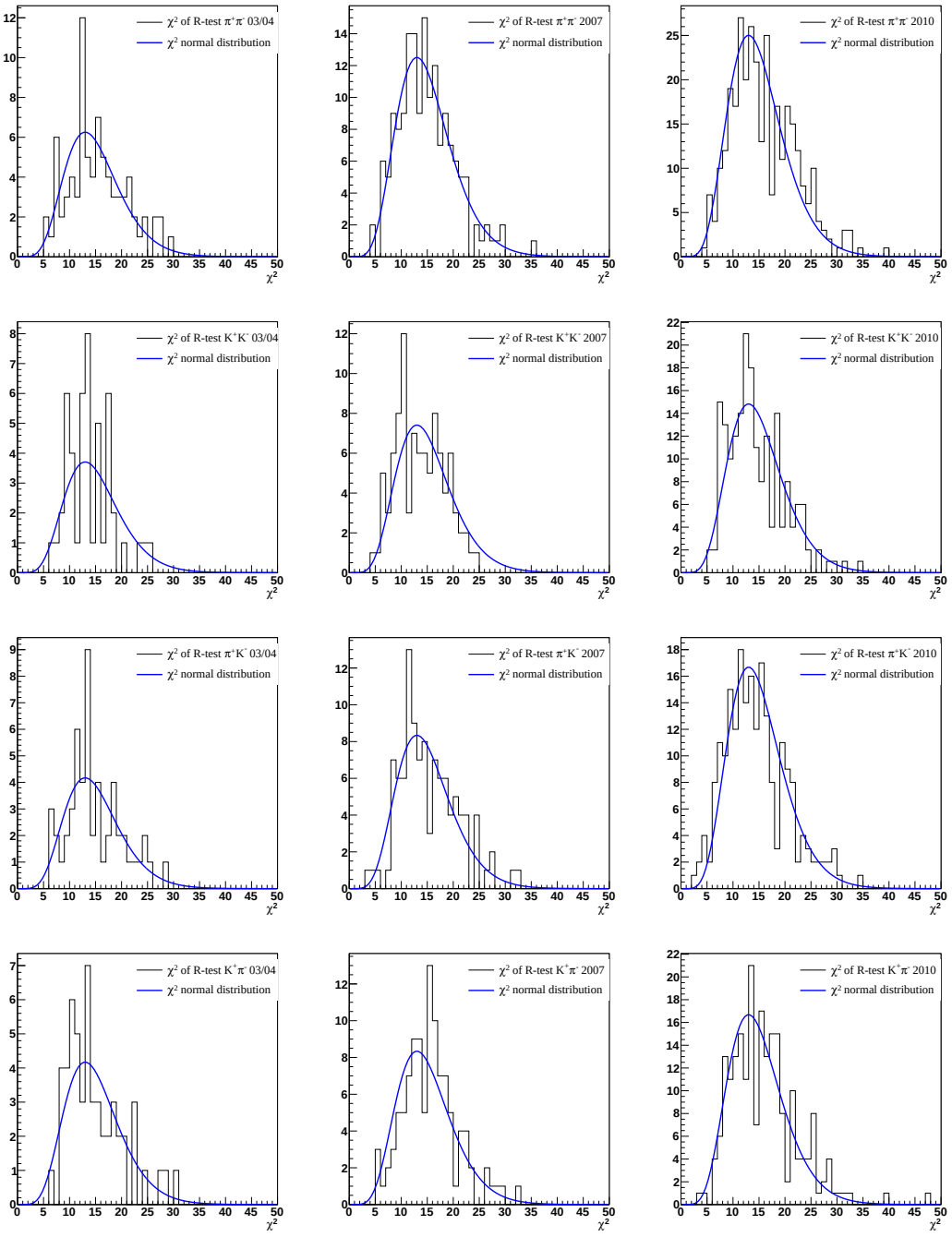

Figure 4.11.: Distributions of χ^2 values of the R-test on the deuteron (left column), 2007 (center column) and 2010 (right column) proton data in comparison to a χ^2 normal distribution (blue line): $\pi^+\pi^-$ pairs (1^{st} row), K^+K^- pairs (2^{nd} row), π^+K^- pairs (3^{rd} row), $K^+\pi^-$ pairs (4^{th} row).

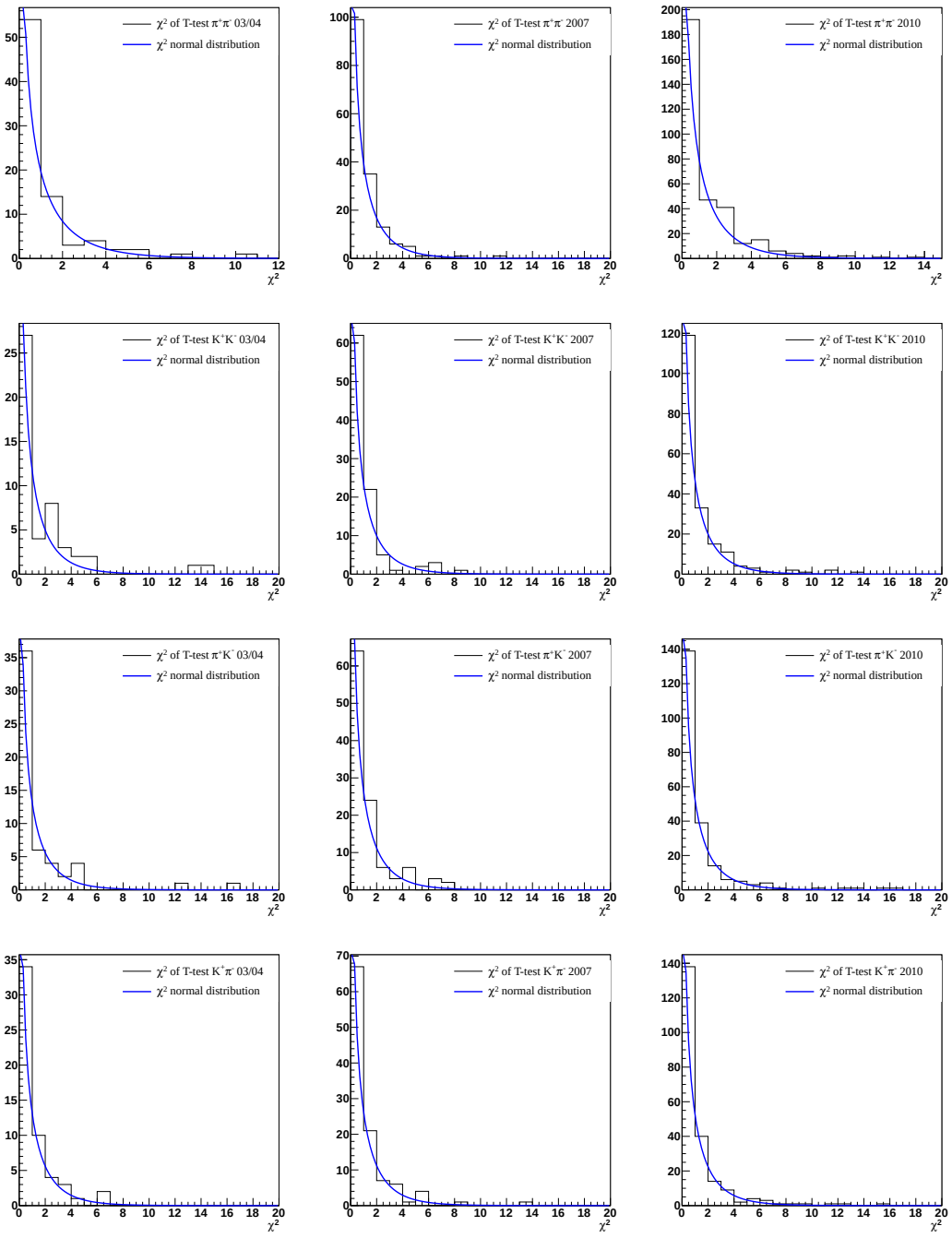

Figure 4.12.: Distributions of χ^2 values of the T-test on the deuteron (left column), 2007 (center column) and 2010 (right column) proton data in comparison to a χ^2 normal distribution (blue line): $\pi^+\pi^-$ pairs (1^{st} row), K^+K^- pairs (2^{nd} row), π^+K^- pairs (3^{rd} row), $K^+\pi^-$ pairs (4^{th} row).

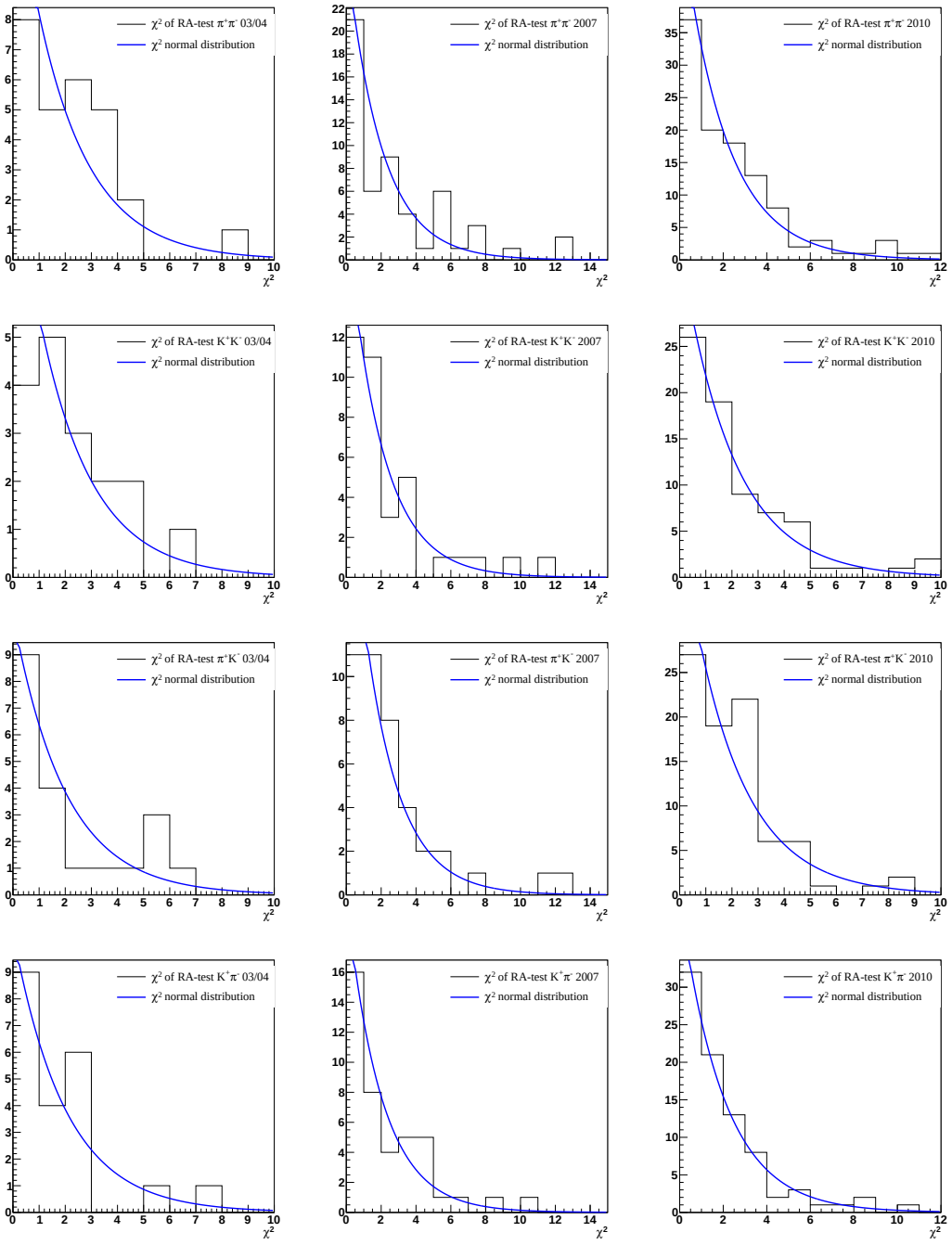

Figure 4.13.: Distributions of χ^2 values of the RA-test on the deuteron (left column), 2007 (center column), and 2010 (right column) proton data in comparison to a χ^2 normal distribution (blue line): $\pi^+\pi^-$ pairs (1^{st} row), K^+K^- pairs (2^{nd} row), π^+K^- pairs (3^{rd} row), $K^+\pi^-$ pairs (4^{th} row).

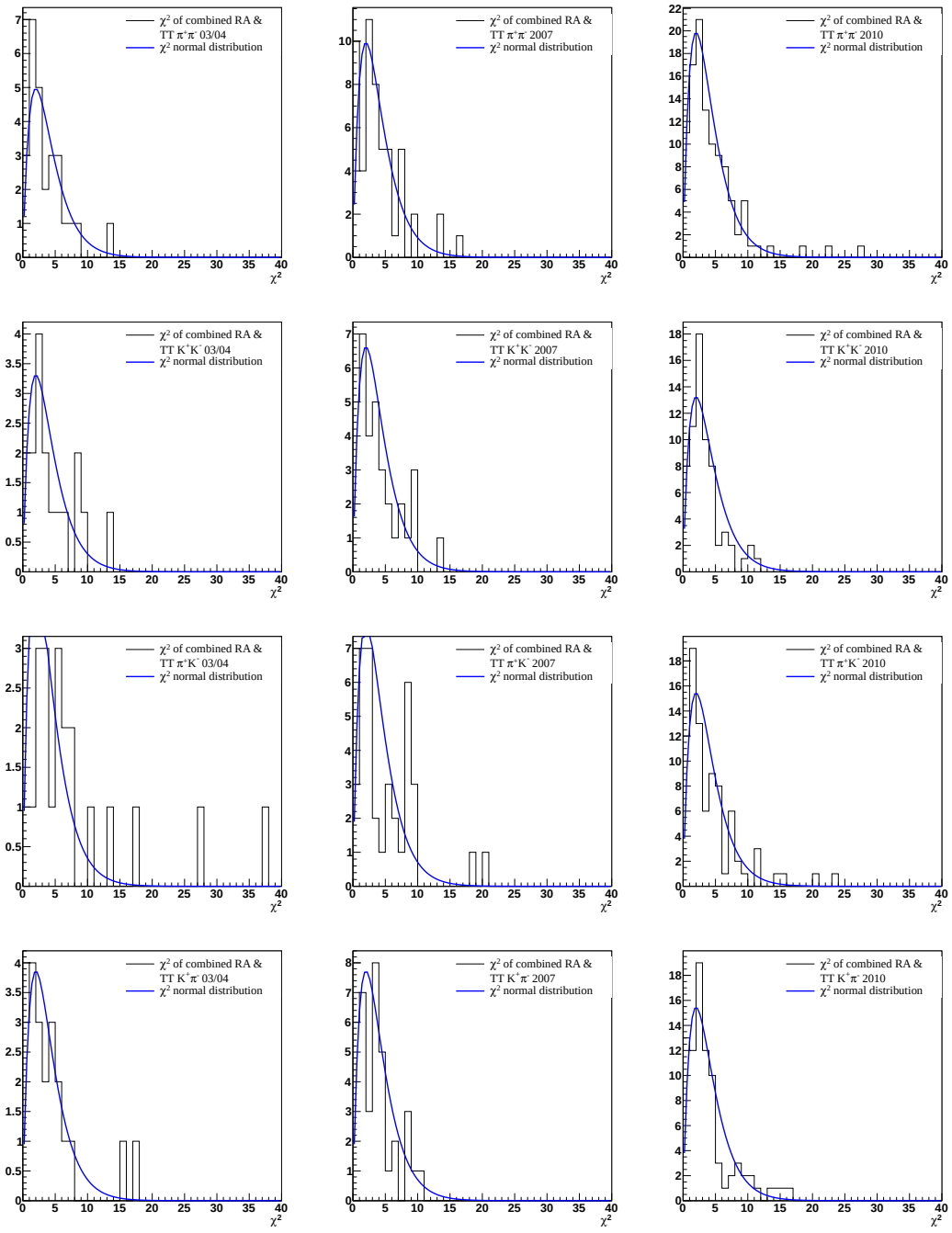

Figure 4.14.: Distributions of χ^2 values of the combined T-test and RA-test on the deuteron (left column), 2007 (center column), and 2010 (right column) proton data in comparison to a χ^2 normal distribution (blue line): $\pi^+\pi^-$ pairs (1$^{\text{st}}$ row), K^+K^- pairs (2$^{\text{nd}}$ row), π^+K^- pairs (3$^{\text{rd}}$ row), $K^+\pi^-$ pairs (4$^{\text{th}}$ row).

4.6.2. False asymmetries

A possible change of the acceptance between two sub-periods can be extracted from a dedicated combination of the target cells, since in the ideal case the measured asymmetries cancel out if target cells with the same spin orientation are combined. The so-called "false asymmetries" are evaluated for two cell combinations of the targets, according to

$$\begin{aligned} \mathrm{FA}_{ext}(\phi) &= \frac{N_1(\phi)N_4'(\phi)}{N_1'(\phi)N_4(\phi)}, \\ \mathrm{FA}_{int}(\phi) &= \frac{N_2(\phi)N_3'(\phi)}{N_2'(\phi)N_3(\phi)}. \end{aligned} \tag{4.19}$$

The asymmetries calculated for these configurations are shown in Figs. A.25, A.26, and A.27 for deuteron, 2007 and 2010 proton data, respectively. In the case of the two-cell deuteron target the configurations are $\mathrm{FA}_{upstream}$ and $\mathrm{FA}_{downstream}$. The FA_{ext} and FA_{int} distributions are fitted in bins of x for each period with $f_{\mathrm{FA}}(\phi) = C \cdot (1 + A_{\mathrm{FA}^{ext/int}} \sin\phi)$. In the ideal case of a constant acceptance the amplitude of the sine modulation is zero. The amplitudes obtained from the fit are added and subtracted with a normalization to the statistical uncertainty in order to generate an upper limit:

$$\mathrm{FA}_+ = \frac{|A_{\mathrm{FA}_{ext}} + A_{\mathrm{FA}_{int}}|}{\sqrt{\sigma_{ext}^2 + \sigma_{int}^2}}, \qquad \mathrm{FA}_- = \frac{|A_{\mathrm{FA}_{ext}} - A_{\mathrm{FA}_{int}}|}{\sqrt{\sigma_{ext}^2 + \sigma_{int}^2}}. \tag{4.20}$$

Since one standard deviation is expected, a value of 0.68 is subtracted in quadrature from both $\mathrm{FA}_\pm$ and the arithmetic mean α is calculated for each period and bin

$$\alpha = \frac{\sqrt{\mathrm{FA}_+^2 - 0.68^2} + \sqrt{\mathrm{FA}_-^2 - 0.68^2}}{2}. \tag{4.21}$$

If $\mathrm{FA}_\pm$ is already smaller or equal than 0.68, α is set to zero. Before calculating the overall arithmetic mean over all x bins and periods

$$\sigma_{sys,FA} = \frac{\sum_i \alpha_i}{\#\text{bins} \cdot \#\text{periods}}, \tag{4.22}$$

the α_i are checked to be stable as a function of the periods.
The Tab. 4.6 shows the systematic uncertainties obtained from the false asymmetry test, the given values are in units of the statistical uncertainty.
The obtained systematic uncertainties for all data sets from this test are smaller than the statistical uncertainties. The results for the deuteron data have to be considered under the constraint of the low statistics which causes statistical fluctuations, as well as the 2010 results under the constraint of the high statistics. The two results for the proton target periods are well compatible among each other and also among the different pair combinations.

Table 4.6.: Systematic uncertainty from the false asymmetry test in units of the statistical uncertainty for identified hadron-pairs from the deuteron, 2007, and 2010 proton data.

period	h^+h^-	$\pi^+\pi^-$	K^+K^-	π^+K^-	$K^+\pi^-$
deuteron	0.38	0.58	0.81	0.72	0.57
2007	0.66	0.65	0.53	0.65	0.47
2010	0.71	0.61	0.53	0.58	0.50

4.6.3. Compatibility among periods

Since the measurements were made over a long period of time, deuteron data has been taken over three years and proton data the whole years 2007 and 2010, the overall stability between the single periods is a quantity which has to be monitored. Therefore the asymmetries evaluated from each single period are checked for systematic deviations. As an example Fig. 4.15 shows the hadron-pair asymmetries of pion pairs from deuteron, 2007, and 2010 data from each of the 6 or 12 individual periods as a function of x. The corresponding mean asymmetries in the x dependence can be found in Fig. A.28. The corresponding period-by-period asymmetries of the K^+K^-, π^+K^-, and $K^+\pi^-$ pairs can be found in Figs. A.29 to A.31.
To quantify the difference between the single periods a pull distribution with the entries

$$\frac{A_{i,j} - \langle A_i \rangle}{\sqrt{\sigma^2_{A_{i,j}} - \sigma^2_{\langle A_i \rangle}}} \tag{4.23}$$

is calculated, where $A_{i,j}$ is the asymmetry value of bin i in x, z, and M_{inv} of period j and $\langle A_i \rangle$ is the mean of all periods in bin i. The obtained pull distributions for all pair combinations, shown in Fig. 4.16 are well centered with a sigma around 1. This result and the observation that the overall trend is the same for all periods without significant deviations allow one to use all periods for the final data sample.

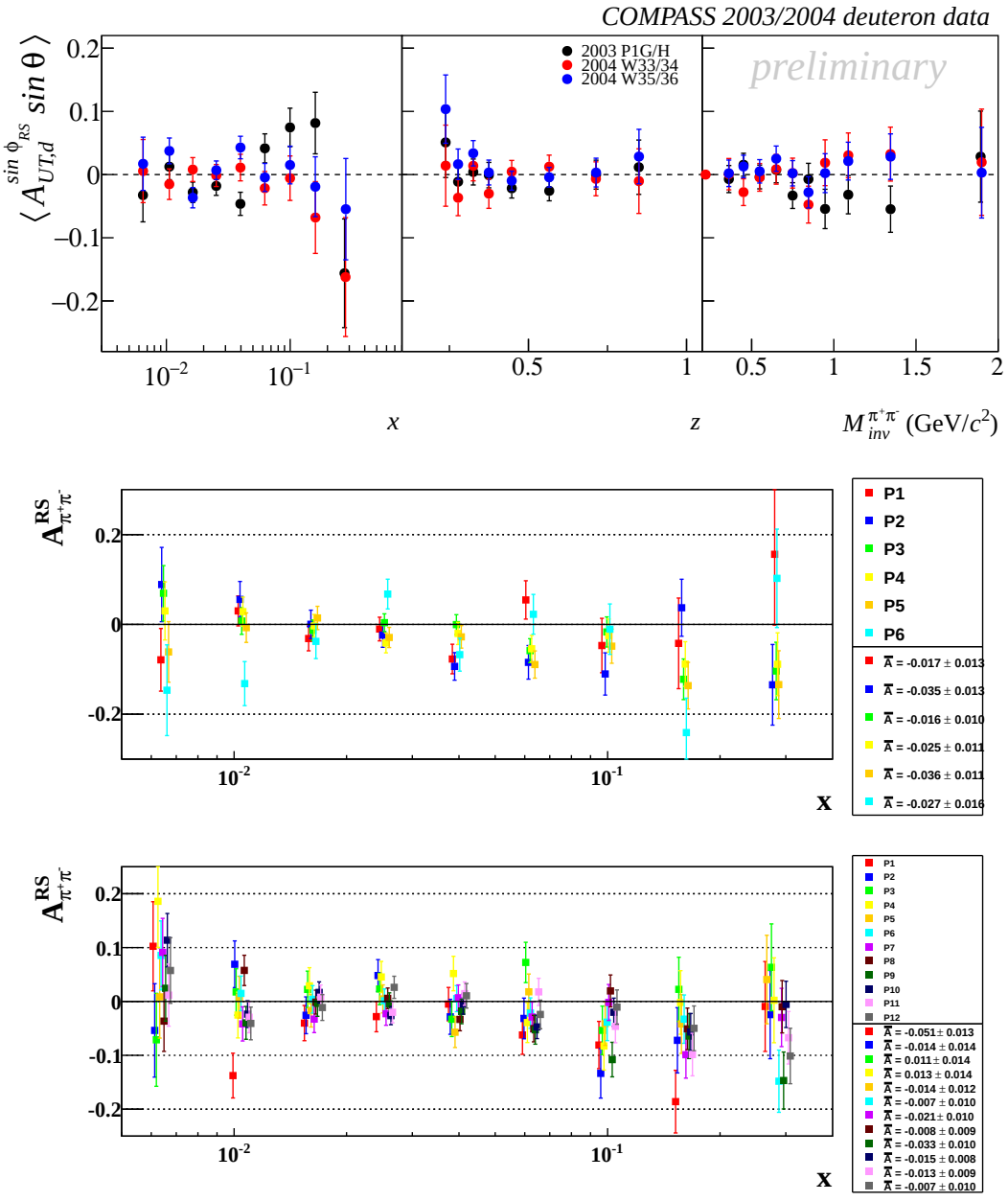

Figure 4.15.: The hadron-pair asymmetries of pion pairs as a function of x from deuteron (1st row), 2007 (2nd row), and 2010 (3rd row) data from each of the 3, 6 or 12 individual periods, respectively.

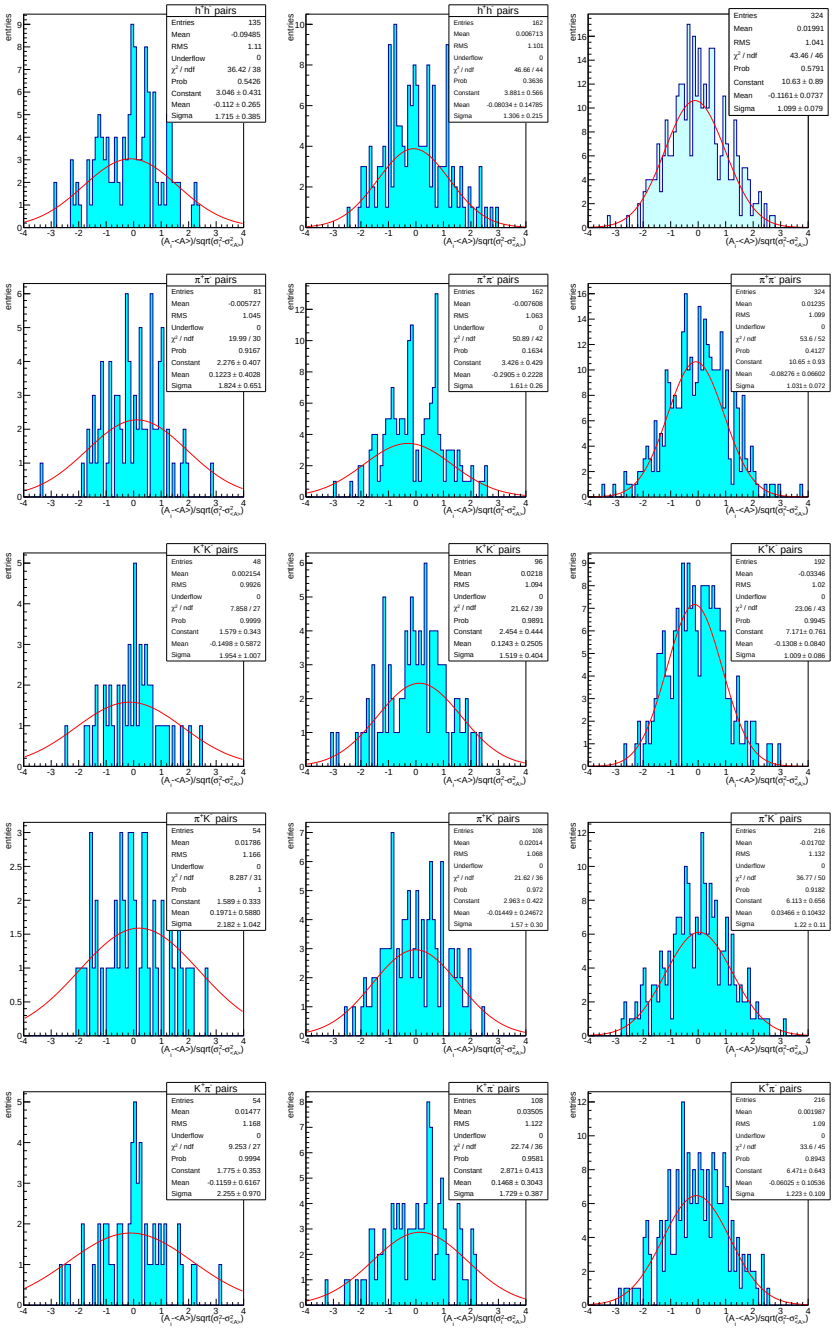

Figure 4.16.: The pull distributions as in Eq. 4.23 between the asymmetries from each individual period and the mean asymmetry from the deuteron (1st column), 2007 (2nd column), and 2010 data (3rd column) of h^+h^- pairs (1st row), $\pi^+\pi^-$ pairs (2nd row), K^+K^- pairs (3rd row), π^+K^- pairs (4th row), and $K^+\pi^-$ pairs (5th row).

4.6.4. Comparison of estimators

The two estimators used in this work, the one-dimensional quadrupole method 1D-QR (Sec. 4.5.1) and the unbinned maximum likelihood method UL (Sec. 4.5.2) give results for the asymmetries which are in good agreement. Nevertheless there are fundamental differences between both, of which the dimension of the fit is just one topic. It is common sense that the UL method is the most advanced method e.g. dealing with small event numbers, on the other hand the 1D-QR method is based on a well controlled one-dimensional fit.
Therefore a comparison of the results obtained with the different methods is also an useful indicator of the stability of the extraction method in general. An example of a direct comparison of the extracted asymmetry from both estimators is given in Fig. 4.17. The comparison is performed by a pull of the form

$$\frac{A_{i,j}^{UL} - A_{i,j}^{1D}}{\sigma_{i,j}}, \tag{4.24}$$

where $\sigma_{i,j}$ is the statistical uncertainty of bin i of period j, which does not depend on the used method. Fig. 4.18 shows the pull distributions for the different pairs from 2010 data. All of them are well centered while the sigma increases fairly for pairs with smaller sample sizes e.g. $\sigma_{\pi\pi} = 0.15$ and $\sigma_{KK} = 0.28$. This effect is expected since the one-dimensional method is prone to low statistic bins in ϕ_{RS}. Besides of that, no systematic influence can be observed. This is also the case for the deuteron and 2007 proton data, see Figs. A.32 to A.36. Therefrom and due to the fact that the unbinned likelihood estimator is the best one known at the moment, all final results are obtained using the UL.

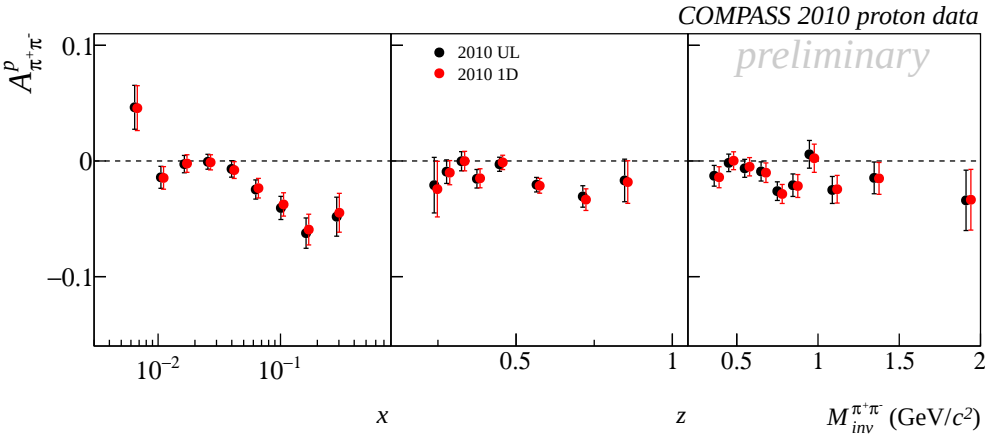

Figure 4.17.: The $\pi^+\pi^-$ hadron-pair asymmetries from 2010 data obtained with the 1D-QR (red dots) and the UL estimator (black dots). The agreement is nearly perfect.

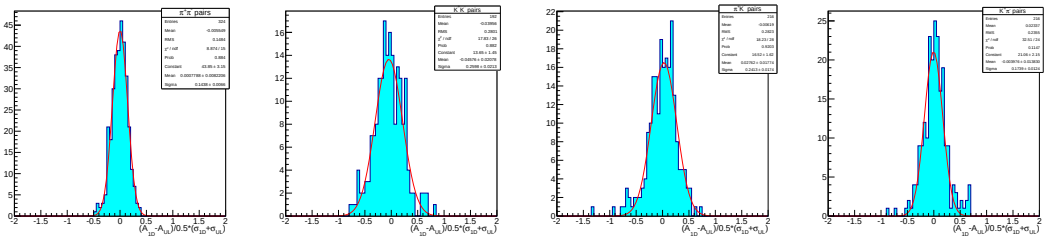

Figure 4.18.: Pulls between the hadron-pair asymmetries from 2010 data obtained with the 1D-QR and the UL estimator $\pi^+\pi^-$ pairs (1st column), K^+K^- pairs (2nd column), π^+K^- pairs (3rd column), and $K^+\pi^-$ pairs (4th column).

4.6.5. Cross-check of results

All COMPASS results need to be cross-checked independently before it is allowed to show them to the public. The results presented in this work are cross-checked between the groups of Trieste, Turino and Erlangen. In a first step the number of hadron-pairs which survived the cuts described in Sec. 4.3 are compared, which agree perfectly. The raw and the final asymmetries are then compared by building a pull distribution according to

$$\frac{A_{i,j}^{analysis1} - A_{i,j}^{analysis2}}{\frac{1}{2}(\sigma_{i,j}^{analysis1} + \sigma_{i,j}^{analysis2})}. \tag{4.25}$$

The Figure 4.19 shows the obtained distributions from the analyses of deuteron, 2007, and 2010 data. The agreement of the cross-check analysis of 2010 data is perfect and the agreement in the cases of deuteron and 2007 data is still very good. However the direct comparison of the calculated asymmetries shows (see Figs. A.37, A.38, and A.39) that the larger deviations in the pulls are caused by very small deviations of the asymmetries due to the lower sample size of the deuteron and the 2007 proton data. Furthermore the deuteron and 2007 cross-checks was only performed on the level of the 1D-QR method, which is more sensitive to small statistics.
The agreement for all years and pair combinations is almost perfect and no systematic error is taken into account from this test.

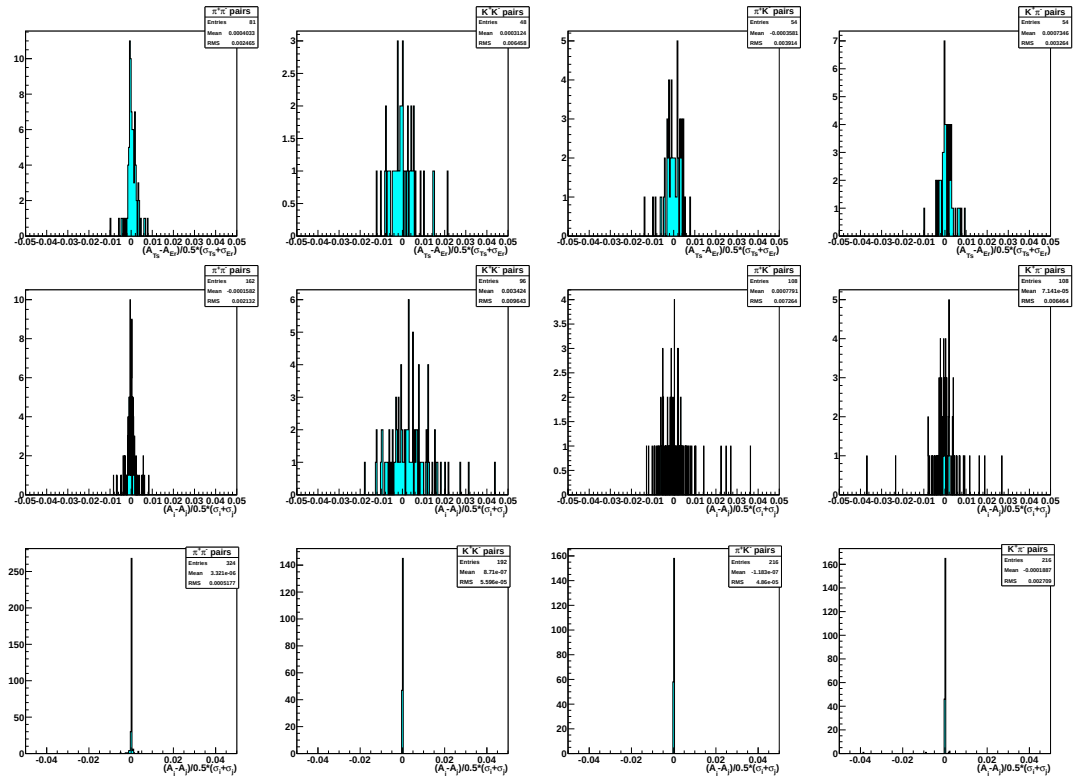

Figure 4.19.: Cross-check pulls between of the hadron-pair asymmetries from deuteron (1st row), 2007 (2nd row), and from 2010 data (3rd row): $\pi^+\pi^-$ pairs (1st column), K^+K^- pairs (2nd column), π^+K^- pairs (3rd column), and $K^+\pi^-$ pairs (4th column).

4.6.6. Systematic effects from the spectrometer acceptance

Possible acceptance effects of the target were already discussed in the Sec. 4.6.1. A way to study the acceptance of the spectrometer itself can be performed by splitting it virtually into segments. Therefore a segmentation into two parts, one time into top and bottom and second into right and left seen in beam direction is performed. The single events are assigned to the parts by the azimuthal polar angle of the scattered muon in the laboratory frame ϕ'. As described, the COMPASS spectrometer is almost symmetrical w.r.t. the horizontal axis, but not w.r.t. the vertical axis, due to the deflection of positively charged particles by the magnets SM1 and SM2 towards the Jura side. Hence at first order one would expect more compatible asymmetries from the top-bottom split then from the left-right split. The limited sample sizes of the deuteron and 2007 proton data just allow for a reasonable evaluation of the $\pi^+\pi^-$ asymmetry (Fig. 4.20 top, middle) while for the 2010 data this exercise was possible for all identified pairs (Fig. 4.20 (bottom) and Fig. A.40). To quantify the compatibility between the horizontal and vertical splits

the statistical normalized differences of the obtained bin-by-bin asymmetries is calculated by

$$A_{\text{top-bottom}} = \frac{\left|A_{\text{top}} - A_{\text{bottom}}\right|}{\sqrt{\sigma^2_{\text{top}} + \sigma^2_{\text{bottom}}}}, \qquad A_{\text{left-right}} = \frac{\left|A_{\text{left}} - A_{\text{right}}\right|}{\sqrt{\sigma^2_{\text{left}} + \sigma^2_{\text{right}}}}. \tag{4.26}$$

After subtracting the value of one standard deviation in quadrature from them

$$\alpha = \sqrt{A^2_{\text{top-bottom/left-right}} - 0.68^2} \tag{4.27}$$

for each x bin and each period separately, the systematic uncertainty is calculated as the arithmetic mean over all periods and bins

$$\sigma_{sys,tblr} = \frac{\sum_i \alpha_i}{\#\text{bins} \cdot \#\text{periods}} \tag{4.28}$$

in units of the statistical uncertainty. The resulting values are shown in Tab. 4.7. Almost all uncertainties are smaller then one unit of the corresponding statistical uncertainties and mostly higher in the left-right case than in the top-bottom case, as expected.
As shown in Sec. 4.4 the statistics available on the deuteron and the 2007 proton target are small w.r.t. the 2010 data. In this study, the resulting statistical fluctuations lead to uncertainties which are around one unit of the statistical uncertainties for h^+h^- pairs and half the statistical uncertainties for pion pairs. The deuteron and proton 2007 sample size of pairs which include kaons after the virtual splitting of the spectrometer into segments is not sufficient any more. Thus these are omitted in this study.
From these considerations, no systematic error from this test is taken into account in the case of the deuteron and the 2007 data. For the high statistic sample of 2010 the values in some bins differ by more than one standard deviation and therefore the highest of the two uncertainties is included into the overall uncertainty, see next section.

Table 4.7.: Systematic uncertainties from the spectrometer acceptance test in units of the statistical uncertainty for hadron-pairs from the deuteron, 2007, and 2010 proton data.

year/target	segmentation	h^+h^-	$\pi^+\pi^-$	K^+K^-	π^+K^-	$K^+\pi^-$
deuteron	top/bottom	0.82	0.54	–	–	–
deuteron	left/right	1.09	0.53	–	–	–
2007	top/bottom	0.87	0.85	–	–	–
2007	left/right	0.93	0.97	–	–	–
2010	top/bottom	0.73	0.76	0.54	0.75	0.46
2010	left/right	0.81	0.77	0.48	0.51	0.52

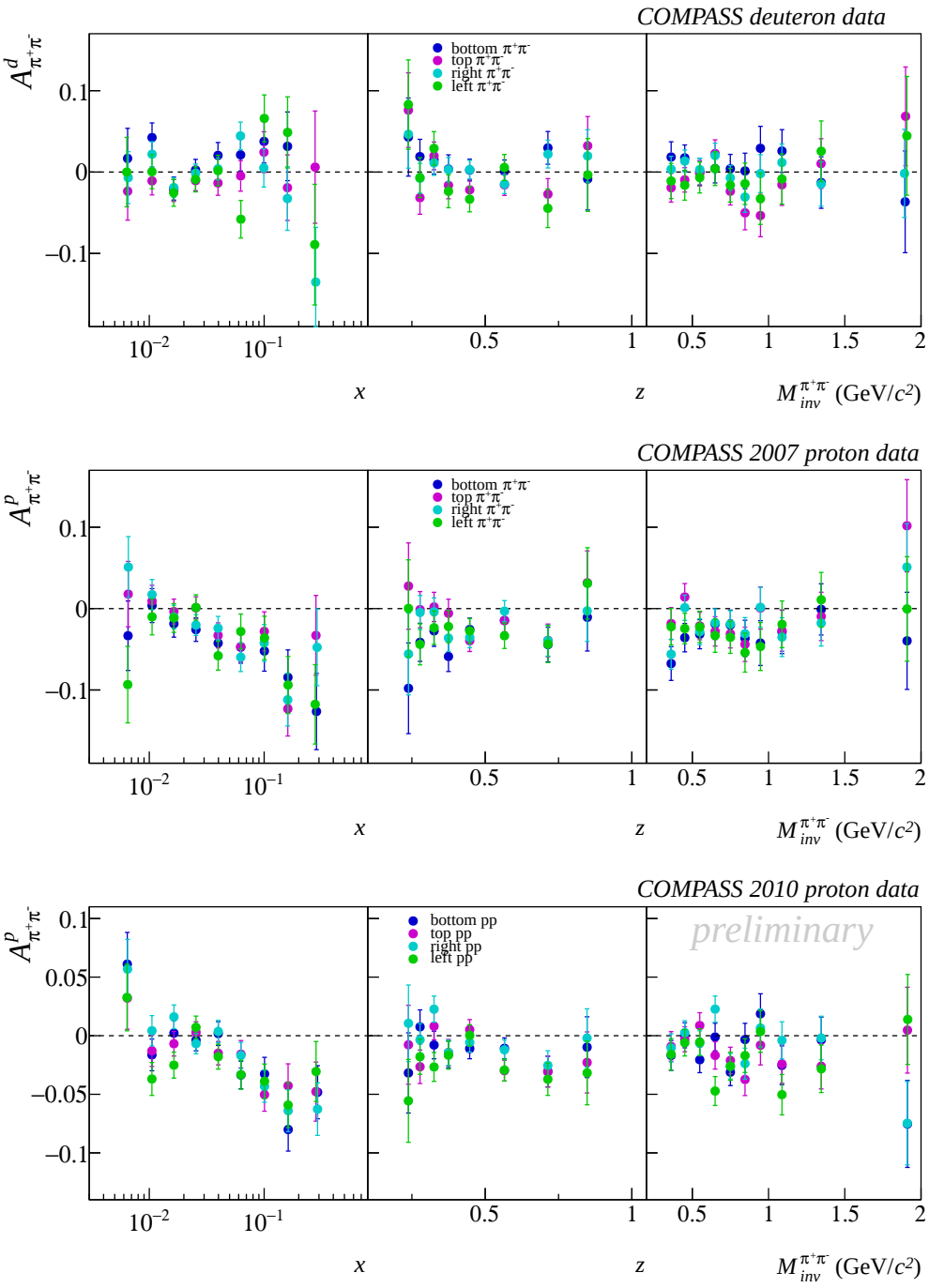

Figure 4.20.: The pion-pair asymmetry evaluated for a split of the spectrometer into top, bottom, left and right from deuteron (top), 2007 data (middle) and 2010 data (bottom).

4.6.7. Overall systematic uncertainty

The calculation of the overall systematic uncertainty from the single uncertainties described above is slightly different for each data sample and could also vary from all hadron-pairs to identified hadron-pairs, depending on the decisions which have been made by the responsible board of the collaboration. In common to all data samples, some tests did not show significant deviations from the expected values, these are: all azimuthal stability tests (R-test, T-test, RA-test), compatibility among periods, cross-check of independent analyses. Further all identified data samples have in common, that no uncertainty from the estimators is taken into account, since the used UL method is the most advanced method known.
In the case of the deuteron and 2007 proton data identified pairs it was decided to use as the only contribution to the overall systematical uncertainty the contribution by the false asymmetry test, as shown in the Tabs. 4.8, since the reliability of the spectrometer segmentation test suffers from the low statistics, see Sec. 4.6.6.
In the case of the 2010 identified pairs, the largest value out of three, namely the false asymmetry test and the two spectrometer acceptance tests, is used.
An additional scale uncertainty of $5.4\,\%$ for deuteron and $3\,\%$ for proton data has to be considered due to the uncertainty in the measurement of the target polarization.

Table 4.8.: The overall systematic uncertainty in units of the statistical uncertainty for unidentified and identified hadron-pairs from the deuteron $2003(2)$-2004, the proton 2007, and 2010 data.

target	year(s)	h^+h^-	$\pi^+\pi^-$	K^+K^-	π^+K^-	$K^+\pi^-$
deuteron	$2003(2)$-2004	0.4	0.6	0.8	0.7	0.6
proton	2007	0.7	0.7	0.5	0.7	0.5
proton	2010	0.8	0.8	0.5	0.8	0.5

4.7. Purity correction

The identification of the produced hadrons is performed via a ring-imaging Cherenkov detector (RICH), which is described in Sec. 3.4.1. The identification probabilities are close to 1 and thus the separation of pions, kaons and protons is very high, but a correction to the measured asymmetries due to a possible misidentification might be appropriate and needs to be studied.
The method to obtain the probabilistic values of identifying for instance a pion as a kaon $P_{\pi\to K}$, is based on the identification of known particles coming from certain decays [SSM06, Pes10, Joo13b]. A source of pure K^+K^- pairs is the decay of a $\phi(1020)$ meson, and the decay of a K^0 meson gives pure $\pi^+\pi^-$ pairs [PDG12]. In a first step these decays are selected from the data with dedicated cuts which do not involve information coming from the RICH detector. The second step is to pin down the selected particles in the RICH data and evaluate the probability to be correctly identified. Some assumptions have to be made, such as that the contribution from other particles e.g. protons is negligible.
In the case of single hadron asymmetries the purity correction is simpler and can be written as

$$A_{m,\pi} = P_{\pi\to\pi}A_{t,\pi} + P_{K\to\pi}A_{t,K}, \qquad A_{m,K} = P_{K\to K}A_{t,K} + P_{\pi\to K}A_{t,\pi}, \tag{4.29}$$

where $A_{m,K/\pi}$ are the measured asymmetries and $A_{t,K/\pi}$ the true asymmetries. Writing these equations in a matrix way, they can be solved via an inversion of it.
Concerning the hadron-pair case the corresponding equation(s) get more complicated, due to the twofold intrinsic pair probabilities. The purity for e.g. the kaon sample is defined as $P_{K\to K} = \epsilon_{K\to K}\frac{N_{t,K}}{N_{m,K}}$, where $\epsilon_{x\to y}$ is the efficiencies/mis-identification probabilities for the RICH identification. The terms $N_{t,x}$ or $N_{m,x}$ are the number of true or measured hadrons of type x.
Thus a pion pair can be mis-identified as a pure kaon pair but also as a π^+K^- or a $K^+\pi^-$ pair and the purity is $P_{\pi^+\pi^-\to\pi^+\pi^-} = \epsilon_{\pi\to\pi}\epsilon_{\pi\to\pi}\frac{N_{t,\pi\pi}}{N_{m,\pi\pi}}$. Like in the single hadron case one can write the purity correction as an equation of the form: $A_m = P\cdot A_t$, where the vectors $A_{m/t}$ contain the four hadron-pair asymmetry values for a certain x, z or M_{inv} bin. The full equation reads:

$$\begin{pmatrix} A_{m,\pi\pi} \\ A_{m,\pi K} \\ A_{m,K\pi} \\ A_{m,KK} \end{pmatrix} = \begin{pmatrix} P_{\pi\pi\to\pi\pi} & P_{\pi K\to\pi\pi} & P_{K\pi\to\pi\pi} & P_{KK\to\pi\pi} \\ P_{\pi\pi\to\pi K} & P_{\pi K\to\pi K} & P_{K\pi\to\pi K} & P_{KK\to\pi K} \\ P_{\pi\pi\to K\pi} & P_{\pi K\to K\pi} & P_{K\pi\to K\pi} & P_{KK\to K\pi} \\ P_{\pi\pi\to KK} & P_{\pi K\to KK} & P_{K\pi\to KK} & P_{KK\to KK} \end{pmatrix} \begin{pmatrix} A_{t,\pi\pi} \\ A_{t,\pi K} \\ A_{t,K\pi} \\ A_{t,KK} \end{pmatrix}. \tag{4.30}$$

It is solved via matrix inversion: $A_t = P^{-1}\cdot A_m$. And the corresponding error propagation gives $\mathrm{cov}(A_t) = P^{-1}\cdot\,\mathrm{cov}(A_m)\cdot(P^{-1})^T$. The entries of the purity matrix are

$$P = \begin{pmatrix} \epsilon_{\pi\pi}\epsilon_{\pi\pi}\frac{N_{t,\pi\pi}}{N_{m,\pi\pi}} & \epsilon_{\pi\pi}\epsilon_{K\pi}\frac{N_{t,\pi K}}{N_{m,\pi\pi}} & \epsilon_{K\pi}\epsilon_{\pi\pi}\frac{N_{t,K\pi}}{N_{m,\pi\pi}} & \epsilon_{K\pi}\epsilon_{K\pi}\frac{N_{t,KK}}{N_{m,\pi\pi}} \\ \epsilon_{\pi\pi}\epsilon_{\pi K}\frac{N_{t,\pi\pi}}{N_{m,\pi K}} & \epsilon_{\pi\pi}\epsilon_{KK}\frac{N_{t,\pi K}}{N_{m,\pi K}} & \epsilon_{K\pi}\epsilon_{\pi K}\frac{N_{t,K\pi}}{N_{m,\pi K}} & \epsilon_{K\pi}\epsilon_{KK}\frac{N_{t,KK}}{N_{m,\pi K}} \\ \epsilon_{\pi K}\epsilon_{\pi\pi}\frac{N_{t,\pi\pi}}{N_{m,K\pi}} & \epsilon_{\pi K}\epsilon_{K\pi}\frac{N_{t,\pi K}}{N_{m,K\pi}} & \epsilon_{KK}\epsilon_{\pi\pi}\frac{N_{t,K\pi}}{N_{m,K\pi}} & \epsilon_{KK}\epsilon_{K\pi}\frac{N_{t,KK}}{N_{m,K\pi}} \\ \epsilon_{\pi K}\epsilon_{\pi K}\frac{N_{t,\pi\pi}}{N_{m,KK}} & \epsilon_{\pi K}\epsilon_{KK}\frac{N_{t,\pi K}}{N_{m,KK}} & \epsilon_{KK}\epsilon_{\pi K}\frac{N_{t,K\pi}}{N_{m,KK}} & \epsilon_{KK}\epsilon_{KK}\frac{N_{t,KK}}{N_{m,KK}} \end{pmatrix}. \tag{4.31}$$

The global efficiency for pions is ≈ 0.97 and ≈ 0.94 for kaons. There are two probabilities in each term since the probability for a pair is the product of the probabilities for the single hadrons of the pair. So each term of the purity matrix is given by the probability for a pair $l\,m$ to be identified as $x\,y$, times the percentage of true pairs of type $l\,m$ in the measured sample $x\,y$. Note that the purity of hadron-pairs does not factorize into a product of the single purities since the number of the pairs $x\,y$ is not the product of the number of single hadrons, e.g. for kaon pairs $N_{m,KK} \neq N_{m,K}\ N_{m,K}$.
The purity corrected asymmetries A_t in comparison to the measured asymmetries A_m are shown in Fig. 4.21 for 2007 proton and in Fig. 4.22 for 2010 proton data, where the pulls between both are shown on the right side. No purity correction is applied on the deuteron data, since the absence of a signal is interpreted as a close-to-complete cancellation of the u and d quark transversities and thus a correction by a signal which is zero is not meaningful. Due to the ≈ 3.5 times larger rest mass of the kaons w.r.t. the pions the correction of the asymmetries as a function of the M_{inv} is not possible for the first 6 bins.
The difference between the measured A_m and the purity corrected/true asymmetry A_t is almost zero (see pulls) and therefore negligible for pion pairs of both proton data sets. The true asymmetries of the other pairs show a very small influence of the purity correction of the order of a few percent of the statistical uncertainties without systematic effects. It is much smaller than the uncertainties given by the systematic checks, thus are well covered by the overall systematic uncertainty, see Sec. 4.6.7.

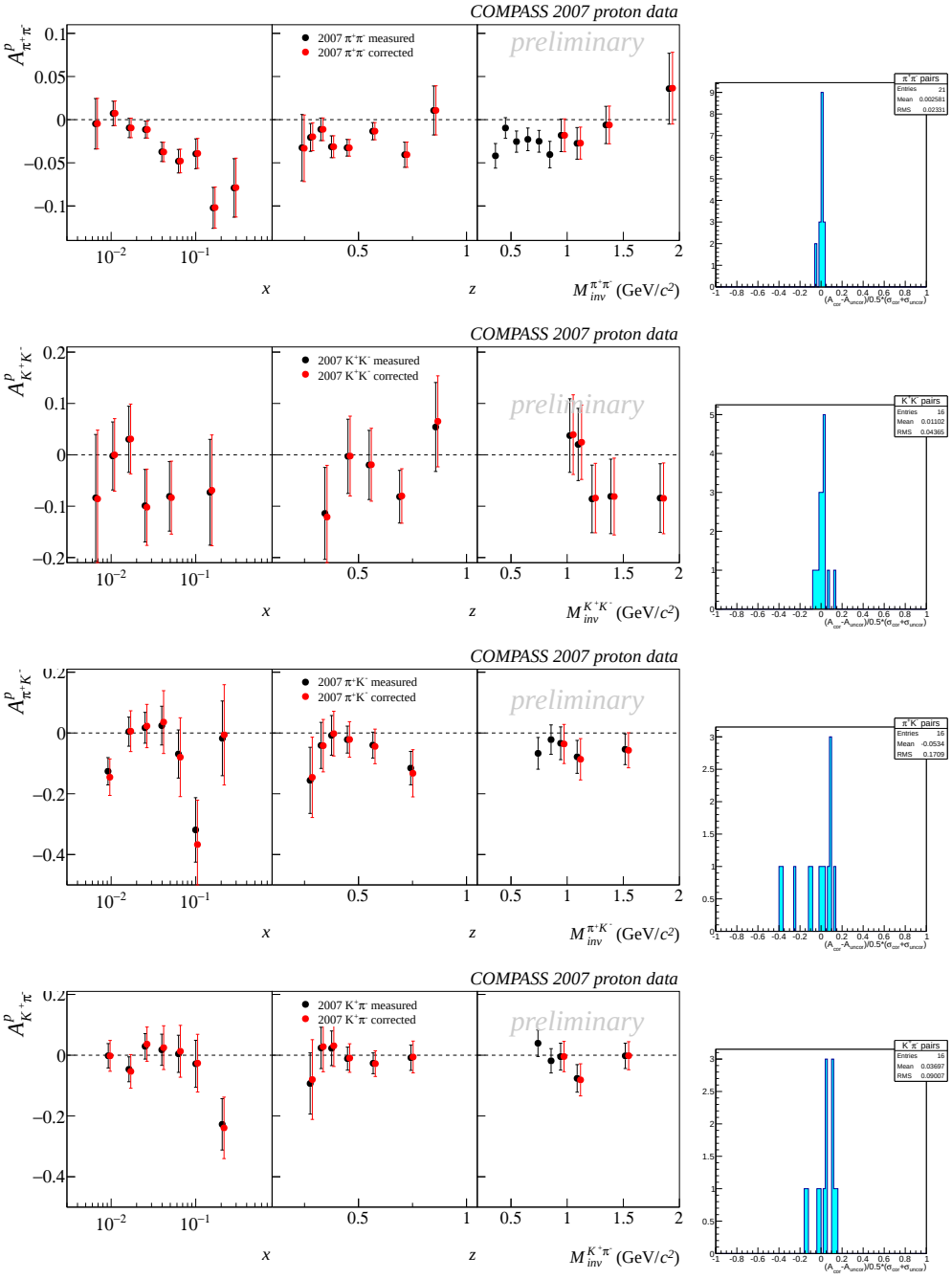

Figure 4.21.: Purity corrected true hadron-pair asymmetries A_t (red dots) in comparison to the measured asymmetries A_m (black dots) of 2007 proton data ans the corresponding pull between both: $\pi^+\pi^-$ pairs (1st row), K^+K^- pairs (2nd row), π^+K^- pairs (3rd row), $K^+\pi^-$ pairs (4th row) .

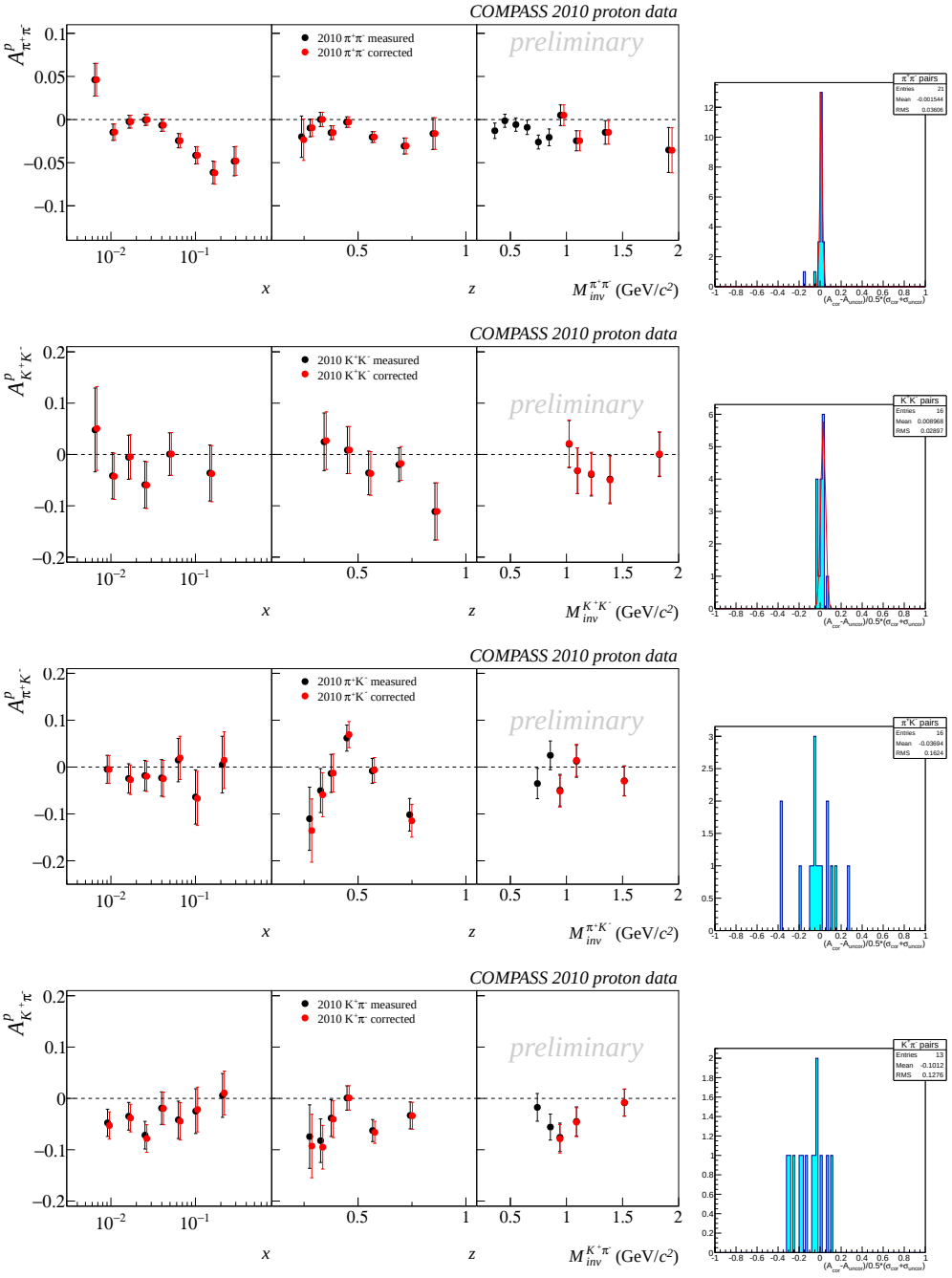

Figure 4.22.: Purity corrected true hadron-pair asymmetries A_t (red dots) in comparison to the measured asymmetries A_m (black dots) of 2010 proton data ans the corresponding pull between both: $\pi^+\pi^-$ pairs (1$^{\text{st}}$ row), K^+K^- pairs (2$^{\text{nd}}$ row), π^+K^- pairs (3$^{\text{rd}}$ row), $K^+\pi^-$ pairs (4$^{\text{th}}$ row) .

4.8. Improvements to previous analyses of deuteron and 2007 proton data

The hadron-pair asymmetries of unidentified pairs h^+h^- from the deuteron and 2007 proton data were already published in [COMPASS12c]. So far only a unreleased analysis of identified hadron-pairs from these data samples by Wollny in [Wol10] has been performed. The main goal of the evaluation of azimuthal spin asymmetries of hadron-pairs is the extraction of the transversity distributions. Therefore a reliable and homogeneous analysis of all identified pairs from all data sets of the COMPASS experiment is necessary. Thus a reanalysis of the deuteron and 2007 proton data was performed, in which the data selection and methods as well as the binning is unified. The analysis of the 2010 proton data was taken as a reference, but also differences due to the data processing by CORAL were considered and retained. The unification compromises five main topics. Among these are two for formal reasons, since they do not change the overall statistics significantly. First the COMPASS spectrometer has an acceptance in x of 0.003 to 0.7 which is now used for all samples, while in [COMPASS12c] the upper limit of x was set to 1. Second the cut on the momentum of the incoming beam muons is specified to $140\,\mathrm{GeV}/c < p_\mu < 180\,\mathrm{GeV}/c$, while $0\,\mathrm{GeV}/c < p_\mu < 200\,\mathrm{GeV}/c$ was used in the publication. Moreover, due to the applicability of model calculations by Bacchetta and Radici (see Sec. 6.3.3) the range of the invariant mass of the pair was optionally limited to $M_{inv} < 1.5\,\mathrm{GeV}/c^2$. In general, this cut is not used for the final results here, but a sample with this cut is provided in addition to the full range sample.
In the analysis of [COMPASS12c] dedicated cuts where performed based on the data of the hadronic calorimeters, in order to reject a so-called "low energy band" which was thought to be the result of muons misidentified as hadrons. It was shown that these particles which deposit only a small fraction of their energy in the calorimeter are muons, but not elastically scattered beam muons [Soz11]. In fact these muons are produced in the decay of pions coming from SIDIS processes. The deviation on the track direction of muons produced in the pion decay and the track direction of the pions was found to be small and thus the angle information carried by the muons is still usable for this analysis. Thus no calorimeter cuts have been applied in this work, see also Sec. 6.3.3.
The fifth difference w.r.t. the published h^+h^- results is related to the unbinned likelihood fit method, where the kinematic values of each pair were weighted with the fraction of polarizable material inside the target f and the depolarization factor[4] D_{nn} before the fit is performed. In this analysis a raw asymmetry without any weighting is calculated and afterwards it is corrected in each kinematic bin with the mean f, D_{nn} and target polarization P_T in order to get the final asymmetry. The UL fit of the single hadron analysis is also performed on the pure angular distributions without any preceding weighting, thus a compatibility between the single hadron results, such as Collins and Sivers, with the hadron-pair results is given. This procedure has also the advantage that one can go one step backward in the analysis, i.e. from the final to the raw asymmetry by dividing the amplitude value (and its error) in each bin by the mean values of f, D_{nn}, and P_T the mean target polarization.

[4] The fraction of the spin of the lepton which is transfered to the virtual photon.

Table 4.9.: Influence of the unitized cuts on the deuteron 2002-2004 data (top table) and on the 2007 proton data (bottom table). The difference is shown for each individual cut w.r.t. the original number of hadron-pairs. Note that the total difference is not the sum of the individual differences due to possible overlaps of the cuts.

2002-2004 cut	h^+h^- published	h^+h^- this study	difference	difference (%)
M_{inv}	5,806,180	5,951,546	+145,366	+2.50
p_μ	5,806,180	5,799,646	-6,534	-0.11
x	5,806,180	5,806,149	-31	
calo	5,806,180	6,351,078	+544,898	+9.38
total	**5,806,180**	**6,508,375**	**702,195**	**+12.1**
2007 cut	h^+h^- published	h^+h^- this study	difference	difference (%)
M_{inv}	10,913,078	11,211,281	+298,203	+2.73
p_μ	10,913,078	10,858,102	-54,976	-0.50
x	10,913,078	10,912,967	-111	-0.001
calo	10,913,078	12,299,588	+1,386,510	+12.7
total	**10,913,078**	**12,596,359**	**+1,683,281**	**+15.4**

A comparison of the influences of these modified cuts is given in Tab. 4.9 (top table) for the deuteron data and in Tab. 4.9 (bottom table) for the 2007 proton data, the overall gain in statistics is $12.1\,\%$ and $15.4\,\%$ respectively. The abolition of the M_{inv} cuts leads to an increase by around $3\,\%$ and the major increase is generated by the abolition of the calorimetry cuts at around $10\,\%$. The other cuts on p_μ and x do not have a significant influence.
More important than the influence on the statistics is the influence on the obtained asymmetries by the modifications. A detailed comparison of the published results and the asymmetries calculated with each modified cut individually is shown in Figs. A.41 to A.45 for both deuteron and 2007 proton data. Figure 4.23 shows the comparison including all five modifications listed above, for deuteron (top) and 2007 proton (bottom) data.
The overall difference between the published results and the asymmetries obtained with the modified cuts and methods is visible but small, it does not change the main characteristics of the signal such as slopes and dips. As can be seen in Fig. A.42 and Fig. A.43 the stricter cut on the beam momentum and on x has no influence on the amplitudes obtained. The additional pairs of the invariant mass region above $1.5\,\mathrm{GeV}/c^2$ have a weak influence on the amplitudes in the high x and high z region, see Fig. A.41. The main contributions to the small overall difference in Fig. 4.23 is clearly related to the calorimetry cut, see Fig. A.44, while the non-weighted fit leads to small and non-systematic deviations, see Fig. A.45.

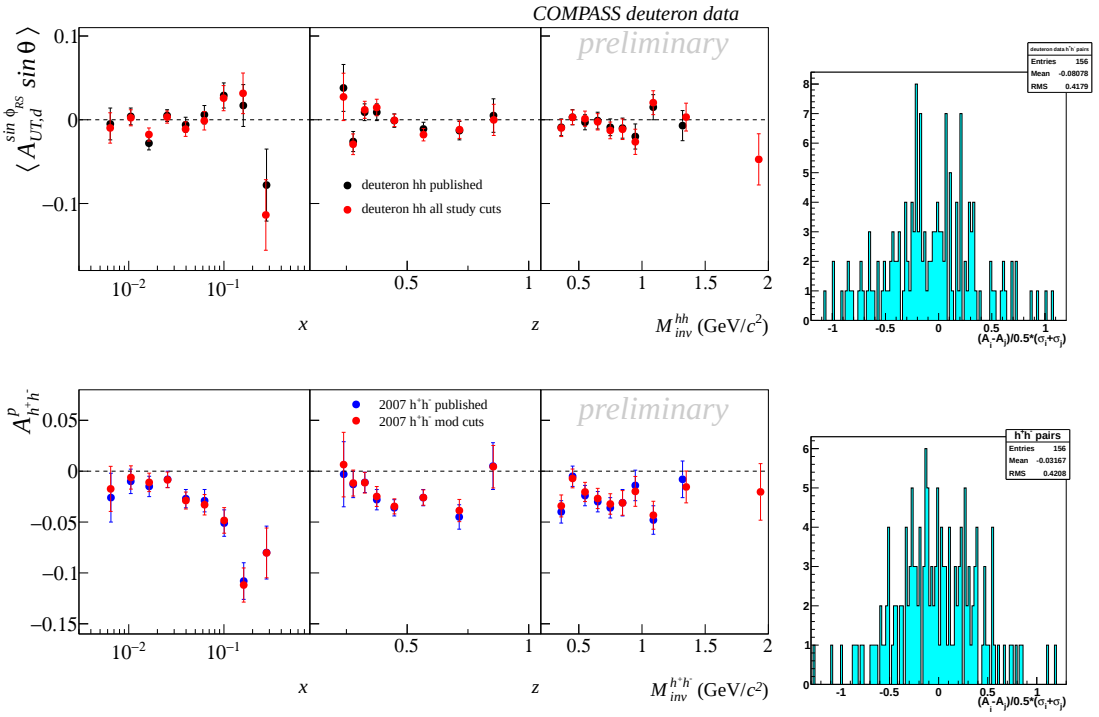

Figure 4.23.: The published hadron-pair asymmetries of all pairs h^+h^- from deuteron data (top, black dots) and from 2007 proton data (bottom, blue dots) in comparison with the results obtained with the modified cuts and methods (red dots). The corresponding pull distributions between the data points from the publication [COMPASS12c] and from this work are shown in the right column.

4.9. Combination of 2007 and 2010 proton data

In the following section the procedure of combining the two independent results of the hadron-pair asymmetries from the 2007 and the 2010 proton data is described. For this, two different methods have been studied and the corresponding results are compared. The same methods were also used to combine the single hadron asymmetries, such as the Collins and the Sivers asymmetry [BDMS12]. A detailed study was performed in this COMPASS note because of an absolute scale uncertainty of ± 0.01 in the Sivers asymmetry of positive hadrons from the 2007 data due to systematic effects, which has to be taken into account properly by the methods.
The first method, "method A" in the following is based on the normalization of the asymmetry amplitudes to their overall weighted mean, which is a more direct approach compared to the second method which is based on the standard linear least squares fit, "method B" in the following.

Method A

Method A uses standard formulas in order to normalize the two sets of data to the overall mean value. A possible absolute scale uncertainty α can be taken into account, but is not present in the hadron-pair case, which means $\alpha = 0$ in the following. The mean asymmetry of all bins i of a data set $k \in [07, 10]$ referring to 2007, and 2010, respectively, and its variance are calculated by

$$\bar{X}_k = \frac{\sum_i \frac{X_{k,i}}{\sigma^2_{X_{k,i}}}}{\sum_i \frac{1}{\sigma^2_{X_{k,i}}}}, \qquad \sigma^2_{\bar{X}_k} = \frac{1}{\sum_i \frac{1}{\sigma^2_{X_{k,i}}}} + \alpha^2, \tag{4.32}$$

where $\sigma^2_{X_{k,i}} = \sigma^2_{stat,X_{k,i}} + \sigma^2_{sys,X_{k,i}}$. From this, the overall mean of two data sets is

$$\bar{Z} = \frac{\frac{\bar{X}_{07}}{\sigma^2_{\bar{X}_{07}}} + \frac{\bar{X}_{10}}{\sigma^2_{\bar{X}_{10}}}}{\frac{1}{\sigma^2_{\bar{X}_{07}}} + \frac{1}{\sigma^2_{\bar{X}_{10}}}}, \qquad \sigma^2_{\bar{Z}} = \frac{1}{\frac{1}{\sigma^2_{\bar{X}_{07}}} + \frac{1}{\sigma^2_{\bar{X}_{10}}}}. \tag{4.33}$$

Then the differences of the overall to the individual mean values are calculated $c_k = \bar{Z} - \bar{X}_k$ in order to built the "normalized asymmetries" on the level of the individual data sets $X^n_{k,i} = X_i + c_k$. Finally the combined asymmetry amplitude in each bin i is

$$Z_i = \frac{\frac{X^n_{07,i}}{\sigma^2_{X_{07,i}}} + \frac{X_{10,i}}{\sigma^2_{X_{10,i}}}}{\frac{1}{\sigma^2_{X_{07,i}}} + \frac{1}{\sigma^2_{X_{10,i}}}}, \qquad \sigma^2_{Z_i} = \frac{1}{\frac{1}{\sigma^2_{X_{07,i}}} + \frac{1}{\sigma^2_{X_{10,i}}}}. \tag{4.34}$$

Note that the statistical uncertainties on c_k have been ignored, since they are very small and negligible w.r.t. the bin-by-bin uncertainties.
The statistical and the systematical uncertainties can be obtained from $\sigma^2_{Z_i}$ by

$$\sigma^2_{stat,Z_i} = \frac{1}{\frac{1}{\sigma^2_{stat,X_{07,i}}} + \frac{1}{\sigma^2_{stat,X_{10,i}}}}, \qquad \sigma^2_{sys,Z_i} = \sigma^2_{Z_i} - \sigma^2_{stat,Z_i}. \tag{4.35}$$

Method B

Method B was developed to deal with data having multiplicative normalization uncertainties [NNPDF10]. These can be taken into account by a χ^2 minimization of the corresponding covariance matrix of the variances of m bins

$$V_k = \begin{pmatrix} \sigma^2_{k,1} + \alpha^2 & \alpha^2 & ... & \alpha^2 \\ \alpha^2 & \sigma^2_{k,2} + \alpha^2 & ... & \alpha^2 \\ ... & ... & ... & ... \\ \alpha^2 & \alpha^2 & ... & \sigma^2_{k,m} + \alpha^2. \end{pmatrix} \tag{4.36}$$

The asymmetry amplitude values are contained in the vectors $\vec{X}_k$.
The χ^2 of V_k then is

$$\chi^2 = \left(\vec{X}_k - \vec{\Lambda}\right)^{\mathrm{T}} V_k^{-1} \left(\vec{X}_k - \vec{\Lambda}\right), \tag{4.37}$$

where $\vec{\Lambda} = C\,\vec{\Psi}$ are linear functions of the parameter Ψ which can be written as

$$\vec{\Psi} = \left(C^{\mathrm{T}} V_k^{-1} C\right)^{-1} C^{\mathrm{T}} V_k^{-1} \vec{X}_k = D_k \vec{X}_k \tag{4.38}$$

and the covariance matrix as

$$V_\Psi^{-1} = D_k^{\mathrm{T}} V_k^{-1} D_k. \tag{4.39}$$

In the present case two independent measurements, 07 and 10 with the same expectation values $\vec{E}$ are given. Then the χ^2 becomes

$$\chi^2 = \left(\vec{X}_{07} - \vec{E}\right)^{\mathrm{T}} V_{07}^{-1} \left(\vec{X}_{07} - \vec{E}\right) + \left(\vec{X}_{10} - \vec{E}\right)^{\mathrm{T}} V_{10}^{-1} \left(\vec{X}_{10} - \vec{E}\right). \tag{4.40}$$

The minimization is performed by demanding the derivatives to be zero, yielding

$$V_{07}^{-1}\,\vec{X}_{07} + V_{10}^{-1}\,\vec{X}_{10} = \left(V_{07}^{-1} + V_{10}^{-1}\right)\vec{E}. \tag{4.41}$$

Solving for the expectation values one gets

$$\vec{E} = \left(V_{07}^{-1} + V_{10}^{-1}\right)^{-1} V_{07}^{-1} \vec{X}_{07} + \left(V_{07}^{-1} + V_{10}^{-1}\right)^{-1} V_{10}^{-1} \vec{X}_{10}, \tag{4.42}$$

which can be simplified with $B_k = \left(V_{07}^{-1} + V_{10}^{-1}\right)^{-1} V_k^{-1}$ to

$$\vec{E} = B_{07}\vec{X}_{07} + B_{10}\vec{X}_{10}, \qquad V_E = B_{07}\vec{X}_{07}B_{07}^{\mathrm{T}} + B_{10}\vec{X}_{10}B_{10}^{\mathrm{T}}. \tag{4.43}$$

The overall statistical and the systematic uncertainties, the latter is shown in Tab. 4.10, can be calculated from the single uncertainties as described for method A.

Table 4.10.: Overall systematic uncertainty in units of the statistical uncertainty for the 2007/2010 combined proton data, obtained with method A.

	h^+h^-	$\pi^+\pi^-$	K^+K^-	π^+K^-	$K^+\pi^-$
overall systematic uncertainty	0.8	0.6	0.5	0.6	0.5

Comparison of results

In Fig. 4.24 (top panel) the results obtained with methods A and B are compared in the case of the pion pair asymmetries, for all other pairs see Fig. A.46. They are almost identical, only a pull between both shows difference in the order of $0.02\,\sigma$. As method B is regarded as the more correct routine as the more general one, all combined 2007/2010 results are calculated using it. As an example the individual results and the combined result of the pion pair asymmetry is shown in Fig. 4.24 (bottom panel), while all other pairs can be found in the Fig. A.47. The total χ^2_{red} from this procedure is 0.95 for $\pi^+\pi^-$, 0.49 for K^+K^-, 0.53 for π^+K^-, and 0.89 for $K^+\pi^-$. The bin-by-bin χ^2_{red} can be found in Tab. A.7.

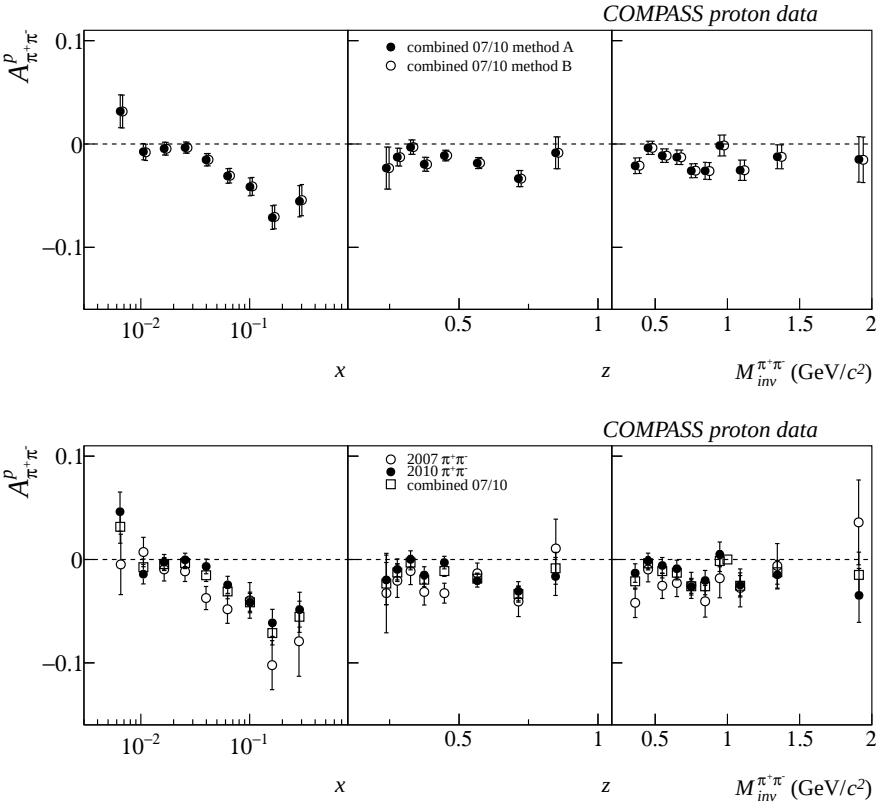

Figure 4.24.: The upper panel shows the comparison of the results obtained with method A (black dots) and method B (open circles) of the combination of the 2007 and 2010 proton pion pair asymmetries. The individual results from 2007 (open circles) and 2010 (black dots) proton data in comparison with the combined results (open squares) are presented in the bottom panel.

5. Results

In the following the final results on the hadron-pair asymmetries from the analyses described in the last section are presented. They are plotted as functions of x, z and M_{inv}, where x is the Bjørken scaling variable, z is the sum of the fractional energies carried by the observed final state hadrons $z = z_1 + z_2$ and M_{inv}, the invariant mass of the pair. Error bars of the data points represent the statistical uncertainties only, while the systematic uncertainties, discussed in Sec. 4.6.7 are indicated by the gray bands, which also indicate the binning (see Tab. A.8).
The results from the 2010 data taking period, the main part of this work, are shown in Sec. 5.2.1 for all hadron-pairs and in Sec. 5.2.2 for identified hadron-pairs. The data samples collected on the deuteron target in the years 2002 until 2004 and from the 2007 data taking period on the proton target have been analyzed in addition afterwards, in order to provide a complete set of results on the dihadron asymmetry of identified hadron-pairs by COMPASS. Even though a preliminary analysis of the identified deuteron data was available before, see Fig. 2.19, a complete reanalysis of this data was necessary to ensure common cuts and common binning, as well as improvements in terms of the particle, track, and vertex identification algorithms. Also for the 2007 proton data, see Fig. 2.20, the cuts have been unified w.r.t. the analysis of 2010 data where the particle identification was introduced. The differences between the previous analyses and this work on the deuteron and 2007 proton data are described in detail in Sec. 4.8.
The identical framework of the analyses on the two proton target data sets from 2007 and 2010 allows, by methods described in Sec. 4.9 for a combination of the asymmetries obtained, which are shown in Sec. 5.2.2.
All numerical values of the results presented in this chapter and the corresponding bin-by-bin mean values of selected quantities are given in Tabs. A.9 to A.30 and in Figs. A.48 to A.49.

5.1. Results from the deuteron data

The COMPASS experiment took data on a polarized deuteron target in the years 2002, 2003, and 2004, therefrom five periods of data with transverse polarization were collected. The data from the 2002 running, being two out of these five periods corresponding to 20 % of the total sample, are not applicable to particle identification since the RICH detector was not yet fully functioning in this first year of COMPASS running. The unification of cuts and methods (see Sec. 4.8) as in the analysis of the 2010 proton data was also applied on the deuteron data.

5.1.1. All hadron-pair asymmetry from the deuteron data

The hadron-pair azimuthal asymmetry of all pairs h^+h^- on a deuteron target from the running periods of 2002, 2003, and 2004 as a function of x, z, and M_{inv} is shown in Fig. 5.1. The amplitudes of the asymmetry are zero in bins of z and M_{inv}, as well as in the region of $x < 0.1$. In the three highest x bins it is still compatible with zero within the uncertainties, but may indicate a certain trend.

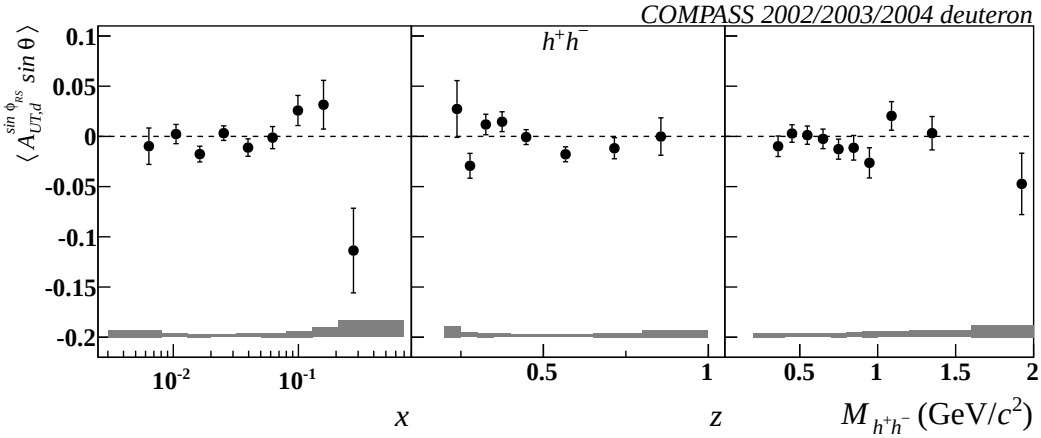

Figure 5.1.: The hadron-pair azimuthal asymmetry on a deuteron target of all pairs h^+h^- from the 2002-04 data.

5.1.2. Identified hadron-pair asymmetry from the deuteron data

In Sec. 2.4.2 the preliminary results of identified hadron-pair asymmetries from the deuteron data are shown. With the advanced cuts, methods and an equal binning w.r.t. the proton data analysis the new results are shown in Fig. 5.2. The asymmetry of identified pion pairs (1st row) is zero in all three dependencies, even more clearly than for the h^+h^- pairs, except of the ρ meson mass ($m_\rho = 775.5\,\mathrm{MeV}/c^2$ [PDG12]) region. The pure kaon pair asymmetry (2nd row), with larger statistical uncertainties is small, fluctuating and compatible with zero. An indication of positive nonzero amplitudes between an invariant mass of $1.15\,\mathrm{GeV}/c^2$ and $1.5\,\mathrm{GeV}/c^2$ is given. The mixed pairs, π^+K^- (3rd row), and $K^+\pi^-$ (4th row) are compatible with zero within the uncertainties in bins of z and M_{inv}. The dependence in x shows a weak indication of a positive or negative rise at high x for π^+K^- and $K^+\pi^-$, respectively.

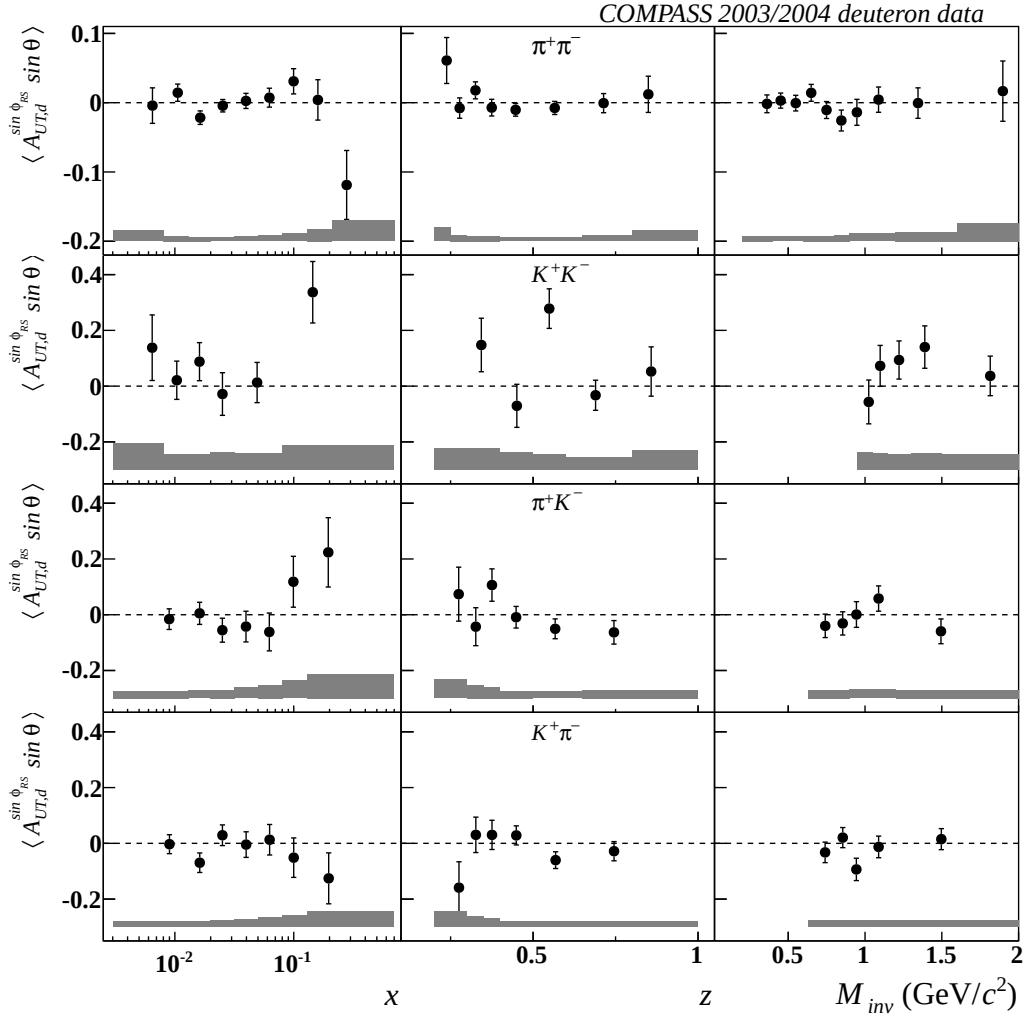

Figure 5.2.: Results of the hadron-pair azimuthal asymmetries measured by the COMPASS experiment on the deuteron target for identified hadron-pairs $\pi^+\pi^-$ (1st row), K^+K^- (2nd row), π^+K^- (3rd row), and $K^+\pi^-$ (4th row) with advanced cuts. Please note the different scale used for pairs which include kaons w.r.t. the scale used for pure pion pairs.

5.2. Results from the proton target

The available statistics on the transversely polarized proton targets are approximately a factor of five times larger than on the deuteron target.

5.2.1. All hadron-pair asymmetry from the proton data

In this section the results of unidentified hadron-pairs are shown. This is the first step of the analysis (since no particle identification is applied here). The pairs are denoted as h^+h^- and the pion mass was assigned to all of them.

2007 data

The hadron-pair azimuthal asymmetry of all hadron-pairs from the data collected during the 2007 running are shown in Fig. 5.3. These results are obtained with the advanced set of cuts described in Sec. 4.8 [COMPASS13] w.r.t. to the published results of [COMPASS12c]. Even though the difference between both analyses is small, the unification of cuts and methods was applied in foresight of the combination of the 2007 and 2010 data. A direct comparison of the results can be found in the Sec. 4.8.
As can be seen in Fig. 5.3, large negative asymmetry amplitudes up to -0.10 are observed in the so-called "valence region" $x > 0.032$, while for $x < 0.032$, the asymmetries are compatible with zero. The asymmetry is negative in the whole z range, without a clear trend. An indication of nonzero asymmetry amplitudes in the M_{inv} dependence between $500\,\mathrm{MeV}/c^2$ and $1\,\mathrm{GeV}/c^2$ is visible

2010 data

With the large amount of data collected in the 2010 running the statistical uncertainties could be reduced significantly. The obtained asymmetries are shown in Fig. 5.4 [COMPASS14a]. The clear rise of the magnitude of the amplitudes with increasing values of x already seen in the 2007 data results is confirmed, even though the asymmetry reaches $6\,\%$ at its maximum. The structure of the dependence in z changed to a shape with a moderate decrease of the amplitude down to almost zero for the fifth bin, with a subsequent increase for higher values of z. The negative dip around the ρ meson mass in the asymmetry as a function of the invariant mass is more pronounced in this data set, since the amplitude becomes again compatible with zero in the seventh bin (0.9 – $1.0\,\mathrm{GeV}/c^2$).

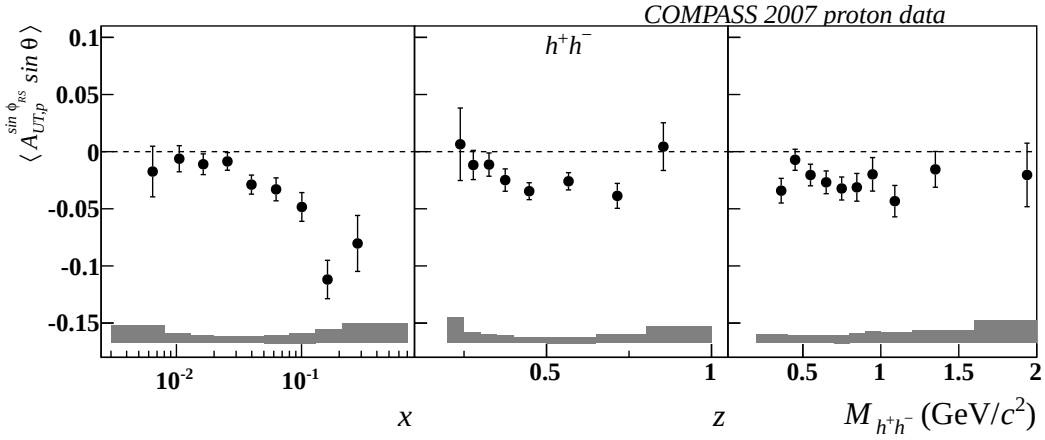

Figure 5.3.: The Hadron-pair azimuthal asymmetry on a proton target of all hadron-pairs h^+h^- from the 2007 data [COMPASS14a].

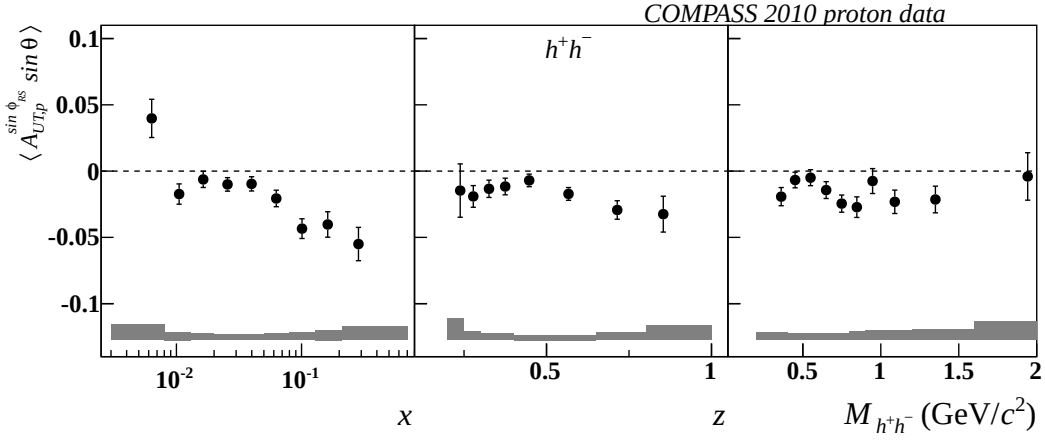

Figure 5.4.: The hadron-pair azimuthal asymmetry on a proton target of all hadron-pairs h^+h^- from the 2010 data [COMPASS14a].

Combined 2007 and 2010 data

The final 2007 hadron-pair data set contains around one third of the statistics w.r.t. the 2010 data set. Therefore the statistical uncertainties could be reduced by a factor larger than 1.6.
Thus the 2010 data are the dominant part in the combined signal, which is shown in Fig. 5.5. All significant features, which were described above are still present. The slope in x is smoothed, with very small error bars also in the high x region. The asymmetry as a function of z is compatible with a constant function over the whole range. The negative dip at the ρ meson mass is very pronounced, the amplitudes decrease almost down to zero at its edges and are negative in the very low M_{inv} region and between 1 and 1.5 GeV$/c^2$.

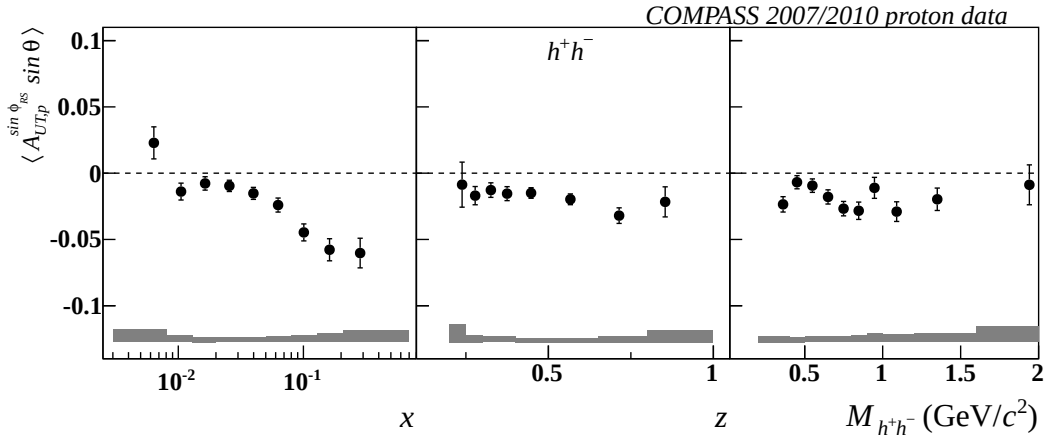

Figure 5.5.: The hadron-pair azimuthal asymmetry on a proton target of all hadron-pairs h^+h^- from the combined 2007 and 2010 data [COMPASS14a].

5.2.2. Identified hadron-pair asymmetries from the proton data

The identification of the hadrons was performed with the method described in Sec. 4.3.4. A possible influence of the misidentification of hadrons was checked and found to be negligible, see Sec. 4.7.

2007 data

The asymmetries of the four possible combinations of pairs from the 2007 proton target data are shown in Fig. 5.6. A trend of large amplitudes at high x values is clearly visible for the pion pairs, as well as clear negative mean values in their z and M_{inv} dependencies. The kaon pairs also show negative mean values in all three dependencies, without clear trends being compatible with zero. The asymmetries of both mixed pairs are compatible with zero within their uncertainties, with slightly negative mean value for π^+K^- pairs.

2010 data

The 2010 data sample offers three times more statistics than the 2007 data sample, accordingly the picture gets more precise also for the pairs which contain kaons. Except for the pion pairs asymmetry amplitudes with their clear increase at large x (see Fig. 5.7) the signal of all other pairs is compatible with zero within the uncertainties in the x dependence. In the case of the $K^+\pi^-$ pairs (4^{th} row) an indication of a negative mean value is given. The fluctuating amplitudes without a clear trend for the pion pair asymmetry as a function of z allow one to compare it with a constant function. The negative dip around the ρ meson mass has a more distinct tendency than in the 2007 results. Being still compatible with zero, the other pairs show some interesting structures in their dependencies on z and M_{inv}, for instance the triangular shape including a double sign change in the z dependence of π^+K^- or the negative dip in the M_{inv} dependence of $K^+\pi^-$ around $\approx 1\,\text{GeV}/c^2$.

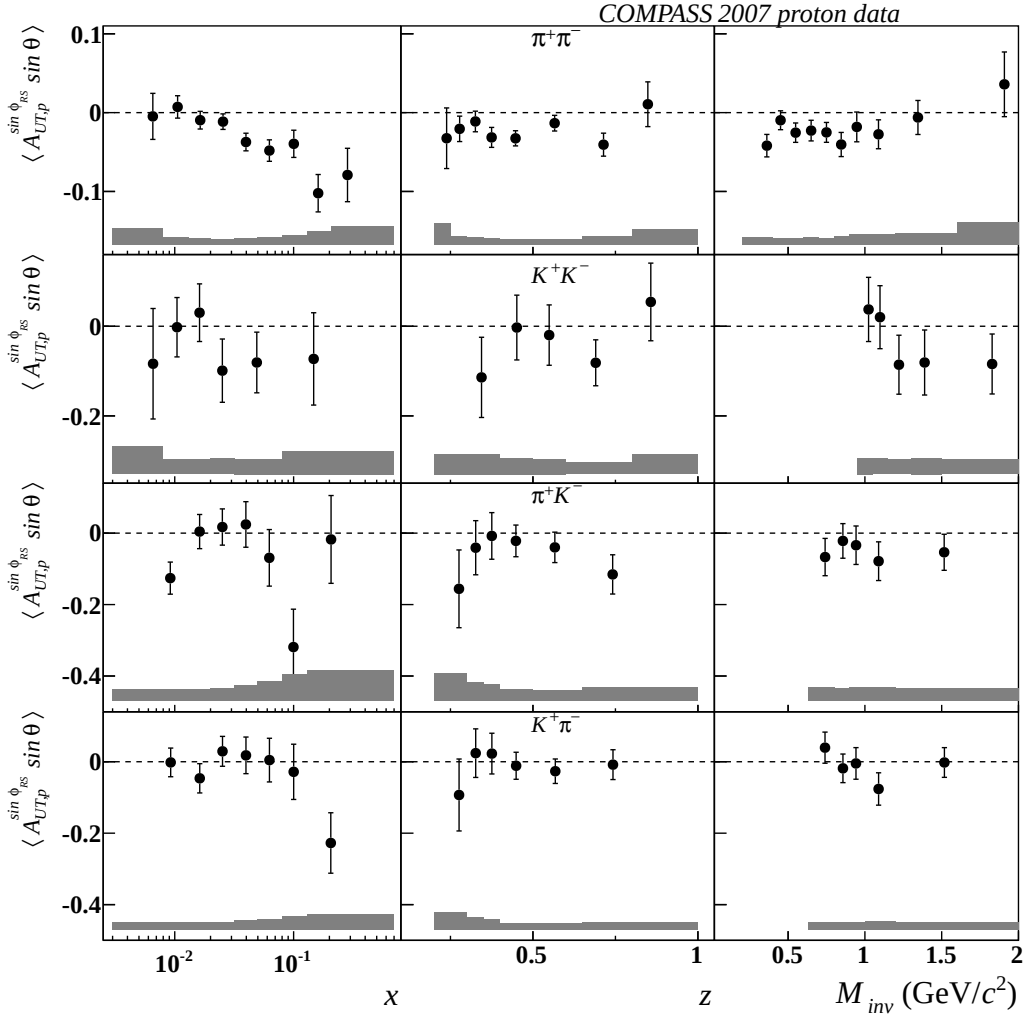

Figure 5.6.: The Hadron-pair azimuthal asymmetries on a proton target of identified pairs from the 2007 data [COMPASS13]: $\pi^+\pi^-$ pairs (1st row), K^+K^- pairs (2nd row), π^+K^- pairs (3rd row), and $K^+\pi^-$ pairs (4th row).

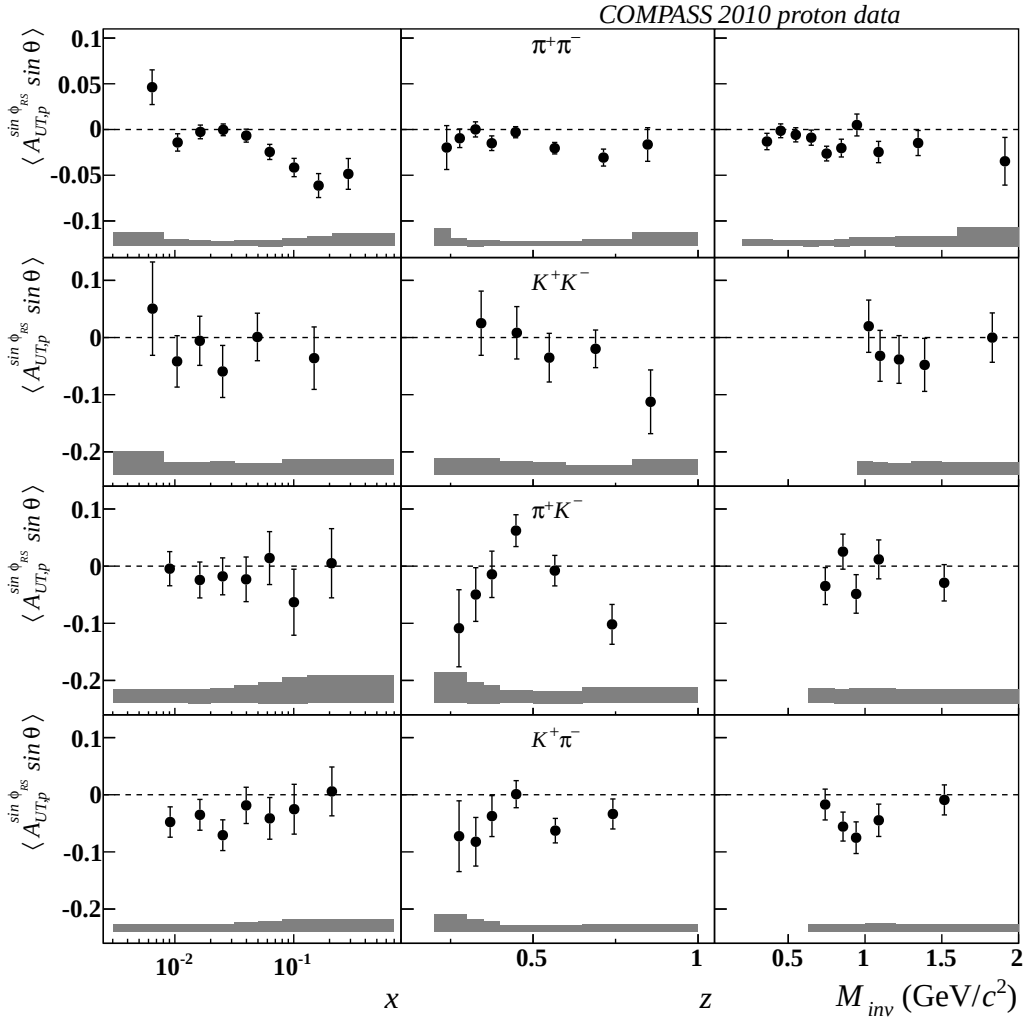

Figure 5.7.: The hadron-pair azimuthal asymmetries on a proton target of identified pairs from the 2010 data [COMPASS14b]: $\pi^+\pi^-$ pairs (1st row), K^+K^- pairs (2nd row), π^+K^- pairs (3rd row), and $K^+\pi^-$ pairs (4th row).

Combined 2007 and 2010 data

The results of the combination of the asymmetry amplitudes obtained from the 2007 and the 2010 proton data sets using the method described in 4.9 are shown in Fig. 5.8. The distribution of the amplitudes is smoothed by the increase of statistics, without loosing its characteristics. A detailed interpretation of the results obtained will be given in the next chapter as well as a comparison of the obtained results to each other (deuteron vs. proton), to other experimental results, and to model predictions. Furthermore an extraction of the transversity distributions of u and d quarks was carried out using these results.

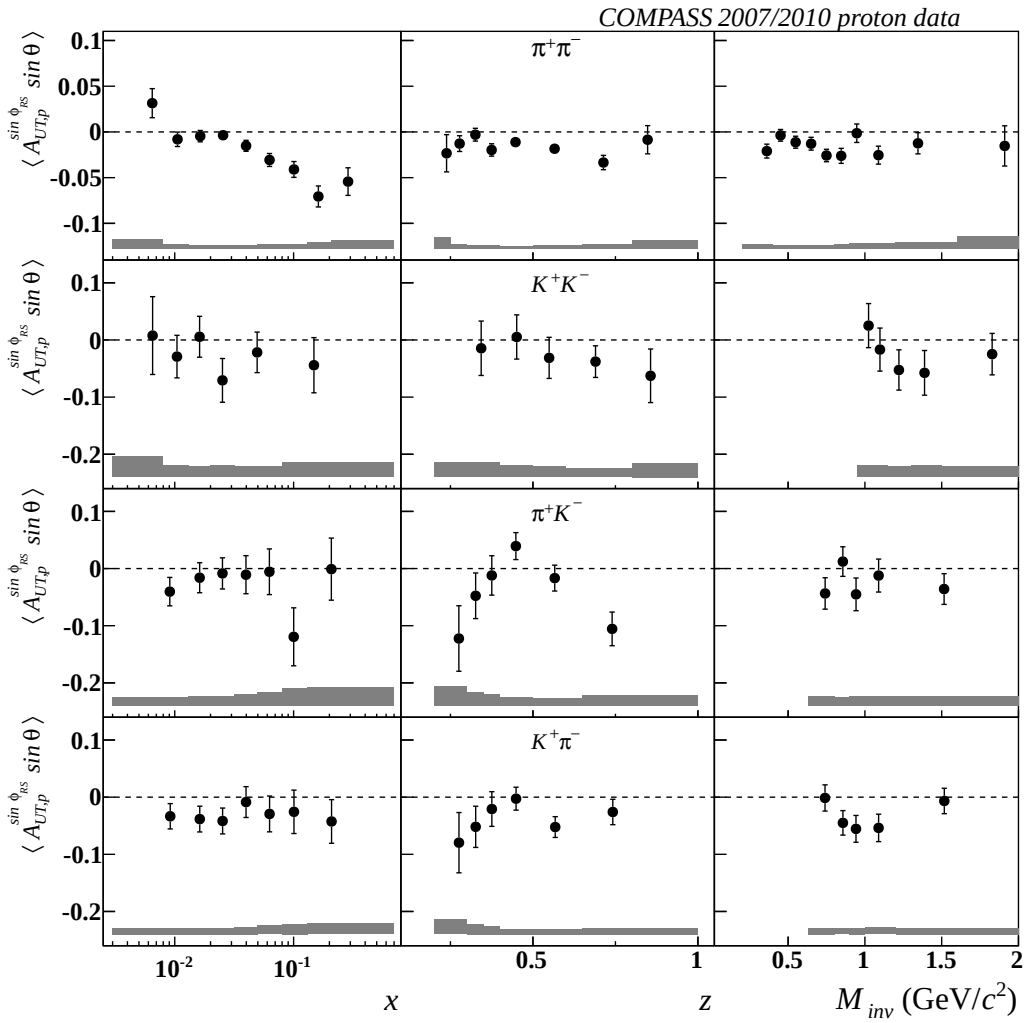

Figure 5.8.: The hadron-pair azimuthal asymmetries on a proton target of identified pairs from the combined 2007 and 2010 data [COMPASS13]: $\pi^+\pi^-$ pairs (1st row), K^+K^- pairs (2nd row), π^+K^- pairs (3rd row), and $K^+\pi^-$ pairs (4th row).

6. Interpretation of the results and extraction of the transversity PDF

This Chapter gives descriptions, comparisons and interpretations on the results on the transverse spin dependent hadron-pair asymmetries, or often referred as a dihadron asymmetries[1], which were presented in Chap. 5. For this purpose general assumptions on some quantities of the underlying theoretical framework from Chap. 2 are introduced. This is done with regard to the single hadron asymmetries in order to give a complete picture, reveal possible commonalities, and in anticipation of future measurements at COMPASS-II, see Chap. 7.2. A comparison of the obtained results is possible to other experimental data from the HERMES collaboration and to the available model predictions. The main focus, however, is on the extraction of the transversity distribution functions of u and d valence quarks using the COMPASS deuteron and proton hadron-pair data, representing the main finding of this thesis. Finally, promising interpretation approaches to the observed asymmetries of identified hadron-pairs are presented.

6.1. General assumptions on the parton distribution and fragmentation functions

The distribution functions and fragmentation functions have been introduced as flavor dependent quantities in Secs. 2.2.1, 2.3.1, and 2.3.4. However, a set of reasonable assumptions on both types of functions is well-founded and facilitate the interpretation of the results. The first assumption is a Gaussian distribution of the parton transverse momenta (if it is nonzero); this ansatz is also used in common model calculations, cf. [ABD$^+$09b, BR06]. The second assumption concerns the x range, where in the following only the valence quark region $0.1 \lesssim x \lesssim 0.3$ is considered since the results show nonzero asymmetry amplitudes in this x range. Assuming this the sea quark contributions to the distribution functions can be neglected for the number density f_1, the Sivers PDF $f_{1T}^{\perp}$, and the Transversity PDF h_1 [ABD$^+$07]

$$\begin{aligned} f_{1(T)}^{(\perp),\bar{u}} \;&:=\; f_{1(T)}^{(\perp),\bar{d}} \;:=\; f_{1(T)}^{(\perp),s} \;:=\; f_{1(T)}^{(\perp),\bar{s}} \;:=\; 0, \\ h_1^{\bar{u}} \;&:=\; h_1^{\bar{d}} \;:=\; h_1^{s} \;:=\; h_1^{\bar{s}} \;:=\; 0. \end{aligned} \tag{6.1}$$

[1] In this work both terms are used synonymously, like in most of the literature.

The fragmentation process is also flavor dependent meaning that the quark's flavor determines the so-called "favored" and "unfavored" fragmentation. For instance the fragmentation of a u quark into a positively charged pion is favored (fav) since the original quark is also a valence quark of this meson; vice versa the fragmentation into a negatively charged pion is unfavored (unf). From this perception the following qualities on the FF can be derived for the single pion hadron production process [ABD$^+$07]

$$\begin{aligned} D_1^{\text{fav},\pi} &:= D_{1,u}^{\pi^+} = D_{1,d}^{\pi^-}, \\ D_1^{\text{unf},\pi} &:= D_{1,d}^{\pi^+} = D_{1,u}^{\pi^-}, \end{aligned} \tag{6.2}$$

$$\begin{aligned} H_1^{\perp\text{fav},\pi} &:= H_{1,u}^{\perp,\pi^+} = H_{1,d}^{\perp,\pi^-}, \\ H_1^{\perp\text{unf},\pi} &:= H_{1,d}^{\perp,\pi^+} = H_{1,u}^{\perp,\pi^-}. \end{aligned} \tag{6.3}$$

Similar equations can be written also for the production of charged kaons [ABD$^+$07]

$$\begin{aligned} D_1^{\text{fav},K} &:= D_{1,u}^{K^+}, \\ D_1^{\text{unf},K} &:= D_{1,d}^{K^+} = D_{1,d}^{K^-} = D_{1,u}^{K^-}, \end{aligned} \tag{6.4}$$

$$\begin{aligned} H_1^{\perp\text{fav},K} &:= H_{1,u}^{\perp,K^+}, \\ H_1^{\perp\text{unf},K} &:= H_{1,d}^{\perp,K^+} = H_{1,d}^{\perp,K^-} = H_{1,u}^{\perp,K^-}. \end{aligned} \tag{6.5}$$

In the case of the fragmentation of a quark into a $\pi^+\pi^-$ pair the isospin symmetry of the doublet of u and d quarks and the charge conjugation motivate for the following assumptions [BCR13]

$$\begin{aligned} D_1^{\sphericalangle u} &= D_1^{\sphericalangle \bar{u}}, \\ D_1^{\sphericalangle d} &= D_1^{\sphericalangle \bar{d}}, \\ D_1^{\sphericalangle s} &= D_1^{\sphericalangle \bar{s}}, \\ H_1^{\sphericalangle u} &= -H_1^{\sphericalangle \bar{u}} = -H_1^{\sphericalangle d} = H_1^{\sphericalangle \bar{d}}, \\ H_1^{\sphericalangle s} &= H_1^{\sphericalangle \bar{s}} = 0. \end{aligned} \tag{6.6}$$

The application of the charge conjugation and the isospin asymmetry corresponds to an interchange of the charges of the hadrons produced and thus also to the exchange of a u quark with a d quark in the fragmentation. Since the vector $\boldsymbol{R}_T$ in Eq. 2.56a points from the negatively to the positively charged hadron $H_1^{\sphericalangle}$ changes its sign due to its linear dependence on $\boldsymbol{R}_T$ [BCR13], see Eq. 6.23a. The unpolarized DiFF $D_1^{\sphericalangle}$ is not affected by the sign changes, since it does not depend directly on $\boldsymbol{R}_T$.
Note that the sea quark distributions are neglected in the set of DiFFs and $H_1^{\sphericalangle}$ is equal in magnitude for u, $\bar{u}$, d and $\bar{d}$.

6.2. Interpretation of the asymmetries from single hadron production

Starting with a brief interpretation of the single hadron asymmetries is useful, since they reveal a basic understanding of the topic. In addition an interconnection of the Collins asymmetry to the hadron-pair asymmetry might be given and both quantities give access to the Transversity PDF. In the following, considerations on the Collins and Sivers asymmetries are made that concern the involved PDFs, FFs, and the flavor dependent contributions of them to the measured asymmetries. Regarding the interpretation of the hadron-pair asymmetries which follows in Sec. 6.3, these are not necessarily required. However, these considerations continue the discussion on the single hadron asymmetries started in Sec. 2.3.3, which will again be of importance for the future program of COMPASS, see Sec. 7.2. The derivations below follow Joosten [Joo13b], which has been briefly summarized.

Collins and Sivers asymmetries of charged pions

Using the set of general assumptions from Sec. 6.1 (Eq. 6.1, 6.2, and 6.4) the equations of the Collins asymmetry (Eq. 2.45) and the Sivers asymmetry (Eq. 2.46) can be expanded in dependence on the target nucleon for instance the proton and the produced meson (here π^+) [2]

$$A_{\text{Coll}}^{p,\pi^+} \approx \frac{\frac{4}{9}h_1^u H_1^{\perp\text{fav},\pi} + \frac{1}{9}h_1^d H_1^{\perp\text{unf},\pi}}{\frac{4}{9}f_1^u D_1^{\text{fav},\pi} + \frac{1}{9}f_1^d D_1^{\text{unf},\pi}}. \tag{6.7}$$

With the rough approximations [Joo13b]

$$\begin{aligned} f_1^u &:\approx 2f_1^d, \\ D_1^{\text{fav}} &:\approx D_1^{\text{unf}} \end{aligned} \tag{6.8}$$

suggested by measurements of the spin-independent quantities, for instance see MSTW 2008 leading-order parametrization in Fig. A.55 [MSTW09]. Neglecting the contribution from the d quark due to its suppression factor of one fourth, one obtains for Eq. 6.7

$$A_{\text{Coll}}^{p,\pi^+} \approx \frac{4h_1^u H_1^{\perp\text{fav},\pi}}{4.25 f_1^u D_1^{\text{fav},\pi}} \approx \frac{h_1^u H_1^{\perp\text{fav},\pi}}{f_1^u D_1^{\text{fav},\pi}}. \tag{6.9}$$

The corresponding result for the production of negatively charged pions on a proton target is

$$A_{\text{Coll}}^{p,\pi^-} \approx \frac{4h_1^u H_1^{\perp\text{unf},\pi}}{2.5 f_1^u D_1^{\text{fav},\pi}} \approx 1.6\,\frac{h_1^u H_1^{\perp\text{unf},\pi}}{f_1^u D_1^{\text{fav},\pi}}. \tag{6.10}$$

[2] Note that this derivation on the single hadron asymmetries are just presented for the proton target for the sake of simplicity.

The results of the Collins asymmetries of charged pions from the 2010 proton data, as presented in Fig. 2.17 (top panel), show in magnitude slightly larger amplitudes for π^- than the asymmetries of π^+ with opposite signs in all three dependencies.
Thus the unfavored Collins FF $H_1^{\perp\text{unf},\pi}$ has to be nonzero with an opposite sign w.r.t. the favored one $H_1^{\perp\text{fav},\pi}$ and together with Eq. 6.10 both should be approximate equal in magnitude [Joo13b]

$$H_1^{\perp\text{unf},\pi} \approx -H_1^{\perp\text{fav},\pi}. \tag{6.11}$$

This evolves Eq. 6.10 to

$$A_{\text{Coll}}^{p,\pi^-} \approx -\frac{4h_1^u H_1^{\perp\text{fav},\pi}}{2.25 f_1^u D_1^{\text{fav},\pi}} \approx -\frac{4}{2.5} A_{\text{Coll}}^{p,\pi^+}. \tag{6.12}$$

The same assumptions can also be applied on the Sivers asymmetry (Eq. 2.46) on a proton target, leading to the following approximations

$$\begin{aligned} A_{\text{Siv}}^{p,\pi^+} &\approx \frac{4f_{1T}^{\perp,u} + 0.5 f_{1T}^{\perp,d}}{4.5 f_1^u} \approx \frac{f_{1T}^{\perp,u}}{f_1^u}, \\ A_{\text{Siv}}^{p,\pi^-} &\approx \frac{2f_{1T}^{\perp,u} + f_{1T}^{\perp,d}}{2.5 f_1^u}. \end{aligned} \tag{6.13}$$

The u quark dominance in the first equation by a factor of 8 w.r.t. the d quark motivates for the neglect of the $f_{1T}^{\perp,d}$ term, while the suppression in the second equation is negligible. The measured Sivers asymmetries of charged pions and kaons, which are presented in Fig. 2.14 (top panel), show clear nonzero amplitudes for π^+. This observation requires $f_{1T}^{\perp,u}$ to be nonzero. Together with the amplitudes of the π^- signal (Fig. 2.14) being compatible with zero within the uncertainties, this implies that the numerator of Eq. 6.13 cancels out through [MSTW09, Joo13b]

$$f_{1T}^{\perp,u} \approx -0.5\, f_{1T}^{\perp,d}. \tag{6.14}$$

Collins and Sivers asymmetries of charged kaons

The 2010 data set with its high statistics offers for the first time the possibility to draw some qualitative conclusions on the PDFs and FFs involved in the production of charged kaons. The corresponding results to Eq. 6.9, 6.10 and 6.13 for the single kaon in the Collins and Sivers case neglecting the sea quark contribution are [Joo13b]

$$\begin{aligned} A_{\text{Coll}}^{p,K^+} &\approx \frac{4h_1^u H_1^{\perp\text{fav},K} + h_1^d H_1^{\perp\text{unf},K}}{4.25 f_1^u D_1^{\text{fav},K}}, \\ A_{\text{Coll}}^{p,K^-} &\approx \frac{4(h_1^u + h_1^d) H_1^{\perp\text{unf},K}}{2.25 f_1^u D_1^{\text{fav},K}}, \end{aligned} \tag{6.15}$$

$$\begin{aligned} A_{\text{Siv}}^{p,K^+} &\approx \frac{4f_{1T}^{\perp,u} + 0.5 f_{1T}^{\perp,d}}{4.5 f_1^u} \approx \frac{f_{1T}^{\perp,u}}{f_1^u}, \\ A_{\text{Siv}}^{p,K^-} &\approx \frac{4f_{1T}^{\perp,u} + f_{1T}^{\perp,d}}{4.5 f_1^u}. \end{aligned} \tag{6.16}$$

Where A_{Siv}^{p,K^+} is already approximated under the assumptions of $f_{1T}^{\perp,u} \neq 0$ and $f_{1T}^{\perp,u} \approx -0.5\, f_{1T}^{\perp,d}$. The Collins asymmetry of negatively charged kaons was found to be small and compatible with zero, see Fig. 2.17 (bottom panel) while for positively charged kaons the asymmetries are sizeable and compatible in magnitude with the π^+ results. Translated into the naïve framework, this brings the conclusion that [Joo13b]

$$H_1^{\perp,\text{fav},K} \approx H_1^{\perp,\text{fav},\pi}, \tag{6.17}$$

under the assumption that the unpolarized DiFFs are approximately equal. The measured amplitudes of the Sivers asymmetry of charged kaons, presented in Fig. 2.14 (bottom panel), are compatible with zero for K^- and sizeable with a positive sign for K^+. The naïve formalism suggests by Eq. 6.13 and 6.15 the same sign and approximately the same strength for both positively charged mesons, while the measurement indicates ≈ 1.5 times larger amplitudes for K^+ than for π^+. An additional contribution could arise from the $\bar{s}$ quark contribution which has been neglected here. For the negatively charged kaons the results of the measurement and the conclusions from the naïve model are again not congruent, since the $f_{1T}^{\perp,u}$ should have a contribution two times larger (cf. Eq. 6.15) and the measured asymmetry is compatible with zero. Here the sea contribution from the s quark might have the opposite effect by compensating the valence quark contribution. This gives a strong hint that the s and $\bar{s}$ contributions are nonzero.

6.2.1. Analyses of the Transversity and the Sivers PDF from single hadron asymmetries

The results of the Sivers and Collins single hadron asymmetries by the HERMES and the COMPASS collaborations were shown in Secs. 2.4.1 and 2.4.1. To allow for a direct comparison an additional cut at $x > 0.032$ on the COMPASS data is introduced and the resulting asymmetries are shown in Figs. 6.1 (Sivers) and 6.2 (Collins).

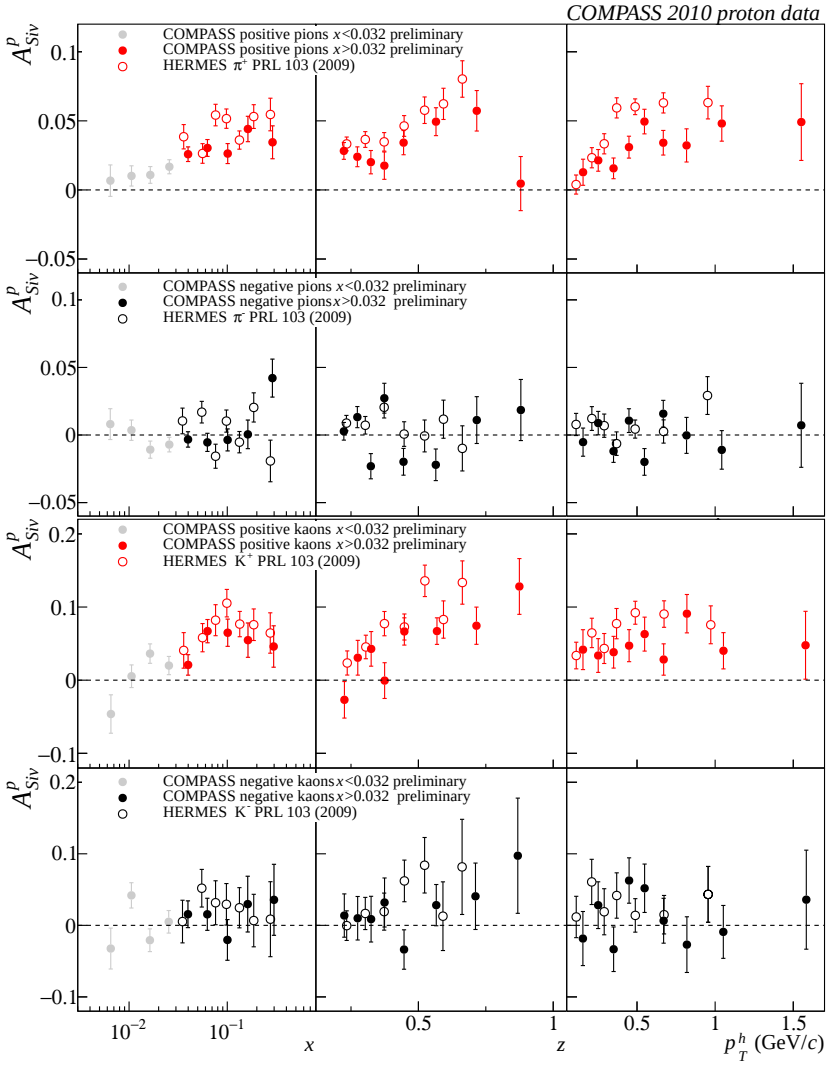

Figure 6.1.: Results of the Sivers single hadron asymmetry of $\pi^{\pm}$ (top panels) and $K^{\pm}$ (bottom panels) on proton targets measured by the HERMES collaboration [HERMES09] (circles) and by the COMPASS collaboration from the 2010 data (dots) [COMPASS14d].

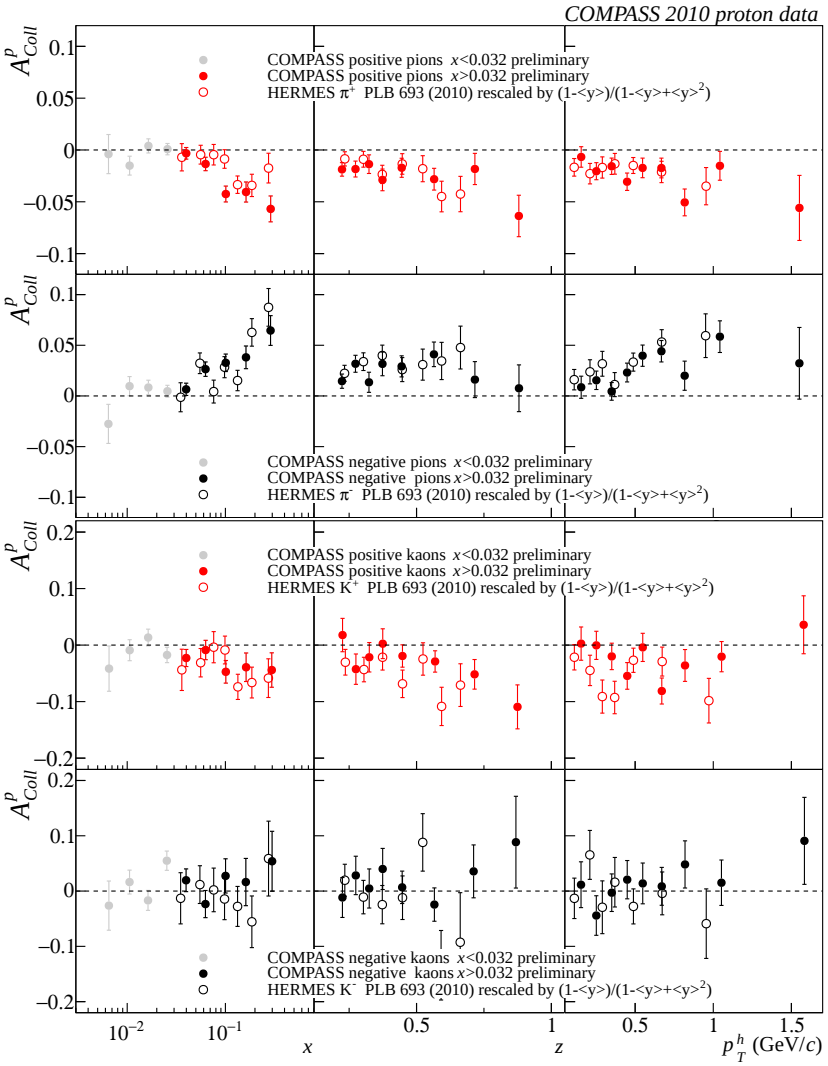

Figure 6.2.: Results of the Collins single hadron asymmetry of $\pi^{\pm}$ (top panels) and $K^{\pm}$ (bottom panels) on proton targets measured by the HERMES collaboration [HERMES10] (circles) and by the COMPASS collaboration from the 2010 data (dots) [COMPASS14d].

The Collins results for pions are compatible within the uncertainties for both charges and in all dependencies, while some differences in the amplitudes of the Sivers asymmetry, slightly larger asymmetries of π^+ are visible. As a reason for these systematically larger Sivers asymmetry amplitudes measured by the HERMES collaboration a possible Q^2 dependence of them is recently under discussion, since the two experiments cover different ranges in the negative squared four-momentum transfer of the virtual photon. The mean Q^2 in bins of x at HERMES ranges from 1.3 to 6.2 $(\mathrm{GeV}/c)^2$, while in the COMPASS case the range is 1.27 to 20.5 $(\mathrm{GeV}/c)^2$, resulting in a total $\langle Q^2 \rangle$ of $\approx 2.4\,(\mathrm{GeV}/c)^2$ for the HERMES measurement and $\approx 3.8\,(\mathrm{GeV}/c)^2$

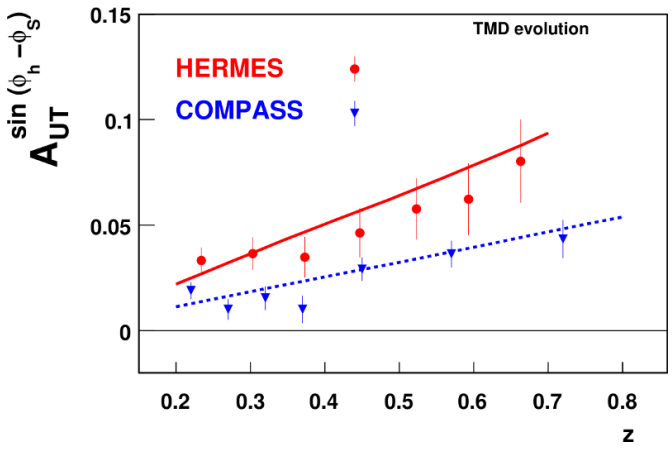

Figure 6.3.: Sivers asymmetries from HERMES (red dots) and COMPASS (blue triangles) for positively charged pions as a function of z. The solid red line is a fit from Anselmino *et al.* [ABD$^+$11] and the blue dashed line is the result of evolving it to the COMPASS Q^2 scale by Aybat *et al.* [APR12] using TMD evolution [APR12].

in the COMPASS case. Aybat *et al.* [APR12] modeled this so called "Q^2 evolution" and used it together with with a TMD evolution scheme [ACQR12] to evolve the fit of the Sivers asymmetry for π^+ of HERMES [ABD$^+$11] to the $\langle Q^2 \rangle$ value of the COMPASS data. The result is shown in Fig. 6.3, where the standard HERMES and COMPASS results are the red dots and blue triangles, respectively. The red line is the fit result [ABD$^+$11] which is then evolved to the mean Q^2 of COMPASS indicated by the dashed blue line. The agreement of the evolved fit from HERMES data with the COMPASS results is visible. The Collins and the dihadron asymmetries from HERMES and COMPASS do not show such a significantly deviant behavior, see Figs. 6.2, 6.5, which indicates a negligible Q^2 dependence of the transversity PDF.
A recent theoretical work by Echevarria *et al.* [EIKV14] studies the QCD evolution of the Sivers TMD in SIDIS as well as in the Drell-Yan process, which will play an important role in the future program of the COMPASS experiment, see Sec. 7.2.
With the presented data sets from both experiments it is possible to extract the underlying Sivers PDF and the transversity PDF. The essentially needed information on the unpolarized DiFFs, see Eq. 2.46 and Eq. 2.45, is obtained from the e^+e^- BELLE collider data [BELLE11]. This work was done for the first time by the group of Anselmino *et al.* [ABD$^+$07], updates including more data followed [ABD$^+$09b, ABD$^+$13]. The fit is based on a Gaussian parametrization of the shape of the unpolarized parton distribution and the FFs. Using this result, in a next step the corresponding distribution functions can be extracted. The most recent extraction of h_1^u and h_1^d by Anselmino *et al.* is presented later in this Chapter (see Sec. 6.3.4) in comparison to the corresponding results obtained from the hadron-pair asymmetry.

The results for the transversity distribution functions clearly show that they are of opposite sign for u and d quarks and that h_1^u is larger in magnitude than h_1^d. The Soffer bound is not violated by the data. A point-by-point extraction of transversity PDFs of valence u and d quarks from the hadron-pair asymmetries is carried out later in this work, whose result will be compared to results from the single hadron channel. Also the extracted Sivers distributions for u and d quarks are of opposite sign, but here $f_{1T}^{\perp d}$ is larger in its maximum than $f_{1T}^{\perp u}$.

6.2.2. Advanced interpretation of the single hadron asymmetries

A well established interpretation of the Collins effect, the so-called "string fragmentation", can also be used in order to describe the hadron-pair asymmetry thus this approach will be discussed in the hadron-pair section of this chapter, Sec. 6.3.5.
The Sivers asymmetry, however, can be interpreted as the association of two effects. When the struck quark is leaving the nucleon remnants a final-state interaction carried by gluons between them is taking place, which attracts the fragmenting quark towards the geometrical center of the nucleon with increasing distance until the hadronization process is initiated by the breakdown of the flux tube. This effect, called "chromodynamic lensing" (see Fig. A.50) alone cannot explain a left-right azimuthal asymmetry of the hadrons since a symmetric distribution of quarks inside the nucleon would cause a symmetric distribution of the hadrons deflected by the final-state interaction. By polarizing the nucleon an asymmetric distribution of quarks can be generated so that a quark leaving the nucleon from the more dense side is bent less than the ones from the other side, since the density of interaction partners is also reduced. Results for probability distributions of finding unpolarized quarks as functions of the impact parameter $b_\perp$ for certain x values inside of an unpolarized and a transversely polarized proton calculated by Burkardt [Bur02] are shown in Fig. A.51. The distributions get asymmetric due to the polarization with an opposite trend for u and d quarks caused by their orbital angular momentum which is of opposite sign. This asymmetric probability distribution together with the final-state interaction generates a left-right asymmetry with a modulation as a function of the Sivers angle $\sin\phi_{Siv} = \sin(\phi_h - \phi_S)$. The center of gravity of the spacial distribution of u and d quarks is not centered any more, but located on opposite sides w.r.t. their common center in the unpolarized case. This charge separation also caused an opposite behavior in the Sivers asymmetry of positively and negatively charged hadrons, since the hadronization of u quarks in positively charged pions is favored w.r.t. the hadronization in negatively charged pions, and vice versa for d quarks.
Further information could be provided by a multi-dimensional analysis of the Sivers asymmetry evaluated for different kinematic regions, namely in two y ranges ($0.1 < y < 0.2$ and $y > 0.2$), three z regions ($z < 0.2$, $0.2 < z < 0.35$, and $0.35 < z < 1$) partly in the full x range or in the valence region $x > 0.032$, the plots and an interpretation can be found in [COMPASS12b]. For an interpretation of the six other single hadron asymmetries see also [COMPASS12b].

6.3. Interpretation of the asymmetry from hadron-pair production

Figure 6.4 shows the comparison of the final results on the hadron-pair asymmetries of identified hadron-pairs from the 2003-2004 deuteron data to the combined 2007/2010 proton data.

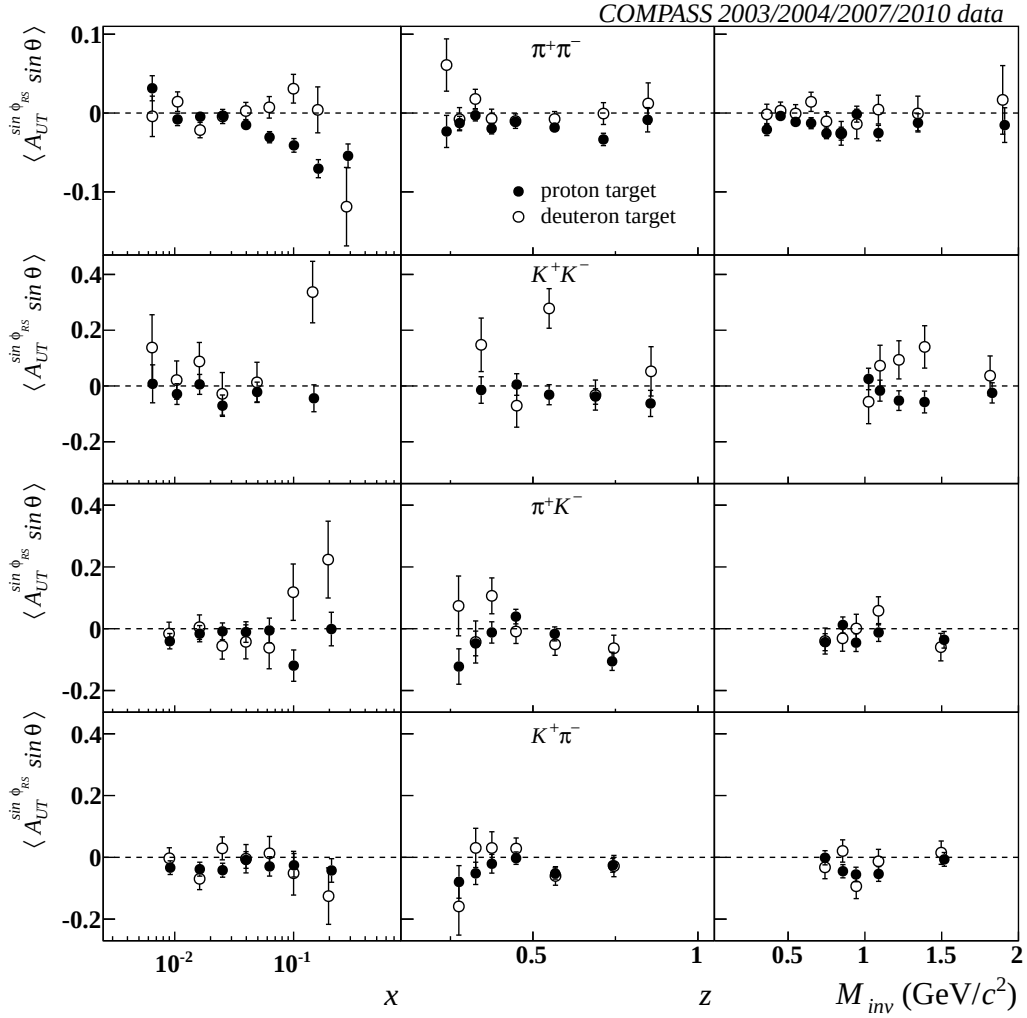

Figure 6.4.: The hadron-pair azimuthal asymmetries of identified pairs from the combined 2007/2010 proton data (black dots) and from the 2003-2004 deuteron data (circles): $\pi^+\pi^-$ pairs (1st row), K^+K^- pairs (2nd row), π^+K^- pairs (3rd row), and $K^+\pi^-$ pairs (4th row) as a function of x, z, and M_{inv}.

The following interpretation will focus on the identified pairs, since these are more suited for dedicated studies and interpretations than all h^+h^- pair results (Figs. 5.5, 5.1), for instance the comparison with the corresponding $\pi^+\pi^-$ results from the HERMES collaboration (Sec. 6.3.3). Also the available models focus on the description of the amplitudes being observed in the pion pair asymmetries (Sec. 6.3.3). Furthermore, approaches to the other pair combinations are briefly introduced. The extraction of the valence quark Transversity PDFs from $\pi^+\pi^-$ pair data will be the final outcome of this thesis (Sec. 6.3.4), supplemented by a review on selected interpretation approaches on the Transversity phenomena (Sec. 6.3.5).

6.3.1. Description of the observations

The asymmetry of pion pairs from the proton target shows clear nonzero amplitudes up to -0.07 in the region of $x > 0.03$ with an increasing trend. The results from the deuteron data are compatible with zero within the uncertainties in the whole x range. No clear dependence on z is present in both data sets, while the proton data has negative amplitudes in the whole range. The dependence on the invariant mass of the pair is congruent for both data sets in the ρ mass region (around $770\,\mathrm{MeV}/c^2$) with amplitudes of ≈ -0.025. In the proton case the amplitude decreases to zero before it increases again in the region of $M_{inv} > 1\,\mathrm{GeV}/c^2$.
The asymmetry of pure kaon pairs is compatible with zero within the uncertainties for both data sets in the dependencies on x and z, with a reduced significance of the deuteron data being affected by the low statistics. However, the asymmetry amplitudes of the proton data have tentatively negative signs for all three variables, while the amplitudes from the deuteron data show tentatively positive signs. The M_{inv} dependence, however, shows an opposite sign for proton and deuteron target results with an indication of a mirror symmetric shape of the signal between 1 and $\approx 1.5\,\mathrm{GeV}/c^2$. In the case of π^+K^- pairs the proton results are tentatively negative but still compatible with zero within the uncertainties, and the available statistics on the deuteron are too small to allow for conclusions. No significant dependence on x and z of the proton data is present for the $K^+\pi^-$ pairs in the indication of a negative mean value, while the deuteron results are compatible with zero within the uncertainties. Most interesting is again the M_{inv} dependence, due to negative dips for both target types just below $\approx 1\,\mathrm{GeV}/c^2$; where the dip of the proton data covers a broader range.
Tables of the numerical values of the asymmetry amplitudes of all pairs from both target data sets can be found in Tabs. A.9 to A.30.

6.3.2. Comparison with other experimental results

The HERMES collaboration was first to publish asymmetries of pion pairs on a proton target in the year 2008 [HERMES08], the COMPASS collaboration followed in the year 2010 with its first data on the proton target [COMPASS10b](not shown here). To adapt to the smaller kinematic range of HERMES ($0.023 < x < 0.4$) an additional cut on the COMPASS sample at $x > 0.032$ has been applied. Since COMPASS takes the depolarization factor D_{nn} (see Eq. 2.43) into account in the shown figures and HERMES published their results without D_{nn} (see Eq. 2.43), it was added here to ensure comparability using numerical values of y from [Lu08]. Moreover the HERMES asymmetry amplitudes are multiplied by -1 to compensate for the additional phase of π in the sine modulation used by COMPASS, see Sec. 2.3.4. Further differences are present in the cut on W at larger $3.16\,\mathrm{GeV}/c^2$ and no minimum cuts on z, x_F, E_{miss}, and $\boldsymbol{R}_T$ are applied in the HERMES analysis. Also the M_{inv} range is smaller, running from 0.3 to 2.5, due to smaller beam momentum ($27.6\,\mathrm{GeV}/c$). A minor difference in the definition of the vector $\boldsymbol{R}$ is present, which is neglected here, see for details Sec. 2.3.4.
The comparison of the HERMES results with the final proton results from this work is presented in Fig. 6.5. The two experimental results are in very good agreement within the uncertainties. The trend of increasing magnitude of asymmetry amplitudes with rising x is evident in both analyses, as well as the comparability with a negative constant in the z dependence.

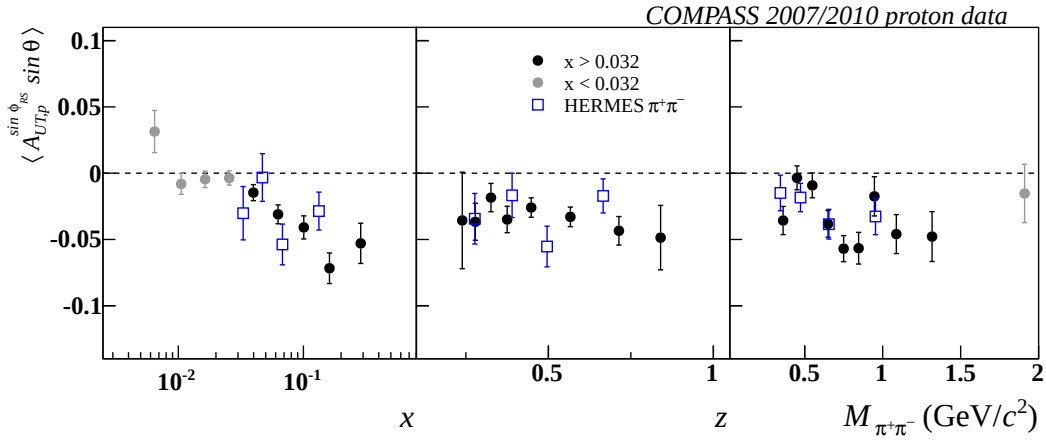

Figure 6.5.: The comparison of the $\pi^+\pi^-$ pair azimuthal asymmetry measured by the HERMES collaboration [HERMES08] (blue open squares) with the results from the COMPASS collaboration extracted from the combined 2007/2010 proton target data (black dots). A cut on $x > 0.032$ has been applied on the COMPASS results to ensure comparability of the results, the data with $x < 0.032$ (gray dots) is not taken into account for the z and M_{inv} dependence. Note that the third HERMES data point in the M_{inv} dependence has almost the same amplitude value as the data point from COMPASS.

The M_{inv} binning of the HERMES data is more coarse than the one of COMPASS, thus the dip around the ρ mass is not that pronounced, but the amplitudes at its edges are in very good agreement. The additional x cut on the COMPASS data has an amplifying effect on the asymmetry amplitudes of the z and M_{inv} dependencies, which increase by approximately a factor of 1.5.
The numerical values obtained from the analysis of this sub-sample can be found in Tab. A.27.

6.3.3. Comparison with model predictions

The significant dip structure around the ρ mass in the M_{inv} dependence of the $\pi^+\pi^-$ pair asymmetries (see Fig. 6.4) motivates for a more detailed consideration of how the observed structures in this dependence can be explained. This is the starting point of two model calculations performed by the Pavia group (Bacchetta *et al.*) and the group around Ma from Beijing. The first one will be described in detail, while in the case of the Beijing model only main aspects will be highlighted since it is partly based in the Pavia model.

The Pavia model

A model to explain the observed hadron-pair asymmetries for pion pairs in the HERMES data has been proposed by Bacchetta and Radici [BR06]. In this work they assume the invariant mass M_{inv} of the hadron-pair system to be small, namely smaller then $1.5\,\mathrm{GeV}/c^2$, as it is the case if both produced hadrons are pions. Thus, an ansatz can be made in which these pions are produced in relative s or p wave channels. The FFs were extracted from a correlator function [BR03a]

$$\Delta^q(z,\cos\theta,M_{inv}^2,\phi_R) = \frac{z|\boldsymbol{R}|}{16M_{inv}}\int \mathrm{d}^2\boldsymbol{k}_T\,\mathrm{d}k^+\Delta^q(k;P_h,R)\Big|_{k^-=\frac{P_h^-}{z}}, \tag{6.18}$$

with [BR04, BMP03]

$$\Delta^q(k;P_h,R)_{ij} = \tag{6.19}$$
$$\sum_X\int\frac{\mathrm{d}^4\xi}{(2\pi)^4}e^{+\imath k\cdot\xi}\left\langle 0\left|\mathcal{U}^{n+}_{(-\infty,\xi)}\psi^q_i(\xi)\right|P_h,R;X\right\rangle\left\langle P_h,R;X\left|\bar\psi^q_j(0)\mathcal{U}^{n+}_{(0,-\infty)}\right|0\right\rangle.$$

The angle θ is the angle between the direction of P_1 in center-of-mass system of the pairs and the direction of P_h. see Fig. 2.10.

In the cm frame the emission of the two hadrons occurs back-to-back. In this framework the pair's difference vector can be written as[3] [BR03a]

$$R^\mu = \Bigg[\frac{\sqrt{M_1^2+|\boldsymbol{R}|^2}-\sqrt{M_2^2+|\boldsymbol{R}|^2}-2|\boldsymbol{R}|\cos\theta}{2\sqrt{2}}, \tag{6.20}$$
$$\frac{\sqrt{M_1^2+|\boldsymbol{R}|^2}-\sqrt{M_2^2+|\boldsymbol{R}|^2}+2|\boldsymbol{R}|\cos\theta}{2\sqrt{2}}, |\boldsymbol{R}|\sin\theta\cos\phi_R, |\boldsymbol{R}|\sin\theta\sin\phi_R \Bigg],$$

$$\zeta = \frac{2R^-}{P_h^-} = \frac{1}{M_{inv}}\left(\sqrt{M_1^2+|\boldsymbol{R}|^2}-\sqrt{M_2^2+|\boldsymbol{R}|^2}-2|\boldsymbol{R}|\cos\theta\right), \tag{6.21}$$

with its absolute value

$$|\boldsymbol{R}| = \frac{1}{2M_{inv}}\sqrt{M_{inv}^2-2(M_1^2+M_2^2)+(M_1^2-M_2^2)^2}. \tag{6.22}$$

After the integration of $\Delta^q(k;P_h,R)_{ij}$ in Eq. 6.19 over $\boldsymbol{k}_T$, where the Wilson lines $\mathcal{U}$ (*c.f.* Eq. 2.63) can be reduced to unity using the light-cone gauge, only two dihadron fragmentation functions survive [BBJR00, BR03a, BR06]

$$D_1^{\sphericalangle q}(z,\cos\theta,M_{inv}^2) = 4\pi\,\mathrm{Tr}\left[\Delta^q(z,\cos\theta,M_{inv}^2,\phi_R)\gamma^-\right], \tag{6.23a}$$

$$\frac{\epsilon_T^{ij}R_{Tj}}{M_{inv}}H_1^{\sphericalangle q}(z,\cos\theta,M_{inv}^2) = 4\pi\,\mathrm{Tr}\left[\Delta^q(z,\cos\theta,M_{inv}^2,\phi_R)\imath\sigma^{i-}\gamma_5\right]. \tag{6.23b}$$

Their linear dependence on $\cos\theta$ in the cm frame allows for an expansion in the basis of Legendre polynomials $\mathcal{P}_n$ in $\cos\theta$. Thus the DiFFs can be written as [BR06]

$$\frac{2|\boldsymbol{R}|}{M_{inv}}D_1^{\sphericalangle}\big(z,\cos\theta,M_{inv}^2)\big) = \sum_n D_{1,n}^{\sphericalangle}\big(z,M_{inv}^2\big)\,\mathcal{P}_n(\cos\theta), \tag{6.24a}$$

$$\frac{2|\boldsymbol{R}|}{M_{inv}}H_1^{\sphericalangle}\big(z,\cos\theta,M_{inv}^2)\big) = \sum_n H_{1,n}^{\sphericalangle}\big(z,M_{inv}^2\big)\,\mathcal{P}_n(\cos\theta), \tag{6.24b}$$

with [BR06]

$$D_{1,n}^{\sphericalangle}\big(z,M_{inv}^2\big) = \int_{-1}^{1}\mathrm{d}\cos\theta\,\mathcal{P}_n(\cos\theta)\frac{2|\boldsymbol{R}|}{M_{inv}}D_1^{\sphericalangle}\big(z,\zeta(\cos\theta),M_{inv}^2\big), \tag{6.25a}$$

$$H_{1,n}^{\sphericalangle}\big(z,M_{inv}^2\big) = \int_{-1}^{1}\mathrm{d}\cos\theta\,\mathcal{P}_n(\cos\theta)\frac{2|\boldsymbol{R}|}{M_{inv}}H_1^{\sphericalangle}\big(z,\zeta(\cos\theta),M_{inv}^2\big). \tag{6.25b}$$

Due to the reasonable assumption of pure s and p wave interference, where $L\in[0,1]$, it is sufficient to perform the expansion in terms of the Legendre polynomials $\mathcal{P}_n$ up to the first

[3] The simplification which occurs due to the equal masses is not executed here in order to keep the equations as general as possible.

three terms $n \in [0, 1, 2]$ to be able to describe all three polarization states. Accordingly the unpolarized and the polarized DiFF reads [BR03a]

$$D_1^{\sphericalangle}(z, \cos\theta, M_{inv}^2) \approx$$
$$D_{1,UU}(z, M_{inv}^2) + D_{1,UL}^{\sphericalangle}(z, M_{inv}^2)\cos\theta + D_{1,LL}^{\sphericalangle}(z, M_{inv}^2)\frac{1}{4}(3\cos^2\theta - 1), \tag{6.26a}$$
$$H_1^{\sphericalangle}(z, \cos\theta, M_{inv}^2) \approx$$
$$H_{1,UT}^{\sphericalangle}(z, M_{inv}^2) + H_{1,LT}^{\sphericalangle}(z, M_{inv}^2)\cos\theta, \tag{6.26b}$$

where the subscripts U, L and T denote the polarization state as unpolarized, longitudinally, and transversely polarized, respectively. The first letter represents the beam polarization state and the second letter the target polarization state.
The DiFF $D_{1,UU}^{\sphericalangle}$ has no dependence on θ and therefore can only contain contributions from s and p waves, but not from the interference between them. The $D_{1,LL}^{\sphericalangle}$ term receives contributions from separated p waves. The interference between s and p waves is described by $D_{1,UL}^{\sphericalangle}$ and $H_{1,UT}^{\sphericalangle}$, while pure p interference gives rise to $H_{1,LT}^{\sphericalangle}$.
In the case of a transversely polarized target, only the functions $H_{1,UT}^{\sphericalangle}$ and $H_{1,LT}^{\sphericalangle}$ become relevant and the cross-section reads [BR03a]

$$\frac{\mathrm{d}^7\sigma}{\mathrm{d}\cos\theta\,\mathrm{d}M_{inv}^2\,\mathrm{d}\phi_R\,\mathrm{d}z\,\mathrm{d}x\,\mathrm{d}y\,\mathrm{d}\phi_S} = \sum_q e_q^2 \frac{\alpha^2\hbar^2}{2\pi Q^2 y} B(y) \frac{|\boldsymbol{S}_T||\boldsymbol{R}|}{M_{inv}} \sin\big(\phi_R + \phi_S + \pi\big) \tag{6.27a}$$
$$h_1^q(x)\sin\theta\Big[H_{1,UT}^{\sphericalangle q}(z, M_{inv}^2) + H_{1,LT}^{\sphericalangle q}(z, M_{inv}^2)\cos\theta\Big],$$

where $h_1(x)$ is the transversity PDF, which can be matched by two chiral-odd and T-odd FF. From the experimental point of view, the measurement by COMPASS is only sensitive to $H_{1,UT}^{\sphericalangle}$ for pure pion and kaon pairs. The reason is, that the $H_{1,LT}^{\sphericalangle}$ term depends on $\cos\theta$ which is symmetric around zero for these pairs (Fig. A.20) and thus is strongly suppressed closed to zero. Hence, the LT term can only contribute in the case of non equal masses of the two hadrons of a pair with their asymmetric $\cos\theta$ distributions, see Fig. A.20. The less advanced interpretation approaches w.r.t. the pion pairs, see also Sec. 6.3.5, make this study a task for future analysis and model calculations, see Sec. 7.1.
The differential cross sections of Eq. 2.67 can be written in terms of the partial wave expanded FFs in leading-twist [BR06]

$$\mathrm{d}^7\sigma_{UU} = \sum_q \frac{\alpha^2\hbar^2 e_q^2}{\pi y Q^2} \frac{1 - y + \frac{y^2}{2} + \frac{y^2\gamma^2}{4}}{1 + \gamma^2} f_1^q(x) D_{1,UU}^{\sphericalangle q}(z, M_{inv}^2), \tag{6.28a}$$

$$\mathrm{d}^7\sigma_{UT} = -\sum_q \frac{\alpha^2\hbar^2 e_q^2}{\pi y Q^2} \frac{1 - y - \frac{y^2\gamma^2}{4}}{1 + \gamma^2} \sin(\phi_R + \phi_S + \pi) h_1^q(x) \frac{|\boldsymbol{R}|}{M_{inv}} H_{1,UT}^{\sphericalangle q}(z, M_{inv}^2), \tag{6.28b}$$

where $\gamma = \frac{2Mx}{q}$ and M is the mass of the target. Additional sub-leading contributions are described in [BR04], further corrections at the level of α_S can be found in [dFV04].

The full asymmetry amplitude then reads [BR06]

$$A_{UT}^{\sin(\phi_R+\phi_S-\pi)}(x,y,z,M_{inv}^2) = \frac{\frac{1-y-y^2\gamma^2/4}{xy^2(1+\gamma^2)}}{\frac{1-y+y^2/2+y^2\gamma^2/4}{xy^2(1+\gamma^2)}} \frac{\pi}{4} \frac{|\boldsymbol{R}|}{M_{inv}} \frac{\sum_q e_q^2 h_1^q(x) H_{1,UT}^{\sphericalangle q}(z,M_{inv}^2)}{\sum_q e_q^2 f_1^q(x) D_{1,UU}^q(z,M_{inv}^2)}. \tag{6.29a}$$

The relevant channels contributing to this process are evaluated with the PYTHIA event generator [SEF+01] which is known to give good results for unpolarized processes. These are [BR06]

1. $q \to \pi^+\pi^- X_1$: fragmentation into an incoherent $\pi^+\pi^-$ pair contributing to the background ($70.77\,\%$);

2. $q \to \rho\, X_2 \to \pi^+\pi^- X_2$: fragmentation into a ρ resonance, which decays into a pion pair creating a peak around $M_{inv} \approx 770\,\text{MeV}/c^2$ ($14.81\,\%$);

3. $q \to \omega\, X_3 \to \pi^+\pi^- X_3$: fragmentation into an ω resonance decaying into a pion pair causing a small peak around $M_{inv} \approx 782\,\text{MeV}$ ($0.31\,\%$);

4. $q \to \omega\, X_4' \to \pi^+\pi^- X_4$ with $X_4 = \pi^0\, X_4'$: fragmentation into an ω resonance decaying into $\pi^+\pi^-\pi^0$ (π^0 stays unobserved), responsible for a broad peak around $M_{inv} \approx 500\,\text{MeV}$ ($8.65\,\%$);

5. $q \to \eta\, X_5' \to \pi^+\pi^- X_5$ with $X_5 = \mathcal{X}\, X_5'$: fragmentation into an $\eta(547)$ or $\eta'(958)$ which decays into $\pi^+\pi^-\,\mathcal{X}$ ($\mathcal{X}$ stays unobserved), creating a peak around $M_{inv} \approx 350\,\text{MeV}$ ($2.05\,\%$);

6. $q \to K^0\, X_6 \to \pi^+\pi^- X_6$: fragmentation into a K^0 resonance decaying into $\pi^+\pi^-$, which causes a narrow peak at $M_{inv} \approx 498\,\text{MeV}$ ($3.41\,\%$).

Bacchetta *et al.* chose a spectator model as the framework for the description of the fragmentation process. This means that the sum over all possible intermediate states X is replaced by an effective on-shell state, called the spectator. The quantum numbers of the spectator are the same as of the initial quark and its mass is one of the parameters of the model.
In the channels 2. and 3. the decays of vector mesons are assumed. Since a vector meson has a J^P of 1^- the pions must be produced in a relative p wave. Also a fraction of the pion pairs originating from channel 4. are produced in a relative p wave, since each charged pion can be in a relative p wave with respect to the other one or to the π^0. Only channel 1. is a pure s wave channel. This restriction to s and p waves and their interference terms limits the invariant mass to an upper limit of $1.5\,\text{GeV}/c^2$. The data sample was tuned with a corresponding cut, not showing any significant effects w.r.t. the full invariant mass range sample. The numerical values obtained from the analysis of this sub-sample can be found in Tab. A.27. Bacchetta *et al.* [BR06] model the correlation function $\Delta^q(k, P_h, R)$ in terms of s and p wave contributions to the vertex, taking into account the equality of the fragmentation correlators for u and $\bar{d}$ quarks as motivated by the isospin symmetry, cf. Eq. 6.6.

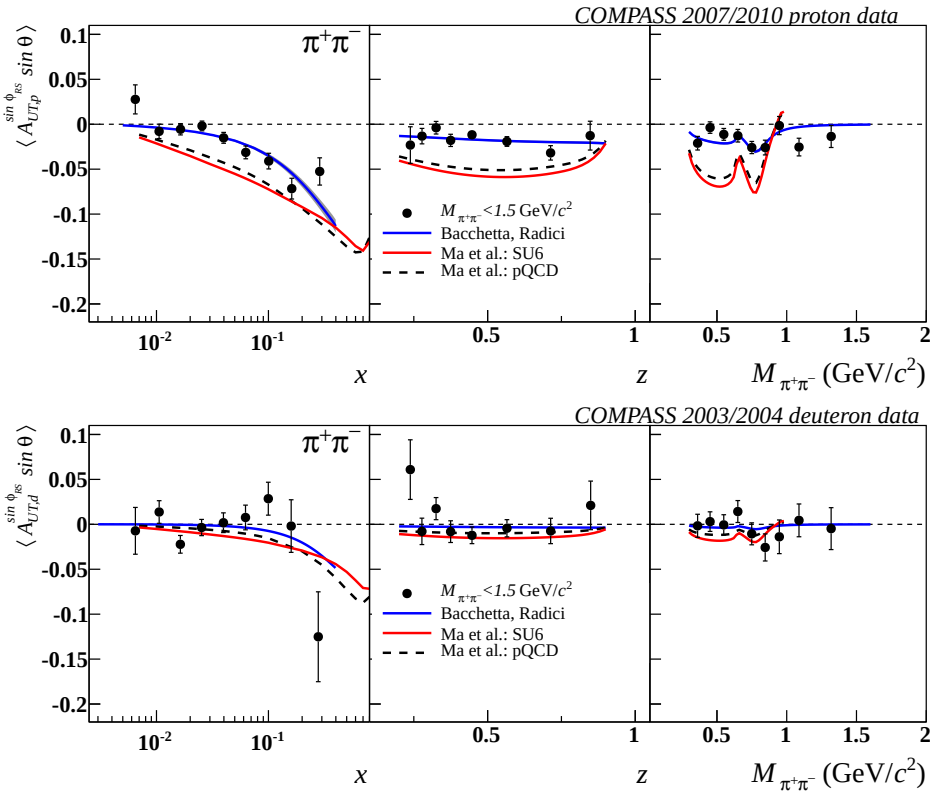

Figure 6.6.: The proton pion pair asymmetries (top panel) and the deuteron pion pair asymmetries (bottom panel) in comparison with the model predictions from Bacchetta and Radici [BR06] (blue line) and from Ma *et al.* the $\mathrm{SU}(6)$ quark-diquark model (red line) and the pQCD based model (black dashed line) [SHBM08].

This ansatz for the fragmentation correlators is then inserted into Eq. 6.18. The free parameters of this model are then fixed by a fit of the ansatz to the output of the PYTHIA event generator [SEF+01], adapted to the kinematics of the HERMES or the COMPASS experiment. The obtained results are shown in Fig. 6.6 (top panel) in comparison with the combined proton results for pion pairs.
The model curve reproduces the distribution in x in shape and strength, only the highest x bin shows an approximately 1σ smaller magnitude of the amplitude than the model curve. The linear functional form with a small slope towards high z extracted from the model is highly compatible with the data points within their uncertainties. The full M_{inv} range can be divided in three sub-ranges, below the ρ mass, around it, and above the ρ mass. In the first sub-range the model predicts a dip caused by channels $4.$, $5.$, and $6.$ corresponding to the decays of an ω resonance, the $\eta(547)$, the $\eta'(958)$ and the K^0. But the data does not indicate a clear signal generated by these decays. Around the ρ mass of $770\,\mathrm{MeV}/c^2$ the model matches perfectly the data both in shape and strength. Above $1\,\mathrm{MeV}/c^2$ the measured amplitude is nonzero, while the model curve rapidly approaches zero due to the restriction on s and p waves.

Bacchetta *et al.* have also applied their model to the quark composition of the deuteron target. The obtained results are shown in Fig. 6.6 (bottom panel) in comparison with the measured asymmetry amplitudes of the pion pairs. The model curves are mostly compatible with zero, apart from the very high x region where a sizeable asymmetry amplitude is predicted. This trend is also present in the data, however, subject to a large uncertainty. In general the model prediction is fully compatible with the results of this analysis.

The Beijing model

The second model calculation to be discussed on the asymmetries of pion pairs has been developed by Ma and collaborators [SHBM08]. In this publication two different approaches to the transversity functions are discussed, namely a $\mathrm{SU}(6)$ quark-diquark model [Fey72, Ma96] and the pQCD based counting rule analysis [FJ75, BBS95, GRSV01, HKS04]. For the $\mathrm{SU}(6)$ quark-diquark model the authors used a set of unpolarized valence quark distributions as input, which were connected by theoretical relations [Ma96, MSS98] to the valence quark transversity distributions [SHBM08]

$$h_1^{u_v}(x) = \big(f_1^{u_v}(x) - \frac{1}{2} f_1^{d_v}(x)\big)\hat{W}_S(x) - \frac{1}{6} f_1^{d_v}(x)\hat{W}_V(x), \tag{6.30a}$$

$$h_1^{d_v}(x) = -\frac{1}{3} f_1^{d_v}(x)\hat{W}_V(x), \tag{6.30b}$$

where $\hat{W}_S(x)$ and $\hat{W}_V(x)$ are the Melosh-Wigner rotation factors [MSS98, MS98, SS97] for a spectator scalar and vector diquarks, which have their origin in the relativistic effect of quark transverse motions [Ma93].
On the other hand the pQCD based counting rule approach uses transversity distributions from a pQCD [MSY01, MSSY01] theoretical calculations which have been adjusted with the usage of the $\mathrm{CTEQ6L}$ [PSH$^+$02] parametrization of unpolarized parton distribution functions. $\mathrm{CTEQ6L}$ results are also used in the $\mathrm{SU}(6)$ model. Both models by Ma *et al.* use the parametrization of the FFs $D_1^{\sphericalangle}$ and $H_1^{\sphericalangle}$ proposed by Bacchetta *et al.* [BR06] as well as the partial wave expansion from Bacchetta *et al.* [BR03a], see previous section. The final results of the model calculations of Ma *et al.* are shown in Fig. 6.6 for the proton target (top panel) and for the deuteron target (bottom panel). Both results, of the $\mathrm{SU}(6)$ and the pQCD parametrization tend to overestimate the strength of the measured pion pair asymmetry in all three dependencies of the proton data. The deviation between the model curves and the proton data results is more extensive than for the Bacchetta *et al.* model. But in the case of the deuteron target the agreement with the measured asymmetry amplitudes is of similar quality as for the Pavia model. Moreover the negative dip in the ρ mass region is also present in the model, see Fig. 6.6 (bottom panel), which is not that pronounced in the Pavia model [BR06]. By the introduction of a cut on the x valence region at > 0.032 (see Fig. A.52) being equivalent to a selection of a x range with significant asymmetry amplitudes a data sample with improved agreement to the Ma *et al.* results can be generated. From the available range of data a distinction between the two models of Ma and collaborators is not possible.

6.3.4. Extraction of the Transversity PDF from hadron-pair data

The extraction of the transversity distributions of u and d valence quarks via the pion pair asymmetry is one of the final goals of this work. The complete set of dihadron asymmetries obtained from the data taken on the transversely polarized deuteron and proton targets at the COMPASS experiment gives the unique possibility to extract $xh_1^q(x)$ of the u_v and d_v valence quarks separately, without the necessity to evolve results between different kinematic domains. The procedure executed in the following is based on the method by Bacchetta *et al.* [BCR13] and their previous works [BCR11, CBR12].

Framework

The starting point is the final asymmetries of pion pairs as a function of x, as shown in the upper panel of Fig. 6.4. As described in Sec. 2.3.4, the measured hadron-pair asymmetries depend on the transversity PDF h_1^q, the polarized DiFF $H_{1,sp}^{\sphericalangle q}$, the number density f_1^q and the unpolarized FF $D_1^{\sphericalangle q}$. Thus these measured asymmetries presented in this work together with additional knowledge on the polarized DiFFs, the number densities, and the unpolarized FFs of u and d valence quarks inside the deuteron and the proton give access to the transversity PDFs. Even only one of the two target types would allow for an extraction of a linear combination of $h_1^{u_v}$ and $h_1^{d_v}$ for certain x values depending also on Q^2, namely for the

$$\begin{aligned} \text{proton target} \quad & xh_{1,p}(x;Q^2) \equiv xh_1^{u_v}(x;Q^2) - \frac{1}{4}xh_1^{d_v}(x;Q^2), \\ \text{deuteron target} \quad & xh_{1,d}(x;Q^2) \equiv xh_1^{u_v}(x;Q^2) + xh_1^{d_v}(x;Q^2). \end{aligned} \tag{6.31}$$

The valence quark transversity function of a quark q is defined as

$$h_1^{q_v} \equiv h_1^q - h_1^{\bar{q}}, \tag{6.32}$$

to exclude sea quark contributions generated in the gluon decay by their cancellation.
For the first time this exercise was performed by Bacchetta, Courtoy and Radici [BCR11] with the HERMES results on the proton target. An extraction which included the COMPASS data on the deuteron and the proton target [COMPASS12c] followed in [CBR12].
The linear combinations in Eq. 6.31 follow from Eq. 2.68 if the reasonable assumptions for the unpolarized FFs and the DiFFs in Eqs. 6.6 are inserted and the sum over all quark flavors depending on the target nucleon. The dependence of the asymmetry on x factorizes from the dependence on the doublet of $(z; M_{inv})$ in the way that only the involved PDFs depend on x. Thus an integration of the two DiFFs can be used to reduce the dependence down to one on x for a certain quantity (cf. $xh_{1,p}$ and $xh_{1,d}$ Eq. 6.33) at fixed values of Q^2.

The integration over the considered ranges in z and M_{inv} is performed according to [BCR13]

$$n_q(Q^2) = \iint \mathrm{d}z\ \mathrm{d}M_{inv} D_1^{\sphericalangle q}(z, M_{inv}; Q^2), \tag{6.33}$$

$$n_q^{\uparrow}(Q^2) = \iint \mathrm{d}z\ \mathrm{d}M_{inv} \frac{|\boldsymbol{R}_T|}{M_{inv}} H_{1,sp}^{\sphericalangle q}(z, M_{inv}; Q^2). \tag{6.34}$$

The DiFF $H_{1,sp}^{\sphericalangle q}$ was obtained from the e^+e^- collider data by the BELLE collaboration [BELLE11], while the spin-independent DiFF $D_1^{\sphericalangle}$ has been parametrized by a reproduction of the dihadron yield of the PYTHIA event generator [SEF+01] in the BELLE Monte-Carlo. Details on the extraction of $H_{1,sp}$ from the BELLE data can be found in [BCR11]. Table A.54 shows the numerical values where $n_u^{\uparrow}(Q^2)$ is sufficient due to the approximations made in Eqs. 6.6. These also hold true for the integrated DiFFs:

$$\begin{aligned} n_u &= n_{\bar{u}}, \\ n_d &= n_{\bar{d}}, \\ n_s &= n_{\bar{s}}, \\ n_u^{\uparrow} &= -n_{\bar{u}}^{\uparrow} = -n_d^{\uparrow} = n_{\bar{d}}^{\uparrow}, \\ n_s^{\uparrow} &= -n_{\bar{s}}^{\uparrow} = 0. \end{aligned} \tag{6.35}$$

Using this expressions, the hadron-pair asymmetry in Eq. 6.33 can be written as

$$A_{UT}^{\sin\phi_{RS}} \propto \frac{\sum_q e_q^2 h_1^q(x) n_q^{\uparrow}(Q^2)}{\sum_q e_q^2 f_1^q(x) n_q(Q^2)}\,. \tag{6.36}$$

Executing the sums explicitly leads to

$$A_{UT,p}^{\sin\phi_{RS}} \propto \frac{\frac{4}{9}\left(h_1^u n_u^{\uparrow} + h_1^{\bar{u}} n_{\bar{u}}^{\uparrow}\right) + \frac{1}{9}\left(h_1^d n_d^{\uparrow} + h_1^{\bar{d}} n_{\bar{d}}^{\uparrow} + h_1^s n_s^{\uparrow} + h_1^{\bar{s}} n_{\bar{s}}^{\uparrow}\right)}{\frac{4}{9}\left(f_1^u n_u + f_1^{\bar{u}} n_{\bar{u}}\right) + \frac{1}{9}\left(f_1^d n_d + f_1^{\bar{d}} n_{\bar{d}} + f_1^s n_s + f_1^{\bar{s}} n_{\bar{s}}\right)} \tag{6.37}$$

for a proton. Taking into account the approximations in Eqs. 6.35 this further simplifies to

$$A_{UT,p}^{\sin\phi_{RS}} \propto \frac{\left(h_1^{u_v} - \frac{1}{4} h_1^{d_v}\right) n_u^{\uparrow}}{\left(f_1^u + f_1^{\bar{u}}\right) n_u + \frac{1}{4}\left(f_1^d + f_1^{\bar{d}}\right) n_d + \frac{1}{4}\left(f_1^s + f_1^{\bar{s}}\right) n_s}\,. \tag{6.38}$$

In order to calculate an analog expression for the deuteron target, the isospin symmetry of the strong force, such that the d quark in the neutron can be regarded as being equivalent to the u quark in the proton, can be used. Thus the neutron PDFs $h_{1,n}^q$ and $f_{1,n}^q$ are related to the proton PDFs by an interchange of the quark flavor of u and d quarks. The contribution of the s quark as a pure sea quark is assumed to be the same for proton and neutron. The fragmentation functions are not affected by this interchange [BCR13].

The full conversion reads

$$\begin{aligned} h_{1,n}^{u/\bar{u}} = h_1^{d/\bar{d}},\ h_{1,n}^{d/\bar{d}} = h_1^{u/\bar{u}},\ h_{1,n}^{s/\bar{s}} = h_1^{s/\bar{s}}, \\ f_{1,n}^{u} = f_1^{d},\ f_{1,n}^{d} = f_1^{u},\ f_{1,n}^{s} = f_1^{s}. \end{aligned} \tag{6.39}$$

Therefore the hadron-pair asymmetry on a pure neutron target would be

$$A_{UT,n}^{\sin\phi_{RS}} \propto \frac{\left(h_1^{d_v} - \frac{1}{4}h_1^{u_v}\right)n_u^{\uparrow}}{\left(f_1^{d} + f_1^{\bar{d}}\right)n_u + \frac{1}{4}\left(f_1^{u} + f_1^{\bar{u}}\right)n_d + \frac{1}{4}\left(f_1^{s} + f_1^{\bar{s}}\right)n_s}\,. \tag{6.40}$$

Because a pure neutron target is not feasible, a deuteron target has been used by COMPASS, for which the equivalent of Eq. 6.36 is the sum of the proton and the neutron contributions. Therefore, the hadron-pair asymmetry on a deuteron target can be written as [BCR11]

$$A_{UT,d}^{\sin\phi_{RS}} \propto \frac{\left(h_1^{u_v} + h_1^{d_v}\right)n_u^{\uparrow}}{\frac{4}{3}\left(f_1^{u} + f_1^{\bar{u}} + f_1^{d} + f_1^{\bar{d}}\right)\left(n_u + \frac{1}{4}n_d\right) + \frac{2}{3}\left(f_1^{s} + f_1^{\bar{s}}\right)n_s}\,. \tag{6.41}$$

Here the isoscalar nature of the two nucleons is reflected by the equal weight of the u and d quark terms, while in the case of the proton target the d quark contribution is suppressed by a factor of $\frac{1}{4}$.
With the asymmetry as the measured quantity the Eqs. 6.38, 6.41 can be solved for the linear combinations of h_1^u and h_1^d, as given in Eqs. 6.31, leading to [BCR11]

$$\begin{aligned} x h_{1,p}(x;Q^2) = &- \frac{A_{UT,p}^{\sin\phi_{RS}}(x;Q^2)}{C(y)n_u^{\uparrow}(Q^2)} \\ &\times \left[n_u(Q^2) x f_1^{u+\bar{u}}(x;Q^2) + \frac{1}{4} n_d(Q^2) x f_1^{d+\bar{d}}(x;Q^2) + \frac{1}{4} n_s(Q^2) x f_1^{s+\bar{s}}(x;Q^2) \right] \end{aligned} \tag{6.42}$$

for the proton target and [BCR11]

$$\begin{aligned} x h_{1,d}(x;Q^2) = &- \frac{A_{UT,d}^{\sin\phi_{RS}}(x;Q^2)}{C(y)n_u^{\uparrow}(Q^2)} \frac{4}{3} \\ &\times \left[\left(x f_1^{u+\bar{u}}(x;Q^2) + x f_1^{d+\bar{d}}(x;Q^2) \right) \left(n_u(Q^2) + \frac{n_d(Q^2)}{4} \right) + \frac{n_s(Q^2)}{2} x f_1^{s+\bar{s}}(x;Q^2) \right] \end{aligned} \tag{6.43}$$

for the deuteron target, with $f_1^{q+\bar{q}} := f_1^q + f_1^{\bar{q}}$ and $C(y) = \frac{B(y)}{A(y)}$ cf. Eq. 2.68. The equations have been multiplied by x by the authors of [BCR11] for a convenient study, since the dependence of the measured asymmetry comes only from the involved PDFs. The unpolarized PDFs are taken from the MSTW08LO set [MSTW09], see Fig. A.55, in combination with the DSSV parameterization [dFSSV09].

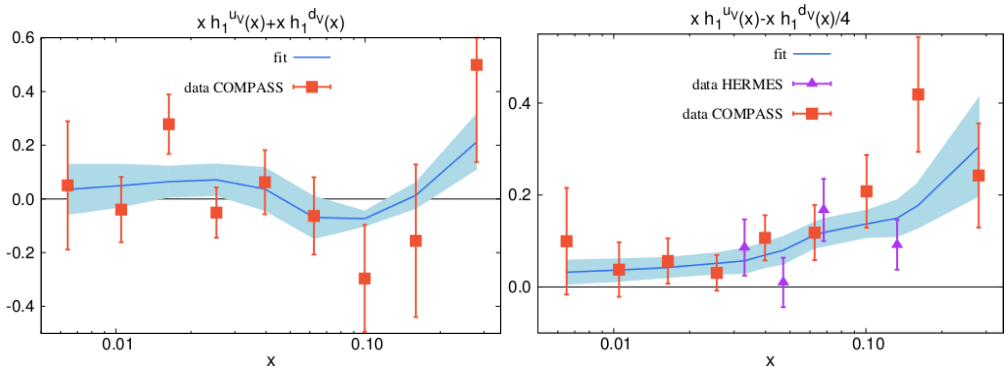

Figure 6.7.: The COMPASS (2002-2004 deuteron and 2007 proton data; red full squares) and HERMES results (purple triangles) for $xh_{1,d}$ (left panel), and $xh_{1,p}$ (right panel) as in Eq. 6.44 from Bacchetta *et al.* [BCR13]. The best-fit result using the flexible scenario form as described in Sec. 6.3.4 is indicated by the blue line, while the error band is the sum of all straight lines connecting the statistical uncertainties of the fit at each data point.

With the results from both target types, proton and deuteron, it is possible to solve the Eq. 6.31 and for $xh_1^{u_v}$ and $xh_1^{d_v}$:

$$xh_1^{u_v} = \frac{1}{5}\Big(xh_{1,d} + 4xh_{1,p}\Big), \tag{6.44}$$

$$xh_1^{d_v} = \frac{4}{5}\Big(xh_{1,d} - xh_{1,p}\Big). \tag{6.45}$$

This has been performed for the first time by Bacchetta and collaborators in [CBR12], later also by Elia [Eli12]. A recently published calculation by Bacchetta *et al.* [BCR13] including the published COMPASS results [COMPASS12c] of h^+h^- pairs from proton and deuteron targets is shown in Fig. 6.7.
The authors used all hadron h^+h^- results, because no identified hadron-pair results had been published by COMPASS at that time. This approximation is well founded, because $\approx 60\,\%$ of the h^+h^- pairs are pure pion pairs (see Tab. 4.5) and the asymmetry values are mostly determined by the $\pi^+\pi^-$ signal (see Figs. 5.5,5.8 and Tabs. A.25, A.26).

Transversity extraction with the new and full data sets

The COMPASS results shown in Fig. 6.7 are obtained from the h^+h^- pair asymmetries of [COMPASS12c] only. The new results presented in this work allow for a more precise evaluation of the quantities discussed above due to the high statistics and the particle identification. The unitized analysis methods for all data sets, proton and deuteron, contribute to a reduction of the systematic uncertainties. A simplified ansatz to do this has been chosen in consultation with A. Bacchetta.
Table 1 of [BCR13] quoting the published $\langle x \rangle$, $\langle Q^2 \rangle$ and $A_{UT}^{\sin\phi_{RS}}$ values from [COMPASS12c] is shown in Fig. A.53. Using this table the bin-by-bin ratios

$$\frac{x h_1^{u_v} + x h_1^{d_v}}{A_{UT,d}^{\sin\phi_{RS}}}, \qquad \frac{x h_1^{u_v} - \frac{1}{4} x h_1^{d_v}}{A_{UT,p}^{\sin\phi_{RS}}} \tag{6.46}$$

are calculated. These ratios are conversion factors containing the information on the unpolarized process, for instance the denominator in Eq.2.68 as well as of the polarized DiFFs $H_{1,sp}^{\sphericalangle}$ in the given x and Q^2 range. The kinematic mean values are almost the same values as the final proton and deuteron data sample of this work, see Tabs. A.26 and A.10. Small differences in the $\langle Q^2 \rangle$ values at large x are the results of the implementation of the LAS trigger in 2010, see Sec. 3.5. These can be neglected in this simple approach w.r.t. the statistical and systematical uncertainties of the data.
In a next step these conversion factors can be used to scale the new asymmetry amplitudes obtained in this work to get again $h_{1,p}$ and $h_{1,d}$. The results obtained with the new pion pair asymmetries of the COMPASS deuteron and proton data are shown in Fig. 6.8, left and right panel. The distributions of $h_{1,p/d}$ are very similar in magnitude to the original asymmetry amplitudes, since the conversion factors are almost constant over a wide x range. They can be found in Tabs. A.31 and A.32.
The final u and d valence quark transversity distributions are obtained by solving the system of equations, the two linear combinations as in Eq. 6.44. Figure 6.9 shows the results for $x h_1^{u_v}$ and $x h_1^{d_v}$. A nonzero trend at large x values is evident in both distributions, the four highest x bins being at least $1\,\sigma$ away from zero. From the present data, sign changes in the distribution of $x h_1^{d_v}$, for instance at very large x, can not be excluded due to the limited statistics. Furthermore the d and u quark transversity PDFs are of opposite signs and the strength of their signals is compatible within the uncertainties. The numerical values are given in Tab. A.33.

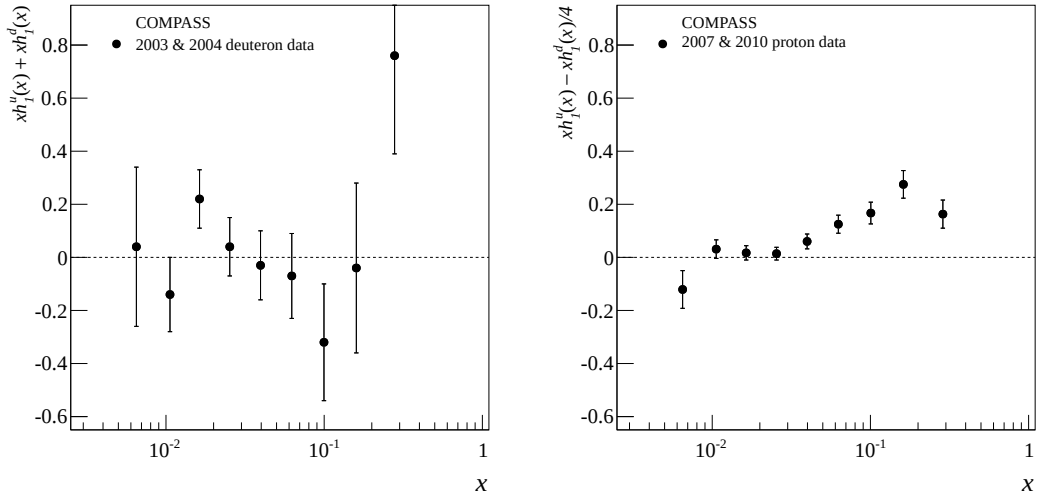

Figure 6.8.: Results of $xh_{1,d}$ (left panel) and $xh_{1,p}$ (right panel) obtained from the $\pi^+\pi^-$ asymmetries of the COMPASS deuteron 2003-2004 and combined proton 2007/2010 data from Fig. 6.4.

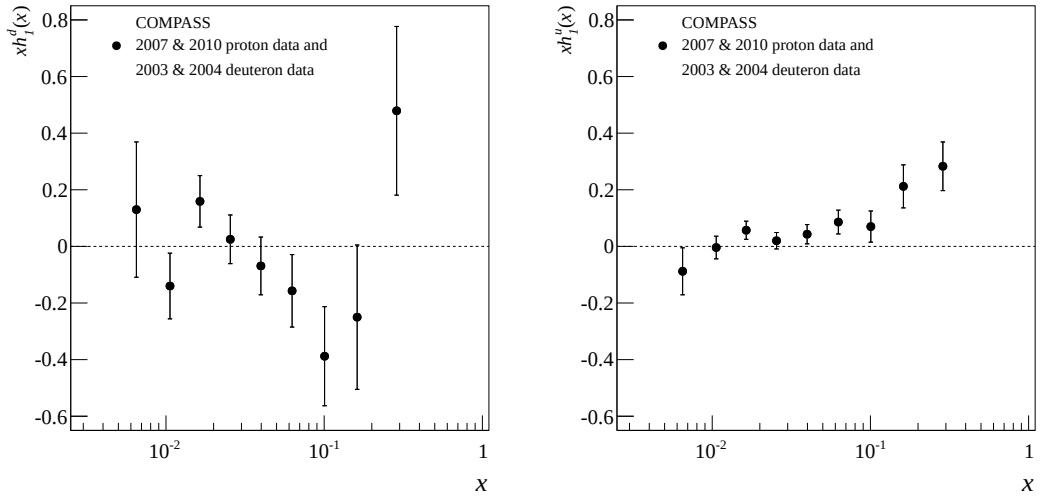

Figure 6.9.: Results of $xh_1^{d_v}$ (left panel) and $xh_1^{u_v}$ (right panel) obtained from the $\pi^+\pi^-$ asymmetries of the COMPASS deuteron 2003-2004 and combined proton 2007/2010 data from Fig. 6.4.

Comparison with results from single hadron production

As described in Sec. 6.3.5, the Collins asymmetry in the single hadron production process also gives access to the transversity PDFs. In the global fit from Anselmino and collaborators the available data from the HERMES and the COMPASS collaborations on the Collins asymmetry and the e^+e^- collider data from the BELLE collaboration are used for a fit of the transversity PDFs. In Fig. 6.10 the results of this work are compared to the two results from the recent global fit of Anselmino *et al.* [ABD+13] denoted as A_{12} and A_0, including two different asymmetry sets by BELLE [BELLE08], see Fig. A.1. The difference between the two curves is inter alia triggered by the very last point of the HERMES π^+ Collins asymmetry, whose amplitude decreases in the their 2010 [HERMES10] analysis w.r.t. the one from 2007 [HERMES07].
The agreement of the d valence quark transversity with the results from the global fit is good enough accounting for the overall systematic uncertainty. All points are within two standard deviations of the curves, still indicating some larger amplitudes at high x. The obtained u_v quark transversity PDF agrees very well with the fits, in trend and magnitude. A possible explanation is the similarity of the hadron-pair asymmetries and the Collins asymmetry of charged pions, which will be discussed in detail in Sec.6.3.5. A global fit to the transversity PDFs from the hadron-pair data was carried out by Bacchetta *et al.* [BCR13], see next section.

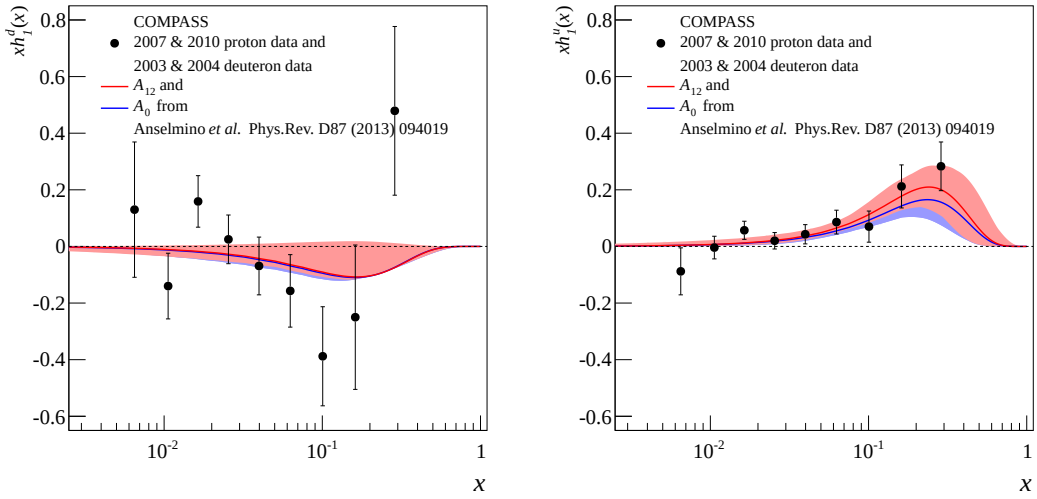

Figure 6.10.: Results of $xh_1^{d_v}$ (left panel) and $xh_1^{u_v}$ (right panel) in comparison to the corresponding results extracted from the single hadron Collins asymmetries from Anselmino *et al.* [ABD+13] (2013) with the A_{12} asymmetry (red curve) and the A_0 asymmetry (blue curve), both from BELLE [BELLE08] see Fig. A.1.

Global fit to the valence quark Transversity PDFs

Bacchetta and collaborators have used the published HERMES and COMPASS (deuteron and 2007 proton h^+h^- data only) to extract the valence quark transversity PDFs [BCR13], see previous section. Their next step is to perform a global fit to the valence quark transversity distributions using the functional form [BCR13]

$$xh_1^{q_v} = \tanh\Big(\sqrt{x}\Big(A_q + B_q x + C_q x^2 + D_q x^3\Big)\Big)\,\Big(x\,\mathrm{SB}^q(x,Q^2) + x\,\mathrm{SB}^{\bar{q}}(x,Q^2)\Big), \quad (6.47)$$

where SB^q is the Soffer bound of a quark q (cf. Eq. 2.28). The behavior of the fit result in the very low x region, where no experimental data is available, is fixed by the $\sqrt{x}$ factor which is a reasonable assumption of the authors. The choice of the parametrization of the arguments of the hyperbolic tangent allows for three scenarios with different levels of freedom

- a rigid scenario of 4 free parameters, with $C_u = C_d = D_u = C_d = 0$,
- a flexible scenario of 6 free parameters, with $D_u = C_d = 0$ and
- an extra-flexible scenario with all 8 parameters fitted.

From the rigid to the extra-flexible scenario the number of possible nodes increases from one up to three.
The different $\langle Q^2 \rangle$ values in each data bin are taken into account by the implementation of the HOPPET code [SR09] in the minimizer of the fitting procedure. For more details on the framework see [BCR13]. The result of a standard χ^2 minimized fit was already shown in Fig. 6.7, while in Fig. 6.11 the output of a replica fit method is presented. Therefore $N = 100$ replicas of the data points were created by applying a Gaussian noise on them with a variance equal to the uncertainties of the points. Each replica set is then fitted separately with an error minimization. Afterwards the most divergent, too low or too high, $32\,\%$ replicas for each data point are rejected and the remaining $68\,\%$ form the uncertainty band (green shaded area) in Fig. 6.11. Since the event samples presented and used in this work to extract the pion pair asymmetries are sub-samples of the sample used by Bacchetta *et al.* or vice versa, the results are not independent from each other. Thus the good agreement of the new valence quark transversity PDF extraction and the fit result to the published asymmetries is not surprising.
The flexible and extra-flexible scenarios create larger uncertainties than the rigid scenario, since these can adapt further to the data points due to the increased number of free parameters. This should not be equated with a physically more correct solution. The positive asymmetry amplitude in the highest x bin of $xh_1^{d_v}$ for example brings the fit to an additional sign change despite of its large uncertainty.
By including the new results of this work in the fit it will be possible to decrease the uncertainties slightly, but a larger data sample on a deuteron target is indispensable for a significant improvement.

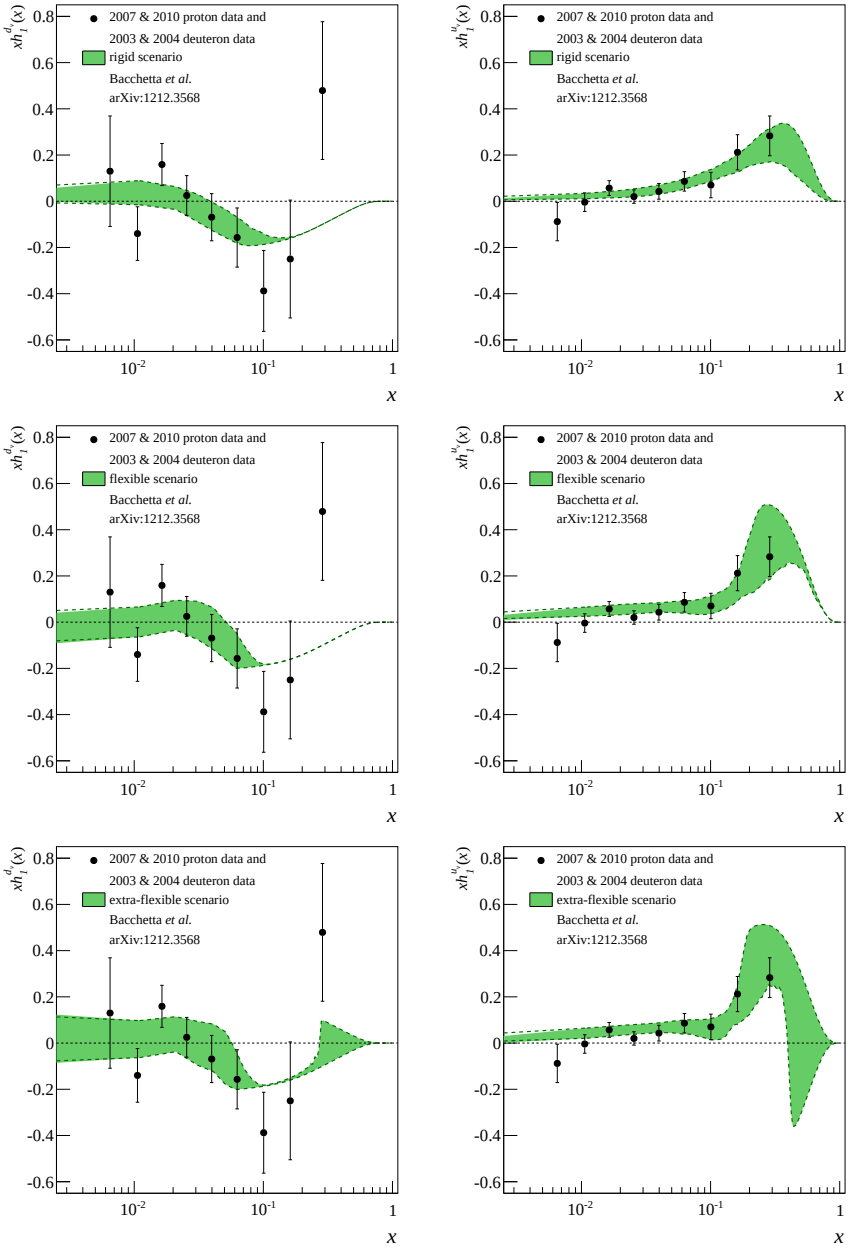

Figure 6.11.: Results of $xh_1^{d_v}$ (left column) and $xh_1^{u_v}$ (right column) from this work (see Sec. 6.3.4) in comparison to the corresponding fit results from Bacchetta *et al.* [BCR13]. The green shaded area includes $68\,\%$ of all fitting replicas (100 replicas of the data, where each point is shifted by a Gaussian noise with the same variance as the measurement.) obtained in the Monte Carlo approach. From top to bottom, results of the rigid, flexible, and extra-flexible scenarios (see Eq. 6.47) are shown.

6.3.5. Interpretation approaches

The similarity of Collins and hadron-pair asymmetries

When comparing the results of the single hadron Collins asymmetry in e.g. Fig. 6.1 to the hadron-pair asymmetry e.g. in Fig. 5.4 a compatible strength of the signals and of the distributions is noticeable. In Fig. 6.12 a direct comparison of these asymmetries of single hadron and dihadrons as a function of x from the 2007/2010 combined proton data is shown. It is observed that the Collins asymmetry of positively and negatively charged hadrons is essentially identical in magnitude with opposite signs [COMPASS12a]. Moreover, a striking similarity in magnitudes between the hadron-pair and the Collins asymmetry is obvious. The study of this effect is also discussed in a recent COMPASS publication of the h^+h^- pair asymmetries from the combined 2007/2010 proton data of this work in [COMPASS14a]. In the following a brief summary of the investigation and conclusion carried out in this publication is given.
As described in Sec. 6.2 [ABD+09b] the first observation on the Collins asymmetry is interpreted as an indication for the transversity distributions of u and d quarks having almost equal magnitude and opposite signs for favored and unfavored Collins fragmentation functions. The latter observation of hadron-pair asymmetry amplitude values being slightly larger in magnitude, but very close to the values of the Collins asymmetry amplitudes for h^+, is an object of recent and ongoing discussions. The event samples on which these asymmetries have been evaluated are not completely independent, since events with more than one hadron being produced also enter the single hadron sample.

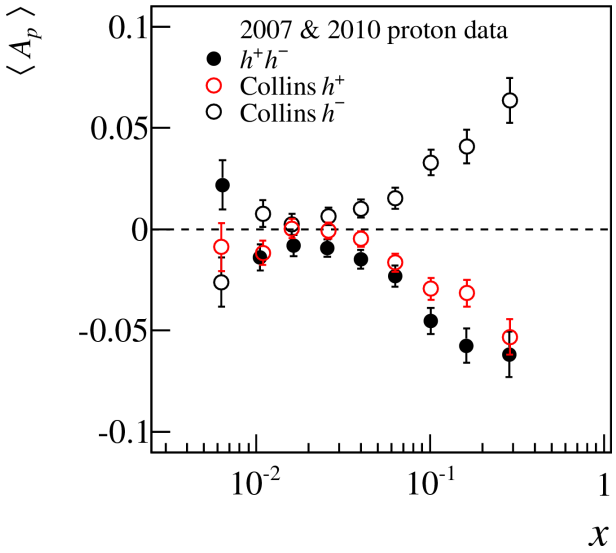

Figure 6.12.: Comparison of the asymmetry vs. x obtained in the analysis of hadron-pair production to the corresponding Collins asymmetry for the combined 2007/2010 proton data [COMPASS14a].

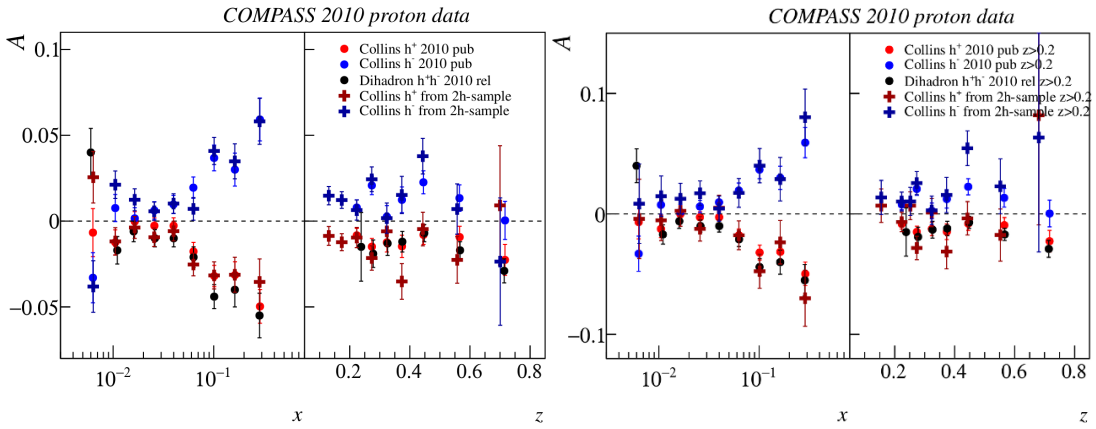

Figure 6.13.: The Collins (red and blue crosses) and hadron-pair asymmetry (black dots) extracted from a common hadron-pair sample as a function of x and z_i with two different cuts on $z_i > 0.1$ (left panel) and $z_i > 0.2$ (right panel) compared to the published results from the standard sample [COMPASS12a] (red and blue dots).

In order to be able to investigate the similarity without a possible bias induced by different cuts, both asymmetries have been evaluated on a common hadron sample. Thus, the cut on the fractional energy of the single hadrons z_i was unitized to $z_i > 0.2$ or $z_i > 0.1$. Furthermore the cut on the transverse momentum of the hadrons p_T at $0.1\,\mathrm{GeV}/c$ used in the single hadron analysis was adopted. Finally two oppositely charged hadrons from the primary vertex were required to create a common sample for the single and the hadron-pair analysis. The results are presented in Fig. 6.13 showing that the similarity persists, giving a strong indication of equal analyzing powers in both channels.

A first approach in order to understand this observation can be performed by an investigation on the angles involved. As a reminder, the Collins asymmetry is the amplitude of the sine modulation of the Collins angle $\phi_{C^\pm} = \phi_{h^\pm} + \phi_S - \pi$, where $\phi_{h^\pm}$ are the azimuthal angles of positive and negative hadrons in the γ^*-nucleon system. The almost equal magnitudes with opposite signs for different charges suggest that in the fragmentation of the struck quark the azimuthal angles of positive and negative hadrons created in the event differ by $\approx \pi$ and thus the hadrons produced have antiparallel transverse momenta. This oppositeness between ϕ_{h^+} and ϕ_{h^-} can be a consequence of the conservation of a local transverse momentum in the fragmentation process, see next section. This can also be reproduced by the Monte Carlo spin-independent DIS event generator LEPTO [EIR97]. If this holds true, the asymmetry amplitudes of an angle ϕ_{2h} defined as the arithmetic mean of the azimuthal angles of the two hadrons of a hadron-pair should give almost equal results compared to the standard dihadron angle ϕ_{RS}, see Eq. 2.68. Accordingly the angle ϕ_{2h} is defined as the azimuthal angle of the vector [COMPASS12a]

$$\boldsymbol{R}_N = \hat{\boldsymbol{p}}_{T,h^+} - \hat{\boldsymbol{p}}_{T,h^-}, \tag{6.48}$$

where $\hat{\boldsymbol{p}}_{T,h^\pm}$ are the unit vectors of the transverse momenta of the hadrons[4].

[4] In the calculation a correct 2π periodicity of the angles has to be ensured

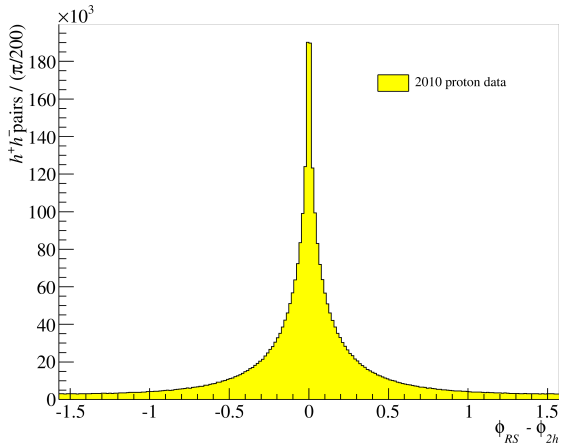

Figure 6.14.: Difference between the two dihadron angles ϕ_{RS} and $\phi_{2h,S}$ [COMPASS14a].

Figure 6.14 shows the difference between the standard dihadron angle ϕ_{RS} and the new angle ϕ_{2h} confirming their similarity in magnitude.
The target spin is taken into account by subtracting $\phi_{S'}$ from ϕ_{2h}, the resulting angle $\phi_{2h,S}$ can be regarded as a mean of the Collins angle of the positive and negative hadrons from the hadron-pair. Correspondingly, the asymmetry amplitudes obtained from these angles are well compatible, see Fig. 6.15. Here the cut on p_T and the demand for $z_i > 0.1$ have been considered. These results are hinting at a common physical origin for the Collins mechanism and the DiFF. A possible explanation could be given by the $^3P_0$ Lund model [AGIS83] and by the recursive string fragmentation model [Art02, Art10] introduced in the next section.

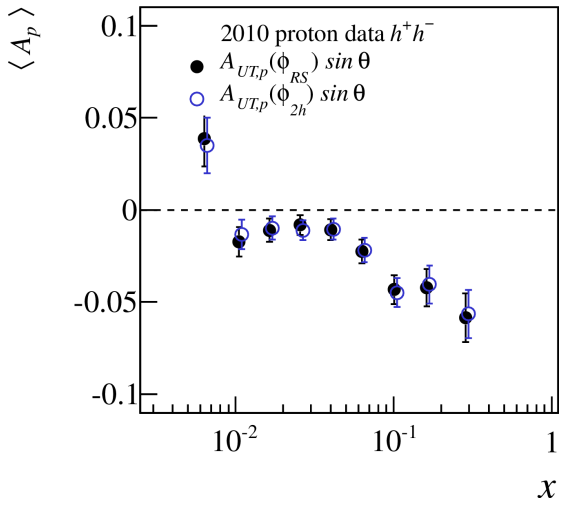

Figure 6.15.: Comparison between the hadron-pair asymmetry (black points) and the Collins-like asymmetry for the hadron-pair (open blue points) as a function of x for the 2010 data [COMPASS14a].

The string fragmentation model

The framework of a (recursive) string fragmentation model can be used for an interpretation of the Collins asymmetry occurring in single hadron production in SIDIS as well as of the hadron-pair asymmetry. Already the semi-classical Lund ${}^3P_0$ string fragmentation model [AGIS83] can generate a Collins-like effect, while Artru [Art02, Art10] has expanded this model to multiple numbers of hadrons produced. The interpretation of the Collins effect, which was postponed from Sec. 6.2.2 to this section, is the starting point.
A valence quark receiving a momentum transfer q from the virtual photon starts to move away from the diquark remnant of the nucleon. Both are color charged and thus connected by a flux tube. If the momentum transfer is high enough, the tearing of the flux tube creates an quark-antiquark pair $q_0\bar{q}_{-1}$ with the quantum numbers of the vacuum $J^{PC} = 0^{++}$. Consequently, its orbital angular momentum $\boldsymbol{L}_y$ is 1 and its spin $\boldsymbol{S}_y$ is -1 w.r.t. the quantization axis, which is given by the transverse spin direction in this case. The struck quark and the generated antiquark $\bar{q}_{-1}$ form a meson e.g. a pion. Then a preferred direction of motion of the pion is given due to the conservation of angular momentum. Thus it depends on the direction of the spin of the struck quark. Hence, in the case of an upwards polarized quark a counter-clockwise rotation is induced while a downwards polarized quarks causes a clockwise movement of the hadron produced, see Fig. 6.16. Therefore a nonzero transversity PDF will lead to a left-right asymmetry in the distribution of the hadrons produced, which is the so-called “Collins effect”.

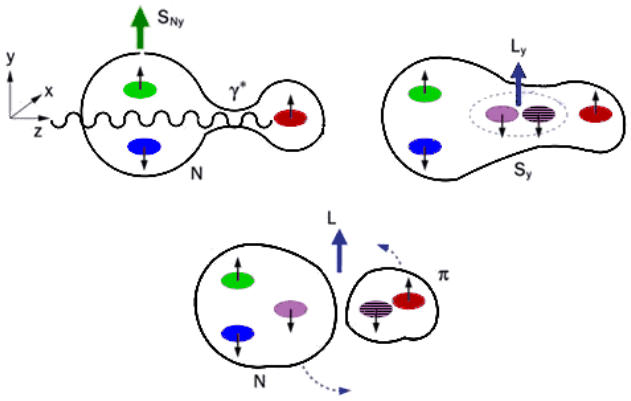

Figure 6.16.: Schematic description of the Collins mechanism in the framework of the string fragmentation model [RvdS04]. In the top-left part the flux tube still exists after the quark (red) has been struck by the virtual photon γ^*, while in the top-right the breaking of the tube has created a quark-antiquark pair with angular momentum $\boldsymbol{L}_y$ and spin $\boldsymbol{S}_y$. Finally a meson, for instance a pion, is created in the hadronization process which preferably moves in a direction depending on the direction of the spin of the struck quark.

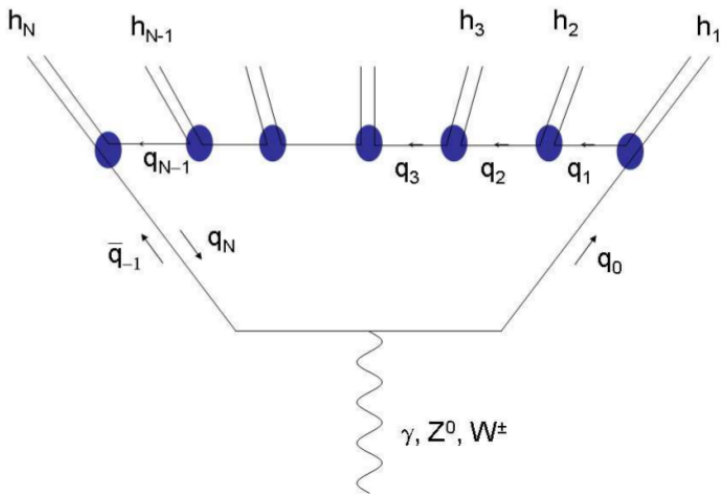

Figure 6.17.: Decay of an electroweak boson γ, Z^0 or $W^{\pm}$ into a quark-antiquark pair $q\bar{q}$, which then hadronizes into N mesons $h_1, ..., h_N$, see Eq. 6.50 [Art10].

Artru suggests that the effect of the interference fragmentation of a quark into a hadron-pair, which is described by the DiFF $H_1^{\sphericalangle}$, might be a so-called "two-particle relative Collins effect" [Art10]. This effect is extendable up to arbitrary numbers of hadrons produced

$$q_0 + \bar{q}_{-1} \rightarrow h_1 + h_2 + ... + h_N. \tag{6.49}$$

In general, Artru assumes that in the decay of an electroweak boson such as the γ a quark-antiquark pair $q_0\bar{q}_{-1}$ is produced, connected by a gluon string, see Fig. 6.17. Then the recursive process can be divided into the sub-process [Art02]

$$\begin{aligned} q_0(\boldsymbol{k}_0) &\rightarrow h_1(\boldsymbol{p}_1) + q_1(\boldsymbol{k}_1), \\ q_1(\boldsymbol{k}_1) &\rightarrow h_2(\boldsymbol{p}_2) + q_2(\boldsymbol{k}_2), \\ &... \\ q_{N-1}(\boldsymbol{k}_{N-1}) &\rightarrow h_N(\boldsymbol{p}_N) + q_N(\boldsymbol{k}_N). \end{aligned} \tag{6.50}$$

where $\boldsymbol{k}_i$ and $\boldsymbol{p}_i$ are the three-momenta of a quark q_i and a hadron h_i, respectively. The recursive fragmentation process is illustrated in Fig. 6.17. From this scheme it is clear that q_N is equal to $\bar{q}_{-1}$ which is a quark propagating backward in time.
If the available energy provided by the virtual photon is high enough, additional quark-antiquark pairs can be produced along the fragmenting string. The total energy, momentum and torsional moment, is conserved in this process. Expanded to a multi-hadron production, the scheme could be modified as shown in Fig. 6.18. The quark-antiquark pairs $q_i\bar{q}_{i+1}$ have the transverse momenta $-\boldsymbol{k}_{i,T}$ and $+\boldsymbol{k}_{i+1,T}$, respectively. The neighboring quarks q_i and $\bar{q}_i$ are not part of the same hadron in the final state, but they carry a torsional moment of $\boldsymbol{L}_i$. The sum of the torsional moment of $\boldsymbol{L}_i$ gives the initial torsional momenta. The transverse hadron-pair momenta are generated by the orbital motions of the single quarks which form a pair. The quark q_3 remains in the target remnant.

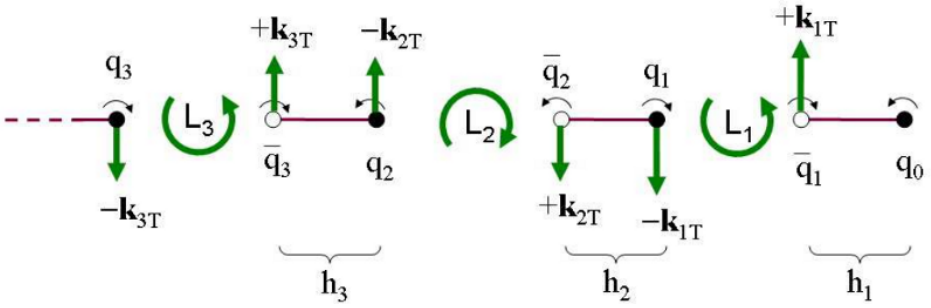

Figure 6.18.: Decay of a string into pseudoscalar mesons h_1,h_2 and h_3 [Art10].

This could be an explanation of the almost equal magnitudes with opposite signs of $\phi_{h^\pm}$ for different charges as in the Collins asymmetry amplitudes extracted from single hadrons taken from the hadron-pair sample as in Fig. 6.13.
The scheme of a decaying string under the conservation of certain quantities does not only explain the creation of a pion pair or multiple numbers of pions, but also holds true for the production of kaon pairs and mixed pion-kaon pairs. Indications of nonzero hadron-pair asymmetry amplitudes of such pairs are given in the results discussed in Sec. 6.3.1. Possible combinations of involved quark flavors in the hadronization process into $\pi^+\pi^-$, K^+K^-, π^+K^-, and $K^+\pi^-$ are

$$\bar{d} = u \div \bar{u} = d \rightarrow \pi^+\pi^-, \tag{6.51}$$
$$\bar{s} = u \div \bar{u} = s \rightarrow K^+K^-, \tag{6.52}$$
$$\bar{d} = u \div \bar{u} = s \rightarrow \pi^+K^-, \quad s = \bar{u} \div u = \bar{d} \rightarrow \pi^+K^- \tag{6.53}$$
$$\bar{s} = u \div \bar{u} = d \rightarrow K^+\pi^-, \quad d = \bar{u} \div u = \bar{s} \rightarrow \pi^+K^-. \tag{6.54}$$

where the $\div$ symbolizes a down-breaking part of the flux tube and $=$ a persisting part. An additional illustration corresponding to the scheme of Fig. 6.18 in shown in Fig. 6.19 and 6.20.

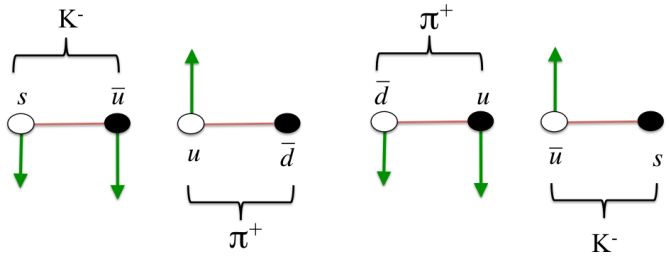

Figure 6.19.: The production scheme of π^+K^- pairs in the string fragmentation model [Eli12].

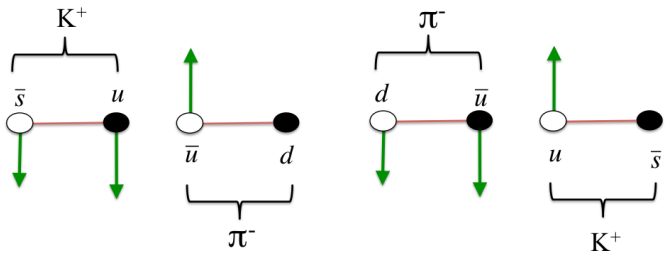

Figure 6.20.: The production scheme of $K^+\pi^-$ pairs in the string fragmentation model [Eli12].

Quark hadronization via the NJL-jet model

Very recently Matevosyan and collaborators [MKT14] described the production of a single hadron or a hadron-pair in the hadronization of the struck quark by a NJL-jet model based on the Field and Feynman quark-jet picture [FF78]. A functional scheme of this process is shown in Fig. 6.21. They assume that the quark has a certain probability to flip its spin after the emission of a hadron, which is indicated by the double-lined arrows in the Figure. The fragmenting quark runs through a decay chain cascade, where the hadron emission probabilities are calculated in the NJL model at each vertex under momentum conservation. In the single pion emission the authors observe an elementary "Collins"-like effect for spin flip probabilities higher then 0.5 appearing as a sine modulation of the azimuthal angle of charged pions. In Sec. 6.3.5 the correlation between the azimuthal angles of the two oppositely charged pions of a hadron-pair was described experimentally. Matevosyan *et al.* also found this correlation in the results produced by their model. The origin of this effect is that in the emission of the first pion the remnant quark gets an opposite signed recoil transverse momentum, as depicted in Fig. 6.21. When the second pion is produced, a fraction of this transverse momentum is transfered to it. This leads to a difference of π in the azimuthal angle of the two hadrons, which is in accordance to the Lund $^3P_0$ string fragmentation model [AGIS83].

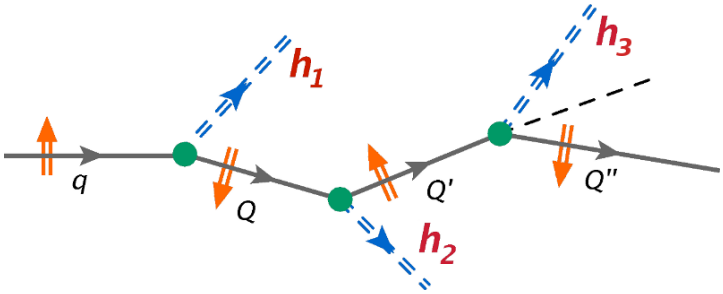

Figure 6.21.: Functional scheme of the production of three hadrons via the NJL-jet model [MKT14]. The double-lined arrows (orange) indicate the spin of the fragmenting quark producing hadrons in a quark decay cascade.

Resonant production of hadron-pairs

Further sources of hadron-pairs are resonance decays. The mass signatures of some mesons decays are clearly visible in the M_{inv} spectra, see Fig 6.22. In the distribution of pion pairs, some of the resonant decays described in Sec. 6.3.3 are clearly visible in both deuteron and proton data. Such as the K^0 channel around $\approx 500\,\mathrm{MeV}/c^2$, the ρ channel around $\approx 770\,\mathrm{MeV}/c^2$ and the f_0/f_2 channel around $\approx 980\,\mathrm{MeV}/c^2$ and $\approx 1270\,\mathrm{MeV}/c^2$, respectively. Other decays with more than two hadrons in the outgoing channel are supposed to generate broader peaks such that decays of ω, η and η' contribute less to the overall pion pair invariant mass spectra, see Sec. 6.3.3. The M_{inv} distribution of pure kaon pairs shows a very pronounced signal, right above their production threshold, originating from the $\phi(1020)$ resonance. The ϕ meson can also contribute to the pion pair spectra via $\phi(1020) \rightarrow \rho\pi \rightarrow \pi^+\pi^-\pi^0$. The high statistics of the proton data sets indicates further broad peaks around $\approx 1300\,\mathrm{MeV}/c^2$ and $\approx 1500\,\mathrm{MeV}/c^2$ which might be caused by the $f_2(1270)$ and the $f_2'(1525)$. The invariant mass distributions of π^+K^- and $K^+\pi^-$ also show in each case one dominant channel caused by the decays of $K^*(892)$. Further possible candidates for peaks in the M_{inv} spectra of the mixed pairs are $K^*(1430)$ and $K_4^*(2045)$.
When comparing the invariant mass spectra to the final pion pair asymmetry of the proton target data sets in Fig. 5.8, a correlation with the ρ^0 mass and with the f_2 mass peak is visible. Artru [Art10] also gives an interpretation of the appearance of a Collins-like asymmetry for decay pions of a ρ meson associated with the polarization of the ρ meson. A transversity signal of the K^+K^- from the $\phi(1020)$ resonance however, is not observed, while an indication of a broad peak in the asymmetry amplitudes from incoherent K^+K^- pairs is given. The only significant transversity signal in the case of the mixed pairs is observed for $K^+\pi^-$ pairs in the mass region of the $K^*(892)$. A meaningful interpretation of the deuteron target results is difficult, only the ρ peak for pion pairs is significant.

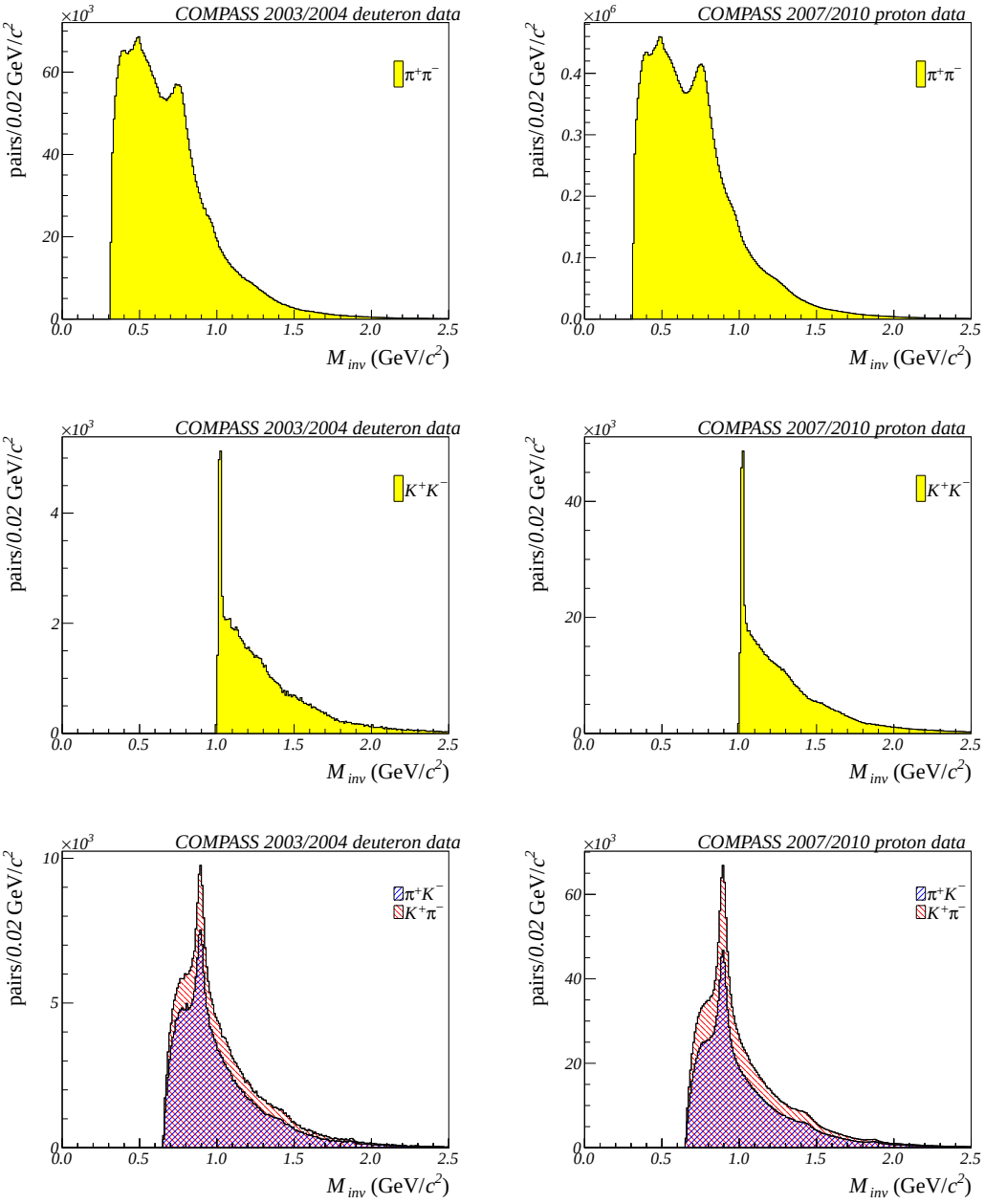

Figure 6.22.: The final M_{inv} distributions from the 2003-2004 deuteron data (left column) and from the combined 2007/2010 proton data (right column) of: $\pi^+\pi^-$ pairs (1st row) , K^+K^- pairs (2nd row), and the mixed pairs π^+K^- and $K^+\pi^-$ (3rd row) (for resonance masses see text).

7. Future prospects

7.1. Further prospects on the hadron-pair asymmetry

The results on the hadron-pair or dihadron asymmetries of identified pion pairs on transversely polarized deuteron and proton targets presented in Chap. 5 are an important milestone, since they allowed for an extraction of the valence transversity PDFs of u and d quarks (Sec. 6.3.4). Model calculations from the Pavia and the Beijing groups, see Sec. 6.3.3, try to setup up a framework to describe the observations made by the HERMES and the COMPASS collaborations (Sec. 6.3.2). The data presented in this work will allow for an improvement of the assumptions made in these models, hence, the contributing channels and their relative strength could be adjusted using the invariant mass distributions from Sec. 6.3.5. A multidimensional extraction of the pion pair asymmetry in bins of (M_{inv}, x) adapted to the masses of the resonances could deliver additional important information. Furthermore, analog models for the pure kaon and the mixed pair asymmetries should be developed. Although the available sample sizes are limited, the results of these dihadrons should allow for an improved flavor separation of the Transversity PDF. This is a basic requirement for a deeper understanding of the role of the strangeness and sea quarks in general.
The tensor charge g_T as introduced in Eq. 2.18a is the integrated transversity PDF. Bacchetta and collaborators [BCR13] made a first attempt to calculate it from the parameters obtained by the fit to the data. In the available x range, g_T of u and d quarks was found to be ≈ 0.3 and ≈ -0.26, respectively. These values strongly depend on the functional form of the fit and the minimization procedure being used. This procedure should be redone including the latest results presented in this work.
In Sec. 6.3.4 it was briefly described how Bacchetta *et al.* [BCR13] obtained the information on the unpolarized DiFF $D_1^{\sphericalangle}$ and that this procedure is based on Monte-Carlo (MC) simulations, since there is no experimental data available yet. The so-called "dihadron multiplicities", the probabilities of producing a pair of hadrons from the initial quark q in the fragmentation process, allow access to $D_1^{\sphericalangle}$, see Eq. A.1. Using the parametrizations of f_1 from e.g. the MSTW 2008 set [MSTW09] shown in Fig. A.55, it is possible to extract the unpolarized DiFF and use this as an input for the transversity extraction instead of the MC generated values. In Sec. A.7 the analysis and results on the multiplicities from the 2004 (deuteron) and the 2010 (proton) data sets are described. Their extraction was also part of this work, but the results are not used in the extraction of the transversity function yet.

Also other pair combinations with mesons such as the π^0 are part of the future dihadron analysis program. At the COMPASS experiment the uncharged pions are detected via their decay products (high energetic photons) in the electro-magnetic calorimeters. A production of the raw data of 2010 including a dedicated energy calibration of the ECALs is ongoing. From there, the asymmetries of $\pi^+\pi^0$, $\pi^0\pi^-$, and $\pi^0\pi^0$ pairs will be extracted if adequate statistics is available. Underlying models to explain the basic Collins and dihadron effect — such as the Lund model and the recursive string fragmentation model — are confirmed in their conclusions and extended by new approaches such as the NJL-jet model (Sec. 6.3.5). Theoretical and experimental efforts will be required in order to develop a framework which can explain the results being observed for all four pair combinations. Predictions made by the models should be tested, for instance, the NJL-jet model predicts sizeable asymmetries also for pairs including π^0 [MKT14].

7.2. The Drell-Yan measurement at COMPASS-II

Semi-inclusive deep inelastic scattering is not the only process where the PDFs described in Sec. 2.3.2 occur. There are more options, among them the so-called "Drell-Yan" (DY) process can be interpreted as space- and time-reversed version of a SIDIS reaction. The measurement of Drell-Yan processes using a polarized target is also part of the COMPASS-II proposal [MM10]. For this an upgrade of the apparatus is necessary, of which an important part is a vertex detector inside the necessary absorber. The development and construction of the scintillating fiber based vertex detector was also performed in the framework of this thesis and is described in detail in Sec. 7.2.3. The setup of a SciFi beam telescope for this measurement is introduced in Sec. A.6.1.

7.2.1. The Drell-Yan process

In the Drell-Yan process a dilepton is produced from the collision of two spin-$\frac{1}{2}$ hadrons which might be polarized, as

$$H_a(P_a, \mathbf{S}_a) + H_b(P_b, \mathbf{S}_b) \to \gamma^*(q) + X \to \ell^-(l) + \ell^+(l') + X, \tag{7.1}$$

where $P_{a/b}$ are the four-momenta of the beam/target hadron and $\mathbf{S}_{a/b}$ the vector of their spin polarizations while the four-momenta of the lepton, the antilepton and of the virtual photon are l, l' and $q = l + l'$, respectively. Additional variables are constructed for the description of the process, such as

the momentum fraction carried by a parton from $H_{a/b}$	$x_{a/b} = \frac{q^2}{P_{a/b} \cdot q}$,
the total center-of-mass energy squared	$s = \left(P_a + P_b\right)^2$,
the Feynman variable	$x_F = x_a - x_b$,
the invariant mass of the dilepton squared	$M^2_{\ell\ell'} = Q^2 = -q^2 = s x_a x_b$.

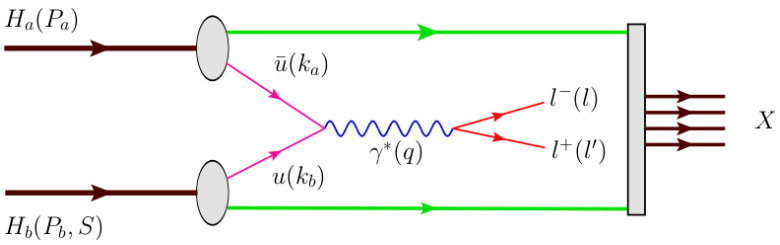

Figure 7.1.: Scheme of the Drell-Yan process where a quark-antiquark pair from two hadrons annihilates into a pair of oppositely charged leptons [MM10].

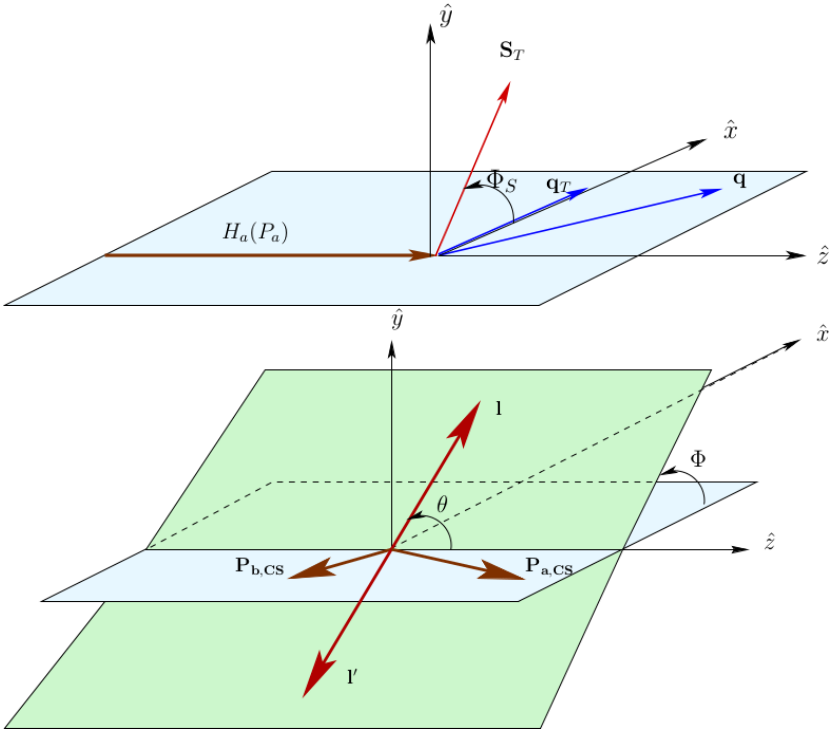

Figure 7.2.: Definition of the azimuthal angle ϕ_S of the target spin polarization $\boldsymbol{S}_T$ in the target rest frame (top) and of the azimuthal and polar angles Φ and θ of the momenta of the leptons in the Collins-Soper frame (bottom) [MM10].

A scheme of the Drell-Yan process is shown in Fig. 7.1 illustrating the case where just the target nucleon has a defined polarization. The following introduction into the theoretical framework of the Drell-Yan process is based on the work by Arnold, Metz, and Schlegel [AMS09].
In the following, two coordinate systems are used to describe the Drell-Yan cross-section, the target rest frame (TRF) and the Collins-Soper frame (CSF). The unit vectors of the first one are defined by the momentum of the beam hadron $\hat{z}$, the transverse component q_T of the virtual photon $\hat{x}$, and finally $\hat{y} = \hat{z} \times \hat{x}$. The latter system is the rest frame of the virtual photon, which is obtained by a boost along $\hat{z}$ and $\hat{x}$. As shown in Fig. 7.2 (top panel) the azimuthal angle ϕ_S of the target spin polarization $\boldsymbol{S}_T$ is defined in the TRF. The azimuthal angle of the lepton

momentum Φ is defined as the angle between the hadron scattering plane and the lepton plane in the CSF. While their polar angle θ is the angle between the intersecting line of these two planes and the momentum of the negative lepton, also in the CSF, see Fig. 7.2 (bottom panel).
In Sec. 2.3.2 it has been shown, that the azimuthal modulations in the single hadron production in polarized SIDIS arise from a convolution of PDFs and FFs. The same formalism holds true for the Drell-Yan process, where the convolutions are defined in the intrinsic momentum space this time as convolutions of two PDFs [AMS09]

$$\mathcal{C}\Big[w\big(\boldsymbol{k}_{a,T},\boldsymbol{k}_{b,T}\big)f_1\bar{f}_2\Big] \equiv \frac{1}{3}\sum_{q=1}^{3} e_q^2 \int \mathrm{d}^2\boldsymbol{k}_{a,T}\,\mathrm{d}^2\boldsymbol{k}_{b,T}\,\delta^{(2)}\big(\boldsymbol{q}_T-\boldsymbol{k}_{a,T}-\boldsymbol{k}_{b,T}\big)w\big(\boldsymbol{k}_{a,T},\boldsymbol{k}_{b,T}\big)\times \Big[f_1^q\big(x_a,\boldsymbol{k}_{a,T}^2\big)f_2^{\bar{q}}\big(x_b,\boldsymbol{k}_{b,T}^2\big)+f_1^{\bar{q}}\big(x_a,\boldsymbol{k}_{a,T}^2\big)f_2^{q}\big(x_b,\boldsymbol{k}_{b,T}^2\big)\Big], \tag{7.2}$$

where $\boldsymbol{k}_T$ is the intrinsic transverse momentum of a quark q inside the hadron.
The Drell-Yan cross-section for an unpolarized beam and a polarized target contains ten modulations depending on ϕ and/or ϕ_S [AMS09], cf. the SIDIS cross-section in Eq. 2.38a. The parts containing the Sivers and the Boer-Mulders PDFs on a transversely polarized target in the QCD parton model in leading order (LO) read [AMS09]

$$\frac{\mathrm{d}^6\sigma}{\mathrm{d}^4q\mathrm{d}\Omega} \propto \frac{\alpha^2}{4q^2\sqrt{(P_a\cdot P_b)^2-M_a^2M_b^2}}\hat{\sigma}_U|\boldsymbol{S}_T|\Big(D_{nn}^{\sin\phi_S}A_T^{\sin\phi_S}\sin\phi_S+ D_{nn}^{\sin(2\phi+\phi_S)}A_T^{\sin(2\phi+\phi_S)}\sin(2\phi+\phi_S)+D_{nn}^{\sin(2\phi-\phi_S)}A_T^{\sin(2\phi-\phi_S)}\sin(2\phi-\phi_S)\Big), \tag{7.3}$$

where $\hat{\sigma}_U$ is the spin-independent part of the cross section.
In leading-order of the QCD parton model applied on the DY process with a transversely polarized target hadron only four terms survive the integration. Among them are the $\sin\phi_S$, which gives access to the Sivers function of the target nucleon and the $\sin(2\phi\pm\phi_S)$ modulations, related to the Boer-Mulders functions of the incoming hadron [AMS09]

$$A_T^{\sin\phi_S} = \frac{\mathcal{C}\Big[\hat{q}\cdot\boldsymbol{k}_{b,T}\,f_1\bar{f}_{1T}^{\perp}\Big]}{M_b\,\mathcal{C}\big[f_a\bar{f}_a\big]}, \tag{7.4}$$

$$A_T^{\sin(2\phi+\phi_S)} = \frac{-\mathcal{C}\Big[\Big(2\big(\hat{q}\cdot\boldsymbol{k}_{b,T}\big)\big[2\big(\hat{q}\cdot\boldsymbol{k}_{a,T}\big)\big(\hat{q}\cdot\boldsymbol{k}_{b,T}\big)-\boldsymbol{k}_{a,T}\cdot\boldsymbol{k}_{b,T}\big]-\boldsymbol{k}_{b,T}^2\big(\hat{q}\cdot\boldsymbol{k}_{a,T}\big)\Big)h_1^{\perp}\bar{h}_{1T}^{\perp}\Big]}{4M_aM_b^2\,\mathcal{C}\big[f_a\bar{f}_a\big]}, \tag{7.5}$$

$$A_T^{\sin(2\phi-\phi_S)} = \frac{-\mathcal{C}\Big[\hat{q}\cdot\boldsymbol{k}_{a,T}\,h_1^{\perp}\bar{h}_1\Big]}{2M_a\,\mathcal{C}\big[f_a\bar{f}_a\big]}, \tag{7.6}$$

where $\hat{q}=\frac{\boldsymbol{q}_T}{q_T}$ and PDFs of antiquarks are indicated by a bar. Thus the $\sin\phi_S$ modulation in the COMPASS case arises by a convolution of the pion number density f_1 and the nucleon Sivers function $f_{1T}^{\perp}$, see Tab. 2.4. Accordingly the $\sin(2\phi+\phi_S)$ and the $\sin(2\phi-\phi_S)$ modulations

have their origin in convolutions of the Boer-Mulders $h_1^\perp$ with the Pretzelosity PDF $h_{1T}^\perp$ and the Boer-Mulders $h_1^\perp$ with the Transversity PDF h_1.
As described in Sec. 2.3.3 and 2.3.3 the Sivers and Boer-Mulders PDFs are both T-odd objects. Their non-local quark-quark correlators in the operator definition have gauge-link operators which include Wilson lines, see also Eq. 2.63. The Drell-Yan process can be interpreted as a space- and time-reversed version of the SIDIS process, therefore the future-pointing (on the light-cone) Wilson lines are replaced by past-pointing Wilson lines [Col02]. This accounts for a sign change of the Sivers and the Boer-Mulders asymmetry in Drell-Yan w.r.t. the SIDIS case [Col02]

$$f_{1T}^\perp\Big|_{DY} = -f_{1T}^\perp\Big|_{SIDIS} \text{ and } h_1^\perp\Big|_{DY} = -h_1^\perp\Big|_{SIDIS}. \tag{7.7}$$

7.2.2. Measuring Drell-Yan at COMPASS-II

The Sivers asymmetry in polarized SIDIS has been measured to be clearly nonzero by the HERMES and the COMPASS collaboration, see Sec. 2.4.1. With the Drell-Yan measurement of the COMPASS-II program, COMPASS will be the first experiment to be able to verify the sign-reversal property of the Sivers and the Boer-Mulders functions, which is an important relation for the understanding of the transverse momentum dependent phenomena. The expected statistical uncertainties on the Sivers asymmetry for the COMPASS Drell-Yan measurement are shown in Fig. 7.3 for two years of data taking together with model predictions from Anselmino *et al.* [A$^+$08]. With the proposed setup it will be possible to give a clear statement on the signs.

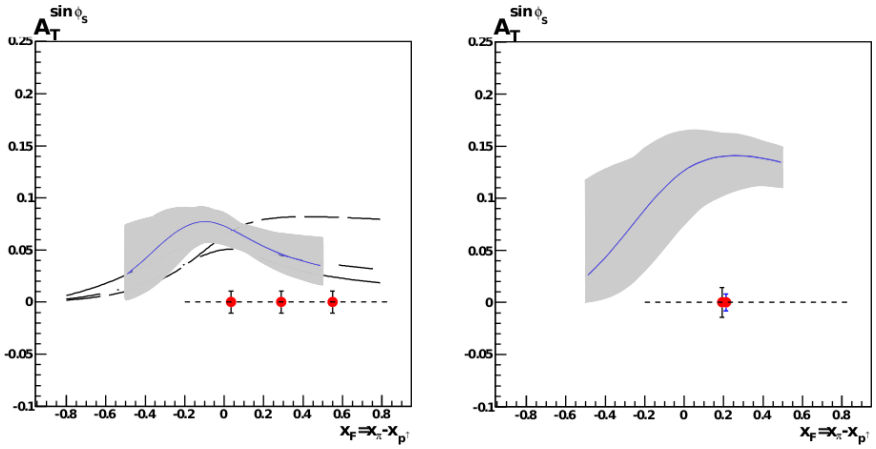

Figure 7.3.: Expected statistical uncertainties on the Sivers asymmetry in the Drell-Yan process for the COMPASS measurement of two years of data taking in an intermediate dimuon mass region $2\,\mathrm{GeV}/c^2 < M_{\mu\mu} < 2.5\,\mathrm{GeV}/c^2$ (left panel) and a high mass region $4\,\mathrm{GeV}/c^2 < M_{\mu\mu} < 9\,\mathrm{GeV}/c^2$ (right panel, the smaller error bar represents the expected systematic uncertainty). Model predictions from Anselmino *et al.* [A$^+$08] are indicated by the blue line and its gray uncertainty band [MM10].

Since the Drell-Yan cross section is relatively small with a few nanobarns (nb) in the actual case the achievable luminosity plays an important role in order to collect the required statistics. One key ingredient is the hadron beam intensity, which is planned to reach $I_{\text{beam}} = 6 \times 10^7 \frac{\pi^-}{\text{s}}$ [MM10]. The full expression of the luminosity reads

$$\mathcal{L} = I_{\text{beam}} L_{\text{eff}} \frac{\rho_{\text{NH}_3} F_f N_A}{A_{\text{eff}}}, \tag{7.8}$$

where the effective target length L_{eff} cannot exceed $\approx 90\,\text{cm}$ to avoid multiple beam interactions along the target and fit into the target cryostat. The target magnet and cooling system, see Sec. 3.2, used already in 2007 and 2010 will be used for the Drell-Yan measurement. Again the target material will be solid-state ammonia ($\rho_{\text{NH}_3} = 0.85\,\text{g/cm}^3$), for which a packing factor $F_f = 0.5$ has to be considered. With the effective mass number of ammonia being $A_{\text{eff}} = 11.71\,\text{g/mol}$, the expected Luminosity is $1.186 \times 10^{32}\,\text{cm}^{-2}\text{s}^{-1} = 118.6\,\text{nb}\,\text{s}^{-1}$. Using a tuned PYTHIA Monte Carlo event generator the Drell-Yan cross-section has been calculated as a function of the momentum of the beam hadrons and the mass of the dimuons in two ranges, an intermediate $2\,\text{GeV}/c^2 < M_{\mu\mu} < 2.5\,\text{GeV}/c^2$ and in a high mass $4\,\text{GeV}/c^2 < M_{\mu\mu} < 9\,\text{GeV}/c^2$ region. Taking into account the ratio of protons and neutrons of the ammonia, one obtains the overall cross-section of the process, shown in Tab. 7.1.
With the knowledge on the cross-section and on the Luminosity it is possible to calculate the expected number of DY events, for instance per day [MM10]

$$R = \mathcal{L} \sigma^{DY \to \mu\mu}_{\pi^-,\text{NH}_3} K_{DY} d_{\text{spill}} n_{\text{spill}} E_{\text{tot}}, \tag{7.9}$$

where $K_{DY} = 2$ is a scaling factor[1], $d_{\text{spill}} = 9.6\,\text{s}$ the duration of the SPS spill (see Sec. 3.1) and $n_{\text{spill}} = 1800$ the maximum number of spills per day. The efficiencies of the event reconstruction, the trigger, the SPS accelerator, the spectrometer are taken into account by the total efficiency E_{tot}, which is estimated to reach ≈ 0.146 [Qui13].

Table 7.1.: The PYTHIA Drell-Yan $\pi^-\text{NH}_3$ cross sections in nanobarn for an ammonia target in the $\mu^+\mu^-$ channel for two invariant mass ranges, and for different beam momenta [MM10].

π^- momentum (GeV/c)	$\sigma^{DY\to\mu\mu}_{\pi^-,\text{NH}_3}$(nb)	
	$2\,\text{GeV}/c^2 < M_{\mu\mu} < 2.5\,\text{GeV}/c^2$	$4\,\text{GeV}/c^2 < M_{\mu\mu} < 9\,\text{GeV}/c^2$
106	5.147	0.702
160	5.922	1.109
190	6.231	1.291
213	6.428	1.419

[1] K_{DY} is the scaling factor between the experimentally measured Drell-Yan cross-section and LO calculations from theory in e.g. the PYTHIA MC generator [SEF+01] adapted on the experiment's kinematics.

Table 7.2.: Number of Drell-Yan events per day (R), depending on the dimuon mass range considered, and for different beam momenta [MM10].

π^- momentum (GeV/c)	$R\,(\frac{1}{\text{day}})$	
	$2\,\text{GeV}/c^2 < M_{\mu\mu} < 2.5\,\text{GeV}/c^2$	$4\,\text{GeV}/c^2 < M_{\mu\mu} < 9\,\text{GeV}/c^2$
106	4013	440
160	4617	695
190	4858	809
213	5012	889

Due to a cut on the transverse momenta of the muons produced at $M_{\mu\mu} < 2\,\text{GeV}/c^2$, a fraction of $\approx 9\,\%$ of the events will be rejected [Qui13], leading to an effective E_{tot} of 0.133. Table 7.2 gives the number of good Drell-Yan events per day corresponding to the cross-section given in Tab. 7.1. A typical year of COMPASS data taking has about 140 days. Assuming two years for the Drell-Yan program 0.23×10^6 DY events in the high-mass region and 1.4×10^6 events in the intermediate mass-region will be collected. This allows for a sufficient statistical precision of the measurement, as shown in Fig. 7.3.
Note that unlike in the proposed schedule for the COMPASS-II program [MM10], the time provided for the Drell-Yan measurement will not be two years, but a pilot run of nine weeks in the end of 2014 followed by a full year of data taking in 2015. An option to catch up the second year in 2018 may be given. Thus the arguments of the statistics being required weights even stronger, scaling the results down to one single year.
The option of increasing the beam intensity to $I_{\text{beam}} = 1 \times 10^8\,\frac{\pi^-}{\text{s}}$ was checked for feasibility and is the current state of planning [Qui13]. The beam intensity and its momentum are not independent of each other as they are properties of the beam line. The best compromise in balancing was found at a beam momentum of $190\,\text{GeV}/c$. Thus the luminosity increases according to Eq. 7.8 from $1.18 \times 10^{32}\,\text{cm}^{-2}\text{s}^{-1}$ to $1.97 \times 10^{32}\,\text{cm}^{-2}\text{s}^{-1}$, which is a factor of about 1.67. Also the number of number of spills per day could be increased up to ≈ 2450 since indications are given that the CNGS experiment will not run in 2014/2015, thus the length of a super-cycle decreases to $33.6\,\text{s}$ [Qui13], see also Sec. 3.1. Taking into account the mentioned innovations in Eq. 7.9 one expects ≈ 1550 Drell-Yan events per day in the high mass region. Hence, in one year of data taking 0.22×10^6 are expected [Qui13], which is about the same number as calculated in the original proposal [MM10].
The kinematic domain of the Drell-Yan process is different w.r.t. the one of the previous SIDIS experiments at COMPASS, most significant are the thresholds of $Q^2 > 15\,(\text{GeV}/c)^2$ and $x > 0.04$. Figure 7.4 shows the $Q^2(x)$ distribution of single hadron h^+ events from 2010 data, used for the extraction of the Sivers asymmetry, while the DY kinematic range is indicated by the red box. In order to make a clear statement on the expected amplitude of the Sivers asymmetry in the DY process an extraction of it in the SIDIS case taking into account the new kinematic regime has been performed. The results are shown in Fig. 7.5.

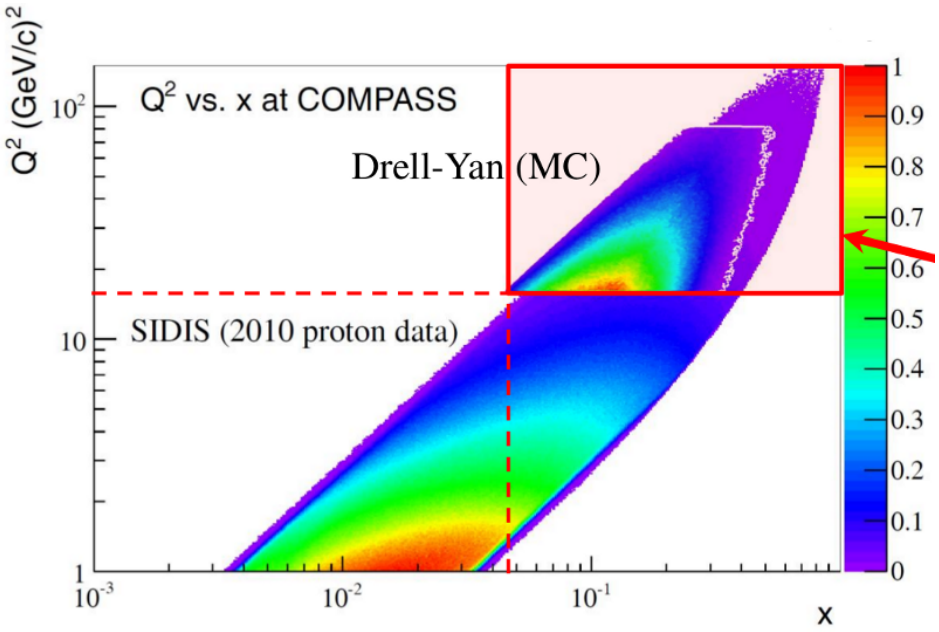

Figure 7.4.: The $Q^2(x)$ distribution of charged single hadron events from 2010 data. The kinematic range of the future COMPASS Drell-Yan experiment is indicated by the red box in the upper right corner with the thresholds $Q^2 > 15\,(\mathrm{GeV}/c)^2$ and $x > 0.04$. The overlayed distribution is the result of a Monte Carlo simulation [Par13].

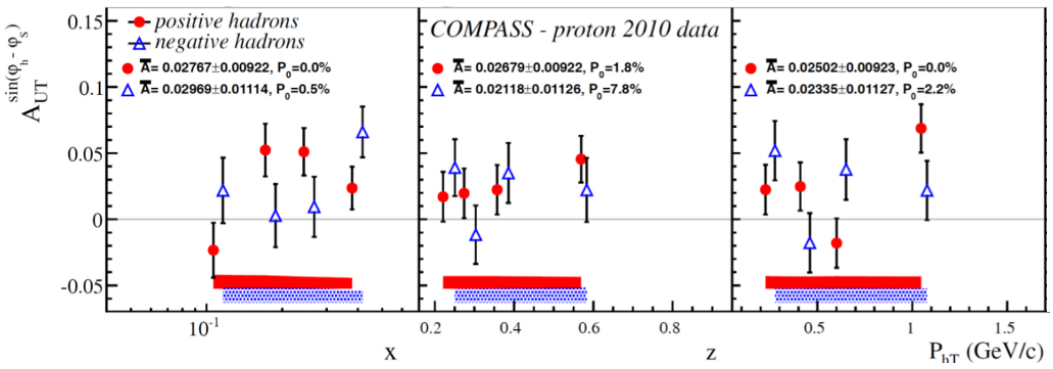

Figure 7.5.: The Sivers asymmetry of charged hadrons from the 2010 data extracted in the Drell-Yan kinematic range. Note that the binning had to be adapted to the limited statistics of the sub-sample [Par13].

The amplitudes in the x dependence for positive hadrons are of the same order as of the full sample, as shown in Fig. 2.14, while the asymmetry amplitudes for negative hadrons are still compatible with zero within the uncertainties.
For theoretical predictions on the strength of the Sivers asymmetry in the Drell-Yan process at COMPASS see [EIKV14], where also the influence of the Q^2 evolution (see Sec. 6.2.1) is

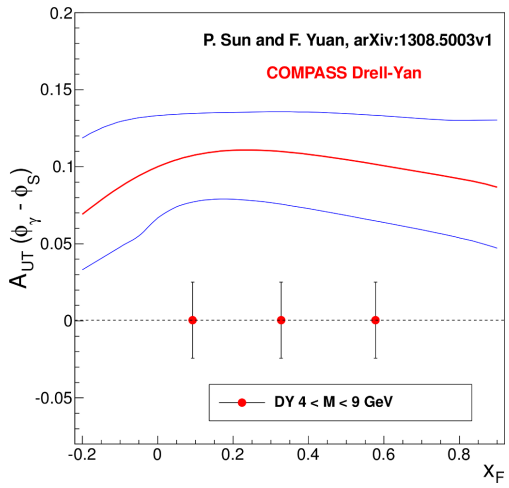

Figure 7.6.: Expected statistical uncertainties on the Sivers asymmetry for the COMPASS Drell-Yan measurement in the high mass region $4\,\mathrm{GeV}/c^2 < M_{\mu\mu} < 9\,\mathrm{GeV}/c^2$ in comparisons to recent model predictions [SY13], indicated by the red line and the limits of an uncertainty band (blue lines) [Qui13].

discussed. According to their calculations an asymmetry of $4\,\%$ can be expected at COMPASS. Recently Sun and Yuan [SY13] published predictions on the strength of the Drell-Yan signal for different experiments, among them also COMPASS, taking also the TMD evolution (see Sec. 6.2.1) into account. Figure 7.6 shows the result of this model calculation in comparison to the expected statistical uncertainties of two years of data taking with parameters in the proposal [MM10], which is of the same order as calculated for the new setup. The consideration of the TMD evolution leads to a decrease of the expected signal amplitudes compared to Fig. 7.3. Nevertheless, the statistical precision will be sufficiently high in order to proof or disproof the model predictions.

7.2.3. A new absorber vertex detector for the Drell-Yan measurement

The hadron beam used for the future Drell-Yan measurement and the need to detect the two muons produced in the process require for certain modifications of the COMPASS spectrometer setup. While the beam intensity has to be as high as possible, the identification probability of the muons suffers from the high occupancy of the detectors. This issue can be solved by the presence of a hadron absorber right after the polarized target to stop the primary beam hadrons and the hadrons produced in secondary processes. The composition and design of the absorber, which is shown in Fig. 7.7 is optimized for high stopping power to the beam, minimal emission of secondaries and space requirements along the beam direction.

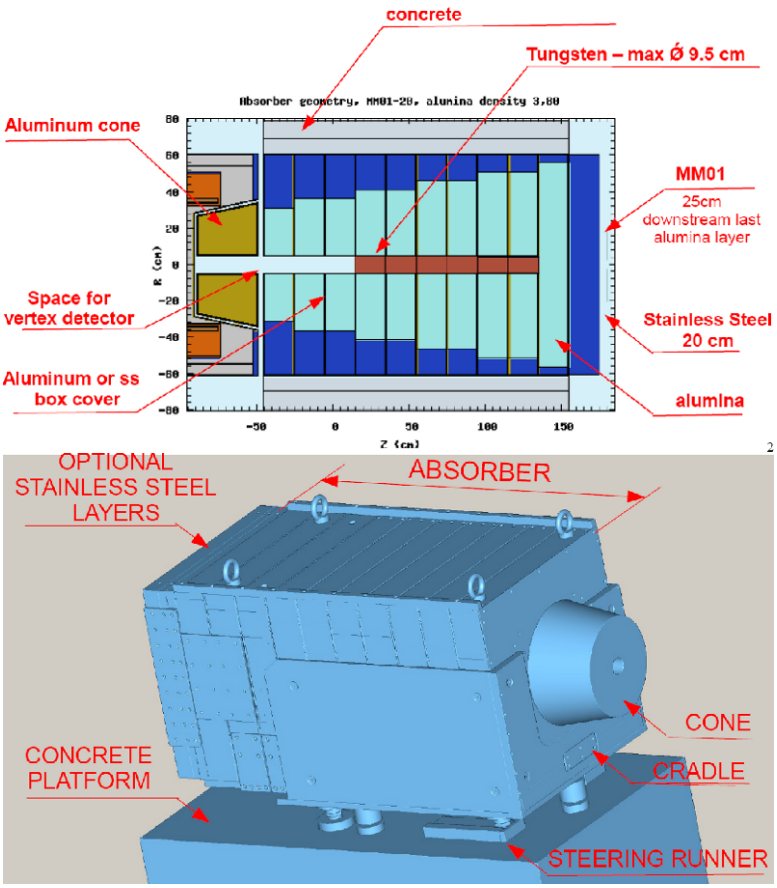

Figure 7.7.: The hadron absorber for the future Drell-Yan program in cross section [Mag12b] (top panel) and as a three-dimensional model (bottom panel) [Pan13].

The absorber structure consists of a conical piece made of aluminum, which fits into the concave end cover of the targets cryostat, see Fig. 3.2. The second part is a box-shaped frame which contains a central beam-plug made of tungsten with a diameter of 9.5 cm surrounded by an inner alumina and an outer stainless steel cone. To fulfill radiation protection requirements, the absorber is situated inside of a larger concrete structure, see Fig. A.56.
The disadvantage of this new absorber structure is, that the first tracking stations, namely the MM01 (see Sec. 3.3.3) has to be placed at a distance of 5.5 m to the target, while is was ≈ 0.9 m for instance during the SIDIS measurements. The same applies in relation to all other detectors [2]. This has the effect that the resolution of the primary vertex position decreases due to the increased uncertainties in the back-propagation of the reconstructed particle tracks. Since the Drell-Yan program measures asymmetry amplitudes of different target polarization states in the target cells, it is necessary to have a precise assignment of the primary vertex to one of the two target cells.

[2] The target will be moved upstream w.r.t. its previous position to create the needed space for the absorber.

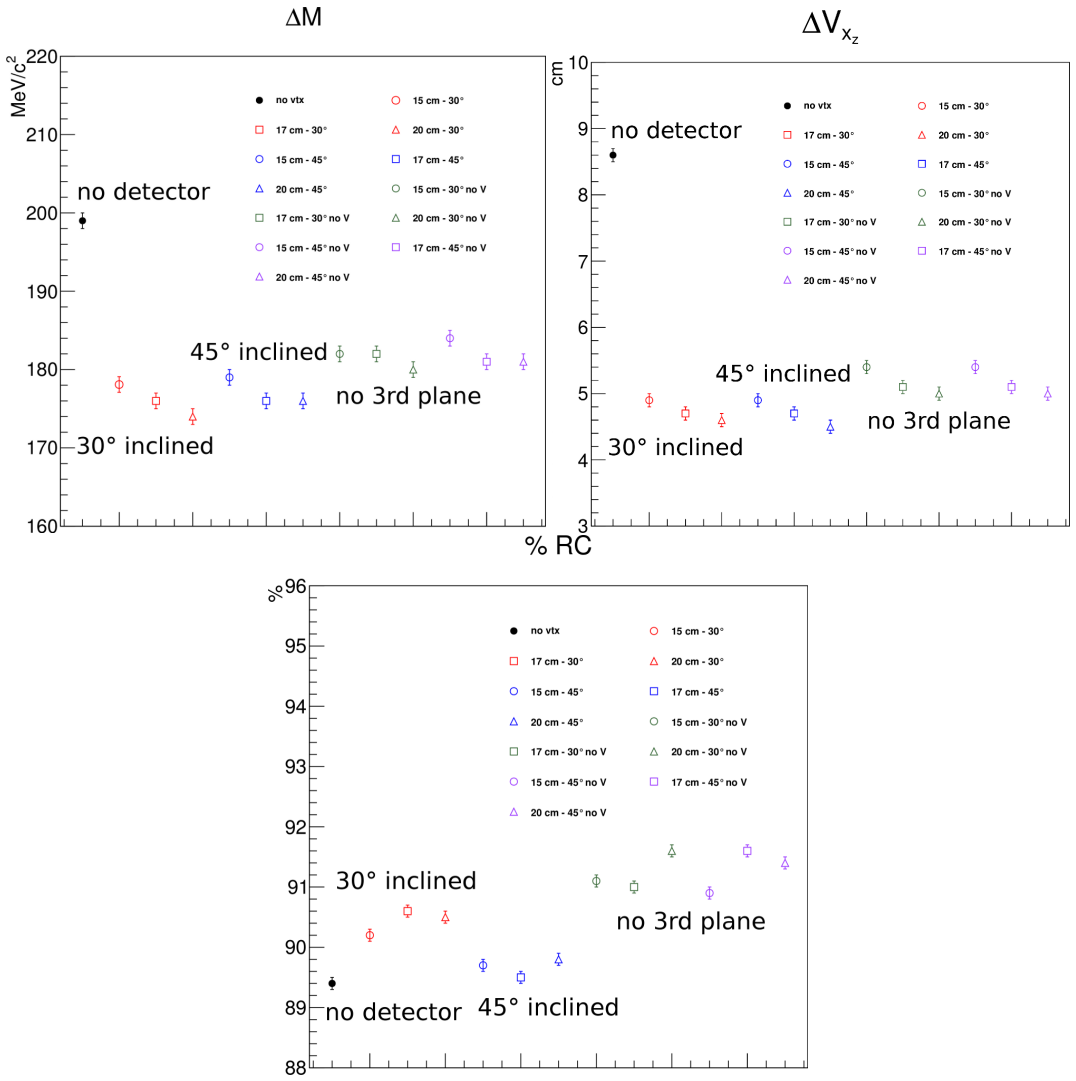

Figure 7.8.: Results of simulations on the mass resolution ΔM (top left panel), the resolution of the reconstructed primary vertex position along the beam axis ΔV_{x_z} (top right panel) and the overall reconstruction efficiency RC (bottom panel) without (black dot) and without a vertex detector of different possible configurations in the size of active area (rectangular 15, 17 or 20 cm edge length) and the inclinations of the diagonal plane (30° or 45°) with 3 planes or just 2 planes ("no 3rd plane") [Tak13].

The degradation of the vertex position resolution would lead to a decrease in the length of usable target volume, in terms of a precise assignment of a vertex to one of the target cells. Each cell will have a length of 55 cm separated by a gap of 20 cm. When applying a $\pm 3\sigma$ cut on the vertex Z position, events originating from 11.6 cm of the total target length would be rejected, if each

vertex is required to be clearly assignable to one target cell and not to the other[3]. This would lead to a decrease of usable events by $\approx 10\,\%$.
The requirement described above make a detector made of scintillation fibers (see Sec. 3.3.1) the only promising candidate for this so-called "vertex detector" in the region upstream of the box-shaped part of the absorber, see Fig. A.57. The groups of Bonn and Erlangen, which already have built the existing SciFi detectors, took over the task to develop and built the crucial element of the COMPASS Drell-Yan setup, which is also a part of this thesis.
Simulations have shown that the resolution of the reconstructed position of the primary vertex along the beam axis ΔV_{x_z} with a detector consisting of three planes of an active area of $15 \times 15\,\mathrm{cm}^2$, see Fig. 7.8 left panel, will improve from $\approx 8.5\,\mathrm{cm}$ to $\approx 5\,\mathrm{cm}$ [Tak13]. The additional uncertainty on the vertex coordinates would also propagate in the mass resolution of the virtual photon ΔM. With a vertex detector inside the absorber the mass resolution could be improved from $\approx 200\,\mathrm{MeV}/c^2$ to smaller than $180\,\mathrm{MeV}/c^2$, see Fig. 7.8 right panel [Tak13]. The dependence on the inclination angle of the third plane at 30° or 45° is negligible. In the same simulation also the fraction of muons which cross the active area of the vertex detector (geometrical acceptance) and will be detected there (detection efficiency) was investigated. For approximately $21\,\%$ of the Drell-Yan events both muons produced will cross a $15 \times 15\,\mathrm{cm}^2$ large detector and will be detected there [Tak13]. But also detecting only one of the two muons, which occurs in $\approx 55\,\%$ of the cases, is indispensable for a precise vertex reconstruction [Tak13]. The reconstruction efficiency (Fig. 7.8 bottom panel) shows an increase of $\approx 0.8\,\%$. This behavior and its dependence on the inclination angle of the third plane is counter-intuitive at first sight, as well as the larger reconstruction efficiency with 30° inclination and without a third plane. It is a consequence of the intrinsic behavior of the event reconstruction algorithm, see Sec. 3.7, which uses a hit-to-track association in each inclination, so that the reconstruction efficiency increases with less planes and less overlap [Tak13].
Thus the luminosity and the number of collected DY events would decrease by the same factor, resulting in either a less significant statement on the sign and strength of the asymmetries in the available measuring time or even making it impossible to draw a definite conclusion.
This detector must have an excellent time resolution, in the order of a few hundred ps to be able to make a time-like separation of the particle tracks crossing the detector with extreme high rates.
In addition to the primary beam hadrons, also secondary particles produced in the interaction of beam with material along its direction increase the rate. This could happen upstream, inside and downstream of the target, including also a back-scattered component from the box-shaped part of the absorber. Again these are strong arguments in favor of using a scintillating-fiber hodoscope as a vertex detector inside of the absorber.

[3] In this assumption the wrong assignment of a vertex from the gap volume between the two cells to one cells is allowed.

Final requirements to the vertex detector

A scintillating fiber detector was set as the appropriate detector for the improvement of the primary vertex resolution. Before the design process could be started, the requirements to it had to be defined in a reliable way. Here the expected particle rate is the most important variable, which has a strong impact on the granularity that means the spacial resolution which is determined by the fiber diameter. The limiting components here are the photomultipliers, which had been tested for the existing SciFi station in the COMPASS detector at a rate per channel of up to 5 MHz [BEE+02]. Simulations on the flux of secondary particles, charged and neutrals (e.g. neutrons and photons) in the plane perpendicular to the beam have been performed. The computed rates for charged particle, corresponding to 1 mm fiber diameter, are shown in Fig. 7.9. They reach a level of up to $\approx$ 10 MHz in the very central beam spot and decrease to $\approx$ 3 MHz at a distance of 10 cm, while the rates for 0.75 mm fibers are smaller, accordingly. Due to the handling of the fibers in production process and the costs of additional read-out channels for small pitches, the fiber diameter is favored to be 1 mm, with a pitch of 0.71 mm. The necessary rate stability was proven in a test at the Erlangen Tandem accelerator for a new type of Hamamatsu multi-anode PMTs R11265-100-M16. An example of PMT signals recorded directly with an oscilloscope with a rates of $\approx$ 14.7 MHz per channel is shown in Fig. 7.10, where the amplitudes of single events reach 70 mV. The analysis of all taken data is shown in Fig. 7.11, where the rate stability, by means of signal amplitude as a function of the rate is plotted for three different types of 16-channel Hamamatsu PMTs. Type 6568 PMT is the one already in use in the COMPASS SciFi stations, type 6568-100 has an increased quantum efficiency due to a improved cathode material (used in SciFi station FI15, see Sec. 3.3.1).

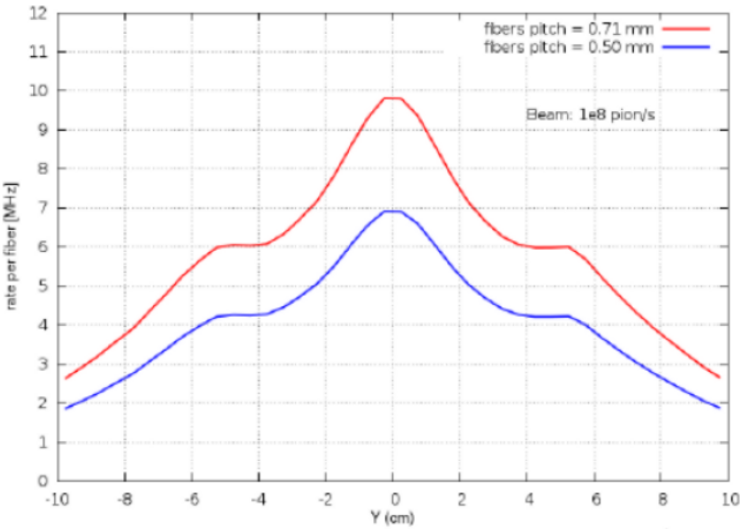

Figure 7.9.: Rate of particles, charged in the plane of the vertex detector for two different fiber diameters 1 mm (red) and 0.75 mm (blue) [Mag12a, Joo13a].

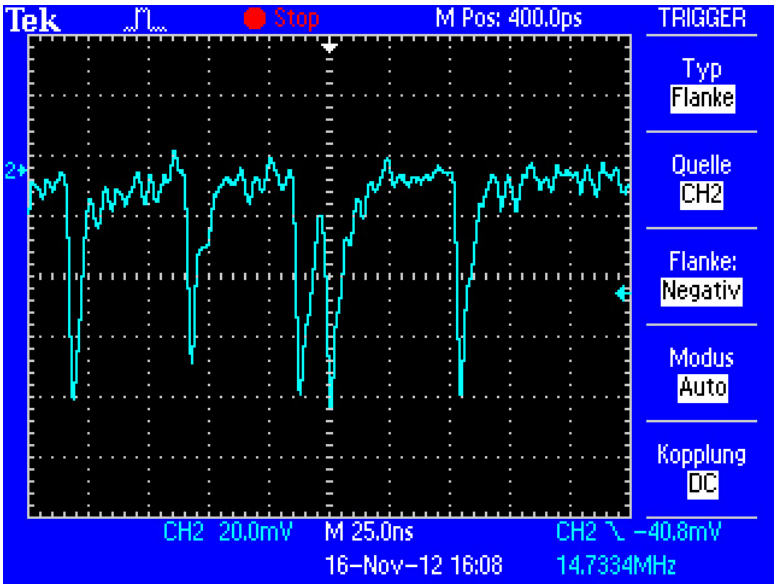

Figure 7.10.: Example from the rate test of the R11265-100-M16 Hamamatsu multi-anode PMTs at the Erlangen Tandem accelerator. The oscilloscope screen shows events of protons crossing a scintillating fiber at a rate of > 14 MHz, while the amplitudes are still in the order of 70 to 80 mV and the signals are well separated.

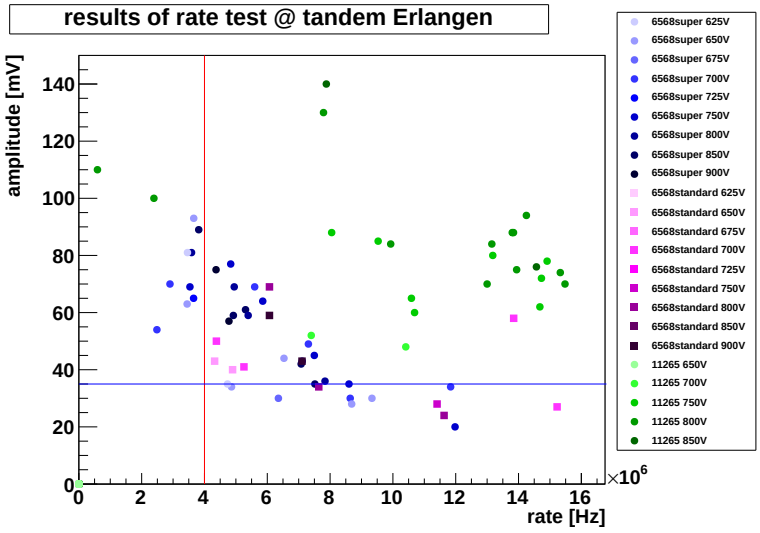

Figure 7.11.: Comparison of rate stability, by means of signal amplitude as a function of the rate, for the type 6568 PMT (blue dots), the type 6568-100 (magenta dots) with improved quantum efficiency and the new type R11265-100-M16 (green dots) all from Hamamatsu. The red line indicates the already proven rate stability of type 6568 [BEE+02] and the blue line an estimate of the minimal required amplitude.

Finally, type R11265-100-M16 is the new candidate to be used in the vertex detector. Even at rates higher then $14\,\text{MHz}$ the amplitudes of type R11265-100-M16 are still in the order of $80\,\text{mV}$ showing no significant decrease, while type 6568 and 6568-100 behave equally in their significant decrease of the amplitudes. At rates above $\approx 8\,\text{MHz}$ the older types fall below the conservative estimate of the required minimal amplitude, which is determined by the observed background noise. Based on these results the PMT type R11265-100-M16 was selected for the vertex detector.
In this high rate environment also the dose deposited inside the scintillating fibers could become an issue. A study for the COMPASS SciFi stations was performed in Erlangen by Teufel *et al.* [Teu03] where scintillating fibers of the type SCSF-78MJ from Kuraray have been irradiated in a central range of $8\,\text{cm}$ by a ^{90}Sr source with $100\,\text{kGy}$. Afterwards, the light transmission coefficient of the fibers has been tested by generating scintillation light via protons from the Erlangen tandem accelerator at different points, before, at and after the previously damaged section. The results is shown in Fig. 7.12 (left panel), revealing that the scintillating property has decreased by a factor of 0.34 in the damaged area. In the case of the DY vertex detector simulations show an accumulated dose of maximum $5\,\text{kGy}$ in two years of data taking for fibers at the very central beam spot ($3\,\text{cm}$ around the center) and around $2\,\text{kGy}$ in the surrounding, see Fig. 7.12 (right panel).
The experience made with this type of fiber in the existing SciFi stations with its general properties such as the long attenuation length ($> 4.0\text{m}$ [Kur98]) and its fast decay time ($2.8\,\text{ns}$ [Kur98]) made it the ideal candidate for the use in the vertex detector.
The high rate of particles to be detected causes an increase in the probability of coinciding hits in the detector, meaning that the time difference of two subsequent events is below the time resolution of the detector for a significant fraction of the events. The decomposition of these ambiguities (see Fig. A.7) requires three detector planes with different inclinations. The choice of the angles of the three planes had to be made under the ancillary condition of the mechanical design of the absorber.

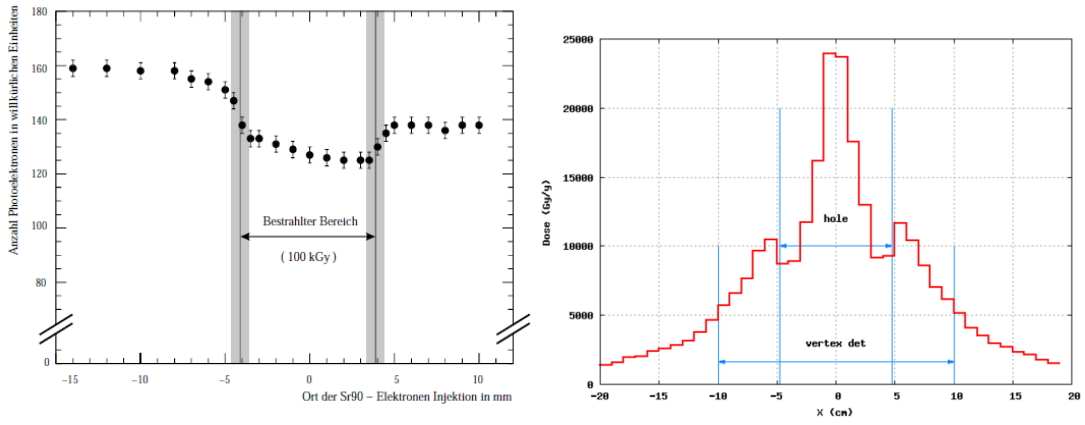

Figure 7.12.: Results of an fiber irradiation test (left panel) [Teu03] and simulated dose per year on the vertex detector (right panel) [Mag12a].

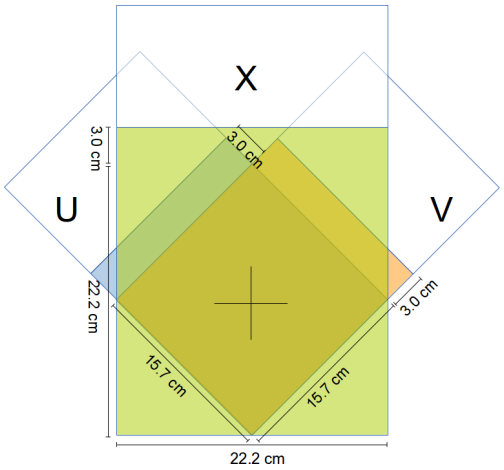

Figure 7.13.: The orientation of the three planes of the vertex detector, beam is traveling into the plane of projection.

The conical part will be mounted on the frame of the box-shaped part, which also provides a gap for the vertex detector. To ensure the mechanical stability this gap will have a "V"-like shape with $\pm 45°$ angles w.r.t. the vertical (Y) axis, with a rectangular bottom part. The two diagonal planes will also be inclined by $\pm 45°$, see Fig. 7.13.
The overall allowed space for the vertex detector in beam direction is $6.5\,\text{cm}$, limited by the various factors, such as the target position, the position of the spectrometer along the beam and the required thickness of the absorber. Taking into account mechanical parts, such as the holders of the detector planes and the housing, the remaining space offers the possibility of eight SciFi half-layers per plane plus a doubling in the central region. The purpose of the doubling will be explained in the following. A simulation of the angular distribution of the muons produced in the Drell-Yan process has shown that the very central beam does not contain a significant fraction of reconstructed tracks. Furthermore, the high occupancy of the fibers crossing the central region will lead to a decrease of the detection efficiency, due to the high rate on the PMT channels. Different scenarios have been discussed how this central region could be deactivated, while still collecting the hits around it.
The most practicable way to implement this was found in using shorter scintillating fibers in the main detector plane, which end below the beam spot region and secondly add a doubling of fibers onto the main plane where the scintillating region starts above the beam spot. The hole thus produced will be adapted to a circle by adding a step, which is illustrated in Fig. 7.14. This approach has the advantage that, as for the other SciFi station, the fibers have to have only one welding point to the clear light guides. The manufacturing process is described in detail in Sec. 7.2.3.
The proximity to the polarized target causes the presence of strong magnetic fields induced by the superconducting solenoid magnet and the dipole field used for transverse measurements. The usual way applied at all COMPASS SciFi detectors to protect the PMT tube from the magnetic field is to shield them in a rectangular tube made of steel or soft iron.

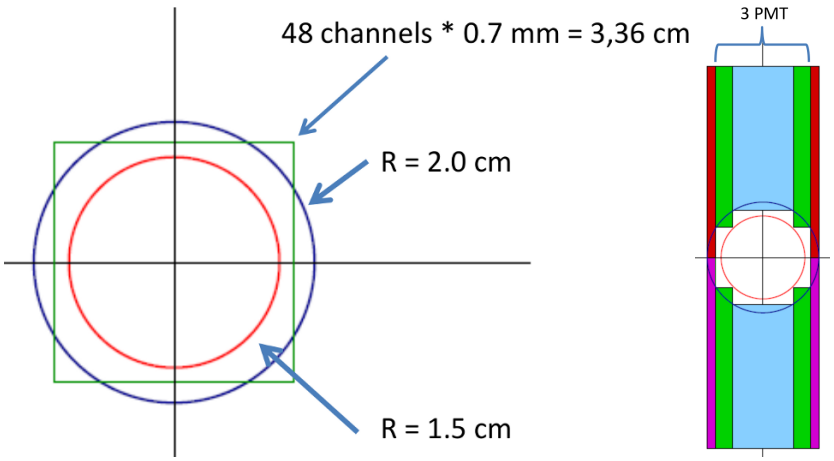

Figure 7.14.: The scheme of the hole (left panel) in one of the detector planes [Joo13a]. The beam spot was adapted as a rectangular with one step, with an inner deactivated spot of diameter $1.5\,\text{cm}$ (red circle) and an outer one of $2.0\,\text{cm}$ (blue circle) in diameter. The red area in the right panel shows the continuous scintillating fibers and the green and blue area is covered by the shortened scintillating fibers at the bottom part and the fibers of the doubling in the upper part the circles from the left scheme are indicated [Joo13a]. Circles in both panels are to scale.

For instance the readout of FI03 is situated $\approx 1.5\,\text{m}$ below the target. Horikawa *et al.* [H$^+$04] have shown that the relative pulse height of the PMT signal is constant over a range from 0 to $4 \times 10^{-2}\,\text{T}$. The use of clear light guides thermally welded to the scintillating fibers allows to place the PMT read-out at a certain distance to the active area. Even though the attenuation length of clear fibers, type "Clear-PSM" from Kuraray has been selected, is fairly long, appropriately $> 10\,\text{m}$ [Kur98], a length of $2\,\text{m}$ of the clear fibers is regarded as sufficient.
Because the magnetic field of the target magnet is well known, its strength can be calculated for any position in space. Thus it has been shown that none of the components of the solenoidal field as well as of the dipole field exceeds $2 \times 10^{-2}\,\text{T}$ or $1 \times 10^{-2}\,\text{T}$, respectively [Joo13a]. The distributions of the magnetic field strength are shown on the App. Fig. A.58. A soft iron shield will be implemented in the vertex detector housing.

Manufacturing process of the vertex detector

The manufacturing process of the vertex detector is based on the experience, which was accumulate during the fabrication of the existing SciFi stations [BEE$^+$02, H$^+$04, Nae02, Teu03].

Final design and specifications of the vertex detector

The design freeze of the vertex detector took place in August 2013, with a presentation at the technical board of the COMPASS collaboration [Joo13a]. The vertex detector will consist of three detector planes X, U, and V, the latter two are orientated in angles of $\pm 45^\circ$ w.r.t. the X layer. Each plane consists of eight half-layers of fibers cf. Fig. 3.4, leading to four fibers per read-out channel. Scintillating fibers of the type SCSF-78MJ from KURARAY with a diameter of 1 mm will be used, with a pitch of $1\,\text{mm}/\sqrt{2} = 0.71\,\text{mm}$. The two diagonal planes, having a width of $15.95\,\text{cm}$ are orthogonal to each other and the width of the X layer is chosen to cover their full width at $22.2\,\text{cm}$. The precise widths of the planes were chosen to fit to a multiple of 16 fiber channels, the number of read-out channels per Hamamatsu multi-anode R11265-100-M16 PMT, so each diagonal plane requires 14 and the X plane 20 PMTs, while the doubling leads to addition three PMTs per plane. In total the vertex detector has 912 channels made of 3648 single fibers, which are read out by 57 PMTs.

Treatment of the fibers

The fibers, scintillating and clear ones, have been ordered in pieces of 2 m thus the light guides already had the appropriate length. The scintillating fiber had to be cut in six different lengths, of which three arise from the geometry of the central beam hole (see Fig. 7.14) and the three others are duplicates of them with just a small variation of the length of $+5$ mm to avoid thickening at the weldings in the final fiber stack[4]. The exact values of the fiber lengths e.g. for the diagonal planes are $(159.5\,\text{mm}\ \&\ 164.5\,\text{mm})$, $(69.5\,\text{mm}\ \&\ 74.5\,\text{mm})$, and $(62.5\,\text{mm}\ \&\ 67.5\,\text{mm})$.
All front surfaces of the fibers had to be polished to prepare them for the welding process and to allow tests on the light transmission coefficient of the weldseam. The groups of Bonn and Erlangen have shown, that a good weldseam between the scintillator and the light guide yields a transmission coefficient of at least $90\,\%$ [Nae02, Teu03]. To prevent the fibers from damage through the polishing, for instance the cladding could burst off the core due to mechanical stress, and to ensure a plain front surface being perpendicular fiber, they have bin clamped in polishing block made of PMMA. This Polymethylmethacrylate is also a component of the fibers themselves, thus it has the same abrasiveness as the fibers. One of those blocks holds 64 fibers, which are pressed with their end faces on a water cooled rotating disc of abrasive paper.

[4] The material of the fibers expands irreversible during the welding process in a range of < 0.1 mm.

Decreasing grain sizes in four steps from 22 to 6 µm of the SiC material allowed for a fine polishing, which has been found to be appropriate [Teu03].
The welding set-up consists of a glass tube with in inner diameter of 1.1 mm with a winding of a tungsten filament in a groove. The filament is heated by a power source. In order to weld a piece of scintillating fiber to a clear fiber, one inserts them from opposite sides into the glass pipe meeting at the position of the tungsten filament. By pressing both fibers together under a certain force and switching on the heating for ≈ 18 s the link between the two pieces is established. The duration of the heating and the proper pressure were determined by try-and-error studies in advance. Likewise the cool down phase is of great importance, the hot weldseam is sensitive to mechanical stress and thus should be kept inside the pipe for approximately 30 s. The set-up had been improved with a second welding tube, which made the parallel welding of two fibers possible, and allowed for a sufficient long cool down time before a fiber was carefully removed from the pipe. Each of the first few hundred fibers has been checked for its light transmission by coupling blue light from a LED into the welded fiber and measuring the transmitted intensity at the other sides. The transmission of the clear light guides served as a reference. Later the sequence was changed to a random test of approx 10 % of the fibers. The reason for this were the good results before, where it turned out that all fibers which persist the mechanical stress of the pull out from the glass tube had a transmission rate of $> 90\,\%$ with a mean value at $\approx 95\,\%$. Furthermore bad weldseams could also be identified by the appearing notches.
The stacking of the fibers to the detector plane is the final step of the fiber treatment. A plate made of cast aluminum with parallel triangular milled strips adapted to the fiber diameter and the stacking pattern serves as a stacking matrix [Teu03, Bra10]. The special feature of this detector is, that the matrix will not be removed from the detector plane, rather the matrix will remain as an part of the detector housing keeping the module in its designated position. The additional material budget in the near halo region is not significant compared to the already present material of the absorbers itself. A hole in the matrix at the beam spot with a diameter of 4 cm ensures that the production of secondary particles is minimized. The matrix including the first half-layer of fibers is shown in Fig. A.59 top, while the front surface of a final plane during a test of the fiber ordering is shown in Fig. A.59 bottom. During the stacking of a half-layer the loose fibers are fixated in the gap between the fibers of the underlying half-layer by bridges, put perpendicular to the fibers exerting soft pressure onto them.
When a half-layer is completed white, water-based paint applied as a thin film $\ll 0.1$ mm is used to "glue" the fibers to each other. This procedure has been applied for all COMPASS SciFi detectors. Subsequently the additional doubling layers, described above, are placed on top of the completed four layer high plane. The mechanical stability of these fibers against movement to the sides was accomplished by adding non-used fibers as spacers in a triangular shape, as can be seen in Fig. A.60. For a final fixation and protection of the detector planes a layer of black paint and a layer of two-component epoxy resin adhesive is applied on its surface, Fig. 7.15 shows a picture of a final detector plane. Already during the stacking process, the channel ordering of fibers has been indicated by threading them into plastic blocks with 16 holes. This allows for a convenient assembly of the fibers heads which connect the fiber ends with the entry windows of the PMTs.

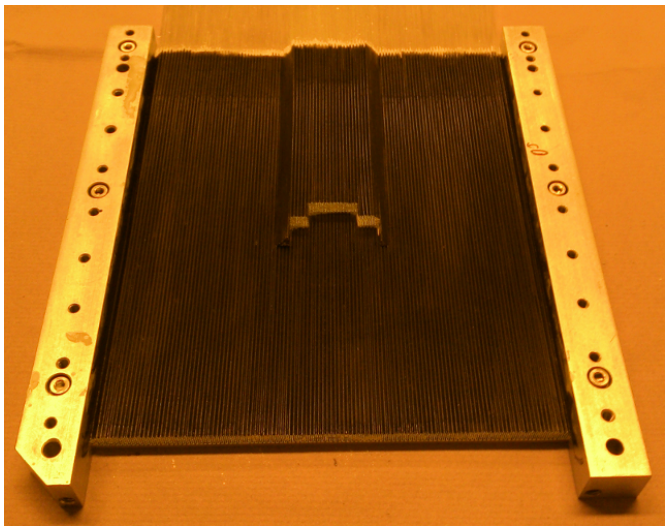

Figure 7.15.: Picture of one a final diagonal detector plane with doubling and protection layer of a two-component epoxy resin adhesive.

Detector housing

The housing of the detector has been designed in a CAD program by a technical engineer, K. Kärcher, of the Physikalisches Institut according to the specifications by the Bonn and Erlangen groups. With a computer model of the complete Drell-Yan COMPASS setup provided by the Turino group [Pan13], it was possible to design an accurately fitting housing for the vertex detector. The lower part has to fit exactly into the gap of the absorber, while the upper part must ensure mechanical stability and provide space for the readout of the detector channels at a maximum distance to the target magnet. These requirements lead to a triangular shape, depicted in Fig. A.61 (top panel). The detector placed in its final position is shown in the bottom panel of Fig. A.61. While the setup of the planes inside of the housing is shown in Fig. A.62.

Detector readout

The analog output signal of the PMTs has to be discriminated since only the time information is of interest for the track reconstruction. The discriminator cards used up to now at the COMPASS SciFi detectors are not available any more. Thus a modern type is intended to be used for the vertex detector. These so-called “PADIWA” (**PA**nda **DI**RC and **WA**SA) discriminators have a very compact design ($5.2 \times 9.4\,\mathrm{cm}$), a very low power consumption $1\,\mathrm{watt}/16\,\mathrm{channels}$ w.r.t. to the old ones and the single channel thresholds are set using FPGA. It is possible to integrate the discriminators into the housing, which will significantly reduce the cabling efforts.

8. Summary

With the results of the analysis of the 2007 data on a transversely polarized proton target, the COMPASS collaboration has been able to verify the first observation of a sizeable Collins asymmetry with opposite sign for charged hadrons made by the HERMES collaboration. This single hadron asymmetry is not the only asymmetry related to the transversity PDF h_1. From the measurement, the hadron-pair or dihadron asymmetry, which is also a h_1-dependent quantity, was also found to be clearly nonzero. These results encouraged the COMPASS collaboration to dedicate a whole year of data taking to the transverse spin effects occurring in the scattering of muons off a transversely polarized proton target, since the 2007 beam time has been split with the longitudinal target mode. This long-awaited high-statistics data set was then collected in the year 2010, reaching more than three times the statistics of the previous set. This allowed for a significant decrease of the statistical uncertainties. In addition, the systematic uncertainties were found to be considerably lower due to a variety of efforts during the data taking and subsequent systematic studies on the stability of the data. The observations made by using the first proton data set were confirmed. The large statistics and the stable operation of the apparatus motivated the implementation of particle identification. Hence, the single hadron asymmetries of charged pions and kaons became available and the hadron-pair analysis could be extended not only on pure pion pairs $\pi^+\pi^-$ but also on kaon K^+K^- and mixed pairs, like π^+K^- and $K^+\pi^-$.
Subsequently, the idea of a comprehensive reanalysis including the 2007 and the 2002-2004 data, collected on a deuteron target using unitized methods and requirements on the data, was implemented. This work achieves one of the final goals, namely having a complete sample of identified hadron-pair asymmetries on deuteron and proton targets. It is the largest available sample on this process so far, including for instance 28 million pion pairs on the proton and almost 4 million on the deuteron target.
The hadron-pair asymmetry amplitudes on the deuteron target of all pair combinations are compatible with zero within the uncertainties; but their significance is diluted by their relatively large statistical uncertainties. Only the highest bin in x and the region around the ρ meson mass for pion pairs, the invariant mass dependence of the pure kaon pairs and mixed pair's x dependence, might give weak indications of nonzero amplitudes. The combined 2007/2010 proton results, however, are clearly nonzero for $\pi^+\pi^-$ pairs in the high x region with a rise up to $-7\,\%$. Also, in their dependence on the invariant mass, significant nonzero amplitudes, for instance around the ρ meson mass with an amplitude of $\approx -2.5\,\%$, are present. Tentatively negative amplitudes are also observed in the asymmetries of K^+K^- and $K^+\pi^-$ pairs in all three dependences, including indications for significant amplitudes in some M_{inv} bins.

A comparison with the pion pair results from the HERMES collaboration, the first results on the hadron-pair asymmetry from a transversely polarized proton target ever published, shows a very good agreement.
Theoretical models, trying to describe the distributions of the asymmetry amplitudes of pion pairs in Monte-Carlo simulations are in good agreement with the measured results. An adjustment in terms of the relative strengths between incoherent and resonant pair production might lead to further improvement.
Other models try to explain the underlying mechanisms of the struck quark leaving the parental nucleon and its subsequent hadronization. The $^3P_0$ Lund model and Artru's recursive string fragmentation model are already well-established approaches to this concept. Recently, complementary techniques like the NJL-jet model based on an idea by Field and Feynman are achieving promising first results.
What these approaches have in common is that a link between the single hadron Collins and the dihadron asymmetry is established via the mechanisms proposed. A very recent COMPASS publication, which includes parts of the results from this thesis, also discusses the observation of a striking similarity between the shape and strength of the Collins and the dihadron asymmetry amplitudes. Studies suggesting a strong correlation between the azimuthal angles of the two hadrons of the pairs might be related to an underlying basic two-particle relative Collins effect.
The dihadron results from both target types offer the unique possibility of extracting the transversity PDFs of u and d valence quarks. This has been performed before, but in this work the first bin-by-bin extraction using the full $\pi^+\pi^-$ proton and deuteron results from the unique data sets is performed. A nonzero trend at large x values is evident in the distributions of $xh_1^{u_v}$ and $xh_1^{d_v}$. Furthermore, they are of opposite sign and approximately equal strength within the uncertainties.
The hardware-related part of this thesis describes the R&D and construction of a high-rate capable vertex detector made of scintillating fibers, which is a crucial part for the Drell-Yan investigation, one of the physics cases of the second phase of the COMPASS experiment. This process reveals also transverse spin effects when using a polarized target. A sign change of certain PDFs w.r.t. the SIDIS process, for instance the Sivers function, is predicted by perturbative QCD calculations. Confirming this relation is one of the main goals of this upcoming measurement. Furthermore, the beam definition by the beam telescope for the Drell-Yan program will rely exclusively on scintillating fiber detectors with a modified and extended beam telescope as described in the hardware-related part of this work.
Summarizing the results presented within this thesis, the initial analysis of the 2010 data and the resulting observations motivated for a comprehensive reanalysis of the previous data samples on transversely polarized deuteron and proton targets. From this data the pion pair asymmetry has been extracted with unique precision and the results on further pair combinations allow access to the role of strangeness in this topic for the first time. In a second step the u and d quark transversity PDFs were extracted from pure pion pair data for the first time, showing sizeable signals for both flavors.
All this clearly shows that transverse spin effects, like these being related to the transversity PDF, are important in the determination of the spin structure of the nucleon. Finally, a comparison with a transversity extraction from the world data on the Collins asymmetry demonstrates that both ways to access h_1 are of equal power.

A. Appendix

A.1. Theory and experimental overview

Table A.1.: Convolutions of the type $A \propto \mathbf{PDF} \otimes \mathbf{FF}$ of the eleven asymmetry modulations. Among them are eight modulations which include a transverse target polarization [BDG+07].

Twist-2	unpolarized	$A_{UU}^{\cos\phi_h} \propto f_1 \otimes D_1 + h_{1T}^{\perp} \otimes H_1^{\perp}$
		$A_{UU}^{\cos 2\phi_h} \propto f_1 \otimes D_1 + h_{1T}^{\perp} \otimes H_1^{\perp}$
	single spin	$A_{UT}^{\sin(\phi_h+\phi_S)} \propto h_1 \otimes H_1^{\perp}$
		$A_{UT}^{\sin(\phi_h-\phi_S)} \propto f_{1T}^{\perp} \otimes D_1$
		$A_{UT}^{\sin(3\phi_h-\phi_S)} \propto h_{1T}^{\perp} \otimes H_1^{\perp}$
	double spin	$A_{LT}^{\cos(\phi_h-\phi_S)} \propto g_{1T} \otimes D_1$
Twist-3	unpolarized	$A_{LU}^{\sin\phi_h}$
	single spin	$A_{UT}^{\sin\phi_S} \propto \frac{M}{Q}(h_1 \otimes H_1^{\perp} + f_{1T}^{\perp} \otimes D_1)$
		$A_{UT}^{\sin(2\phi_h-\phi_S)} \propto \frac{M}{Q}(h_{1T}^{\perp} \otimes H_1^{\perp} + f_{1T}^{\perp} \otimes D_1)$
	double spin	$A_{LT}^{\cos\phi_S} \propto \frac{M}{Q} g_{1T} \otimes D_1$
		$A_{LT}^{\cos(2\phi_h-\phi_S)} \propto \frac{M}{Q} g_{1T} \otimes D_1$

Table A.2.: Depolarization factors D_{nn}, target dilution factors f, target polarizations P_T, and beam polarizations λ for the calculation of the physical asymmetries from the raw asymmetry [BDG+07]

$D_{nn}^{\sin(\phi_h-\phi_S)}(y)$			$= 1$
$D_{nn}^{\cos(2\phi_h)}(y)$	$= D_{nn}^{\sin(\phi_h+\phi_S)}(y)$	$= D_{nn}^{\sin(3\phi_h-\phi_S)}(y)$	$= \varepsilon \approx \frac{2(1-y)}{1+(1-y)^2}$
$D_{nn}^{\cos(\phi_h-\phi_S)}(y)$			$= \sqrt{1-\varepsilon^2} \approx \frac{y(2-y)}{1+(1-y)^2}$
$D_{nn}^{\cos(\phi_h)}(y)$	$= D_{nn}^{\sin(2\phi_h-\phi_S)}(y)$	$= D_{nn}^{\sin(\phi_S)}(y)$	$= \sqrt{2\varepsilon(1+\varepsilon)} \approx \frac{2(2-y)\sqrt{1-y}}{1+(1-y)^2}$
$D_{nn}^{\sin(\phi_h)}(y)$	$= D_{nn}^{\cos(2\phi_h-\phi_S)}(y)$	$= D_{nn}^{\cos(\phi_S)}(y)$	$= \sqrt{2\varepsilon(1-\varepsilon)} \approx \frac{2y\sqrt{1-y}}{1+(1-y)^2}$
$A_{UU}^{\omega(\phi_h,\phi_S)}$	$= \frac{A_{UU,raw}^{\omega(\phi_h,\phi_S)}}{D^{\omega(\phi_h,\phi_S)}(y)}$		
$A_{LU}^{\omega(\phi_h,\phi_S)}$	$= \frac{A_{LU,raw}^{\omega(\phi_h,\phi_S)}}{D^{\omega(\phi_h,\phi_S)}(y)\lambda}$		
$A_{UT}^{\omega(\phi_h,\phi_S)}$	$= \frac{A_{UT,raw}^{\omega(\phi_h,\phi_S)}}{D^{\omega(\phi_h,\phi_S)}(y) f \lvert P_T \rvert}$		
$A_{LT}^{\omega(\phi_h,\phi_S)}$	$= \frac{A_{LT,raw}^{\omega(\phi_h,\phi_S)}}{D^{\omega(\phi_h,\phi_S)}(y) f \lambda \lvert P_T \rvert}$		

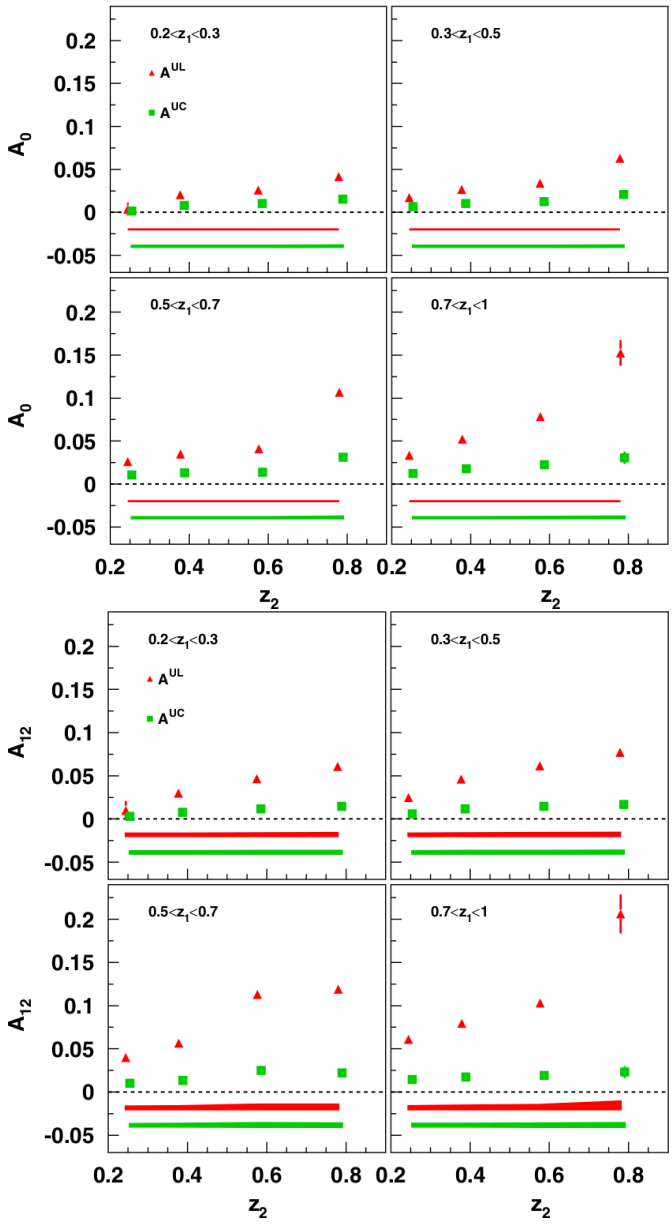

Figure A.1.: The BELLE collaboration A_0 asymmetry amplitudes (top panel) and A_{12} asymmetry amplitudes (bottom panel in different z_i and ranges of the hadrons produced. The index 0 refers to the hadron method, while the index 12 refers to the thrust method for the event reconstruction. The superscripts U, L, and C refer to $\pi^+\pi^-$ pairs with unlike-sign (e.g. $+-$), like-sign (e.g. $++$) and charge-conjugates [BELLE08].

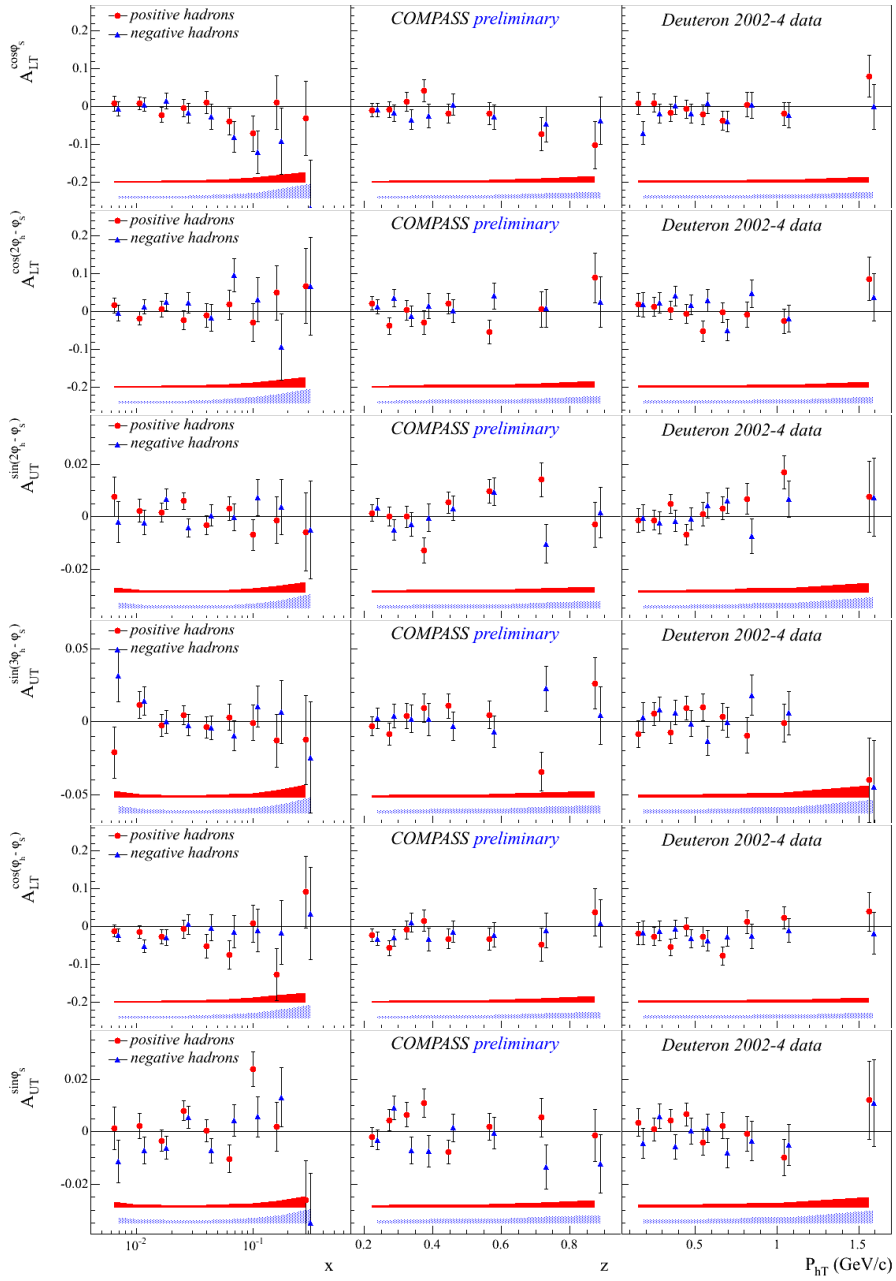

Figure A.2.: Results of the $A_{LT}^{\cos\phi_S}$, $A_{LT}^{\cos(2\phi_h-\phi_S)}$, $A_{UT}^{\sin(2\phi_h-\phi_S)}$, $A_{UT}^{\sin(3\phi_h-\phi_S)}$, $A_{LT}^{\cos(\phi_h-\phi_S)}$, $A_{UT}^{\sin\phi_S}$ single hadron asymmetry measured by the the COMPASS experiment from the 2002-2004 deuteron data of charged hadrons $h^{\pm}$ [COMPASS14e].

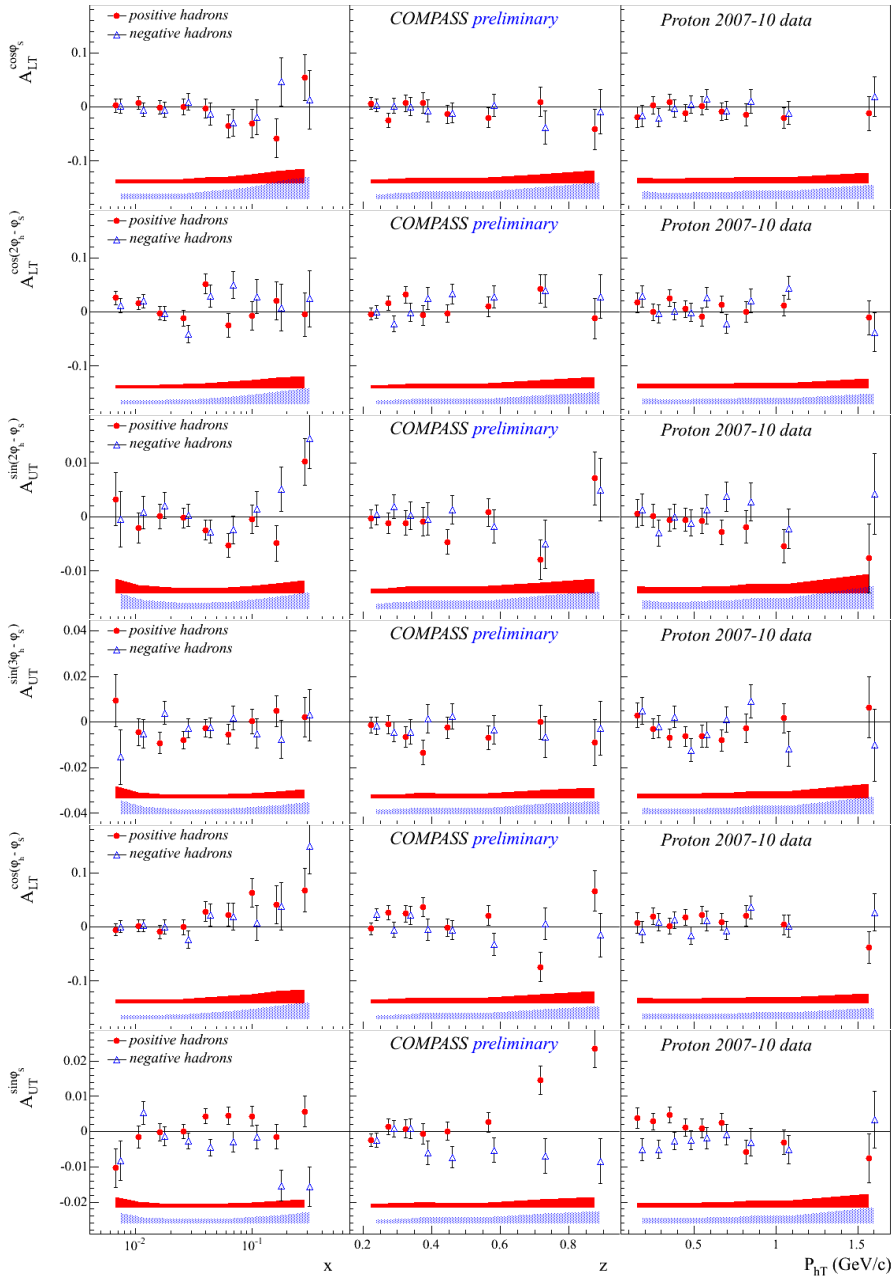

Figure A.3.: Results of the $A_{LT}^{\cos\phi_S}$, $A_{LT}^{\cos(2\phi_h-\phi_S)}$, $A_{UT}^{\sin(2\phi_h-\phi_S)}$, $A_{UT}^{\sin(3\phi_h-\phi_S)}$, $A_{LT}^{\cos(\phi_h-\phi_S)}$, $A_{UT}^{\sin\phi_S}$ single hadron asymmetry measured by the the COMPASS experiment from the combined 2007/2010 proton data of charged hadrons $h^{\pm}$ [COMPASS14e].

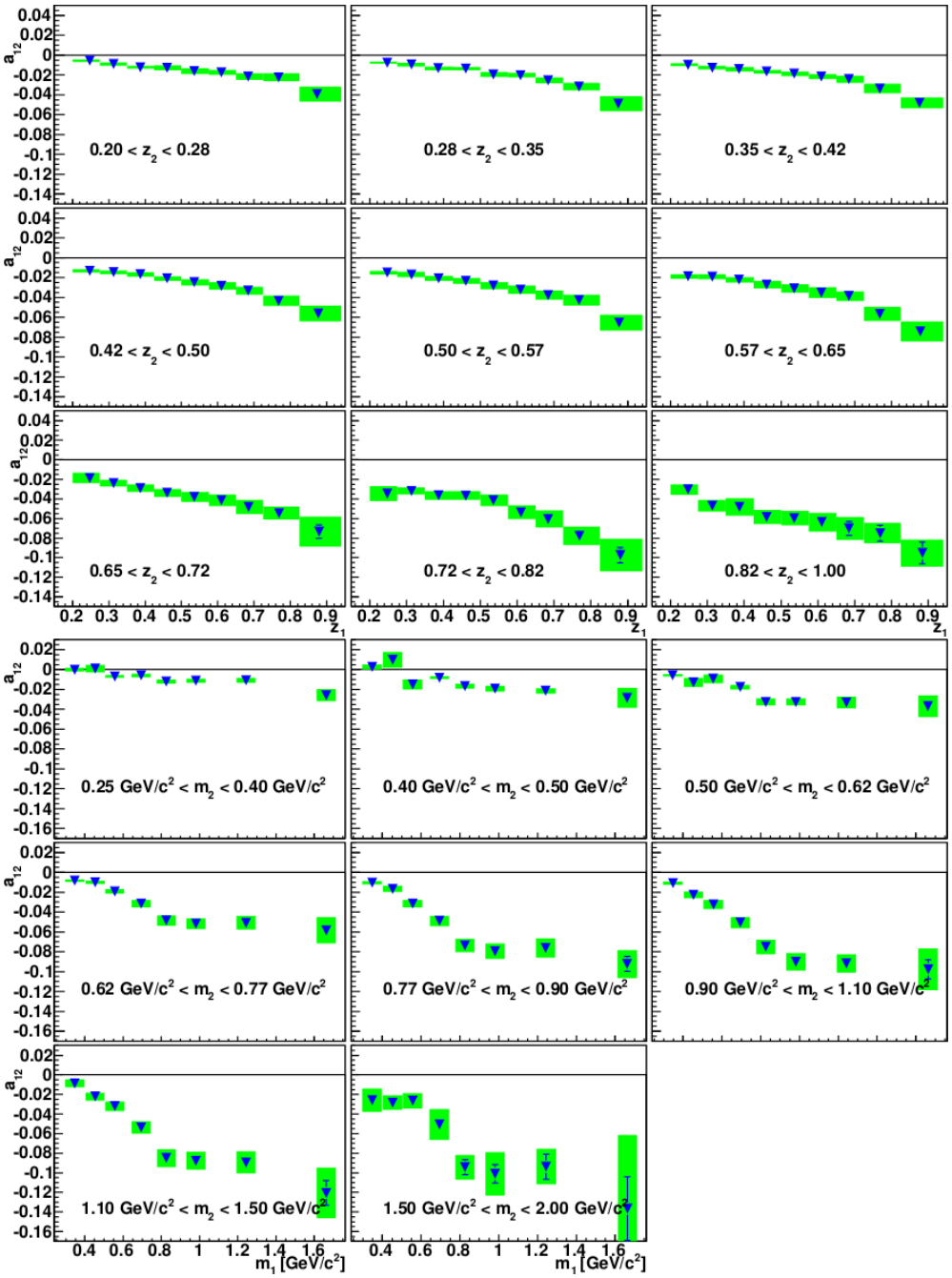

Figure A.4.: Asymmetries of hadron-pairs produced in polarized e^+e^- collisions from the BELLE experiment as a function of z_1 in bins of z_2 (top panel) and as a function of M_1 in bins of M_2 (bottom panel) [BELLE11].

Further possibilities to access transversity and Sivers PDF

As already pointed out, the transversity PDF is a chiral-odd function and can therefore only be measured in combination with another chiral-odd function. Besides of the Collins FF (see Sec. 2.3.3) and the DiFF (see Sec. 2.3.4), another FF allows access to h_1 and the space of possible functions is not limited to FF, if the experimental conditions are chosen in an appropriate way. Using a polarized fixed target experiment, such as HERMES or COMPASS, performing SIDIS measurements at sufficient energies the production of Λ (uds) and $\bar{\Lambda}$ hyperon is another option. The related Λ fragmentation function is chiral-odd and couples to the transversity PDF. The Λ hyperons produced in the fragmentation carries a certain fraction of the polarization of the initial quark. The subsequent weak decay $\Lambda \to p\,\pi$ is self-analyzing, meaning that the angular distribution of the protons is constrained by the polarization of the Λ, which in turn depends on the polarization of the struck quark. The polarizations of Λ and $\bar{\Lambda}$ were measured at the COMPASS experiment on the deuteron and proton 2007 target [COMPASS07c, COMPASS09c] and found to be small and compatible with zero within the uncertainties. An analysis of this channel using the large 2010 proton data sample is ongoing.
Not only the investigation of the transversity PDF is part of the physics program of the experiments mentioned above, also the Sivers function is accessible in the reactions described. Especially the access via the Drell-Yan reaction is one of the main goals of the upcoming PAX [PAX05] (FAIR at GSI), RHIC [BSSV00] (BNL) and COMPASS-II [MM10] (CERN) experiments. All three aim at a proof of a fundamental prediction of the QCD, which is the sign change of the Sivers function if one goes from a final-state interaction, such as SIDIS, to a process with initial state interactions, such as in the Drell-Yan process due to its T-odd nature. The PAX experiment plans to investigate this by the production of D mesons in collisions of antiprotons with polarized protons and *vice versa*, while the RHIC experiment will make use of the collisions of unpolarized protons with polarized protons. The COMPASS collaborations has already proven their capability to measure Drell-Yan reactions during tests in the years 2007 and 2009. Pairs of muons will be produced in scattering π^- off a transversely polarized proton target $\pi^- p^\uparrow \to \mu^+ \mu^- X$. The clear separation of the muons from hadronic background brings experimental challenges, of which the Bonn and the Erlangen groups will contribute significantly, as described in Sec. 7.2.

A.2. The COMPASS experiment

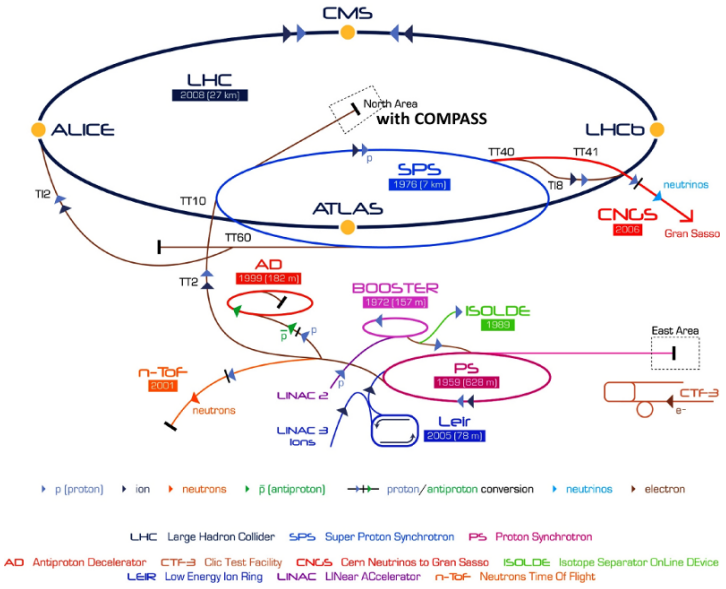

Figure A.5.: Schematic view of CERN's accelerator facilities: The North Area including COMPASS is supplied with a primary proton beam from the SPS [CERN14].

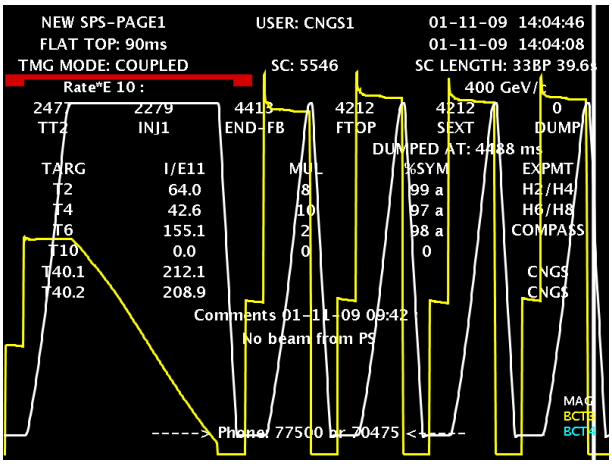

Figure A.6.: An example of the structure of a SPS super-cycle from the running period 2009 [CERN09], white lines indicate the bending field of the magnets, yellow lines the beam current. The first bump, indicated by the red bracket above, belongs to the COMPASS extraction, with the flat top visible as the long diagonal line and the four following bumps are extractions for the CNGS experiment.

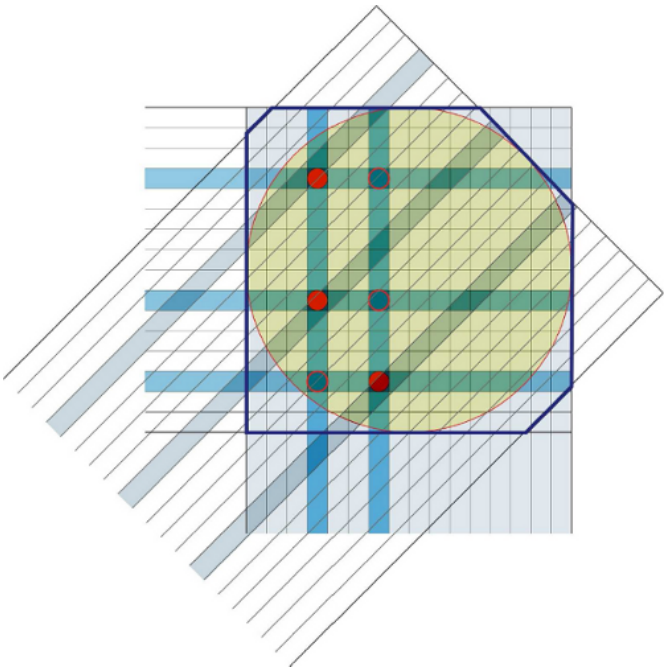

Figure A.7.: Resolving ambiguities appearing in an array of two detector planes in horizontal and vertical orientation by a third diagonal plane [Teu03]. The blue shaded strip indicate the fired strips, the full red circles at the intercept points of the fired channels are the real particle penetration points and the open red circles are the fake ambiguities.

Table A.3.: Parameters of SciFi stations in COMPASS. Column 3 specifies the number of fiber layers per plane, columns 4 and 7 give the size of the square active area and the number of channels for each plane, respectively. Column 8 lists the thickness of the respective station in units of radiation lengths (X_0).

No.	Proj.	# of layers	Size (cm^2)	Fiber ø (mm)	Pitch (mm)	# of ch.	Thickness (X_0)
1,2	X, Y	14	$3.9^2, 3.9^2$	0.5	0.41	96, 96	1.64%
15	X, Y	4	$4.5^2, 4.5^2$	1.0	0.71	64, 64	0.98%
3,4	X, Y, U	14	$5.3^2, 5.3^2, 5.3^2$	0.5	0.41	128, 128, 128	2.46%
5	X, Y	12	$8.4^2, 8.4^2$	0.75	0.53	160, 160	2.10%
55	U, V	8	12.3×6.3	1.00	0.71	96, 96	1.86%
6	X, Y, U	8	$10.0^2, 10.0^2, 12.3^2$	1.0	0.71	143, 143, 176	2.79%
7	X, Y	8	$10.0^2, 10.0^2$	1.0	0.71	143, 143	1.86%
8	X, Y	8	$12.3^2, 12.3^2$	1.0	0.71	176, 176	1.86%

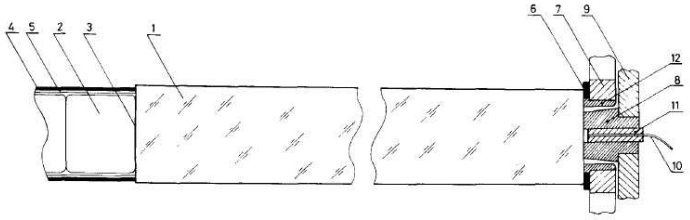

Figure A.8.: A counter of the ECAL2 calorimeter: 1) TF1-000 lead glass radiator, 2) FEU-84-3 PMT, 3) permalloy magnetic screen, 4) quartz fiber to distribute the light pulse of the monitoring system, 5) light guide connector [COMPASS07a]

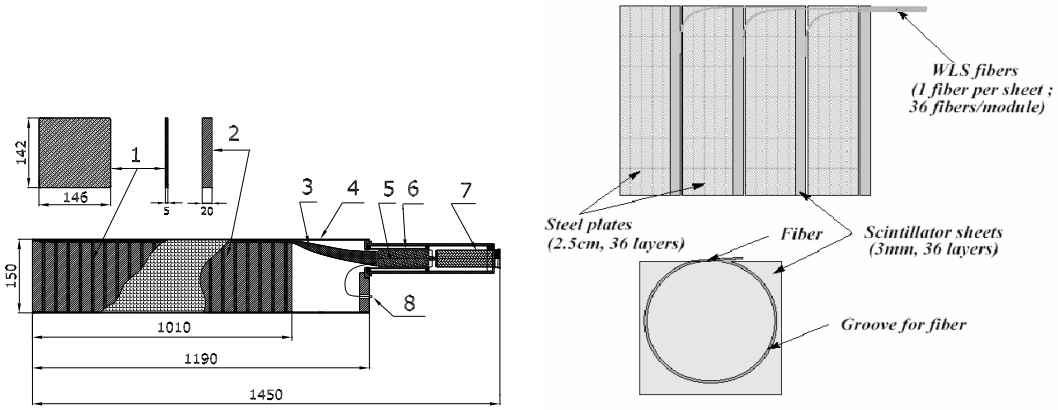

Figure A.9.: Structure of the HCAL1 module (left): 1) scintillators, 2) iron plates, 3) light guide, 4) container, 5) PMT, 6) PMT magnetic shielding, 7) Cockcroft-Walton divider, 8) optical connector for LED control. Dimensions are in mm. Principle of the fiber light readout of HCAL2 (right panel), top: side view of part of a module, bottom: front view of a scintillator plate with the fiber readout [COMPASS07a]

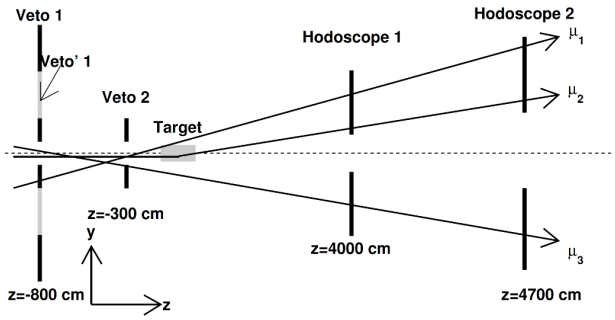

Figure A.10.: Scheme of the veto system: Only the track μ_2 is accepted. In the cases of the μ_1 and μ_3 tracks the hits in Veto 1 and Veto 2 lead to a rejection of the event/particle [COMPASS07a].

A.3. Data analysis

Table A.4.: Full list of detectors, which were excluded due to the results from the detector profile analysis of the 2010 proton data.

Period	Detector (TB Name)	Missing channels	Run range concerned	Comment
W23 (P1)	PA03U1	0-187	85034-85041; 85094-85164	Exclude for all P1
	PA04V1	188-379	85030 (62 spills)	Exclude for run 85134 (69 spills) to balance
W24 (P2)	DC01X2	0-63	85414-85445	Exclude for all P2
	DC04X1	192-255	85414-85441	Exclude for all P2
	HL04X1,Y1,05X1,Y1	All	85414	Exclude run 85414 for production
	HO04Y2_m	0	85197-85381	Exclude for all P2
	PA03U1	0-187	85207-85286	Exclude for all P2
	PA05U1	380-571	85295-85300	Exclude for runs 85367,85422,85424,85428 to balance
	Beam Unstable		85384,85385,85387	Exclude these runs for production
W26 (P3)	DC00U1	0-111	85473	Exclude run 85473 for production (also probs. on other DC, and GM05)
	DC04U1,V1,X1		85489	Exclude run 85489 for production
	DC04X1	192-255	All P3	(Exclude for all P3)
	PA03U1	0-187	85498-85638	Exclude for all P3
	PA05U1	380-571	85580-85638	Exclude for all P3
W27 (P4)	GM01X1	384-511	85831-85850	Exclude for all P4
	MA01Y1	1,2,3,4	85702	Exclude for run 85822 to balance
	MB01Y1ul,dl	All	85694-85713	Exclude for all P4
	PS01X1	0-187	85712,85713	Exclude for runs 85776,85843 to balance
	PS01X1	572-759	85684-85713	Exclude for all P4
W29 (P5)	BM01P1	47	86323-86446	Exclude for all P5
	DC01V2	48-111	86202-86228	Exclude for runs 86367,68,69,71,72,73 to balance
	FI03Y1	All	86390,86391	Exclude for run 86291 to balance
	GM01U1,V1	All	86219,86240-86242	Exclude for runs 86362,86367,86368,86369 to balance
W31 (P6)	DC04Y2	64-127	86681-86703	Exclude for all P6
	GM09X,Y	All	All P6	(Exclude for all P6)
W33 (P7)	GM08	All	86789	Exclude run 86789 for production
	GM09X	All	All P7	(Exclude for all P7)
	HO01Y1_j	5,27	All P7	Exclude for all P7
	PS01X1	572-759	86945-87135	Exclude for all P7
W35 (P8)	GM04X,Y,U,V	All	87521	Exclude for run 87426 to balance
	PS01V1	572-759	87355,87356,87357	Exclude for runs 87551,87552 to balance
	ST02U1da,ua	0-31	87354-87413	Exclude for all P8
W37 (P9)	DC04Y1	128-191	87853-87859	Exclude for runs 87704-87708 to balance
W39 (P10)	DC04Y1	128-191	87979-87980	Exclude for runs 88097-88098 to balance
	DC01Y2	48-111	>88071	Exclude for all P10
W42 (P11)	DC04Y1 ,Y2	all	>88567	Exclude for all P11 (via Traf DetNameOff)
W44 (P12)	DC04Y1 ,Y2	all	all runs	Exclude for all P12 (via Traf DetNameOff)
	DC01Y2	48-111	88850,51,52,53,54	Exclude for runs 89093,94,95,96 to balance
	DC04X1	192-255	>89065	Exclude for all P12
	HM05X1_d	0	88811-88897	Exclude for all P12 (not done yet, have to check with Johannnes)
	HI04X1 ; HL04X1	some channels	88811,88822,88823,88824	Exclude these runs for production
	GP02; GP03	almost all	89202,89206,89209	Exclude these runs for production

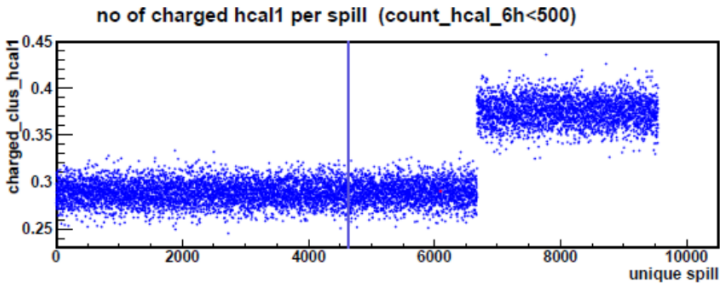

Figure A.11.: An exemplary distribution of a step in the number of charged clusters per spill of HCAL1 from period 2010_P5 [Eli12]. The blue vertical line marks the boundary of the two sub-periods.

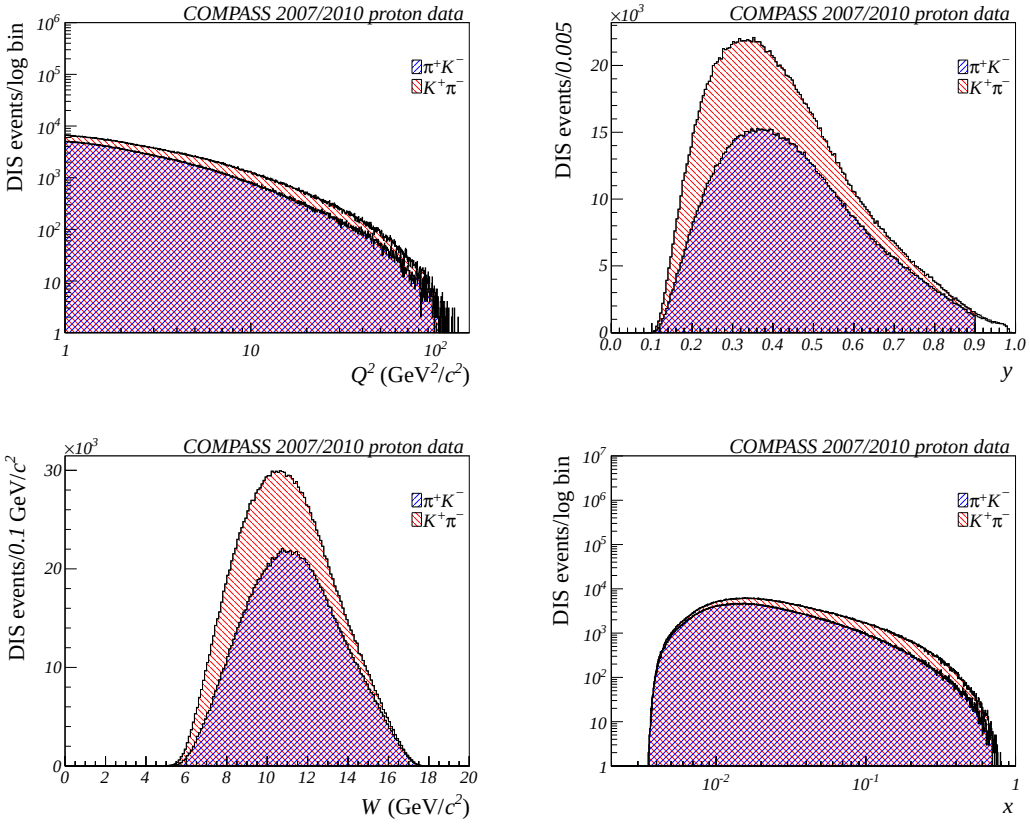

Figure A.12.: Kinematic distribution of DIS events before and after the specific cuts from the combined 2007/2010 proton data for π^+K^- (blue shaded, see legend) and $K^+\pi^-$ pairs (red shaded). From left to right in the 1$^{\text{st}}$ row: Q^2 distribution and y distribution; 2$^{\text{nd}}$ row: W distribution and x distribution.

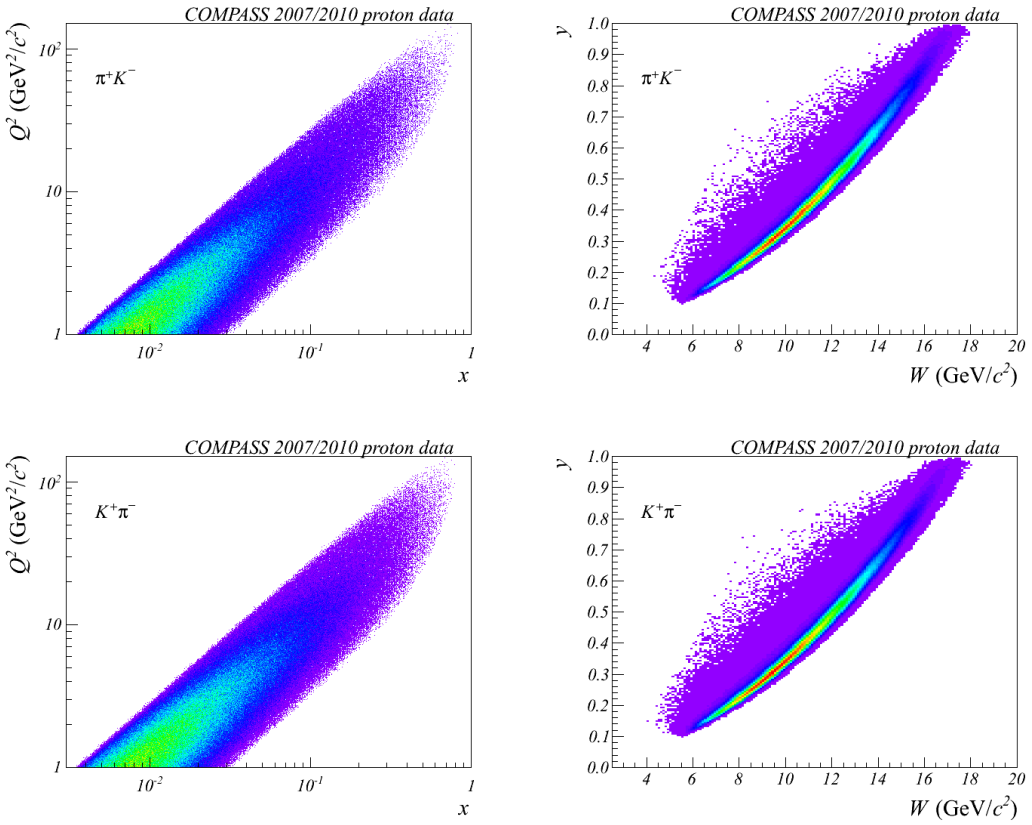

Figure A.13.: Kinematic distribution of DIS events from the combined 2007/2010 proton data for π^+K^- and $K^+\pi^-$ pairs. From left to right in the 1$^{\text{st}}$ row: $Q^2(x)$ and $y(W)$ distribution of π^+K^-; 2$^{\text{nd}}$ row: $Q^2(x)$ and $y(W)$ distribution of $K^+\pi^-$.

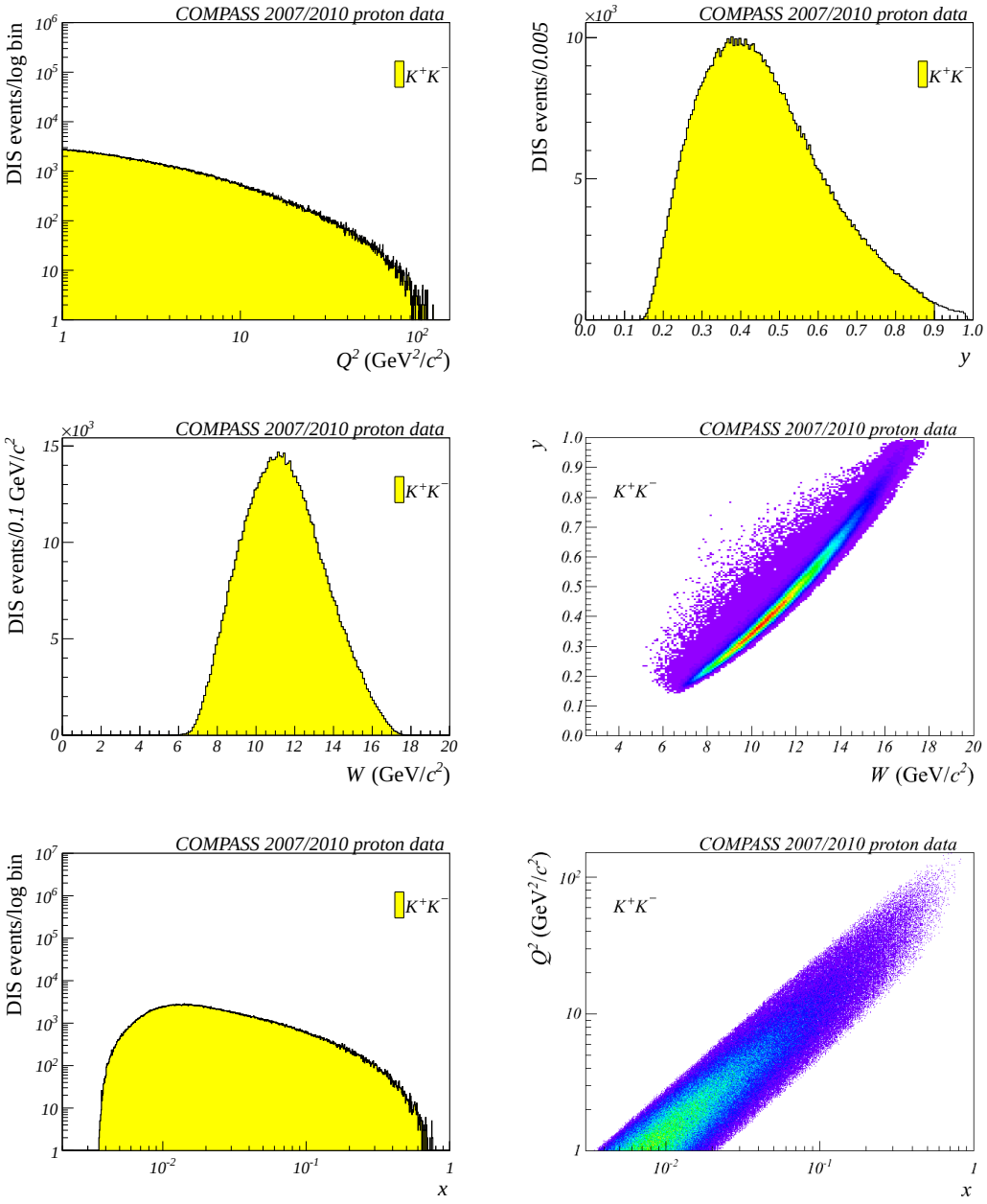

Figure A.14.: Kinematic distribution of DIS events of the K^+K^- sample before and after the specific cuts from the combined 2007/2010 proton data for kaon pairs. From left to right in the 1st row: Q^2 distribution and y distribution; 2nd row: W distribution and $y(W)$ distribution; 3rd row: x distribution and $Q^2(x)$ distribution.

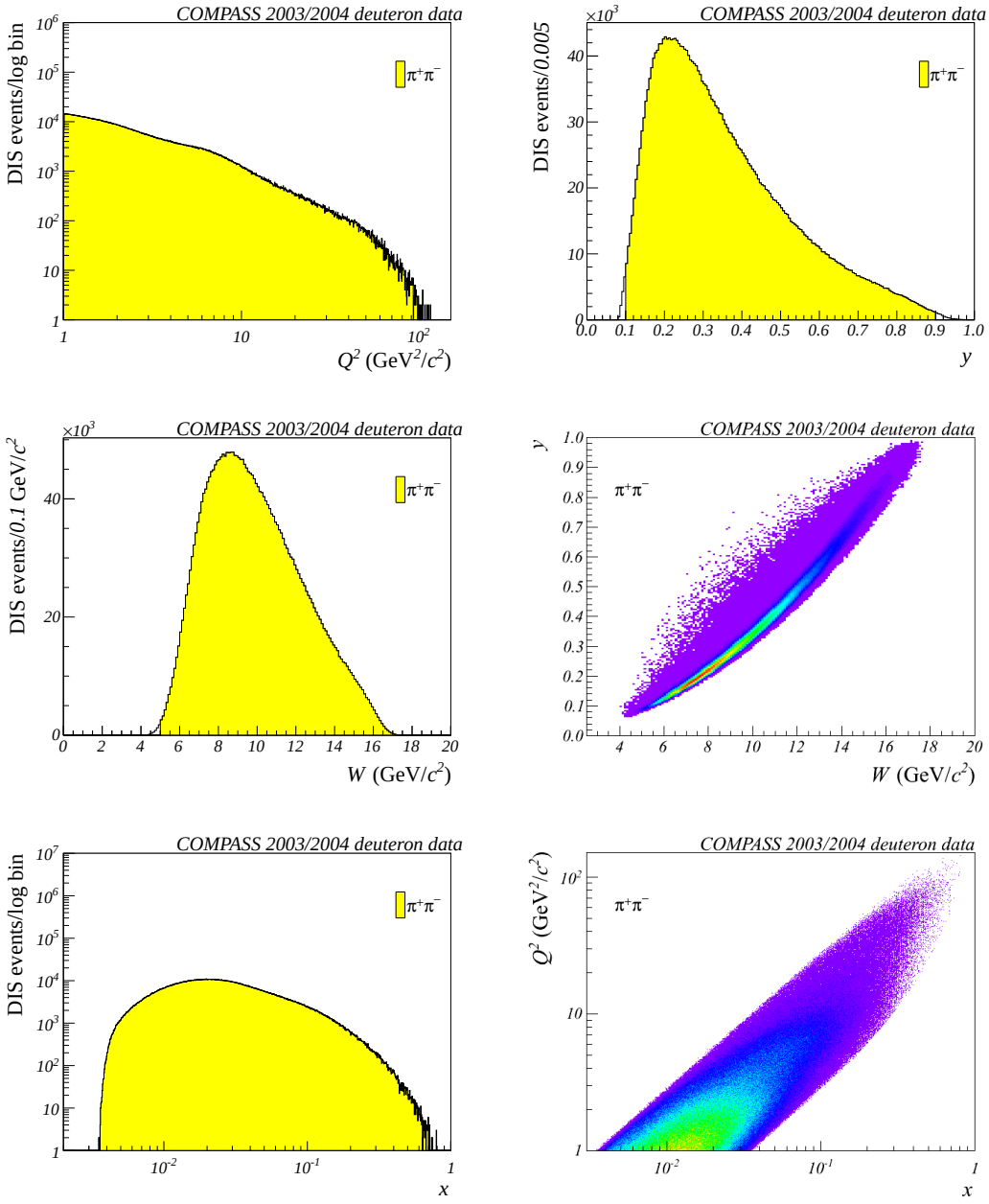

Figure A.15.: Kinematic distribution of DIS events of the $\pi^+\pi^-$ sample before (white) and after the specific cuts (yellow) from the deuteron 2003-2004 data for $\pi^+\pi^-$ pairs. From left to right in the 1st row: Q^2 distribution and y distribution; 2nd row: W distribution and $y(W)$ distribution; 3rd row: x distribution and $Q^2(x)$ distribution.

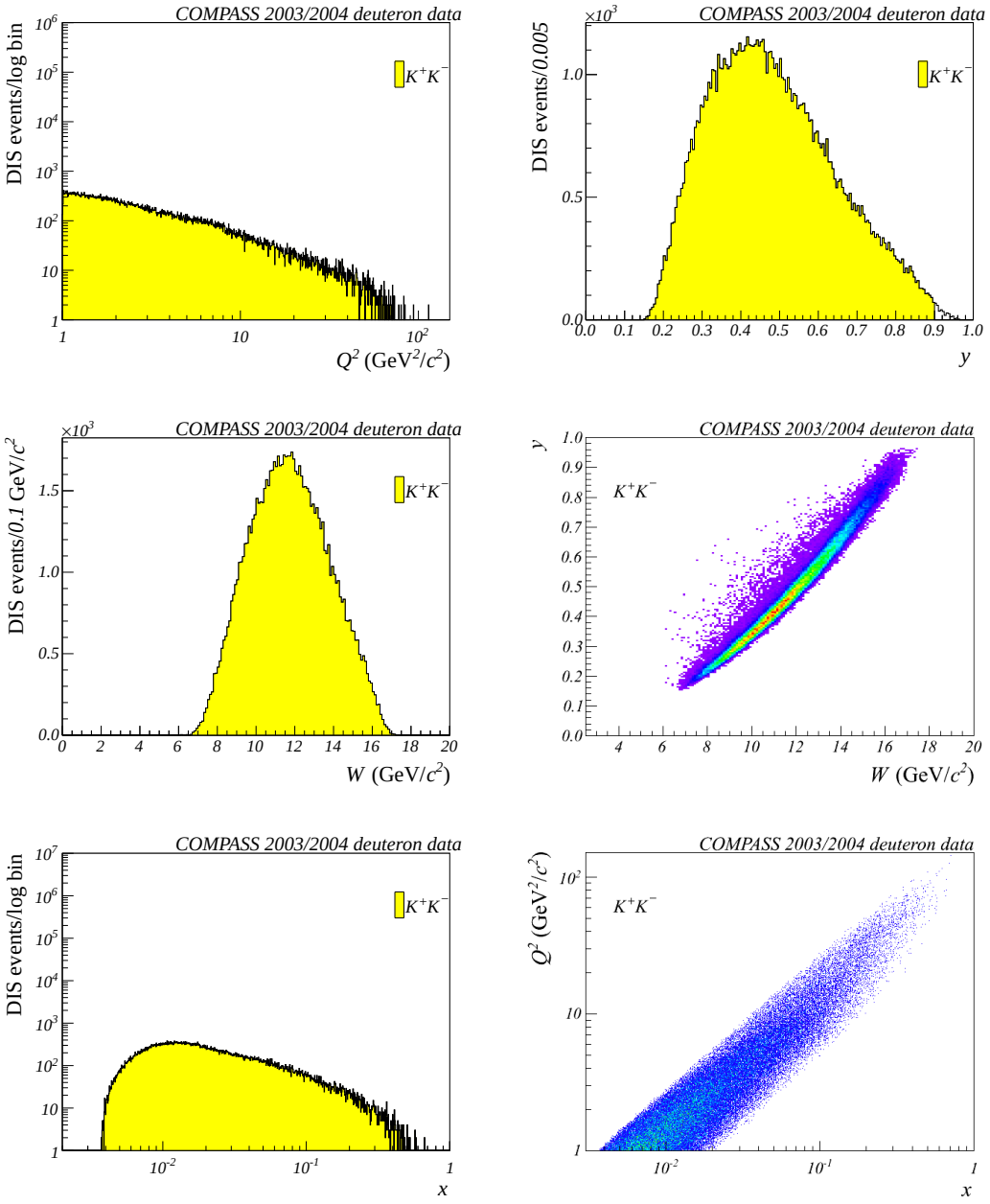

Figure A.16.: Kinematic distribution of DIS events of the K^+K^- sample before (white) and after the specific cuts (yellow) from the deuteron for kaon pairs. From left to right in the 1st row: Q^2 distribution and y distribution; 2nd row: W distribution and $y(W)$ distribution; 3rd row: x distribution and $Q^2(x)$ distribution.

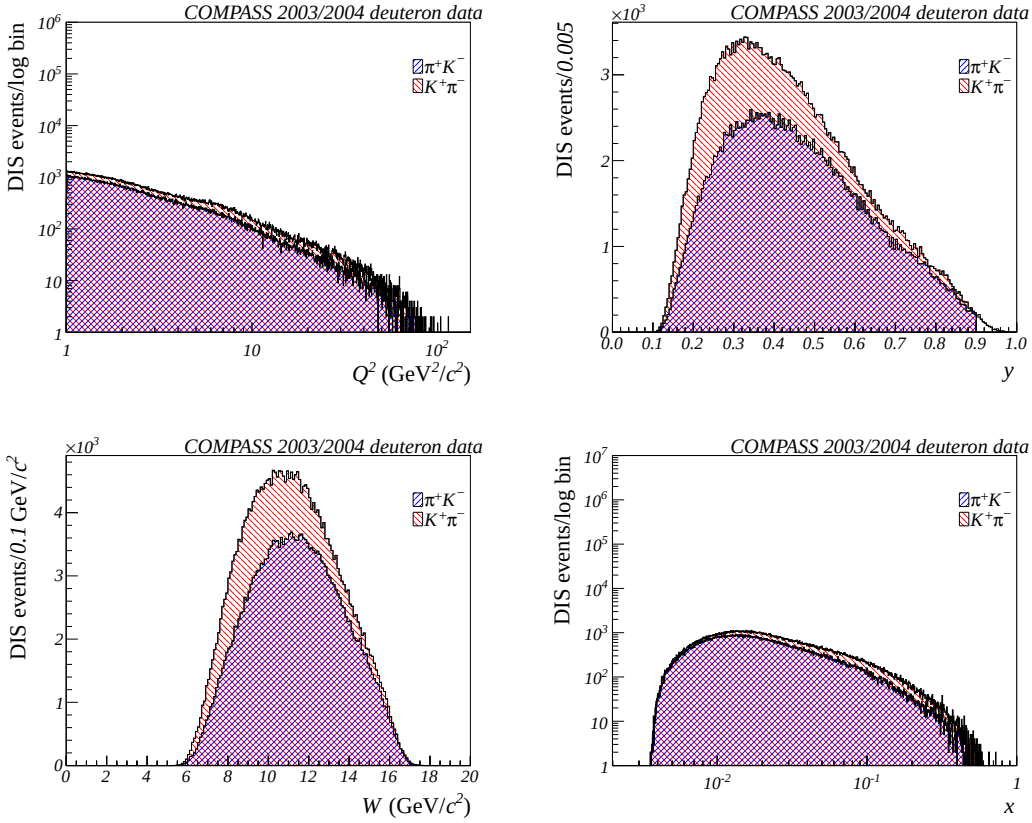

Figure A.17.: Kinematic distribution of DIS events before and after the specific cuts from the deuteron data for π^+K^- (blue shaded, see legend) and $K^+\pi^-$ (red shaded) pairs. From left to right in the 1$^{\text{st}}$ row: Q^2 distribution and y distribution; 2$^{\text{nd}}$ row: W distribution and x distribution.

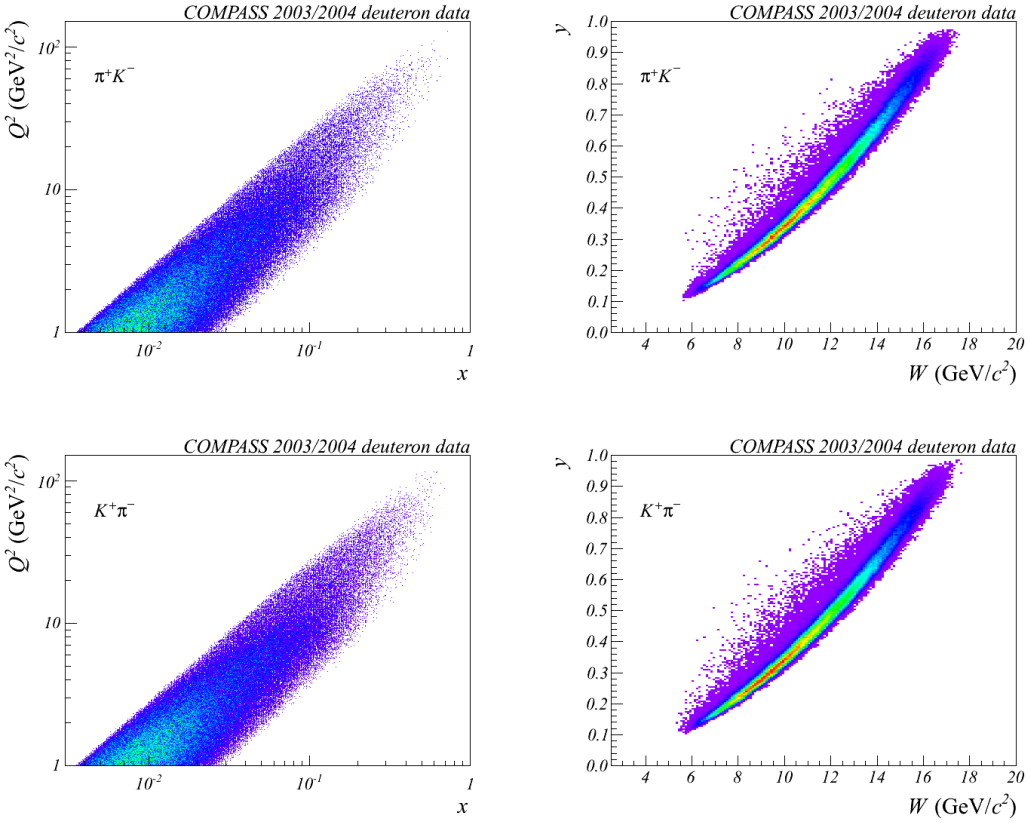

Figure A.18.: Kinematic distribution of DIS events from the deuteron data for π^+K^- and $K^+\pi^-$ pairs. From left to right in the 1$^{\text{st}}$ row: $Q^2(x)$ and $y(W)$ distribution of π^+K^-; 2$^{\text{nd}}$ row: $Q^2(x)$ and $y(W)$ distribution of $K^+\pi^-$.

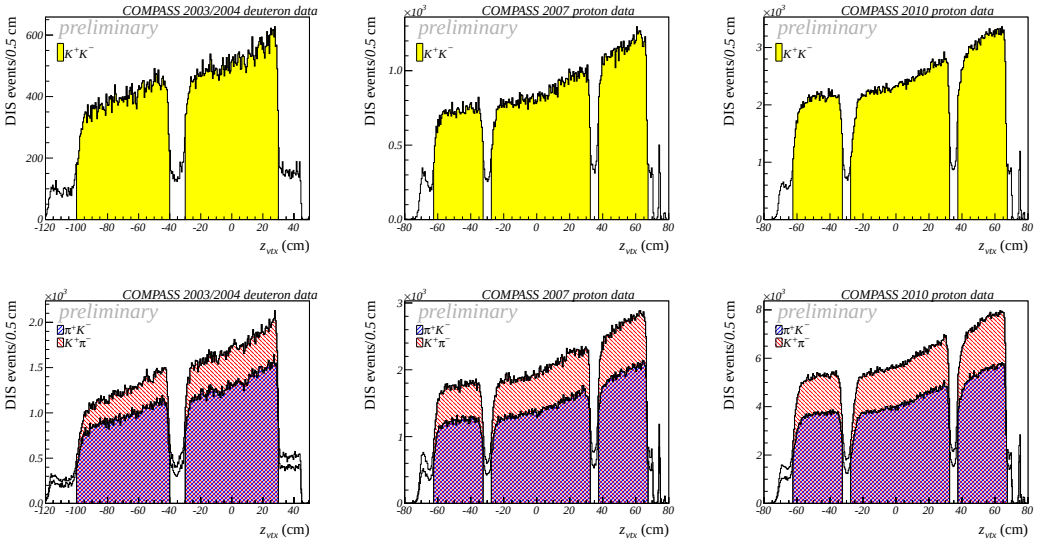

Figure A.19.: Distribution the reconstructed primary vertex position along the beam axis from deuteron (left) and combined 2007/2010 proton data (right) before (white) and after the cuts of kaon pairs (1st row), π^+K^- (blue shaded), and $K^+\pi^-$ (red shaded) (2nd row).

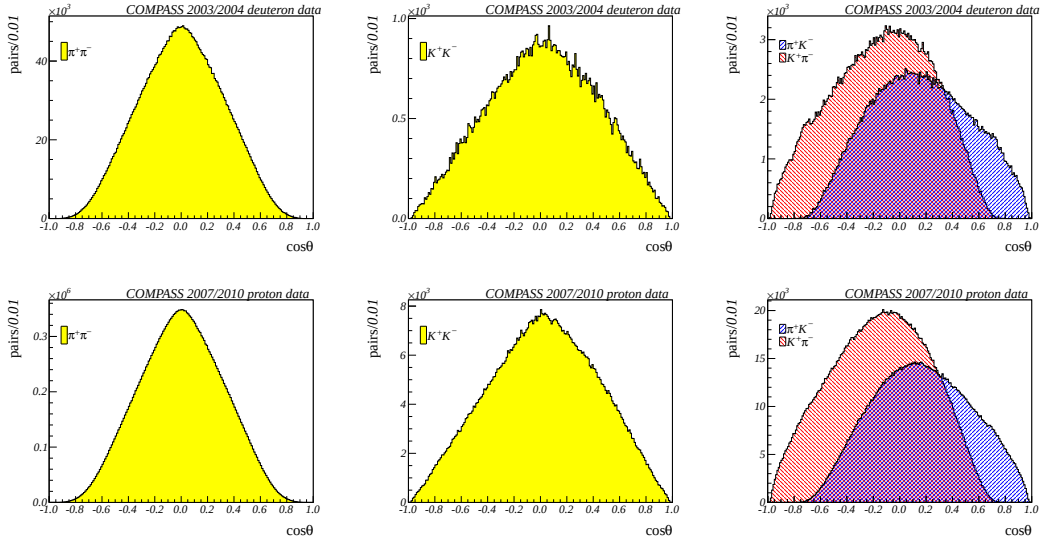

Figure A.20.: Distributions of $\cos\theta$ from the deuteron data 2003-2004 (1st row) and combined 2007/2010 proton data (2nd row) of $\pi^+\pi^-$ pairs (1st column), kaon pairs (2nd column), and π^+K^- & $K^+\pi^-$ (3rd column).

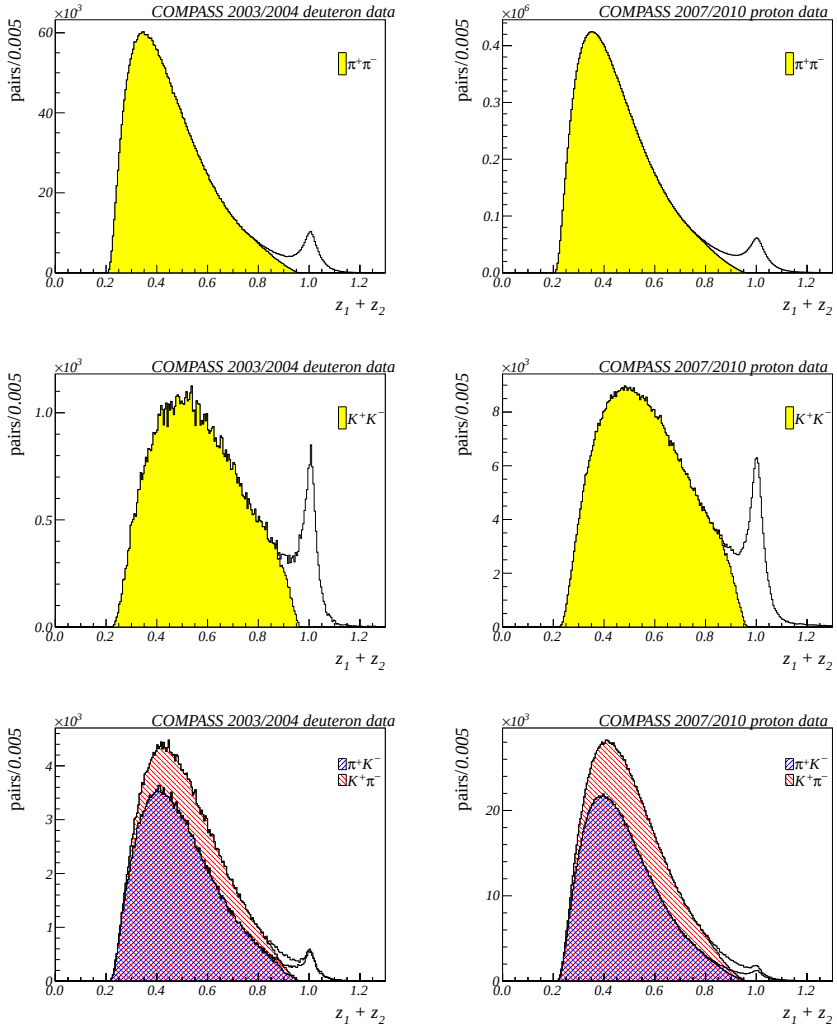

Figure A.21.: Distribution of the $z = z_1 + z_2$ from deuteron (1st column) and combined 2007/2010 proton data (2nd column) before (white) and after the cuts (yellow) of pion pairs (1st row), kaon pairs (2nd row), and π^+K^- & $K^+\pi^-$ (3rd row).

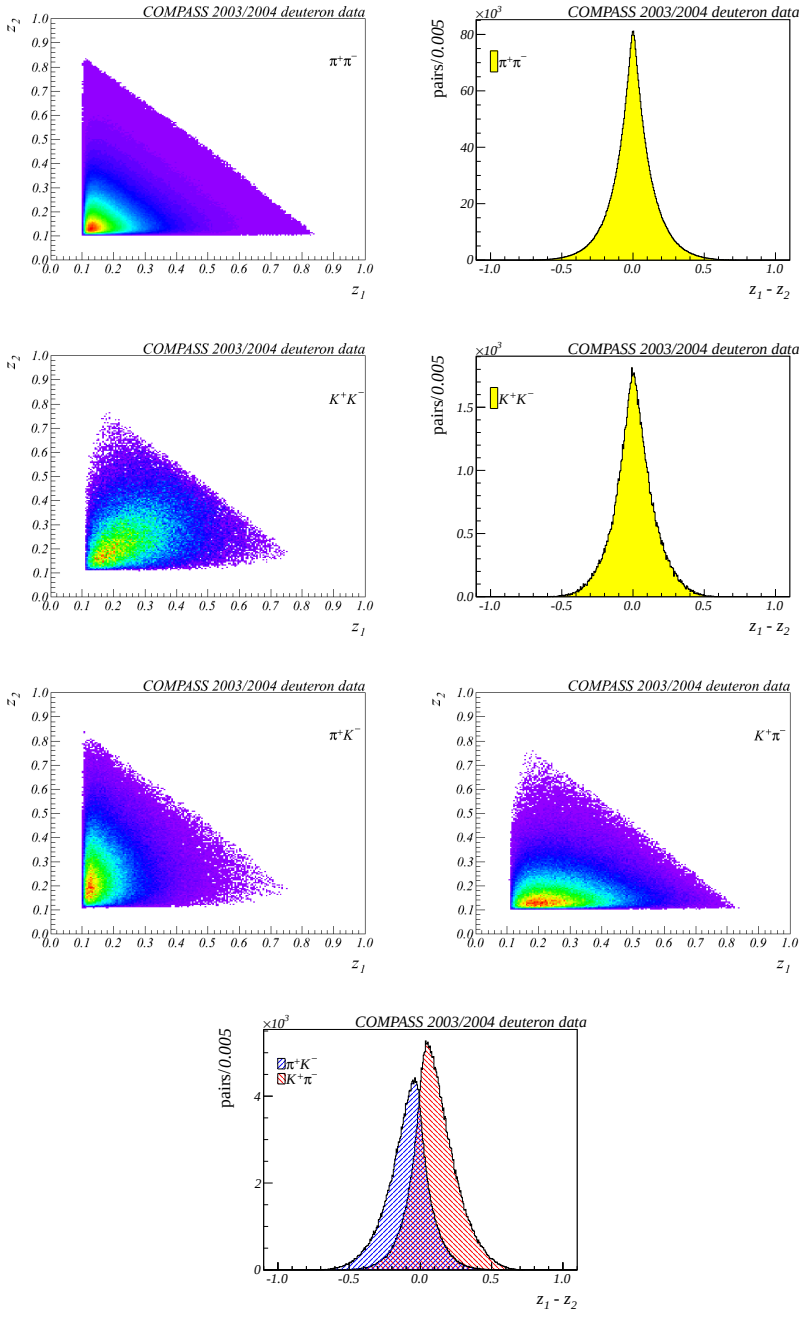

Figure A.22.: Distributions of z_2 as a function of z_1 (1st column) and $z_1 - z_2$ (2nd column) both from the 2003-2004 deuteron data of $\pi^+\pi^-$ pairs (1st row), kaon pairs (2nd row), and π^+K^- & $K^+\pi^-$ (3rd and 4th row).

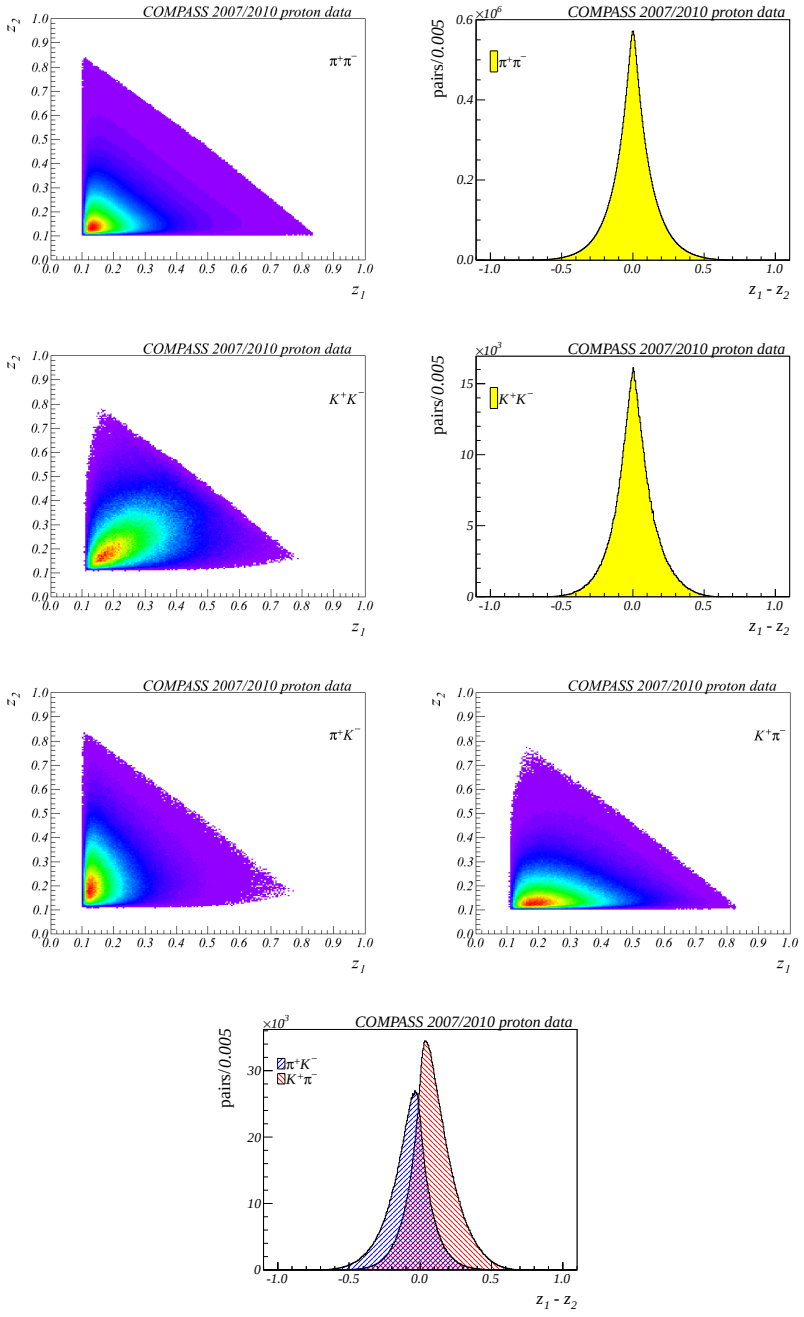

Figure A.23.: Distributions of z_2 as a function of z_1 (1st column) and $z_1 - z_2$ (2nd column) both from the 2007/2010 proton data of $\pi^+\pi^-$ pairs (1st row), kaon pairs (2nd row), and π^+K^- & $K^+\pi^-$ (3rd and 4th row).

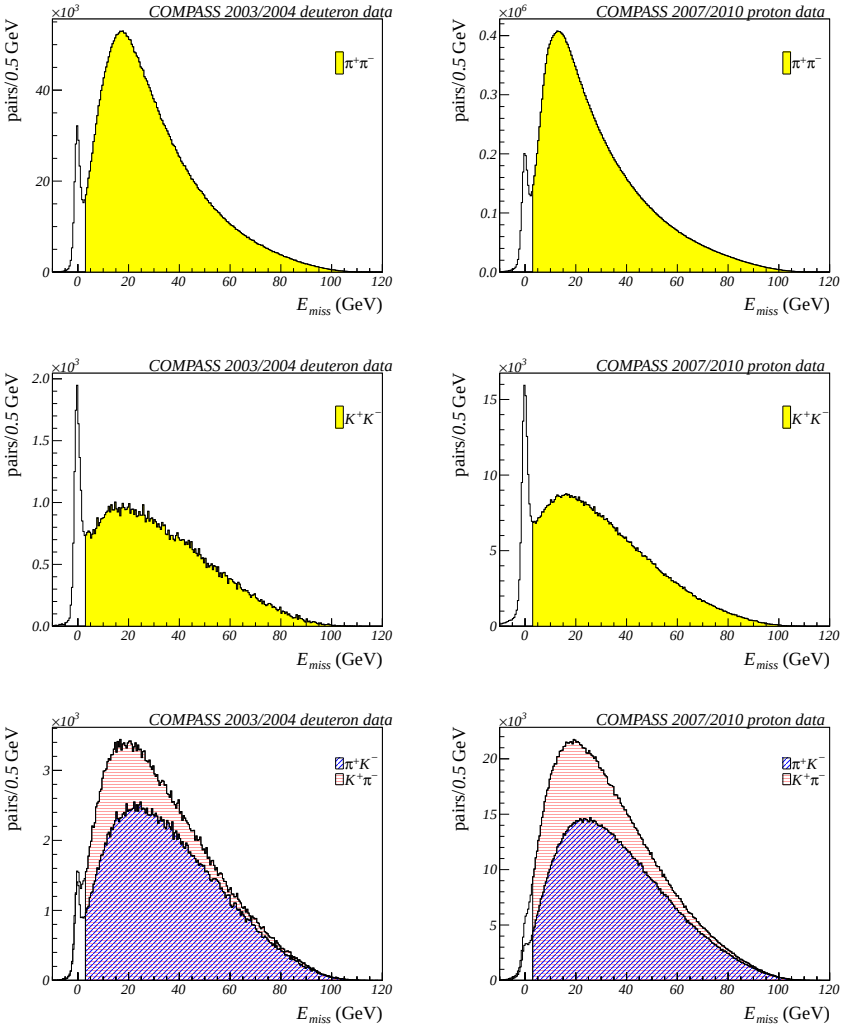

Figure A.24.: Distributions of the missing energy E_{miss} from deuteron (1st column) and combined 2007/2010 proton data (2nd column) before (white) and after the cuts (yellow) of pion pairs(1st row), kaon pairs (2nd row), and π^+K^- & $K^+\pi^-$ (3rd row).

Table A.5.: The χ^2 probability values of the R-test (right sub-table) and of the T-test (left sub-table) on the deuteron data without making any bin on the kinematic variables of deuteron, 2007, and 2010 proton data.

R-test	h^+h^-	$\pi^+\pi^-$	K^+K^-	π^+K^-	$K^+\pi^-$
deuteron_1	0.60	–	–	–	–
deuteron_2	0.91	–	–	–	–
deuteron_3	0.20	0.27	0.75	0.50	0.27
deuteron_4	0.72	0.79	0.44	0.80	0.80
deuteron_5	0.47	0.58	0.93	0.89	0.58
2007_1	0.52	0.22	0.89	0.87	0.96
2007_2	0.95	0.85	0.79	0.53	0.14
2007_3	0.65	0.34	0.67	0.58	0.30
2007_4	0.17	0.35	0.64	0.84	0.14
2007_5	0.60	0.31	0.43	0.37	0.58
2007_6	0.87	0.82	0.68	0.29	0.76
2010_1	0.37	0.04	0.49	0.21	0.12
2010_2	0.49	0.96	0.61	0.74	0.50
2010_3	0.43	0.44	0.29	0.73	0.29
2010_4	0.71	0.41	0.70	0.87	0.28
2010_5	0.70	0.65	0.84	0.84	0.57
2010_6	0.01	0.06	0.43	0.38	0.50
2010_7	0.02	0.03	0.85	0.67	0.10
2010_8	0.05	0.43	0.12	0.56	0.69
2010_9	0.67	0.05	0.99	0.55	0.38
2010_10	0.01	0.01	0.92	0.49	0.18
2010_11	0.78	0.71	0.10	0.52	0.46
2010_12	0.02	0.07	0.18	0.69	0.46

T-test	h^+h^-	$\pi^+\pi^-$	K^+K^-	π^+K^-	$K^+\pi^-$
deuteron_1	0.99	–	–	–	–
deuteron_2	0.52	–	–	–	–
deuteron_3	0.21	0.80	0.91	0.63	0.09
deuteron_4	0.94	0.60	0.06	0.65	0.36
deuteron_5	0.17	0.02	0.78	0.49	0.36
2007_1	0.11	0.07	0.81	0.37	0.15
2007_2	0.97	0.72	0.18	0.80	0.66
2007_3	0.21	0.07	0.71	0.47	0.97
2007_4	0.14	0.04	0.68	0.57	0.47
2007_5	0.60	0.79	0.93	0.36	0.87
2007_6	0.38	0.25	0.42	0.59	0.11
2010_1	0.12	0.21	0.94	0.56	0.27
2010_2	0.07	0.83	0.84	0.73	0.58
2010_3	0.74	0.63	0.89	0.92	0.97
2010_4	0.31	0.28	0.66	0.65	0.60
2010_5	0.42	0.88	0.50	0.30	0.84
2010_6	0.15	0.44	0.75	0.75	0.98
2010_7	0.18	0.54	0.93	0.68	0.94
2010_8	0.45	0.31	0.37	0.45	0.85
2010_9	0.02	0.41	0.69	0.78	0.60
2010_10	0.48	0.10	0.98	0.57	0.70
2010_11	0.02	0.51	0.81	0.83	0.69
2010_12	0.02	0.24	0.98	0.51	0.63

Table A.6.: The χ^2 probability values of the RA-test (right sub-table) and of the combined RA- and T-test (left sub-table) on the deuteron data without making any bin on the kinematic variables of deuteron, 2007, and 2010 proton data.

RA-test	h^+h^-	$\pi^+\pi^-$	K^+K^-	π^+K^-	$K^+\pi^-$
deuteron_1	0.34	–	–	–	–
deuteron_2	0.27	–	–	–	–
deuteron_3	0.95	0.38	0.17	0.93	0.37
deuteron_4	0.39	0.51	0.33	0.45	0.74
deuteron_5	0.94	0.60	0.53	0.52	0.36
2007_1	0.01	0.17	0.09	0.13	0.84
2007_2	0.08	0.81	0.40	0.98	0.35
2007_3	0.30	0.18	0.23	0.59	0.98
2007_4	0.67	0.78	0.65	0.94	0.55
2007_5	0.54	0.34	0.23	0.74	0.69
2007_6	0.10	0.17	0.82	0.14	0.24
2010_1	0.73	0.90	0.33	0.32	0.78
2010_2	0.24	0.36	0.10	0.11	0.01
2010_3	0.57	0.47	0.99	0.91	0.05
2010_4	0.54	0.05	0.88	0.81	0.61
2010_5	0.60	0.66	0.35	0.58	0.75
2010_6	0.22	0.24	0.36	0.03	0.79
2010_7	0.56	0.41	0.24	0.20	0.83
2010_8	0.78	0.74	0.60	0.29	0.96
2010_9	0.69	0.30	0.06	0.84	0.36
2010_10	0.38	0.02	0.35	0.10	0.64
2010_11	0.09	0.10	0.54	0.54	0.87
2010_12	0.47	0.17	0.64	0.02	0.63

RA&TT	h^+h^-	$\pi^+\pi^-$	K^+K^-	π^+K^-	$K^+\pi^-$
deuteron_1	0.99	–	–	–	–
deuteron_2	0.74	–	–	–	–
deuteron_3	0.12	0.87	0.86	0.88	0.94
deuteron_4	0.98	0.86	0.93	0.86	0.87
deuteron_5	0.08	0.93	0.83	0.86	0.97
2007_1	0.64	0.02	0.08	0.06	0.04
2007_2	1.00	0.97	0.69	0.97	0.96
2007_3	0.76	0.22	0.46	0.41	0.48
2007_4	0.58	0.31	0.95	0.94	0.91
2007_5	0.94	0.69	0.70	0.55	0.70
2007_6	0.93	0.30	0.38	0.13	0.19
2010_1	0.57	0.90	0.33	0.32	0.78
2010_2	0.50	0.36	0.10	0.11	0.01
2010_3	0.96	0.47	0.99	0.91	0.05
2010_4	0.81	0.05	0.88	0.81	0.61
2010_5	0.87	0.66	0.35	0.58	0.75
2010_6	0.64	0.24	0.36	0.03	0.79
2010_7	0.66	0.41	0.24	0.20	0.83
2010_8	0.17	0.74	0.60	0.29	0.96
2010_9	0.88	0.30	0.06	0.84	0.36
2010_10	0.07	0.02	0.35	0.10	0.64
2010_11	0.99	0.10	0.54	0.54	0.87
2010_12	0.12	0.17	0.64	0.02	0.63

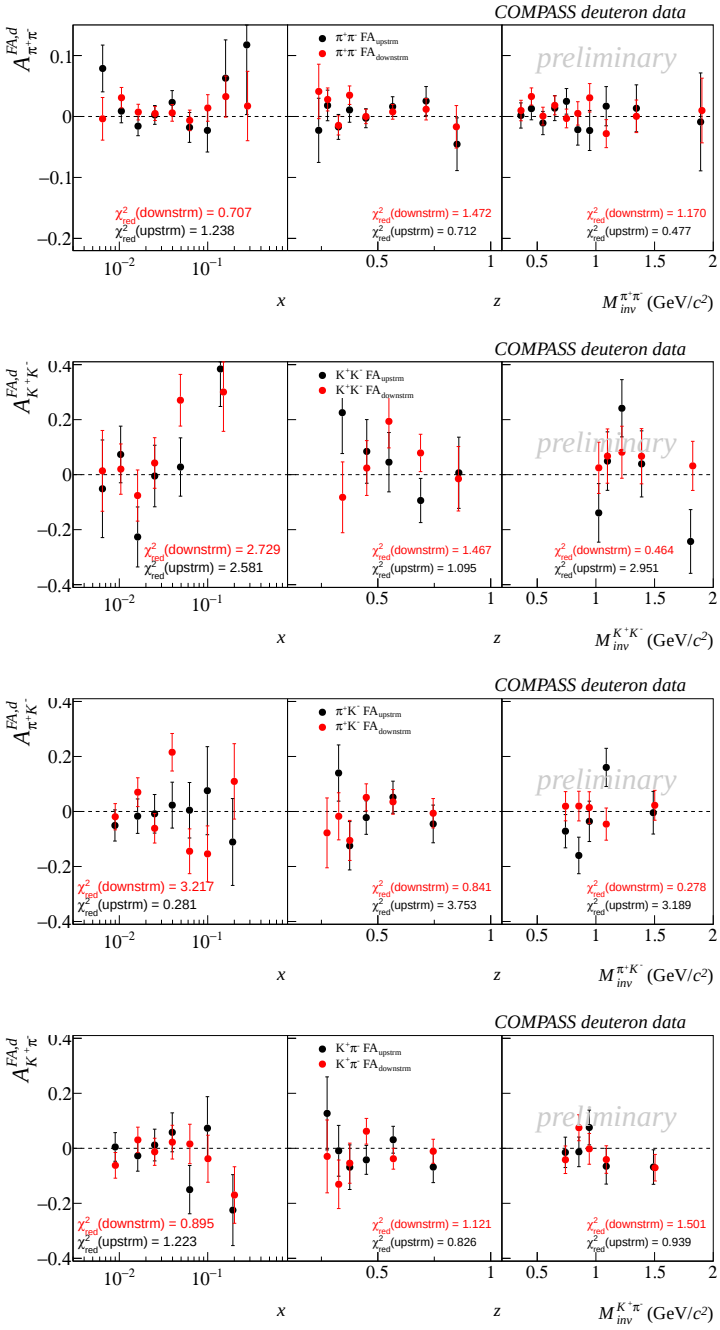

Figure A.25.: False asymmetries in the configurations FA_{upstrm} and $\mathrm{FA}_{downstrm}$ of the deuteron data: h^+h^- pairs (1st row), $\pi^+\pi^-$ pairs (2nd row), K^+K^- pairs (3rd row), π^+K^- pairs (4th row), $K^+\pi^-$ pairs (5th row)

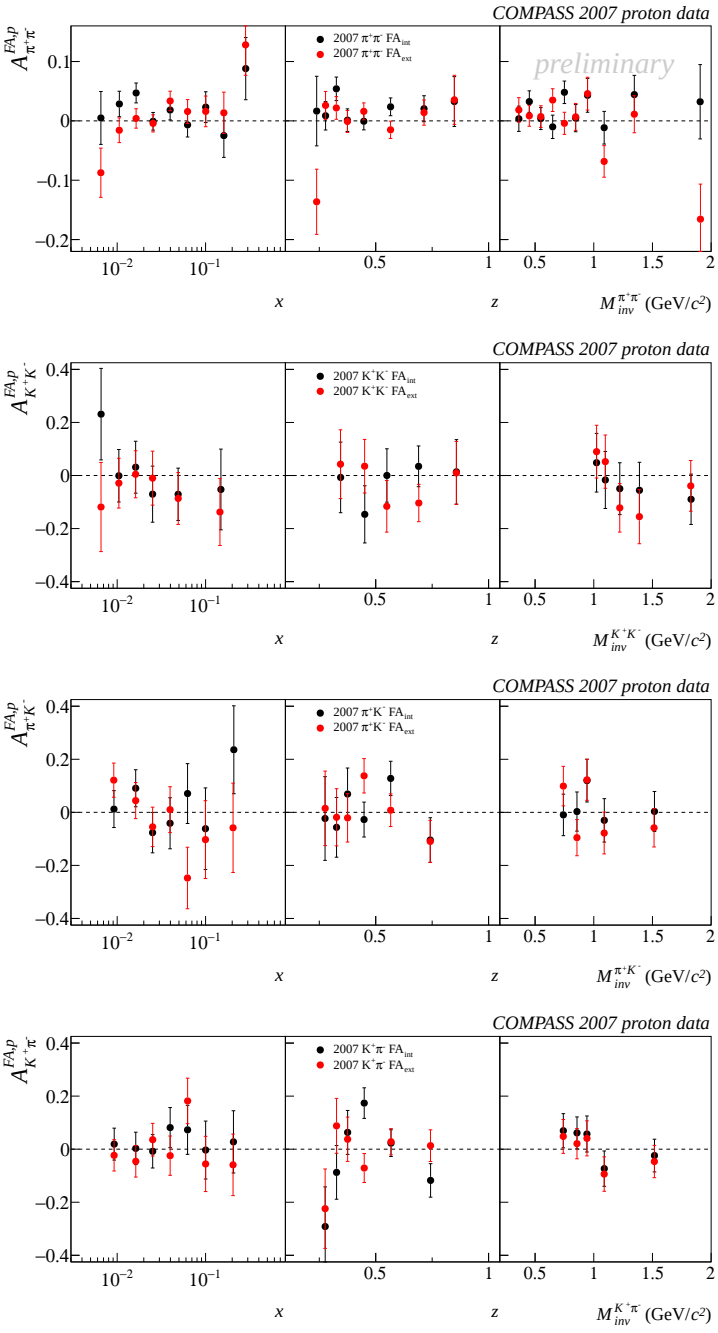

Figure A.26.: False asymmetries in the configurations FA_{ext} and FA_{int} of the 2007 proton data: $\pi^+\pi^-$ pairs (1st row)), K^+K^- pairs (2nd row), π^+K^- pairs (3rd row), $K^+\pi^-$ pairs (4th row)

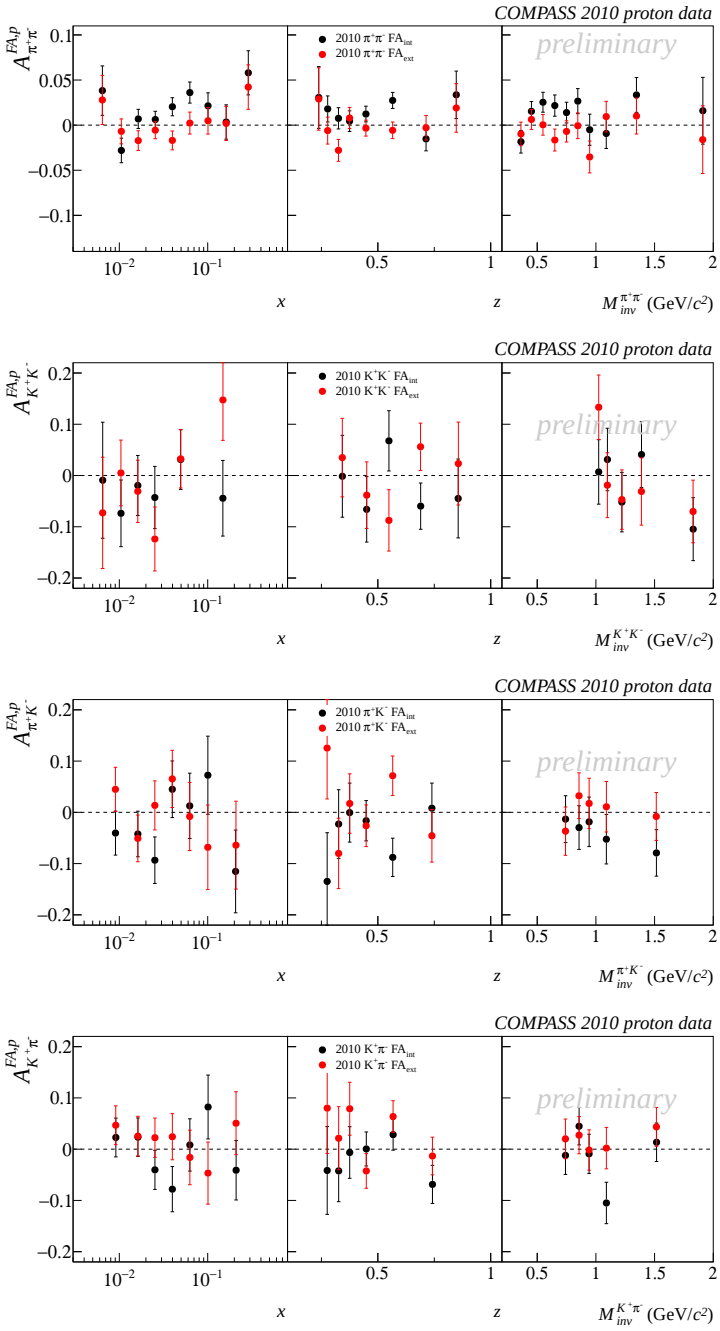

Figure A.27.: False asymmetries in the configurations FA_{ext} and FA_{int} of the 2010 proton data: h^+h^- pairs (1st row), $\pi^+\pi^-$ pairs (2nd row), K^+K^- pairs (3rd row), π^+K^- pairs (4th row), $K^+\pi^-$ pairs (5th row)

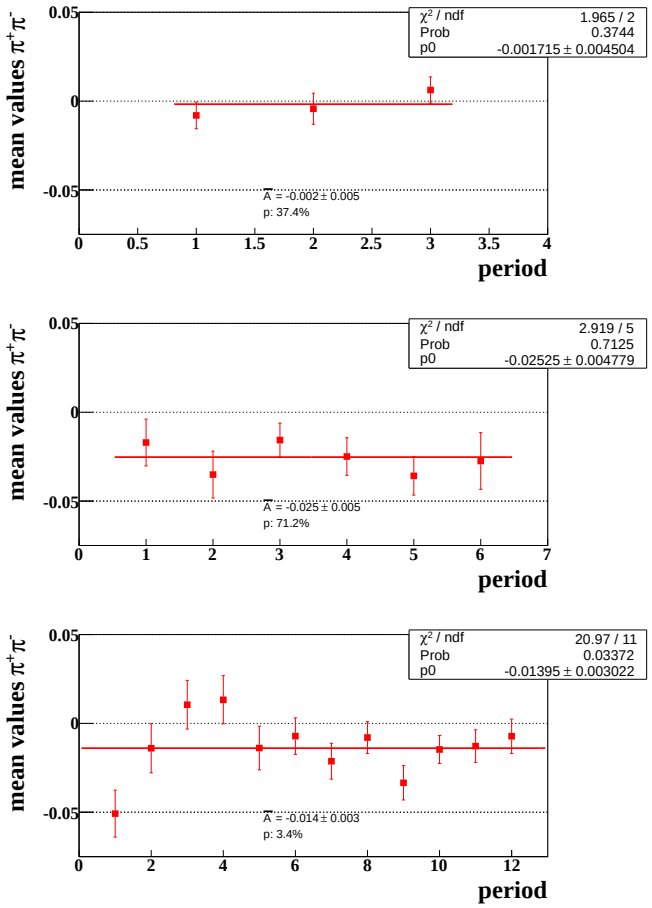

Figure A.28.: The mean values of the hadron-pair asymmetry in x for $\pi^+\pi^-$ pairs as a function of x from deuteron (1st row), 2007 (2nd row), and 2010 (3rd row) data from each of the 3, 6 or 12 individual periods.

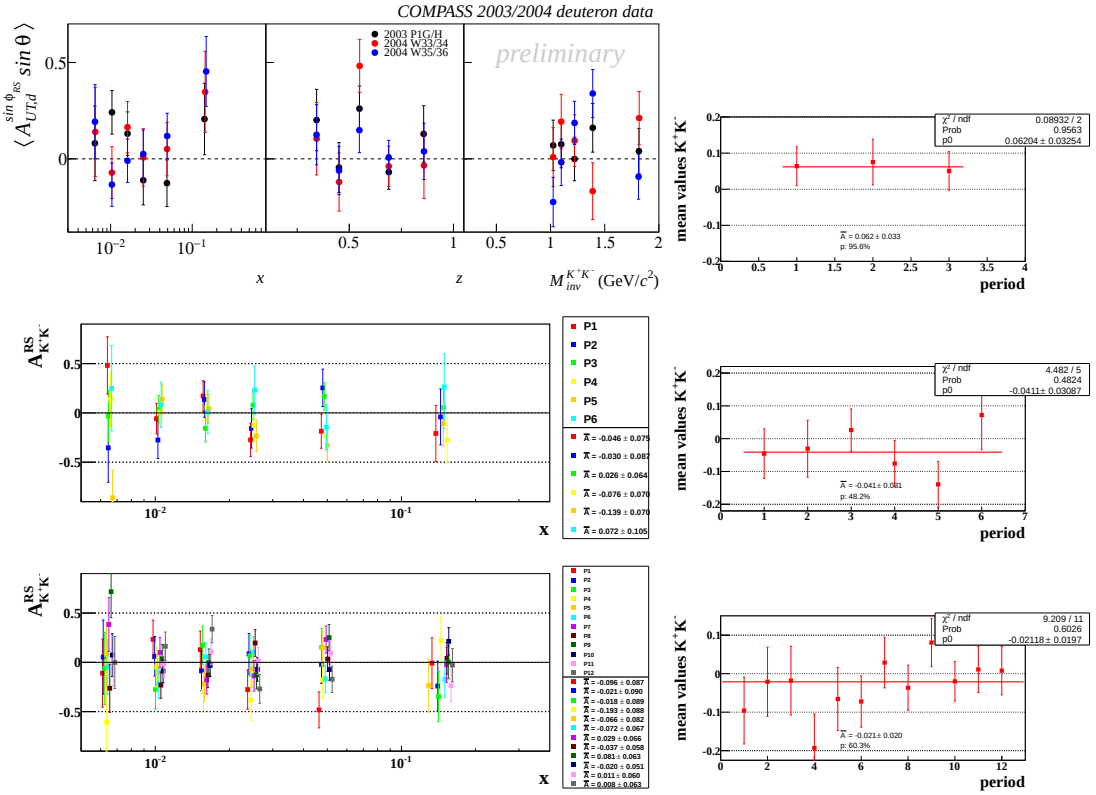

Figure A.29.: The hadron-pair asymmetries of K^+K^- pairs as a function of x from deuteron (1st row), 2007 (2nd row, and 2010 (3rd from each of the 6 or 12 individual periods. row its mean values. The mean values of the asymmetry in x are shown in the right column.

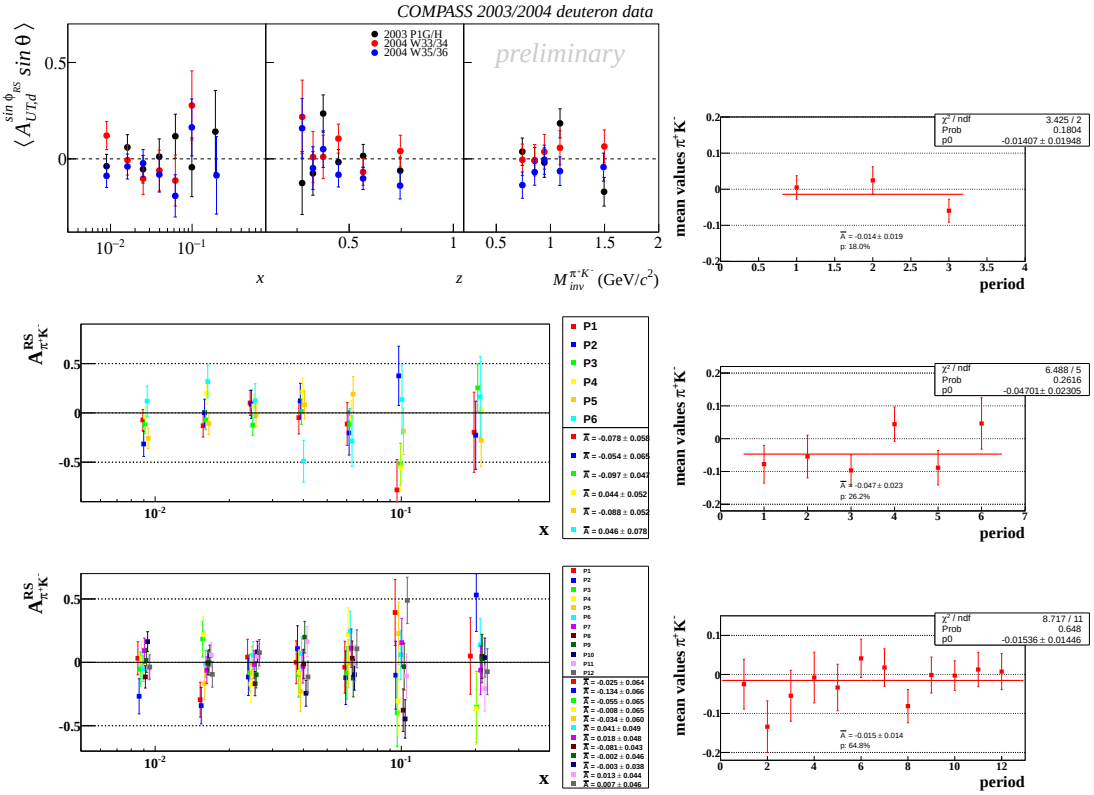

Figure A.30.: The hadron-pair asymmetries of π^+K^- pairs as a function of x from deuteron (1st row), 2007 (2nd row), and 2010 (3rd row) data from each of the 3, 6 or 12 individual periods. The mean values of the asymmetry in x are shown in the right column.

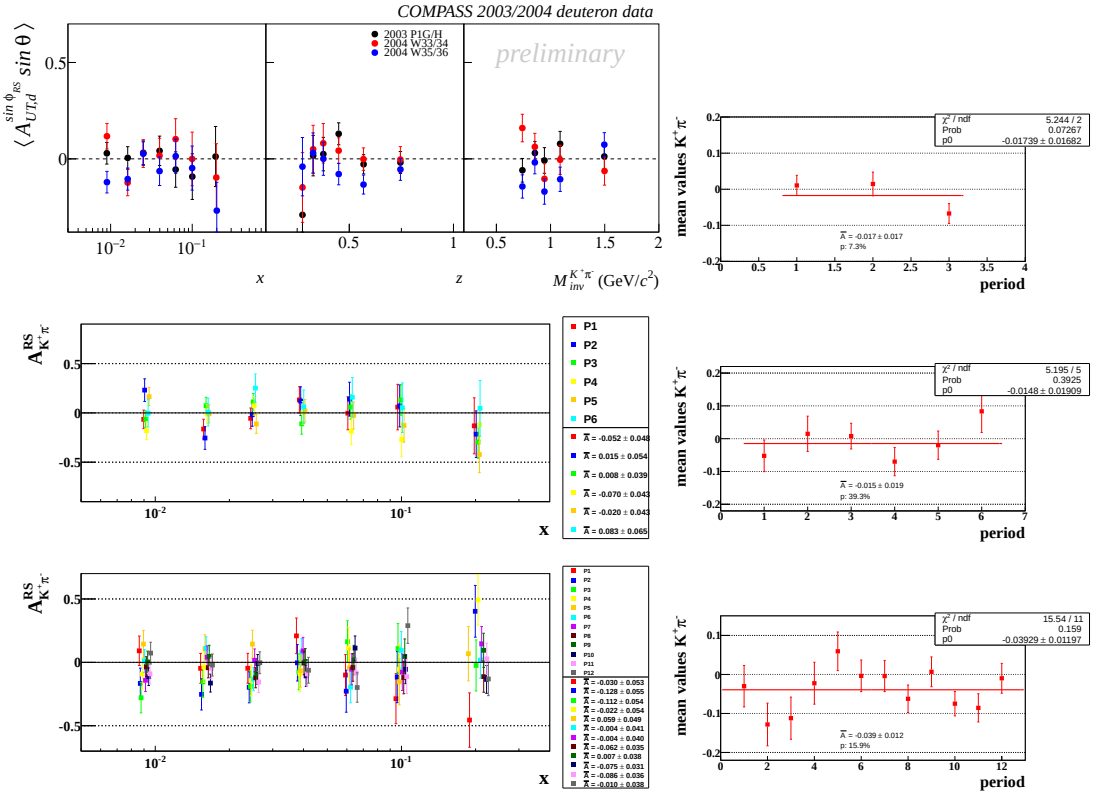

Figure A.31.: The hadron-pair asymmetries of $K^+\pi^-$ pairs as a function of x from deuteron (1st row), 2007 (2nd row), and 2010 (3rd row) data from each of the 3, 6 or 12 individual periods. The mean values of the asymmetry in x are shown in the right column.

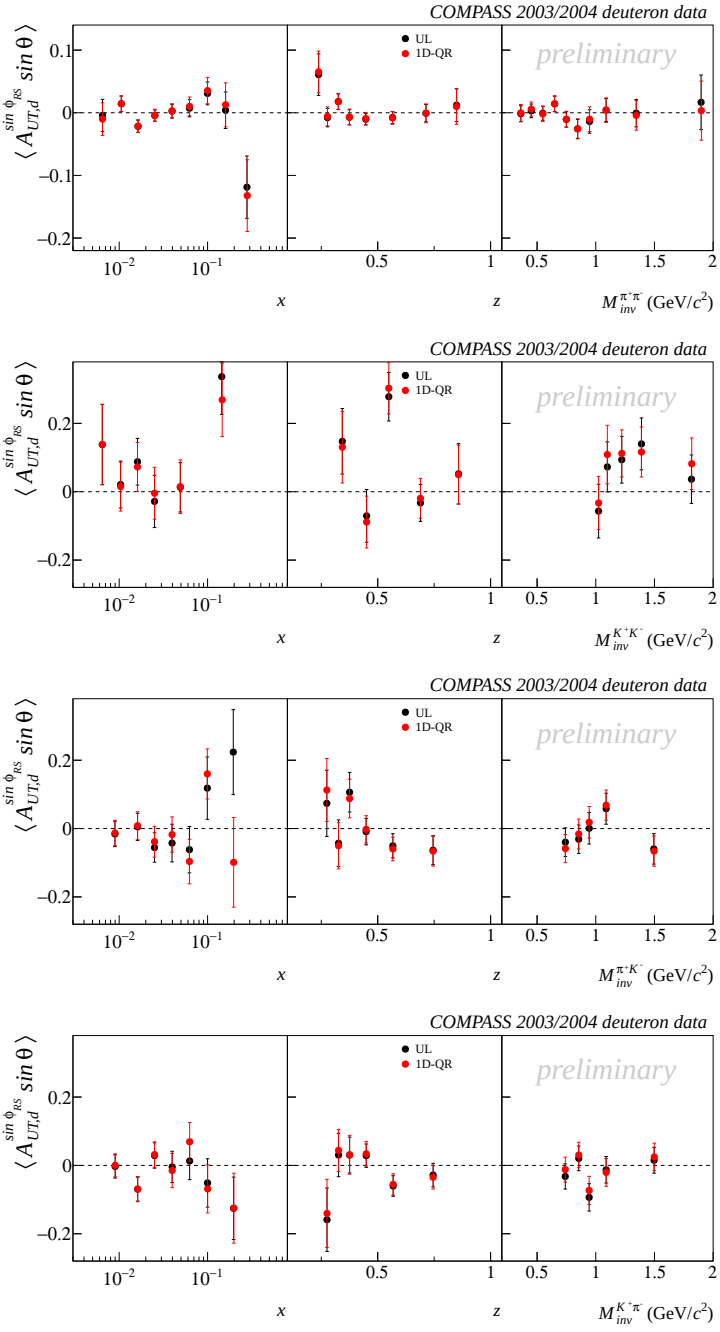

Figure A.32.: The $\pi^+\pi^-$ (from top to bottom right), K^+K^-, π^+K^-, and $K^+\pi^-$ pair asymmetries from deuteron data obtained with the 1D-QR (red dots) and the UL estimator (black dots).

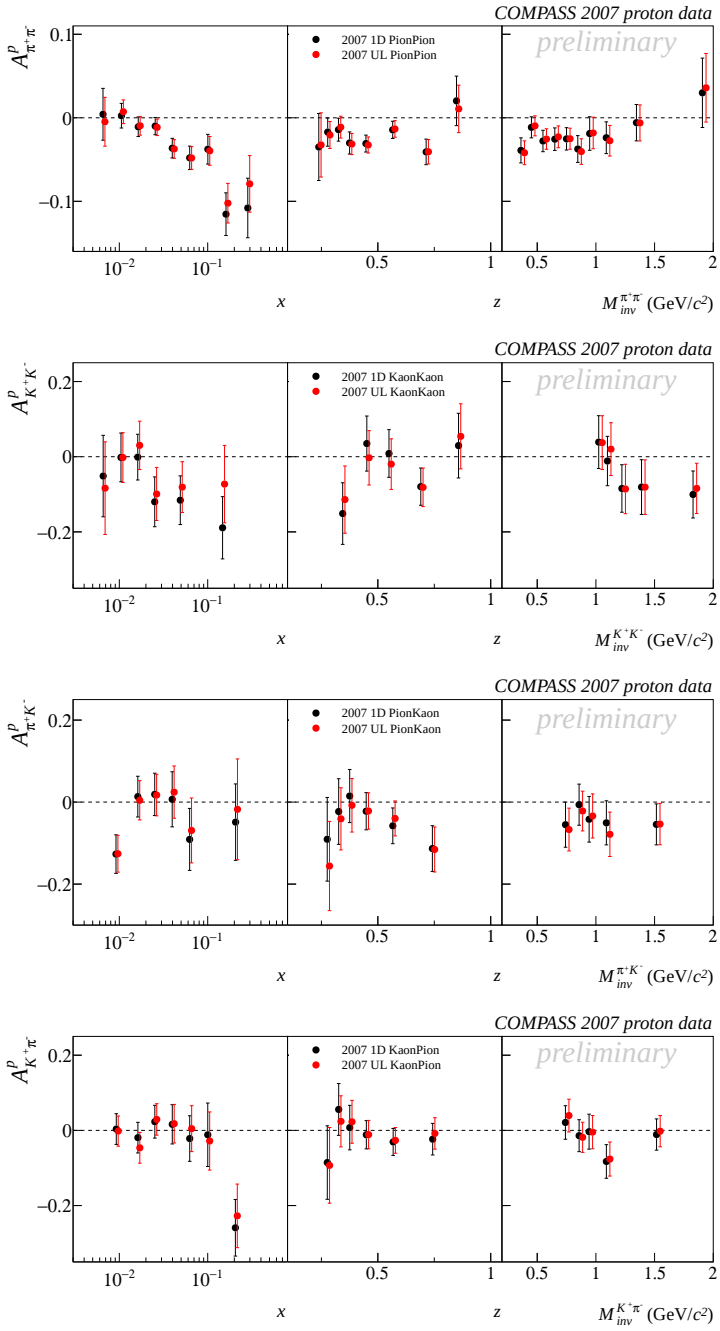

Figure A.33.: The $\pi^+\pi^-$ (from top left to bottom right), K^+K^-, π^+K^-, and $K^+\pi^-$ pair asymmetries from 2007 data obtained with the 1D-QR (red dots) and the UL estimator (black dots).

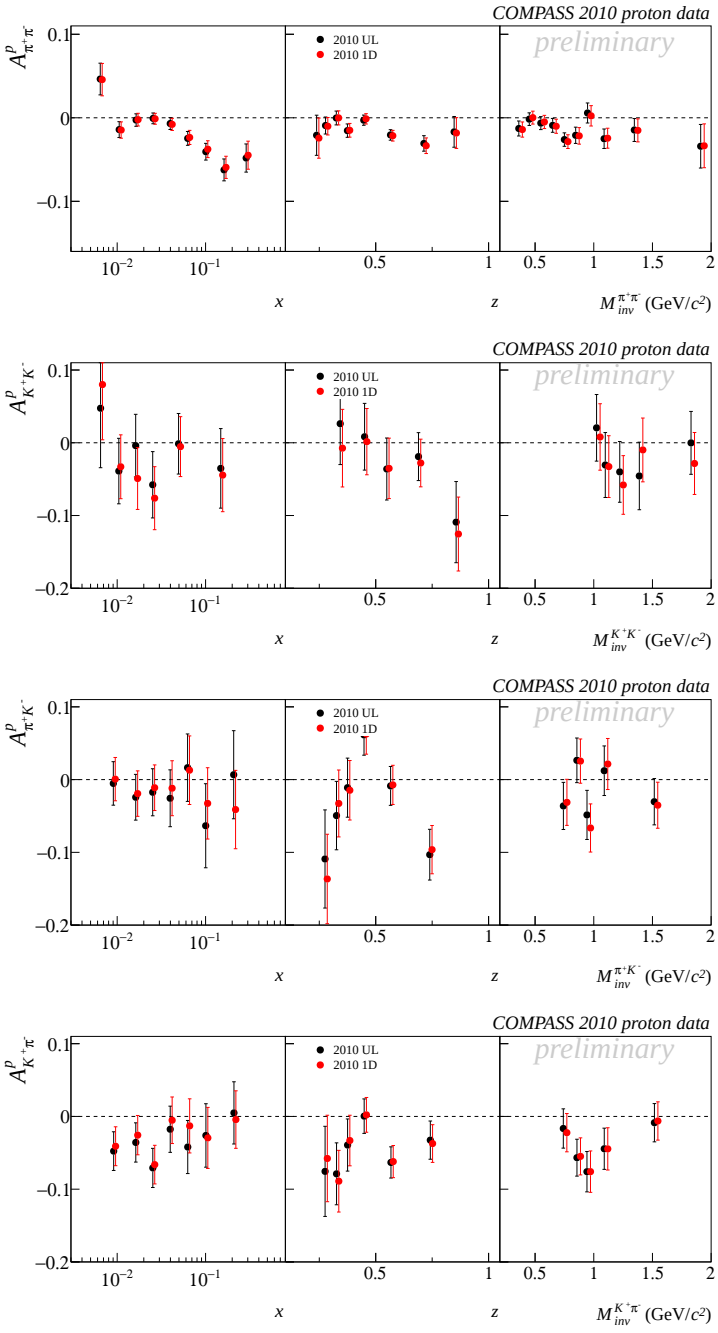

Figure A.34.: The $\pi^+\pi^-$ (from top left to bottom right), K^+K^-, π^+K^-, and $K^+\pi^-$ pair asymmetries from 2010 data obtained with the 1D-QR (red dots) and the UL estimator (black dots).

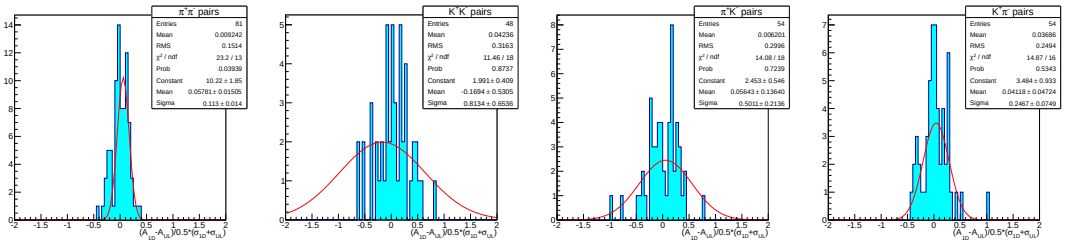

Figure A.35.: Pulls between the hadron-pair asymmetries from deuteron data obtained with the 1D-QR and the UL estimator $\pi^+\pi^-$ pairs (1$^{\text{st}}$ column), K^+K^- pairs (2$^{\text{nd}}$ column), π^+K^- pairs (3$^{\text{rd}}$ column), and $K^+\pi^-$ pairs (4$^{\text{th}}$ column).

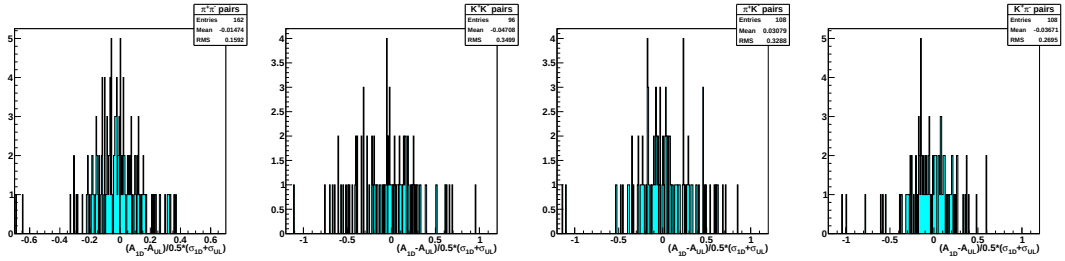

Figure A.36.: Pulls between the hadron-pair asymmetries from 2007 data obtained with the 1D-QR and the UL estimator $\pi^+\pi^-$ pairs (1$^{\text{st}}$ column), K^+K^- pairs (2$^{\text{nd}}$ column), π^+K^- pairs (3$^{\text{rd}}$ column), and $K^+\pi^-$ pairs (4$^{\text{th}}$ column).

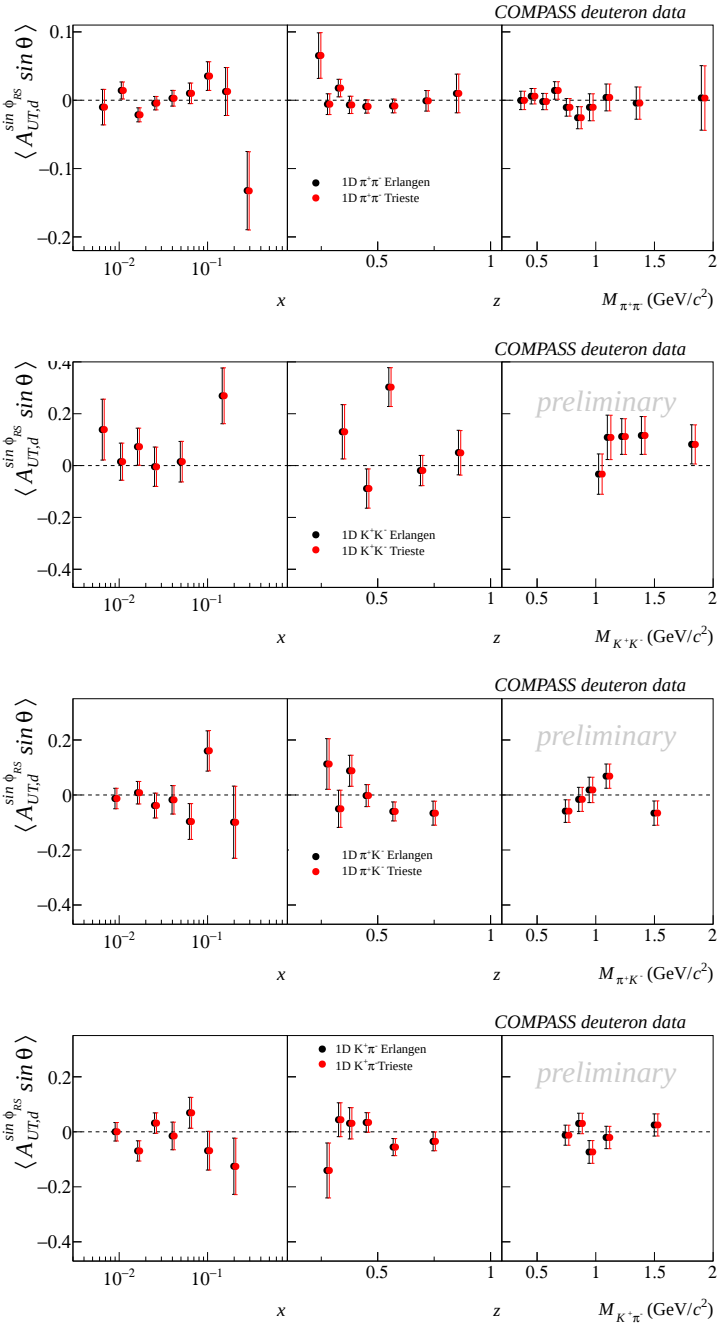

Figure A.37.: Cross-check of $\pi^+\pi^-$ (from top left to bottom right), K^+K^-, π^+K^-, and $K^+\pi^-$ pair asymmetries from deuteron data obtained with the 1D-QR method: Trieste analysis (red dots) and Erlangen analysis (black dots).

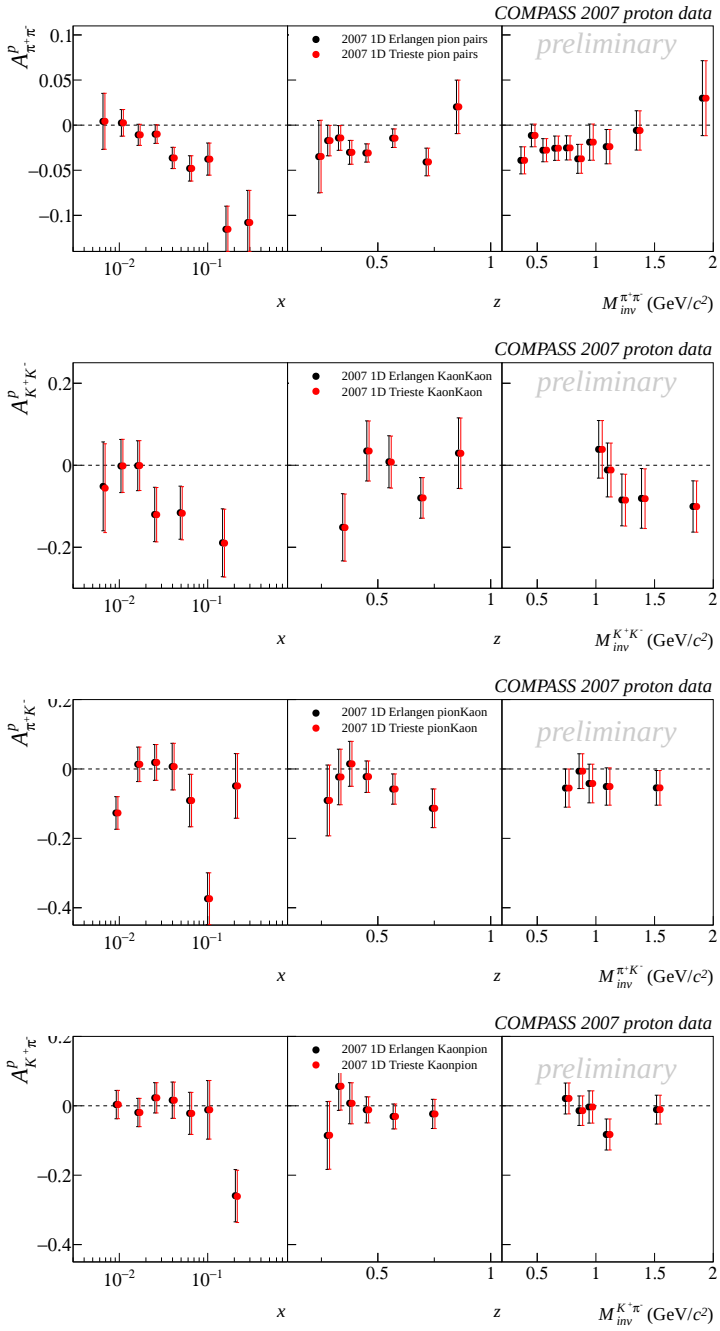

Figure A.38.: Cross-check of $\pi^+\pi^-$ (from top left to bottom right), K^+K^-, π^+K^-, and $K^+\pi^-$ pair asymmetries from 2007 data obtained with the 1D-QR method: Trieste analysis (red dots) and Erlangen analysis (black dots).

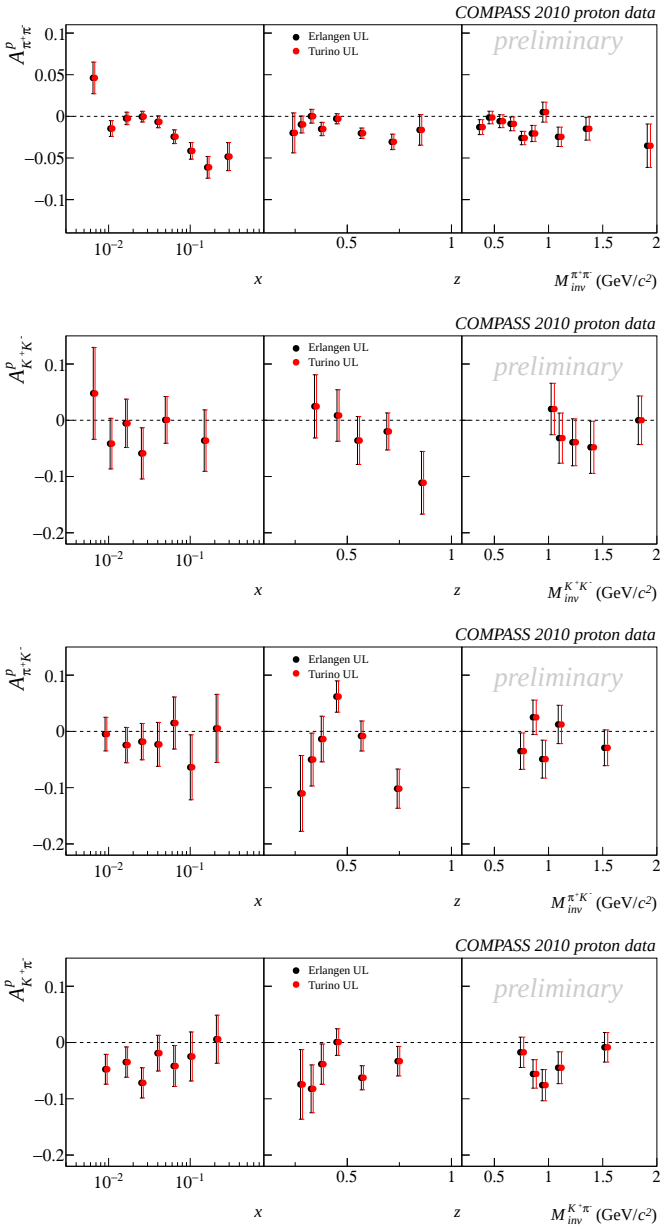

Figure A.39.: Cross-check of $\pi^+\pi^-$ (from top left to bottom right), K^+K^-, π^+K^-, and $K^+\pi^-$ pair asymmetries from 2007 data obtained with the UL method: Turino analysis (red dots) and Erlangen analysis (black dots).

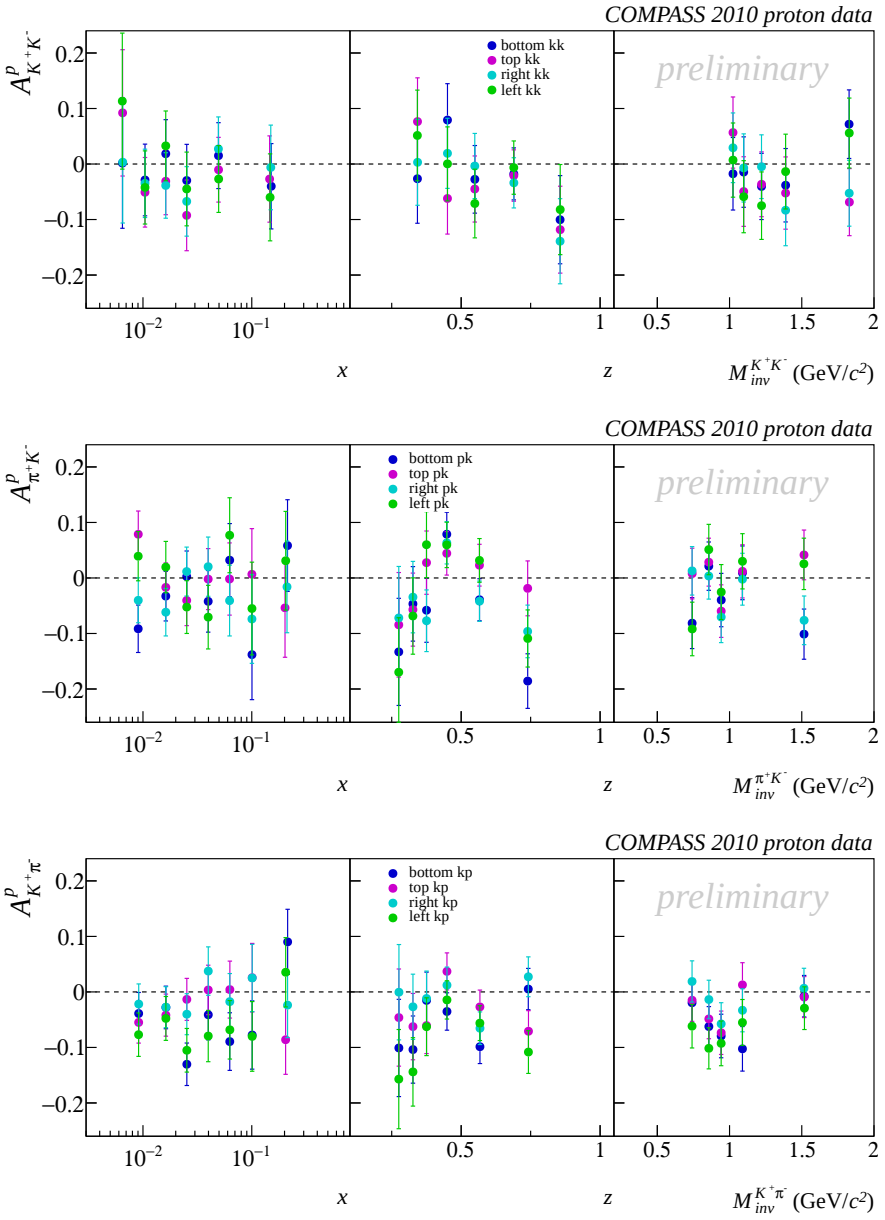

Figure A.40.: The pion pair asymmetry evaluated for a split of the spectrometer into top, bottom, left and right from 2007 data (top), and 2010 data (bottom): K^+K^- pairs (1$^{\text{st}}$ column), π^+K^- pairs (2$^{\text{nd}}$ column), and $K^+\pi^-$ pairs (3$^{\text{rd}}$ column).

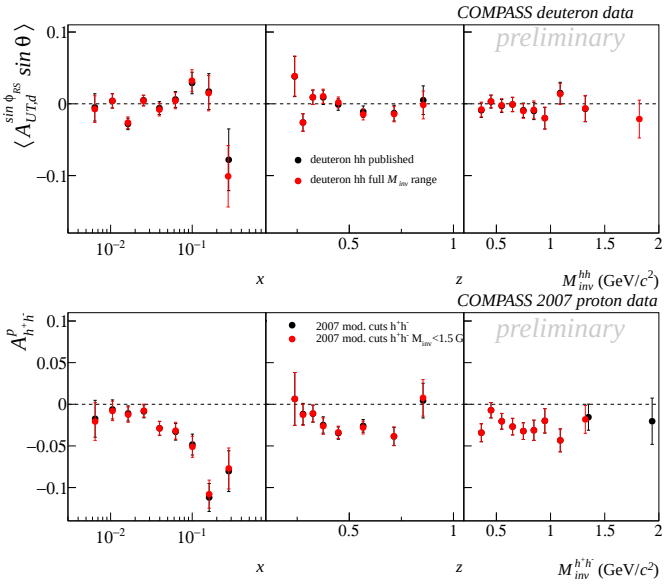

Figure A.41.: The published hadron-pair asymmetry (black dots) of h^+h^- pairs from deuteron data (top panel) and from 2007 proton data (bottom panel) in comparison with the results obtained without a cut on M_{inv} (red dots).

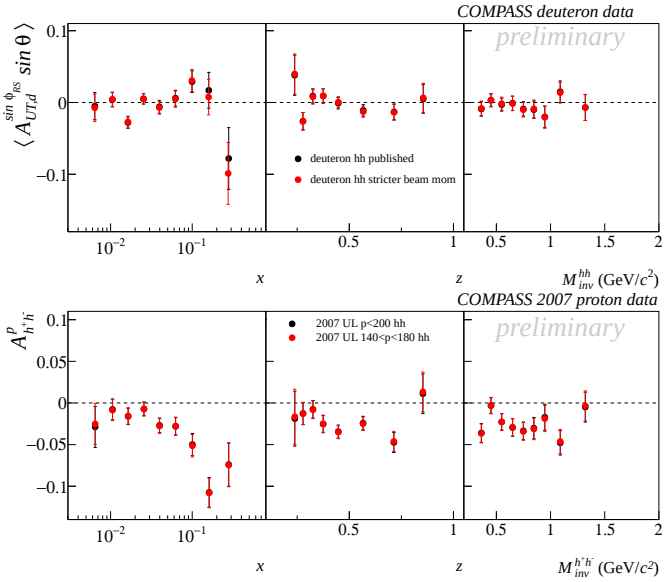

Figure A.42.: The published hadron-pair asymmetry (black dots) of h^+h^- pairs from deuteron data (top panel) and from 2007 proton data (bottom panel) in comparisonn with the results obtained with a stricter cut p_{beam} (red dots).

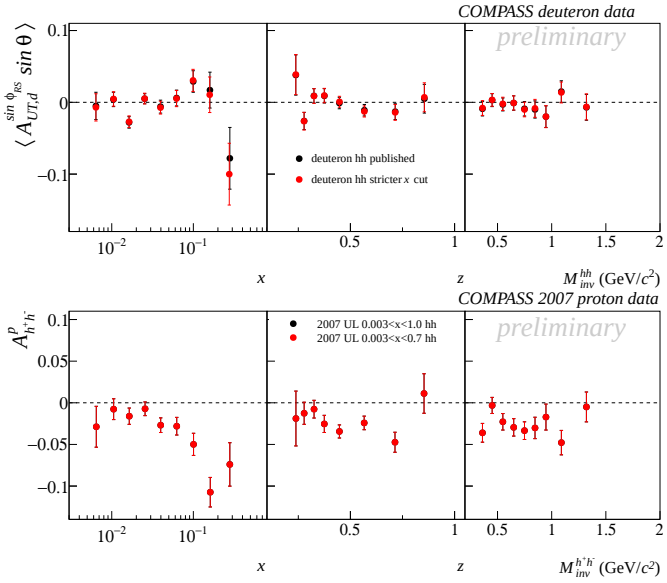

Figure A.43.: The published hadron-pair asymmetry (black dots) of h^+h^- pairs from deuteron data (top panel) and from 2007 proton data (bottom panel) in comparison with the results obtained with the stricter cut on x (red dots).

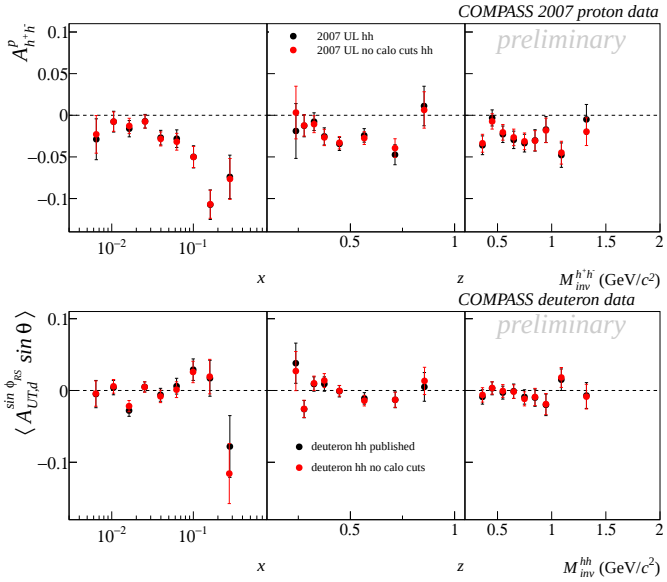

Figure A.44.: The published hadron-pair asymmetry (black dots) of h^+h^- pairs from deuteron data (top panel) and from 2007 proton data (bottom panel) in comparison with the results obtained without any cuts an calorimeter data (red dots).

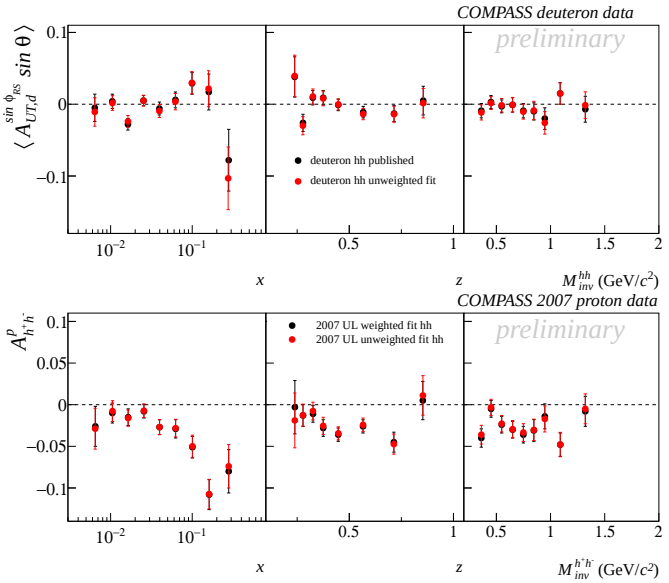

Figure A.45.: The published hadron-pair asymmetry (black dots) of h^+h^- pairs from deuteron (top panel) and from 2007 proton data (bottom panel) in comparison with the results obtained without pre-weightening before the UL fit with y and D_{nn} (red dots).

Table A.7.: χ^2 values of the minimization of method B bin-by-bin. Statistical and systematical uncertainties have been considered.

$\pi^+\pi^-$	1	2	3	4	5	6	7	8	9	10
x	1.52	1.17	0.20	0.63	3.82	1.57	0.01	1.62	0.47	
z	0.05	0.23	0.38	0.83	4.83	0.25	0.24	0.45		
M_{inv}	2.10	0.24	1.29	0.56	0.00	0.85	0.76	0.01	0.08	1.52
K^+K^-	1	2	3	4	5	6				
x	0.62	0.19	0.17	0.18	0.82	0.08				
z	1.35	0.01	0.03	0.80	2.01					
M_{inv}	0.03	0.30	0.28	0.11	0.87					
π^+K^-	1	2	3	4	5	6	7			
x	3.61	0.18	0.25	0.29	0.59	0.02	0.09			
z	0.01	0.01	0.00	1.83	0.28	0.03				
M_{inv}	0.19	0.48	0.04	1.44	0.12					
$K^+\pi^-$	1	2	3	4	5	6	7			
x	0.73	0.05	3.34	0.30	0.34	0.00	4.93			
z	0.02	1.43	0.67	0.06	0.65	0.21				
M_{inv}	1.00	0.50	1.51	0.28	0.014					

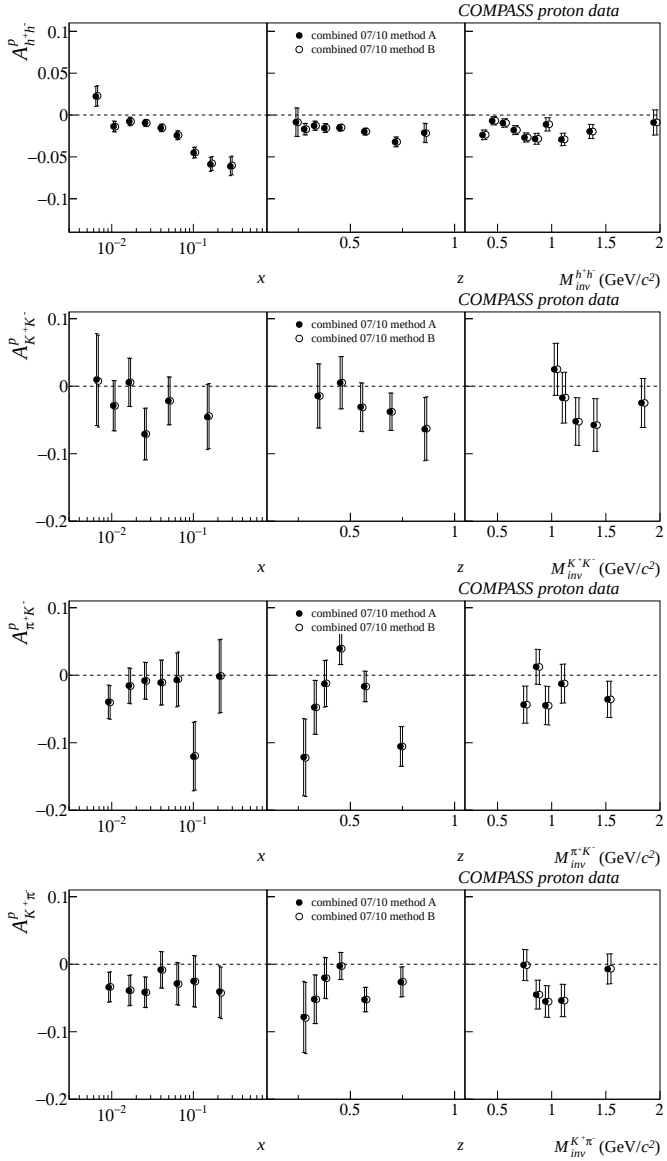

Figure A.46.: Comparison of the results obtained with method A (black dots) ad method B (red dots) of the combination of the 2007, and 2010 proton identified hadron-pair asymmetries: h^+h^- pairs (1$^{\text{st}}$ row), $\pi^+\pi^-$ pairs (2$^{\text{nd}}$ row), K^+K^- pairs (3$^{\text{rd}}$ row), π^+K^- pairs (4$^{\text{th}}$ row), and $K^+\pi^-$ pairs (5$^{\text{th}}$ row).

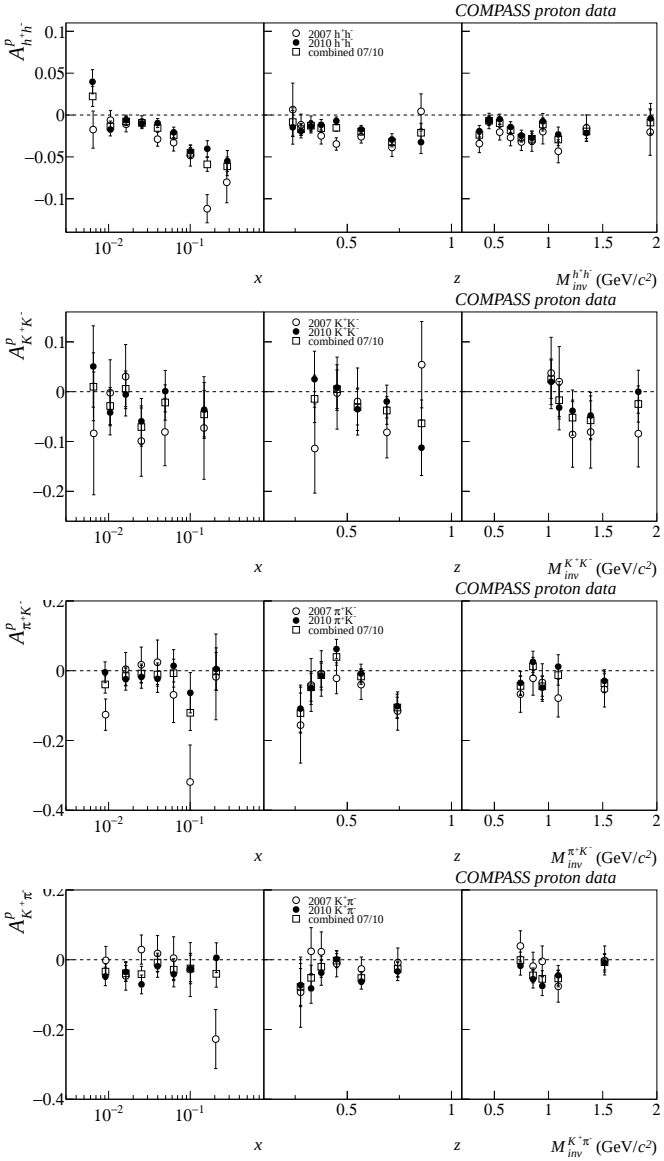

Figure A.47.: Hadron-pair asymmetries obtained from the 2007 proton data (black dots), the 2010 proton data (red dots) and the result of their combination (blue dots): h^+h^- pairs (1st row), $\pi^+\pi^-$ pairs (2nd row), K^+K^- pairs (3rd row), π^+K^- pairs (4th row), and $K^+\pi^-$ pairs (5th row).

A.4. Results

Table A.8.: Binning for h^+h^-, $\pi^+\pi^-$, K^+K^-, π^+K^- and $K^+\pi^-$ pair samples: For the K^+K^- binning x bins 6 & 7 and 8 & 9, z bins 1 to 4 have been merged w.r.t. the pion pair standard sample, while for the mixed pairs π^+K^- and $K^+\pi^-$ sample x bins 1 & 2 and 8 & 9, z bins 1 & 2 and 7 & 8, M_{inv} bins 1 to 5 of the the pion pair standard sample have been merged; in order to assure maximum compliance between the binning of the different pair combinations taking also in account the available statistic.

sample	$h^+h^-/\pi^+\pi^-$ standard	$h^+h^-/\pi^+\pi^-$ $x > 0.032$	$h^+h^-/\pi^+\pi^-$ $M_{inv} < 1.5\,\mathrm{GeV}/c^2$	$h^+h^-/\pi^+\pi^-$ $x > 0.032$ & $M_{inv} < 1.5\,\mathrm{GeV}/c^2$	K^+K^-	π^+K^- $K^+\pi^-$
bins in x						
1	$[0.003, 0.008[$	$[0.032, 0.050[$	$[0.003, 0.008[$	$[0.032, 0.050[$	$[0.003, 0.008[$	$[0.003, 0.013[$
2	$[0.008, 0.013[$	$[0.050, 0.080[$	$[0.008, 0.013[$	$[0.050, 0.080[$	$[0.008, 0.013[$	$[0.013, 0.020[$
3	$[0.013, 0.020[$	$[0.080, 0.130[$	$[0.013, 0.020[$	$[0.080, 0.130[$	$[0.013, 0.020[$	$[0.020, 0.032[$
4	$[0.020, 0.032[$	$[0.130, 0.210[$	$[0.020, 0.032[$	$[0.130, 0.210[$	$[0.020, 0.032[$	$[0.032, 0.050[$
5	$[0.032, 0.050[$	$[0.210, 1.000[$	$[0.032, 0.050[$	$[0.210, 1.000]$	$[0.032, 0.080[$	$[0.050, 0.080[$
6	$[0.050, 0.080[$		$[0.050, 0.080[$		$[0.080, 1.000]$	$[0.080, 0.130[$
7	$[0.080, 0.130[$		$[0.080, 0.130[$			$[0.130, 1.000]$
8	$[0.130, 0.210[$		$[0.130, 0.210[$			
9	$[0.210, 1.000]$		$[0.210, 1.000]$			
bins in z						
1	$[0.20, 0.25[$	$[0.20, 0.25[$	$[0.20, 0.25[$	$[0.20, 0.25[$	$[0.20, 0.40[$	$[0.20, 0.30[$
2	$[0.25, 0.30[$	$[0.25, 0.30[$	$[0.25, 0.30[$	$[0.25, 0.30[$	$[0.40, 0.50[$	$[0.30, 0.35[$
3	$[0.30, 0.35[$	$[0.30, 0.35[$	$[0.30, 0.35[$	$[0.30, 0.35[$	$[0.50, 0.65[$	$[0.35, 0.40[$
4	$[0.35, 0.40[$	$[0.35, 0.40[$	$[0.35, 0.40[$	$[0.35, 0.40[$	$[0.65, 0.80[$	$[0.40, 0.50[$
5	$[0.40, 0.50[$	$[0.40, 0.50[$	$[0.40, 0.50[$	$[0.40, 0.50[$	$[0.80, 1.00]$	$[0.50, 0.65]$
6	$[0.50, 0.65[$	$[0.50, 0.65[$	$[0.50, 0.65[$	$[0.50, 0.65[$		$[0.65, 1.00[$
7	$[0.65, 0.80[$	$[0.65, 0.80[$	$[0.65, 0.80[$	$[0.65, 0.80[$		
8	$[0.80, 1.00]$	$[0.80, 1.00]$	$[0.80, 1.00]$	$[0.80, 1.00]$		
bins in M_{inv}						
1	$[0.0, 0.4[$	$[0.0, 0.4[$	$[0.0, 0.4[$	$[0.0, 0.4[$	$[0.90, 1.05[$	$[0.0, 0.8[$
2	$[0.4, 0.5[$	$[0.4, 0.5[$	$[0.4, 0.5[$	$[0.4, 0.5[$	$[1.05, 1.15[$	$[0.8, 0.9[$
3	$[0.5, 0.6[$	$[0.5, 0.6[$	$[0.5, 0.6[$	$[0.5, 0.6[$	$[1.15, 1.30[$	$[0.9, 1.0[$
4	$[0.6, 0.7[$	$[0.6, 0.7[$	$[0.6, 0.7[$	$[0.6, 0.7[$	$[1.30, 1.50[$	$[1.0, 1.2[$
5	$[0.7, 0.8[$	$[0.7, 0.8[$	$[0.7, 0.8[$	$[0.7, 0.8[$	$[1.50, 100.]$	$[1.2, 100]$
6	$[0.8, 0.9[$	$[0.8, 0.9[$	$[0.8, 0.9[$	$[0.8, 0.9[$		
7	$[0.9, 1.0[$	$[0.9, 1.0[$	$[0.9, 1.0[$	$[0.9, 1.0[$		
8	$[1.0, 1.2[$	$[1.0, 1.2[$	$[1.0, 1.2[$	$[1.0, 1.2[$		
9	$[1.2, 1.6[$	$[1.2, 1.6[$	$[1.2, 1.5]$	$[1.2, 1.5]$		
10	$[1.6, 100]$	$[1.6, 100]$				

Table A.9.: All h^+h^- pair deuteron data (2002-2004) data azimuthal asymmetry and corresponding mean kinematic values; Q^2 in $(\mathrm{GeV}/c)^2$, W and M_{inv} in GeV/c^2.

bin range x	A	σ_{stat}	σ_{sys}	$\langle x\rangle$	$\langle Q^2\rangle$	$\langle y\rangle$	$\langle z\rangle$	$\langle x\rangle$	$\langle W\rangle$	$\langle M_{inv}\rangle$	$\langle D_{nn}\rangle$
$[0.003, 0.008[$	-0.0098	0.0181	0.0109	0.0064	1.240	0.650	0.396	0.006	13.891	0.750	0.605
$[0.008, 0.013[$	0.0023	0.0096	0.0058	0.0105	1.471	0.471	0.427	0.011	11.739	0.731	0.803
$[0.013, 0.020[$	-0.0176	0.0078	0.0047	0.0163	1.738	0.359	0.448	0.016	10.154	0.706	0.886
$[0.020, 0.032[$	0.0032	0.0073	0.0044	0.0253	2.208	0.293	0.470	0.025	9.077	0.683	0.922
$[0.032, 0.050[$	-0.0112	0.0087	0.0052	0.0396	3.320	0.280	0.479	0.040	8.766	0.672	0.926
$[0.050, 0.080[$	-0.0012	0.0110	0.0066	0.0624	5.346	0.286	0.476	0.062	8.774	0.667	0.924
$[0.080, 0.130[$	0.0258	0.0150	0.0090	0.0998	8.578	0.287	0.474	0.100	8.615	0.658	0.923
$[0.130, 0.210[$	0.0316	0.0242	0.0145	0.1599	14.578	0.303	0.472	0.160	8.529	0.650	0.910
$[0.210, 1.000[$	-0.1137	0.0421	0.0253	0.2810	30.950	0.362	0.467	0.281	8.635	0.651	0.876
bin range z				$\langle z\rangle$							
$[0.20, 0.25[$	0.0273	0.0283	0.0170	0.2381	3.411	0.483	0.238	0.026	11.712	0.517	0.775
$[0.25, 0.30[$	-0.0293	0.0124	0.0074	0.2775	3.363	0.428	0.278	0.029	10.981	0.587	0.823
$[0.30, 0.35[$	0.0119	0.0102	0.0061	0.3254	3.314	0.398	0.325	0.031	10.544	0.632	0.846
$[0.35, 0.40[$	0.0146	0.0099	0.0059	0.3747	3.306	0.376	0.375	0.033	10.221	0.664	0.861
$[0.40, 0.50[$	-0.0007	0.0074	0.0044	0.4471	3.260	0.352	0.447	0.035	9.868	0.702	0.877
$[0.50, 0.65[$	-0.0178	0.0074	0.0044	0.5657	3.162	0.319	0.556	0.038	9.363	0.754	0.902
$[0.65, 0.80[$	-0.0118	0.0105	0.0063	0.7138	2.972	0.279	0.714	0.040	8.767	0.809	0.930
$[0.80, 1.00[$	-0.0002	0.0186	0.0112	0.8489	2.778	0.282	0.849	0.035	8.914	0.865	0.935
bin range M_{inv}				$\langle M_{inv}\rangle$							
$[0.0, 0.4[$	-0.0098	0.0102	0.0061	0.3614	3.313	0.336	0.405	0.038	9.607	0.361	0.888
$[0.4, 0.5[$	0.0029	0.0088	0.0053	0.4506	3.267	0.340	0.426	0.037	9.678	0.451	0.886
$[0.5, 0.6[$	0.0012	0.0091	0.0055	0.5488	3.247	0.347	0.434	0.036	9.782	0.549	0.881
$[0.6, 0.7[$	-0.0025	0.0097	0.0058	0.6495	3.207	0.354	0.446	0.034	9.892	0.649	0.876
$[0.7, 0.8[$	-0.0127	0.0100	0.0060	0.7493	3.171	0.360	0.473	0.033	9.984	0.749	0.872
$[0.8, 0.9[$	-0.0113	0.0122	0.0073	0.8458	3.191	0.369	0.483	0.033	10.115	0.846	0.866
$[0.9, 1.0[$	-0.0263	0.0151	0.0091	0.9470	3.223	0.378	0.487	0.032	10.257	0.947	0.859
$[1.0, 1.2[$	0.0204	0.0143	0.0086	1.0880	3.190	0.389	0.502	0.031	10.413	1.088	0.852
$[1.2, 1.5[$	0.0032	0.0166	0.0100	1.3450	3.207	0.406	0.539	0.029	10.674	1.345	0.841
$[1.5, 100[$	-0.0473	0.0306	0.0184	1.8997	3.290	0.450	0.581	0.027	11.293	1.900	0.807

Table A.10.: Identified $\pi^+\pi^-$ deuteron data (2003-2004) data azimuthal asymmetry and corresponding mean kinematic values; Q^2 in $(\mathrm{GeV}/c)^2$, W and M_{inv} in GeV/c^2.

bin range x	A	σ_{stat}	σ_{sys}	$\langle x\rangle$	$\langle Q^2\rangle$	$\langle y\rangle$	$\langle z\rangle$	$\langle x\rangle$	$\langle W\rangle$	$\langle M_{inv}\rangle$	$\langle D_{nn}\rangle$
$[0.003, 0.008[$	-0.0042	0.0256	0.0154	0.0065	1.257	0.667	0.446	0.007	14.087	0.775	0.578
$[0.008, 0.013[$	0.0144	0.0124	0.0074	0.0106	1.523	0.489	0.454	0.011	11.967	0.750	0.783
$[0.013, 0.020[$	-0.0216	0.0098	0.0059	0.0164	1.816	0.375	0.466	0.016	10.378	0.722	0.872
$[0.020, 0.032[$	-0.0044	0.0090	0.0054	0.0253	2.282	0.303	0.482	0.025	9.208	0.692	0.913
$[0.032, 0.050[$	0.0026	0.0109	0.0065	0.0396	3.334	0.281	0.488	0.040	8.755	0.674	0.923
$[0.050, 0.080[$	0.0072	0.0137	0.0082	0.0625	5.341	0.286	0.486	0.062	8.741	0.671	0.921
$[0.080, 0.130[$	0.0309	0.0182	0.0109	0.1000	8.651	0.289	0.485	0.100	8.622	0.664	0.918
$[0.130, 0.210[$	0.0040	0.0291	0.0175	0.1599	14.783	0.308	0.485	0.160	8.562	0.658	0.905
$[0.210, 1.000[$	-0.1188	0.0498	0.0300	0.2813	31.539	0.369	0.482	0.281	8.705	0.663	0.869
bin range z				$\langle z\rangle$							
$[0.20, 0.25[$	0.0609	0.0332	0.0199	0.2381	3.255	0.488	0.238	0.025	11.775	0.515	0.765
$[0.25, 0.30[$	-0.0078	0.0147	0.0088	0.2776	3.218	0.435	0.278	0.028	11.047	0.585	0.812
$[0.30, 0.35[$	0.0178	0.0123	0.0074	0.3255	3.188	0.408	0.326	0.030	10.665	0.632	0.833
$[0.35, 0.40[$	-0.0071	0.0120	0.0072	0.3748	3.189	0.391	0.375	0.032	10.414	0.666	0.846
$[0.40, 0.50[$	-0.0103	0.0092	0.0055	0.4476	3.163	0.373	0.448	0.033	10.144	0.707	0.858
$[0.50, 0.65[$	-0.0076	0.0095	0.0057	0.5671	3.110	0.352	0.567	0.035	9.817	0.764	0.872
$[0.65, 0.80[$	-0.0007	0.0138	0.0083	0.7151	3.004	0.332	0.715	0.036	9.517	0.830	0.885
$[0.80, 1.00[$	0.0121	0.0262	0.0157	0.8558	2.874	0.369	0.856	0.030	10.109	0.898	0.862
bin range M_{inv}				$\langle M_{inv}\rangle$							
$[0.0, 0.4[$	-0.0016	0.0128	0.0077	0.3615	3.155	0.347	0.415	0.036	9.744	0.361	0.875
$[0.4, 0.5[$	0.0030	0.0109	0.0065	0.4505	3.132	0.353	0.437	0.035	9.831	0.450	0.872
$[0.5, 0.6[$	-0.0006	0.0113	0.0068	0.5490	3.135	0.364	0.448	0.034	10.003	0.549	0.864
$[0.6, 0.7[$	0.0142	0.0122	0.0073	0.6495	3.120	0.375	0.463	0.033	10.172	0.649	0.857
$[0.7, 0.8[$	-0.0106	0.0122	0.0073	0.7489	3.088	0.382	0.490	0.032	10.277	0.749	0.852
$[0.8, 0.9[$	-0.0257	0.0151	0.0091	0.8461	3.126	0.392	0.499	0.031	10.430	0.846	0.845
$[0.9, 1.0[$	-0.0139	0.0187	0.0112	0.9471	3.161	0.403	0.505	0.030	10.587	0.947	0.837
$[1.0, 1.2[$	0.0044	0.0183	0.0110	1.0892	3.162	0.416	0.520	0.029	10.786	1.089	0.827
$[1.2, 1.5[$	-0.0006	0.0220	0.0132	1.3492	3.187	0.440	0.558	0.027	11.116	1.349	0.809
$[1.5, 100[$	0.0167	0.0435	0.0261	1.9292	3.284	0.494	0.605	0.025	11.852	1.929	0.762

Table A.11.: Identified $\pi^+\pi^-$ pair deuteron data (2003-2004) data azimuthal asymmetry with a cut on $x > 0.032$ (left sub-table), on $M_{inv} < 1.5\,\mathrm{GeV}/c^2$ (center sub-table) and both cuts (right sub-table); Q^2 in $(\mathrm{GeV}/c)^2$, W and M_{inv} in GeV/c^2.

bin range x	A	σ_{stat}	σ_{sys}	$\langle x \rangle$
$[0.032, 0.050[$	0.0026	0.0109	0.0065	0.0396
$[0.050, 0.080[$	0.0072	0.0137	0.0082	0.0624
$[0.080, 0.130[$	0.0309	0.0182	0.0109	0.0997
$[0.130, 0.210[$	0.0040	0.0291	0.0175	0.1597
$[0.210, 1.000[$	-0.1188	0.0498	0.0299	0.2787
bin range z				$\langle z \rangle$
$[0.20, 0.25[$	0.0463	0.0653	0.0392	0.2386
$[0.25, 0.30[$	0.0123	0.0269	0.0161	0.2780
$[0.30, 0.35[$	0.0172	0.0215	0.0129	0.3258
$[0.35, 0.40[$	-0.0121	0.0202	0.0121	0.3751
$[0.40, 0.50[$	-0.0005	0.0148	0.0089	0.4479
$[0.50, 0.65[$	0.0005	0.0146	0.0088	0.5673
$[0.65, 0.80[$	0.0240	0.0205	0.0123	0.7146
$[0.80, 1.00[$	0.0398	0.0428	0.0257	0.8427
bin range M_{inv}				$\langle M_{inv} \rangle$
$[0.0, 0.4[$	0.0273	0.0197	0.0118	0.3612
$[0.4, 0.5[$	-0.0122	0.0170	0.0102	0.4502
$[0.5, 0.6[$	0.0111	0.0180	0.0108	0.5483
$[0.6, 0.7[$	0.0196	0.0198	0.0119	0.6489
$[0.7, 0.8[$	-0.0064	0.0203	0.0122	0.7489
$[0.8, 0.9[$	-0.0063	0.0254	0.0152	0.8455
$[0.9, 1.0[$	0.0110	0.0320	0.0192	0.9464
$[1.0, 1.2[$	0.0152	0.0320	0.0192	1.0868
$[1.2, 1.5[$	-0.0210	0.0401	0.0241	1.3403
$[1.5, 100[$	0.1116	0.0846	0.0508	1.8866

bin range x	A	σ_{stat}	σ_{sys}	$\langle x \rangle$
$[0.003, 0.008[$	-0.0072	0.0260	0.0156	0.0065
$[0.008, 0.013[$	0.0137	0.0126	0.0076	0.0106
$[0.013, 0.020[$	-0.0223	0.0098	0.0059	0.0163
$[0.020, 0.032[$	-0.0036	0.0090	0.0054	0.0253
$[0.032, 0.050[$	0.0018	0.0110	0.0066	0.0396
$[0.050, 0.080[$	0.0076	0.0137	0.0082	0.0624
$[0.080, 0.130[$	0.0285	0.0183	0.0110	0.0997
$[0.130, 0.210[$	-0.0019	0.0293	0.0176	0.1597
$[0.210, 1.000[$	-0.1251	0.0500	0.0300	0.2787
bin range z				$\langle z \rangle$
$[0.20, 0.25[$	0.0609	0.0332	0.0199	0.2381
$[0.25, 0.30[$	-0.0078	0.0147	0.0088	0.2774
$[0.30, 0.35[$	0.0175	0.0123	0.0074	0.3254
$[0.35, 0.40[$	-0.0082	0.0121	0.0073	0.3747
$[0.40, 0.50[$	-0.0123	0.0093	0.0056	0.4470
$[0.50, 0.65[$	-0.0044	0.0096	0.0058	0.5654
$[0.65, 0.80[$	-0.0074	0.0141	0.0085	0.7135
$[0.80, 1.00[$	0.0211	0.0270	0.0162	0.8490
bin range M_{inv}				$\langle M_{inv} \rangle$
$[0.0, 0.4[$	-0.0016	0.0128	0.0077	0.3613
$[0.4, 0.5[$	0.0030	0.0109	0.0065	0.4505
$[0.5, 0.6[$	-0.0006	0.0113	0.0068	0.5488
$[0.6, 0.7[$	0.0142	0.0122	0.0073	0.6494
$[0.7, 0.8[$	-0.0106	0.0122	0.0073	0.7493
$[0.8, 0.9[$	-0.0257	0.0151	0.0091	0.8458
$[0.9, 1.0[$	-0.0139	0.0187	0.0112	0.9469
$[1.0, 1.2[$	0.0044	0.0182	0.0109	1.0880
$[1.2, 1.5[$	-0.0048	0.0233	0.0140	1.3183

bin range x	A	σ_{stat}	σ_{sys}	$\langle x \rangle$
$[0.032, 0.050[$	0.0018	0.0110	0.0066	0.0396
$[0.050, 0.080[$	0.0076	0.0137	0.0082	0.0624
$[0.080, 0.130[$	0.0285	0.0183	0.0110	0.0997
$[0.130, 0.210[$	-0.0019	0.0293	0.0176	0.1597
$[0.210, 1.000[$	-0.1251	0.0502	0.0301	0.2787
bin range z				$\langle z \rangle$
$[0.20, 0.25[$	0.0463	0.0653	0.0392	0.2386
$[0.25, 0.30[$	0.0132	0.0269	0.0161	0.2780
$[0.30, 0.35[$	0.0170	0.0215	0.0129	0.3258
$[0.35, 0.40[$	-0.0135	0.0202	0.0121	0.3751
$[0.40, 0.50[$	-0.0009	0.0149	0.0089	0.4479
$[0.50, 0.65[$	0.0001	0.0147	0.0088	0.5672
$[0.65, 0.80[$	0.0184	0.0208	0.0125	0.7144
$[0.80, 1.00[$	0.0429	0.0441	0.0265	0.8422
bin range M_{inv}				$\langle M_{inv} \rangle$
$[0.0, 0.4[$	0.0273	0.0197	0.0118	0.3612
$[0.4, 0.5[$	-0.0122	0.0170	0.0102	0.4502
$[0.5, 0.6[$	0.0111	0.0180	0.0108	0.5483
$[0.6, 0.7[$	0.0196	0.0198	0.0119	0.6489
$[0.7, 0.8[$	-0.0064	0.0203	0.0122	0.7489
$[0.8, 0.9[$	-0.0063	0.0254	0.0152	0.8455
$[0.9, 1.0[$	0.0110	0.0320	0.0192	0.9464
$[1.0, 1.2[$	0.0152	0.0320	0.0192	1.0868
$[1.2, 1.5[$	-0.0356	0.0423	0.0254	1.3159

Table A.12.: Identified K^+K^- pair deuteron data (2003-2004) data azimuthal asymmetry and corresponding mean kinematic values; Q^2 in $(\mathrm{GeV}/c)^2$, W and M_{inv} in GeV/c^2.

bin range x	A	σ_{stat}	σ_{sys}	$\langle x \rangle$	$\langle Q^2 \rangle$	$\langle y \rangle$	$\langle z \rangle$	$\langle x \rangle$	$\langle W \rangle$	$\langle M_{inv} \rangle$	$\langle D_{nn} \rangle$
$[0.003, 0.008[$	0.1378	0.1176	0.0941	0.0064	1.250	0.657	0.467	0.006	13.981	1.342	0.595
$[0.008, 0.013[$	0.0211	0.0686	0.0549	0.0104	1.586	0.514	0.538	0.010	12.280	1.340	0.762
$[0.013, 0.020[$	0.0878	0.0683	0.0546	0.0161	2.154	0.448	0.586	0.016	11.377	1.329	0.818
$[0.020, 0.032[$	-0.0283	0.0765	0.0612	0.0251	3.223	0.428	0.602	0.025	11.064	1.313	0.834
$[0.032, 0.080[$	0.0129	0.0721	0.0577	0.0492	6.252	0.426	0.604	0.049	10.900	1.304	0.836
$[0.080, 1.000[$	0.3368	0.1103	0.0882	0.1467	19.527	0.436	0.603	0.147	10.420	1.280	0.825
bin range z				$\langle z \rangle$							
$[0.20, 0.40[$	0.1476	0.0960	0.0768	0.3432	4.024	0.617	0.343	0.023	13.417	1.244	0.645
$[0.40, 0.50[$	-0.0706	0.0772	0.0618	0.4508	4.174	0.544	0.451	0.027	12.531	1.308	0.727
$[0.50, 0.65[$	0.2781	0.0710	0.0568	0.5490	4.265	0.486	0.549	0.031	11.791	1.329	0.784
$[0.65, 0.80[$	-0.0327	0.0539	0.0431	0.6894	4.119	0.409	0.689	0.035	10.774	1.356	0.854
$[0.80, 1.00[$	0.0524	0.0884	0.0707	0.8577	3.703	0.351	0.858	0.037	9.988	1.378	0.900
bin range M_{inv}				$\langle M_{inv} \rangle$							
$[0.90, 1.05[$	-0.05668	0.0786	0.0629	1.0241	4.025	0.468	0.549	0.031	11.526	1.024	0.793
$[1.05, 1.15[$	0.07266	0.0734	0.0587	1.0986	4.422	0.491	0.543	0.033	11.801	1.099	0.773
$[1.15, 1.30[$	0.09368	0.0684	0.0547	1.2214	4.290	0.488	0.558	0.032	11.778	1.221	0.778
$[1.30, 1.50[$	0.14005	0.0760	0.0608	1.3891	4.082	0.484	0.574	0.030	11.737	1.389	0.782
$[1.50, 100.[$	0.03666	0.0710	0.0568	1.8174	3.684	0.490	0.598	0.027	11.848	1.817	0.777

Table A.13.: Identified π^+K^- pair deuteron data (2003-2004) data azimuthal asymmetry and corresponding mean kinematic values; Q^2 in $(\mathrm{GeV}/c)^2$, W and M_{inv} in GeV/c^2.

bin range x	A	σ_{stat}	σ_{sys}	$\langle x\rangle$	$\langle Q^2\rangle$	$\langle y\rangle$	$\langle z\rangle$	$\langle x\rangle$	$\langle W\rangle$	$\langle M_{inv}\rangle$	$\langle D_{nn}\rangle$
$[0.003, 0.013[$	-0.0158	0.0370	0.0259	0.0090	1.450	0.563	0.451	0.009	12.846	1.040	0.703
$[0.013, 0.020[$	0.0050	0.0397	0.0278	0.0161	2.020	0.420	0.506	0.016	10.993	1.022	0.839
$[0.020, 0.032[$	-0.0555	0.0430	0.0301	0.0251	2.886	0.385	0.528	0.025	10.425	1.013	0.862
$[0.032, 0.050[$	-0.0425	0.0551	0.0386	0.0396	4.548	0.384	0.530	0.040	10.324	1.008	0.862
$[0.050, 0.080[$	-0.0617	0.0679	0.0475	0.0623	7.074	0.380	0.527	0.062	10.159	0.999	0.865
$[0.080, 0.130[$	0.1183	0.0912	0.0638	0.0994	11.308	0.380	0.528	0.099	9.940	0.993	0.862
$[0.130, 1.000[$	0.2238	0.1243	0.0870	0.1976	24.796	0.414	0.509	0.198	9.795	0.984	0.838
bin range z				$\langle z\rangle$							
$[0.20, 0.30[$	0.0738	0.0968	0.0678	0.2746	3.674	0.624	0.275	0.020	13.514	0.922	0.636
$[0.30, 0.35[$	-0.0429	0.0681	0.0477	0.3264	3.637	0.561	0.326	0.023	12.748	0.967	0.708
$[0.35, 0.40[$	0.1065	0.0581	0.0407	0.3755	3.597	0.517	0.375	0.025	12.192	0.991	0.751
$[0.40, 0.50[$	-0.0090	0.0388	0.0272	0.4487	3.535	0.471	0.449	0.027	11.582	1.017	0.791
$[0.50, 0.65[$	-0.0505	0.0355	0.0249	0.5671	3.323	0.409	0.567	0.030	10.738	1.050	0.842
$[0.65, 1.00[$	-0.0632	0.0422	0.0295	0.7451	2.988	0.336	0.745	0.033	9.711	1.085	0.899
bin range M_{inv}				$\langle M_{inv}\rangle$							
$[0.0, 0.8[$	-0.0399	0.0420	0.0294	0.7410	3.455	0.431	0.475	0.030	11.007	0.741	0.821
$[0.8, 0.9[$	-0.0311	0.0416	0.0291	0.8546	3.465	0.459	0.477	0.028	11.391	0.855	0.797
$[0.9, 1.0[$	0.0008	0.0461	0.0323	0.9440	3.466	0.462	0.491	0.028	11.437	0.944	0.794
$[1.0, 1.2[$	0.0581	0.0454	0.0318	1.0882	3.389	0.468	0.500	0.027	11.511	1.088	0.790
$[1.2, 100[$	-0.0595	0.0445	0.0312	1.4960	3.306	0.472	0.532	0.026	11.587	1.496	0.786

Table A.14.: Identified $K^+\pi^-$ pair deuteron data (2003-2004) data azimuthal asymmetry and corresponding mean kinematic values; Q^2 in $(\mathrm{GeV}/c)^2$, W and M_{inv} in GeV/c^2.

bin range x	A	σ_{stat}	σ_{sys}	$\langle x\rangle$	$\langle Q^2\rangle$	$\langle y\rangle$	$\langle z\rangle$	$\langle x\rangle$	$\langle W\rangle$	$\langle M_{inv}\rangle$	$\langle D_{nn}\rangle$
$[0.003, 0.013[$	-0.0030	0.0340	0.0204	0.0090	1.447	0.559	0.455	0.009	12.800	1.052	0.707
$[0.013, 0.020[$	-0.0695	0.0350	0.0210	0.0162	1.985	0.412	0.515	0.016	10.884	1.033	0.845
$[0.020, 0.032[$	0.0290	0.0371	0.0223	0.0251	2.785	0.371	0.542	0.025	10.233	1.020	0.872
$[0.032, 0.050[$	-0.0045	0.0459	0.0275	0.0398	4.402	0.370	0.544	0.040	10.138	1.013	0.873
$[0.050, 0.080[$	0.0129	0.0547	0.0328	0.0627	6.812	0.364	0.546	0.063	9.940	1.002	0.877
$[0.080, 0.130[$	-0.0514	0.0708	0.0425	0.1002	10.812	0.361	0.548	0.100	9.686	0.990	0.877
$[0.130, 1.000[$	-0.1256	0.0913	0.0548	0.1984	23.805	0.393	0.538	0.198	9.537	0.981	0.855
bin range z				$\langle z\rangle$							
$[0.20, 0.30[$	-0.1589	0.0928	0.0557	0.2754	3.684	0.626	0.275	0.020	13.532	0.933	0.633
$[0.30, 0.35[$	0.0305	0.0635	0.0381	0.3265	3.796	0.562	0.327	0.024	12.751	0.975	0.707
$[0.35, 0.40[$	0.0303	0.0525	0.0315	0.3755	3.844	0.513	0.376	0.027	12.136	0.996	0.755
$[0.40, 0.50[$	0.0285	0.0342	0.0205	0.4492	3.770	0.463	0.449	0.030	11.470	1.017	0.798
$[0.50, 0.65[$	-0.0603	0.0300	0.0180	0.5684	3.675	0.395	0.568	0.034	10.527	1.047	0.854
$[0.65, 1.00[$	-0.0283	0.0345	0.0207	0.7453	3.355	0.322	0.745	0.038	9.489	1.094	0.908
bin range M_{inv}				$\langle M_{inv}\rangle$							
$[0.0, 0.8[$	-0.0324	0.0368	0.0221	0.7400	3.799	0.414	0.488	0.035	10.764	0.740	0.834
$[0.8, 0.9[$	0.0206	0.0361	0.0217	0.8551	3.778	0.440	0.491	0.032	11.124	0.855	0.813
$[0.9, 1.0[$	-0.0935	0.0401	0.0241	0.9435	3.711	0.447	0.503	0.031	11.217	0.944	0.806
$[1.0, 1.2[$	-0.0129	0.0388	0.0233	1.0885	3.594	0.451	0.512	0.030	11.274	1.088	0.803
$[1.2, 100[$	0.0151	0.0378	0.0227	1.4986	3.480	0.458	0.544	0.028	11.381	1.499	0.799

Table A.15.: All h^+h^- pair 2007 proton data azimuthal asymmetry and corresponding mean kinematic values; Q^2 in $(\mathrm{GeV}/c)^2$, W and M_{inv} in GeV/c^2.

bin range x	A	σ_{stat}	σ_{sys}	$\langle x\rangle$	$\langle Q^2\rangle$	$\langle y\rangle$	$\langle z\rangle$	$\langle x\rangle$	$\langle W\rangle$	$\langle M_{inv}\rangle$	$\langle D_{nn}\rangle$
$[0.003, 0.008[$	-0.0174	0.0222	0.0155	0.0065	1.234	0.649	0.449	0.007	13.875	0.785	0.608
$[0.008, 0.013[$	-0.0062	0.0114	0.0080	0.0105	1.485	0.477	0.455	0.011	11.807	0.766	0.797
$[0.013, 0.020[$	-0.0110	0.0091	0.0064	0.0164	1.766	0.365	0.464	0.016	10.213	0.745	0.880
$[0.020, 0.032[$	-0.0085	0.0077	0.0054	0.0256	2.140	0.284	0.474	0.026	8.879	0.721	0.924
$[0.032, 0.050[$	-0.0289	0.0083	0.0058	0.0398	2.885	0.244	0.480	0.040	8.120	0.703	0.941
$[0.050, 0.080[$	-0.0330	0.0100	0.0070	0.0626	4.470	0.240	0.480	0.063	7.964	0.696	0.943
$[0.080, 0.130[$	-0.0484	0.0126	0.0088	0.1006	7.055	0.236	0.480	0.101	7.749	0.689	0.945
$[0.130, 0.210[$	-0.1119	0.0168	0.0118	0.1614	11.068	0.230	0.482	0.161	7.376	0.678	0.945
$[0.210, 1.000[$	-0.0803	0.0245	0.0172	0.2805	22.606	0.263	0.483	0.281	7.260	0.674	0.928
bin range z				$\langle z\rangle$							
$[0.20, 0.25[$	0.0065	0.0317	0.0222	0.2386	3.497	0.452	0.239	0.030	11.243	0.509	0.799
$[0.25, 0.30[$	-0.0117	0.0128	0.0090	0.2781	3.411	0.382	0.278	0.036	10.241	0.581	0.852
$[0.30, 0.35[$	-0.0113	0.0102	0.0071	0.3257	3.374	0.349	0.326	0.039	9.743	0.635	0.875
$[0.35, 0.40[$	-0.0249	0.0098	0.0069	0.3748	3.365	0.332	0.375	0.042	9.479	0.676	0.885
$[0.40, 0.50[$	-0.0346	0.0074	0.0052	0.4476	3.354	0.318	0.448	0.044	9.253	0.724	0.894
$[0.50, 0.65[$	-0.0259	0.0076	0.0053	0.5667	3.330	0.304	0.567	0.045	9.022	0.789	0.903
$[0.65, 0.80[$	-0.0387	0.0109	0.0076	0.7145	3.239	0.293	0.715	0.046	8.848	0.861	0.909
$[0.80, 1.00[$	0.0044	0.0209	0.0146	0.8543	2.999	0.348	0.854	0.034	9.773	0.922	0.879
bin range M_{inv}				$\langle M_{inv}\rangle$							
$[0.0, 0.4[$	-0.0342	0.0108	0.0076	0.36127	3.375	0.307	0.412	0.046	9.064	0.361	0.901
$[0.4, 0.5[$	-0.0071	0.0092	0.0064	0.45056	3.348	0.309	0.433	0.045	9.099	0.451	0.900
$[0.5, 0.6[$	-0.0204	0.0094	0.0066	0.54921	3.353	0.316	0.445	0.044	9.212	0.549	0.896
$[0.6, 0.7[$	-0.0268	0.0100	0.0070	0.64958	3.337	0.323	0.460	0.043	9.321	0.650	0.891
$[0.7, 0.8[$	-0.0322	0.0101	0.0071	0.74908	3.286	0.327	0.486	0.041	9.392	0.749	0.889
$[0.8, 0.9[$	-0.0312	0.0121	0.0085	0.84622	3.309	0.334	0.496	0.041	9.502	0.846	0.884
$[0.9, 1.0[$	-0.0199	0.0147	0.0103	0.94724	3.359	0.341	0.502	0.040	9.607	0.947	0.880
$[1.0, 1.2[$	-0.0433	0.0137	0.0096	1.08975	3.318	0.351	0.518	0.038	9.768	1.090	0.873
$[1.2, 1.5[$	-0.0155	0.0156	0.0109	1.34974	3.321	0.371	0.555	0.036	10.070	1.350	0.859
$[1.5, 100[$	-0.0204	0.0278	0.0195	1.93684	3.394	0.422	0.603	0.031	10.816	1.937	0.822

Table A.16.: Identified $\pi^+\pi^-$ pair 2007 proton data azimuthal asymmetry and corresponding mean kinematic values; Q^2 in $(\mathrm{GeV}/c)^2$, W and M_{inv} in GeV/c^2.

bin range x	A	σ_{stat}	σ_{sys}	$\langle x\rangle$	$\langle Q^2\rangle$	$\langle y\rangle$	$\langle z\rangle$	$\langle x\rangle$	$\langle W\rangle$	$\langle M_{inv}\rangle$	$\langle D_{nn}\rangle$
$[0.003, 0.008[$	-0.0048	0.0292	0.0204	0.0065	1.221	0.634	0.396	0.007	13.715	0.751	0.628
$[0.008, 0.013[$	0.0072	0.0142	0.0099	0.0106	1.450	0.465	0.430	0.011	11.658	0.739	0.811
$[0.013, 0.020[$	-0.0096	0.0112	0.0078	0.0164	1.734	0.358	0.451	0.016	10.136	0.725	0.887
$[0.020, 0.032[$	-0.0114	0.0099	0.0069	0.0255	2.159	0.287	0.468	0.025	8.951	0.707	0.925
$[0.032, 0.050[$	-0.0373	0.0112	0.0078	0.0397	3.051	0.258	0.479	0.040	8.387	0.698	0.937
$[0.050, 0.080[$	-0.0482	0.0136	0.0095	0.0626	4.769	0.256	0.478	0.063	8.263	0.692	0.938
$[0.080, 0.130[$	-0.0396	0.0173	0.0121	0.1004	7.526	0.252	0.477	0.100	8.036	0.684	0.940
$[0.130, 0.210[$	-0.1022	0.0237	0.0166	0.1609	11.996	0.249	0.478	0.161	7.699	0.675	0.938
$[0.210, 1.000[$	-0.0791	0.0339	0.0237	0.2840	24.603	0.284	0.473	0.284	7.549	0.668	0.918
bin range z				$\langle z\rangle$							
$[0.20, 0.25[$	-0.0325	0.0385	0.0270	0.2384	3.570	0.473	0.238	0.028	11.560	0.518	0.786
$[0.25, 0.30[$	-0.0206	0.0161	0.0113	0.2779	3.511	0.408	0.278	0.033	10.660	0.590	0.838
$[0.30, 0.35[$	-0.0112	0.0131	0.0092	0.3256	3.464	0.372	0.326	0.036	10.124	0.640	0.864
$[0.35, 0.40[$	-0.0314	0.0127	0.0089	0.3747	3.429	0.349	0.375	0.039	9.777	0.676	0.879
$[0.40, 0.50[$	-0.0326	0.0096	0.0067	0.4472	3.378	0.326	0.447	0.041	9.422	0.718	0.894
$[0.50, 0.65[$	-0.0134	0.0099	0.0069	0.5658	3.264	0.295	0.566	0.044	8.948	0.774	0.916
$[0.65, 0.80[$	-0.0406	0.0146	0.0102	0.7140	3.073	0.260	0.714	0.046	8.420	0.834	0.940
$[0.80, 1.00[$	0.0107	0.0284	0.0199	0.8482	2.773	0.271	0.848	0.038	8.726	0.882	0.941
bin range M_{inv}				$\langle M_{inv}\rangle$							
$[0.0, 0.4[$	-0.0419	0.01425	0.0100	0.3614	3.473	0.322	0.405	0.043	9.361	0.361	0.897
$[0.4, 0.5[$	-0.0097	0.01198	0.0084	0.4507	3.404	0.321	0.427	0.042	9.351	0.451	0.897
$[0.5, 0.6[$	-0.0254	0.01229	0.0086	0.5489	3.385	0.326	0.436	0.041	9.421	0.549	0.894
$[0.6, 0.7[$	-0.0228	0.01310	0.0092	0.6498	3.349	0.330	0.448	0.040	9.488	0.650	0.891
$[0.7, 0.8[$	-0.0251	0.01261	0.0088	0.7497	3.269	0.329	0.476	0.040	9.473	0.750	0.892
$[0.8, 0.9[$	-0.0404	0.01531	0.0107	0.8457	3.277	0.335	0.486	0.039	9.568	0.846	0.888
$[0.9, 1.0[$	-0.0181	0.01889	0.0132	0.9470	3.328	0.342	0.490	0.039	9.676	0.947	0.883
$[1.0, 1.2[$	-0.0275	0.01834	0.0129	1.0885	3.275	0.351	0.503	0.037	9.811	1.088	0.878
$[1.2, 1.5[$	-0.0062	0.02158	0.0151	1.3454	3.248	0.363	0.542	0.035	10.008	1.345	0.871
$[1.5, 100[$	0.0359	0.04103	0.0287	1.9084	3.284	0.398	0.585	0.031	10.551	1.908	0.847

Table A.17.: Identified K^+K^- pair 2007 proton data azimuthal asymmetry and corresponding mean kinematic values; Q^2 in $(\mathrm{GeV}/c)^2$, W and M_{inv} in GeV/c^2.

bin range x	A	σ_{stat}	σ_{sys}	$\langle x\rangle$	$\langle Q^2\rangle$	$\langle y\rangle$	$\langle z\rangle$	$\langle x\rangle$	$\langle W\rangle$	$\langle M_{inv}\rangle$	$\langle D_{nn}\rangle$
$[0.003, 0.008[$	-0.0837	0.1232	0.0616	0.0066	1.220	0.630	0.464	0.007	13.675	1.340	0.635
$[0.008, 0.013[$	-0.0022	0.0662	0.0331	0.0105	1.509	0.487	0.539	0.010	11.955	1.341	0.792
$[0.013, 0.020[$	0.0302	0.0643	0.0322	0.0162	2.039	0.424	0.583	0.016	11.059	1.324	0.841
$[0.020, 0.032[$	-0.0991	0.0706	0.0353	0.0252	3.035	0.404	0.599	0.025	10.734	1.318	0.854
$[0.032, 0.080[$	-0.0809	0.0677	0.0339	0.0490	5.785	0.396	0.604	0.049	10.493	1.307	0.859
$[0.080, 1.000[$	-0.0729	0.1030	0.0515	0.1475	18.383	0.408	0.604	0.148	10.020	1.292	0.844
bin range z				$\langle z\rangle$							
$[0.20, 0.40[$	-0.1141	0.0895	0.0448	0.3442	4.099	0.581	0.344	0.024	12.980	1.236	0.690
$[0.40, 0.50[$	-0.0029	0.0723	0.0362	0.4511	4.061	0.504	0.451	0.028	12.033	1.302	0.770
$[0.50, 0.65[$	-0.0197	0.0673	0.0337	0.5492	4.053	0.448	0.549	0.032	11.296	1.331	0.821
$[0.65, 0.80[$	-0.0816	0.0512	0.0256	0.6903	3.925	0.381	0.690	0.037	10.381	1.361	0.875
$[0.80, 1.00[$	0.0542	0.0866	0.0433	0.8572	3.407	0.336	0.857	0.036	9.754	1.378	0.909
bin range M_{inv}				$\langle M_{inv}\rangle$							
$[0.90, 1.05[$	0.0375	0.0716	0.0358	1.0239	3.784	0.437	0.552	0.031	11.122	1.024	0.823
$[1.05, 1.15[$	0.0202	0.0703	0.0352	1.0983	4.221	0.451	0.548	0.034	11.295	1.098	0.813
$[1.15, 1.30[$	-0.0858	0.0658	0.0329	1.2217	4.190	0.453	0.561	0.033	11.317	1.222	0.812
$[1.30, 1.50[$	-0.0809	0.0725	0.0363	1.3889	3.967	0.453	0.576	0.032	11.330	1.387	0.813
$[1.50, 100.[$	-0.0842	0.0669	0.0335	1.8285	3.618	0.456	0.604	0.029	11.397	1.828	0.810

Table A.18.: Identified π^+K^- pair 2007 proton data azimuthal asymmetry and corresponding mean kinematic values; Q^2 in $(\mathrm{GeV}/c)^2$, W and M_{inv} in GeV/c^2.

bin range x	A	σ_{stat}	σ_{sys}	$\langle x\rangle$	$\langle Q^2\rangle$	$\langle y\rangle$	$\langle z\rangle$	$\langle x\rangle$	$\langle W\rangle$	$\langle M_{inv}\rangle$	$\langle D_{nn}\rangle$
$[0.003, 0.013[$	-0.1260	0.0449	0.0314	0.0092	1.422	0.538	0.442	0.009	12.557	1.064	0.734
$[0.013, 0.020[$	0.0044	0.0478	0.0335	0.0162	1.992	0.414	0.490	0.016	10.914	1.040	0.846
$[0.020, 0.032[$	0.0171	0.0507	0.0355	0.0252	2.843	0.380	0.511	0.025	10.352	1.029	0.868
$[0.032, 0.050[$	0.0243	0.0638	0.0447	0.0397	4.396	0.372	0.515	0.040	10.153	1.022	0.871
$[0.050, 0.080[$	-0.0692	0.0792	0.0554	0.0624	6.810	0.366	0.515	0.062	9.950	1.012	0.874
$[0.080, 0.130[$	-0.3190	0.1060	0.0742	0.0997	10.793	0.363	0.517	0.100	9.686	1.004	0.872
$[0.130, 1.000[$	-0.0176	0.1229	0.0860	0.2066	24.613	0.393	0.506	0.207	9.428	0.996	0.849
bin range z				$\langle z\rangle$							
$[0.20, 0.30[$	-0.1559	0.1088	0.0762	0.2759	3.929	0.596	0.276	0.022	13.162	0.933	0.673
$[0.30, 0.35[$	-0.0409	0.0758	0.0531	0.3265	3.798	0.534	0.326	0.025	12.408	0.982	0.739
$[0.35, 0.40[$	-0.0078	0.0653	0.0457	0.3753	3.723	0.490	0.375	0.027	11.840	1.007	0.780
$[0.40, 0.50[$	-0.0217	0.0443	0.0310	0.4484	3.633	0.440	0.448	0.030	11.171	1.035	0.821
$[0.50, 0.65[$	-0.0399	0.0426	0.0298	0.5664	3.448	0.383	0.566	0.034	10.358	1.073	0.865
$[0.65, 1.00[$	-0.1156	0.0549	0.0384	0.7416	3.150	0.327	0.742	0.036	9.535	1.114	0.907
bin range M_{inv}				$\langle M_{inv}\rangle$							
$[0.0, 0.8[$	-0.0670	0.0522	0.0365	0.7409	3.675	0.411	0.463	0.033	10.728	0.741	0.842
$[0.8, 0.9[$	-0.0218	0.0484	0.0339	0.8566	3.599	0.433	0.472	0.031	11.042	0.857	0.823
$[0.9, 1.0[$	-0.0338	0.0539	0.0377	0.9424	3.585	0.439	0.481	0.030	11.124	0.942	0.818
$[1.0, 1.2[$	-0.0786	0.0542	0.0379	1.0892	3.616	0.447	0.483	0.030	11.221	1.089	0.812
$[1.2, 100[$	-0.0536	0.0505	0.0354	1.5163	3.394	0.456	0.520	0.027	11.361	1.516	0.804

Table A.19.: Identified $K^+\pi^-$ pair 2007 proton data azimuthal asymmetry and corresponding mean kinematic values; Q^2 in $(\mathrm{GeV}/c)^2$, W and M_{inv} in GeV/c^2.

bin range x	A	σ_{stat}	σ_{sys}	$\langle x\rangle$	$\langle Q^2\rangle$	$\langle y\rangle$	$\langle z\rangle$	$\langle x\rangle$	$\langle W\rangle$	$\langle M_{inv}\rangle$	$\langle D_{nn}\rangle$
$[0.003, 0.013[$	-0.0019	0.0401	0.0201	0.0092	1.413	0.532	0.448	0.009	12.475	1.072	0.741
$[0.013, 0.020[$	-0.0464	0.0410	0.0205	0.0162	1.946	0.404	0.500	0.016	10.777	1.045	0.855
$[0.020, 0.032[$	0.0292	0.0418	0.0209	0.0252	2.734	0.364	0.526	0.025	10.135	1.030	0.879
$[0.032, 0.050[$	0.0179	0.0513	0.0257	0.0397	4.195	0.354	0.533	0.040	9.908	1.023	0.885
$[0.050, 0.080[$	0.0046	0.0611	0.0306	0.0626	6.460	0.346	0.538	0.063	9.678	1.014	0.889
$[0.080, 0.130[$	-0.0283	0.0773	0.0387	0.1001	10.128	0.339	0.545	0.100	9.360	1.001	0.890
$[0.130, 1.000[$	-0.2275	0.0846	0.0423	0.2055	22.679	0.363	0.537	0.206	9.063	0.990	0.872
bin range z				$\langle z\rangle$							
$[0.20, 0.30[$	-0.0931	0.1007	0.0504	0.276	3.888	0.594	0.276	0.022	13.140	0.937	0.675
$[0.30, 0.35[$	0.0240	0.0680	0.0340	0.327	3.931	0.528	0.327	0.025	12.331	0.982	0.746
$[0.35, 0.40[$	0.0228	0.0570	0.0285	0.376	3.940	0.481	0.376	0.029	11.721	1.006	0.789
$[0.40, 0.50[$	-0.0113	0.0378	0.0189	0.449	3.913	0.429	0.449	0.033	11.004	1.029	0.831
$[0.50, 0.65[$	-0.0266	0.0343	0.0172	0.568	3.874	0.367	0.568	0.039	10.110	1.063	0.877
$[0.65, 1.00[$	-0.0081	0.0418	0.0209	0.743	3.532	0.310	0.743	0.043	9.260	1.114	0.917
bin range M_{inv}				$\langle M_{inv}\rangle$							
$[0.0, 0.8[$	0.0394	0.0436	0.0218	0.7402	3.986	0.391	0.476	0.038	10.435	0.740	0.857
$[0.8, 0.9[$	-0.0185	0.0400	0.0200	0.8570	3.921	0.411	0.489	0.036	10.709	0.857	0.841
$[0.9, 1.0[$	-0.0047	0.0442	0.0221	0.9419	3.924	0.418	0.499	0.035	10.803	0.942	0.835
$[1.0, 1.2[$	-0.0763	0.0453	0.0227	1.0891	3.819	0.427	0.499	0.034	10.938	1.089	0.828
$[1.2, 100[$	-0.0021	0.0416	0.0208	1.5178	3.586	0.437	0.536	0.031	11.095	1.517	0.820

Table A.20.: All h^+h^- pair 2010 proton data azimuthal asymmetry and corresponding mean kinematic values; Q^2 in $(\mathrm{GeV}/c)^2$, W and M_{inv} in GeV/c^2.

bin range x	A	σ_{stat}	σ_{sys}	$\langle x\rangle$	$\langle Q^2\rangle$	$\langle y\rangle$	$\langle z\rangle$	$\langle x\rangle$	$\langle W\rangle$	$\langle M_{inv}\rangle$	$\langle D_{nn}\rangle$
$[0.003, 0.008[$	0.040	0.014	0.011	0.006	1.267	0.646	0.446	0.006	14.192	0.783	0.563
$[0.008, 0.013[$	-0.017	0.008	0.006	0.011	1.558	0.474	0.453	0.011	12.088	0.763	0.770
$[0.013, 0.020[$	-0.006	0.006	0.005	0.016	1.878	0.360	0.462	0.016	10.504	0.744	0.869
$[0.020, 0.032[$	-0.010	0.005	0.004	0.026	2.303	0.277	0.472	0.026	9.169	0.726	0.908
$[0.032, 0.050[$	-0.010	0.005	0.004	0.040	3.113	0.237	0.477	0.040	8.394	0.706	0.928
$[0.050, 0.080[$	-0.021	0.006	0.005	0.063	4.796	0.233	0.478	0.063	8.120	0.700	0.933
$[0.080, 0.130[$	-0.044	0.007	0.005	0.101	7.496	0.229	0.479	0.101	7.945	0.694	0.937
$[0.130, 0.210[$	-0.040	0.010	0.008	0.162	11.885	0.223	0.481	0.162	7.623	0.685	0.939
$[0.210, 1.000[$	-0.055	0.013	0.010	0.285	23.014	0.256	0.485	0.285	7.321	0.678	0.931
bin range z				$\langle z\rangle$							
$[0.20, 0.25[$	-0.015	0.020	0.015	0.238	3.968	0.481	0.238	0.032	11.604	0.513	0.766
$[0.25, 0.30[$	-0.019	0.008	0.006	0.278	3.902	0.406	0.278	0.039	10.539	0.583	0.828
$[0.30, 0.35[$	-0.013	0.007	0.005	0.326	3.875	0.369	0.326	0.043	9.995	0.636	0.854
$[0.35, 0.40[$	-0.012	0.006	0.005	0.375	3.865	0.351	0.375	0.045	9.708	0.677	0.867
$[0.40, 0.50[$	-0.007	0.005	0.004	0.448	3.860	0.335	0.448	0.048	9.460	0.724	0.878
$[0.50, 0.65[$	-0.017	0.005	0.004	0.567	3.837	0.319	0.567	0.050	9.207	0.789	0.889
$[0.65, 0.80[$	-0.029	0.007	0.005	0.714	3.740	0.306	0.714	0.051	9.015	0.862	0.897
$[0.80, 1.00[$	-0.033	0.014	0.011	0.854	2.930	0.336	0.854	0.035	0.810	0.732	0.873
bin range M_{inv}				$\langle M_{inv}\rangle$							
$[0.0, 0.4[$	-0.019	0.007	0.005	0.361	3.863	0.324	0.412	0.050	9.294	0.361	0.885
$[0.4, 0.5[$	-0.007	0.006	0.005	0.451	3.848	0.325	0.432	0.049	9.309	0.451	0.885
$[0.5, 0.6[$	-0.005	0.006	0.005	0.549	3.846	0.332	0.443	0.048	9.421	0.549	0.880
$[0.6, 0.7[$	-0.014	0.006	0.005	0.650	3.839	0.340	0.458	0.047	9.536	0.650	0.875
$[0.7, 0.8[$	-0.025	0.006	0.005	0.749	3.785	0.344	0.483	0.046	9.609	0.759	0.872
$[0.8, 0.9[$	-0.027	0.008	0.006	0.846	3.821	0.352	0.494	0.045	9.724	0.846	0.866
$[0.9, 1.0[$	-0.008	0.009	0.007	0.947	3.866	0.359	0.501	0.044	9.833	0.947	0.861
$[1.0, 1.2[$	-0.023	0.009	0.007	1.090	3.844	0.371	0.516	0.042	10.012	1.090	0.853
$[1.2, 1.5[$	-0.021	0.010	0.008	1.350	3.839	0.391	0.554	0.040	10.325	1.350	0.838
$[1.5, 100[$	-0.004	0.018	0.014	1.942	3.889	0.446	0.601	0.034	11.111	1.942	0.795

Table A.21.: Identified $\pi^+\pi^-$ pair 2010 proton data azimuthal asymmetry and corresponding mean kinematic values; Q^2 in $(\mathrm{GeV}/c)^2$, W and M_{inv} in GeV/c^2.

bin range x	A	σ_{stat}	σ_{sys}	$\langle x\rangle$	$\langle Q^2\rangle$	$\langle y\rangle$	$\langle z\rangle$	$\langle x\rangle$	$\langle W\rangle$	$\langle M_{inv}\rangle$	$\langle D_{nn}\rangle$
$[0.003, 0.008[$	0.046	0.019	0.015	0.006	1.252	0.661	0.392	0.006	14.007	0.748	0.588
$[0.008, 0.013[$	-0.015	0.010	0.008	0.011	1.512	0.484	0.426	0.011	11.898	0.735	0.788
$[0.013, 0.020[$	-0.002	0.007	0.006	0.016	1.828	0.376	0.447	0.016	10.375	0.723	0.870
$[0.020, 0.032[$	-0.000	0.006	0.005	0.026	2.297	0.303	0.464	0.026	9.192	0.708	0.911
$[0.032, 0.050[$	-0.007	0.007	0.006	0.040	3.256	0.273	0.474	0.040	8.628	0.700	0.926
$[0.050, 0.080[$	-0.024	0.008	0.006	0.063	5.060	0.269	0.473	0.063	8.473	0.695	0.929
$[0.080, 0.130[$	-0.041	0.010	0.008	0.101	7.975	0.265	0.474	0.101	8.234	0.688	0.932
$[0.130, 0.210[$	-0.061	0.013	0.010	0.162	12.816	0.264	0.475	0.162	7.947	0.680	0.932
$[0.210, 1.000[$	-0.048	0.017	0.014	0.288	24.864	0.283	0.476	0.288	7.572	0.670	0.924
bin range z				$\langle z\rangle$							
$[0.20, 0.25[$	-0.020	0.024	0.019	0.238	4.093	0.498	0.238	0.031	11.863	0.520	0.756
$[0.25, 0.30[$	-0.010	0.010	0.008	0.278	4.052	0.429	0.278	0.036	10.911	0.591	0.816
$[0.30, 0.35[$	0.000	0.008	0.006	0.326	4.024	0.389	0.326	0.041	10.336	0.640	0.846
$[0.35, 0.40[$	-0.015	0.008	0.006	0.375	3.983	0.364	0.375	0.043	9.958	0.676	0.863
$[0.40, 0.50[$	-0.003	0.006	0.005	0.447	3.934	0.339	0.447	0.046	9.570	0.718	0.881
$[0.50, 0.65[$	-0.020	0.006	0.005	0.566	3.816	0.302	0.566	0.050	9.033	0.775	0.909
$[0.65, 0.80[$	-0.031	0.009	0.007	0.714	3.581	0.263	0.714	0.052	8.452	0.835	0.937
$[0.80, 1.00[$	-0.016	0.018	0.014	0.847	3.194	0.274	0.847	0.042	8.754	0.887	0.939
bin range M_{inv}				$\langle M_{inv}\rangle$							
$[0.0, 0.4[$	-0.013	0.009	0.007	0.361	4.034	0.337	0.403	0.048	9.543	0.361	0.883
$[0.4, 0.5[$	-0.001	0.008	0.006	0.451	3.965	0.335	0.424	0.047	9.513	0.451	0.885
$[0.5, 0.6[$	-0.006	0.008	0.006	0.549	3.936	0.339	0.433	0.046	9.585	0.549	0.881
$[0.6, 0.7[$	-0.009	0.008	0.006	0.650	3.890	0.344	0.445	0.045	9.654	0.650	0.878
$[0.7, 0.8[$	-0.026	0.008	0.006	0.750	3.809	0.343	0.471	0.044	9.643	0.750	0.878
$[0.8, 0.9[$	-0.021	0.010	0.008	0.846	3.826	0.349	0.482	0.044	9.735	0.846	0.874
$[0.9, 1.0[$	0.005	0.012	0.010	0.947	3.868	0.355	0.487	0.043	9.830	0.947	0.870
$[1.0, 1.2[$	-0.025	0.012	0.010	1.088	3.823	0.365	0.500	0.042	9.978	1.088	0.863
$[1.2, 1.5[$	-0.015	0.014	0.011	1.346	3.780	0.377	0.538	0.040	10.162	1.346	0.856
$[1.5, 100[$	-0.035	0.026	0.021	1.911	3.811	0.414	0.580	0.035	10.723	1.911	0.830

Table A.22.: Identified K^+K^- pair 2010 proton data azimuthal asymmetry and corresponding mean kinematic values; Q^2 in $(\mathrm{GeV}/c)^2$, W and M_{inv} in GeV/c^2.

bin range x	A	σ_{stat}	σ_{sys}	$\langle x\rangle$	$\langle Q^2\rangle$	$\langle y\rangle$	$\langle z\rangle$	$\langle x\rangle$	$\langle W\rangle$	$\langle M_{inv}\rangle$	$\langle D_{nn}\rangle$
$[0.003, 0.008[$	0.049	0.082	0.041	0.006	1.244	0.650	0.451	0.006	13.897	1.335	0.603
$[0.008, 0.013[$	-0.042	0.045	0.023	0.010	1.563	0.504	0.528	0.010	12.155	1.333	0.772
$[0.013, 0.020[$	-0.005	0.043	0.022	0.016	2.144	0.443	0.573	0.016	11.314	1.325	0.821
$[0.020, 0.032[$	-0.059	0.046	0.023	0.025	3.225	0.427	0.586	0.025	11.037	1.315	0.833
$[0.032, 0.080[$	0.001	0.042	0.021	0.049	6.182	0.418	0.592	0.049	10.784	1.307	0.841
$[0.080, 1.000[$	-0.036	0.055	0.028	0.148	18.460	0.409	0.599	0.148	10.077	1.294	0.849
bin range z				$\langle z\rangle$							
$[0.20, 0.40[$	0.025	0.056	0.028	0.343	4.563	0.605	0.343	0.026	13.254	1.236	0.657
$[0.40, 0.50[$	0.008	0.046	0.023	0.451	4.779	0.519	0.451	0.032	12.201	1.300	0.753
$[0.50, 0.65[$	-0.036	0.043	0.022	0.549	4.776	0.457	0.549	0.037	11.399	1.329	0.813
$[0.65, 0.80[$	-0.020	0.033	0.017	0.689	4.648	0.385	0.689	0.043	10.420	1.357	0.873
$[0.80, 1.00[$	-0.111	0.056	0.028	0.856	4.020	0.335	0.856	0.042	9.7346	1.387	0.910
bin range M_{inv}				$\langle M_{inv}\rangle$							
$[0.90, 1.05[$	0.020	0.046	0.023	1.024	4.450	0.457	0.537	0.035	11.358	1.024	0.802
$[1.05, 1.15[$	-0.032	0.045	0.023	1.098	4.948	0.466	0.540	0.039	11.460	1.098	0.797
$[1.15, 1.30[$	-0.039	0.042	0.021	1.221	4.838	0.467	0.553	0.038	11.484	1.221	0.797
$[1.30, 1.50[$	-0.048	0.046	0.023	1.388	4.621	0.467	0.569	0.036	11.498	1.388	0.797
$[1.50, 100.[$	0.000	0.043	0.022	1.829	4.264	0.470	0.597	0.033	11.549	1.829	0.795

Table A.23.: Identified π^+K^- pair 2010 proton data azimuthal asymmetry and corresponding mean kinematic values; Q^2 in $(\mathrm{GeV}/c)^2$, W and M_{inv} in GeV/c^2.

bin range x	A	σ_{stat}	σ_{sys}	$\langle x\rangle$	$\langle Q^2\rangle$	$\langle y\rangle$	$\langle z\rangle$	$\langle x\rangle$	$\langle W\rangle$	$\langle M_{inv}\rangle$	$\langle D_{nn}\rangle$
$[0.003, 0.013[$	-0.005	0.030	0.024	0.009	1.465	0.561	0.432	0.009	12.835	1.063	0.703
$[0.013, 0.020[$	-0.024	0.031	0.025	0.016	2.101	0.434	0.481	0.016	11.179	1.041	0.826
$[0.020, 0.032[$	-0.018	0.032	0.026	0.025	3.026	0.401	0.502	0.025	10.648	1.031	0.848
$[0.032, 0.050[$	-0.023	0.039	0.031	0.040	4.664	0.392	0.507	0.040	10.439	1.024	0.855
$[0.050, 0.080[$	0.015	0.046	0.037	0.063	7.219	0.385	0.508	0.063	10.227	1.017	0.860
$[0.080, 0.130[$	-0.064	0.058	0.046	0.100	11.424	0.380	0.508	0.100	9.947	1.009	0.864
$[0.130, 1.000[$	0.005	0.060	0.048	0.208	23.916	0.381	0.507	0.208	9.344	1.000	0.865
bin range z				$\langle z\rangle$							
$[0.20, 0.30[$	-0.110	0.067	0.054	0.275	4.317	0.622	0.275	0.024	13.461	0.937	0.636
$[0.30, 0.35[$	-0.050	0.047	0.038	0.326	4.389	0.556	0.326	0.028	12.655	0.985	0.712
$[0.35, 0.40[$	-0.014	0.041	0.033	0.375	4.384	0.509	0.375	0.031	12.060	1.010	0.758
$[0.40, 0.50[$	0.062	0.028	0.022	0.448	4.256	0.455	0.448	0.034	11.343	1.038	0.806
$[0.50, 0.65[$	-0.008	0.027	0.022	0.566	4.081	0.388	0.566	0.039	10.408	1.073	0.861
$[0.65, 1.00[$	-0.102	0.035	0.028	0.739	3.711	0.321	0.739	0.043	9.454	1.113	0.910
bin range M_{inv}				$\langle M_{inv}\rangle$							
$[0.0, 0.8[$	-0.035	0.032	0.026	0.741	4.290	0.422	0.458	0.038	10.861	0.741	0.830
$[0.8, 0.9[$	0.025	0.031	0.025	0.856	4.231	0.449	0.464	0.035	11.229	0.856	0.805
$[0.9, 1.0[$	-0.050	0.034	0.027	0.942	4.209	0.455	0.474	0.035	11.301	0.942	0.801
$[1.0, 1.2[$	0.012	0.034	0.027	1.089	4.186	0.465	0.476	0.034	11.437	1.089	0.792
$[1.2, 100[$	-0.029	0.032	0.026	1.516	4.003	0.474	0.512	0.031	11.562	1.516	0.784

Table A.24.: Identified $K^+\pi^-$ pair 2010 proton data azimuthal asymmetry and corresponding mean kinematic values; Q^2 in $(\mathrm{GeV}/c)^2$, W and M_{inv} in GeV/c^2.

bin range x	A	σ_{stat}	σ_{sys}	$\langle x\rangle$	$\langle Q^2\rangle$	$\langle y\rangle$	$\langle z\rangle$	$\langle x\rangle$	$\langle W\rangle$	$\langle M_{inv}\rangle$	$\langle D_{nn}\rangle$
$[0.003, 0.013[$	-0.048	0.027	0.014	0.009	1.457	0.554	0.439	0.009	12.746	1.068	0.712
$[0.013, 0.020[$	-0.035	0.027	0.014	0.016	2.050	0.423	0.493	0.016	11.034	1.044	0.835
$[0.020, 0.032[$	-0.072	0.027	0.014	0.025	2.925	0.387	0.517	0.025	10.449	1.034	0.859
$[0.032, 0.050[$	-0.019	0.032	0.016	0.040	4.461	0.375	0.524	0.040	10.198	1.025	0.868
$[0.050, 0.080[$	-0.042	0.036	0.018	0.063	6.897	0.367	0.530	0.063	9.971	1.017	0.874
$[0.080, 0.130[$	-0.025	0.044	0.022	0.101	10.825	0.358	0.535	0.101	9.657	1.008	0.880
$[0.130, 1.000[$	0.006	0.043	0.022	0.209	22.730	0.358	0.539	0.209	9.032	0.992	0.882
bin range z				$\langle z\rangle$							
$[0.20, 0.30[$	-0.074	0.062	0.031	0.276	4.392	0.619	0.276	0.025	13.420	0.938	0.641
$[0.30, 0.35[$	-0.082	0.042	0.021	0.326	4.532	0.551	0.326	0.029	12.594	0.985	0.717
$[0.35, 0.40[$	-0.038	0.037	0.019	0.375	4.617	0.502	0.375	0.033	11.960	1.007	0.765
$[0.40, 0.50[$	0.001	0.024	0.012	0.449	4.616	0.444	0.449	0.038	11.187	1.031	0.815
$[0.50, 0.65[$	-0.063	0.021	0.011	0.568	4.560	0.374	0.568	0.045	10.189	1.062	0.871
$[0.65, 1.00[$	-0.033	0.026	0.013	0.742	4.263	0.308	0.742	0.051	9.223	1.112	0.918
bin range M_{inv}				$\langle M_{inv}\rangle$							
$[0.0, 0.8[$	-0.017	0.027	0.014	0.740	4.694	0.404	0.472	0.044	10.587	0.740	0.844
$[0.8, 0.9[$	-0.056	0.025	0.013	0.857	4.614	0.428	0.482	0.041	10.919	0.857	0.823
$[0.9, 1.0[$	-0.076	0.028	0.014	0.942	4.602	0.433	0.493	0.040	10.989	0.942	0.818
$[1.0, 1.2[$	-0.045	0.028	0.014	1.089	4.497	0.444	0.494	0.038	11.137	1.089	0.809
$[1.2, 100[$	-0.009	0.026	0.013	1.517	4.225	0.453	0.530	0.035	11.273	1.517	0.802

Table A.25.: All h^+h^- pair combined $2007/2010$ proton data azimuthal asymmetry and corresponding mean kinematic values; Q^2 in $(\mathrm{GeV}/c)^2$, W and M_{inv} in GeV/c^2.

bin range x	A	σ_{stat}	σ_{sys}	$\langle x \rangle$							
$[0.003, 0.008[$	0.0229	0.0121	0.0097	0.0064	1.259	0.647	0.447	0.0064	14.116	0.783	0.574
$[0.008, 0.013[$	-0.0139	0.0064	0.0051	0.0105	1.540	0.475	0.453	0.0105	12.021	0.764	0.776
$[0.013, 0.020[$	-0.0077	0.0051	0.0040	0.0164	1.851	0.361	0.462	0.0164	10.434	0.744	0.872
$[0.020, 0.032[$	-0.0096	0.0043	0.0034	0.0256	2.264	0.279	0.472	0.0256	9.099	0.725	0.912
$[0.032, 0.050[$	-0.0152	0.0045	0.0036	0.0398	3.058	0.239	0.478	0.0398	8.328	0.705	0.931
$[0.050, 0.080[$	-0.0241	0.0053	0.0042	0.0628	4.718	0.235	0.478	0.0628	8.083	0.699	0.935
$[0.080, 0.130[$	-0.0447	0.0064	0.0051	0.1008	7.390	0.231	0.479	0.1008	7.898	0.693	0.939
$[0.130, 0.210[$	-0.0578	0.0083	0.0067	0.1617	11.689	0.225	0.481	0.1617	7.564	0.683	0.940
$[0.210, 1.000[$	-0.0603	0.0112	0.0089	0.2841	22.916	0.258	0.485	0.2841	7.306	0.677	0.930
bin range z				$\langle z \rangle$							
$[0.20, 0.25[$	-0.0087	0.0170	0.0136	0.2385	3.855	0.474	0.2385	0.032	11.517	0.512	0.774
$[0.25, 0.30[$	-0.0170	0.0069	0.0055	0.2781	3.784	0.400	0.2781	0.038	10.467	0.583	0.834
$[0.30, 0.35[$	-0.0128	0.0055	0.0044	0.3256	3.755	0.364	0.3256	0.042	9.935	0.636	0.859
$[0.35, 0.40[$	-0.0154	0.0053	0.0042	0.3748	3.745	0.346	0.3748	0.044	9.653	0.677	0.871
$[0.40, 0.50[$	-0.0150	0.0040	0.0032	0.4475	3.739	0.331	0.4475	0.047	9.410	0.724	0.882
$[0.50, 0.65[$	-0.0197	0.0041	0.0033	0.5667	3.715	0.315	0.5667	0.049	9.163	0.789	0.892
$[0.65, 0.80[$	-0.0320	0.0059	0.0047	0.7144	3.620	0.303	0.7144	0.050	8.975	0.862	0.900
$[0.80, 1.00[$	-0.0216	0.0114	0.0091	0.8539	2.947	0.339	0.8539	0.035	2.961	0.778	0.874
bin range M_{inv}				$\langle M_{inv} \rangle$							
$[0.0, 0.4[$	-0.0235	0.0058	0.0046	0.3612	3.746	0.320	0.412	0.049	9.239	0.3612	0.889
$[0.4, 0.5[$	-0.0068	0.0050	0.0040	0.4505	3.728	0.321	0.432	0.048	9.259	0.4505	0.889
$[0.5, 0.6[$	-0.0094	0.0051	0.0041	0.5492	3.728	0.328	0.443	0.047	9.371	0.5492	0.884
$[0.6, 0.7[$	-0.0179	0.0054	0.0043	0.6496	3.719	0.336	0.458	0.046	9.484	0.6496	0.879
$[0.7, 0.8[$	-0.0268	0.0054	0.0044	0.7491	3.665	0.340	0.484	0.045	9.557	0.7491	0.876
$[0.8, 0.9[$	-0.0284	0.0065	0.0052	0.8463	3.698	0.348	0.494	0.044	9.671	0.8463	0.870
$[0.9, 1.0[$	-0.0111	0.0079	0.0063	0.9473	3.744	0.355	0.501	0.043	9.779	0.9473	0.866
$[1.0, 1.2[$	-0.0290	0.0074	0.0059	1.0896	3.718	0.366	0.516	0.041	9.953	1.0896	0.858
$[1.2, 1.5[$	-0.0197	0.0085	0.0068	1.3501	3.715	0.386	0.554	0.039	10.264	1.3501	0.843
$[1.5, 100[$	-0.0088	0.0151	0.0120	1.9407	3.770	0.440	0.601	0.033	11.040	1.9407	0.801

Table A.26.: Identified $\pi^+\pi^-$ pair combined $2007/2010$ proton data azimuthal asymmetry and corresponding mean kinematic values; Q^2 in $(\mathrm{GeV}/c)^2$, W and M_{inv} in GeV/c^2.

bin range x	A	σ_{stat}	σ_{sys}	$\langle x \rangle$	$\langle Q^2 \rangle$	$\langle y \rangle$	$\langle z \rangle$	$\langle x \rangle$	$\langle W \rangle$	$\langle M_{inv} \rangle$	$\langle D_{nn} \rangle$
$[0.003, 0.008[$	0.0314	0.0159	0.0095	0.0065	1.244	0.654	0.393	0.0065	13.933	0.748	0.598
$[0.008, 0.013[$	-0.0081	0.0079	0.0047	0.0106	1.495	0.479	0.427	0.0106	11.831	0.736	0.795
$[0.013, 0.020[$	-0.0046	0.0062	0.0037	0.0164	1.801	0.371	0.448	0.0164	10.308	0.723	0.875
$[0.020, 0.032[$	-0.0036	0.0054	0.0032	0.0255	2.259	0.298	0.465	0.0255	9.126	0.708	0.915
$[0.032, 0.050[$	-0.0152	0.0060	0.0036	0.0398	3.202	0.269	0.475	0.0398	8.564	0.699	0.929
$[0.050, 0.080[$	-0.0307	0.0071	0.0042	0.0627	4.987	0.266	0.475	0.0627	8.421	0.694	0.931
$[0.080, 0.130[$	-0.0410	0.0087	0.0052	0.1006	7.870	0.262	0.475	0.1006	8.188	0.687	0.934
$[0.130, 0.210[$	-0.0706	0.0115	0.0069	0.1616	12.637	0.261	0.475	0.1616	7.893	0.679	0.933
$[0.210, 1.000[$	-0.0543	0.0151	0.0091	0.2871	24.815	0.283	0.475	0.2871	7.568	0.670	0.923
bin range z				$\langle z \rangle$							
$[0.20, 0.25[$	-0.0233	0.0204	0.0122	0.2382	3.963	0.492	0.2382	0.030	11.788	0.519	0.763
$[0.25, 0.30[$	-0.0128	0.0086	0.0052	0.2778	3.912	0.423	0.2778	0.036	10.846	0.591	0.821
$[0.30, 0.35[$	-0.0030	0.0070	0.0042	0.3255	3.877	0.384	0.3255	0.039	10.281	0.640	0.850
$[0.35, 0.40[$	-0.0197	0.0068	0.0041	0.3747	3.837	0.360	0.3747	0.042	9.911	0.676	0.867
$[0.40, 0.50[$	-0.0112	0.0051	0.0031	0.4472	3.787	0.335	0.4472	0.045	9.531	0.718	0.885
$[0.50, 0.65[$	-0.0184	0.0053	0.0032	0.5656	3.668	0.300	0.5656	0.048	9.011	0.774	0.911
$[0.65, 0.80[$	-0.0335	0.0078	0.0047	0.7136	3.443	0.262	0.7136	0.050	8.443	0.835	0.938
$[0.80, 1.00[$	-0.0085	0.0154	0.0093	0.8476	3.077	0.273	0.8476	0.041	8.746	0.886	0.940
bin range M_{inv}				$\langle M_{inv} \rangle$							
$[0.0, 0.4[$	-0.0210	0.0076	0.0046	0.3613	3.887	0.333	0.404	0.046	9.495	0.3613	0.887
$[0.4, 0.5[$	-0.0037	0.0064	0.0038	0.4507	3.817	0.331	0.425	0.046	9.471	0.4507	0.888
$[0.5, 0.6[$	-0.0113	0.0066	0.0039	0.5489	3.791	0.336	0.434	0.045	9.542	0.5489	0.885
$[0.6, 0.7[$	-0.0129	0.0070	0.0042	0.6498	3.747	0.340	0.445	0.044	9.610	0.6498	0.881
$[0.7, 0.8[$	-0.0258	0.0068	0.0041	0.7497	3.665	0.339	0.472	0.043	9.597	0.7497	0.882
$[0.8, 0.9[$	-0.0262	0.0082	0.0049	0.8457	3.680	0.345	0.483	0.042	9.690	0.8457	0.878
$[0.9, 1.0[$	-0.0014	0.0101	0.0061	0.9471	3.725	0.352	0.488	0.042	9.789	0.9471	0.873
$[1.0, 1.2[$	-0.0254	0.0098	0.0059	1.0882	3.678	0.361	0.501	0.040	9.934	1.0882	0.867
$[1.2, 1.5[$	-0.0124	0.0116	0.0069	1.3456	3.639	0.373	0.539	0.038	10.121	1.3456	0.860
$[1.5, 100[$	-0.0153	0.0220	0.0132	1.9103	3.672	0.410	0.582	0.034	10.678	1.9103	0.835

Table A.27.: Identified $\pi^+\pi^-$ pair combined $2007/2010$ proton data azimuthal asymmetry with a cut on $x > 0.032$ (left sub-table), on $M_{inv} < 1.5\,\mathrm{GeV}/c^2$ (center sub-table) and both cuts (right sub-table); Q^2 in $(\mathrm{GeV}/c)^2$, W and M_{inv} in GeV/c^2.

bin range x	A	σ_{stat}	σ_{sys}	$\langle x \rangle$
$[0.032, 0.050[$	-0.0148	0.0060	0.0036	0.0398
$[0.050, 0.080[$	-0.0306	0.0071	0.0042	0.0627
$[0.080, 0.130[$	-0.0414	0.0087	0.0052	0.1006
$[0.130, 0.210[$	-0.0713	0.0115	0.0069	0.1616
$[0.210, 1.000[$	-0.0559	0.0151	0.0091	0.2871
bin range z				$\langle z \rangle$
$[0.20, 0.25[$	-0.0356	0.0364	0.0218	0.2390
$[0.25, 0.30[$	-0.0362	0.0140	0.0084	0.2785
$[0.30, 0.35[$	-0.0185	0.0107	0.0064	0.3260
$[0.35, 0.40[$	-0.0355	0.0099	0.0060	0.3751
$[0.40, 0.50[$	-0.0258	0.0073	0.0044	0.4479
$[0.50, 0.65[$	-0.0332	0.0073	0.0044	0.5668
$[0.65, 0.80[$	-0.0442	0.0105	0.0063	0.7140
$[0.80, 1.00[$	-0.0428	0.0234	0.0141	0.8405
bin range M_{inv}				$\langle M_{inv} \rangle$
$[0.0, 0.4[$	-0.0357	0.0106	0.0064	0.3615
$[0.4, 0.5[$	-0.0035	0.0090	0.0054	0.4506
$[0.5, 0.6[$	-0.0092	0.0093	0.0056	0.5487
$[0.6, 0.7[$	-0.0383	0.0101	0.0060	0.6496
$[0.7, 0.8[$	-0.0569	0.0098	0.0059	0.7496
$[0.8, 0.9[$	-0.0566	0.0119	0.0072	0.8457
$[0.9, 1.0[$	-0.0175	0.0148	0.0089	0.9469
$[1.0, 1.2[$	-0.0459	0.0147	0.0088	1.0875
$[1.2, 1.5[$	-0.0432	0.0178	0.0107	1.3420
$[1.5, 100[$	-0.0547	0.0362	0.0217	1.8938

bin range x	A	σ_{stat}	σ_{sys}	$\langle x \rangle$
$[0.003, 0.008[$	0.0277	0.0162	0.0097	0.0065
$[0.008, 0.013[$	-0.0079	0.0080	0.0048	0.0106
$[0.013, 0.020[$	-0.0056	0.0063	0.0038	0.0164
$[0.020, 0.032[$	-0.0019	0.0054	0.0033	0.0255
$[0.032, 0.050[$	-0.0151	0.0060	0.0036	0.0398
$[0.050, 0.080[$	-0.0313	0.0071	0.0043	0.0627
$[0.080, 0.130[$	-0.0410	0.0087	0.0052	0.1007
$[0.130, 0.210[$	-0.0717	0.0115	0.0069	0.1616
$[0.210, 1.000[$	-0.0525	0.0152	0.0091	0.2871
bin range z				$\langle z \rangle$
$[0.20, 0.25[$	-0.0232	0.0204	0.0122	0.2382
$[0.25, 0.30[$	-0.0132	0.0086	0.0052	0.2778
$[0.30, 0.35[$	-0.0039	0.0070	0.0042	0.3255
$[0.35, 0.40[$	-0.0180	0.0068	0.0041	0.3747
$[0.40, 0.50[$	-0.0117	0.0052	0.0031	0.4471
$[0.50, 0.65[$	-0.0192	0.0054	0.0032	0.5654
$[0.65, 0.80[$	-0.0319	0.0080	0.0048	0.7133
$[0.80, 1.00[$	-0.0127	0.0160	0.0096	0.8474
bin range M_{inv}				$\langle M_{inv} \rangle$
$[0.0, 0.4[$	-0.0211	0.0076	0.0046	0.3613
$[0.4, 0.5[$	-0.0037	0.0064	0.0038	0.4507
$[0.5, 0.6[$	-0.0113	0.0066	0.0039	0.5489
$[0.6, 0.7[$	-0.0128	0.0070	0.0042	0.6498
$[0.7, 0.8[$	-0.0259	0.0068	0.0041	0.7497
$[0.8, 0.9[$	-0.0259	0.0082	0.0049	0.8457
$[0.9, 1.0[$	-0.0015	0.0101	0.0061	0.9471
$[1.0, 1.2[$	-0.0254	0.0098	0.0059	1.0882
$[1.2, 1.5[$	-0.0136	0.0123	0.0074	1.3188

bin range x	A	σ_{stat}	σ_{sys}	$\langle x \rangle$
$[0.032, 0.050[$	-0.0147	0.0060	0.0036	0.0398
$[0.050, 0.080[$	-0.0310	0.0071	0.0043	0.0627
$[0.080, 0.130[$	-0.0409	0.0087	0.0052	0.1007
$[0.130, 0.210[$	-0.0717	0.0115	0.0069	0.1616
$[0.210, 1.000[$	-0.0529	0.0152	0.0091	0.2871
bin range z				$\langle z \rangle$
$[0.20, 0.25[$	-0.0357	0.0364	0.0218	0.2390
$[0.25, 0.30[$	-0.0367	0.0140	0.0084	0.2785
$[0.30, 0.35[$	-0.0184	0.0107	0.0064	0.3260
$[0.35, 0.40[$	-0.0349	0.0100	0.0060	0.3750
$[0.40, 0.50[$	-0.0259	0.0073	0.0044	0.4479
$[0.50, 0.65[$	-0.0329	0.0074	0.0044	0.5666
$[0.65, 0.80[$	-0.0435	0.0108	0.0065	0.7137
$[0.80, 1.00[$	-0.0486	0.0243	0.0146	0.8401
bin range M_{inv}				$\langle M_{inv} \rangle$
$[0.0, 0.4[$	-0.0357	0.0106	0.0064	0.3615
$[0.4, 0.5[$	-0.0035	0.0090	0.0054	0.4506
$[0.5, 0.6[$	-0.0092	0.0093	0.0056	0.5487
$[0.6, 0.7[$	-0.0383	0.0101	0.0060	0.6496
$[0.7, 0.8[$	-0.0569	0.0098	0.0059	0.7496
$[0.8, 0.9[$	-0.0566	0.0119	0.0072	0.8457
$[0.9, 1.0[$	-0.0175	0.0148	0.0089	0.9469
$[1.0, 1.2[$	-0.0459	0.0147	0.0088	1.0875
$[1.2, 1.5[$	-0.0478	0.0188	0.0113	1.3168

Table A.28.: Identified K^+K^- pair combined $2007/2010$ proton data azimuthal asymmetry and corresponding mean kinematic values; Q^2 in $(\mathrm{GeV}/c)^2$, W and M_{inv} in GeV/c^2.

bin range x	A	σ_{stat}	σ_{sys}	$\langle x \rangle$	$\langle Q^2 \rangle$	$\langle y \rangle$	$\langle z \rangle$	$\langle x \rangle$	$\langle W \rangle$	$\langle M_{inv} \rangle$	$\langle D_{nn} \rangle$
$[0.003, 0.008[$	0.0077	0.0681	0.0340	0.0065	1.237	0.0065	0.454	0.007	13.838	1.337	0.612
$[0.008, 0.013[$	-0.0291	0.0372	0.0186	0.0104	1.548	0.0104	0.532	0.010	12.098	1.335	0.778
$[0.013, 0.020[$	0.0056	0.0357	0.0179	0.0162	2.115	0.0162	0.576	0.016	11.242	1.325	0.827
$[0.020, 0.032[$	-0.0707	0.0383	0.0191	0.0252	3.174	0.0252	0.589	0.025	10.956	1.316	0.839
$[0.032, 0.080[$	-0.0217	0.0354	0.0177	0.0493	6.083	0.0493	0.595	0.049	10.711	1.307	0.846
$[0.080, 1.000[$	-0.0442	0.0483	0.0241	0.1482	18.444	0.1482	0.600	0.148	10.065	1.294	0.848
bin range z				$\langle z \rangle$							
$[0.20, 0.40[$	-0.0145	0.0476	0.0238	0.3431	4.449	0.599	0.3431	0.026	13.186	1.236	0.665
$[0.40, 0.50[$	0.0052	0.0387	0.0194	0.4508	4.592	0.515	0.4508	0.031	12.157	1.301	0.757
$[0.50, 0.65[$	-0.0313	0.0360	0.0180	0.5491	4.584	0.455	0.5491	0.036	11.372	1.330	0.815
$[0.65, 0.80[$	-0.0379	0.0277	0.0138	0.6897	4.450	0.384	0.6897	0.041	10.409	1.358	0.874
$[0.80, 1.00[$	-0.0627	0.0469	0.0234	0.8565	3.849	0.335	0.8565	0.040	9.740	1.384	0.910
bin range M_{inv}				$\langle M_{inv} \rangle$							
$[0.90, 1.05[$	0.0251	0.0385	0.0193	1.0239	4.274	0.452	0.541	0.034	11.296	1.0239	0.808
$[1.05, 1.15[$	-0.0169	0.0377	0.0188	1.0981	4.757	0.462	0.542	0.037	11.417	1.0981	0.801
$[1.15, 1.30[$	-0.0525	0.0352	0.0176	1.2215	4.668	0.463	0.556	0.037	11.440	1.2215	0.801
$[1.30, 1.50[$	-0.0576	0.0391	0.0195	1.3884	4.448	0.463	0.571	0.035	11.454	1.3884	0.801
$[1.50, 100.[$	-0.0248	0.0363	0.0181	1.8286	4.090	0.466	0.599	0.032	11.508	1.8286	0.799

Table A.29.: Identified π^+K^- pair combined $2007/2010$ proton data azimuthal asymmetry and corresponding mean kinematic values; Q^2 in $(\mathrm{GeV}/c)^2$, W and M_{inv} in GeV/c^2.

bin range x	A	σ_{stat}	σ_{sys}	$\langle x\rangle$	$\langle Q^2\rangle$	$\langle y\rangle$	$\langle z\rangle$	$\langle x\rangle$	$\langle W\rangle$	$\langle M_{inv}\rangle$	$\langle D_{nn}\rangle$
$[0.003, 0.013[$	-0.0404	0.0249	0.0149	0.0091	1.453	0.556	0.435	0.0091	12.760	1.063	0.712
$[0.013, 0.020[$	-0.0160	0.0263	0.0158	0.0162	2.071	0.429	0.484	0.0162	11.106	1.041	0.831
$[0.020, 0.032[$	-0.0085	0.0272	0.0163	0.0252	2.978	0.396	0.504	0.0252	10.571	1.030	0.853
$[0.032, 0.050[$	-0.0108	0.0333	0.0200	0.0397	4.598	0.387	0.509	0.0397	10.368	1.024	0.859
$[0.050, 0.080[$	-0.0056	0.0400	0.0240	0.0625	7.123	0.381	0.509	0.0625	10.162	1.016	0.863
$[0.080, 0.130[$	-0.1194	0.0507	0.0304	0.1002	11.290	0.376	0.510	0.1002	9.891	1.008	0.866
$[0.130, 1.000[$	-0.0010	0.0543	0.0326	0.2077	24.048	0.384	0.507	0.2077	9.360	0.999	0.862
bin range z				$\langle z\rangle$							
$[0.20, 0.30[$	-0.1224	0.0573	0.0344	0.2755	4.224	0.616	0.275	0.2755	13.389	0.936	0.645
$[0.30, 0.35[$	-0.0477	0.0399	0.0240	0.3263	4.243	0.550	0.326	0.3263	12.594	0.984	0.719
$[0.35, 0.40[$	-0.0120	0.0345	0.0207	0.3753	4.217	0.504	0.375	0.3753	12.005	1.010	0.764
$[0.40, 0.50[$	0.0393	0.0236	0.0142	0.4482	4.095	0.451	0.448	0.4482	11.298	1.037	0.810
$[0.50, 0.65[$	-0.0167	0.0226	0.0136	0.5660	3.914	0.386	0.566	0.5660	10.395	1.073	0.862
$[0.65, 1.00[$	-0.1056	0.0294	0.0177	0.7400	3.558	0.323	0.740	0.7400	9.476	1.113	0.909
bin range M_{inv}				$\langle M_{inv}\rangle$							
$[0.0, 0.8[$	-0.0436	0.0275	0.0165	0.7410	4.132	0.419	0.459	0.037	10.826	0.7410	0.833
$[0.8, 0.9[$	0.0122	0.0259	0.0155	0.8563	4.066	0.445	0.466	0.034	11.180	0.8563	0.810
$[0.9, 1.0[$	-0.0451	0.0286	0.0172	0.9423	4.049	0.451	0.476	0.034	11.256	0.9423	0.805
$[1.0, 1.2[$	-0.0123	0.0288	0.0173	1.0893	4.039	0.460	0.478	0.033	11.381	1.0893	0.797
$[1.2, 100[$	-0.0358	0.0269	0.0161	1.5157	3.845	0.469	0.514	0.030	11.510	1.5157	0.789

Table A.30.: Identified $K^+\pi^-$ pair combined $2007/2010$ proton data azimuthal asymmetry and corresponding mean kinematic values; Q^2 in $(\mathrm{GeV}/c)^2$, W and M_{inv} in GeV/c^2.

bin range x	A	σ_{stat}	σ_{sys}	$\langle x\rangle$	$\langle Q^2\rangle$	$\langle y\rangle$	$\langle z\rangle$	$\langle x\rangle$	$\langle W\rangle$	$\langle M_{inv}\rangle$	$\langle D_{nn}\rangle$
$[0.003, 0.013[$	-0.0334	0.0222	0.0111	0.0092	1.445	0.548	0.441	0.0092	12.673	1.069	0.720
$[0.013, 0.020[$	-0.0383	0.0225	0.0113	0.0162	2.021	0.418	0.495	0.0162	10.963	1.045	0.840
$[0.020, 0.032[$	-0.0417	0.0226	0.0113	0.0253	2.874	0.381	0.519	0.0253	10.366	1.033	0.864
$[0.032, 0.050[$	-0.0086	0.0270	0.0135	0.0398	4.394	0.370	0.527	0.0398	10.125	1.024	0.872
$[0.050, 0.080[$	-0.0294	0.0313	0.0157	0.0628	6.793	0.362	0.532	0.0628	9.901	1.016	0.877
$[0.080, 0.130[$	-0.0257	0.0380	0.0190	0.1007	10.670	0.354	0.537	0.1007	9.591	1.007	0.882
$[0.130, 1.000[$	-0.0425	0.0382	0.0191	0.2086	22.720	0.359	0.539	0.2086	9.038	0.992	0.880
bin range z				$\langle z\rangle$							
$[0.20, 0.30[$	-0.0796	0.0527	0.0264	0.2758	4.272	0.613	0.276	0.2758	13.354	0.938	0.649
$[0.30, 0.35[$	-0.0519	0.0361	0.0180	0.3265	4.383	0.545	0.327	0.3265	12.528	0.984	0.725
$[0.35, 0.40[$	-0.0208	0.0303	0.0152	0.3754	4.445	0.497	0.375	0.3754	11.899	1.007	0.771
$[0.40, 0.50[$	-0.0027	0.0201	0.0100	0.4489	4.434	0.440	0.449	0.4489	11.140	1.030	0.819
$[0.50, 0.65[$	-0.0523	0.0182	0.0091	0.5676	4.379	0.372	0.568	0.5676	10.168	1.063	0.872
$[0.65, 1.00[$	-0.0260	0.0222	0.0111	0.7421	4.067	0.309	0.742	0.7421	9.233	1.112	0.917
bin range M_{inv}				$\langle M_{inv}\rangle$							
$[0.0, 0.8[$	-0.0014	0.0229	0.0115	0.7403	4.512	0.401	0.473	0.043	10.548	0.7403	0.847
$[0.8, 0.9[$	-0.0449	0.0214	0.0107	0.8568	4.433	0.424	0.484	0.039	10.864	0.8568	0.827
$[0.9, 1.0[$	-0.0555	0.0235	0.0117	0.9419	4.428	0.429	0.495	0.039	10.941	0.9419	0.823
$[1.0, 1.2[$	-0.0538	0.0240	0.0120	1.0892	4.323	0.440	0.496	0.037	11.086	1.0892	0.814
$[1.2, 100[$	-0.0067	0.0222	0.0111	1.5171	4.058	0.449	0.532	0.034	11.227	1.5171	0.807

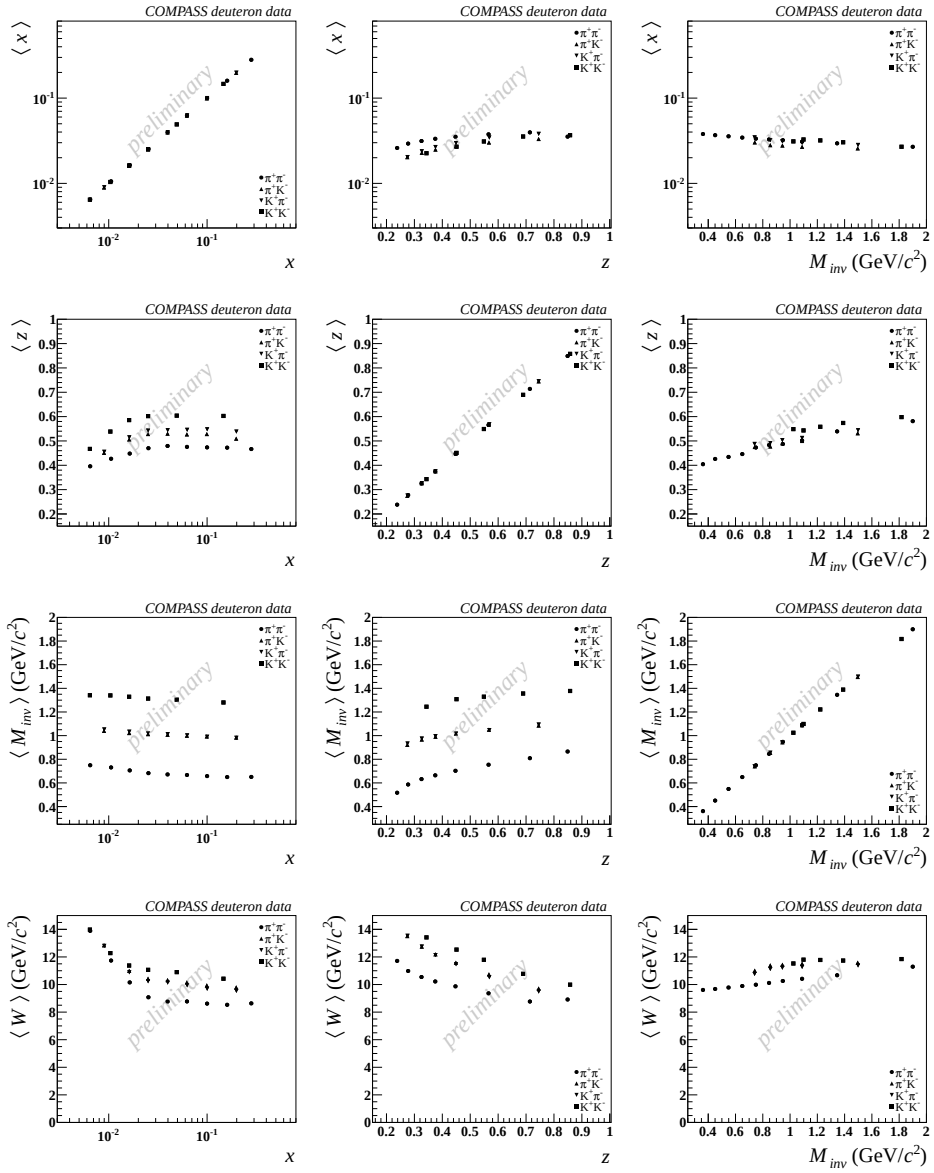

Figure A.48.: The 2003/2004 deuteron data hadron-pair kinematic mean values $\pi^+\pi^-$, K^+K^-, π^+K^- and $K^+\pi^-$ pairs:
1st column in x bins, 2nd column in z bins, 3rd column in M_{inv} bins
1st row $\langle x \rangle$, 2nd row $\langle z \rangle$, 3rd row $\langle M_{inv} \rangle$ and 4th row $\langle W \rangle$.

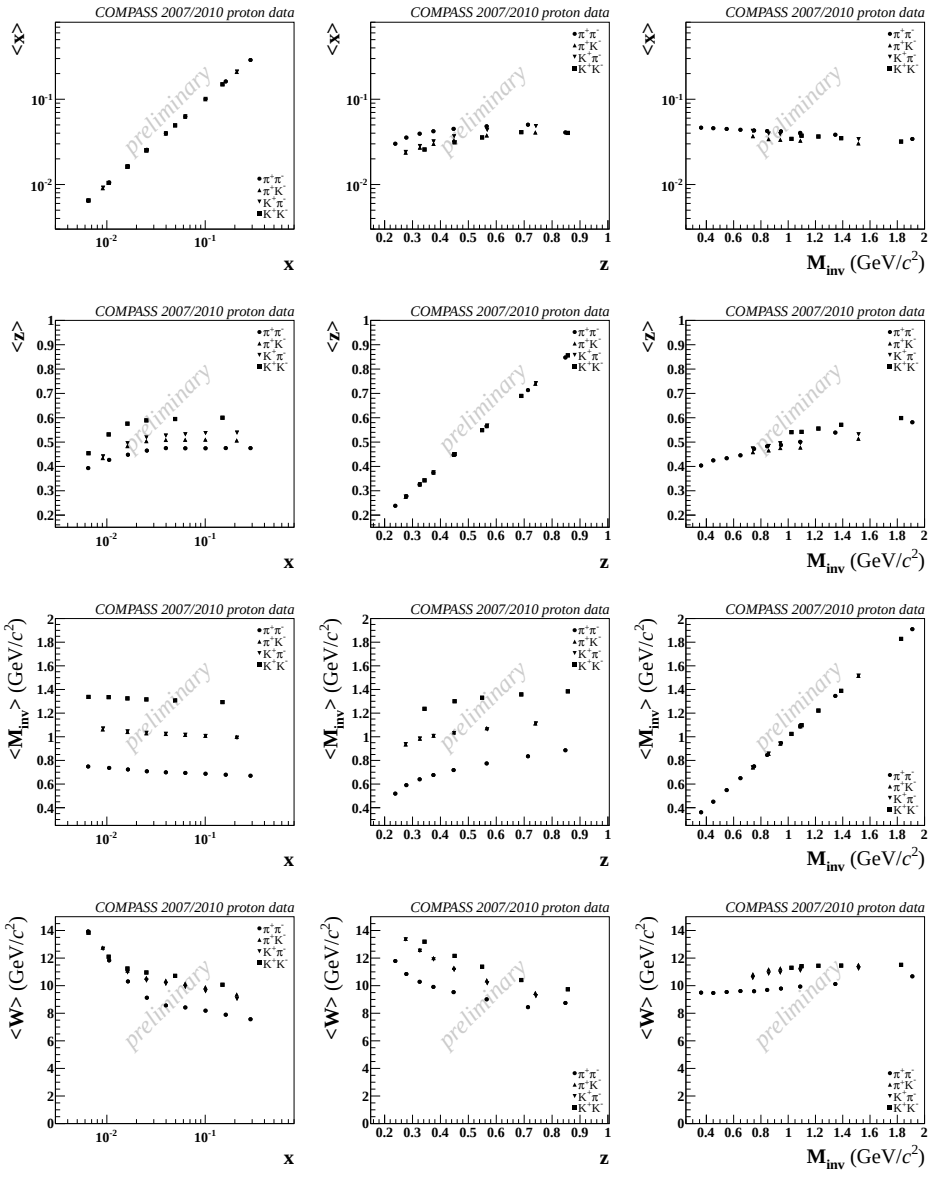

Figure A.49.: The combined 0710 and 2010 proton data hadron-pair kinematic mean values $\pi^+\pi^-$, K^+K^-, π^+K^-, and $K^+\pi^-$ pairs:
1st column in x bins, 2nd column in z bins, 3rd column in M_{inv} bins
1st row $\langle x \rangle$, 2nd row $\langle z \rangle$, 3rd row $\langle M_{inv} \rangle$, and 4th row $\langle W \rangle$.

A.5. Interpretation of the results and extraction of the transversity PDF

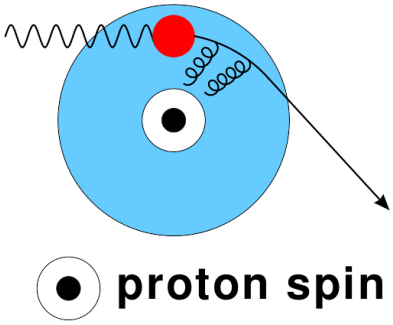

Figure A.50.: Scheme of the principle of chromodynamic lensing [Wol10].

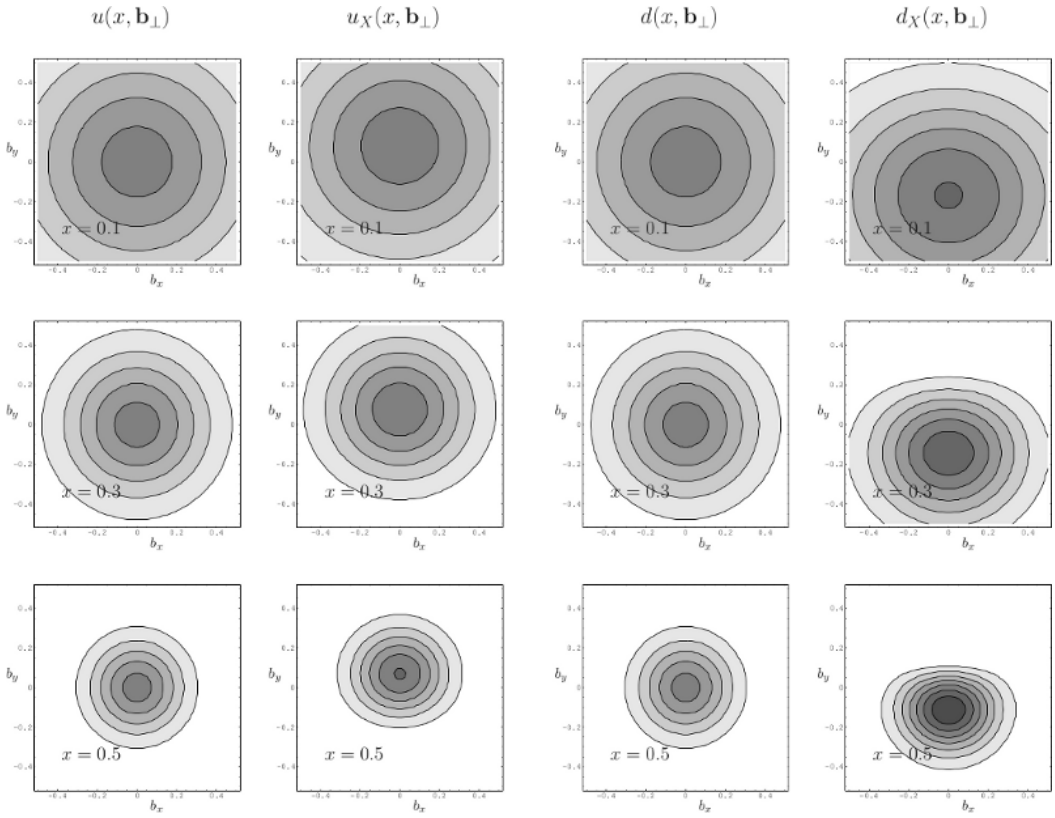

Figure A.51.: Model predictions of the probability distributions of finding unpolarized u-quarks (left) and d-quarks (right) shown in the transverse plane for three values of x: $u(x, \boldsymbol{b}_\perp)$ and $d(x, \boldsymbol{b}_\perp)$ are calculated for an unpolarized proton and $u_X(x, \boldsymbol{b}_\perp)$ and $d_X(x, \boldsymbol{b}_\perp)$ for an in direction b_x transversely polarized proton [Bur02].

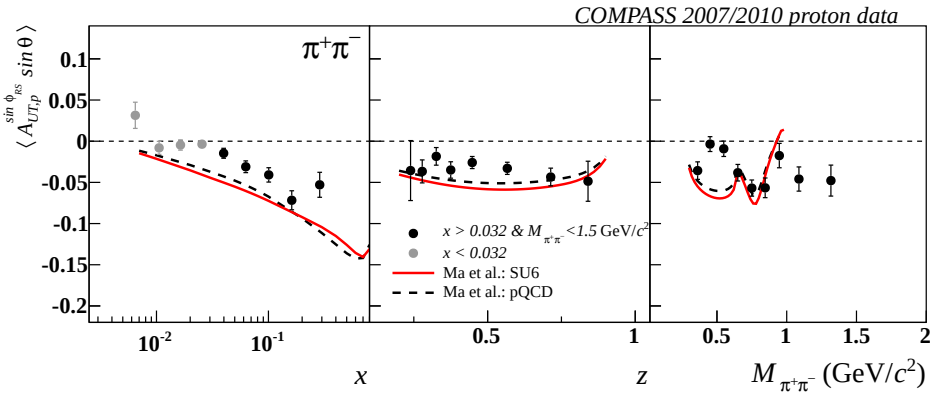

Figure A.52.: The combined 2007/2010 pion pair asymmetries with a cut at $x > 0.032$ in comparison with the model predictions from Ma *et al.* [SHBM08] the SU(6) quark-diquark model (red line), the pQCD based model (black dashed line). The numerical values obtained from the analysis of this sub-sample can be found in Tab. A.27.

	HERMES	data		
x	y	Q^2[GeV^2]	A_{SIDIS}	$h_1^{u_v} - h_1^{d_v}/4$
0.033	0.734	1.232	0.015 ± 0.010	0.086 ± 0.061
0.047	0.659	1.604	0.002 ± 0.011	0.010 ± 0.054
0.068	0.630	2.214	0.035 ± 0.011	0.167 ± 0.069
0.133	0.592	4.031	0.020 ± 0.010	0.092 ± 0.054
	COMPASS	proton	data	
x		Q^2[GeV^2]	A_{SIDIS}	$h_1^{u_v} - h_1^{d_v}/4$
0.0065		1.232	0.026 ± 0.030	0.10 ± 0.12
0.0105		1.476	0.010 ± 0.016	0.038 ± 0.059
0.0164		1.744	0.015 ± 0.013	0.057 ± 0.049
0.1330		2.094	0.008 ± 0.010	0.031 ± 0.039
0.0398		2.802	0.027 ± 0.011	0.107 ± 0.049
0.0626		4.342	0.029 ± 0.014	0.118 ± 0.060
0.1006		6.854	0.051 ± 0.016	0.208 ± 0.079
0.1613		10.72	0.108 ± 0.023	0.42 ± 0.12
0.2801		21.98	0.080 ± 0.033	0.24 ± 0.11
	COMPASS	deuteron	data	
x		Q^2[GeV^2]	A_{SIDIS}	$h_1^{u_v} + h_1^{d_v}$
0.0064		1.253	0.005 ± 0.024	0.05 ± 0.24
0.0105		1.508	-0.004 ± 0.012	-0.04 ± 0.12
0.0163		1.792	0.028 ± 0.010	0.28 ± 0.11
0.0253		2.266	-0.005 ± 0.009	-0.051 ± 0.094
0.0396		3.350	0.006 ± 0.011	0.06 ± 0.12
0.0623		5.406	-0.006 ± 0.014	-0.06 ± 0.14
0.0996		8.890	-0.029 ± 0.019	-0.30 ± 0.20
0.1597		15.65	-0.017 ± 0.030	-0.16 ± 0.28
0.2801		33.22	0.078 ± 0.054	0.50 ± 0.36

Figure A.53.: Table 1 of [BCR13] quoting HERMES and COMPASS $\langle x \rangle$, $\langle Q^2 \rangle$ and $A_{UT}^{\sin\phi_{RS}}$ values from Refs. [HERMES08] and [COMPASS12c], respectively. The last column contains the numerical values of the linear combinations $xh_{1,p}$ and $xh_{1,d}$ as in Eq. 6.31.

	HERMES	range	for proton		
Q^2 [GeV^2]	n_u	n_d	n_s	$n_u^\uparrow$
1.232	0.607	0.614	0.393	-0.157 ± 0.037
1.604	0.589	0.595	0.380	-0.152 ± 0.037
2.214	0.569	0.575	0.365	-0.146 ± 0.037
4.031	0.536	0.542	0.341	-0.137 ± 0.037
	COMPASS	range	for proton		
Q^2 [GeV^2]	n_u	n_d	n_s	$n_u^\uparrow$
1.232	0.897	0.906	0.580	-0.183 ± 0.031
1.476	0.876	0.885	0.565	-0.178 ± 0.031
1.744	0.858	0.867	0.552	-0.175 ± 0.031
2.094	0.840	0.849	0.539	-0.171 ± 0.031
2.802	0.813	0.822	0.520	-0.165 ± 0.031
4.342	0.776	0.785	0.494	-0.158 ± 0.031
6.854	0.742	0.751	0.471	-0.151 ± 0.031
10.720	0.713	0.721	0.451	-0.145 ± 0.031
21.985	0.671	0.679	0.422	-0.136 ± 0.031
	COMPASS	range	for deuteron		
Q^2 [GeV^2]	n_u	n_d	n_s	$n_u^\uparrow$
1.253	0.895	0.904	0.578	-0.182 ± 0.031
1.508	0.874	0.883	0.563	-0.178 ± 0.031
1.792	0.855	0.865	0.550	-0.174 ± 0.031
2.266	0.832	0.841	0.534	-0.169 ± 0.031
3.350	0.797	0.806	0.509	-0.162 ± 0.031
5.406	0.759	0.768	0.483	-0.154 ± 0.031
8.890	0.725	0.733	0.459	-0.147 ± 0.031
15.652	0.690	0.698	0.435	-0.140 ± 0.031
33.219	0.650	0.657	0.408	-0.132 ± 0.031

Figure A.54.: Results of the integrated unpolarized DiFF $n_q(Q^2)$ of u, d and s quarks and of the integrated polarized DiFF $n_q^\uparrow(Q^2)$ of u quarks in HERMES and COMPASS asymmetries binning [BCR13]. For the integral see Eq. 6.33 and for assumption on the flavor dependence see Eq. 6.35.

Table A.31.: Table for the calculation of $x\,h_1^{u_v} + x\,h_1^{d_v}$. The first three columns of the upper sub-table are the h^+h^- from the deuteron 2002-2004 data from [COMPASS12c], while the first three columns in the second sub-table are the final results for identified $\pi^+\pi^-$ from the deuteron 2003-2004 extracted in this work. Bacchetta *et al.* [BCR13] extracted $x\,h_1^{u_v} + x\,h_1^{d_v}$ from the h^+h^- results (see Fig. A.53) shown in column 4 of the first sub-table and the column 5 are the bin-by-bin ratios $\frac{x\,h_1^{u_v}+x\,h_1^{d_v}}{A_{UT,d}^{\sin\phi_{RS}}}$. These ratios are used in the second sub-table to convert the final asymmetries of $\pi^+\pi^-$ to $x\,h_1^{u_v} + x\,h_1^{d_v}$, shown in column 5 of the lower sub-table. The quoted uncertainties are combined statistical and systematic uncertainties from the data sets.

2002-2004 deuteron h^+h^-

$\langle x \rangle$	$\langle Q^2 \rangle$	$A_{UT,d}^{\sin\phi_{RS}}$	$xh_{1,d}$	$\frac{xh_{1,d}}{A_{UT,d}^{\sin\phi_{RS}}}$
0.0064	1.253	0.005 ± 0.024	0.05 ± 0.24	10.0
0.0105	1.508	-0.004 ± 0.012	-0.04 ± 0.12	10.0
0.0163	1.792	0.028 ± 0.010	0.28 ± 0.11	10.0
0.0253	2.266	-0.005 ± 0.009	-0.05 ± 0.09	10.2
0.0396	3.350	0.006 ± 0.011	0.06 ± 0.12	10.0
0.0623	5.406	-0.006 ± 0.014	-0.06 ± 0.14	10.0
0.0996	8.890	-0.029 ± 0.019	-0.30 ± 0.20	10.3
0.1597	15.650	-0.017 ± 0.030	-0.16 ± 0.28	9.4
0.2801	33.220	0.078 ± 0.054	0.50 ± 0.36	6.4

2003 & 2004 deuteron $\pi^+\pi^-$

$\langle x \rangle$	$\langle Q^2 \rangle$	$A_{UT,d}^{\sin\phi_{RS}}$	$\frac{xh_{1,d}}{A_{UT,d}^{\sin\phi_{RS}}}$	$xh_{1,d}$
0.0065	1.257	0.004 ± 0.030	10.0	0.04 ± 0.30
0.0106	1.523	-0.014 ± 0.014	10.0	-0.14 ± 0.14
0.0163	1.816	0.022 ± 0.011	10.0	0.22 ± 0.11
0.0253	2.282	0.004 ± 0.011	10.2	0.04 ± 0.11
0.0396	3.334	-0.003 ± 0.013	10.0	-0.03 ± 0.13
0.0624	5.341	-0.007 ± 0.016	10.0	-0.07 ± 0.16
0.0997	8.651	-0.031 ± 0.021	10.3	-0.32 ± 0.22
0.1597	14.783	-0.004 ± 0.034	9.4	-0.04 ± 0.32
0.2787	31.539	0.119 ± 0.058	6.4	0.76 ± 0.37

Table A.32.: Table for the calculation of $x\,h_1^{u_v} - \frac{1}{4}x\,h_1^{d_v}$. The first three columns of the upper sub-table are the h^+h^- from the proton 2007 data from [COMPASS12c], while the first three columns in the second sub-table are the final results for identified $\pi^+\pi^-$ from the proton 2007 & 2010 extracted in this work. Bacchetta *et al.* [BCR13] extracted $x\,h_1^{u_v} - \frac{1}{4}x\,h_1^{d_v}$ from the h^+h^- results (see Fig. A.53) shown in column 4 of the first sub-table and the column 5 are the bin-by-bin ratios $\frac{x\,h_1^{u_v} - \frac{1}{4}x\,h_1^{d_v}}{A_{UT,p}^{\sin\phi_{RS}}}$. These ratios are used in the second sub-table to convert the final asymmetries of $\pi^+\pi^-$ to $x\,h_1^{u_v} - \frac{1}{4}x\,h_1^{d_v}$, shown in column 5 of the lower sub-table. The quoted uncertainties are combined statistical and systematic uncertainties from the data sets.

2007 proton h^+h^-

$\langle x \rangle$	$\langle Q^2 \rangle$	$A_{UT,p}^{\sin\phi_{RS}}$	$xh_{1,p}$	$\frac{xh_{1,p}}{A_{UT,p}^{\sin\phi_{RS}}}$
0.0065	1.232	0.026 ± 0.030	0.10 ± 0.12	3.85
0.0105	1.476	0.010 ± 0.016	0.038 ± 0.059	3.80
0.0164	1.744	0.015 ± 0.013	0.057 ± 0.049	3.80
0.0256	2.094	0.008 ± 0.010	0.031 ± 0.039	3.88
0.0398	2.802	0.027 ± 0.011	0.107 ± 0.049	3.96
0.0626	4.342	0.029 ± 0.014	0.118 ± 0.060	4.07
0.1006	6.854	0.051 ± 0.016	0.208 ± 0.079	4.08
0.1613	10.72	0.108 ± 0.023	0.42 ± 0.12	3.89
0.2801	21.98	0.080 ± 0.033	0.24 ± 0.11	3.00

2007 & 2010 proton $\pi^+\pi^-$

$\langle x \rangle$	$\langle Q^2 \rangle$	$A_{UT,p}^{\sin\phi_{RS}}$	$\frac{xh_{1,p}}{A_{UT,p}^{\sin\phi_{RS}}}$	$xh_{1,p}$
0.0065	1.244	-0.0314 ± 0.0185	3.85	-0.121 ± 0.071
0.0106	1.495	0.0081 ± 0.0092	3.80	0.031 ± 0.035
0.0164	1.801	0.0046 ± 0.0072	3.80	0.017 ± 0.027
0.0255	2.259	0.0036 ± 0.0063	3.88	0.014 ± 0.024
0.0398	3.202	0.0152 ± 0.0070	3.96	0.060 ± 0.028
0.0627	4.987	0.0307 ± 0.0083	4.07	0.125 ± 0.034
0.1006	7.870	0.0410 ± 0.0101	4.08	0.167 ± 0.041
0.1616	12.637	0.0706 ± 0.0134	3.89	0.275 ± 0.052
0.2871	24.815	0.0543 ± 0.0176	3.00	0.163 ± 0.053

Table A.33.: The final results of the u and d valence quark transversities distribution extracted from the final deuteron and proton $\pi^+\pi^-$ pair asymmetry. The quoted uncertainties are combined statistical and systematic uncertainties from the data sets.

$\langle x \rangle$	$xh_1^{u_v}$	$xh_1^{d_v}$
0.0065	-0.088 $\pm$ 0.083	0.130 $\pm$ 0.239
0.0106	-0.004 $\pm$ 0.040	-0.140 $\pm$ 0.116
0.0164	0.057 $\pm$ 0.032	0.159 $\pm$ 0.091
0.0255	0.020 $\pm$ 0.029	0.025 $\pm$ 0.086
0.0398	0.043 $\pm$ 0.034	-0.069 $\pm$ 0.102
0.0627	0.086 $\pm$ 0.042	-0.157 $\pm$ 0.128
0.1006	0.070 $\pm$ 0.055	-0.388 $\pm$ 0.175
0.1616	0.212 $\pm$ 0.076	-0.250 $\pm$ 0.255
0.2871	0.283 $\pm$ 0.086	0.479 $\pm$ 0.298

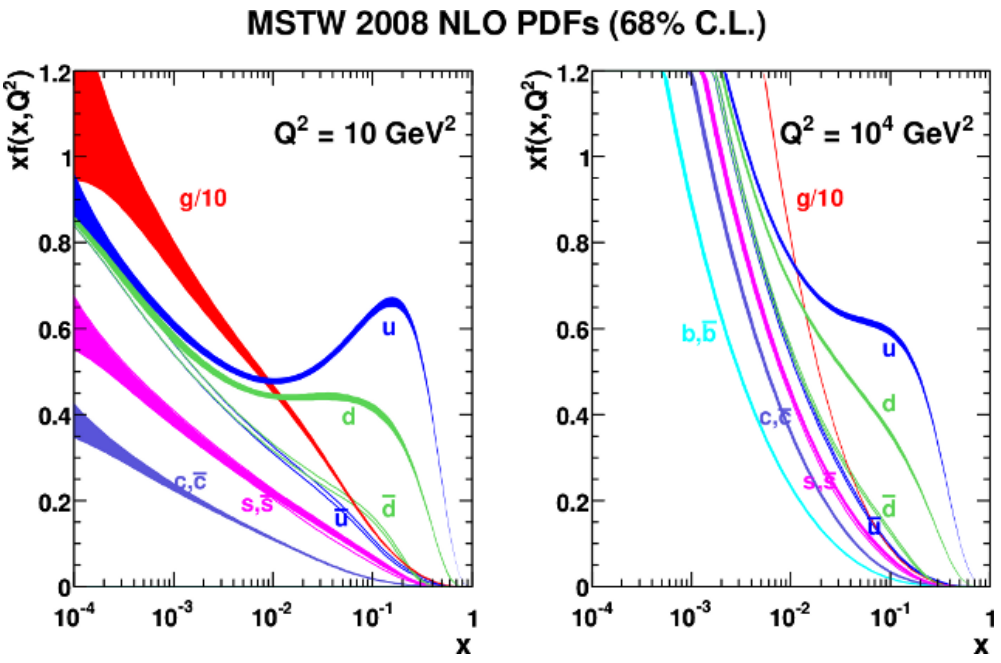

Figure A.55.: Results for the unpolarized PDF xf_1 as obtained from the MSTW 2008 leading-order parametrization at $\langle Q^2 \rangle = 10\,\mathrm{GeV}/c^2$ (left panel) and at $\langle Q^2 \rangle = 1 \times 10^4\,\mathrm{GeV}/c^2$ (right panel) [MSTW09].

A.6. Future prospects

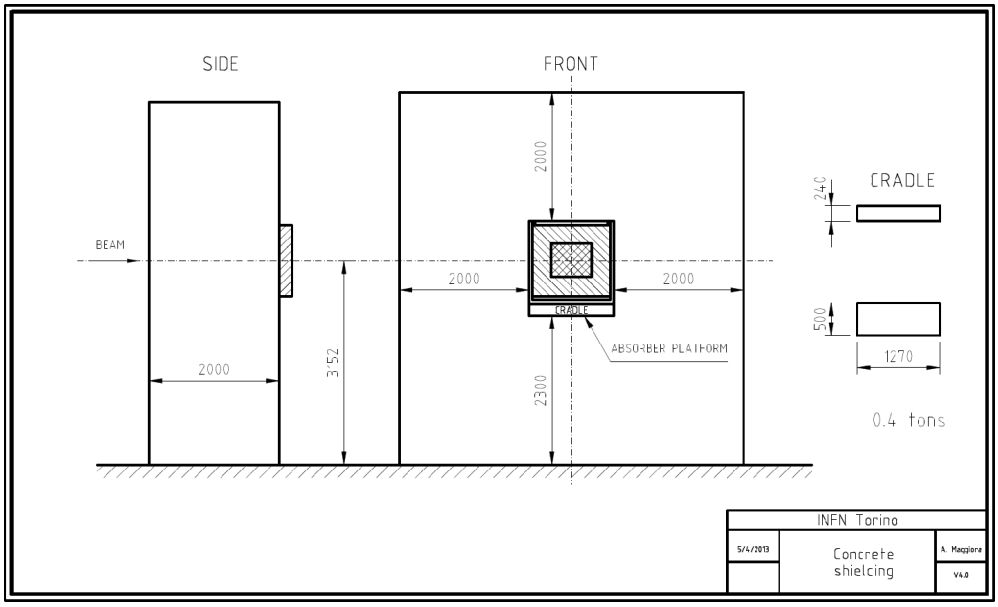

Figure A.56.: A technical drawing of the concrete shielding as a part of the Drell-Yan hadron absorber [Pan13].

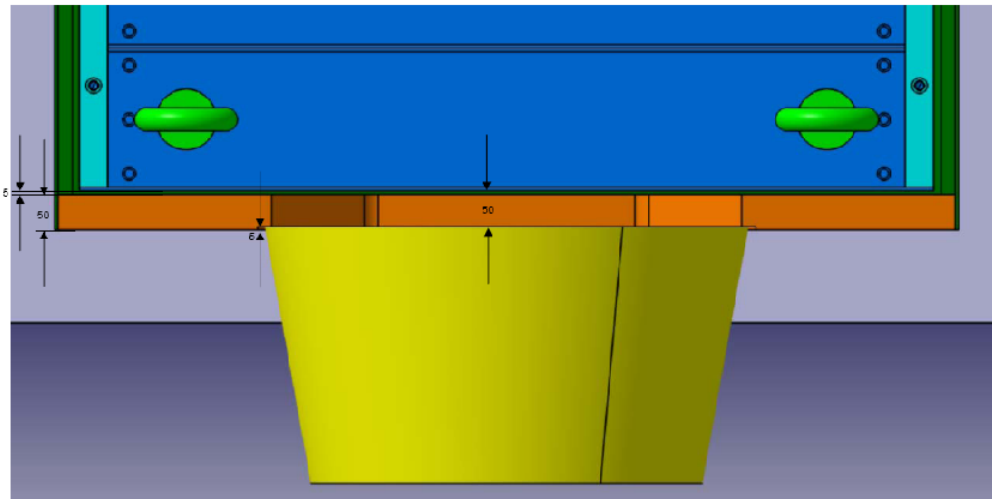

Figure A.57.: Top view of the absorber. The vertex detector will be placed between the conical part (yellow) and the box-shaped part (blue) inside a gap of its frame (orange). The size of this gap was enlarged from 50 to the maximum available 65 mm during the design process [Pan13].

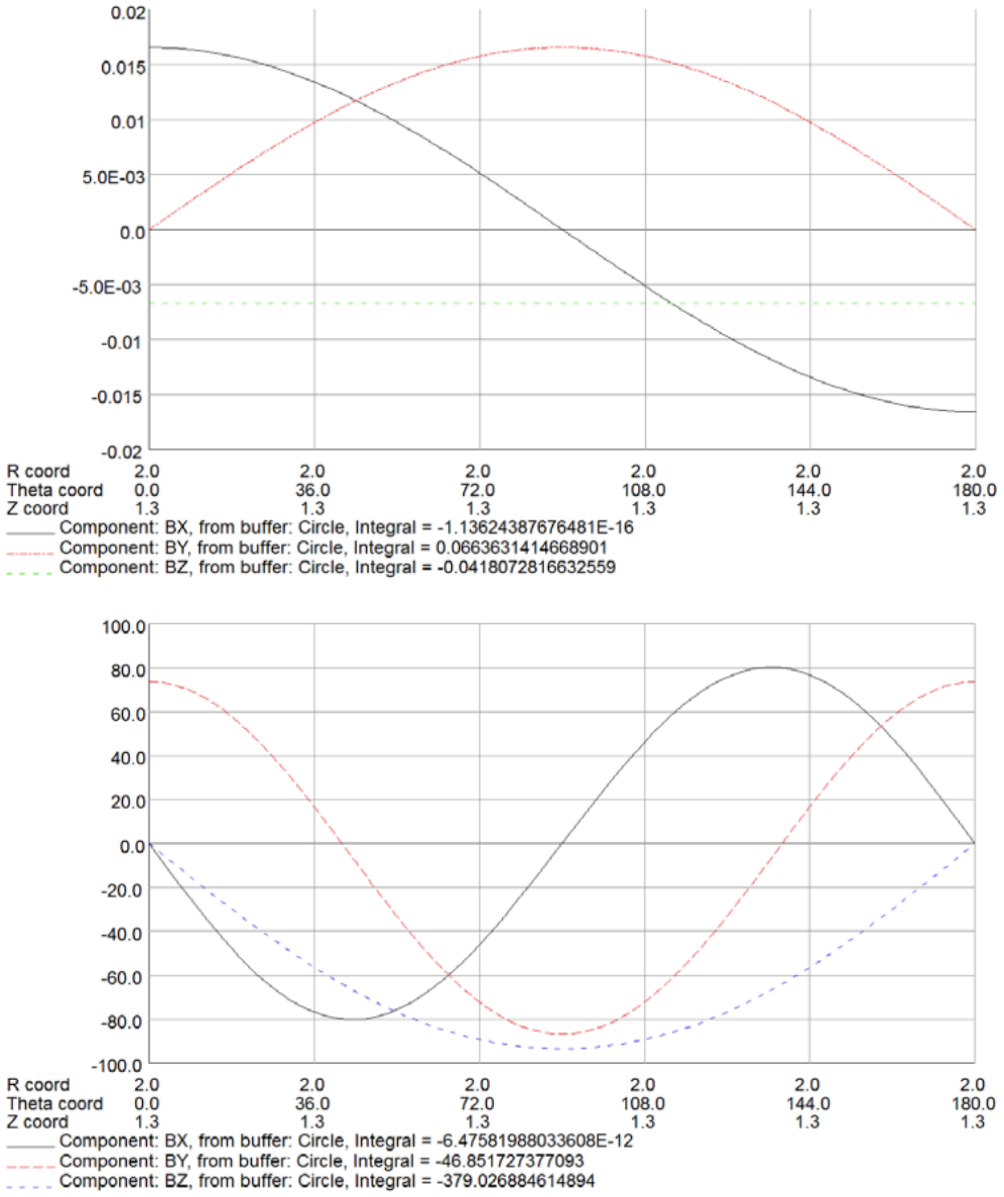

Figure A.58.: The distribution of magnetic field strength generated by the target magnet at the position of the photomultiplier of the vertex detector. The distance to beam axis R is 2 m and the angle coordinate θ starts at the Jura side going clock-wise seen in beam direction. In the top panel the solenoidal components of the field strengths in Tesla are given and in the bottom panel the ones of the dipole field in Gauss ($1\,\mathrm{Gs} = 1 \times 10^{-4}\,\mathrm{T}$) [Gau13].

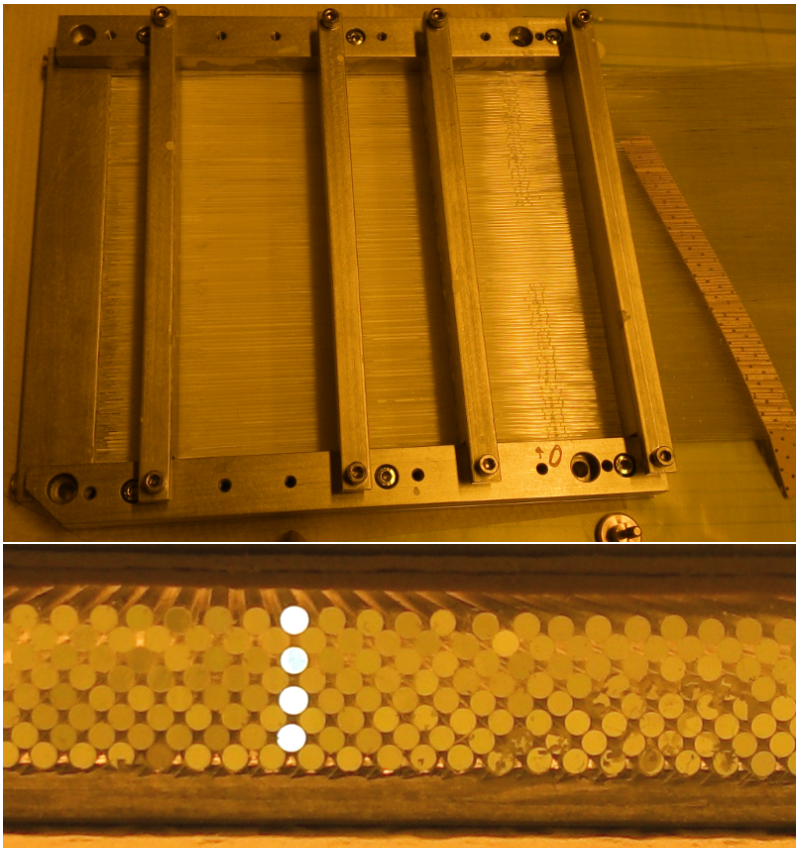

Figure A.59.: Picture of one of the planes of the vertex detector taken during the fiber stacking (top) and front surface with one read-out channel illuminated (bottom).

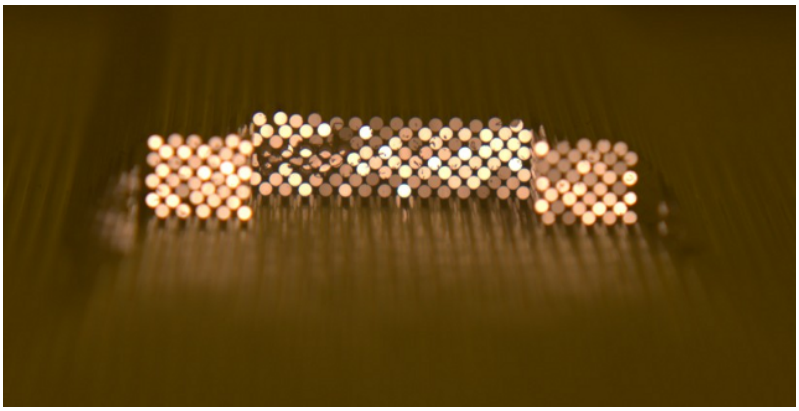

Figure A.60.: Picture of one of the planes doubling fibers stack of one of the diagonal planes, the step function is visible and the supporting spacer fibers are left and right of the active scintillating fibers.

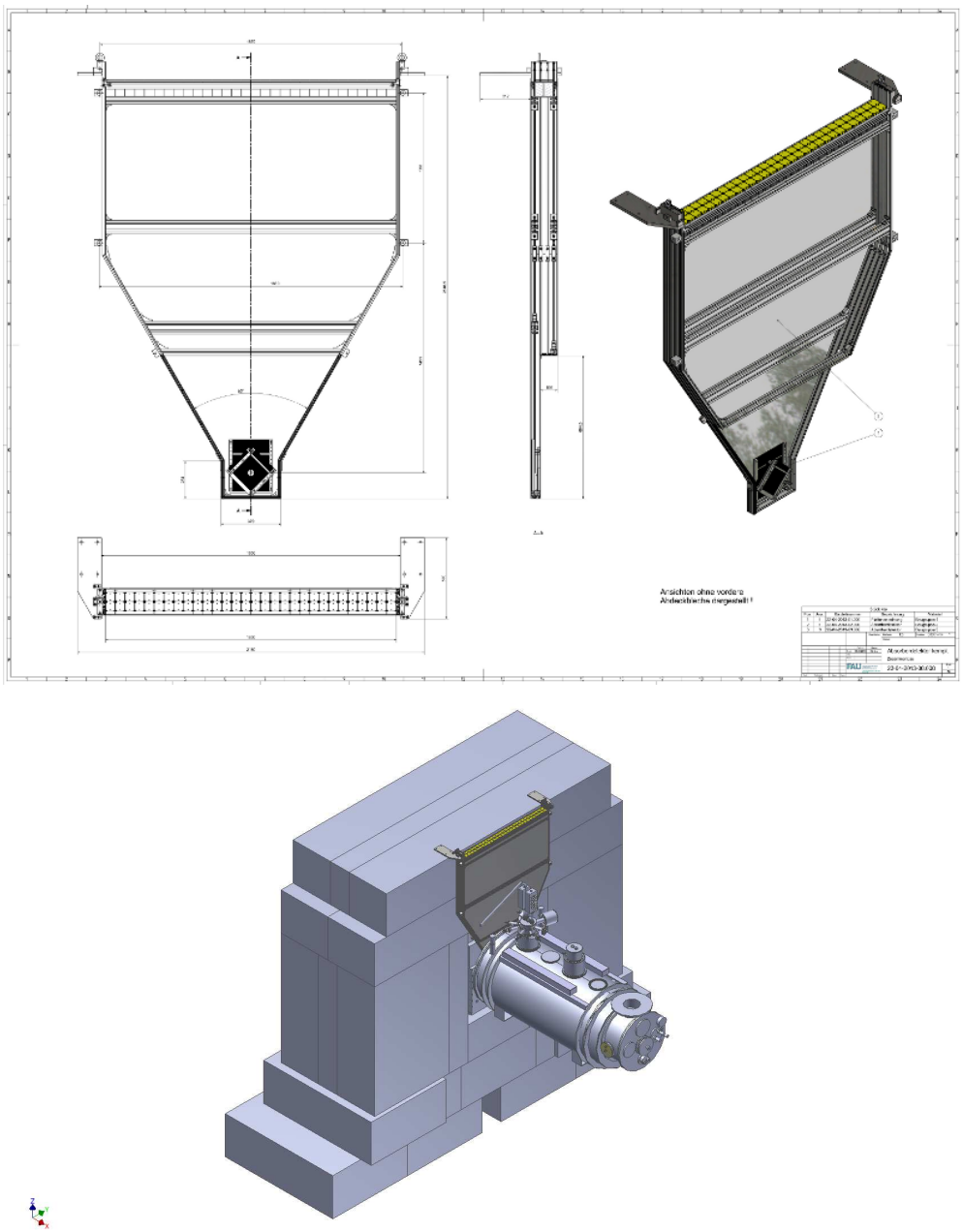

Figure A.61.: CAD drawing (by courtesy of K. Kärcher) of the housing for the vertex detector (top picture): front, side, top and three-dimensional view. The vertex detector in its designated position inside of the Drell-Yan setup mounted at the upstream side of the concrete shielding of the absorber.

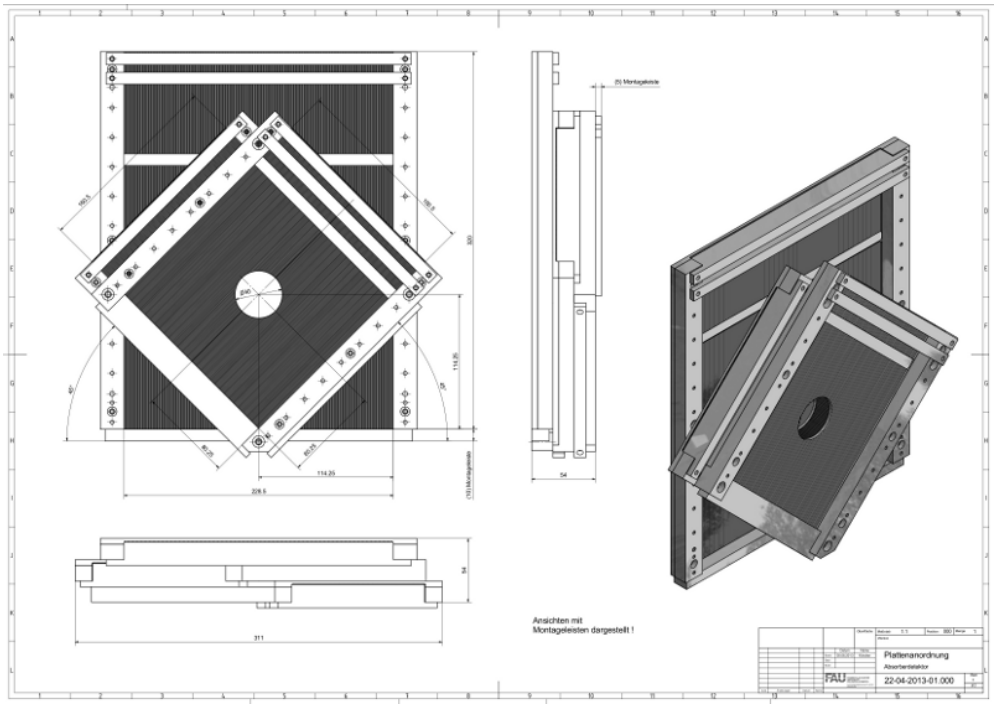

Figure A.62.: CAD drawing (by courtesy of K. Kärcher) of the active detector area inside of the housing, seen from beam direction (left).

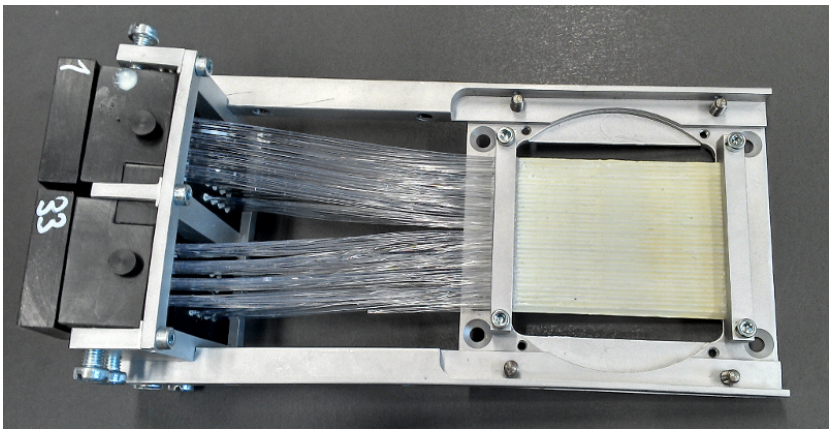

Figure A.63.: Picture of the additional third plane for FI15, which is identical to the existing planes of FI15.

A.6.1. A SciFi beam telescope for the Drell-Yan measurement at COMPASS

As for the previous SIDIS measurements a beam telescope in the region before the polarized target is also needed for the Drell-Yan measurement. The available space in front of the target has been decreased w.r.t. the SIDIS setup, since the target is shifted upstream to provide space for the absorber. This prevents for a parallel use of the scintillating-fiber hodoscopes (see Sec. 3.3.1) and silicon microstrip detectors (see Sec. 3.3.2), which also might suffer under a reduced efficiency due to the very high rates. The need for a good time resolution outweighs the spacial resolution here, hence a beam telescope made of Scintillating-Fiber detectors was requested by the Drell-Yan COMPASS group.
A setup of three SciFi detectors at the positions BT01-03 as in the SIDIS measurements is maintained as the basic concept, illustrated in Fig. A.64. These should be distributed in almost equal distances in the available space. Several boundary conditions on the properties of the detectors to be used exist, such as BT03 is exposed to the magnetic field of the polarized target. Since FI03 (see Tab. A.3) was originally designed to operate directly at the downstream end of the target, being exposed to the same field, it is to only suitable candidate for position BT03. For the central detector, BT02, FI15 (see Sec. 3.3.1) is a reasonable candidate, due to its compact design and the width of its active area being larger then the diameter of the target.

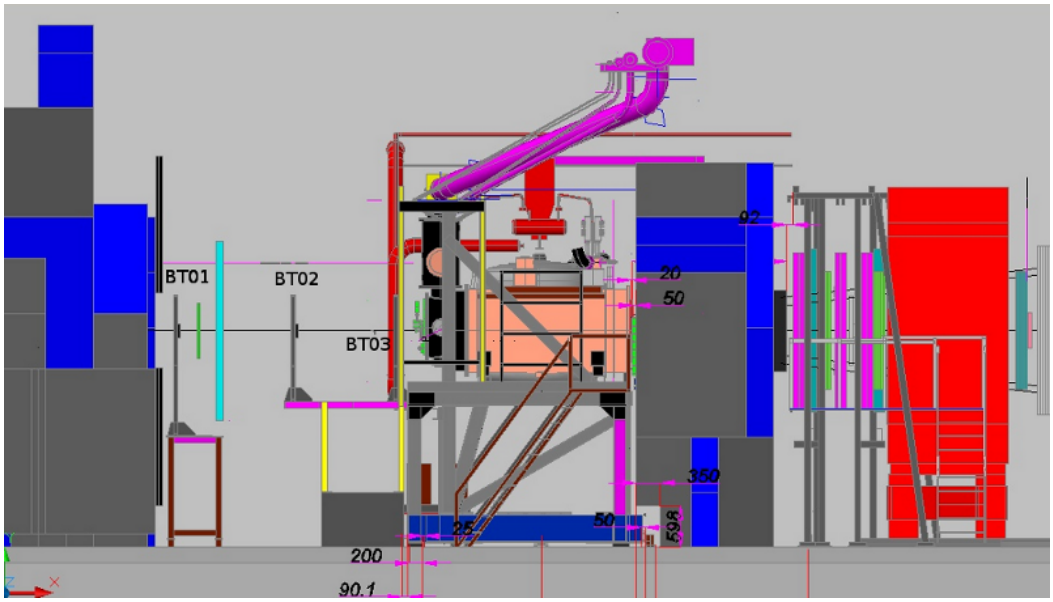

Figure A.64.: Schematic view of the Drell-Yan target area [Den14]. The beam enters from the right side, the target cryostat is indicated in orange and SM1 in red. The SciFi beam telescope will consist of three stations at the positions BT01, BT02, and BT03.

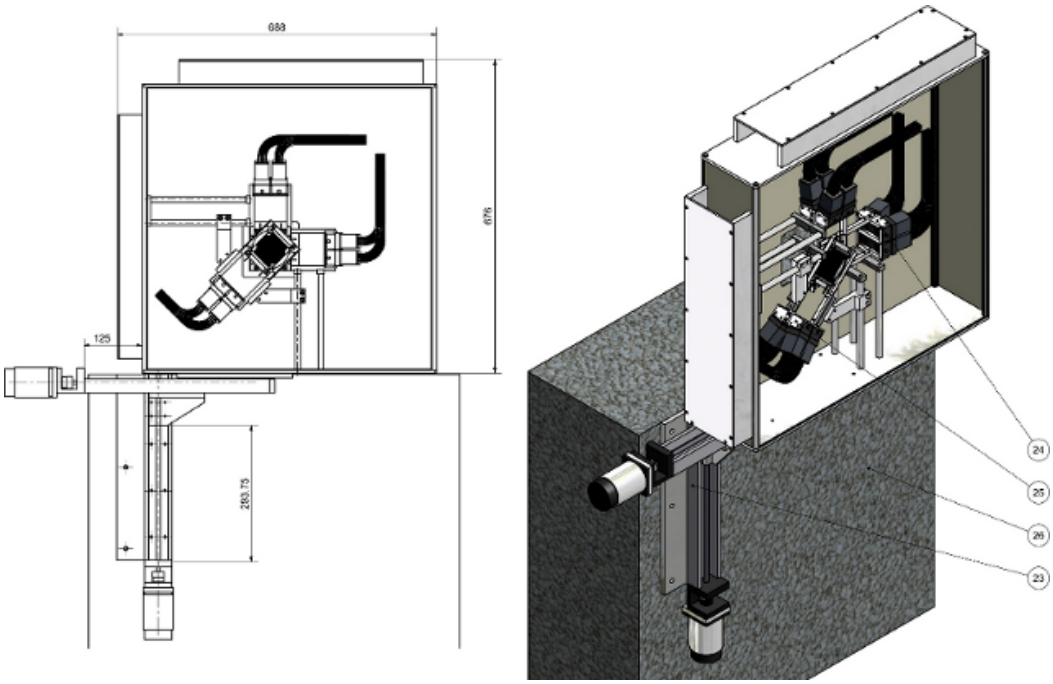

Figure A.65.: Technical drawing of the extended FI15 (BT02) with three planes X, Y, and V with housing and motorized two-dimensional positioning stage (by courtesy of K. Kärcher).

However, its two planes do not offer redundancy and the possibility to resolve ambiguities, see Fig. A.7, thus a third plane is useful to add.
Figure A.63 shows a picture of the third plane, which has been produced. A new housing has to be constructed, where all three planes fit in; a technical drawing of it is shown in Fig. A.65.
The two options of using FI01 or FI04 as BT01 have been considered, where both have advantages and disadvantages. FI01 has only two planes, X and Y, and an active area of $3.9 \times 3.9\,\mathrm{mm}^2$, which is not covering the full $4\,\mathrm{cm}$ of the target diameter[1]. But it has been used previously in this position and thus is expected to be sufficient. FI04 has three planes, each $5.3 \times 5.3\,\mathrm{mm}^2$. But it has a large housing which will require either a complete modification or a dedicated mounting, which feasibility is not yet clarified. Both options are currently under investigation and a final decision by the technical board is expected by end of April 2014. Recent MC simulations by Takekawa have shown that with a beam telescope with a total number of nine planes (three planes per detector) $89.6\,\%$ of the primary vertices are reconstructed, compared to $85.8\,\%$ with a beam telescope consisting of eight planes [Tak14]. Since one also might have to face failures during the data taking an appropriate redundancy has to be foreseen. In particular, because the reconstruction efficiency drops dramatically, down to $\approx 75\,\%$ if only seven planes are functioning. Hence, a nine plane solution is strongly favored.

[1] In the case of the final SIDIS data a radial cut at $3.9\,\mathrm{cm}$ on the primary vertex in the target material has been applied.

A.7. Multiplicities

The data set which is used for the results presented above can also provide important information on the so-called "dihadron multiplicities" $M^{h^+h^-}$. In this section a short overview is given about the results which are obtained from the 2004 and the 2010 data sets. The cross-check of these results was also part of this thesis, while Makke [COMPASS14c] is primarily responsible for this analysis.

The multiplicity of the hadron-pair production is the probability of producing a pair of hadrons from the initial quark q by the double fragmentation process [dFV04]. The knowledge of this quantity is crucial to determine the polarized and unpolarized DiFFs and thus to access the transversity function h_1^q in SIDIS.

The available model calculations are based on an indirect approach via invariant mass spectra of hadron-pairs produced in e^+e^-, proton-proton collisions and SIDIS, but these data suffer from large systematics and do not offer multi-dimensional information in z and M_{inv} simultaneously. The multiplicity for instance of h^+h^- pairs is related to the unpolarized DiFF via [COMPASS14c]

$$M^{h^+h^-}(x,z) = \frac{1}{N^{\text{DIS}}}\frac{\mathrm{d}N^{h^+h^-}}{\mathrm{d}Q^2\,\mathrm{d}z\,\mathrm{d}M_{inv}} = \frac{\sum_q e_q^2 f_1(x,Q^2) D_1^{\sphericalangle q}(z,M_{inv},Q^2)}{\sum_q e_q^2 f_1(x,Q^2)}. \tag{A.1}$$

The method of extraction from the data is the following. For a given kinematic bin i the experimental/raw dihadron multiplicity is determined by $M^{h^+h^-}_{\text{raw},i} = {}^{N_i^{h^+h^-}}/_{N_i^{\text{DIS}}}$. The acceptance, defined as $\varepsilon_i = {}^{M^{h^+h^-}_{\text{raw},i}}/_{M^{h^+h^-}_{\text{MC},i}}$ is estimated using a Monte Carlo simulation. Thus the final dihadron multiplicity is $M_i^{h^+h^-} = {}^{M^{h^+h^-}_{\text{raw},i}}/_{\varepsilon_i}$. The dihadron multiplicities from a deuteron target, 2004 data, and from a proton target, 2010 data, are shown in Figs. A.66 and A.67, with different orders of the dependencies on Q^2 and M_{inv}. The results are found to be compatible within $10\,\%$. The dihadron multiplicity shows a weak dependence on Q^2 (see Fig. A.67), which is barely visible at low and mid z-M_{inv} region, reaching its maximum in the highest z and Q^2 bin. This is a clear indication that Q^2 evolution can be neglected in the case of the hadron-pair azimuthal asymmetry and the comparison of results from the HERMES and the COMPASS experiment is not affected by the different Q^2 ranges. A stronger dependence of the dihadron multiplicity on z and M_{inv} is observed (see Fig. A.66) being driven by dependence on the unpolarized DiFF. This effect can be reproduced with the results of simulations using unpolarized LEPTO.

Although these results are not yet used for the extraction of the transversity distributions of u and d valence quarks (see Sec. 6.3.4), they will be an important ingredient to future analyses, see Sec. 7.1.

The hadron-pair samples used for the multiplicity extraction have been cross-checked by the author of this thesis.

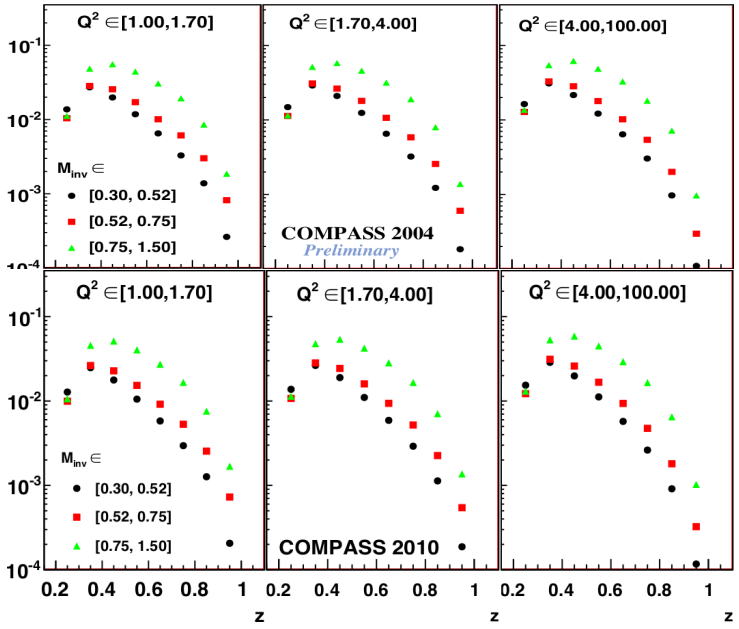

Figure A.66.: The dihadron h^+h^- multiplicities from the 2004 deuteron (top panel) and 2010 proton data (bottom panel) as a function of z, in bins of Q^2 (panels) and M_{inv} (marker) [COMPASS14c].

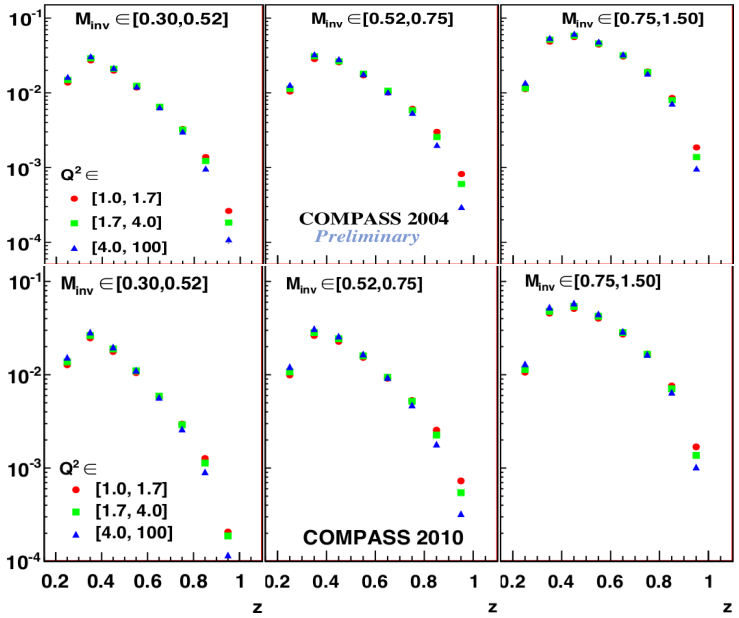

Figure A.67.: The dihadron h^+h^- multiplicities from the 2004 deuteron (top panel) and 2010 proton data (bottom panel) as a function of z, in bins of M_{inv} (panels) and Q^2 (marker) [COMPASS14c].

A.8. Notations and conventions

Metric tensor

The metric tensor is

$$g^{\mu\nu} = \begin{pmatrix} 1 & 0 & 0 & 0 \\ 0 & -1 & 0 & 0 \\ 0 & 0 & -1 & 0 \\ 0 & 0 & 0 & -1 \end{pmatrix} \tag{A.2}$$

with Greek indices running from 0 to 3. Repeated indices are summed in all cases. Four vectors are written in light italic roman type, while boldface italic is used for three-vectors. The imaginary unit is denoted as $\imath$ with $\imath^2 = -1$. Please note the difference w.r.t. i, which is used for indices. In the following section natural units ($\hbar := c := 1$) are used for reasons of better readability.

Light-cone vectors

The Light-cone vectors are defined as [Min09]

$$a^\mu := [a^-, a^+, \boldsymbol{a}_T] = \left[\frac{a^0 - a^3}{\sqrt{2}}, \frac{a^0 + a^3}{\sqrt{2}}, a^1, a^2\right]. \tag{A.3}$$

Thus the dot-product in light-cone components is

$$\begin{aligned} a \cdot b &= a^+ b^- + b^- a^+ - \boldsymbol{a}_T \cdot \boldsymbol{b}_T \\ &= a^+ b^- + b^- a^+ - a^i b^i \\ &= a^+ b^- + b^- a^+ - a_x b_x - a_y b_y. \end{aligned} \tag{A.4}$$

The two-dimensional transverse part of a light-cone vector a^μ is

$$\begin{aligned} \boldsymbol{a}_T &= (a_x, a_y), \\ a^\mu_T &= \big[0, 0, \boldsymbol{a}_T\big], \\ a_{T\mu} &= \big[0, 0, -\boldsymbol{a}_T\big]. \end{aligned} \tag{A.5}$$

In terms of the Sudakov vectors $n_+ := (1, 0, 0, 0)$ and $:= (0, 1, 0, 0)$, a^μ can be written as

$$a^\mu = a^+ n_+ + a^- n_- + \boldsymbol{a}_T. \tag{A.6}$$

For instance the four-momentum $p^\mu = (p^0, p^1, p^2, p^3)$ of a particle which moves in z direction ($p^1 = p^2 = 0$) becomes in light-cone coordinates in the collinear frame

$$p^\mu = \left(\frac{p^0 + p^3}{\sqrt{2}}, \frac{p^0 - p^3}{\sqrt{2}}, 0, 0 \right) = \left(p^+, \frac{2M^2}{p^+}, 0, 0 \right), \tag{A.7}$$

since $p^\mu p_\mu = M^2 = (p^0)^2 - (p^3)^2 = (p^0 - p^3)(p^0 + p^3)$.

Dirac matrices

The Dirac matrices γ^μ are defined as [LLZP91]

$$\gamma^0 := \begin{pmatrix} 1 & 0 & 0 & 0 \\ 0 & 1 & 0 & 0 \\ 0 & 0 & -1 & 0 \\ 0 & 0 & 0 & -1 \end{pmatrix}, \gamma^1 := \begin{pmatrix} 0 & 0 & 0 & 1 \\ 0 & 0 & 1 & 0 \\ 0 & -1 & 0 & 0 \\ -1 & 0 & 0 & 0 \end{pmatrix}, \tag{A.8}$$

$$\gamma^2 := \begin{pmatrix} 0 & 0 & 0 & -\imath \\ 0 & 0 & \imath & 0 \\ 0 & \imath & 0 & 0 \\ -\imath & 0 & 0 & 0 \end{pmatrix}, \gamma^3 := \begin{pmatrix} 0 & 0 & 1 & 0 \\ 0 & 0 & 0 & -1 \\ -1 & 0 & 0 & 0 \\ 0 & 1 & 0 & 0 \end{pmatrix}. \tag{A.9}$$

In addition one defines the dirac matrix γ^5 with $\gamma^5\gamma^5 = \mathbb{1}$ and $\gamma^5\gamma^\mu = -\gamma^\mu\gamma^5$ as

$$\gamma^5 := \imath\gamma^0\gamma^1\gamma^2\gamma^3 = \begin{pmatrix} 0 & 0 & 0 & 1 \\ 0 & 0 & 1 & 0 \\ 0 & 1 & 0 & 0 \\ 1 & 0 & 0 & 0 \end{pmatrix}. \tag{A.10}$$

The dirac matrices can be written in light-cone representation (see Sec. A.8) as

$$\gamma^+ = \frac{1}{2}\left(\gamma^0 + \gamma^3\right) \text{ and } \gamma^- = \frac{1}{2}\left(\gamma^0 - \gamma^3\right). \tag{A.11}$$

Feynman slash notation and Pauli matrices

The Feynman-slash is defined as [PS95]

$$\not{A} := \sum_{\mu=0}^{3} \gamma^{\mu} A_{\mu}, \tag{A.12}$$

where A is a covariant vector and γ are the Dirac matrices. For instance $\not{p}$ of a four-momentum vector $p = (E, -\boldsymbol{p})$ is

$$\begin{aligned} \not{p} &= \sum_{\mu=0}^{3} \gamma^{\mu} p_{\mu} = \gamma^{0} p_{0} + \sum_{\mu=1}^{3} \gamma^{i} p_{i} \\ &= \begin{pmatrix} p_{0} & 0 \\ 0 & -p_{0} \end{pmatrix} + \begin{pmatrix} 0 & \sigma^{i} p_{i} \\ -\sigma^{i} p_{i} & 0 \end{pmatrix} \\ &= \begin{pmatrix} E & -\sigma \cdot \boldsymbol{p} \\ \sigma \cdot \boldsymbol{p} & -E \end{pmatrix}, \end{aligned} \tag{A.13}$$

where σ^{i} are the Pauli matrices [LLZP91]

$$\sigma_{1} := \begin{pmatrix} 0 & 1 \\ 1 & 0 \end{pmatrix}, \sigma_{2} := \begin{pmatrix} 0 & -\imath \\ \imath & 0 \end{pmatrix}, \sigma_{3} := \begin{pmatrix} 1 & 0 \\ 0 & -1 \end{pmatrix}. \tag{A.14}$$

Logarithmic binning

For convenience in plots of kinematic distributions involving Q^2 or x, the corresponding axes are always plotted in logarithmic scale. The x scale ranges from 1×10^{-3} to 1.0, while Q^2 covers 1.0 to $150.0\,(\mathrm{GeV}/c)^2$. The number of bins in both cases is 1×10^{3}. Then the upper limit $k_{bin}(i+1)$ of a bin i with a lower limit $k_{bin}(i)$ is given by

$$k_{bin}(i+1) = k_{bin}(i) \cdot 10^{c}, \tag{A.15}$$

with

$$c = \frac{|\log_{10}(range_{\text{max}}) - \log_{10}(range_{\text{min}})|}{\#\,\text{bins}}. \tag{A.16}$$

List of Figures

2.1. Simplified scheme of the DIS process 6
2.2. Definition of the azimuthal angle ϕ 8
2.3. Results on the proton structure function F_2^p 9
2.4. Inclusive DIS handbag diagram 13
2.5. Helicity amplitudes handbag diagrams 15
2.6. Semi-inclusive DIS handbag diagram 17
2.7. Single hadron production in SIDIS process 22
2.8. Scheme of the dihadron process 27
2.9. SIDIS dihadron handbag diagram 27
2.10. Hadron-pair center of mass frame 29
2.11. Difference between $\boldsymbol{R}_T$ and $\boldsymbol{R}_T^{\mathrm{H}}$ 32
2.12. Sivers asymmetry of charged pions and kaons from HERMES 35
2.13. Sivers asymmetry of charged pions and kaons from COMPASS deuteron data . 36
2.14. Sivers asymmetry of charged pions and kaons from COMPASS proton data . . 36
2.15. Collins asymmetry of charged pions and kaons from HERMES 37
2.16. Collins asymmetry of charged pions and kaons from COMPASS deuteron data . 38
2.17. Collins asymmetry of charged pions and kaons from COMPASS proton data . . 39
2.18. Hadron-pair asymmetry of pion pairs from HERMES 40
2.19. Asymmetry of h^+h^- and identified pairs from COMPASS deuteron data 41
2.20. Hadron-pair asymmetry of h^+h^- pairs from COMPASS proton data 2007 . . . 42

3.1. Schematic view of beam momentum station 45
3.2. Schematic view of polarized target 46
3.3. Schematic view of COMPASS spectrometer 48
3.4. Scintillating fiber hodoscope 50
3.5. Micromegas detector 52
3.6. GEM detector 53
3.7. Drift chamber detector 53
3.8. Ring-imaging Cherenkov detector 56
3.9. Cherenkov rings in RICH 57
3.10. Muon wall detector 59
3.11. COMPASS trigger components 61
3.12. Kinematic coverage of trigger sub-systems 61
3.13. COMPASS trigger concept 62

3.14. Architecture of the COMPASS DAQ system 63

4.1. Examples of detector profile analysis 69
4.2. Examples of bad spill analysis 70
4.3. Example of K^0 stability test 72
4.4. Kinematic distribution of DIS events: $\pi^+\pi^-$ pairs 74
4.5. Coordinate distributions of BPV along beam axis 75
4.6. Distributions of $z = z_1 + z_2$ 78
4.7. Distributions of missing energy 78
4.8. Fraction of pion and kaon pairs to all hadron-pairs 80
4.9. Target cell polarization configuration 85
4.10. Weighted and unweighted UL fit comparison 87
4.11. R-test χ^2 distributions 91
4.12. T-test χ^2 distributions 92
4.13. Reasonable assumption χ^2 distributions 93
4.14. Combined reasonable assumption and T-test χ^2 distributions 94
4.15. Compatibility among individual periods 97
4.16. Pull distribution between individual periods 98
4.17. Comparison of estimators 99
4.18. Pulls between 1D-QR and the UL estimator results 100
4.19. Cross-check pulls 101
4.20. Hadron-pair asymmetries from spectrometer split 103
4.21. Purity corrected true hadron-pair asymmetries 2007 data 107
4.22. Purity corrected true hadron-pair asymmetries 2010 data 108
4.23. Published hadron-pair asymmetries of h^+h^- pairs from deuteron and proton data 111
4.24. Comparison of combined results 114

5.1. Hadron-pair asymmetry h^+h^- pairs 2002-04 deuteron data 116
5.2. Hadron-pair asymmetry identified pairs 2002-04 deuteron data 117
5.3. Hadron-pair asymmetry h^+h^- pairs 2007 proton data 119
5.4. Hadron-pair asymmetry h^+h^- pairs 2010 proton data 119
5.5. Hadron-pair asymmetry h^+h^- pairs combined 2007/2010 data 120
5.6. Hadron-pair asymmetry identified pairs 2007 proton data 122
5.7. Hadron-pair asymmetry identified pairs 2010 proton data 123
5.8. Hadron-pair asymmetry identified pairs combined 2007/2010 data 124

6.1. Sivers asymmetry of pions and kaons: HERMES vs. COMPASS 130
6.2. Collins asymmetry of pions and kaons: HERMES vs. COMPASS 131
6.3. Sivers asymmetry Q^2 evolution: HERMES vs. COMPASS 132
6.4. Hadron-pair asymmetry identified pairs from deuteron and proton data 134
6.5. Asymmetry of $\pi^+\pi^-$ pairs: HERMES vs. COMPASS 136
6.6. Asymmetry of $\pi^+\pi^-$ pairs: comparison with model predictions 141
6.7. Global fit to HERMES and COMPASS $\pi^+\pi^-$ asymmetries 146

6.8. Extracted linear combinations $xh_{1,d}$ and $xh_{1,p}$ . . . 148
6.9. Extracted transversity distributions of d and u valence quarks . . . 148
6.10. Comparison of transversity extracted from single and hadron-pair channels . . 149
6.11. Global fits to u and d valence quark transversity distributions . . . 151
6.12. Comparison of Collins and hadron-pair asymmetry . . . 152
6.13. Comparison of Collins and hadron-pair asymmetry: common sample . . . 153
6.14. Difference between ϕ_{RS} and $\phi_{2h,S}$ . . . 154
6.15. Standard hadron-pair asymmetry vs. Collins-like hadron-pair asymmetry . . . 154
6.16. Collins mechanism in string fragmentation model . . . 155
6.17. Decay of an electroweak boson in string fragmentation model . . . 156
6.18. Decay of string into pseudoscalar mesons . . . 157
6.19. Production scheme of π^+K^- pairs . . . 157
6.20. Production scheme of $K^+\pi^-$ pairs . . . 158
6.21. Scheme of hadron-pair production in NJL-jet model . . . 158
6.22. Deuteron and proton M_{inv} distributions . . . 160

7.1. Scheme of the Drell-Yan process . . . 163
7.2. Definition of Drell-Yan ϕ_S and Φ . . . 163
7.3. Expected statistical uncertainties on the Sivers asymmetry in Drell-Yan . . . 165
7.4. SIDIS $Q^2(x)$ distributions vs. expected Drell-Yan . . . 168
7.5. SIDIS Sivers asymmetry in Drell-Yan kinematic range . . . 168
7.6. Expected statistical uncertainties on the Sivers asymmetry in Drell-Yan . . . 169
7.7. Hadron absorber for COMPASS Drell-Yan program . . . 170
7.8. Simulated mass and primary vertex position resolution . . . 171
7.9. Particle rates to vertex detector . . . 173
7.10. Example from rate test Hamamatsu R11265-100-M16 . . . 174
7.11. Results of rate test Hamamatsu 6568(-100) and R11265-100-M16 . . . 174
7.12. Results of fiber irradiation test . . . 175
7.13. Orientation of vertex detector planes . . . 176
7.14. Scheme of beam spot hole of vertex detector . . . 177
7.15. Picture of final vertex detector plane . . . 180

A.1. BELLE A_0 and A_{12} asymmetries . . . 185
A.2. Results of six other TMD asymmetries: deuteron data . . . 186
A.3. Results of six other TMD asymmetries: proton data . . . 187
A.4. BELLE hadron-pair asymmetry . . . 188
A.5. Schematic view of CERN's accelerator facilities . . . 190
A.6. SPS super-cycle example . . . 190
A.7. Resolving ambiguities . . . 191
A.8. Counter of the ECAL2 calorimeter . . . 192
A.9. Structure of the HCAL1 module . . . 192
A.10. Scheme of the veto system . . . 192
A.11. Example of kinematic stability studies . . . 194

A.12. Kinematic distribution of DIS events identified pairs combined 2007/2010 data 1 194
A.13. Kinematic distribution of DIS events identified pairs combined 2007/2010 data 2 195
A.14. Kinematic distribution of DIS events identified pairs combined 2007/2010 data 3 196
A.15. Kinematic distribution of DIS events identified pairs 2003-2004 data 1 197
A.16. Kinematic distribution of DIS events identified pairs 2003-2004 data 2 198
A.17. Kinematic distribution of DIS events identified pairs 2003-2004 data 3 199
A.18. Kinematic distribution of DIS events identified pairs 2003-2004 data 4 200
A.19. Reconstructed primary vertex position distributions 201
A.20. Distributions of $\cos\theta$ 201
A.21. Distributions of $z = z_1 + z_2$ combined 2007/2010 proton data 2 202
A.22. Distributions of z_1 and z_2 2003-2004 deuteron data 203
A.23. Distributions of z_1 and z_2 2007/2010 proton data 204
A.24. Distributions of missing energy E_{miss} 205
A.25. False asymmetries of deuteron data 207
A.26. False asymmetries of 2007 proton data 208
A.27. False asymmetries of 2010 proton data 209
A.28. Period's mean x asymmetry amplitudes 210
A.29. Hadron-pair asymmetry of individual periods K^+K^- pairs 211
A.30. Hadron-pair asymmetry of individual periods π^+K^- pairs 212
A.31. Hadron-pair asymmetry of individual periods $K^+\pi^-$ pairs 213
A.32. Comparison of estimators deuteron data 214
A.33. Comparison of estimators 2007 proton data 215
A.34. Comparison of estimators 2010 proton data 216
A.35. Pulls of estimator's results deuteron data 217
A.36. Pulls of estimator's results 2007 proton data 217
A.37. Cross-check deuteron data 218
A.38. Cross-check 2007 proton data 219
A.39. Cross-check 2010 proton data 220
A.40. Systematic effects from spectrometer acceptance 221
A.41. Improvements to previous analyses: M_{inv} cut 222
A.42. Improvements to previous analyses: p_{beam} cut 222
A.43. Improvements to previous analyses: x cut 223
A.44. Improvements to previous analyses: calorimeter cut 223
A.45. Improvements to previous analyses: without pre-weightening 224
A.46. Comparison of the results method A vs. B 225
A.47. Comparison of the results single sets vs. combined 226
A.48. Kinematic mean values deuteron data 238
A.49. Kinematic mean values combined 2007/2010 proton data 239
A.50. Chromodynamic lensing 240
A.51. Sivers distribution model predictions 240
A.52. Hadron-pair asymmetry with $x > 0.032$ compared to [SHBM08] 241
A.53. Table 1 of [BCR13] 242
A.54. Table 2 of [BCR13] 242

A.55. MSTW2008NLO xf_1 results 245
A.56. Technical drawing of concrete shielding 246
A.57. Top view of the Drell-Yan absorber 246
A.58. Magnetic field strength at vertex detector position 247
A.59. Fiber stacking of vertex detector 248
A.60. Fiber doubling of vertex detector 248
A.61. CAD drawing vertex detector housing 249
A.62. CAD drawing vertex detector detail 250
A.63. Third plane for FI15 250
A.64. Schematic view of the Drell-Yan target area 251
A.65. Technical drawing of the extended FI15 252
A.66. Dihadron h^+h^- multiplicities from deuteron data 254
A.67. Dihadron h^+h^- multiplicities from proton data 254

List of Tables

2.1. Kinematic variables for the description of the DIS process 6
2.2. Chirality and time reversal properties of leading-twist PDFs 19
2.3. The five leading-twist transverse momentum dependent PDFs 20
2.4. Quark and parent nucleon polarization matrix 20

4.1. Transversity run periods 67
4.2. RICH likelihood cuts 81
4.3. Final statistics of the deuteron 2002-04 hadron-pair sample 82
4.4. Final statistics of the 2007 hadron-pair sample 83
4.5. Final statistics of the 2010 hadron-pair sample 83
4.6. Results from false asymmetry test 96
4.7. Systematic uncertainties from the spectrometer acceptance 102
4.8. Overall systematic uncertainties 104
4.9. Influence of unitized cuts: deuteron data 110
4.10. Overall systematic uncertainty for the 2007/2010 combined proton data 113

7.1. PYTHIA Drell-Yan $\pi^- \mathrm{NH}_3$ cross sections 166
7.2. Expected number of Drell-Yan events per day 167

A.1. Convolutions of asymmetry modulations 184
A.2. Physical asymmetries D_{nn}, f, P_T, and λ factors 184
A.3. Parameters of COMPASS SciFi stations 191
A.4. Results of 2010 detector profile analysis 193
A.5. R-test χ^2 probability values 206
A.6. R-test χ^2 probability values 206
A.7. Combination of 2007, and 2010 data χ^2 values 224
A.8. Binning for asymmetry extraction 227
A.9. Numerical values: h^+h^- deuteron 228
A.10. Numerical values: $\pi^+\pi^-$ deuteron 228
A.11. Numerical values: $\pi^+\pi^-$ deuteron $x > 0.032$ 229
A.12. Numerical values: K^+K^- deuteron 229
A.13. Numerical values: π^+K^- deuteron 230
A.14. Numerical values: $K^+\pi^-$ deuteron 230
A.15. Numerical values: h^+h^- 2007 proton 231
A.16. Numerical values: $\pi^+\pi^-$ 2007 proton 231

A.17. Numerical values: K^+K^- 2007 proton . . . 232
A.18. Numerical values: π^+K^- 2007 proton . . . 232
A.19. Numerical values: $K^+\pi^-$ 2007 proton . . . 232
A.20. Numerical values: h^+h^- 2010 proton . . . 233
A.21. Numerical values: $\pi^+\pi^-$ 2010 proton . . . 233
A.22. Numerical values: K^+K^- 2010 proton . . . 234
A.23. Numerical values: π^+K^- 2010 proton . . . 234
A.24. Numerical values: $K^+\pi^-$ 2010 proton . . . 234
A.25. Numerical values: h^+h^- combined $2007/2010$ . . . 235
A.26. Numerical values: $\pi^+\pi^-$ combined $2007/2010$ . . . 235
A.27. Numerical values: $\pi^+\pi^-$ proton $x > 0.032$ . . . 236
A.28. Numerical values: K^+K^- combined $2007/2010$ . . . 236
A.29. Numerical values: π^+K^- combined $2007/2010$ . . . 237
A.30. Numerical values: $K^+\pi^-$ combined $2007/2010$ . . . 237
A.31. Calculation of $xh_{1,d}$ . . . 243
A.32. Calculation of $xh_{1,u}$ . . . 244
A.33. Results of u and d valence quark transversities . . . 245

Bibliography

[A+07a] V. Abazov et al., *Results of mass testing of mini drift tubes for the D0 forward muon system*, Instruments and Experimental Techniques **50**(1), 51–60 (2007).

[A+07b] V. Abazov et al., *Test stands for mini drift tubes*, Instruments and Experimental Techniques **50**(1), 41–50 (2007).

[A+08] M. Anselmino et al., *New preliminary results on the transversity distribution and the Collins fragmentation functions*, Proceedings of TRANSVERSITY 2008 conference , 138 (2008).

[A11] X. Qian, K. Allada, C. Dutta et al. (Jefferson Lab Hall A Collaboration), *Single Spin Asymmetries in Charged Pion Production from Semi-Inclusive Deep Inelastic Scattering on a Transversely Polarized* ^{3}He *Target at* $Q^2 = 1.4 - 2.7\,\mathrm{GeV}^2$, Phys. Rev. Lett. **107**, 072003 (2011).

[AAA+08a] P. Abbon, M. Alexeev, H. Angerer et al., *The COMPASS RICH-1 detector upgrade*, The European Physical Journal Special Topics **162**(1), 251–257 (2008).

[AAA+08b] P. Abbon, M. Alexeev, H. Angerer et al., *Pattern recognition and PID for COMPASS RICH-1*, Nuclear Instruments and Methods A **595**(1), 233 – 236 (2008).

[AAB+91] D. Adams, N. Akchurin, N. Belikov et al., *Analyzing power in inclusive* π^+ *and* π^- *production at high* x_F *with a 200 GeV polarized proton beam*, Physics Letters B **264**(3–4), 462 – 466 (1991).

[ABB+05] E. Albrecht, G. Baum, R. Birsa et al., *Status and characterisation of COMPASS RICH-1*, Nuclear Instruments and Methods A **553**(1–2), 215 – 219 (2005).

[ABD+07] M. Anselmino, M. Boglione, U. D'Alesio, A. Kotzinian, F. Murgia et al., *Transversity and Collins functions from SIDIS and e+ e- data*, Phys.Rev. **D75**, 054032 (2007), arXiv:hep-ph/0701006.

[ABD+09a] M. Anselmino, M. Boglione, U. D'Alesio, A. Kotzinian, S. Melis et al., *Sivers Effect for Pion and Kaon Production in Semi-Inclusive Deep Inelastic Scattering*, Eur.Phys.J. **A39**, 89–100 (2009), arXiv:hep-ph/0805.2677.

[ABD+09b] M. Anselmino, M. Boglione, U. D'Alesio, A. Kotzinian, F. Murgia et al., *Update on transversity and Collins functions from SIDIS and e+ e- data*, Nucl.Phys.Proc.Suppl. **191**, 98–107 (2009), arXiv:hep-ph/0812.4366.

[ABD+11] M. Anselmino, M. Boglione, U. D'Alesio, S. Melis, F. Murgia et al., *Sivers Distribution Functions and the Latest SIDIS Data*, (2011), arXiv:hep-ph/1107.4446.

[ABD+13] M. Anselmino, M. Boglione, U. D'Alesio, S. Melis, F. Murgia et al., *Simultaneous extraction of*

transversity and Collins functions from new SIDIS and e+e- data, Phys.Rev. **D87**, 094019 (2013), arXiv:hep-ph/1303.3822.

[Abr83] A. Abragam, *Principles of Nuclear Magnetism (International Series of Monographs on Physics)*, Oxford University Press, USA, 1983.

[ACD+02] C. Altunbas, M. Capéans, K. Dehmelt, J. Ehlers, J. Friedrich, I. Konorov et al., *Construction, test and commissioning of the triple-gem tracking detector for COMPASS*, Nuclear Instruments and Methods A **490**(1–2), 177 – 203 (2002).

[ACQR12] S. M. Aybat, J. C. Collins, J.-W. Qiu and T. C. Rogers, *The QCD Evolution of the Sivers Function*, Phys.Rev. **D85**, 034043 (2012), arXiv:hep-ph/1110.6428.

[ADME+03] H. Angerer, R. De Masi, A. Esposito et al., *Present status of silicon detectors in Compass*, Nuclear Instruments and Methods A **512**(1–2), 229 – 238 (2003).

[Ado09] C. Adolph, *Vermessung von Multianoden Photomultiplieren fuer das WASA@COSY DIRC Upgrade Projekt*, Diploma thesis, Friedrich-Alexander-Universität Erlangen-Nürnberg (FAU), Erlangen, Germany, 2009.

[Ado13] C. Adolph, *One-hadron transverse spin effects on a proton target at COMPASS*, PhD thesis, Friedrich-Alexander-Universität Erlangen-Nürnberg (FAU), Erlangen, Germany, 2013.

[AEL95] M. Anselmino, A. Efremov and E. Leader, *The Theory and phenomenology of polarized deep inelastic scattering*, Phys.Rept. **261**, 1–124 (1995), arXiv:hep-ph/9501369.

[AESY08] H. Avakian, A. Efremov, P. Schweitzer and F. Yuan, *Pretzelosity distribution function* $h_{1T}^{\perp}$, (2008), arXiv:hep-ph/0808.3982.

[AGIS83] B. Andersson, G. Gustafson, G. Ingelman and T. Sjoestrand, *Parton fragmentation and string dynamics*, Physics Reports **97**(2–3), 31 – 145 (1983).

[AMM+00] I. Abt, S. Masciocchi, B. Moshous, T. Perschke, K. Riechmann and B. Wagner, *Double-sided microstrip detectors for the high radiation environment in the HERA-B experiment*, Nuclear Instruments and Methods A **439**(2–3), 442 – 450 (2000).

[AMS09] S. Arnold, A. Metz and M. Schlegel, *Dilepton production from polarized hadron hadron collisions*, Phys. Rev. D **79**, 034005 (2009).

[APR12] S. M. Aybat, A. Prokudin and T. C. Rogers, *Calculation of TMD Evolution for Transverse Single Spin Asymmetry Measurements*, Phys.Rev.Lett. **108**, 242003 (2012), arXiv:hep-ph/1112.4423.

[Art02] X. Artru, *The Transverse spin*, (2002), arXiv:hep-ph/0207309.

[Art10] X. Artru, *Recursive fragmentation model with quark spin. Application to quark polarimetry*, (2010), arXiv:hep-ph/1001.1061.

[B+69] E. D. Bloom et al., *High-Energy Inelastic* $e-p$ *Scattering at* 6° *and* 10°, Phys. Rev. Lett. **23**, 930–934 (Oct 1969).

[B+76] F. Brasse et al., *Construction of a large drift chamber and test measurements*, Internal report, DESY **F21-76**(02) (1976).

[B+05] C. Bernet et al., *The gaseous microstrip detector Micromegas for the high-luminosity COMPASS experiment at CERN*, Nuclear Instruments and Methods A **536**(1–2), 61 – 69 (2005).

[B+06] J. Bisplinghoff et al., *Collins and Sivers asymmetries on hadrons identified as pions and kaons from COMPASS 2003/2004 transverse run*, COMPASS note **12** (2006).

[BBF+13] T. Baumann, M. Buechele, H. Fischer et al., *The GANDALF 128-channel Time-to-Digital Converter*, Journal of Instrumentation **8**(01), C01016 (2013).

[BBH+05] C. Bernet, A. Bravar, J. Hannappel, D. v. Harrach et al., *The COMPASS trigger system for muon scattering*, Nuclear Instruments and Methods A **550**(1–2), 217 – 240 (2005).

[BBJR00] A. Bianconi, S. Boffi, R. Jakob and M. Radici, *Two hadron interference fragmentation functions. Part 1. General framework*, Phys.Rev. **D62**, 034008 (2000), arXiv:hep-ph/9907475.

[BBS95] S. J. Brodsky, M. Burkardt and I. Schmidt, *QCD constraints on the shape of polarized quark and gluon distributions*, Nuclear Physics B **441**(1–2), 197 – 214 (1995).

[BCR11] A. Bacchetta, A. Courtoy and M. Radici, *First Glances at the Transversity Parton Distribution through Dihadron Fragmentation Functions*, Phys. Rev. Lett. **107**, 012001 (2011).

[BCR13] A. Bacchetta, A. Courtoy and M. Radici, *First extraction of valence transversities in a collinear framework*, JHEP **1303**, 119 (2013), arXiv:hep-ph/1212.3568.

[BDD+06] V. Bychkov, N. Dedek, W. Duennweber, M. Faessler, H. Fischer et al., *The large size straw drift chambers of the COMPASS experiment*, Nuclear Instruments and Methods A **556**(1), 66 – 79 (2006).

[BDDM04] A. Bacchetta, U. D'Alesio, M. Diehl and C. A. Miller, *Single-spin asymmetries: The Trento conventions*, Phys.Rev. **D70**, 117504 (2004), arXiv:hep-ph/0410050.

[BDG+07] A. Bacchetta, M. Diehl, K. Goeke, A. Metz, P. J. Mulders et al., *Semi-inclusive deep inelastic scattering at small transverse momentum*, JHEP **0702**, 093 (2007), arXiv:hep-ph/0611265.

[BDMS12] F. Bradamante, V. Duic, A. Martin and F. Sozzi, *Combining transverse spin asymmetries from 2007 and 2010 data*, COMPASS note **3** (2012).

[BDR02] V. Barone, A. Drago and P. G. Ratcliffe, *Transverse polarisation of quarks in hadrons*, Phys.Rept. **359**, 1–168 (2002), arXiv:hep-ph/0104283.

[BEE+02] J. Bisplinghoff, D. Eversheim, W. Eyrich et al., *A scintillating fibre hodoscope for high rate applications*, Nuclear Instruments and Methods A **490**(1–2), 101 – 111 (2002).

[BEG+89] C. Brown, D. Eartly, D. Green et al., *D∅ muon system with proportional drift tube chambers*, Nuclear Instruments and Methods A **279**(1–2), 331 – 338 (1989).

[BELLE08] R. Seidl, M. Grosse Perdekamp, A. Ogawa et al. (BELLE Collaboration), *Measurement of azimuthal asymmetries in inclusive production of hadron pairs in e^+e^- annihilation at $\sqrt{s} = 10.58$ GeV*, Phys. Rev. D **78**, 032011 (2008).

[BELLE11] A. Vossen et al. (BELLE Collaboration), *Observation of transverse polarization asymmetries of charged pion pairs in e^+e^- annihilation near $\sqrt{s} = 10.58$ GeV*, Phys.Rev.Lett. **107**, 072004 (2011), arXiv:hep-ex/1104.2425.

[BGGo79] C. Berger, H. Genzel, R. Grigull and other, *Evidence for gluon bremsstrahlung in e+e− annihilations at high energies*, Physics Letters B **86**(3–4), 418 – 425 (1979).

[BGKW04] Y. Bedfer, S. Gerassimov, A. Korzenev and R. Windmolders, *COMPASS's track reconstruction algorithm*, COMPASS note **1** (2004).

[Bjo69] J. D. Bjorken, *Asymptotic Sum Rules at Infinite Momentum*, Phys. Rev. **179**, 1547–1553 (1969).

[BM98] D. Boer and P. J. Mulders, *Time-reversal odd distribution functions in leptoproduction*, Phys. Rev. D **57**, 5780–5786 (1998).

[BMP03] D. Boer, P. Mulders and F. Pijlman, *Universality of T odd effects in single spin and azimuthal asymmetries*, Nucl.Phys. **B667**, 201–241 (2003), arXiv:hep-ph/0303034.

[BP10] J. Barth and J. Pretz, *Performance of the Large Angle Spectrometer Trigger*, COMPASS note **12** (2010).

[BR03a] A. Bacchetta and M. Radici, *Partial wave analysis of two-hadron fragmentation functions*, Phys.Rev. **D67**, 094002 (2003), arXiv:hep-ph/0212300.

[BR03b] V. Barone and P. Ratcliffe, *Transverse Spin Physics*, World Scientific, 2003.

[BR04] A. Bacchetta and M. Radici, *Two hadron semi-inclusive production including subleading twist*, Phys.Rev. **D69**, 074026 (2004), hep-ph/0311173.

[BR06] A. Bacchetta and M. Radici, *Modeling dihadron fragmentation functions*, Phys.Rev. **D74**, 114007 (2006), arXiv:hep-ph/0608037.

[Bra10] C. Braun, *Construction und tests of a very thin beam counter made of scintillating fibres and software for quality checks for the COMPASS experiment*, Diploma thesis, Friedrich-Alexander-Universität Erlangen-Nürnberg (FAU), Erlangen, Germany, 2010.

[Bro70] C. G. Broyden, *The Convergence of a Class of Double-rank Minimization Algorithms 1. General Considerations*, IMA J Appl Math **6**, 76–90 (1970).

[BSSV00] G. Bunce, N. Saito, J. Soffer and W. Vogelsang, *Prospects for spin physics at RHIC*, Ann.Rev.Nucl.Part.Sci. **50**, 525–575 (2000), arXiv:hep-ph/0007218.

[Bur02] M. Burkardt, *Impact parameter dependent parton distributions and transverse single spin asymmetries*, Phys.Rev. **D66**, 114005 (2002), arXiv:hep-ph/0209179.

[Bus88] W. Busza, *Experience with Iarocci tubes produced on a large scale*, Nuclear Instruments and Methods A **265**(1–2), 210 – 217 (1988).

[CBR12] A. Courtoy, A. Bacchetta and M. Radici, *Status on the transversity parton distribution: the dihadron fragmentation functions way*, PoS **QNP2012**, 042 (2012), arXiv:hep-ph/1206.1836.

[CBT08] I. Cloet, W. Bentz and A. W. Thomas, *Transversity quark distributions in a covariant quark-diquark model*, Phys.Lett. **B659**, 214–220 (2008), arXiv:hep-ph/0708.3246.

[Cer34] P. Cerenkov, *Visible Emission of Clean Liquids by Action of Radiation*, Doklady Akad Nauk SSSR **2**, 451 (1934).

[CERN09] CERN (CERN Collaboration), OP vistars http://op-webtools.web.cern.ch/op-webtools/vistar/vistars.php?usr=LHC, 2009.

[CERN14] CERN (CERN Collaboration), CERN's accelerator complex http://te-dep-epc.web.cern.ch/te-dep-epc/machines/general.stm, 2014.

[CG69] C. G. Callan and D. J. Gross, *High-Energy Electroproduction and the Constitution of the Electric Current*, Phys. Rev. Lett. **22**, 156–159 (1969).

[CLASS13] S. A. Pereira (CLASS Collaboration), *Dihadron production at JLAB*, Presentation at the workshop Structure of Nucleons and Nuclei (2013).

[Col93] J. C. Collins, *Fragmentation of transversely polarized quarks probed in transverse momentum distributions*, Nucl.Phys. **B396**, 161–182 (1993), arXiv:hep-ph/9208213.

[Col02] J. C. Collins, *Leading twist single transverse-spin asymmetries: Drell-Yan and deep inelastic scattering*, Phys.Lett. **B536**, 43–48 (2002), arXiv:hep-ph/0204004.

[COMPASS05] V. Y. Alexakhin et al. (COMPASS Collaboration), *First measurement of the transverse spin asymmetries of the deuteron in semi-inclusive deep inelastic scattering*, Phys.Rev.Lett. **94**, 202002 (2005), arXiv:hep-ex/0503002.

[COMPASS07a] P. Abbon et al. (COMPASS Collaboration), *The COMPASS experiment at CERN*, Nucl.Instrum.Meth. **A577**, 455–518 (2007), arXiv:hep-ex/0703049.

[COMPASS07b] E. Ageev et al. (COMPASS Collaboration), *A New measurement of the Collins and Sivers asymmetries on a transversely polarised deuteron target*, Nucl.Phys. **B765**, 31–70 (2007), arXiv:hep-ex/0610068.

[COMPASS07c] A. Ferrero (COMPASS Collaboration), *Measurement of transverse Lambda and Antilambda polarization at COMPASS*, AIP Conf.Proc. **915**, 436–440 (2007).

[COMPASS09a] M. Alekseev et al. (COMPASS Collaboration), *Collins and Sivers asymmetries for pions and kaons in muon-deuteron DIS*, Phys.Lett. **B673**, 127–135 (2009), arXiv:hep-ex/0802.2160.

[COMPASS09b] M. Alekseev et al. (COMPASS Collaboration), *Gluon polarisation in the nucleon and longitudinal double spin asymmetries from open charm muoproduction*, Physics Letters B **676**(1–3), 31–38

(2009).

[COMPASS09c] T. Negrini (COMPASS Collaboration), *Lambda polarization with a transversely polarized proton target at the COMPASS experiment*, AIP Conf.Proc. **1149**, 656–659 (2009).

[COMPASS10a] M. Alekseev et al. (COMPASS Collaboration), *Measurement of the Collins and Sivers asymmetries on transversely polarised protons*, Physics Letters B **692**(4), 240–246 (2010).

[COMPASS10b] M. Alekseev et al. (COMPASS Collaboration), *Measurement of the Collins and Sivers asymmetries on transversely polarised protons*, Phys.Lett. **B692**, 240–246 (2010), arXiv:hep-ex/1005.5609.

[COMPASS12a] C. Adolph et al. (COMPASS Collaboration), *Experimental investigation of transverse spin asymmetries in muon-p SIDIS processes: Collins asymmetries*, Phys.Lett. **B717**, 376–382 (2012), arXiv:hep-ex/1205.5121.

[COMPASS12b] C. Adolph et al. (COMPASS Collaboration), *Experimental investigation of transverse spin asymmetries in muon-p SIDIS processes: Sivers asymmetries*, Phys.Lett. **B717**, 383–389 (2012), arXiv:hep-ex/1205.5122.

[COMPASS12c] C. Adolph et al. (COMPASS Collaboration), *Transverse spin effects in hadron-pair production from semi-inclusive deep inelastic scattering*, Phys.Lett. **B713**, 10–16 (2012), arXiv:hep-ex/1202.6150.

[COMPASS12d] C. Braun (COMPASS Collaboration), *COMPASS results: new measurements of transverse-spin asymmetries in two-hadron inclusive production*, Il Nuovo Cimento **C2**, 115–120 (2012).

[COMPASS13] C. Braun (COMPASS Collaboration), *COMPASS results on transverse spin dependent azimuthal asymmetries in two-hadron production in semi-inclusive deep-inelastic scattering*, Presentation at the XXI. International Workshop on Deep-Inelastic Scattering and Related Subjects (2013).

[COMPASS14a] C. Adolph et al. (COMPASS Collaboration), *A high-statistics measurement of transverse spin effects in dihadron production from muon-proton semi-inclusive deep-inelastic scattering*, (2014), arXiv:hep-ex/1401.7873.

[COMPASS14b] C. Braun (COMPASS Collaboration), *COMPASS Results on Transverse Spin Asymmetries in Identified Two-Hadron Production in SIDIS*, Physics of Particles and Nuclei, Proceedings of 20th International Symposium on Spin Physics 2012 **45**(1) (2014).

[COMPASS14c] N. Makke (COMPASS Collaboration), *Study of the Hadronization Process from Single-Hadron and Hadron-Pair Production in SIDIS at COMPAS*, Physics of Particles and Nuclei, Proceedings of 20th International Symposium on Spin Physics 2012 **45**(1) (2014).

[COMPASS14d] A. Martin (COMPASS Collaboration), *COMPASS Results on Collins and Sivers Asymmetries for Charged Hadrons*, Physics of Particles and Nuclei, Proceedings of 20th International Symposium on Spin Physics 2012 **45**(1) (2014).

[COMPASS14e] B. Parsamyan (COMPASS Collaboration), *Six «Beyond Collins and Sivers» Transverse Spin Asymmetries at COMPASS*, Physics of Particles and Nuclei, Proceedings of 20th International Symposium on Spin Physics 2012 **45**(1) (2014).

[Den14] O. Denisov, *Sci-Fi based beam telescope*, COMPASS technical board meeting (February 2014).

[dFSSV09] D. de Florian, R. Sassot, M. Stratmann and W. Vogelsang, *Extraction of Spin-Dependent Parton Densities and Their Uncertainties*, Phys.Rev. **D80**, 034030 (2009), arXiv:hep-ph/0904.3821.

[dFV04] D. de Florian and L. Vanni, *Two hadron production in e+e- annihilation to next-to-leading order accuracy*, Phys.Lett. **B578**, 139–149 (2004), arXiv:hep-ph/0310196.

[E15500] P. Anthony et al. (E155 Collaboration), *Measurements of the Q2-dependence of the proton and neutron spin structure functions g1p and g1n*, Physics Letters B **493**(1–2), 19–28 (2000).

[EIKV14] M. G. Echevarria, A. Idilbi, Z.-B. Kang and I. Vitev, *QCD Evolution of the Sivers Asymmetry*, (2014), arXiv:hep-ph/1401.5078.

[EIR97] A. Edin, G. Ingelman and J. Rathsman, *LEPTO 6.5 - A Monte Carlo generator for deep inelastic lepton-nucleon scattering*, COMPUTER PHYSICS COMMUNICATIONS **101**(1-2), 108–134 (1997).

[Eli12] C. Elia, *Measurement of two-hadron transverse spin asymmetries in SIDIS at COMPASS*, PhD thesis, Universita di Trieste, Trieste, Italy, 2012.

[EMC89] J. Ashman et al. (EMC Collaboration), *An investigation of the spin structure of the proton in deep inelastic scattering of polarised muons on polarised protons*, Nuclear Physics B **328**(1), 1–35 (1989).

[Fey69] R. P. Feynman, *Very High-Energy Collisions of Hadrons*, Phys. Rev. Lett. **23**, 1415–1417 (Dec 1969).

[Fey72] R. Feynman, *Photon-Hadron Interactions*, Frontiers in Physics, W. A. Benjamin, 1972.

[FF78] R. Field and R. Feynman, *A parametrization of the properties of quark jets*, Nuclear Physics B **136**(1), 1 – 76 (1978).

[FJ75] G. R. Farrar and D. R. Jackson, *Pion and Nucleon Structure Functions near* $x = 1$, Phys. Rev. Lett. **35**, 1416–1419 (1975).

[Fle69] R. Fletcher, *A new approach to variable metric algorithms*, The Computer Journal **13**, 317–322 (1969).

[Fou] F. S. Foundation, GNU General Public License.

[Gau13] F. Gautheron, *Magnetic field calculations for Drell-Yan vertex detector*, COMPASS technical board meeting (July 2013).

[GKK$^+$06] O. Gavrishchuk, V. Kukhtin, N. Kuzmin, P. Manyakov, A. Maksimov et al., *Calorimeter for detection of hadrons in the energy range 10-GeV - 100-GeV*, Instrum.Exp.Tech. **49**, 41–55 (2006).

[GM64] M. Gell-Mann, *A schematic model of baryons and mesons*, Physics Letters **8**(3), 214–215 (1964).

[Gol70] D. Goldfarb, *A family of variable-metric methods derived by variational means*, Math. Comp. **24**, 23–26 (1970).

[GRSV01] M. Gluck, E. Reya, M. Stratmann and W. Vogelsang, *Models for the polarized parton distributions of the nucleon*, Phys.Rev. **D63**, 094005 (2001), arXiv:hep-ph/0011215.

[Gup97] R. Gupta, *Introduction to lattice QCD: Course*, pages 83–219 (1997), arXiv:hep-lat/9807028.

[GW73] D. J. Gross and F. Wilczek, *Ultraviolet Behavior of Non-Abelian Gauge Theories*, Phys. Rev. Lett. **30**, 1343–1346 (1973).

[H$^+$04] S. Horikawa et al., *Development of a scintillating-fibre detector with position-sensitive photomultipliers for high-rate experiments*, Nuclear Instruments and Methods A **516**(1), 34 – 49 (2004).

[HERMES07] M. Diefenthaler (HERMES Collaboration), *HERMES measurements of Collins and Sivers asymmetries from a transversely polarised hydrogen target*, Proceedings, 15th International Workshop on Deep-inelastic scattering and related subjects (DIS 2007). Vol. 1 and 2 , 579–582 (2007), arXiv:hep-ex/0706.2242.

[HERMES08] A. Airapetian et al. (HERMES Collaboration), *Evidence for a Transverse Single-Spin Asymmetry in Leptoproduction of $\pi^+\pi^-$ Pairs*, JHEP **0806**, 017 (2008), arXiv:hep-ex/0803.2367.

[HERMES09] A. Airapetian et al. (HERMES Collaboration), *Observation of the Naive-T-Odd Sivers Effect in Deep-Inelastic Scattering*, Phys. Rev. Lett. **103**, 152002 (2009).

[HERMES10] A. Airapetian et al. (HERMES Collaboration), *Effects of transversity in deep-inelastic scattering by polarized protons*, Phys.Lett. **B693**, 11–16 (2010), arXiv:hep-ex/1006.4221.

[HERMES11] A. Rostomyan (HERMES Collaboration), *HERMES results: TMD measurements in SIDIS off the transversely polarized p target*, Presentation at TRANSVERSITY 2011 conference (2011).

[HK06] F.-H. Heinsius and S. Koblitz, *COMPASS Luminosity for 2002-2004*, COMPASS note **5** (2006).

[HKS04] M. Hirai, S. Kumano and N. Saito, *Determination of polarized parton distribution functions and their uncertainties*, Phys. Rev. D **69**, 054021 (2004).

[Hof56] R. Hofstadter, *Electron Scattering and Nuclear Structure*, Rev. Mod. Phys. **28**, 214–254 (Jul 1956).

[I$^+$83] E. Iarocci et al., *Electrodeless plastic streamer tubes*, Nuclear Instruments and Methods in Physics Research **217**(3), 429 – 431 (1983).

[Jaf96] R. L. Jaffe, *Spin, twist and hadron structure in deep inelastic processes*, (1996), arXiv:hep-ph/9602236.

[JJ91] R. L. Jaffe and X. Ji, *Chiral-odd parton distributions and polarized Drell-Yan process*, Phys. Rev. Lett. **67**, 552–555 (1991).

[JM90] R. Jaffe and A. Manohar, *The g1 problem: Deep inelastic electron scattering and the spin of the proton*, Nuclear Physics B **337**(3), 509 – 546 (1990).

[Joo13a] R. Joosten, *SciFi vertex detector for DY*, COMPASS technical board meeting (July 2013).

[Joo13b] R. Joosten, *Transverse Spin Effects in Semi-Inclusive Deep Inelastic Scattering from the COMPASS Experiment*, Habil. thesis, Rheinische Friedrich-Wilhelms-University Bonn, Bonn, Germany, 2013.

[K$^+$03] F. Kunne et al., *The gaseous microstrip detector micromegas for the COMPASS experiment at CERN*, Nuclear Physics A **721**, C1087 – C1090 (2003).

[Kur98] Kuraray, *Scintillating Materials*, product brochure edition, 1998.

[Kur07] C. Kurig, *Construction, test and improvement of the trigger system for the electromagnetic calorimeter ECAL1 of the COMPASS experiment*, Diploma thesis, Johannes Gutenberg-Universität Mainz, Mainz, Germany, 2007.

[KWP$^+$04] B. Ketzer, Q. Weitzel, S. Paul, F. Sauli and L. Ropelewski, *Performance of triple GEM tracking detectors in the COMPASS experiment*, Nuclear Instruments and Methods A **535**(1–2), 314 – 318 (2004).

[LAPP81] F. Binon et al. (LAPP Collaboration), *Hodoscope Gamma Spectrometer Gams-200*, CERN preprint CERN-EP **81-27** (1981).

[LAPP86a] D. Alde et al. (LAPP Collaboration), *Production of G (1590) and Other Mesons Decaying Into eta Pairs by 100-GeV/c pi- on Protons*, Nucl.Phys. **B269**, 485–508 (1986).

[LAPP86b] F. Binon et al. (LAPP Collaboration), *Hodoscope multiphoton spectrometer GAMS-2000*, Nuclear Instruments and Methods A **248**, 86 (1986).

[Leo94] W. R. Leo, *Techniques for Nuclear and Particle Physics Experiments*, Springer-Verlag, 2 edition, 1994.

[LLZP91] L. Landau, E. Lifschitz, P. Ziesche and L. Pitaevskij, *Quantenmechanik: mit 11 Tabellen*, Lehrbuch der theoretischen Physik, Akad.-Verlag, 1991.

[Lu08] X.-R. Lu, *Single-Spin Asymmetry in Electro-Production of $\pi^+\pi^-$ Pairs from a Transversely Polarized Proton Target at the HERMES Experiment*, PhD thesis, Tokyo Institute of Technology, Tokyo, Japan, 2008.

[M$^+$02] A. Magnon et al., *Tracking with 40×40 cm^2 MICROMEGAS detectors in the high energy, high luminosity COMPASS experiment*, Nuclear Instruments and Methods A **478**(1–2), 210 – 214 (2002).

[Ma93] B.-Q. Ma, *The Proton spin and the Wigner rotation*, Z.Phys. **C58**, 479–482 (1993), arXiv:hep-ph/9306241.

[Ma96] B.-Q. Ma, *The x dependent helicity distributions for valence quarks in nucleons*, Phys.Lett. **B375**,

320–326 (1996), arXiv:hep-ph/9604423.

[Mag12a] A. Maggiora, *DY Hadron Absorber simulation status*, Drell-Yan hardware meeting (July 2012).

[Mag12b] A. Maggiora, *Final Hadron Absorber simulation status*, Drell-Yan hardware meeting (September 2012).

[Man92] A. V. Manohar, *An Introduction to spin dependent deep inelastic scattering*, (1992), arXiv:hep-ph/9204208.

[Mas08] F. Massmann, *Measurement of transverse spin effects via two-hadron correlations at the COMPASS experiment*, PhD thesis, Rheinische Friedrich-Wilhelms-University Bonn, Bonn, Germany, 2008.

[Mei01] A. Meier, *LiD for the polarized target of the COMPASS experiment*, PhD thesis, Ruhr-Universität Bochum, Bochum, Germany, 2001.

[Min09] H. Minkowski, *Raum und Zeit*, Jahresberichte der Deutschen Mathematiker-Vereinigung, B. G. Teubner, 1909.

[MKT14] H. H. Matevosyan, A. Kotzinian and A. W. Thomas, *Studies of Azimuthal Modulations in Two Hadron Fragmentation of a Transversely Polarised Quark*, Phys.Lett. **B731**, 208–216 (2014), arXiv:hep-ph/1312.4556.

[MM10] G. K. Mallot and A. Magnon, COMPASS-II Proposal, Technical Report CERN-SPSC-2010-014. SPSC-P-340, CERN, Geneva, May 2010.

[MPS$^+$09] A. Martin, G. Pesaro, P. Schiavon, F. Sozzi and H. Wollny, *On the role of the acceptance in the Unbinned Maximum Likelihood Method*, COMPASS note **13** (2009).

[MR01] P. Mulders and J. Rodrigues, *Transverse momentum dependence in gluon distribution and fragmentation functions*, Phys.Rev. **D63**, 094021 (2001), arXiv:hep-ph/0009343.

[MS98] B.-Q. Ma and I. Schmidt, *Quark orbital angular momentum in a light-cone representation*, Phys. Rev. D **58**, 096008 (1998).

[MSS98] B.-Q. Ma, I. Schmidt and J. Soffer, *The Quark spin distributions of the nucleon*, Phys.Lett. **B441**, 461–467 (1998), arXiv:hep-ph/9710247.

[MSSY01] B.-Q. Ma, I. Schmidt, J. Soffer and J.-J. Yang, *Helicity and transversity distributions of the nucleon and Λ hyperon from Λ fragmentation*, Phys. Rev. D **64**, 014017 (2001).

[MSTW09] A. Martin, W. Stirling, R. Thorne and G. Watt, *Parton distributions for the LHC*, Eur.Phys.J. **C63**, 189–285 (2009), arXiv:hep-ph/0901.0002.

[MSY01] B.-Q. Ma, I. Schmidt and J.-J. Yang, *Nucleon transversity distribution from azimuthal spin asymmetry in pion electroproduction*, Phys. Rev. D **63**, 037501 (2001).

[MT96a] P. J. Mulders and R. D. Tangerman, *The complete tree-level result up to order 1/Q for polarized*

deep-inelastic leptoproduction, Nuclear Physics B **461**(1–2), 197 – 237 (1996).

[MT96b] P. Mulders and R. Tangerman, *The Complete tree level result up to order 1/Q for polarized deep inelastic leptoproduction*, Nucl.Phys. **B461**, 197–237 (1996), arXiv:hep-ph/9510301.

[Muon81] O. Allkofer et al. (European Muon Collaboration), *A large magnetic spectrometer system for high-energy muon physics*, Nuclear Instruments and Methods **179**(3), 445 – 466 (1981).

[Nae02] J. N. Naehle, *Faserhodoskope im COMPASS-Experiment zum Nachweis von Teilchenspuren innerhalb des Primaerstrahls*, PhD thesis, Rheinische Friedrich-Wilhelms-University Bonn, Bonn, Germany, 2002.

[NK12] K. Novotny and E.-M. Kabuss, *Performance of the trigger hodoscopes in 2007 and 2010*, COMPASS note **5** (2012).

[NNPDF10] R. D. Ball et al. (NNPDF Collaboration), *Fitting Parton Distribution Data with Multiplicative Normalization Uncertainties*, JHEP **1005**, 075 (2010), arXiv:hep-ph/0912.2276.

[Pan13] D. Panzieri, *DY absorber and DY experimental area lay-out*, Drell-Yan hardware meeting (May 2013).

[Par13] B. Parsamyan, *SIDIS asymmetries in the DY-range*, Drell-Yan analysis meeting (October 2013).

[PAX05] V. Barone et al. (PAX Collaboration), *Antiproton-proton scattering experiments with polarization*, (2005), arXiv:hep-ex/0505054.

[PDG12] J. Beringer et al. (PDG Collaboration), *Review of Particle Physics*, Phys. Rev. D **86**, 010001 (2012).

[Pes10] G. Pesaro, *Measurements at COMPASS of transverse spin effects on identified hadrons on a transversely polarised proton target*, PhD thesis, Universita di Trieste, Trieste, Italy, 2010.

[Pol73] H. D. Politzer, *Reliable Perturbative Results for Strong Interactions?*, Phys. Rev. Lett. **30**, 1346–1349 (1973).

[PRSZ06] B. Povh, K. Rith, C. Scholz and F. Zetsche, *Teilchen und Kerne*, Springer-Verlag, 2006.

[PS95] M. Peskin and D. Schroeder, *An Introduction to Quantum Field Theory*, Advanced book classics, Addison-Wesley Publishing Company, 1995.

[PSH$^+$02] J. Pumplin, D. Stump, J. Huston, H. Lai, P. M. Nadolsky et al., *New generation of parton distributions with uncertainties from global QCD analysis*, JHEP **0207**, 012 (2002), arXiv:hep-ph/0201195.

[Qui13] C. Quintans, *Asymmetry uncertainties and latest predictions*, Drell-Yan analysis meeting (October 2013).

[ROOT13] R. Brun, F. Rademakers et al. (ROOT Collaboration), ROOT web page http://root.cern.ch/, 2013.

[RS79] J. P. Ralston and D. E. Soper, *Production of dimuons from high-energy polarized proton-proton collisions*, Nuclear Physics B **152**(1), 109–124 (1979).

[RvdS04] M. Radici and G. van der Steenhoven, *The new transversity council of Trento*, Cern Courier **44**(8), 51 (2004).

[Sau97] F. Sauli, *GEM: A new concept for electron amplification in gas detectors*, Nuclear Instruments and Methods A **386**(2–3), 531 – 534 (1997).

[Sch09] A. Schmidt, *Radiatorstudien zum DIRC-Detektor am WASA@Cosy Experiment*, Diploma thesis, Friedrich-Alexander-Universität Erlangen-Nürnberg (FAU), Erlangen, Germany, 2009.

[SEF+01] T. Sjostrand, P. Eden, C. Friberg, L. Lonnblad, G. Miu et al., *High-energy physics event generation with PYTHIA 6.1*, Comput.Phys.Commun. **135**, 238–259 (2001), arXiv:hep-ph/0010017.

[Sha70] D. F. Shanno, *Conditioning of quasi-Newton methods for function minimization*, Math. Comp. **124**, 647–656 (1970).

[SHBM08] J. She, Y. Huang, V. Barone and B.-Q. Ma, *Transversity from two pion interference fragmentation*, Phys.Rev. **D77**, 014035 (2008), arXiv:hep-ph/0711.0817.

[Siv90a] D. W. Sivers, *Single Spin Production Asymmetries from the Hard Scattering of Point-Like Constituents*, Physics Review D **41**, 83 (1990).

[Siv90b] D. W. Sivers, *Single Spin Production Asymmetries from the Hard Scattering of Point-Like Constituents*, Phys.Rev. **D41**, 83 (1990).

[SMC99] D. D. Adams et al. (SMC Collaboration), *The polarized double cell target of the SMC*, Nucl. Instr. and Meth. A **437**(1), 23 – 67 (1999).

[Sof95] J. Soffer, *Positivity constraints for spin dependent parton distributions*, Phys.Rev.Lett. **74**, 1292–1294 (1995), arXiv:hep-ph/9409254.

[Soz07] F. Sozzi, *Measurement of transverse spin effects in COMPASS*, PhD thesis, Universita di Trieste, Trieste, Italy, 2007.

[Soz11] F. Sozzi, *Status of two-hadron, Collins and Sivers asymmetries for 2010 with final cuts*, COMPASS analysis meeting talk (July 2011).

[SR09] G. P. Salam and J. Rojo, *A Higher Order Perturbative Parton Evolution Toolkit (HOPPET)*, Comput.Phys.Commun. **180**, 120–156 (2009), arXiv:hep-ph/0804.3755.

[SS97] I. Schmidt and J. Soffer, *Melosh rotation and the nucleon tensor charge*, Phys.Lett. **B407**, 331–334 (1997), arXiv:hep-ph/9703411.

[SSM06] F. Sozzi, P. Schiavon and A. Martin, *A method to extract RICH purity from data*, COMPASS note **12** (2006).

[SY13] P. Sun and F. Yuan, *TMD Evolution: Matching SIDIS to Drell-Yan and W/Z Boson Production*,

Phys.Rev. **D88**, 114012 (2013), arXiv:hep-ph/1308.5003.

[T+01] D. Thers et al., *Micromegas as a large microstrip detector for the COMPASS experiment*, Nuclear Instruments and Methods A **469**(2), 133 – 146 (2001).

[Tak13] S. Takekawa, *Simulations of the vertex detector for the Drell-Yan programn*, COMPASS analysis meeting talk (April 2013).

[Tak14] S. Takekawa, *Beam telescope for DY run*, COMPASS technical board meeting (April 2014).

[Teu03] A. Teufel, *Entwicklung und Bau von Hodoskopen aus szintillierenden Fasern fuer das COMPASS-Experiment*, PhD thesis, Friedrich-Alexander-Universität Erlangen-Nürnberg (FAU), Erlangen, Germany, 2003.

[vdB97] H. van der Bij, *S-LINK, a data link interface specification for the LHC era*, IEEE Trans. Nucl. Sci. **NS-44**, 398 (1997).

[Vos08] A. Vossen, *Transverse Spin Asymmetries at the COMPASS Experiment*, PhD thesis, Albert-Ludwigs-Universität Freiburg, Freiburg, Germany, 2008.

[Wol10] H. Wollny, *Measuring azimuthal asymmetries in semi-inclusive deep-inelastic scattering off transversely polarized protons*, PhD thesis, Albert-Ludwigs-Universität Freiburg, Freiburg, Germany, 2010.

[YS94] T. Ypsilantis and J. Seguinot, *Theory of ring imaging Cherenkov counters*, Nuclear Instruments and Methods A **343**(1), 30 – 51 (1994).

[Zwe64] G. Zweig, *An SU(3) model for strong interaction symmetry and its breaking*, CERN preprints **TH-401,TH-412** (1964).